Summer 8-1-2018

The Feasibility of using Inherent Optical Properties and the Apparent Optical Property Remote Sensing Reflectance to estimate Suspended Particulate Matter, Particularly for use in Airborne Hydrographic Surveys

Sarah Epps
University of Southern Mississippi

The Feasibility of using Inherent Optical Properties and the Apparent Optical Property Remote Sensing Reflectance to estimate Suspended Particulate Matter, Particularly for use in Airborne Hydrographic Surveys

by

Sarah A. Epps

A Dissertation
Submitted to the Graduate School,
the College of Science & Technology
and the School of Ocean Science & Technology
at The University of Southern Mississippi
in Partial Fulfillment of the Requirements
for the Degree of Doctor of Philosophy

Approved by:

Dr. Stephan Howden, Committee Chair
Dr. David Wells
Dr. Steven Lohrenz
Dr. Laodong Guo
Dr. Grady Tuell

Dr. Stephan Howden Committee Chair	Dr. Jerry Wiggert Department Chair	Dr. Karen S. Coats Dean of the Graduate School

August 2018

Published by the Graduate School

ABSTRACT

Airborne hydrographic surveys are routinely used to create and update nautical charts around the world. This research is intended to assist in maximizing the utility of the data products made available from those surveys in accordance with the current survey–once, use–many–times initiatives. Specifically, this project evaluates the feasibility of using the data available airborne hydrographic systems that utilize bathymetric lasers and hyperspectral sensors to estimate the concentration of suspended particulate matter (SPM). SPM is sometimes also called suspended sediment. The ability to chart spatial distributions of SPM utilizing hydrographic survey systems already in operation will assist researchers, managers, and stakeholders of the areas thus surveyed.

Ship-based in situ measurements of multiple IOPs at up to twelve wavelengths were gathered in the northern Gulf of Mexico during five cruises between 2009 and 2010. One hundred sixty-nine IOP based SPM models using all available quality-checked data were developed and evaluated for performance. This large number of algorithms allowed for a comparison of the effectiveness of the IOPs that may be derived from airborne hydrographic surveys with other IOPs that may or may not be so readily available. The results were varied.

The apparent optical property remote sensing reflectance (R_{rs}) is a data product of hyperspectral sensors that are often part of airborne survey systems. A method to predict suspended particulate matter concentration using the wavelength of maximum intensity for R_{rs} is presented. This represents a new way to estimate suspended particulate matter concentration from an airborne platform.

Due to the methods used for gathering the in-situ data, it was necessary to consider the validity of the assumption that consecutive water column profiling events from a ship represent the same sampling environment. Though this research demonstrates that this assumption is false, it does indicate that consecutive profiling events do sample the same water properties in many instances and that with a little care, datasets gathered this way may be used in research efforts similar to this one. Finally, the distribution and selected properties of SPM concentrations in the northern Gulf of Mexico were examined.

ACKNOWLEDGMENTS

This work could not have happened without the assistance, mentorship, and contributions of the following individuals and organizations.

- Dr. Stephan Howden, Advisor, Associate Professor, Ocean Science & Technology, USM
- Dr. David Wells, Committee Member, Professor Emeritus, Ocean Science & Technology, USM
- Dr. Steven Lohrenz, Committee Member, Professor Emeritus, Ocean Science & Technology, USM
- Dr. Grady Tuell, Committee Member, 3D IDEAS, LLC
- Dr. Laodong Gou, Committee Member, Professor, Freshwater Science, University of Wisconsin-Milwaukee
- Ken Barbor, Director of the Hydrographic Science Research Center
- Linda Downs & Diana Lovejoy
- Kevin Martin
- Faculty, staff, and students of USM, School of Ocean Science & Technology, Division of Marine Science
- CZMIL (Coastal Zone Mapping and Imaging Lidar)
- NSF (National Science Foundation)
- SBA, MIST, (U.S. Small Business Administration, Marine Industry Science & Technology cluster)
- MTS, (Marine Technology Society)
- Tenix LADS

DEDICATION

With special appreciation and gratitude to my Heavenly Father and Savior Jesus Christ

who "has made the sea [my] path…"

(2 Nephi 10:20, Book of Mormon: Another Testament of Jesus Christ).

And for my beloved *Family*

TABLE OF CONTENTS

LIST OF TABLES

LIST OF ILLUSTRATIONS

LIST OF ABBREVIATIONS

a	Absorption coefficient (m^{-1})
AC9	Absorption and attenuation sensor by WET Labs, Inc. (9 wavelengths)
ACS	Absorption and attenuation sensor by WET Labs, Inc. (85 wavelengths)
ASD	Hand-held radiometer by Applied Spectral Devices
b	Total scatter
b_b	Total backscatter
b_{bp}	Particulate backscatter
b_t	Total scatter (also b)
BB9	Backscatter sensor by WET Labs, Inc.
c	Attenuation coefficient (m^{-1})
CASI	Compact Airborne Spectrographic Imager
CDOM	Color dissolved organic matter
Chl a	Chlorophyll a
cm	Centimeter
CTD	Conductivity, temperature, and depth sensor
CTD-T	CTD profiler induced turbidity (encountered in situations where the profiler's proximity to the seafloor caused resuspension of particulates)
CZMIL	Coastal Zone Mapping and Imaging Lidar
DC	Dark Current

DN	Digital Number
E_d	Downwelling irradiance
FlC	Fluorescing chlorophyll
FOV	Field of view
GC1	GulfCarbon research cruise: #1: January 8 – 20, 2009
GC2	GulfCarbon research cruise: #2: April 19 – May 1, 2009
GC3	GulfCarbon research cruise: #3: July 18 - 30, 2009
GC4	GulfCarbon research cruise: #4: October 28 – November 9, 2009
GC5	GulfCarbon research cruise: #5: March 10 – 22, 2010
GF/F	Glass fiber filter
IOP	Inherent optical property
IT	Integration time
JALBTCX	Joint Airborne Bathymetric Lidar Center of Expertise
k_d	Diffuse Attenuation
k_{sys}	Attenuation coefficient associated with a specific lidar system
l	Liter
L	Optical path length
LISST	Laser In-Situ Scattering and Transmissometry sensor by Sequoia Scientific
L_w	Water leaving radiance

m	Meter
mg	Milligram
MAD	Median absolute deviation
N	Buoyancy frequency
nm	Nanometer
ns	Nanosecond
NIR	Near Infrared
NSR	Noise to signal ratio
PC	Particulate carbon
PCA	Principle component analysis
POC	Particulate organic carbon
PN	Particulate nitrogen
PSD	Particle size distribution
PSU	Practical salinity unit
QAA	Quasi-analytical algorithm
R_{rs}	Remote sensing reflectance (sr^{-1})
REA	Rapid environmental assessment
R/V	Research vessel
S	Salinity
SBE49	CTD sensor (model SBE49)
SPM	Suspended particulate matter (mg/l)
sr	Steradian
STD	Standard deviation

T	Transmission
TPU	Total propagated uncertainty
TSM	Total suspended matter (µl/L)
USGS	United States Geological Survey
USM	The University of Southern Mississippi
UWS	Underway sample
µl	Microliter
µm	Micron or micrometer
X_{IOP}	The value an IOP (or IOP combination) would need to have in order to predict a specified SPM concentration

CHAPTER I - INTRODUCTION

Overview

The propose of this dissertation research is to maximize the benefits from employing airborne laser systems, hyperspectral imagers, and other sensors routinely used in hydrographic surveys. Hydrographic surveys produce critical data sets needed to create nautical charts. Since the seafloor and coastlines experience frequent changes, regular surveys are performed. The specific research interests for this dissertation are in using the data from airborne hydrographic surveys to estimate concentrations of suspended particulate matter (or SPM) in the nearshore environment.

There are a lot of reasons to find particles in coastal waters. First, sediment and other small particles may be carried into the marine environment on a river plume. Second, colonies of plant and animal life often develop and form blooms. Third, particles on the seafloor may be resuspended into the water by currents or waves. Fourth, where present, sewage outfall pipes emit effluvia into nearshore waters. And fifth, storm drainage injects land-based surface runoff into the coastal environment. Regardless of the sources or types of suspended particulate matter, the presence or absence of SPM plays a role in the quality of the coastal environment. The ability to chart spatial distributions of SPM utilizing hydrographic survey systems already in operation will assist researchers, managers, and stakeholders of the areas thus surveyed.

The terms, “suspended particulate matter” and “suspended sediment” sometimes appear to be used interchangeably in the peer-reviewed literature (J. Lee, Liu, Hung, Lin, & Du, 2016). Different types of research seem to prefer one term over the other. For example, “suspended sediment” often materializes in research on particulates introduced

(or reintroduced) into the water column from seafloor materials (Martín, Puig, Palanques, & Ribó, 2014; Masunaga, Arthur, Fringer, & Yamazaki, 2017) or from terrestrial-fluvial sources (C.-T. A. Chen et al., 2017; Miguel, Castro, & Nehama, 2017; Unverricht et al., 2014; van Maren, Liew, & Hasan, 2014; Vercruysse, Grabowski, & Rickson, 2017). It is also often seen in studies where an apparent optical property based on reflectance is used to estimate suspended matter concentration (Baird et al., 2016; Kumar, Equeenuddin, Mishra, & Acharya, 2016; Umar, Rhoads, & Greenberg, 2018). Model-based research appears to prefer the term suspended sediment to SPM (Gao et al., 2018; Masunaga et al., 2017). Conversely, the term "suspended particulate matter" is frequently used when referring to marine environments (Tiessen, Eleveld, Nauw, Nechad, & Gerkema, 2017), and when the research includes additional biogeochemical implications including metal transport and autotrophic planktonic cycles (Hakspiel-Segura, Martínez-López, Pinedo-González, Verdugo-Díaz, & Acevedo-Acosta, 2016; Hamers, Kamstra, van Gils, Kotte, & van Hattum, 2015; Helali, Zaaboub, Oueslati, Added, & Aleya, 2016; C. Liu et al., 2017).

The presence or absence of suspended particulate matter affects marine organisms by regulating light availability, transport of nutrients and pollutants, even biological materials. It affects anthropogenic activities by in-filling harbors (de-Nijs, Winterwerp, & Pietrzak, 2009) and shipping channels and the fouling of marine instruments. Sources of SPM include fluvial inputs, re-suspension of bottom particulates (Bartholomä, Kubicki, Badewien, & Flemming, 2009) and in situ generation by marine organisms. Each type of SPM constituent will interact differently with the green laser beam (532 nm) of a bathymetric lidar system.

For the purposes of this study, suspended particulate matter is defined as material located in the water column which may be captured on a 0.4 μm filtration membrane. SPM may be composed of many different types of particles. The organic fraction of SPM may consist of living or deceased matter. Mineral particles are also present in the marine environment and become suspended in the water column through aeolian (dust), fluvial or re-suspension processes.

Flocs are aggregates consisting of mineral particles attached to organic membranes. Each one can contain as many as 10^6 component particles (Baugh & Manning, 2007). The formation and disassembly of these aggregates depend upon the availability of constituent materials and the local turbulent flow regime (Bartholomä et al., 2009; Bowers, 2003). It has been demonstrated that floc density and size have an inverse relationship (Bowers, Braithwaite, Nimmo-Smith, & Graham, 2011). The observation of intact flocs becomes problematic due to their fragility, although in situ methods for observing them are improving. Because the flocculation process changes the size distribution of SPM, it is anticipated that IOPs of the observed waters will be affected by their presence or absence. The identification of flocs, as opposed to individual SPM particles, will not be addressed in this project, but these aggregates are expected to be present at some parts of the proposed survey area. The varied sizes and compositions of particles found in natural waters provide a challenge to the quantification of SPM by remote means as light will have unique interactions with individual particles. Characteristics of SPM reported in the literature include a strong correlation between backscatter (b_b) and SPM concentration (D'Sa, Miller, & McKee, 2007). Also, the SPM particle size distribution (PSD) in coastal waters follows a power law, or Jung

distribution (David Doxaran et al., 2008; Twardowski et al., 2001). Finally, near fluvial inputs in the Irish Sea, it has been noted that the mean diameter of surface SPM particles is significantly larger than bottom particles (Krivtsov, Howarth, Jones, Souza, & Jago, 2008). Similar phenomena may be observed in the Northern Gulf of Mexico.

Organic particles appear to have unique spectral signatures according to species (Hunter, Tyler, Présing, Kovács, & Preston, 2008; Jonasz & Fournier, 2007). Lithogenic particles too, appear to have distinct spectral responses (Bowers & Binding, 2006; Jarrard & Vanden-Berg, 2006). Best detection of mineral SPM occurs in the near infrared (700 – 900 nm) color range (Binding, Bowers, & Mitchelson-Jacob, 2005; Bowers, Binding, & Ellis, 2007). IOPs are also highly dependent upon particle composition (refractive index) and size (E. Boss, Stramski, Bergmann, Pegau, & Lewis, 2004). Additionally, similar to the organic matter, the IOPs of the lithogenic fraction of SPM tends to be mineral specific (Bowers & Binding, 2006).

The sensors used in airborne hydrographic surveys record the way specific kinds of light interact with the marine environment. This work involves determining how this light reacts to particles in the water. During this research, the relationship between suspended particulate matter and 167 inherent optical properties was determined. Afterward, an evaluation to gauge the relative value of these SPM predictors was performed.

A way to predict suspended particulate matter concentration using the wavelength of maximum intensity for the apparent optical property remote sensing reflectance is presented. This represents a new way to estimate suspended particulate matter

concentration from an airborne platform. Also, the distribution and selected properties of SPM concentrations in the northern Gulf of Mexico were examined.

Airborne Hydrographic Surveys

Airborne and spaceborne remote sensing instruments can observe large marine areas much faster than in-situ sampling can be performed. To date, most published remote sensing algorithms crafted to estimate suspended particulate matter (SPM) are designed for application to observations from multispectral and hyperspectral instruments. Hyperspectral sensors have been integrated into airborne bathymetric lidar platforms for simultaneous offshore observations (Macon, Wozencraft, Park, & Tuell, 2008; R. Smith, Irish, & Smith, 2000; J. Wozencraft & Millar, 2005). Thus, additional options for estimating SPM by remote sensing methods become possible by extracting properties of natural waters from observations by both sensors.

The primary purpose of this research is to evaluate the feasibility of applying suspended particulate matter (SPM) algorithms for use with potential data products of the Coastal Zone Mapping Imaging Lidar (CZMIL). The system is capable of simultaneous observations of the active (lidar) and passive (hyperspectral) sensors associated with airborne bathymetric lidar surveys. Ideally, this type of research would utilize datasets collected simultaneously from the air and sea. To date, the quantity of quantity of simultaneous air and sea observations performed is too limited to perform a rigorous study of the matter. Fortunately, a lot can be learned about this particular problem from looking at large sets of high-quality data from a ship-based platform. This research evaluated in - situ data from five ship excursions in the northern Gulf of Mexico. During this project, observations of inherent optical properties (IOP), apparent optical properties

(AOP), particulate carbon (PC) and SPM were obtained. Those parameters which may be derived through the use of lidar and hyperspectral data were given special attention. They are also evaluated in relation to other parameters that were obtained in-situ.

The Coastal Zone Mapping and Imaging Lidar (CZMIL) system consists of an airborne topographic and bathymetric lidar co-located with a hyperspectral sensor (Tuell, Barbor, & Wozencraft, 2010; J. M. Wozencraft, 2010). It is used by the stakeholders of the Joint Airborne Bathymetric Lidar Center of Expertise (JALBTCX) for current hydrographic and coastal zone charting projects. The lidar system was produced by Optech International (now Teledyne Optech). The second instrument associated with the lidar system is the CASI - 1500 (Compact Airborne Spectrographic Imager) hyperspectral sensor. When this airborne sensor platform fly's surveys, simultaneous lidar and hyperspectral data are gathered. The CZMIL system is intended to produce multiple data products for coastal researchers and environmental managers. This research is designed to evaluate the potential for suspended particulate matter (SPM) analysis available from these data sets has yet to be fully realized.

There has been a growing interest in combining airborne lidar and hyperspectral data sets to characterize coastal environments (Deronde, Houthys, Henriet, & Van Lancker, 2008; V. I. Feygels et al., 2007; Kopilevich, Feygels, Tuell, & Surkov, 2005; R. Smith et al., 2000). Additionally, developments towards this end have been made through limited studies that have been performed using the fusion of airborne lidar and multi-spectral imagery (Chust, Galparsoro, Borja, Franco, & Uriarte, 2008) to characterize coastal environments.

Considerable effort has been applied to the hypothesis that the IOPs of natural waters may be retrieved from lidar waveforms (Dolina, Dolin, Levin, Rodionov, & Savel'ev, 2007; V. I. Feygels et al., 2007; Zege, Katsev, & Prikhach, 2007). Teledyne Optech has in-house inversion software, called the Rapid Environmental Assessment (REA) and its successor Hydrofusion. Algorithms associated with this software compare simulated lidar waveforms with actual waveforms (Kopilevich et al., 2005). They can also produce vertically integrated values (i.e., a single value that represents the entire water column) for absorption-plus-backscattering ($a + b_b$), which in turn is used to estimate other IOPs (Jing Li, Gao, & Wang, 2010). This value is sometimes referred to as water column attenuation and denoted as $\kappa\lambda$ (Macon et al., 2008) or as the laser system's attenuation coefficient K_{sys} (Minsu Kim, Feygels, Kopilevich, & Park, 2014; Zhao, Zaho, Zhang, & Zhou, 2018).

Hypotheses and Objectives

The hypotheses in this research address necessary considerations related to appropriate sampling (and subsampling) methods for this dissertation. Therefore, this project gives considerable attention to the applicability of using non-concurrent observations of SPM and optical properties in the project area. Since most SPM sampling and optical data collection in this project were gathered from consecutive rather than coincident profiler casts, early consideration of this problem needed to occur. This principle is important not only to this research project but to the application of airborne bathymetric lidar data for the assessment of optical properties in near-shore environments as it is assumed that concurrent coordinated air-based and ship-based operations are rarely cost effective and seldom performed.

Hypothesis 1. Sequential Profiling

Data from sequential casts of the same profiler or of different profilers can be used to represent the same sample space. See Figure 1 for a flowchart of the relationships between sensor outputs and objective fulfillment. (Abbreviations are defined in the front material of this dissertation.)

Objective 1. Similar datasets from each profiler were obtained. These data sets included salinity, attenuation, and chlorophyll-a concentration. More specifically, salinity data sets were obtained at 0.25 m depth increments from SBE49 FastCAT located on the optical profiler and the 911 Plus CTD on the profilers provided by the research vessels. Both sensor types were made by Sea-Bird Electronics. Attenuation data was obtained from the ACS on the optical profiler and the C-Star transmissometer on the profiler belonging to the R/V Cape Hatteras. (No transmissometer data was available from GC4 on the R/V Hugh R. Sharp.) Chlorophyll – a data sets came from an AQUAtracka III by Chelsea Technologies Group Ltd. on the R/V Cape Hatteras, an ECO FL fluorimeter by WET Labs on the Hugh R Sharp, and an ECO FL3 by WET Labs on the optical profiler (Chapter III).

Objective 2. Similar datasets were evaluated relative to each other to detect significant environmental changes between profiler casts. This included determining if profiler induced turbidity occurred near the seafloor for each cast of a sensor bundle. Salinity data sets near the surface (at the 0.75 m – 2 m and 2 m - 4 m depth ranges and at the depths for each SPM sample) were compared to determine if the observed values are within ±1 PSU of each other. Attenuation data sets near the sea floor were evaluated to determine if bottom sediments were resuspended into the water column due to the

proximity the profilers. A similar evaluation on the near-bottom data using chlorophyll – a and fluorescence data sets was performed since a comparison of attenuation data between the profilers was not possible for GC4 (Chapter III).

Objective 3. Dataset quality for SPM algorithm development was improved by eliminating all points associated with specific locations and depths of interest that demonstrated significant change between profiler casts represented by the salinity datasets. This was accomplished using the evaluations performed in Hypothesis 1, Objective 2. Near-surface data points in the 0.75 m – 2 m and 2 m – 4 m depth ranges were eliminated from any future analysis involving data from both profilers. Also, locations of SPM samples where the paired salinity values from each profiler exceed the ±1 PSU acceptance limit were eliminated. Locations where there appeared to have been seafloor disturbance by a profiler were also removed from further analysis (Chapter III).

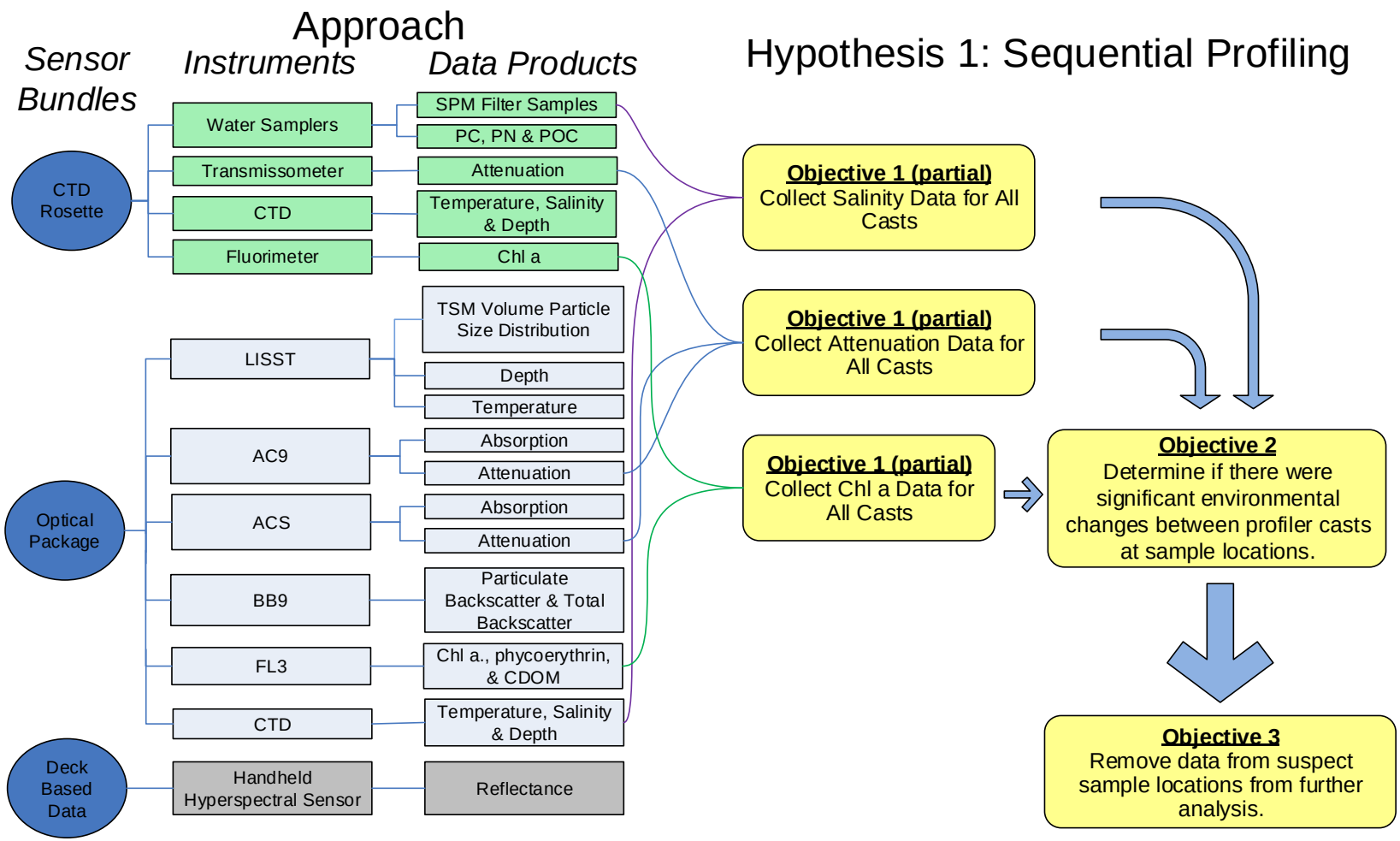

Figure 1. Hypothesis 1 Flow Chart

The underlying premise behind the motivation for this whole project is the idea that SPM concentration prediction can be obtained using CZMIL data. This assumes that optical properties can be used as reliable SPM predictors. A large part of this research addresses that subject.

Hypothesis 2: SPM Algorithm Development from Inherent Optical Properties

All IOPs are equivalent SPM concentration predictors (Chapters IV and V). See Figure 2 for a flowchart of the relationships between sensor outputs and objective fulfillment. (Abbreviations are defined in the front material of this dissertation.)

Objective 1. Using SPM and inherent optical property data, regression-based linear algorithm coefficients were developed to estimate SPM concentrations for absorption, attenuation, and backscattering which were all primary data products of the sensors. Additional IOPs and IOP combinations were calculated and compared to SPM. The backscattering ratio was defined as $\frac{b_b}{b}$ where b_b is backscattering, and b is total scattering. The total scattering was determined through the simple equation $b = c - a$ (m^{-1}). Both the attenuation (c) and the absorption (a) are available from the AC9 and ACS data sets. The IOP combinations of absorption-plus-backscatter ($a + b_b$) and backscatter-divided-by-absorption-plus-backscatter $b_b/(a + b_b)$ (a fundamental part of the definition of the AOP R_{rs}) along with the backscattering coefficient were determined using data from the BB9 and the AC9 or ACS.

Objective 2: The effectiveness of each linear regression of SPM in relation to an IOP or IOP combination as an SPM predictor was evaluated. The linear regressions between SPM and IOPs (or IOP combinations) are evaluated relative to various measured

concentration ranges. The accuracy of predictions relative to filtered SPM is evaluated within each concentration range and for each regression. Sensor limitations and root mean squared error values are also considered.

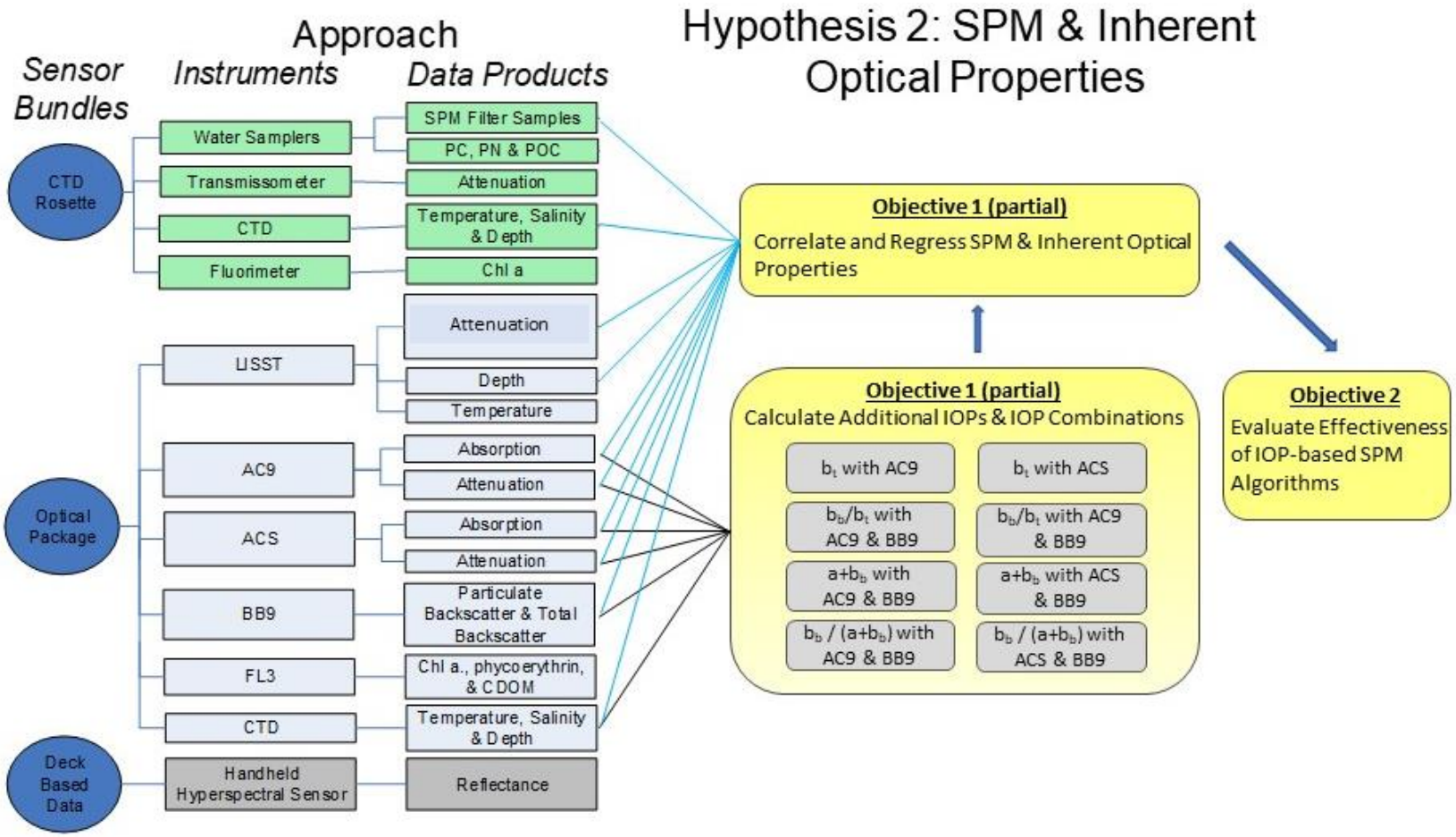

Figure 2. Hypothesis 2 Flow Chart

Hypothesis 3: SPM Algorithm Development from Apparent Optical Property R_{rs}

SPM can be predicted from the apparent optical property R_{rs} (Chapter VI). See Figure 3 for a flowchart of the relationships between sensor outputs and objective fulfillment. (Abbreviations are defined in the front material of this dissertation.)

Objective 1. In situ SPM concentration was compared with apparent optical property remote sensing reflectance data from above deck sensors. Correlation parameters between R_{rs} and SPM were calculated. Remote sensing reflectance was calculated using measurements from an Applied Spectral Devices hand-held spectroradiometer (ASD). Some data from a deck-mounted Satlantic HyperSAS was also made available for this research during GC2. An SPM algorithm was developed using the wavelength of maximum R_{rs} intensity.

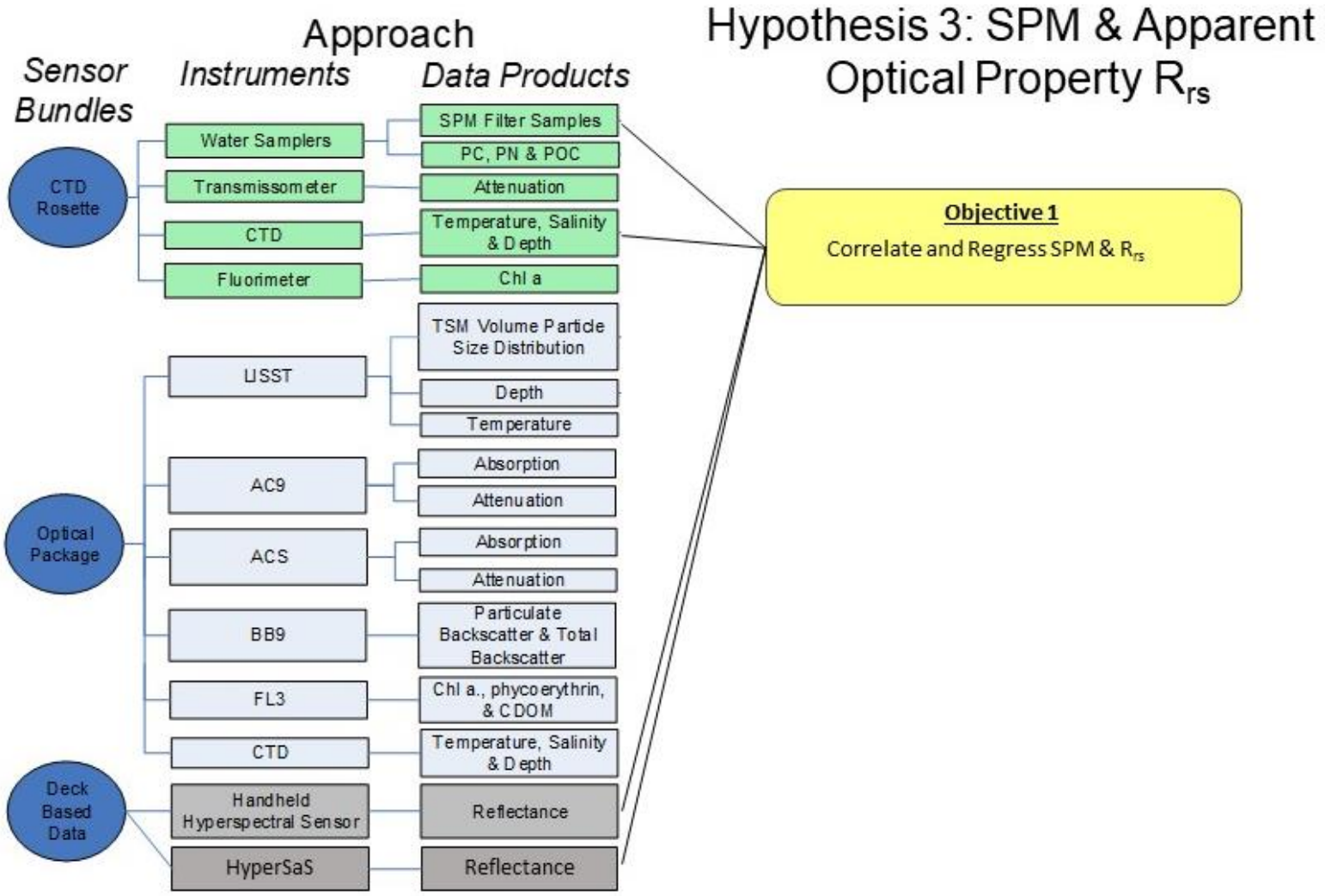

Figure 3. Hypothesis 3 Flowchart

The SPM samples that serve as the baseline dataset can reveal information about the temporal and spatial variation of the project area. The research area of this project includes several water types. Also, the five research cruises were executed over a period of fifteen months. The filter samples and optical sensors utilized in this project allows for the evaluation of SPM properties and distribution.

Hypothesis 4: SPM Distribution and Physical Properties

Regional SPM concentration and composition (lithogenic or organic particle dominated) varied over time (Chapter VII). See Figure 4 for a flowchart of the relationships between sensor outputs and objective fulfillment. (Abbreviations are defined in the front material of this dissertation.)

Objective 1: The aim of this objective was to obtain in-situ SPM samples, both at the surface and at depth. These data sets included total SPM concentration (mg/l), and the particulate carbon content of the material. Using the onboard Seabird SBE32 water sampler systems which were mounted with 10 L (R/V Sharp) or 12 L (R/V Cape Hatteras) Niskin bottles, filter samples for SPM and PC were obtained. These samples were taken for the surface waters of all stations. Additional filter samples were taken at various depths based upon changes observed in the real-time data streams (salinity, temperature, turbidity, florescence, and dissolved oxygen) of the CTD downcast. Where nepheloids were observed in the transmissometer (turbidity) data, filter-samples were also taken. The cost for obtaining and processing PC samples was quite high; therefore, the number of samples in the PC dataset was smaller than the number of samples in the SPM data sets.

SPM samples for this project were filtered through 0.4 µm pore sized polycarbonate hydrophilic membranes. Smaller sets of SPM samples filtered through different pore sized membranes were also taken for comparison. At a few locations, quasi-replicate SPM samples were filtered through 0.2 µm polycarbonate membranes and glass fiber filters (which have an approximate pore size of 0.7 µm). These were compared with samples simultaneously filtered through 0.4 µm filters. Particulate carbon (PC) samples were filtered through 0.45 µm pore sized silver membranes. The quantities of PC on these samples are determined using USM's elemental combustion system (Costech Instruments).

Objective 2: Obtain total particle volume (ml/l) and mean particle size at the same locations as the filtered samples using the Laser In-Situ Scattering and Transmissometry (LISST) sensor and calculate the correlation between these parameters and the SPM concentration. A Sequoia Scientific LISST-100 B was mounted to the optical profiling package and deployed at each station visited. Laser diffraction was used to observe forward scattering at multiple small angles from a 670 nm wavelength collimated beam. These parameters were correlated to the filter SPM samples taken from the same depth.

Objective 3: Using data obtained in Objectives 1 and 2 the distributions of SPM physical properties were evaluated.

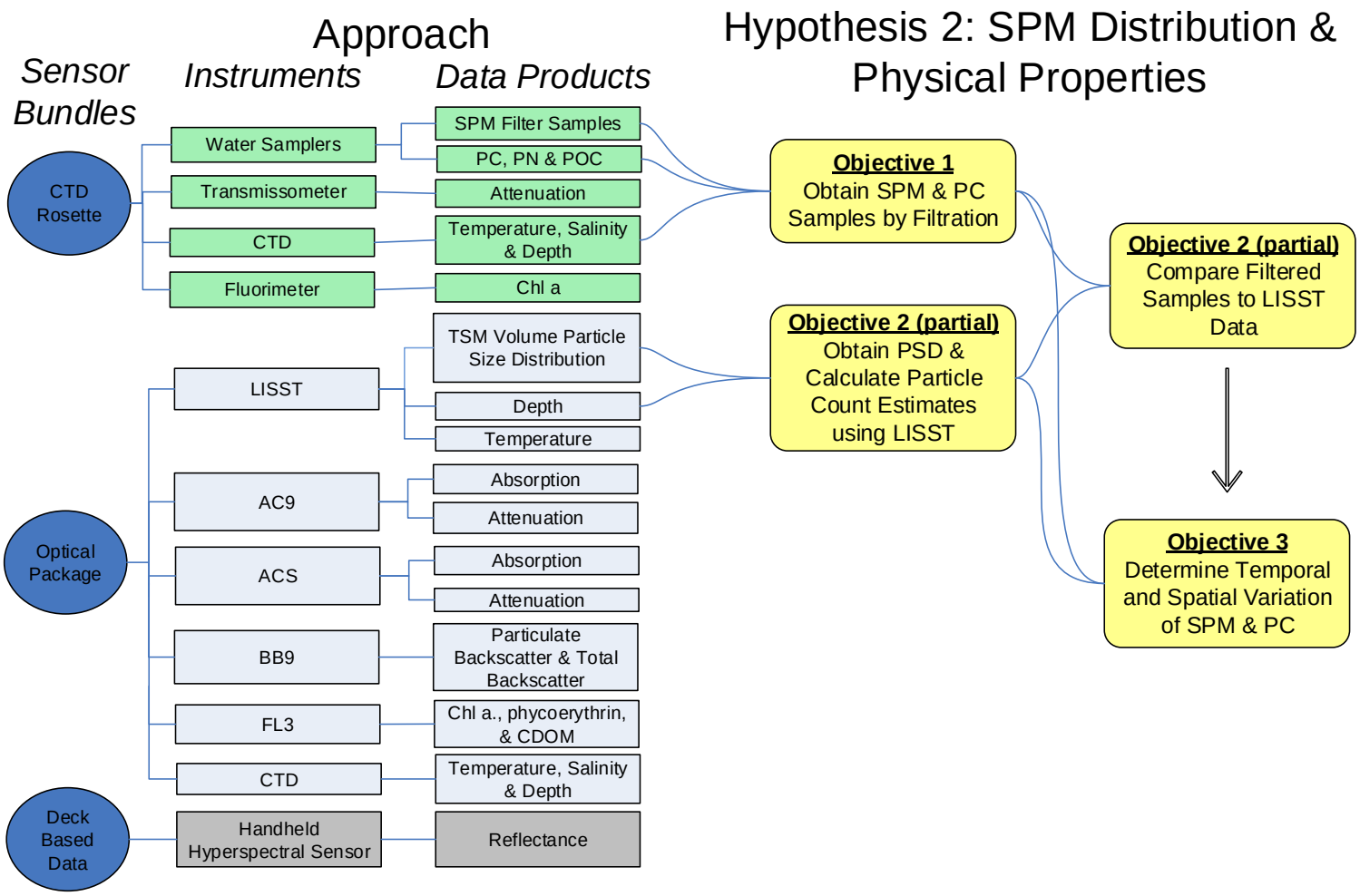

Figure 4. Hypothesis 4 Flowchart

Research Site

In situ IOP and SPM measurements were observed as part of a project funded by the National Science Foundation (Lohrenz & Gundersen, 2008). The survey area extended along the Northern Gulf of Mexico coastal margin from Mobile Bay, Alabama to the Sabine River in Texas and offshore to beyond the 1000 m isobath (Figure 5). This area included turbid coastal waters, as well as oligotrophic marine waters. Though it was presumed that a large percentage of the project area was too deep to be considered appropriate for lidar bathymetric surveys, the objectives of this project were still achievable.

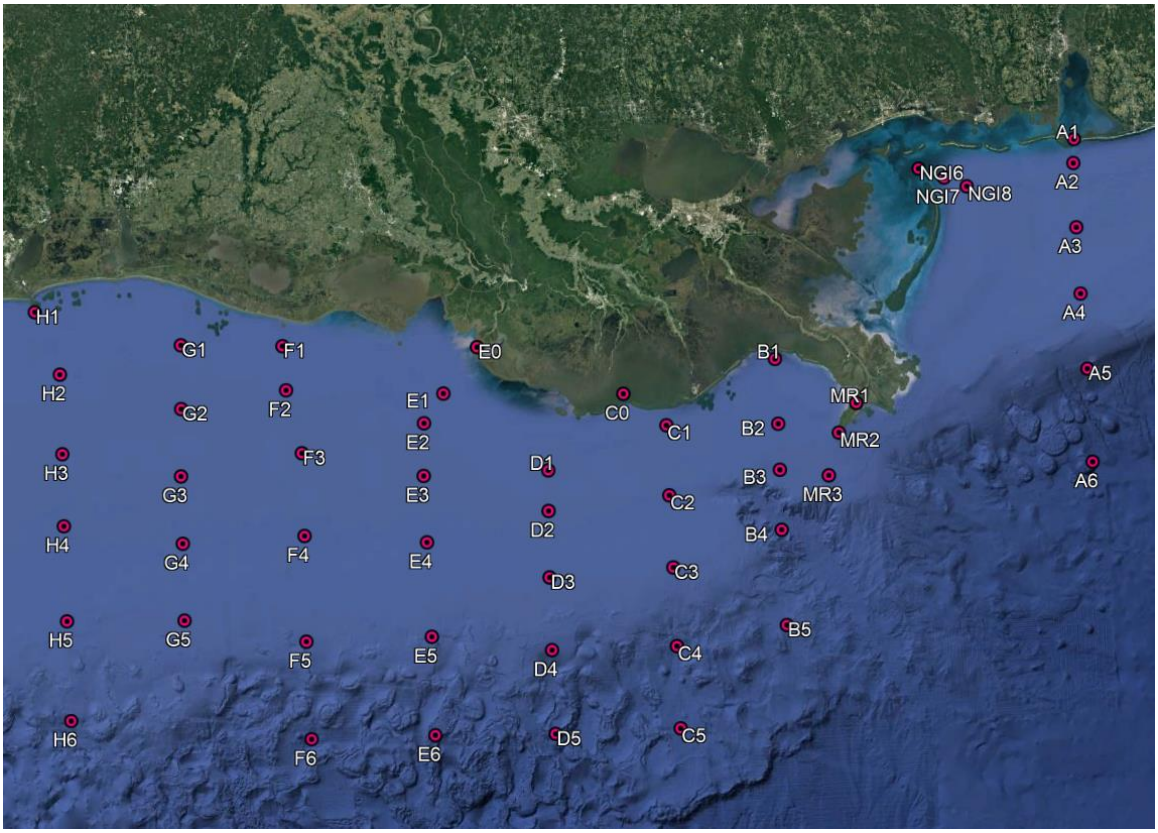

Figure 5. Project Area

The project area is based on (Lohrenz & Gundersen, 2008). The figure was produced using Google Earth.

Forty-nine stations were visited on each of five research cruises (Figure 5). These excursions took place in January, April, July and November 2009 and March 2010. Three additional stations (NGI_6, NGI_7, and NGI_8) were sampled during cruises when time and weather conditions permitted. This study site overlapped other project areas where SPM was previously examined in this region. The entire area studied by D'Sa et al. (D'Sa et al., 2007) is encompassed within the current study region. Additionally, the north-south "A" transect and the "NGI" stations overlap the particulate organic carbon (POC) study area evaluated by Son et al. (Son, Gardner, Mishonov, & Richardson, 2009). For this research, surface water samples were collected at all stations. Stations located where there was enough water under the keel for profiling also had water samples collected at various depths dependent upon on-site assessment of the CTD down-cast data. Figures 1 thru 4, summarize the data types observed and how they related to achieving the objectives of this study.

Uncertainty

It is essential to have a basic understanding of the sources and magnitude of uncertainty in hydrographic projects. International Hydrographic Organization standards for expressing uncertainty is through the use of confidence intervals for depth based products (International_Hydrographic_Organization, 2008). Marine scientists usually express uncertainty through other statistical methods such as standard deviations, median absolute deviations, and root mean squared errors. In this project, most uncertainty estimates are reported using the marine science approach, through confidence intervals are plotted in many figures displaying remote sensing reflectance spectra (Chapter VI).

Uncertainty in this project may be considered in two broad categories: the uncertainty of observational method, and the uncertainty of the environment. Sources of observational uncertainty in this project include horizontal and vertical positioning of in situ observations. For this research, it was important to be cognizant that understanding the relative positions of the nearly simultaneous observations was far more important than knowing the uncertainty involved with accurate cartographic positioning as defined by the International Hydrographic Organization (International_Hydrographic_Organization, 2008).

As with most hydrographic survey projects, the uncertainty associated with vertical positioning of the profilers in motion was difficult to constrain. Depth/pressure sensors were incorporated into several sensors on each of the profiling packages (Figures 1 thru 4). Care was taken to understand the offset relationships between each depth sensor referenced to within the profiling packages. Determining the correlation between the depth sensors of the CTD package and the optics package was simple in theory, but difficult to implement. Ideally, the CTD sensor from the optics package would have been mounted to the CTD profiling package while it was being cast, then transferred back to the optics package for its cast at every station of interest. This procedure would have increased the time the research vessel spent on each station and was therefore not employed. Therefore, it was assumed that the SeaBird CTD sensors on each profiler performed to the manufacturer's specifications (Table 1).

Careful filtering protocols needed to be used in all cases for the collection of water subsamples from the Niskin bottles located on the CTD rosette. The entire bottle

was drained from the bottom (not the spigot) into a clean carboy and agitated before any subsampling occurred at each observation point. This procedure was necessary because settling occurs between the time the bottle captures the sample and the time the profiler returns to the deck. In past research, during the time of carousel recovery, 26% of particles as small as 4 µm in diameter settled below the spigot and thereby became unavailable for subsampling through that means (Gundersen, Orcutt, Purdie, Michaels, & Knap, 2001). Also, in order to establish observational repeatability estimates, replicates of filter samples were taken. The uncertainty associated with the volume of water put through the filters were ascertained in the lab through the calibration of each of the feeder-bottles used for subsampling in the field. Corresponding statistics were generated using the bootstrap resampling method (Zoubir & Iskander, 1998).

Instrument drift of the ship mounted, handheld, profiling, and laboratory sensors was minimized by calibration methods appropriate to each device. Finally, the use of a LISST involved the employment of Mie scattering theory. By using this instrument, two assumptions about SPM in natural waters were made. The first assumption was that the particles were homogenous, therefore having a constant refractive index throughout. The second assumption was that all particles sensed by the LISST were spherical. It is well understood that both assumptions are erroneous and therefore the resultant particle size data need to be considered estimates of equivalent spherical diameters.

Environmental Uncertainty

Uncertainties resulting from dynamic environmental parameters were also expected to have been encountered during this survey. Two examples are mentioned here.

First, the study area encompassed many sites of past and present petroleum production. Oil may be found in the form of surface slicks, film encasing bubbles, or as suspended droplets with a maximum diameter <1 m^{-1} (Stramski, Boss, Bogucki, & Voss, 2004). Any of these forms of oil in the water can create a significant contribution to backscattering (Stramski et al., 2004). Second, bubbles entrained due to wind gusts of 10 m/s can more than double remote sensing reflectance values (Stramski et al., 2004). Environmental uncertainty was addressed by taking multiple samples of the same environment where possible.

CHAPTER II – METHODS: SENSORS, FILTRATION AND PROFILER CONFIGURATION

Introduction

The data sets for this research may be divided into three general categories based upon method of sample collection; first, data obtained through filtration samples, second, observations obtained through water column profiling sensors and finally, above water remote sensing reflectance (R_{rs}) measurements. Data derived from the filtration of sample water are often referred to in this research as "filter samples." From this type of sampling, the sea-truths of SPM and particulate carbon are determined. The optical sensors on the profiling packages represent active optical measurements (where a light source is included in the sensor) whereas the deck-based R_{rs} measurements are passive optical observations (where the light source is natural solar radiation).

An evaluation of data collection methods based upon profiler configuration was performed in this project to determine the compatibility of observations made by the filtration of water samples and the digital outputs of the various sensors used in this work. This evaluation also characterized uncertainty involved in working with datasets obtained using multiple profilers. These procedures facilitated decisions made to trim the data sets used for SPM algorithm development in order to minimize uncertainty produced by using data sets from two profilers deployed sequentially. Since two research vessels were utilized during the course of this project (the R/V Cape Hatteras for cruises GC1, GC2, GC3 and GC5, and the R/V Hugh R Sharp for cruise GC4), the specifications for instrument deployment orientation of each vessel are also detailed in this chapter.

Filtration Method

Profiling sampler systems provided by the research vessels collected the water processed by filtration methods. Similar methods were used to obtain the observational values used for concentration calculations for both SPM and particulate carbon (PC). Since these data sets were derived using filtration methods, these observations are frequently referred to as "filter samples" during this project. A Seabird SBE32 water sampler system was deployed by the R/V Cape Hatteras (cruises GC1-3, GC5) with twelve-liter capacity Niskin bottles mounted to the carousel. During GC1, twelve of these bottles were available for sample collection. The remainder of the R/V Cape Hatteras cruises (GC2, GC3, and GC5) had twenty-three bottles deployed with each cast. The R/V Hugh R Sharp (GC4) employed a General Oceanic Model 1015 water sampler rosette with twelve 10 L sample bottles attached.

At each station, the water sampler system, co-mounted with a CTD, turbidity meter, fluorometer, and dissolved oxygen sensor was lowered to within a few meters of the seafloor. Live data streams from the sensors assisted researchers in deciding at which depths to obtain water samples. Once the water sampler system returned to the deck, the entire contents of selected sampler bottles were drained into carboys which had been rinsed with deionized, MilliQ, or NanoPure water. This was done to capture the particles that may have settled below the level of the spigot prior to drainage thus avoiding concentration biases in the water samples (Wilford D. Gardner, 1977) and similar to methods used by other researchers (McPhee-Shaw, Sternberg, Mullenbach, & Ogston, 2004). For SPM evaluation, subsamples were withdrawn from these carboys and vacuum filtered through pre-tared nucleopore 0.4 µm pore sized filters. For comparison,

nucleopore 0.2 µm pore sized filters were used on replicate SPM samples during GC2 and GC5. Glass GF/F filters were also used for SPM replicate samples during GC5. The PC samples were filtered through 0.45 µm pore sized silver filters. (See Chapter VII for the effects of different pore sizes of the filters on SPM concentration.) In order to ensure homogeneity of the bulk water samples, the carboys containing bulk water samples were agitated before subsamples were withdrawn. Once the SPM and PC samples were filtered, they were stored in either a desiccator or a freezer until returned to the lab at The University of Southern Mississippi, Department of Marine Science.

Additional surface samples of SPM and PC were taken while the ships were in motion. In this document, they are referred to as "under-way" samples. The under-way samples were acquired through the ships' flow-through systems. Through these systems, seawater was continuously taken into the ship near the bow and circulated to accommodate various ships' functions. Most the water was expelled near the stern. Under-way samples were collected from interrupt valves located near the onboard labs. The under-way sample locations were noted from the ship's navigational system. Though the depths of the intake valves for the flow-through systems on the research vessels used on this project were unknown, it was considered reasonable to assume that the actual depths of the water for the under-way samples fell within the range of the surface water samples extracted using the sample bottles.

Following each of the cruises, the SPM and PC samples were oven dried at approximately 60 C. The SPM samples were then weighed at least three times. These repeated mass observations were spread out over several days in an attempt to mitigate environmental factors in the lab that could cause variations in these delicate weight

measurements. Examples of environmental influences on dry weights include vibrations from nearby equipment in the lab (including the building's air circulation system). When weighing events took place on extremely humid days, some of the samples (particularly those with a large percentage of lithogenic materials) would not come to equilibrium on the balance. It was believed that during these occasions, electronegative clay particles actively adsorbed water molecules from the air. Between weighing events, the samples were stored in a desiccator. If necessary, the SPM samples were re-dried in the oven and weighed additional times until the standard deviation of these observations came to within 0.00005g (the approximate uncertainty of the balances used in this study). When more than three weighing events were needed to achieve this low standard deviation, only the final three observations were used in a rolling mean to determine the bulk weight of the samples. Concentrations were then evaluated.

The PC samples were collected from the same water sample bottles as the SPM samples. They were filtered through 0.45 μm pore sized silver filters. As with the SPM samples, these filters were immediately either desiccated or frozen until returned to the lab where they were dried for at least a day at about 60 C. The PC samples were then subjected to a Costech elemental combustion system which yielded the total carbon content of each sample. Concentrations of PC were then calculated.

Vertical Profiling

Two water column profiling systems were employed at each site throughout this project. The first profiling system used in this research was the USM optical package (Figure 6). The sensors on this profiler used in this research are detailed in Figure 6, and Table 1. The second profiler consists of the onboard water sampling profilers with co-

located digital sensors supplied by the research vessels. Data from the CTDs and transmissometers from the water sampler profilers are used in this research. Table 1 also provides details about these sensors. Brief descriptions of these sensors follow the table.

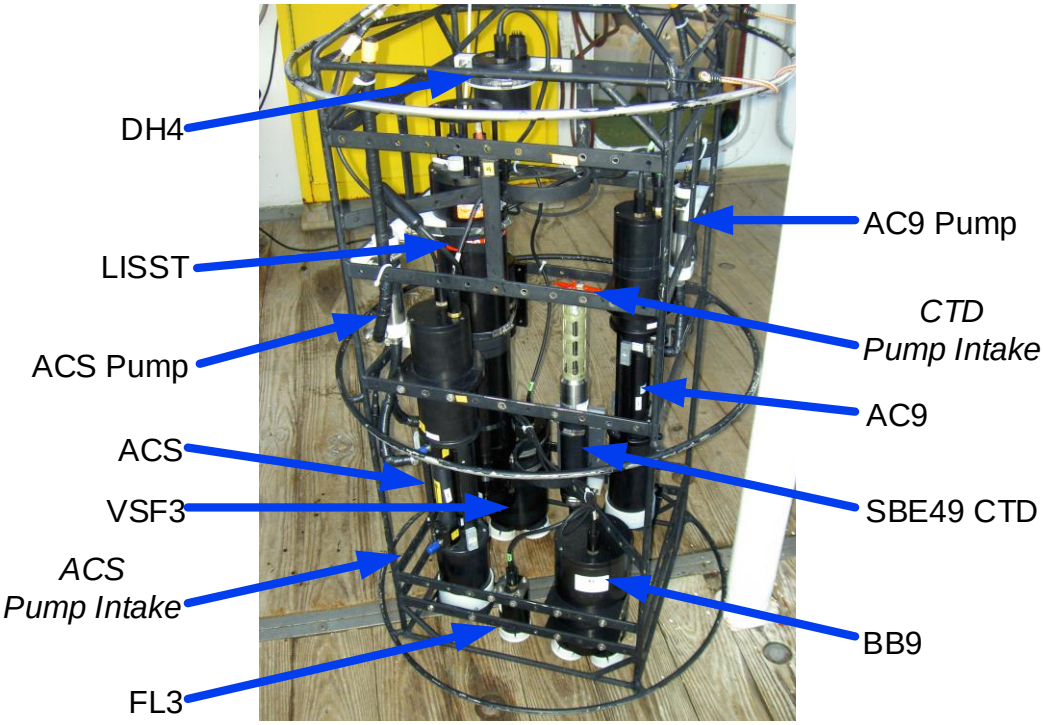

Figure 6. USM Optical Profiler

The USM optical profiler with onboard equipment. The data from the VSF3 were not used in this research.

Table 1

Specifications of Profiling Sensors

Sensor Name (Model)	Company	Final Data Products	Data Units	Data Resolution	Sample Rate Hz	Estimated Uncertainty[a]	Profiler
CTD SBE49 FastCAT 350m rating	Sea-Bird Electronics	Salinity Temperature Depth	none C m	0.4 0.0001 0.007	16	0.00025[b] 0.002 C[b] 0.35 m +.175/yr	Optical
AC9	WET Labs	Absorption[c] Attenuation[c]	m^{-1} m^{-1}	0.01 0.01	6	Precision: 0.003 m^{-1} Precision: 0.003 m^{-1}	Optical
ACS	WET Labs	Absorption[d] Attenuation[d]	m^{-1} m^{-2}	0.01 0.01	4	Precision(450-750nm): 0.001 m^{-1} Precision(400-449nm): 0.005 m^{-1}	Optical
Scattering Meter (ECO BB-9)	WET Labs	Backscatter[e]	m^{-1}	~0.0005	1	Linearity: 0.99 R^2	Optical
Particle Size Analyzer LISST	Sequoa Scientific, Inc.	Particle Size Distribution Attenuation	µl/l m^{-1}	<0.38	1	Not Published	Optical
Eco 3 Measurement Sensor (FL3)	WET Labs	Chlorophyll-a Phycoerythrin-Phycocyanin CDOM	µg/l ppb ppb	0.02 0.04-0.15 0.18	to 8	Linearity: 0.99 R^2	Optical

Table 1 (continued).

Sensor Name (Model)	Company	Final Data Products	Data Units	Data Resolution	Sample Rate Hz	Estimated Uncertainty[a]	Profiler
C-Star Transmissometer	WET Labs	Attenuation[f]	m^{-1}	~0.0002	to 8	Linearity: 0.99 R^2	Sampler R/V Cape Hatteras
AQUAtracka III	Chelsea Technologies Group Ltd.	Chlorophyll-a	µg/l	0.01 µg/l	Not Reported	±0.02 µg/l or 3%	Sampler R/V Cape Hatteras
CTD (911 Plus)[g]	Sea-Bird Electronics	Salinity Temperature Depth	none C m	~0.4 0.0002 0.0068	24	~0.00025[h] 0.00124[i] C 1.36[j] m	Sampler R/V Cape Hatteras
ECO FL Fluorimeter	WET Labs	Chlorophyll-a	µg/l	0.02 µg/l	to 8	Linearity: 0.99 R^2	Sampler R/V Hugh R Sharp
CTD (911 Plus)[j]	Sea-Bird Electronics	Salinity Temperature Depth	none C m	~0.4 0.0002 0.0068	24	~0.00025[h] 0.00124[i] C 1.36[j] m	Sampler R/V Hugh R Sharp

Notes. [a] Unless otherwise specified, the estimated uncertainty is based on published specifications and sensor calibration schedule. [b]Value based on spec sheet and factory calibrations performed on 8/29/08 and 1/26/2011. [c] Wavelengths (nm): 412, 440, 488, 510, 532, 555, 650, 676, 715 [d]85 wavelengths (400-745 nm) [e] Wavelengths (nm): 400, 440, 488, 510, 532, 595, 660, 676, 715. [f] Wavelength 660 nm ±10 nm. [g]The model of the Sea-Bird CTD is not published, but photographs indicate that the model is the CTD 911plus. [h]The published CTD specifications give the same sensor stability value for conductivity. [i]Since the calibration value for this sensor is not available to the public, the calibration

value for USM's CTD is reported. [j]The model is assumed. (Chelsea_Technologies_Group_Ltd; Sea-Bird Electronics, 2011a, 2011b; WET_Labs, 2006, 2008a, 2008b, 2009, 2010a, 2010b, 2010c; WET_Labs_Inc., 2011)

DH4 (WET_Labs, 2010c)

The WET Labs Inc. data handler (DH4) (WET_Labs, 2010c), though not a sensor, was an integral part of optical profiler operations. It received the real-time data feeds from all the sensors on the optical profiler with the exception of the LISST. Through it, all observations of the connected sensors received the same time and depth tags. Later, all data managed by the DH4 was binned to the nearest quarter meter thus coordinating the multi-sensor observations.

CTD (Sea-Bird Electronics, 2010, 2011b)

Conductivity, temperature and depth sensors (CTDs) produced by Sea-Bird Electronics were deployed on the optical profiler and on the ships' water sampler profilers. Depth was calculated from observations of a pressure sensor; temperature was recorded by onboard thermistors and salinity was calculated using conductivity measurements (Sea-Bird Electronics, 2010). The SBE49 located on the optical profiler provided depth information for all of the profilers' sensors except for the LISST which had its' own pressure sensor (Sequoia_Scientific).

The SBE49 calibrations took place prior to this project. Lab and in-cruise adjustments were neither taken deemed necessary as the CTD sensors have an excellent reputation for stability in the field. The other CTDs were maintained by the ships' technical personnel.

BB9 (WET_Labs, 2008b)

An ECO-BB9 sensor by WET Labs Inc. produced particulate backscatter (b_{bp}) and total backscatter (b_{bt}) coefficients at 400, 440, 488, 510, 532, 595, 660, 676, and 715 nm wavelengths. Light sources at these wavelengths were provided by calibrated light

emitting diodes. Scattered light was collected by detectors positioned at 117^O from the boresight direction of light propagation (WET_Labs, 2008b). Particulate backscatter was calculated using the following relationship reported in (Emmanuel Boss & Pegau, 2001; WET_Labs, 2008b).

$$b_{bp} = 2\pi * 1.1 * \beta_p(117^O) \quad (2.1)$$

Here, the volume scattering of particles (β_p) (equation 2.2) at the observation angle of 117^O was calculated (WET_Labs, 2008b) where $\beta_w(117^O, \lambda)$ was estimated using equation 2.3:

$$\beta_p(117^O, \lambda) = \beta(117^O, \lambda) - \beta_w(117^O, \lambda) \quad (2.2)$$

β represented the total volume scattering of the sample space. The volume scattering of water (β_w) at 117^O included salinity (S) and came from (A. Morel, 1974; WET_Labs, 2008b):

$$\beta_w(117^O, \lambda) = 1.38\left(\frac{\lambda}{500nm}\right)^{-4.32}\left(1 + \frac{0.3S}{37}\right)10^{-4}\left(1 + \frac{cos^2 117^O(0.91)}{(1.09)}\right)m^{-1}sr^{-1} \quad (2.3)$$

The total backscattering coefficient (b_{bt}) was calculated at each of these nine wavelengths (λ) and consisted of backscatter contributions from particulates (b_{bp}) (already reported) and from known backscattering values of natural water (b_{bw}).

$$b_{bt}(\lambda) = b_{bp}(\lambda) + b_{bw}(\lambda) \quad (2.4)$$

During the initial processing of the GulfCarbon optical data, backscattering caused by natural water was determined from the observational values using the following equations for brackish water (equation 2.5) published by WET Labs (WET_Labs, 2008b), (b_{bpw}, salinity was <35) and for seawater (equation 2.6) (WET_Labs, 2008b), (WET_Labs, 2008b) (b_{bsw}, salinity was >35) respectively with units of 10^{-4} m^{-1}:

$$b_{bpw}(\lambda) = \frac{0.0022533\left(\frac{\lambda}{500nm}\right)^{-4.23}}{2} \quad (2.5)$$

$$b_{bsw}(\lambda) = \frac{0.0029308\left(\frac{\lambda}{500nm}\right)^{-4.24}}{2} \quad (2.6)$$

Manufacturers' calibrations were performed in the fall of 2008 and 2009. Dark counts were collected as part of each calibration process through the use of electrical tape being placed over each sensor.

AC9 (WET_Labs, 2008a) and ACS (WET_Labs, 2009)

The AC9 and ACS sensors were both WET Labs Inc. products designed to measure the absorption (a) and attenuation (c) coefficients of natural waters. The AC9 operated using 412, 440, 488, 510, 532, 555, 650, 676, and 715 nm wavelengths. The ACS reported spectral absorption and attenuation. ACS absorption was reported in 85 wavelengths ranging from 403.9 nm to 744.8 nm. Similarly, ACS attenuation was reported in 85 wavelengths ranging from 401.2 nm to 743.5 nm (Table 2). Unlike the AC9, the ACS absorption and attenuation output wavelengths did not precisely match. However, the ACS had 4 nm resolution. Therefore a precise wavelength match between the absorption and attenuation coefficients may not have been important in this case. The AC9 did not have a published wavelength resolution, but it utilized a 10 nm band-pass in the signal, whereas the AC9 used a 15 nm bandpass indicating that the AC9 wavelengths resolution may have been a little finer than 4 nm.

Table 2

Absorption and Attenuation Wavelengths of the ACS

Wavelength nm					
a	c	a	c	a	c
	401.2	532.5	534.1	660.1	660.9
403.9	405.5	537.2	538.5	664.6	665.0
408.0	409.6	541.6	543.0	668.7	669.3
412.1	413.9	546.3	547.6	672.9	673.4
416.2	417.8	550.7	552.4	677.1	677.6
420.6	422.6	555.5	556.9	681.2	681.6
425.4	427.0	560.1	561.5	685.0	685.6
429.9	431.5	564.4	565.6	688.9	689.4
434.1	435.6	568.6	570.0	692.6	693.1
438.2	439.8	572.7	574.1	696.0	696.6
442.8	444.4	576.6	578.0	699.6	700.2
447.4	449.0	581.7	582.0	702.9	703.4
452.2	453.6	586.1	586.1	706.2	706.8
456.6	458.2	590.3	590.3	709.5	710.0
461.1	462.7	594.5	594.7	712.8	713.2
465.7	467.1	598.9	599.1	715.8	716.6
470.6	472.0	603.3	603.6	718.9	719.7
475.4	477.1	608.0	608.3	722.2	722.9
480.4	481.8	612.5	612.9	725.1	725.4
485.2	486.7	616.9	617.4	727.8	728.1
489.7	491.1	621.4	621.9	730.4	731.1
494.4	495.8	625.7	626.2	732.7	733.4
498.9	500.5	630.0	630.4	735.3	735.6
503.6	505.4	634.4	634.7	737.0	738.0
508.5	510.4	638.5	639.2	739.4	739.9
513.5	515.2	642.8	643.3	741.5	741.8
518.5	520.3	647.1	647.6	743.2	743.5
523.0	524.8	651.4	652.1	744.8	
527.9	529.4	655.8	656.3		

Notes. a is absorption. c is attenuation

The initial in-situ absorption and attenuation coefficient values recorded included effects of pure natural water, dissolved matter, and suspended particulates. Data

processing through WET Labs Inc.'s' software removed the effects of pure water absorption using Nano-Pure calibrations. Temperature differences caused by sensor operation were also addressed at that time.

The absorption coefficient (a) for each sensor was measured in a 25 cm flow tube lined with clear quartz which in turn was surrounded by a layer of air allowing the propagation of forward scatter up to 41.7^{O} (WET_Labs, 2008a, 2009) towards the receiver. The length of the flow tube reduced the "lost" effects forward scatter between 47.7^{O} and 90^{O} as well as the backscatter since the length of the tube permitted multiple scattering events between the light source at one end and the detector at the other end of the tube thus reducing the net undetectable scatter.

Thermal adjustments related to the sample waters were made using methods developed by Pegau et al. (Pegau, Gray, & Zaneveld, 1997) which utilized the slopes of temperature versus each observed wavelength of the absorption coefficient used by the AC9s in their study. These adjustments were judged likely to be significant in the red and infrared wavelengths and negligible for the remaining visible and ultraviolet wavelengths. For the AC9 and the ACS in this project, 715 nm was used as the reference wavelength in temperature adjustments.

Beam transmission and attenuation are related by the following equation where c is the attenuation coefficient, L is the optical pathlength, and T is transmission.

$$c = -\frac{1}{L} ln(T) \tag{2.7}$$

Attenuation (c) was measured by a second 25 cm length flow through tube on each AC instrument. These tubes were lined with a black material that absorbed any scattered light thus removing it from the system (WET_Labs, 2008a, 2009). Therefore, light transmitted

through the attenuation sample space was reduced by both absorption and scattering processes. As with the absorption measurements, the initial attenuation results included components from natural seawater, dissolved matter and suspended particulate matter. The effects of pure sea water were later removed from these reported values. Thermal adjustments were made using the same methods as was done for the absorption coefficient.

Manufacturers' calibrations were performed in the fall of 2008 and 2009. Additionally, clear water (Nano-Pure) water calibrations were conducted prior to each cruise. Mid-cruise Nano-Pure calibrations were also performed during GC1, GC2, and GC3.

LISST 100X (Type B) (Sequoia_Scientific)

The Laser In-Situ Scattering and Transmissometry (LISST) by Sequioa Scientific, Inc. was deployed with the optics profiler at each station. This sensor used laser diffraction to estimate the total SPM concentration (ml/l) and the particle size distribution (PSD). This was achieved through the measurement of irradiance propagated by small angle forward scattering of particulates in the observation area. Incident light from a collimated laser beam (670 nm) illuminated a 5 cm optical path where it interacted with seawater, including dissolved and particulate obstructions. The scattered light was collected on 32 concentric ring detectors. These detectors were log spaced about the lasers' bore sight. The median angles of these detectors ranged from 0.160^{o} to 17.96^{o}. The associated software inverted the raw observations into the PSD.

For the purposes of this study, the detection of particles smaller than 1.25 μm would have been desirable, however smaller particles scattered light at larger angles

(Jonasz & Fournier, 2007), which in turn would have required a larger detector array. Particle concentration was reported by volumes (µl/l) in 32 bins where the effective diameters of the particles increased logarithmically in size, as detailed in Table 3.

Table 3

Median Size of Particles in each LISST Bin

Median Diameter µm							
1.44	1.68	1.97	2.31	2.72	3.19	3.76	4.43
5.21	6.14	7.24	8.54	10.1	11.9	14	16.5
19.5	23	27.1	31.9	37.6	44.4	52.4	61.7
72.8	85.9	101	119	140	166	196	231

Table published by Sequoia Scientific Inc. (Sequoia Scientific). Used with permission (see appendix).

The calculation of true PSD required that a few things were known a priori, specifically the phase function of the single particles of the sample. (The phase function was the volume scattering, such as the variables used in equations 2.1, 2.2 and 2.3, divided by the total scattering coefficient (b) (Mobley, 1994).) Since such a priori knowledge for field conditions could not be obtained, approximations were used. Specifically, Mie theory was applied to the estimation of the PSD (Agrawal & Pottsmith, 2000; Agrawal, Whitmire, Mikkelsen, & Pottsmith, 2008). Mie theory included the assumption that all observed particles were solid, homogeneous spheres; therefore, the diameters of the constituents of the LISST derived PSDs were reported as the spherical equivalents of the observed particles. A comparative study of standardized spheres and randomly shaped particles of approximately the same size (Agrawal et al., 2008) revealed some of the effects of those different shapes on the appearance of the PSD. Most notably, an enhanced quantity of fines through the inversion calculations were reported in the smallest size bin compared to similar observations of homogeneous spheres. This was

likely caused by the detection of particles smaller than the spherical equivalent of 1.25 μm. This phenomenon also likely occurred in the project area, especially in surface and nearshore waters.

The pressure sensor on the LISST was located at the opposite end of the sensor from the observational portion of the instrument. Therefore, depth values were adjusted for the 0.635 m offset created by the vertical deployment of the LISST and binned to the nearest quarter meter for analysis (Figure 7). Since the pressure sensor could not report elevation above the sea surface, near-surface data holidays were the result. With the center of the optical path of the LISST was located 0.635 m below the pressure sensor, any recorded signal by the instrument recorded at 0 m could have been observed between 0.635 m and the deck of the research vessel. (Occasionally, the LISST recorded several hours of deck observations between stations.) Therefore, since the signal initially reported at 0 m (and later adjusted to 0.635 m before being binned to 0.75 m), the data values at 0.75 m could have represented seawater or air measurements. Therefore, data reported at 0.75 m was not considered in this research effectively giving the LISST data set a 1 m shallow cut-off.

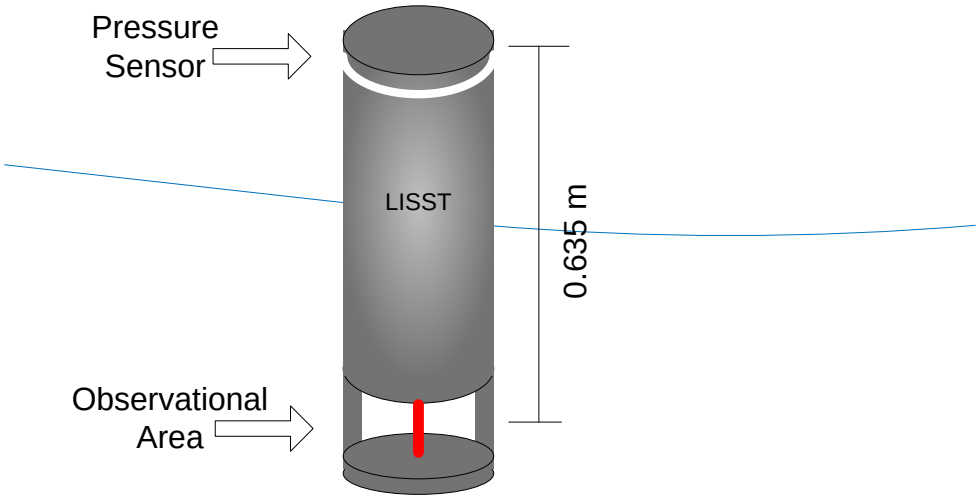

Figure 7. LISST Deployment Configuration

The pressure sensor in relation to the observational area of the LISST in vertical deployment. This scene shows a case where the pressure sensor records 0 m depth, but the observational area records subsurface data.

A manufacturers' calibration was performed in late 2008. In-lab calibrations using Nano-Pure were made for this sensor prior to each cruise and applied to the corresponding data sets.

Transmissometer (WET_Labs, 2010b, 2011)

The R/V Cape Hatteras provided a WET Labs Inc. C-Star Transmissometer on its' CTD profiler for cruises GC1-3 and GC5. This sensor provided attenuation coefficient values at 650 nm with a 10 – 12 nm bandwidth (WET_Labs, 2010b). The attenuation coefficient measured by transmissometer was calculated by the sensors' software using equation 2.7 (Bishop, 1986, 1999; Emmanuel Boss, Slade, Behrenfeld, & Dall'Olmo, 2009; Bunt, Larcombe, & Jago, 1999; Chung, Gardner, Richardson, Walsh, & Landry, 1996; Inthorn, Mohrholz, & Zabel, 2006; McCarthy, Pyle, & Griffin, 1974; McPhee-Shaw et al., 2004; David A. Siegel, Dickey, Washburn, Hamilton, & Mitchell, 1989). Transmissometer observations were made with a 25 cm path-length, open sample space.

Maintenance and calibrations were managed by the R/V Cape Hatteras' technical personnel.

Fluorimeters (Chelsea_Technologies_Group_Ltd; WET_Labs, 2010a; WET_Labs_Inc., 2011)

The fluorimeters located on the ships' CTD profilers reported chlorophyll-a concentration. In this research, they were primarily used to identify incidences of profiler-induced turbidity when the ships' profilers caused resuspension of benthic materials. Maintenance and calibrations were managed by the ships' technical personnel.

The fluorimeter on the optical profiler also reported chlorophyll – a. In this project, the data from this sensor is referred to as fluorescence. As with the other fluorimeters deployed during these cruises, in this project, these data were used only for qualitative analyses, specifically for the identification of profiler induced turbidity.

The Use of Multiple Profilers and Data Types

The CTD profilers on both research vessels employed in this project were configured so that the CTD (and other sensors) were located near the bases of the packages with the sampler bottles affixed a little higher up. All depth measurements related to the water samples provided to the researchers represented the depth of the CTD sensors at the time of sample capture. To more accurately calculate the depth of the water samples, a vertical offset was subtracted from the CTD observations and applied to the metadata of the filter samples (Figure 8). These offsets represented the difference between the depth sensor and the center of the nearest sample bottle. These offset values were 0.936 m for the CTD profiler on the R/V Cape Hatteras and 0.781 m for the CTD profiler on the R/V Hugh R Sharp.

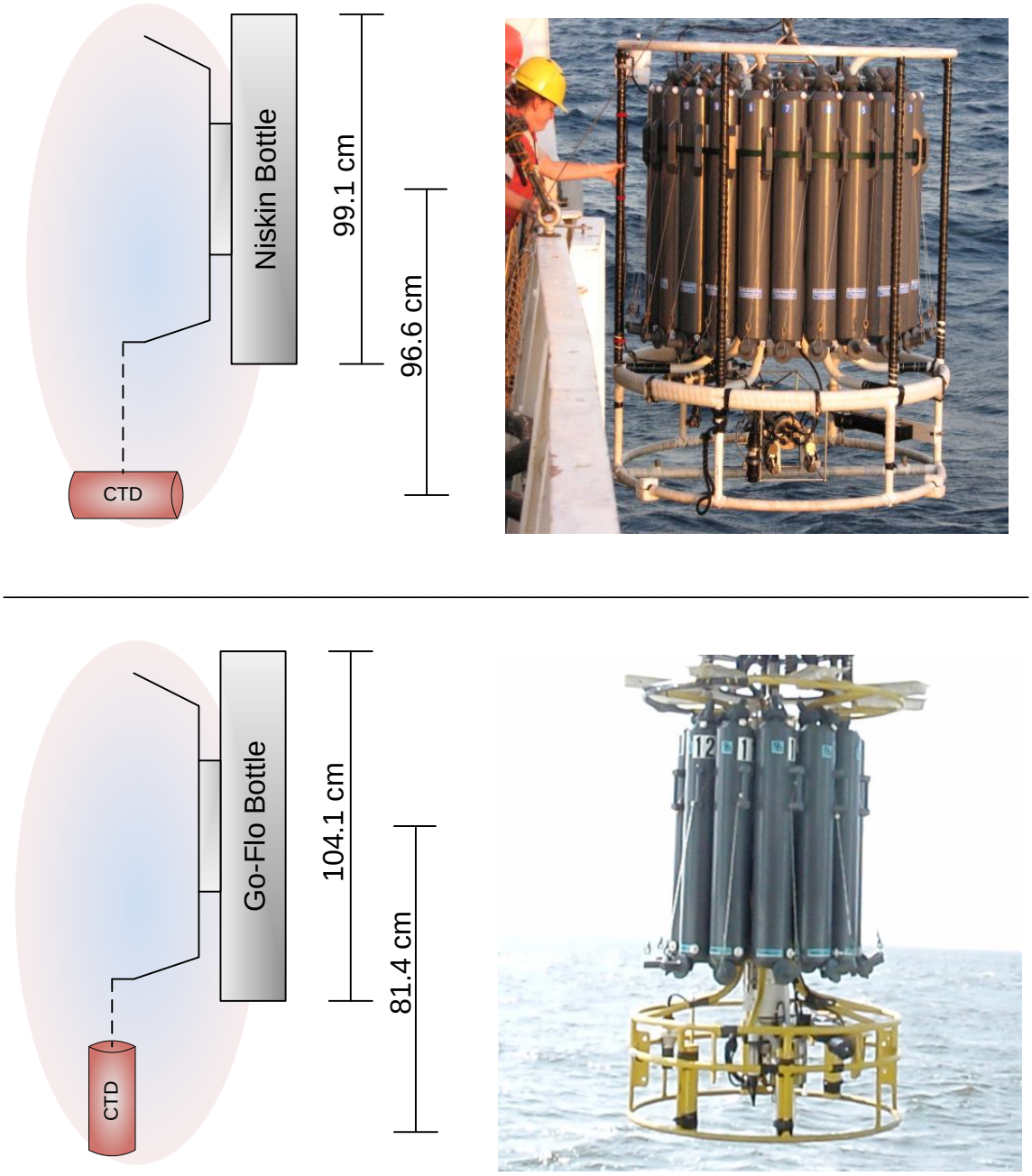

Figure 8. Water Sampler Configurations

Bulk water sampler configuration in relation to the co-located CTD sensors for the R/V Cape Hatteras (top) and the R/V Hugh R. Sharp (bottom). Lengths of the bottle chambers and the vertical offsets between the pressure sensor of the CTD and the center of the sample bottles are also shown.

Several of the sensors used in this research required pumps to supply water into sampling spaces for observation. These sensors included all CTDs, the AC9, and the ACS. The use of pumps combined with variable profiling speeds may have imposed temporal latency issues. Specifically, the time lapse between the water intake and actual observation by the sensor was unknown. (Similar issues have been considered using a towed AC9 (Barth & Bogucki, 2000).) Additionally, the sensors themselves experienced vertical motion of varying rates as the profiler moved up and down through the water column via an onboard winch. The time lag was expected to be exaggerated when the sensor was moving in the downward (Figure 9). There was only one case of where a pump-intake was mounted horizontally on a profiling package; the CTD sensor on the water sampling profiler or the R/V Cape Hatteras. All other pumps were mounted vertically. The time lag and associated uncertainty related to the true depth of the parcel of water under observation in the pump assisted sensors was not quantified in this project.

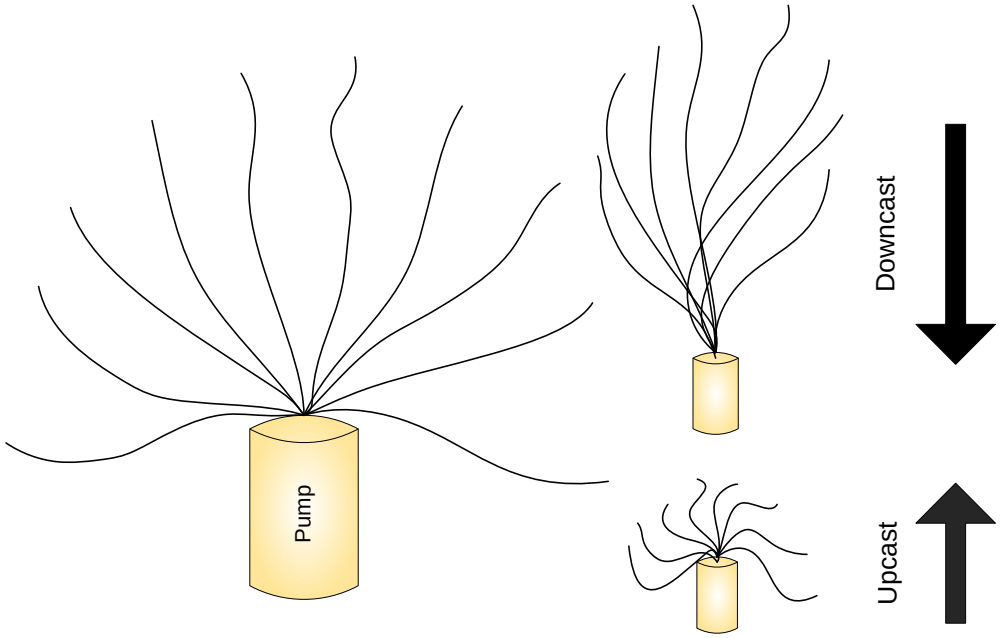

Figure 9. Moving Water Pump Intake

Graphical representation of water intake to a vertically mounted pump. Left: the pump is motionless. Right: the pump is undergoing vertical motion.

Finally, there is a vertical offset between each pump intake location and the depth sensor on the CTDs (Figure 10). On the optical profiler, an effort was made to keep the pump intake valves between the sensors level with one another. These offsets were not measured and adjusted in the subsequent evaluation of the data for several reasons. The most important of which is a lack of understanding of the vertical range of the water pumped into the sensor at any given depth. This behavior would have incorporated parameters such as pump strength and the shear stresses of the natural water, considerations beyond the scope of this project.

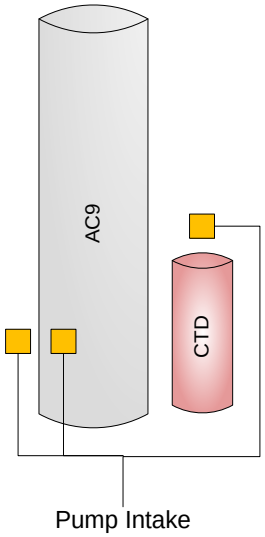

Figure 10. Water Pump Location in Relation to Profiling Sensors

Graphical representation of the pump intake locations of pump-included sensors on the optical profiler. The ACS pump locations are similar to the pump locations of the AC9.

Methods of Improving Profile Data and Filter Sample Spatial Relationships

The original observations from the profiling sensors on the GulfCarbon cruises were adjusted for sensor calibrations, then binned to the nearest quarter-meter before being provided to participating researchers for further analysis. This research required an understanding of the relationship between these digital datasets and the observations made by filtration of bulk water samples. Unlike the data output from the profiling sensors, the method of bulk water extraction from the marine environment used in this research could not provide such a fine scale resolution (quarter-meter) of the vertical component of the sample position.

This coarser resolution for the bulk water samples comes from several different sources. First, the bulk water sampling systems used in this project occupied vertical spaces much greater than 0.25 m (see Figure 8). The sampling system deployed on the R/V Cape Hatteras employed 12 to 23 12L Niskin bottles co-located with two CTDs and

other sensors. This configuration was used for cruises GC1, GC2, GC3, and GC5. For cruise GC4, the R/V Hugh R. Sharp deployed a General Oceanic Model rosette with twelve 10 L sample bottles. In all cases, the sample bottles were deployed vertically. The initial depth reported to the onboard researchers reflects the observations recorded by the primary CTD mounted on the carousels at the time of bulk water sample capture. As seen in Figure 10, these measurements did not reflect the best depth values for the water samplers. In this SPM research, the vertical offset between the CTD and the center of the bulk water sample bottle was subtracted from each depth value for the water samples. These adjusted depth values were used for all filtered samples considered in this research.

Some consideration must be given to the effect the profilers had on the natural environment. A profiling package on its way down (downcast) had the potential to cause mixing, disturbing the fine-scale vertical structure of the water column and possibly adding bubbles into the near-surface environment. This mixing started with the interaction of the base of the profiler's frame as it entered the water and progressed downward. Additionally, when a CTD (located on either a water sampling profiler or on the optical profiler) was first introduced into the marine environment, water pump degassing (adding more bubbles to the near-surface environment) and initiation procedures were conducted. This usually occurred at a depth where the profiler remained completely submerged, yet still close to the sea surface. In rough seas, this meant that these procedures were performed when the sensors were at a greater depth than they were in calm water in order to maintain submersion.

In addition to the vertical offset applied to the bulk water samples that were used in the filtration datasets, more steps were necessary to bring the digital datasets and the

filtered datasets into a more robust state for comparison. Figure 8 shows not only that there was a difference between the depth sensor and the center of the bulk water sampler bottles, but that there was also a sizeable vertical difference between the center of the bulk water sampler bottle and the top and bottom ends of each bottle. These differences were relatively large compared to the 0.25 m depth bins reported for the digital profiling sensors. Therefore, for this project, when the relationships between filtered data and the digital data were analyzed, multiple observations from the profiling sensors (binned at 0.25 m) were considered over a 1.25 m vertical range. Specifically, the medians and median absolute deviations (MADs) of the digital data were calculated from the official (previously vertically offset) depth of each filtered data point as well as the two points above and below that depth. For example, if the filter sample was taken at 10.5 m and compared to the backscatter data at that depth, a median was calculated for the backscatter data to include all five observations in the 10 m to 11 m depth range.

In summary, when the digital datasets from the profiling sensors were compared to the filtered water datasets the following steps were taken:

1. A vertical offset was applied to the filtered water datasets to account for the distance between the center of the sample bottle and the CTD sensor. The value was then rounded off to the nearest quarter meter.
2. For the digital profiling dataset in question, the observational median and median absolute deviation (MAD) values were calculated using the point of comparable depth relative to the filter sample plus the observations within 0.5 m of that central vertical point.

It should be noted that this method does not account for the inherent differences between the CTD pressure sensors used on the optical profiler and the ship's water sampler profilers. In the former case, the CTD had a depth rating of 350 m. The latter had depth ratings of 6800 m. Since the CTD's inherent uncertainty is a small percentage of the depth rating, the sensors with the larger depth ratings carried a higher uncertainty than those with shallower depth ratings. These uncertainties are listed in Table 1.

Uncertainties Related to Profiler Configuration

In order to maximize the quality of the processing procedures of the profiler observations, it is necessary to understand the uncertainties related to profiler deployment. Sources of uncertainties related to profiling observations include disruptions introduced to the structure of the water column by the profiler itself. When the pumps executed initialization procedures, they introduced air and fresh water (from deck-side cleanings between stations) into the surface waters. Even though data recording did not begin until after the pump initialization was complete, the surface waters had been disturbed. Additionally, air bubbles got into the pumps as the profiler rose through the surface at the ends of the upcasts causing anomalies in the observational data. Spikes were consistently seen in the top 0.5 m of profile data from the sensors that employed pumps. Similar spikes were seen in the top 0.25 m of the profile data from the sensors that did not use pumps. Therefore, in all cases for this project (with the exception of the LISST) the upper 0.5 m and 0.25 m observations were removed from the data of sensors with pumps and without pumps respectively.

Additionally, the movements of the profiler as it progressed through the water column had the potential to disturb boundaries such as the halocline and thermocline.

Since the CTD rosettes and the optical profiler were different in dimensions, mass, and onboard attachments (see Figure 11), it was believed that there was a difference in potential water column disturbance. Also interactions between a profiler and the sea floor had the potential to disturb bottom sediments and introduce the effects of profiler-induced re-suspension of bottom matter to the sensor observations.

Figure 11. Vertical Profiling Bundles

Optical profiler (right) next to Ship's CTD profiler system with 12 Niskin Bottles for bulk water samples (left). Photo was taken on the R/V Cape Hatteras during cruise GC1. Note that all other cruises on the R/V Cape Hatteras had 23 Niskin Bottles mounted to the CTD profiler.

The CTD sensors were chosen for methods-related analyses because they were present on all profilers. These analyses included evaluating uncertainties related to downcast versus upcast data (addressed later in this chapter) and examining whether sequential profiling events observed the same environmental conditions as proposed by Hypothesis 1 (Chapters I and III).

Uncertainties Related to Downcast and Upcast Profile Data

Data outputs from the optical profiler and the ship's CTD profilers were divided into two data files per deployment. The downcast files contained data from the downward journey of the profiler. Similarly, the upcast files consisted of the data from the upward path of the profiler.

There was a variable temporal component involved in considering downcasts in relation to upcasts. The near-surface values recorded by a profiling sensor between the downcast and upcast data files represented the points of greatest temporal difference whereas the values recorded at the bottom of each profile had the least temporal difference between them. The near-surface temporal differences were naturally larger when the profiler was deployed to greater depths. Since the depths of the occupied stations for this project area ranged from a few meters to approximately 1750 m, the temporal variability between the downcast data and the upcast data was substantial. The appropriate use of downcast versus upcast data been a consideration for oceanographers for decades (see (Bishop, 1986) and his references), (David A. Siegel et al., 1989).

The first two steps reported earlier in this chapter for relating filtered data to digital sensor reports (e.g., from the CTD, BB9, ACS, etc.) do not address data availability and variability with reference to downcast and upcast data files. The following section evaluates downcast versus upcast data. Analyses regarding data availability and correlation were performed using the salinity data sets in the surface waters (0.75 – 2 m depth) and in slightly deeper waters (2 – 4 m depth). (Waters deeper than 4 m were not considered in order to retain as many stations observed as possible, and not exclude the shallow end-members in the project area.) All profiles, at all stations

of all cruises, were considered. The results of these comparisons are displayed in Figure 12 and relate to *Hypothesis 1* of this project.

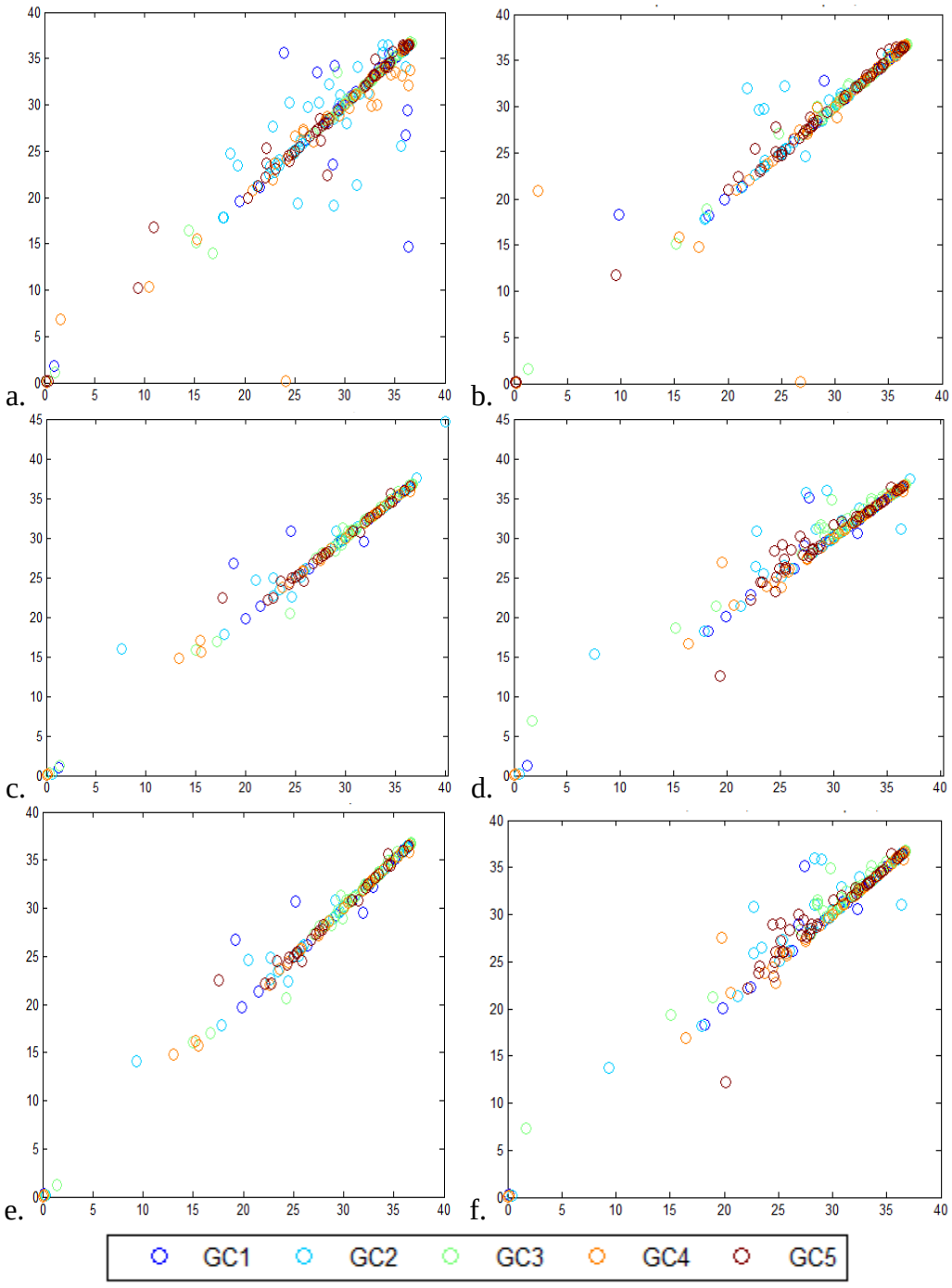

Figure 12. Downcast vs. Upcast Salinity

Downcast is plotted on the x-axes. Upcast data is plotted on the y-axes. All data pairs plotted are from the 0.25 interval depths available within the following depth ranges and related to the specified sensors. a. 0.75-2m depth, SBE49. b. 2-4m depth, SBE49. c. 0.75-2m depth, CTD 1. d. 2-4m depth, CTD 1 e. 0.75-2m depth, CTD 2. f. 2-4m depth, CTD 2.

The salinity values had a strong downcast versus upcast linear relationship at the 0.75 – 2 m depth range as seen in the scatter plots *a*, *c*, and *e* in Figure 12 and by the correlation values in Table 4. The results of downcast versus upcast analysis at 2 – 4 m depth can be seen in Figure 12, plots *b*, *d*, and *f*. The corresponding Spearman correlation values were reported in Table 5. They too had a strong linear relationship. However, plots *d* and *f* (2 – 4 m for the CTDs on the ships' profilers) show more scattered points than the comparable plots for the 0.75 – 2 m depth range (plots *c* and *e*, Figure 12). This apparent increased scatter with depth in the ships' CTDs may have been misleading as the number of downcast-upcast data pairs available for plotting on the 2 – 4 m depth plots (n = 246) (Table 7) was much greater than the 0.75 – 2 m plots (n = 170), (Table 6).

High p-values from the Kruskal-Wallis evaluations indicate that there was no statistical difference in the salinity data used for the downcast-upcast comparisons (Table 4 and Table 5). The Spearman's rank correlation coefficient values also indicate a very strong relationship between the downcast and upcast data. The lowest correlation value ($\rho = 0.82$ for GC1, 0.75 – 2 m, the SBE49 sensor), is also associated with the largest differences of number of observations between the downcasts and the upcasts (Table 6).

Table 4

Downcast-Upcast Evaluation: Relationship Analysis 0.75-2m Depth

Cruise	CTD Sensor	Kruskal-Wallis p	Spearman's Rank Correlation		n
			ρ	p	
GCALL	SBE49	0.92	0.93	0.00	278
GCALL	CTD 1	0.82	0.99	0.00	170
GCALL	CTD 2	0.88	0.99	0.00	170
GC1	SBE49	0.85	0.82	0.00	62
GC1	CTD 1	0.86	0.97	0.00	27
GC1	CTD 2	0.83	0.98	0.00	27
GC2	SBE49	0.81	0.92	0.00	71
GC2	CTD 1	0.85	0.99	0.00	35
GC2	CTD 2	0.91	0.99	0.00	35
GC3	SBE49	0.77	0.97	0.00	50
GC3	CTD 1	0.76	0.99	0.00	50
GC3	CTD 2	0.81	0.99	0.00	50
GC4	SBE49	0.70	0.95	0.00	44
GC4	CTD 1	0.98	1.00	0.00	30
GC4	CTD 2	0.99	1.00	0.00	30
GC5	SBE49	0.78	0.98	0.00	51
GC5	CTD 1	0.97	0.99	0.00	28
GC5	CTD 2	1.00	0.99	0.00	28

Notes. CTD 1 and CTD 2 represent two separate sensors on the ships' water sampler profilers. Cruise "GCALL" was used when the evaluation was performed on the combined dataset for all five cruises.

Table 5

Downcast-Upcast Evaluation: Relationship Analysis, 2-4m Depth

Cruise	CTD Sensor	Kruskal-Wallis p	Spearman's Rank Correlation		n
			ρ	p	
GCALL	SBE49	0.57	0.99	0.00	286
GCALL	CTD 1	0.41	0.96	0.00	246
GCALL	CTD 2	0.42	0.96	0.00	246
GC1	SBE49	0.71	0.99	0.00	65
GC1	CTD 1	0.81	0.98	0.00	47
GC1	CTD 2	0.80	0.98	0.00	47
GC2	SBE49	0.61	0.96	0.00	75
GC2	CTD 1	0.59	0.91	0.00	53
GC2	CTD 2	0.62	0.91	0.00	53
GC3	SBE49	0.90	1.00	0.00	50
GC3	CTD 1	0.28	0.94	0.00	52
GC3	CTD 2	0.32	0.94	0.00	52
GC4	SBE49	0.86	0.99	0.00	45
GC4	CTD 1	0.92	0.99	0.00	47
GC4	CTD 2	0.94	0.99	0.00	47
GC5	SBE49	0.64	0.99	0.00	51
GC5	CTD 1	0.52	0.96	0.00	47
GC5	CTD 2	0.51	0.96	0.00	47

Notes. CTD 1 and CTD 2 represent two separate sensors on the ships' water sampler profilers. Cruise "GCALL" was used when the evaluation was performed on the combined data set for all five cruises.

Table 6

Number of Observations for Downcast-Upcast Comparison, 0.75-2m Depth

Cruise	CTD Sensor	n Casts			n Observations Per Cast Median (MAD)	
		Down	Up	Pairs	Down	Up
GCALL	SBE49	282	286	278	4.5 (1.5)	6 (0)
GCALL	CTD 1	173	232	170	2 (1)	3 (1)
GCALL	CTD 2	173	232	170	2 (1)	3 (1)
GC1	SBE49	63	65	62	4 (1)	6 (0)
GC1	CTD 1	27	46	27	1 (1)	3 (1)
GC1	CTD 2	27	46	27	1 (1)	3 (1)
GC2	SBE49	72	74	71	5 (1)	6 (0)
GC2	CTD 1	36	47	35	2 (2)	3 (1.5)
GC2	CTD 2	36	47	35	2 (2)	3 (1.5)
GC3	SBE49	52	50	50	5 (1)	6 (0)
GC3	CTD 1	50	52	50	2 (1)	3 (1)
GC3	CTD 2	50	52	50	2 (1)	3 (1)
GC4	SBE49	44	46	44	5 (1)	6 (0)
GC4	CTD 1	30	45	30	2 (1)	4 (1)
GC4	CTD 2	30	45	30	2 (1)	4 (1)
GC5	SBE49	51	51	51	5 (1)	6 (0)
GC5	CTD 1	30	42	28	1 (1)	2.5 (0.5)
GC5	CTD 2	30	42	28	1 (1)	2.5 (0.5)

Notes. MAD is the median absolute deviation. CTD 1 and CTD 2 represent two separate sensors on the ships' water sampler profilers. Cruise "GCALL" was used when the evaluation was performed on the combined data set for all five cruises. The maximum number of observations per stations was n = 6.

Table 7

Number of Observations for Downcast-Upcast Comparisons, 2-4 m Depth

Cruise	CTD Sensor	n Casts			n Observations Per Cast Median (MAD)	
		Down	Up	Pairs	Down	Up
GCALL	SBE49	288	288	286	9 (0)	9 (0)
GCALL	CTD 1	247	247	246	9 (0)	9 (0)
GCALL	CTD 2	247	247	246	9 (0)	9 (0)
GC1	SBE49	65	66	65	9 (0)	9 (0)
GC1	CTD 1	48	47	47	9 (0)	9 (0)
GC1	CTD 2	48	47	47	9 (0)	9 (0)
GC2	SBE49	75	75	75	9 (0)	9 (0)
GC2	CTD 1	53	54	53	9 (0)	9 (0)
GC2	CTD 2	53	54	53	9 (0)	9 (0)
GC3	SBE49	52	50	50	9 (0)	9 (0)
GC3	CTD 1	52	52	52	9 (0)	9 (0)
GC3	CTD 2	52	52	52	9 (0)	9 (0)
GC4	SBE49	45	46	45	9 (0)	9 (0)
GC4	CTD 1	47	47	47	9 (0)	9 (0)
GC4	CTD 2	47	47	47	9 (0)	9 (0)
GC5	SBE49	51	51	51	9 (0)	9 (0)
GC5	CTD 1	47	47	47	9 (0)	9 (0)
GC5	CTD 2	47	47	47	9 (0)	9 (0)

Notes. MAD is the median absolute deviation. CTD 1 and CTD 2 represent two separate sensors on the ships' water sampler profilers. Cruise "GCALL" was used when the evaluation was performed on the combined dataset for all five cruises. The maximum number of observations per stations was n = 9.

The number of instances where downcast and upcast paired data occurred was an important consideration in this analysis (Tables 6 and 7). In all cases, the number of available downcast-upcast paired data sets at 2 – 4 m was greater than the instances of paired datasets observed for the 0.75 – 2 m depth range. Furthermore, at the 0.75 - 2 m depth range (Table 6), we can see that the number of upcasts containing CTD data for a given cruise almost always exceeded the number of downcasts, particularly for the

sensors located on the ships' CTD profilers. This phenomenon was attributed to the fact that many downcast files did not have recorded data for the first meter or more of depth. Data gaps near the surface depths of the downcast files occurred because the ships' CTD profilers started logging data after the carousel was completely submerged and initialized. In the upcast direction, logging of the ships' CTD profiler sensors stopped at about the time that the water containers (positioned above the sensors) collected surface samples also resulting in data gaps at the near surface depths of the upcast files. The number of upcast profiles observed by the ships' CTD profilers in the 0.75 – 2 m depth range was greater than the number of downcast profiles at the same depths (Table 6 and Table 7).

The SBE49 CTD attached to the optics profiler acquired more near surface (0.75 – 2 m) observations than the ships' CTD profilers in both the downcast and upcast directions (Table 6). These additional observations were possible because less depth below the sea surface was required for the CTD initialization procedures prior to the downcast of the smaller (optical) profiler than for the more massive CTD profilers (Figure 12). In the upcast direction, the SBE49 on the optical profiler generally stopped recording useful data shallower than 0.5 m.

Regardless of the individual CTD sensor under consideration, the number of down-up pairs available for comparison was usually fewer than the smallest number of either downcasts or upcasts for a given cruise. This apparent mismatch occurred because in some cases the profilers logged either a downcast or upcast profiling event, but not both. Therefore, in several cases, a set of paired data for the depth range under consideration was not observed by the sensor.

The number of observations made per considered depth range per downcast or upcast was also evaluated (Tables 6 and 7). As expected, the number of observations recorded by the CTDs per downcast or upcast within the analyzed depth range had greater stability between two and four meters than between 0.75 and two meters. Furthermore, in the shallower depth range (0.75 – 2 m), the upcast files contained more observations than the downcast files. This indicated that the upcast data better represented near-surface conditions than the downcast data for the SBE49. This tendency was not evident in the 2 – 4 m salinity data. (Both downcast and upcast data files generally had the same number of observations.)

A similar relationship is noted with the other, ship-based CTDs, though to a lesser degree. Both the downcast and upcast data files associated with CTD 1 and CTD 2 have fewer salinity observations than the SBE49 files. However, even these sensors have more observations available for analysis in the upcast rather than the downcast directions. Also, like the SBE49, the CTD 1 and CTD 2 sensors from the research vessels had the same number of observations in both downcast and upcast data sets.

In summary, the ability of all CTD sensors to record data at all 0.25 m depth intervals between 0.75 and 2 m of the sea surface is highly variable given the techniques used in this project for profiler deployment. (This includes considerations for sensor initialization and shut down.) Most significantly, the upcast data files best represent this depth interval based upon the number of observations available for analysis in the data files. (Additionally, water samples are captured by the CTD profilers only on upcasts.) The increased data availability in the upcast direction is an important consideration later on in this research for establishing the process used to determine which subsets of data

are utilized in the near-surface environment for SPM algorithm development. From the downcast versus upcast salinity analysis, a data processing procedure has been integrated into the management of all of the data from sensors located on the optical profiler linked to the DH4. When evaluating any data from 2 m depth or less, only upcast data was considered. This applied both to regional surface data evaluations and to filterdepths within this near surface range.

Deck – Based Hyperspectral Observations

Hyperspectral observations at visible and near-visible wavelengths were carried out in order to calculate various radiances and remote sensing reflectance (R_{rs}) during cruises GC2 – GC5. Observations were performed when the research vessel was on station during daylight hours. For the purposes of this project, radiance was defined as the flux of light (λ = 375 – 1075 nm) transmitted through or reflected from a target of interest, such as the sky, sea or a Lambertian surface, towards the hand-held hyperspectral sensor, within the sensor's field-of-view (FOV) angle, at the azimuth and inclination angles of observation.

Radiance calculations were essential to estimating remote sensing reflectance. R_{rs} was a measure of light departing the water column and moving in a generally upward direction. It was classified as a passive apparent optical property because the radiometric observations required to calculate this parameter were obtained in ambient light conditions (without the aid of artificial illumination). Remote sensing reflectance was further defined as water leaving radiance (L_w) divided by downwelling irradiance (E_d); $R_{rs} \equiv \frac{L_w}{E_d}$ sr^{-1} (Doron, Bélanger, Doxaran, & Babin, 2011; Z. Lee, Ahn, Mobley, & Arnone, 2010; Z. Lee, Shang, Lin, Chen, & Doxaran, 2016; Minu et al., 2016; Mobley,

1999; Neil, Cunningham, & McKee, 2011; Sylvain Ouillon & Petrenko, 2005; S. Wang et al., 2016; Zhu, Yu, & Tian, 2013). Direct measurements of L_w could not be made with existing technology, but it was estimated using in situ observations (Le et al., 2009).

Field Measurements: ASD

Measurements for the calculation of R_{rs} were made with a hand-held spectroradiometer (ASD), by Analytical Spectral Devices, Inc. This instrument output spectral irradiance from 325 nm to 1075 nm wavelengths at 1 nm intervals. Sky observations were measured by orienting the instrument 90^O away from the sun azimuth, and approximately 45^O down from zenith. Azimuth orientation was achieved by positioning oneself so that when one's arms were held straight out to either side, one hand pointed to the sun's azimuth and the other pointed through the shadow of the head. Zenith and nadir related angles were estimated using an inclinometer affixed to the side of the sensor by two reattach-able strips. The sea was observed by pointing the ASD approximately 45^O downwards over the rail of the research vessel. Care was taken to avoid ship-shadow during the sea observations. Also at each station, observations of a calibrated gray Lambertian surface were used to calculate radiance for R_{rs} calculations. A Lambertian surface reflects light intensity equally in all directions. The instrument was optimized by observing a calibrated white Lambertian surface.

Three different field-of-view (FOV) configurations were available, 1^O, 10^O and 25^O through the use of fore-optic attachments. These FOV angles, along with sensor height and angle from the target affected the area observed by the instrument footprint or spot size (Figure 13). Larger FOVs and greater heights of the sensors yielded larger

footprints. Sample spot-sizes were detailed in Table 15 and Table 16 for various bore-site angles and sensor heights.

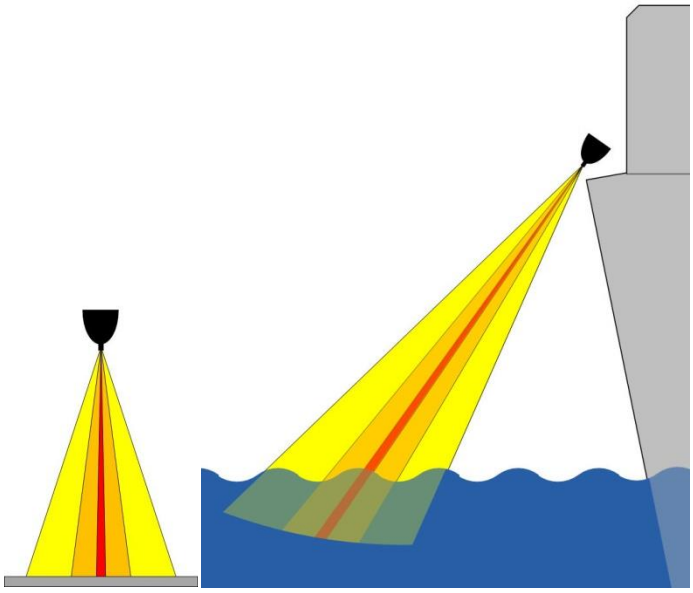

Figure 13. ASD Field of View Options

Field of view options and resultant observational spot-sizes for the ASD handheld hyperspectral sensor. Red, orange and yellow cones represent 1O, 10O and 25O formats used in this research. Left illustration demonstrates vertical observation of a calibrated reference target. Right illustration shows the ASD observing the ocean at ~45O off nadir, over the rail of the research vessel.

The height the sensor was held over the Lambertian reference surfaces at approximately 0.3 m to 0.5 m. Though attempts were made to hold the sensor steady while taking observations, some motion was inevitable during the collection process affecting observational spot size. This motion related footprint size uncertainty was most relevant to observations of the sea surface. Table 8 shows the areas circumscribed by the different field-of-view configurations and at various heights above a calibrated Lambertian surface at nadir angle. Table 9 describes approximate sea surface areas observed by the sensor at various height, elevation angle and FOV options.

Table 8

Viewing Areas of the ASD Held at 90^{O} from Target Surface

Height m	Area cm^2		
	1^{O} FOV	10^{O} FOV	25^{O} FOV
0.3	0.02	2.16	13.9
0.5	0.06	6.01	38.6

Note. FOV is the field of view.

Table 9

Sea Surface Viewing Areas at Various Angles from Nadir, ASD

Boresight Angle Off-Nadir	Height m	Area cm^2		
		1^{O} FOV	10^{O} FOV	25^{O} FOV
35^{O}	2	1.42	135.07	796.75
	3	3.19	303.91	1792.69
45^{O}	2	1.9	176.9	1011.08
	3	4.27	398.02	2274.94
55^{O}	2	2.87	259.9	1425.87
	3	6.46	584.77	3208.21

Note. FOV is the field of view.

Field measurements were collected for the intent of using the data for a semi-empirical method of R_{rs} calculation. Sky, sea and calibrated surface observations were made in groups, or cycles, of about five spectra files per target. Multiple sky and sea cycle pairs were collected at each station. Sky and sea cycles collected consecutively were used in the calculation of a single R_{rs} spectrum. Several R_{rs} spectra were calculated for each station using this method. These spectra were averaged, and the 95% confidence interval (CI) was calculated using the Student-T two-sided distribution. An example of an

R_{rs} spectrum with its' 95% CI was plotted in Figure 14, As seen in this example, the 95% CI typically varied with wavelength.

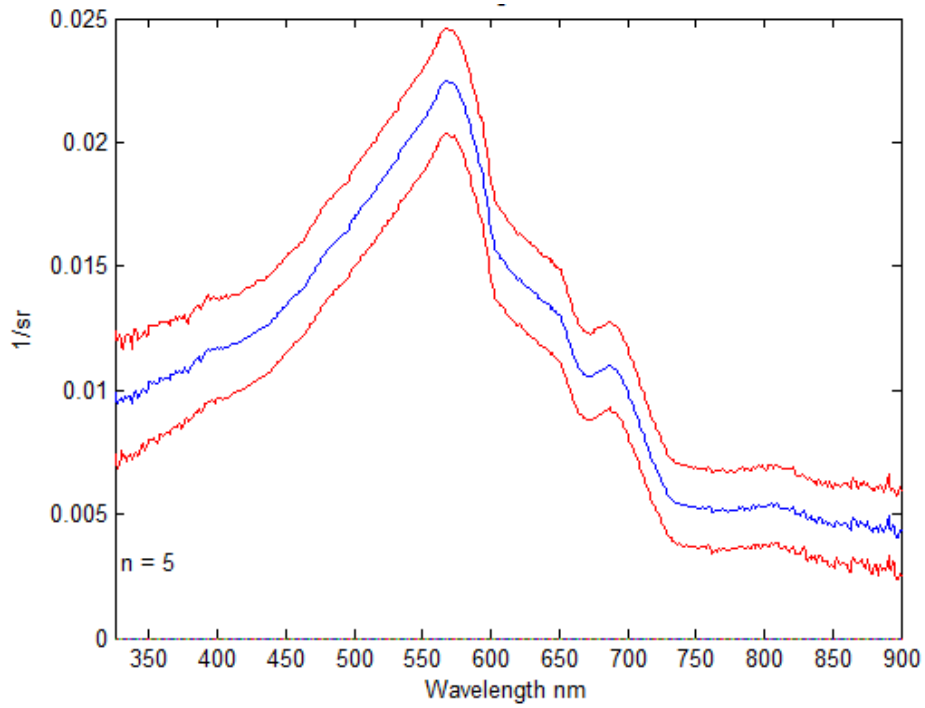

Figure 14. R_{rs} Spectrum

An example of remote sensing reflectance and the 95% CI. From GC5, station C1 with a 1^{O} FOV.

Gray surface observational cycles and dark line spectra cycles were made with each fore-optic attachment in use at each station, but they were not made as frequently as the sky and sea observations. In radiance and R_{rs} calculations these observations were employed in connection with the sky and sea observational cycles of closest temporal proximity.

All spectral measurements in the field were collected by the hyperspectral sensor as “digital numbers” (DN), the term described by ASD for the raw observations of the instrument. The DN observations included influences from photonic energy (hv) emanating from the desired observed target, over a recorded time interval (ns). In

addition to responses from the intended target (sky, sea, calibrated surface), the digital numbers data also represented the physical response (also known as the system response) of the sensor to the environment. It was observed in the field that the instrument was particularly sensitive to heat. On clear summer days, the system response made a significant contribution to the raw data (by about 102 DN). This influence was quantified by periodically taking dark current (DC) measurements, where the light was blocked from passing through the receiver of the instrument while a spectrum was measured. Thus, the only spectral response recorded during a DC measurement came from within the sensor. The DC measurements were subtracted from all other observations in order to calculate radiance and remote sensing reflectance.

Radiance (rad) calculations from the raw digital numbers followed the equation published in (Analytical Spectral Devices, 2002, 2003):

$$rad = \frac{known * input * cal\ IT}{response * input\ IT} \quad W\ m^{-2}\ sr^{-1} \tag{2.8}$$

Here, "known" was the reported radiance of the white target used by ASD Inc. to calibrate the handheld instrument in-house. "Input" was the observed spectra of raw digital numbers from which site-specific dark current values had been subtracted; "cal IT" was the integration time (in ns) used by the instrument during the lab observation of the known surface. "Response" was the spectra determined by ASD Inc. to be the calibration values of the instrument for the specific field-of-view fore-optic attachment used. The "response" was determined at ASD Inc. by observation of the known surface as part of the manufacturer's calibration service. Finally, input IT was the integration time (in ns) of the input spectra.

Field observations and calibration data were substituted into equation 8 yields the following calculation method for radiance values…

$$rad = \frac{ASDwr * (cycleMEAN - dlMEAN) * 544}{fovCAL * cycleIT}\ W\ m^{-2}\ sr^{-1}, \quad (2.9)$$

where *"ASDwr"* was the calibrated target used by the manufacturer for sensor calibration. "C*ycle"* was the set of observations (sky, sea, or target surface) of interest measured in the field. *dl* represented the mean dark current spectra obtained in the field. "*fovCAL"* was the calibration file provided by ASD for each fore-optic. And "*cycleIT* "was the integration time of the in-field observations.

Remote sensing reflectance (R_{rs}) was calculated from the radiance adapted from (Analytical Spectral Devices, 2002; Mobley, 1999).

$$R_{rs} \approx \frac{seaRAD - (0.028 * skyRAD)}{gryRAD * \left(\pi / gryCAL\right)}\ sr^{-1} \quad (2.10)$$

Variables "*seaRAD"*, "*skyRAD"* and "*gryRAD"* stood for the radiances of the sea, sky and gray target observations respectively, calculated using equation 2.9. "*gryCAL"* was the efficiency of the gray reference target reported by the manufacturer.

Since up to a few hundred observational spectra were recorded at each station in a relatively short time-frame from several types of targets, detailed quality assurance and control was necessary. Once onshore, each observational spectrum was examined to ensure that it was correctly classified as a sky, sea, Lambertian surface or DC observation as recorded in the field notes. The obvious outliers were also removed from the working dataset. Outlier spectra usually had much higher DN values than the other spectra of the same observational cycle.

Once the outliers were removed, an average spectrum for each cycle (DC, Lambertian surface, sky or sea observational cycle) was determined. The resultant spectra were used in the radiance and R_{rs} calculations. One sky and sea cycle pair along with the closest temporal observational cycle of the calibrated Lambertian surface radiance and dark current measurements were used to calculate each R_{rs} spectrum. Several R_{rs} spectra were produced for each station occupied during daylight hours. These spectra were later used to calculate the uncertainty of R_{rs} at each FOV employed at each station.

Field Measurements: HyperSAS

R_{rs} data from a Satlantic HyperSAS system is available for GC2 provided by Steven Lohrenz (personal communication). This sensor system was mounted at the rail near the pilot house of the R/V Cape Hatteras. The L_w estimate was observed with a 3^O FOV. The position was approximately 8 m from the sea surface with an approximate 45^O boresight angle. This results in a footprint of approximately 2670 cm^2. The E_d was recorded using a cosine collector. The resulting One hundred thirty-seven R_{rs} wavelengths are available from this sensor and method (Table 10).

Table 10

HyperSAS R_{rs} Wavelengths

HyperSAS Wavelength nm			
λ	λ	λ	λ
349.4	462.9	576.6	690.1
352.8	466.2	579.9	693.4
356.1	469.6	583.3	696.7
359.4	472.9	586.6	700.0
362.7	476.2	589.9	703.4
366.1	479.6	593.3	706.7
369.4	482.9	596.6	710.0
372.7	486.3	600.0	713.4
376.1	489.6	603.3	716.7
379.4	493.0	606.6	720.0
382.7	496.3	610.0	723.3
386.1	499.6	613.3	726.7
389.4	503.0	616.7	730.0
392.7	506.3	620.0	733.3
396.1	509.7	623.4	736.6
399.4	513.0	626.7	740.0
402.8	516.4	630.0	743.3
406.1	519.7	633.4	746.6
409.4	523.1	636.7	749.9
412.8	526.4	640.0	753.2
416.1	529.8	643.4	756.5
419.4	533.1	646.7	759.9
422.8	536.4	650.1	763.2
426.1	539.8	653.4	766.5
429.5	543.1	656.7	769.8
432.8	546.5	660.1	773.1
436.1	549.8	663.4	776.4
439.5	553.2	666.7	779.8
442.8	556.5	670.1	783.1
446.2	559.9	673.4	786.4
449.5	563.2	676.7	789.7
452.8	566.5	680.1	793.0
456.2	569.9	683.4	796.3
459.5	573.2	686.7	799.6
			802.9

Uncertainty related to Hyperspectral Observations

Potential sources of uncertainty associated with ASD hyperspectral measurements included a number of parameters. Misalignment between the inclinometer and the ASD could have introduced error into the nadir and zenith based angles. The spectral observations were also made from the deck of a research vessel, where sensors' orientation relative to the sun and sea surface was in a state of constant motion.

Glare from reflective surfaces of the ship occasionally passed over the calibrated surface while under observation as the research vessel moved. Considerable effort was put into avoiding that circumstance, but it may not have been universally avoided. If glare occurred in the viewing area at the moment of observation, photonic energy in addition to that from a normal ambient environment would have been recorded by the instrument. Conversely, shadows cast by various protrusions of the vessel's structure and onboard equipment onto the calibrated surfaces during observation would have caused a reduction in the total photonic energy recorded by the sensor. These variable conditions also applied to the targeted areas of the sea surface. Additionally, sun glint also produced outlier spectra in some of the sea observations causing abnormally high DN values. Therefore, multiple field observations reduced the influence of these environmental parameters.

During this project, the same DC and radiance spectra of the Lambertian surface were applied to more than one R_{rs} spectrum at a given station and FOV. This resulted in codependency of the R_{rs} spectra upon each other, based upon those values. These parameters, however, were quite small in relation to the sky and sea radiances, in the

future, each sky – sea observational cycle pair will have its own gray surface and DC cycles in order to achieve completely independent R_{rs} spectra.

To evaluate the most appropriate way to manage uncertainty calculation for ASD based R_{rs} data, the 1^{O} FOV field observations from GC5 were tested in three different ways to calculate radiance, R_{rs} and related estimated error. The first method, previously described, employed multiple sequential irradiance and DC observational cycles to produce several R_{rs} spectra per station. From these R_{rs} spectra, descriptive statistics were calculated and 95% CIs were determined using the two-sided Student-T distribution (see Figure 14). This method was ultimately employed in this research. Two other methods of using field data for R_{rs} and uncertainty calculations including total propagated uncertainty (TPU) and the Monte Carlo methods were tested, but not used in the creation of the final data products.

Conclusions

Essential details about this research are provided in this chapter including descriptions of sensors, the process used on filtration samples, explanations of the configurations of all profilers deployed during data collection and the method used in obtaining R_{rs} data. The first two steps in the rules followed by this project relating to comparing filter-data to data collected by the various profiling sensors are established. Downcast versus upcast salinity data sets are analyzed partially meeting the requirements of Hypothesis 1 for this dissertation. Further analysis indicates that when compiling data subsets for SPM algorithm development, where filterdepths occur at or shallower than 2 m, only upcast data should be used to mitigate the effects of depth bias due to a potential

lack of shallower data. Finally, in this chapter, methods for managing R_{rs} uncertainty are explored and a method selected for use with this project.

CHAPTER III - METHODS II: ANALYZING THE SEQUENTIAL DEPLOYMENT OF PROFILERS

Introduction

The use of two different profilers, one to obtain water samples and the other to make optical observations, required profiling events to take place sequentially rather than simultaneously. Also, the optical profiler was regularly deployed twice in succession during cruises GC1 and GC2. To treat the separate casts as sampling the same water column, one needs to be reasonably sure that the water column maintains its character throughout all sampling events. Water properties below the ship can potentially change due to local and advective alterations and any movement of the ship. This chapter addresses that problem using salinity datasets collected by each profiler. Problem areas, defined here as stations where salinity data in the near-surface waters did not agree to within one practical salinity unit (PSU) between sequential profiling events, were identified. Consideration was also given to instances of seafloor disturbance (sediment resuspension) by one or the other of the profilers. Attenuation and fluorescence data sets were utilized to identify instances where this occurred. Results from these analyses lead to the elimination of filtered and optical data at specific locations from algorithm development.

Uncertainties Related to Sequential Deployments of the Optical Profiler

At selected stations during cruises GC1, GC2 and GC5, the optical profiler was deployed twice so that filters could be attached to one of the AC sensors during these casts. Over the course of five cruises, this procedure was performed 45 times. Table 11 lists these double cast events. In most cases, either the AC9 or the ACS was fitted with a

filter for each of these casts while the other AC sensor remained filter-free. (Six exceptions to this practice took place during GC1 where the AC9 was filtered for one cast, and the other cast had all sensors deployed without filters.) This project considered only unfiltered absorption and attenuation data from the AC9 and ACS sensors. Therefore, at 45 stations it was not possible to always choose AC9 or ACS data from the first deployment of the optical profiler (the profiling event occurring nearest in time to the deployment of the ship's CTD profiler). Thus, at some locations, the length of time between the deployment of the research vessel's CTD profiler and unfiltered data from the optical profiler was increased by the time required for an additional cast of the optical profiler.

Table 11

Stations with Double Casts of the Optical Profiler

Cruise	Station	Cruise	Station	Cruise	Station
GC1	E0	GC1	H4	GC2	D2
GC1	E3	GC1	H5	GC2	D3
GC1	E4	GC1	H6	GC2	D4
GC1	E5	GC2	A1	GC2	D5
GC1	F1	GC2	A2	GC2	E0
GC1	F2	GC2	A4	GC2	E1
GC1	F3	GC2	A5	GC2	E2
GC1	G1	GC2	A6	GC2	MR1
GC1	G2	GC2	B1	GC2	MR2
GC1	G3	GC2	B2	GC2	MR3
GC1	G4	GC2	B3	GC2	NGI6
GC1	G5	GC2	B4	GC2	NGI7
GC1	H1	GC2	B5	GC2	NGI8
GC1	H2	GC2	C0	GC5	GC4
GC1	H3	GC2	D1	GC5	GC5

Though data from the AC9 and the ACS acquired using a filter were not used in this research, data from multiple casts of the unfiltered sensors on the optical profiler were utilized in this project (e.g., BB9, LISST, etc.). The decision to use data from multiple casts of the optical profiler was similar to treating the ship's CTD cast as sampling the same water as the optical profiler cast. Therefore, it was important to understand whether or not properties of the observed natural waters remained consistent through all profiling events per station.

The relationships of the salinity datasets between the first and second deployments from the SBE49 on the optical profiler at the 0.75 – 2 m and the 2 – 4 m depth ranges are shown in Figure 15 and Tables 12 and 13. Similar to the downcast versus upcast data (see Chapter II), there is more scatter in the 0.75 – 2 m data than in the

2 – 4 m depth data. Since the scatter occurring in the top layer of the salinity data consists of mostly higher salinity values during the second cast, it might be inferred that the act of occupying the station over the length of time required to perform two casts of the optical profiler may cause near-surface waters to mix with deeper, more saline water in some cases. At the 2 – 4 m depth range, the salinity values of the first and second casts are generally more consistent. In addition to the two depth ranges in the near-surface waters, salinity data pairs from filterdepths are also considered (Figure 15).

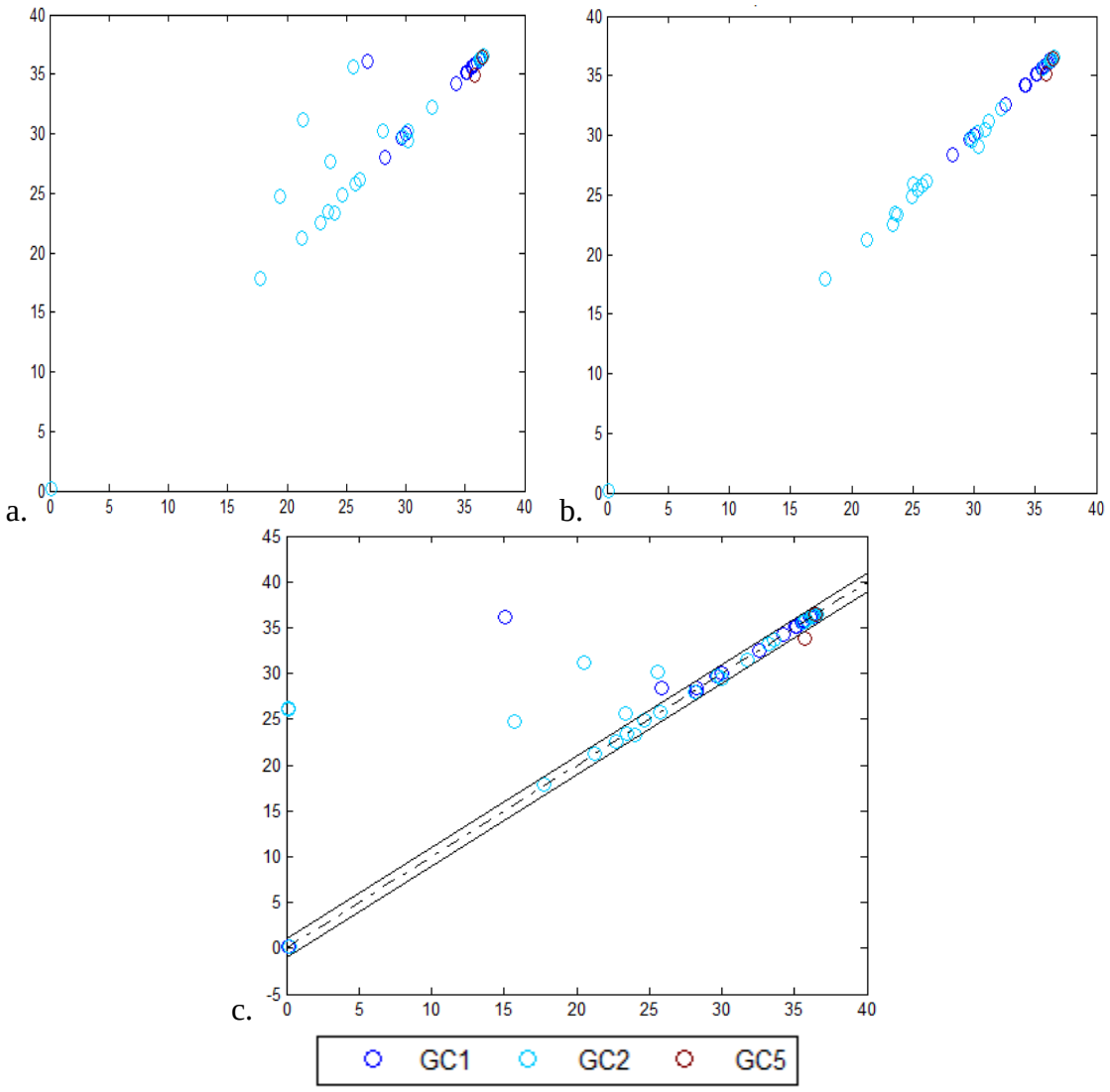

Figure 15. Salinity Comparisons from Multiple Casts of the Optical Profiler

The x-axis represents salinity from the first cast. The y-axis represents salinity from the second cast. Plot *a* shows salinity vs. salinity for the 0.75 – 2 m depth range. Plot *b* shows salinity vs. salinity for the 2 – 4 m depth range. Plot c shows the salinity at filterdepths associated with filtration samples. The 1:1 relationship and the ±1 PSU range beyond that relationship are also marked in Plot c.

When employing the rule used in this dissertation of using only upcast data at depths ≤ 2 m and using both downcast and upcast data below that point (see Chapter II), the maximum number of reported observations possible per deployment is six at the 0.75 – 2 m depth range and 18 at the 2 – 4 m depth range) (Tables 6, 7 and 12). While multiple

deployment comparisons reveal that the salinity data at the 0.75 – 2 m depth range are strongly correlated, the 2 – 4 m depth range demonstrates a stronger relationship (Table 13). These results are similar to the combined cruise comparisons for the downcast versus upcast datasets (Tables 4 and 5).

Table 12

Optical Profiler 1st & 2nd Cast n Observations of Salinity

Cruises	Depth Range m	Data Pairs	n Observations Per Profile Median (MAD)	
			First Cast	Second Cast
GC2, GC3, GC5	0.75 - 2	43	6 (0)	6 (0)
GC2, GC3, GC5	2 - 4	44	18 (0)	18 (0)
GC2, GC3, GC5	Filterdepths	75	5 (4)	5 (4)

Notes. Since only upcast data is used for depths of 2 m or less, the greatest n observations possible per profile are n = 6 for the 0.75 - 2 m depth range while n = 18 is the greatest number of observations per profile for the 2 - 4 m depth range. MAD is the median absolute deviation.

Table 13

Optical Profiler 1st & 2nd Cast Salinity Relationships

Cruises	Depth Range m	Kruskal-Wallis p	Spearman's Rank Correlation		n
			ρ	p	
GC2, GC3, GC5	0.75 - 2	0.59	0.93	0.00	43
GC2, GC3, GC5	2 - 4	0.94	0.99	0.00	44
GC2, GC3, GC5	Filterdepths	0.69	0.96	0.00	75

Note. MAD is the median absolute deviation.

From this exercise, it can be seen that the use of data from two casts of the optical profiler adds some uncertainty to any potential combination of the datasets, especially at very shallow depths. It is assumed that this principle carries over for the observations of the other sensors deployed on the optical profiler. If it was possible to use only data from

the first cast of the optical profiler, this project could have restricted its attention to datasets obtained by that deployment event at each station. However, to have coupled data pairs between filter samples and unfiltered optical sensors, data needed to be adopted from whichever deployment of the optical profiler produced an unfiltered product. Since both casts of the optical profiler needed to be utilized to obtain the AC9 and ACS data, at these 45 stations the observations from both casts were used from the sensors on that package that did not employ filters (e.g., BB9, LISST, etc., see Table 1).

Uncertainties Related to Observations from Different Profilers Deployed Sequentially: Salinity

Ship capabilities did not allow for the deployment of two profilers at the same time. Filter sample data from the ships' CTD profilers were used to determine the relationship between those filter samples and digital data observed from sensors on both the ships' CTD and USMs' optical profilers. Therefore, salinity data from both profilers were used to detect uncertainty inherent to the use of two profilers deployed in sequence. The salinity comparisons in this dissertation serve as proxies for other properties measured at the "same" locations. All data used in this evaluation, and for the remainder of this dissertation, have been subjected to the methods determined by the previous relationship studies in this project.

Salinity comparisons between the two profilers at the 0.75 – 2 m and 2 – 4 m depth ranges are shown in Figure 16. Less scatter is evident in these figures than was plotted in the downcast versus upcast evaluation done at the 0.75 – 2 m depth range (Figure 12). Most of the scattering indicates that in cases where the ships' CTD profiler did not agree with the optical profiler the more saline values were observed by the ship's

CTD systems. There were, however, a few exceptions to this higher-salinity bias during GC1 and GC2 (Figure 16).

Tables 14 and 15 describe the availability of salinity data for the profiler to profiler comparisons. Similar to the results of the downcast versus upcast data analysis from Chapter II, within the 0.75 – 2 m depth range, more data were collected by the SBE49 on the optical profiler than from the CTD sensors on the research vessels' profilers (Table 14 and Figure 17). The number of observations available for the profiler to profiler evaluations increased in similarity below 2 m (Table 15). The employment of multiple casts of the optical profiler during GC1 and GC2 influenced the abundance of data available at both depth ranges for those cruises (Tables 14 and 15).

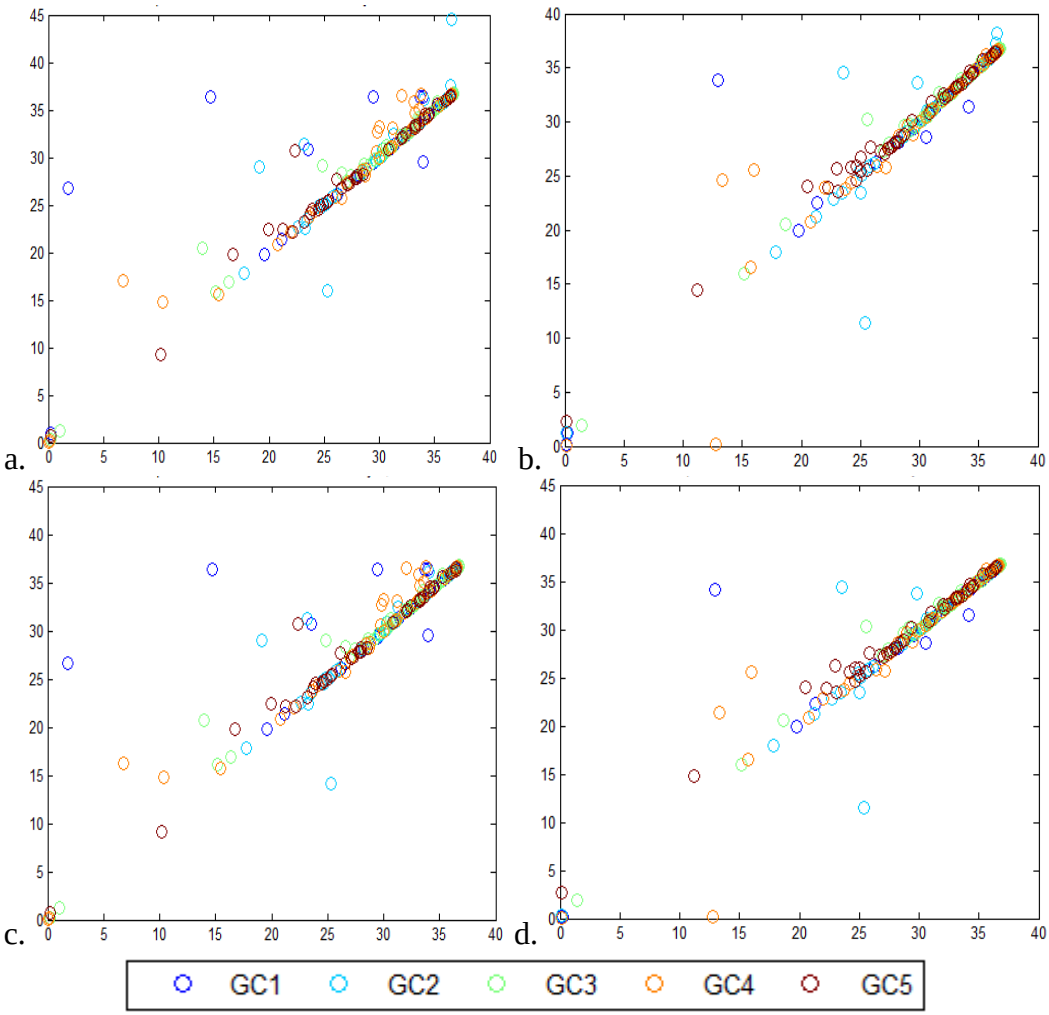

Figure 16. Profiler – Profiler Salinity in Near Surface Waters

The x-axis shows the optical profiler (SBE49) salinity data. The y-axis shows the CTD profiler salinity data. a. Optical profiler salinity versus CTD sensor 1 salinity, 0.75 – 2 m depth range. b. Optical profiler salinity versus CTD sensor 1 salinity, 2 - 4 m depth range. c. Optical profiler salinity versus CTD sensor 2 salinity, 0.75 - 2 m depth range. d. Optical profiler salinity versus CTD sensor 2 salinity, 2 – 4 m depth range.

Table 14

Profiler – Profiler Evaluation: Salinity Data Availability, 0.75-2m Depth

Cruise	CTD Sensor #	n Stations Per Profiler			n Observations Per Station Median (MAD)	
		Optics	CTD	Pairs	Optics	CTD
GCALL	1	243	229	225	6 (0)	3 (1)
GCALL	2	243	229	225	6 (0)	3 (1)
GC1	1	48	46	46	6 (2)	3 (1)
GC1	2	48	46	46	6 (2)	3 (1)
GC2	1	50	44	43	6 (1)	4 (2)
GC2	2	50	44	43	6 (1)	4 (2)
GC3	1	50	52	50	6 (0)	3 (1)
GC3	2	50	52	50	6 (0)	3 (1)
GC4	1	46	46	44	6 (0)	4 (1)
GC4	2	46	46	44	6 (0)	4 (1)
GC5	1	49	42	42	6 (0)	2 (1)
GC5	2	49	42	42	6 (0)	2 (1)

Notes. The SBE49 salinity data from the optical profiler is one member of each comparison. CTD 1 and CTD 2 represent salinity data from two separate sensors on the ships' water sampler profilers. Cruise "GCALL" was used when the evaluation was performed on the combined dataset for all five cruises. MAD is the median absolute deviation. “Pairs” represents the number of instances where the CTD sensors on both profilers recorded observations in the 0.75 – 2 m depth range.

Table 15

Profiler – Profiler Evaluation: Salinity Data Availability: 2-4m Depth

Cruise	CTD Sensor #	n Stations Per Profiler			n Observations Per Station Median (MAD)	
		Optics	CTD	Pairs	Optics	CTD
GCALL	1	241	244	238	18 (0)	18 (0)
GCALL	2	241	244	238	18 (0)	18 (0)
GC1	1	47	48	47	18 (0)	18 (0)
GC1	2	47	48	47	18 (0)	18 (0)
GC2	1	49	51	49	18 (8)	18 (0)
GC2	2	49	51	49	18 (8)	18 (0)
GC3	1	51	51	50	18 (0)	18 (0)
GC3	2	51	51	50	18 (0)	18 (0)
GC4	1	46	47	46	18 (0)	18 (0)
GC4	2	46	47	46	18 (0)	18 (0)
GC5	1	48	47	46	18 (0)	18 (0)
GC5	2	48	47	46	18 (0)	18 (0)

Notes. The SBE49 salinity data from the optical profiler is one member of each comparison. CTD 1 and CTD 2 represent salinity data from two separate sensors on the ships' water sampler profilers. Cruise "ALL" was used when the evaluation was performed on the combined dataset for all five cruises. MAD is the median absolute deviation. “Pairs” represents the number of instances where the CTD sensors on both profilers recorded observations in the 2 – 4 m depth range.

Kruskal-Wallis evaluations reported in Tables 16 and 17 indicate that the salinity data sets from the paired profilers were statistically the same at both depth ranges for all five cruises. The Spearman’s rank correlation coefficients were also generally very strong in both depth ranges. The relatively low value of $\rho = 0.78$ evidenced in the GC1, 0.75 – 2 m data was a notable exception. Table 6 also indicated that there was a lower than normal correlation between the downcast and upcast data from the SBE49 in the same depth range. These observations could indicate the presence of an easily disturbed, shallow halocline at several stations during this cruise.

Table 16

Profiler – Profiler Evaluation: Salinity Relationship Analysis, 0.75-2m

Cruise	CTD Sensor #	Kruskal-Wallis p	Spearman's Rank Correlation		n
			ρ	p	
GCALL	1	0.31	0.94	0.00	225
GCALL	2	0.37	0.94	0.00	225
GC1	1	0.32	0.78	0.00	46
GC1	2	0.53	0.78	0.00	46
GC2	1	0.68	0.95	0.00	43
GC2	2	0.87	0.95	0.00	43
GC3	1	0.73	0.99	0.00	50
GC3	2	0.84	0.99	0.00	50
GC4	1	0.48	0.96	0.00	44
GC4	2	0.49	0.96	0.00	44
GC5	1	0.73	0.98	0.00	42
GC5	2	0.75	0.98	0.00	42

Notes. The SBE49 salinity data from the optical profiler is one member of each comparison. CTD 1 and CTD 2 represent salinity data from two separate sensors on the ships' water sampler profilers. Cruise "GCALL" was used when the evaluation was performed on the combined dataset for all five cruises.

Table 17

Profiler -Profiler Evaluation: Salinity Relationship Analysis, 2-4m Depth

Cruise	CTD Sensor #	Kruskal-Wallis p	Spearman's Rank Correlation		n
			ρ	p	
GCALL	1	0.62	0.98	0.00	238
GCALL	2	0.71	0.98	0.00	238
GC1	1	0.81	0.98	0.00	47
GC1	2	0.84	0.98	0.00	47
GC2	1	0.78	0.97	0.00	49
GC2	2	0.95	0.97	0.00	49
GC3	1	0.75	0.99	0.00	50
GC3	2	0.82	0.99	0.00	50
GC4	1	0.75	0.99	0.00	46
GC4	2	0.8	0.99	0.00	46
GC5	1	0.64	0.99	0.00	46
GC5	2	0.64	0.99	0.00	46

Notes. The SBE49 salinity data from the optical profiler is one member of each comparison. Cruise "GCALL" was used when the evaluation was performed on the combined dataset for all five cruises.

In a proof of concept exercise, all near-surface data (0.75 – 2 m and 2 – 4 m depth ranges) that evidenced at least a ± 1 PSU difference between the median salinity values reported from each profiler were examined more closely. In summary, if the effective median ± MAD ranges of the reported salinity values from each profiler overlapped, then the discrepancies were discounted since the median values could be considered statistically the same. In other cases, where one profiler had a lot more observations upon which to calculate median and MAD values, and no other mitigating factors, were discerned from the salinity data, a depth bias due to undersampling at the top of the water column (Figure 17) was assumed, and the reason for the salinity mismatch attributed to circumstances inherent to near-surface operations. (Here, the term “depth bias” refers to

the potential for the CTD sensor of one profiler to report a more saline value than the CTD on the other profiler due to one or both sensors under-sampling the given depth range (Figure 17).)

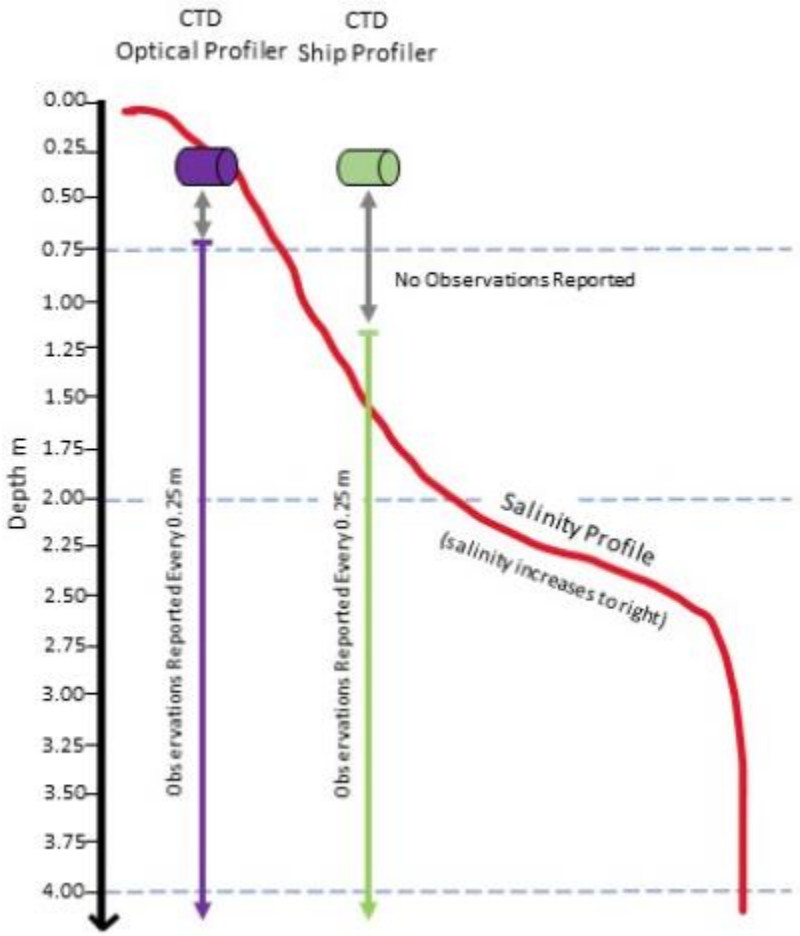

Figure 17. Depth Bias in Profiling Events

Under-sampling within a depth range may cause a higher median salinity value to be reported by one sensor with respect to the other. This circumstance is especially problematic where there is a large salinity gradient in the first few meters of the water column, a condition that often occurs in the presence of river plumes.

Other reasons for a salinity value mismatch could be attributed to environmental change experienced by the sampling area during the period of station occupation. This exercise does not attempt to discern whether environmental change was naturally occurring, caused by ship engines, or produced by equipment-induced mixing of near-

surface waters. In these cases, both CTD sensors had similar n values for the depth range in question even though there was a discrepancy in salinity values. Also, at some locations, a determination could not be made about the cause of the salinity value mismatch. Finally, there were 30 near surface locations that did not produce paired salinity data. Since the profiler to profiler evaluations could not be performed, an unknown level of uncertainty is inherent in any effort that attempted to correlate data originating from the two different profilers at those locations and depths. The results of these analyses are plotted in Figure 18. The waters near the mouth of Mobile Bay (station A1) experienced significant salinity mismatch during three of the five cruises for both of the near surface depth ranges.

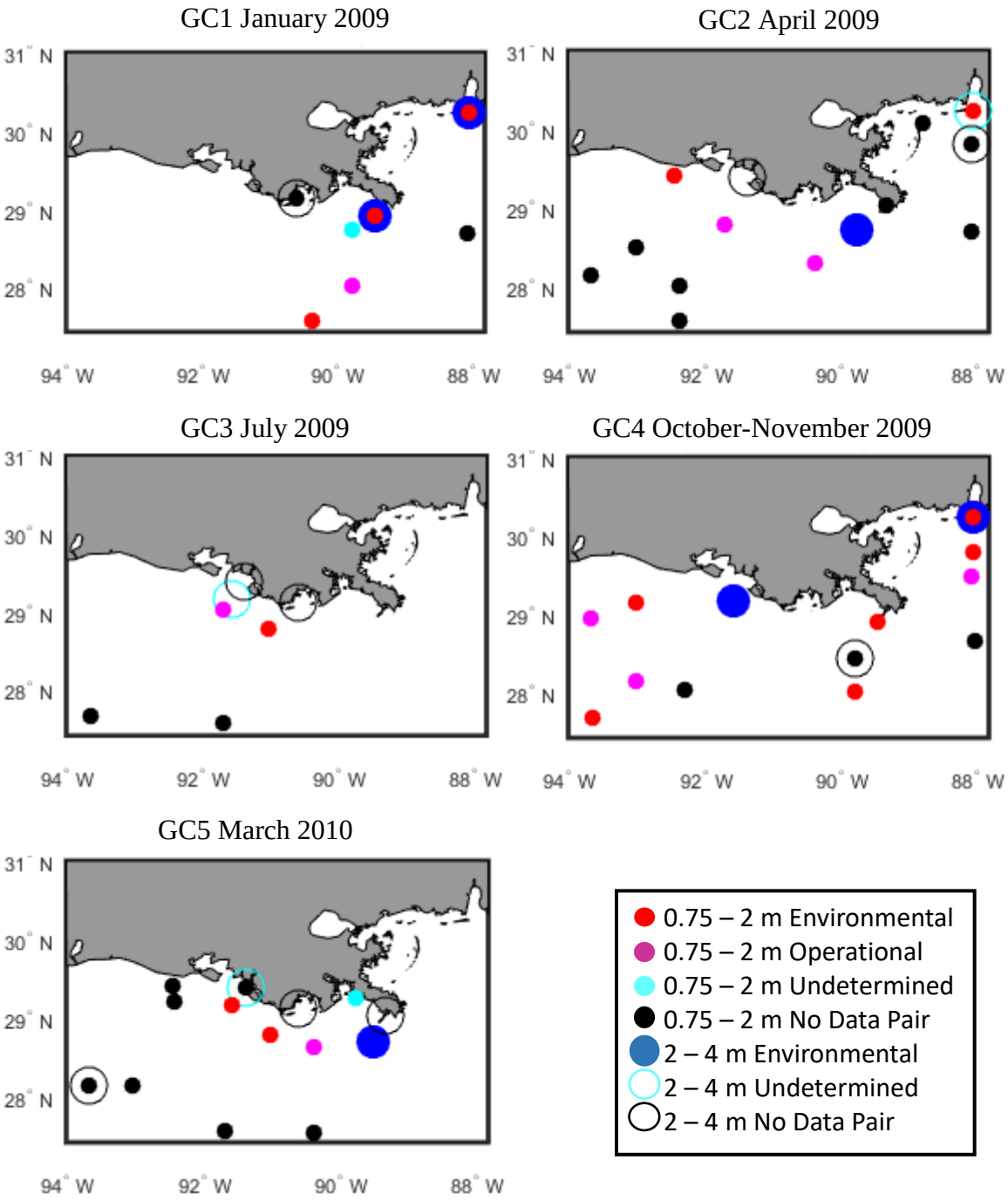

Figure 18. Near Surface Salinity Mismatch Locations

A mismatch is declared if the median salinity values reported by CTDs mounted on the ships' profilers or the optical profiler disagree by ± 1 PSU or more. Operational mismatches represent locations where it is believed that under-sampling in the near-surface waters by one of the profilers occurred. Environmental mismatches represent locations where apparent under-sampling did not occur.

For this research, salinity to salinity comparisons from multiple profilers were also evaluated at the filterdepths to identify locations where the sampling environment changed between profiling events. There was great variety in the number of observations available for salinity calculations at filterdepths (Table 18). Some of this variation was related to the actual depth of interest (whether or not it occurred at or less than 2 m). Some variation in salinity values reported by the different profilers occurred because, during cruises GC1 and GC2, the optical profiler was deployed twice at various stations. (Multiple deployments of the optical profiler also occurred twice during GC5.) Tables 18 and 19 report the salinity evaluations of all filterdepths related to each cruise. The subsets of filterdepths that occurred at 0.75 – 2 m and at greater than 2 m depths were also examined since it was thought that mismatches in the near surface waters could occur (Figure 19, plots c and d).

The number of observations available for the profiler to profiler evaluations varied greatly, from 4 ± 4 paired data points where all GC3 filterdepths were used in the evaluation to 20 ± 0 paired data points in the GC1 dataset where only filterdepths > 2 m were analyzed. As with the surface and near-surface salinity comparisons, these salinity to salinity relationships were closely related to each other with the lowest correlation value occurring during GC1 (Table 19). Occasional scattering on the salinity to salinity plots at filterdepths appeared to be biased towards higher salinity values from the ships' CTD profilers and relatively evenly distributed between all five cruises (Figure 19 plots a and b). Furthermore, nearly all of the scattering of the salinity data from the different profilers occurred at filterdepths that were less than 2 m (Figure 19, plots c and d). Although it is also clear that many of the filterdepths at less than 2 m were well

correlated (Figure 19, plots c and d, Table 19). This analysis indicates that the uncertainty introduced into evaluations involving filter samples from the CTD profiler could mostly be expected at depths less than 2 m.

Table 18

Profiler – Profiler Salinity Evaluation, Filterdepths

Cruise	Depths m	CTD #	n Filterdepths Per Profiler			n Observations Per Filterdepth Median (MAD)	
			Optics	CTD	Pairs	Optics	CTD
GCALL	all	1	414	402	360	8 (3)	10 (0)
GCALL	all	2	414	402	360	8 (3)	10 (0)
GCALL	>2	1	210	248	209	10 (0)	10 (0)
GCALL	>2	2	210	248	209	10 (0)	10 (0)
GC1	all	1	37	36	33	10 (5)	4.5 (4.5)
GC1	all	2	37	36	33	10 (5)	4.5 (4.5)
GC1	>2	1	15	18	15	20 (0)	10 (0)
GC1	>2	2	15	18	15	20 (0)	10 (0)
GC2	all	1	90	97	82	10 (5)	10 (0)
GC2	all	2	90	97	82	10 (5)	10 (0)
GC2	>2	1	51	64	51	10 (8.5)	10 (0)
GC2	>2	2	51	64	51	10 (8.5)	10 (0)
GC3	all	1	98	93	79	4 (4)	10 (0)
GC3	all	2	98	93	79	4 (4)	10 (0)
GC3	>2	1	48	61	48	10 (0)	10 (0)
GC3	>2	2	48	61	48	10 (0)	10 (0)
GC4	all	1	74	78	73	5 (3)	4 (3)
GC4	all	2	74	78	73	5 (3)	4 (3)
GC4	>2	1	30	35	30	10 (0)	10 (0)
GC4	>2	2	30	35	30	10 (0)	10 (0)
GC5	all	1	115	98	93	10 (0)	10 (0)
GC5	all	2	115	98	93	10 (0)	10 (0)
GC5	>2	1	66	70	65	10 (0)	10 (0)
GC5	>2	2	66	70	65	10 (0)	10 (0)

Notes. The SBE49 salinity data from the optical profiler is one member of each comparison. CTD 1 and CTD 2 represent salinity data from two separate sensors on the ships' water sampler profilers. Cruise "GCALL" occurred when the evaluation was performed on the combined dataset for all five cruises. MAD is the median absolute deviation. “Pairs” represents the number of instances where the CTD sensors on both profilers recorded observations at filterdepths.

Table 19

Profiler – Profiler Salinity Relationship Analysis, Filterdepths

Cruise	Depths m	CTD #	Kruskal Wallis p	Spearman's Rank Correlation		n
				ρ	p	
GCALL	all	1	0.36	0.98	0.00	360
GCALL	all	2	0.57	0.98	0.00	360
GCALL	>2	1	0.62	0.99	0.00	209
GCALL	>2	2	0.97	1	0.00	209
GC1	all	1	0.48	0.89	0.00	33
GC1	all	2	0.86	0.89	0.00	33
GC1	>2	1	0.76	1	0.00	15
GC1	>2	2	0.76	1	0.00	15
GC2	all	1	0.6	0.98	0.00	82
GC2	all	2	1	0.98	0.00	82
GC2	>2	1	0.65	0.98	0.00	51
GC2	>2	2	0.81	1	0.00	51
GC3	all	1	0.63	0.99	0.00	79
GC3	all	2	0.85	0.99	0.00	79
GC3	>2	1	0.67	0.99	0.00	48
GC3	>2	2	0.94	0.99	0.00	48
GC4	all	1	0.6	0.98	0.00	73
GC4	all	2	0.65	0.98	0.00	73
GC4	>2	1	0.69	1	0.00	30
GC4	>2	2	0.78	1	0.00	30
GC5	all	1	0.79	0.99	0.00	93
GC5	all	2	0.79	0.99	0.00	93
GC5	>2	1	0.86	1	0.00	65
GC5	>2	2	0.85	1	0.00	65

Notes. The SBE49 salinity data from the optical profiler is one member of each comparison. CTD 1 and CTD 2 represent salinity data from two separate sensors on the ships' water sampler profilers. Cruise "GCALL" occurred when the evaluation was performed on the combined dataset for all five cruises.

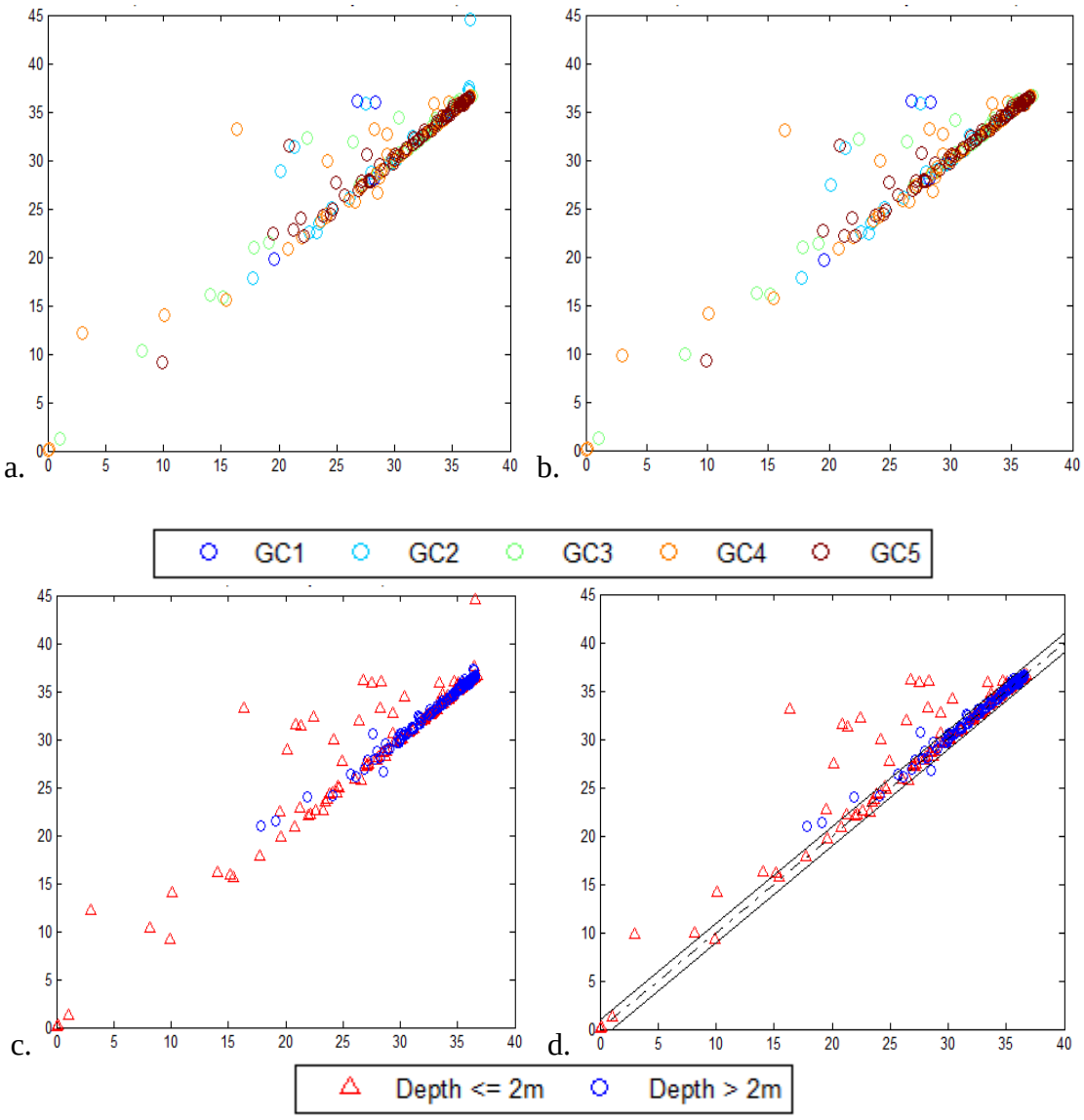

Figure 19. Profiler – Profiler Salinity Comparisons, Filterdepths

Profiler to profiler comparisons of salinity data (PSU) at filterdepths. The x-axes show the optical profiler (SBE49) salinity data. The y-axes show the CTD profiler salinity data. a. Optical profiler salinity versus CTD sensor 1 salinity. b. Optical profiler salinity versus CTD sensor 2 salinity. c. Optical profiler salinity versus CTD sensor 1 salinity; shallow water comparisons are emphasized. d. Optical profiler salinity versus CTD sensor 2 salinity; shallow water comparisons are emphasized. The dashed line shows a 1:1 relationship. Solid lines delineate ±1 PSU from the 1:1 relationship.

Regarding the filterdepth data, the majority of the salinity to salinity comparisons appear to have a 1:1 relationship. To reduce uncertainty introduced into the datasets used to develop algorithms, an acceptance zone of ±1 PSU to the 1:1 relationship of the

salinity data was applied. The locations (stations and depths) where the paired salinity data exceeded that acceptance zone were dropped from the datasets later used for algorithm development. In these cases, median uncertainty ranges were not considered prior to data removal. Locations, where paired salinity data were not available at filterdepths, were also excluded from algorithm development since the compatibility of the of the profiler to profiler observations could not be ascertained at those locations and filterdepths.

Uncertainties Related to Observations from Different Profilers Deployed Sequentially: Attenuation & Fluorescence

Another condition that must be considered in relation to the quality of the data pairs originating from different profilers is the possibility of seafloor disturbance, and the resuspension of SPM, by the sensor packages. If only the ship's CTD profilers were utilized for all observations related to filter samples and optical properties, the occurrence of SPM resuspension from the sea floor would have become a non-issue since all water samples and optical properties would have occurred under the same turbidity conditions. If, however, one profiler induced sea floor disturbance and the other did not then the data from the different profilers represented different sampling environments. To remove data produced under these circumstances an attempt was made to identify locations of seafloor disturbance by examining the profile and bottle capture data from the R/V Cape Hatteras' C-Star transmissometer (which measured attenuation at 650 nm) and the fluorometer sensors attached to the CTD profiler.

When the water sample bottles were given the command to close around the water at the pre-determined depths, the simultaneous sensor data was recorded (including

transmissometer and fluorometer observations). The downcast profile data and the discrete sensor data taken at the time of bottle capture were plotted together (Figure 20). In cases where the CTD profiler was believed to have induced increased turbidity by disturbing the seafloor, there was a sharp increase in the transmissometer values and often a markedly different (either higher or lower) fluorescence value.

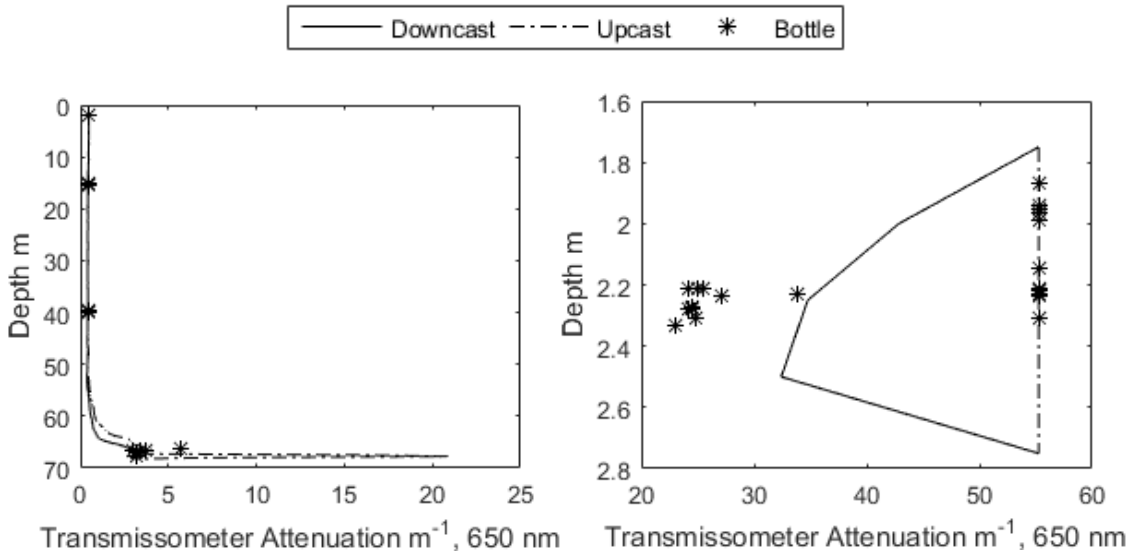

Figure 20. Examples of CTD-T

Examples of CTD-T from C-Star transmissometer data on the CTD profiler of the R/V Cape Hatteras. Left plot shows GC3, station D3. Right plot shows GC5, station C0. Transmissometer data at the time of water-capture by all Niskin bottles on the rosette are also plotted.

CTD profiler induced turbidity (CTD-T) was identified in several locations where near-bottom SPM samples were collected. This subset of filter samples was subsequently removed from consideration in regional SPM distribution and from analyses relating SPM to observations made by the optical profiler. The CTD profiler of the R/V Hugh R Sharp did not have a working transmissometer at the time but did employ a fluorescence sensor. Near-seafloor depths were examined using this data. Likewise, profiler-induced turbidity was evaluated in the attenuation data from the optical profiler.

Conclusions and Project Related Procedures

This chapter evaluated objectives relating to Hypothesis 1 of this project. Contrary to the hypothesis, data from sequential casts of the same profiler (or from sequential casts of different profilers) may not be universally assumed to represent the same sample space. However, this technique appears to observe the same sample space in many cases making sequential profiling a viable observation method so long as data quality methods like the ones described in this chapter are used. The analyses performed here have proven that there are cases, particularly in near-surface waters, where the assumption sequential profiler casts sample under the same conditions cannot be made. As a result of evaluations of multiple deployments of the optical profiler, and sequential deployments of different profilers, the strategy for managing digital profile data in this project has been expanded to include a step for managing these circumstances. The full procedure is summarized here:

1. A vertical offset was applied to the filtered water datasets to account for the distance between the center of the sample bottle and the CTD sensor. The value was then rounded off to the nearest quarter meter.
2. For the digital profiling dataset in question, the observational median and median absolute deviation (MAD) values were calculated using the point of comparable depth plus the observations within 0.5 m of that central vertical point of any filterdepth in question.
3. Regarding data sets from sensors that employed a pump, no data was considered from the top 0.5 m of the water column.

4. Regarding data sets from sensors that did not employ a pump, no data was considered from the top 0.25 m of the water column. The exception to this rule was the LISST data set which had a 1 m shallow cut-off.
5. At depths greater than 2 m, all available observations were used from both the downcast and the upcast data files.
6. At depths less than or equal to 2 m, only data from the upcast profile was used. This step applied to both near-surface data sets and filterdepth data sets.
7. In cases where there were multiple casts of the same profiler, data from both casts were combined and subjected to the previous steps. Data from filter-fitted absorption-attenuation sensors were not assimilated into these calculations.
8. Specific points involving multiple casts of the optical profiler were excluded from further algorithm development where there was a ± 1 PSU difference between the salinity data from sequential casts of the optical profiler.
9. Specific points where there was a ± 1 PSU difference between the salinity data from sequential casts of the different profilers were excluded from algorithm development.
10. Specific points where there was an apparent event of CTD-T were excluded from algorithm development.

CHAPTER IV – METHODS III: PERFORMANCE EVALUATIONS OF IOP SENSORS

Introduction

Chapter IV evaluates the profiling optical sensors used in this research. Some techniques utilized and developed for this dissertation have practical applications beyond this project. Other approaches described here have relevance only to the specific datasets related to this enterprise.

The identification and removal of mid-spectral artifacts in the ACS datasets is an example of a methods application that may have relevance beyond this project. The ACS sensor utilizes a linearly graded filter mounted on a rotating disk located between the source light and the sample space. As a space-saving mechanism, the light filter was cut into two pieces near 550 nm. Some observational overlap exists between the two halves of the complete spectrum (WET_Labs, 2009). Several factors related to the discontinuous or two-piece light filter may contribute to the creation of the mid-spectral artifacts. Physical degradation along the green edges of the optical filters may cause the observed wavelengths to be different than the reported ones. Additionally, slight nutation of the rotating disk could cause latency (timing) issues. In a similar fashion to the case of slight physical filter degradation, a tilting of the rotating disk containing the two halves of the linear filter could cause the source light to shine through a different wavelength than the one recorded at a given time. Latency inherent to healthy sensor operation may also contribute to artifact formation in the 488 μs temporal gap between the observations of the first and second halves of the spectra (WET_Labs, 2009) and the 62.5 ms it takes to

observe each half-spectrum (WET_Labs, 2009) since the particles and colloids in the sample space move both during and between observations.

The AC data were handled in a multi-step process. First, a method was developed to identify mid-spectral artifacts in the ACS products from the split in the filter window. Where artifacts were identified by this method, the affected data were removed, and the data loss due to this procedure was evaluated. Secondly, a comparison of AC9 and ACS was made. Based upon this assessment, all of the AC9 data from GC1 were removed from further analysis. Third, mid-cruise calibrations of the AC sensors were examined for evidence of sensor drift. None was found. Finally, uncertainties involved in the estimation of the absorption of pure water were also considered.

Saturation points for various profiling optical sensors were identified, and instances in the data where this occurred were removed from consideration. A depth-bias (different from the one discussed in Chapter III) is discovered in the GC4 data of the LISST and resolved. Additionally, a calibration-related bias was discovered in the LISST GC2 and GC3 datasets. These difficulties were also solved. Potential artifacts in the LISST data related to schlieren were identified and removed from further analysis. Finally, this chapter provides a discussion about the importance of the acceptance angles of the various attenuation sensors employed in this project relative to the reported c values.

AC9 & ACS Sensors

The AC9 and ACS sensors were deployed side-by-side on the optical profiler. Except for the 45 stations where two casts of the optical profiler were performed (see Chapter III and Table 11 for details), simultaneous observations were made of the

unmodified water column by the AC9 and the ACS. Both sensors were designed to report absorption (a) and attenuation (c) coefficients with the AC9 recording nine wavelengths and the ACS reporting 85 wavelengths. Each AC sensor demonstrated different advantages during this research. For example, both absorption and attenuation spectra produced by the ACS sensors resulted in a much greater resolution of data than the AC9 (Figure 21). However, as will be shown below, there was a serious quality control issue associated with the ACS. This problem resulted in the exclusion of significant quantities of ACS observations from the working datasets.

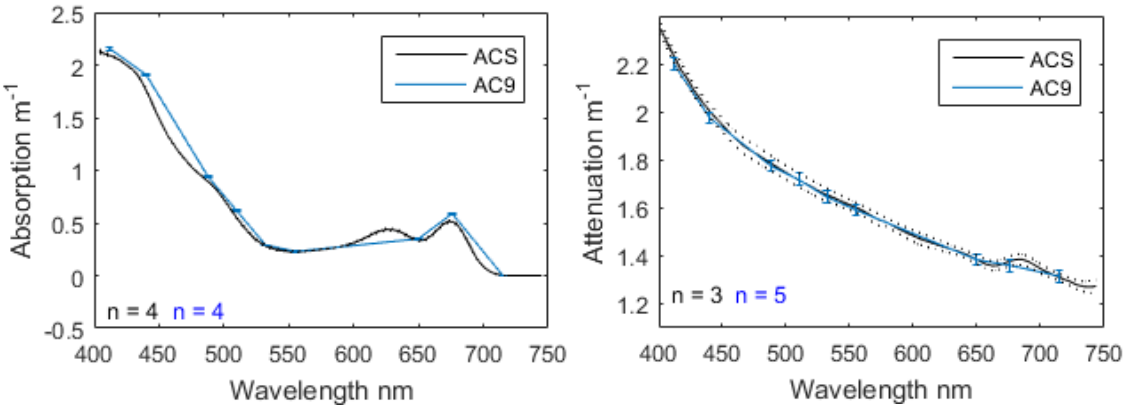

Figure 21. AC9 & ACS a & c Spectra Examples

Examples of the difference in spectral resolution between the AC9 and ACS observations. Median values (solid lines) are plotted along with the median absolute deviations (dotted lines and bars). Absorption spectra (left) are from GC3, station B1, 5.5 m. Attenuation spectra (right) are from GC2 station C2, 1.25 m.

ACS Data Anomalies and Processing Adjustments

Data quality concerns became apparent when absorption and attenuation spectra from the ACS were initially plotted for all filterdepths in this project. Mid-spectral artifacts frequently appeared between 576.6 nm and 581.7 nm in the absorption spectra and between 574.1 nm and 578.0 nm in the attenuation spectra. Figures 22 and 23

demonstrate examples of these mid-spectral artifacts for absorption and attenuation respectively.

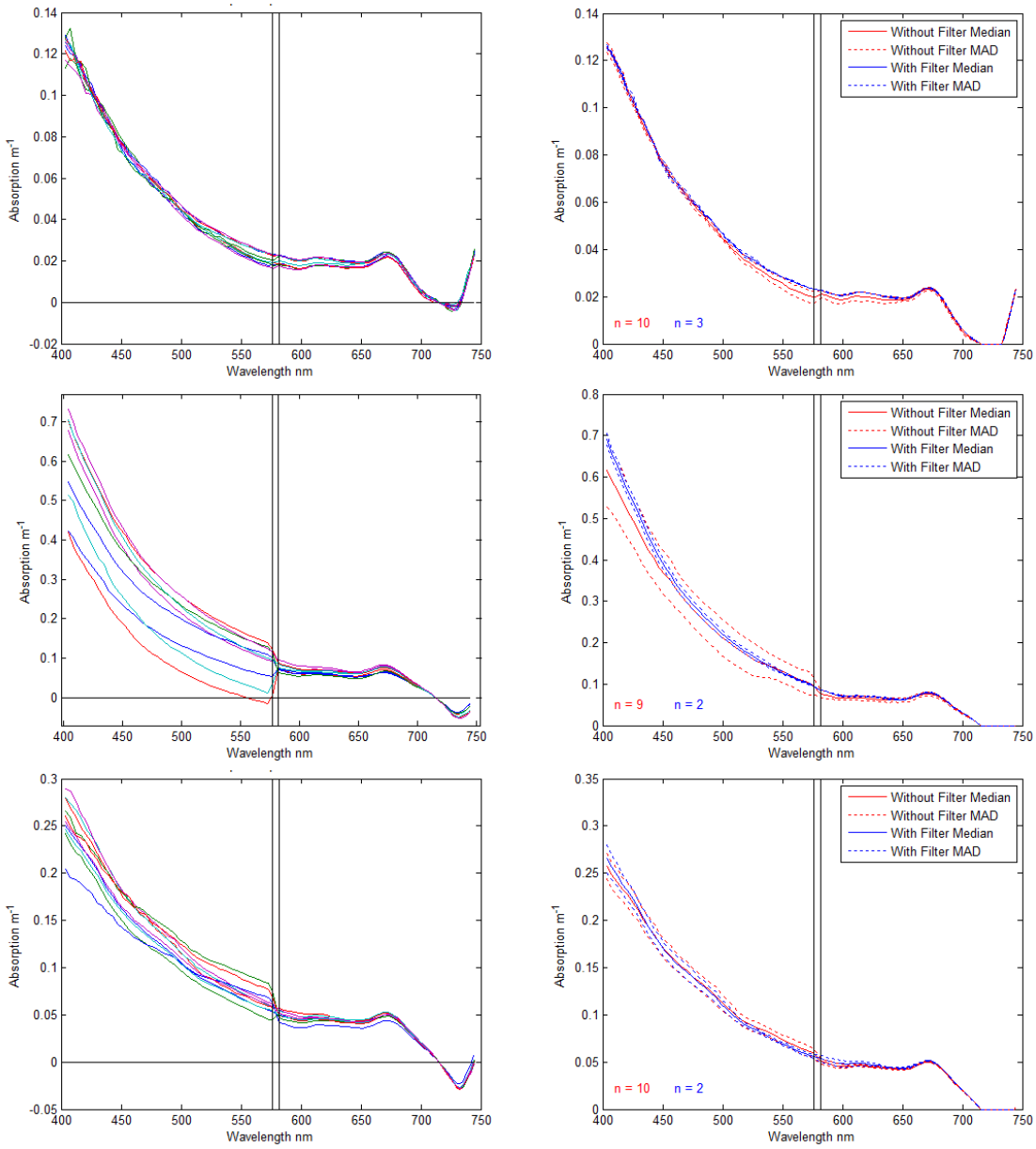

Figure 22. Absorption Mid-Spectral Artifacts

Examples mid-spectral artifacts in the absorption data from the ACS. Plots on the left show all of the individual spectra reported at 0.25 m depth increments included in selected filter depths. Plots on the right show the medians and median absolute deviations of these spectra both before and after spectra removal. Vertical lines denote the locations of 576.6 nm and 581.7 nm. The locations of these examples are GC5, station A6, 19.25 m depth (top), GC2, station G2, 14.25 m depth (middle), and GC2, station E4, 47.75 m depth (bottom).

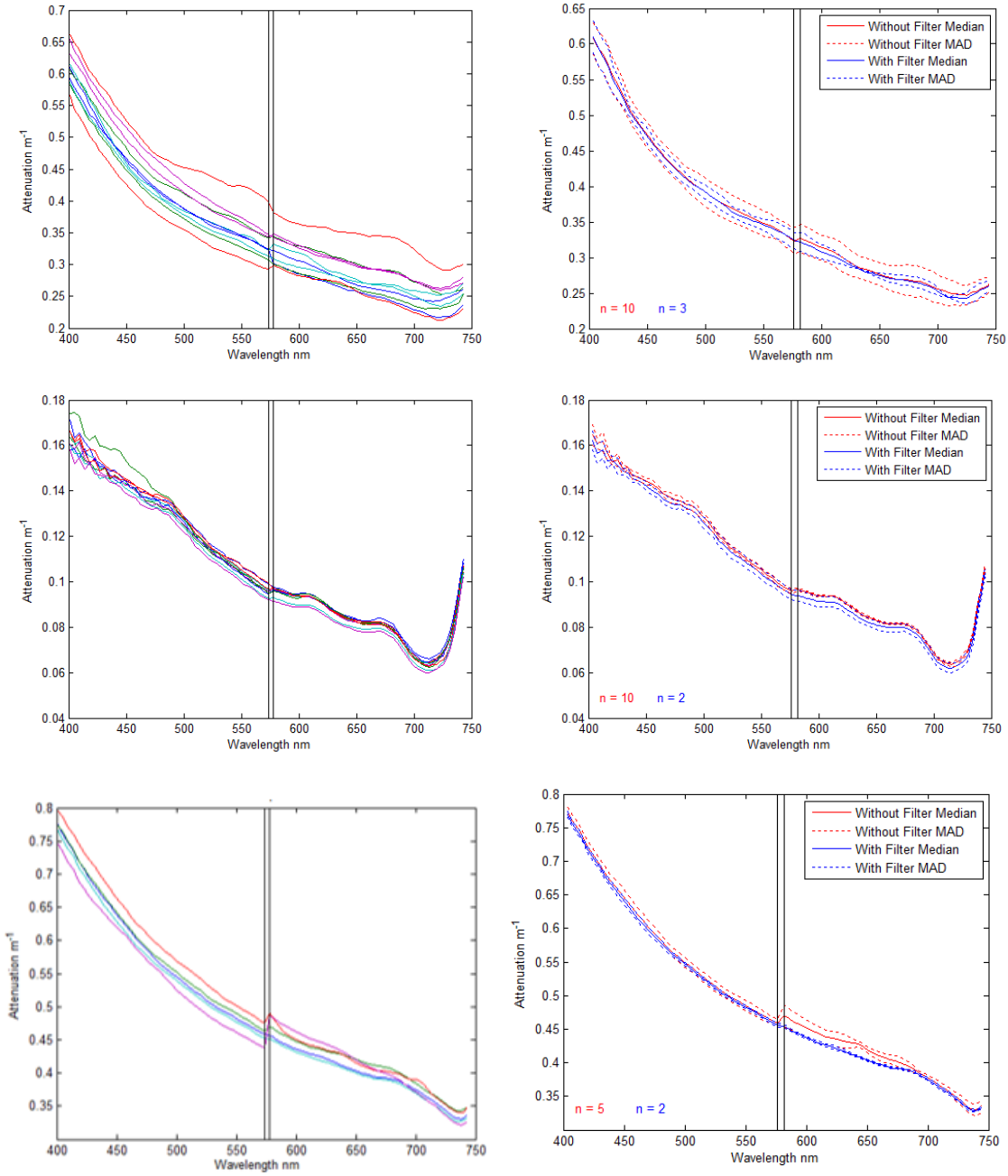

Figure 23. Attenuation Mid-Spectral Artifacts

Examples mid-spectral artifacts in the attenuation data from the ACS. Plots on the left show all of the individual spectra reported at 0.25 m depth increments included in selected filter depths. Plots on the right show the medians and median absolute deviations of these spectra both before and after spectra removal. Vertical lines denote the locations of 574.1 nm and 578.0 nm. The locations of these examples are GC1, station G1, 11 m depth (top), GC2, station H6, 81.5 m depth (middle), and GC4, station A4, 1.75 m depth (bottom).

The ACS absorption and attenuation mid-spectral anomalies may exhibit either positive or negative slope without apparent pattern or regularity. Sometimes the effects of these artifacts are reduced by the smoothing that occurred when the median values of spectral absorption or attenuation coefficients are calculated at filterdepths. However, such mitigation doesn't always result from using median values of the data about each filterdepth (Figures 22 and 23). Even the ACS-derived absorption and attenuation reported at every 0.25 m depth in the profiler data files represent averages of all sensor accepted spectra within the 0.25 m range about the reported depth. Thus, some smoothing was already inherent in the spectra reported in the downcast and upcast data files prior to further analysis performed during this research. These anomalies are present in a large percentage of the reported profile data and subsequently in further-processed filterdepth data. Therefore, the presence of these mid-spectral artifacts could not be removed by simply increasing the number of spectra per sample and calculating the mean or median of those spectra. In other words, there is a bias on one side or the other that cannot be removed by smoothing.

In developing a strategy to manage the ACS mid-spectral artifacts, it was decided that attempting to shift one or the other halves of the affected spectra up or down was impractical. (There was no way to determine which offset was correct.) Therefore, quality control efforts focused on removing complete individual spectra which contained artifacts from further analysis and algorithm development rather than attempting to impose an amplitude adjustment to affected spectra.

The methods used to identify spectra containing mid-spectral artifacts are described in terms of wavelength position along the 85-wavelength observational window

rather than by the wavelength itself since the observed wavelengths of the absorption and attenuation spectra don't match (see Table 1). Figure 24 demonstrates sample absorption and attenuation spectra both with and without these artifacts. The locations of these anomalies within the spectra are also plotted. The artifacts for both absorption and attenuation occur between the 38^{th} and 39^{th} reported wavelengths of the spectra and occasionally extend to a wavelength beyond those two points. Table 20 defines the corresponding wavelengths to these positions as they relate to the absorption and attenuation spectra. There, the amplitudes (A^x) represent the reported value of absorption or attenuation at the corresponding spectral positions (or wavelengths), P^x.

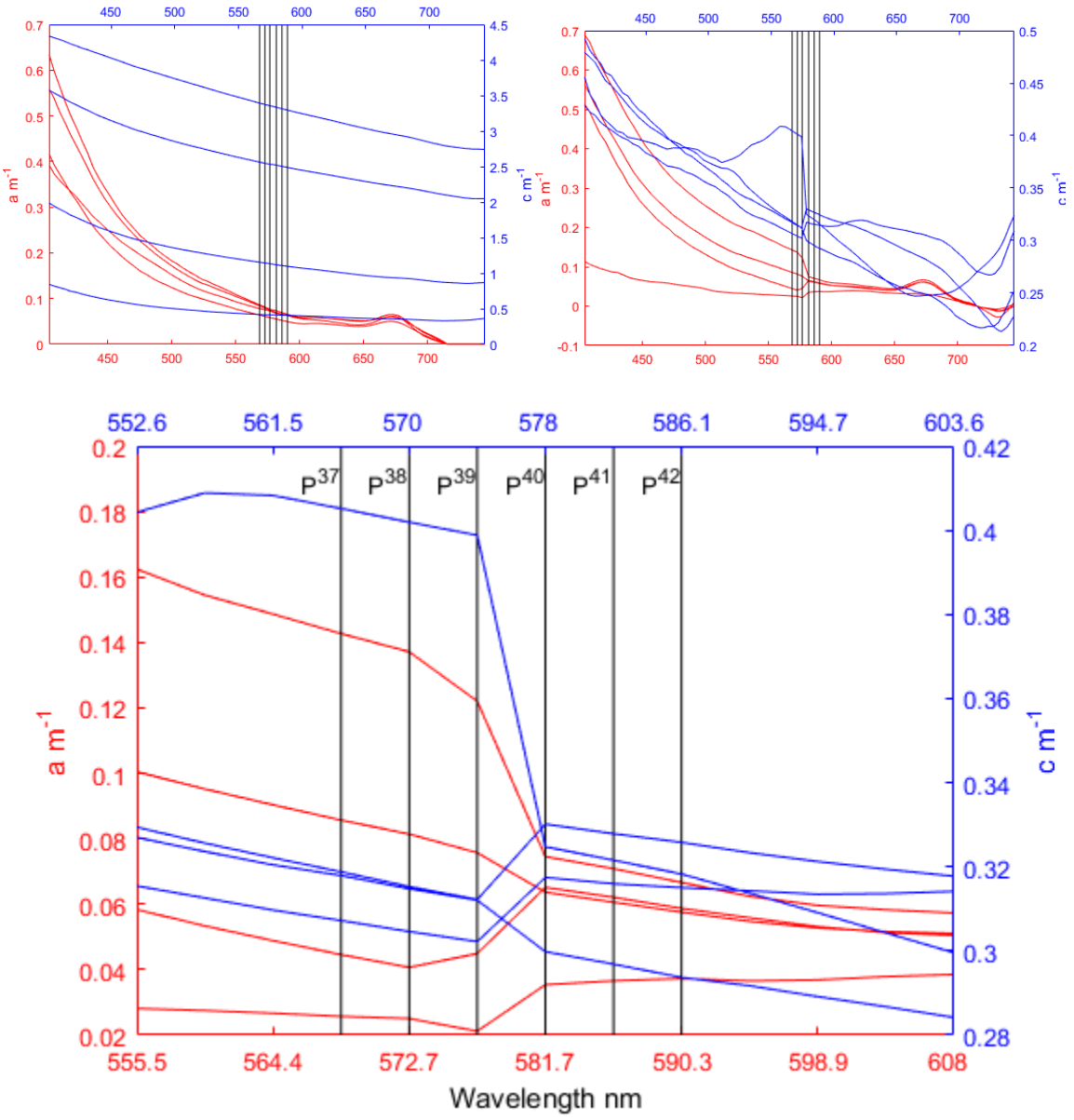

Figure 24. Mid-Spectral Artifact Positions & Wavelengths

ACS Absorption (red) and attenuation (blue) spectra. The top left plot displays median spectral values for quality- passed data. Both absorption and attenuation spectra are from GC2, A2 15.75 m, C1 10.25 m, E3 14.5 m and G4 43.0 m. The top right plot displays spectra that did not pass the quality control test. Absorption spectra come from GC2 C1 (downcast) 9.75 m and 10.25 m, C1 (upcast) 10.0 m, and E4 (upcast) 1.5 m. Attenuation spectra come from GC2 E4 (upcast) 1.5 m, D3 (upcast) 1.25 m, H5 (downcast) 2.75 m and (upcast) 53.05 m. The bottom plot displays a magnification of the upper right plot. Wavelength positions noted in Table 20 are noted in all plots.

Table 20

Variables used to Identify ACS Spectra with Mid-Spectral Artifacts

λ Position	λ Amplitude	a Wavelength nm	c Wavelength nm
P^{37}	A^{37}	568.6	565.6
P^{38}	A^{38}	572.7	570.0
P^{39}	A^{39}	576.6	574.1
P^{40}	A^{40}	581.7	578.0
P^{41}	A^{41}	586.1	582.0
P^{42}	A^{42}	590.3	586.1

Note. To use this table with an ACS absorption spectrum, wavelength position P37 occurs at wavelength 568.6 nm. It has an associated amplitude, A37, which has the value of absorption at 568.6 nm. Likewise, an ACS attenuation spectrum wavelength position, P37, occurs at 565.6 nm. It's associated amplitude, A37, is the value of attenuation at 565.6 nm. The wavelengths reported in this table correspond to the specific ACS used in this research and may not represent the same wavelengths associated with 37th through 42nd absorption and attenuation wavelengths reported by other ACS sensors.

$$v = \left|\frac{A^{38}-A^{37}}{P^{38}-P^{37}}\right| \quad (4.1)$$

$$w = \left|\frac{A^{39}-A^{38}}{P^{39}-P^{38}}\right| \quad (4.2)$$

$$z = \left|\frac{A^{40}-A^{39}}{P^{40}-P^{39}}\right| \quad (4.3)$$

$$d_{crit} = A^{40} - A^{39} \ \text{m}^{-1} \quad (4.4)$$

$$d_{ref} = A^{41} - A^{40} \ \text{m}^{-1} \quad (4.5)$$

$$d_{ref2} = A^{42} - A^{41} \ \text{m}^{-1} \quad (4.6)$$

The calculated values v, w, and z are slopes before, at, and after the critical points of artifact position. Values d_{crit}, $d_{ref,}$ and d_{ref2} represent the spectral amplitude difference at the critical spectral position and to reference positions to the right of the critical position

respectively. Based on these calculations, an absorption or attenuation spectrum was removed from further analysis if it met any of the following conditions:

1. $z > 1.5\ w$
2. $w > 1.5\ v$
3. If $d_{crit} \geq 0$ and either (or both) of the following conditions are true, then the spectrum was removed from further evaluation:
    a. $d_{ref} < 0$
    b. $d_{ref2} < 0$
2. In other words, in this project, if the slope on either side of the critical wavelengths (P^{38} and P^{39}) differed from the critical slope (w) by more than 50%, the entire spectrum was removed from further consideration. (This threshold value was somewhat subjective. However, other slope-percentage criteria were considered, and the critical slope threshold employed in this research appeared to work well for these datasets.) An ACS absorption or attenuation spectrum was also removed from further consideration if the critical slope was positive and either of the reference amplitude differences was negative. Figure 25 demonstrates these data quality decision processes graphically.

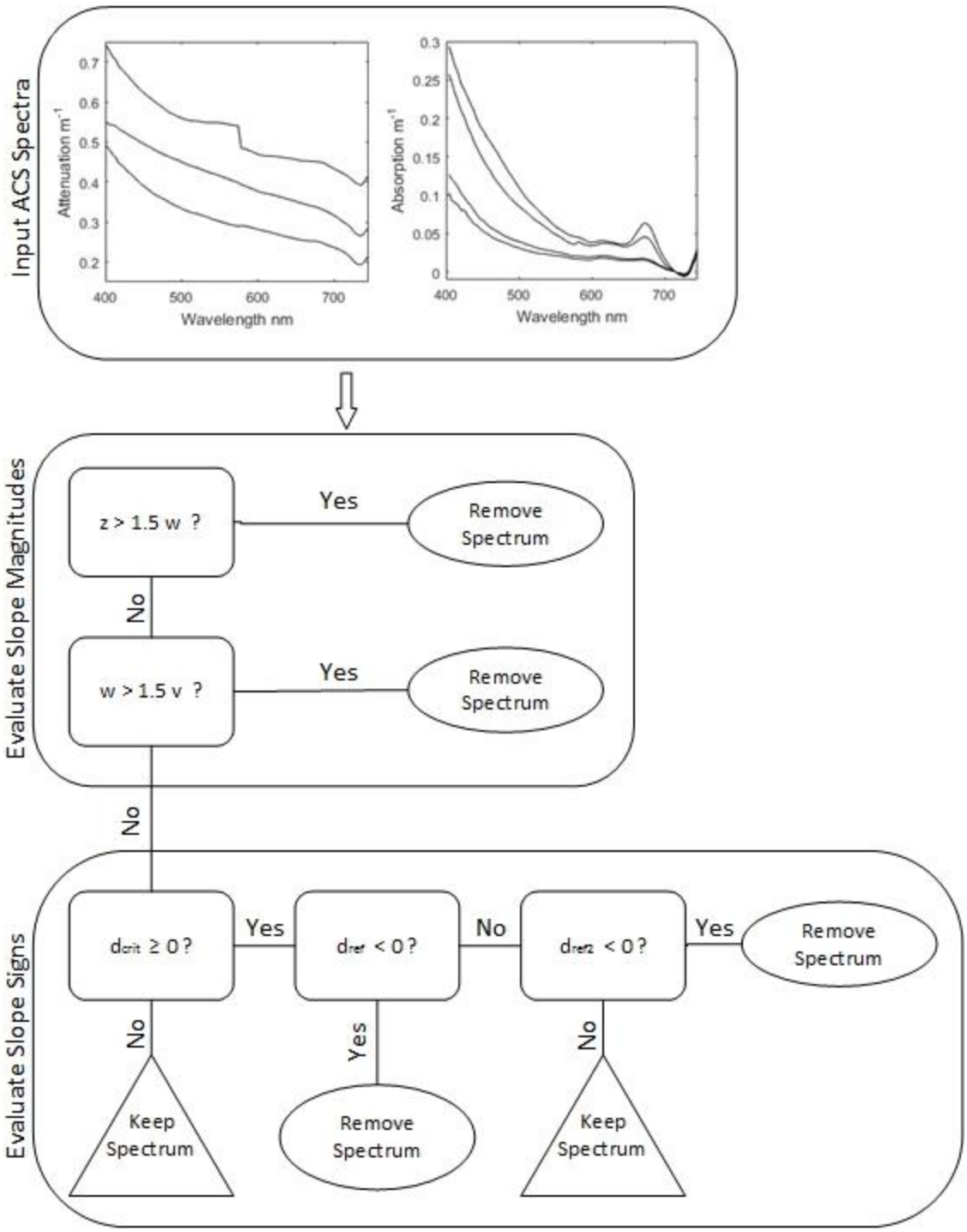

Figure 25. Decision Tree for ACS Spectra Removal

As a result of this artifact removal procedure, the remaining spectra were generally smoother near the critical wavelengths. Sometimes this change was also

accompanied by a visible amplitude shift which affected half of each full spectrum relative to unfiltered data. Examples of the results of this data removal process are seen in Figures 22 and 23.

Applying this quality control procedure resulted in significant data removal. Overall, the median percent absorption removal was 66.7 ± 21.6 (MAD), and the median percent attenuation removal was 55.7 ± 20.6 (MAD) per downcast or upcast file respectively. Distributions of the percent data removal are plotted in Figure 26. This data filter was applied to every ACS absorption and attenuation spectra. Filterdepth spectral values were then recalculated following this process so that only clean data were used for further analysis and algorithm development.

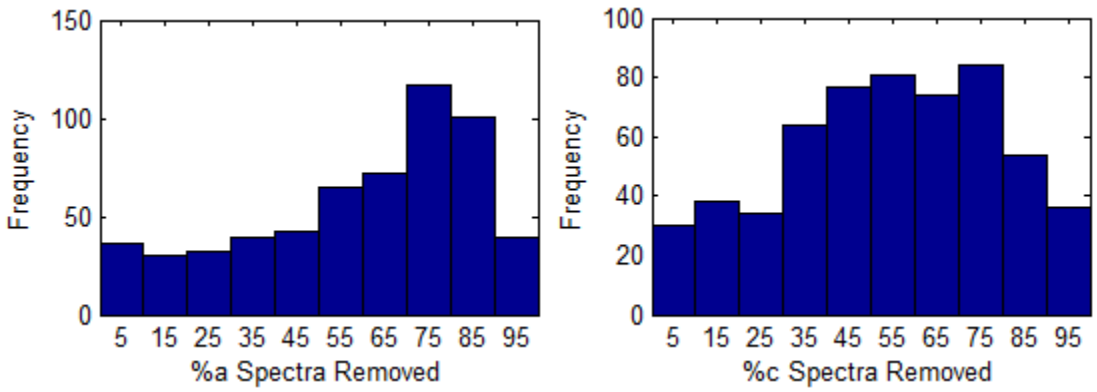

Figure 26. ACS Data Removal

Histograms of the percent data removal of the ACS absorption and attenuation spectra per data file from the downcast and upcast files of the optical profiler for during cruises GC1 through GC5.

AC9 & ACS Data Quality: Absorption

When deploying similar sensors side-by-side, one hopes that each instrument independently reports identical results. While the absorption coefficients reported by the AC9 and the ACS are similar, they frequently do not report the same absorption values, even though they are deployed side-by-side. To quantify how well the AC9 and the ACS

worked in relation to each other, Spearman correlation values were calculated between the absorption coefficients for each of the five cruises (Table 21). Since the AC9 and the ACS do not report the same wavelengths (Table 2), linear interpolation was applied to the ACS data to estimate absorption at the AC9 wavelengths of 412 nm, 440 nm, 488 nm, 510 nm, 532 nm, 555 nm, 650 nm, 676 nm, 715 nm for this analysis.

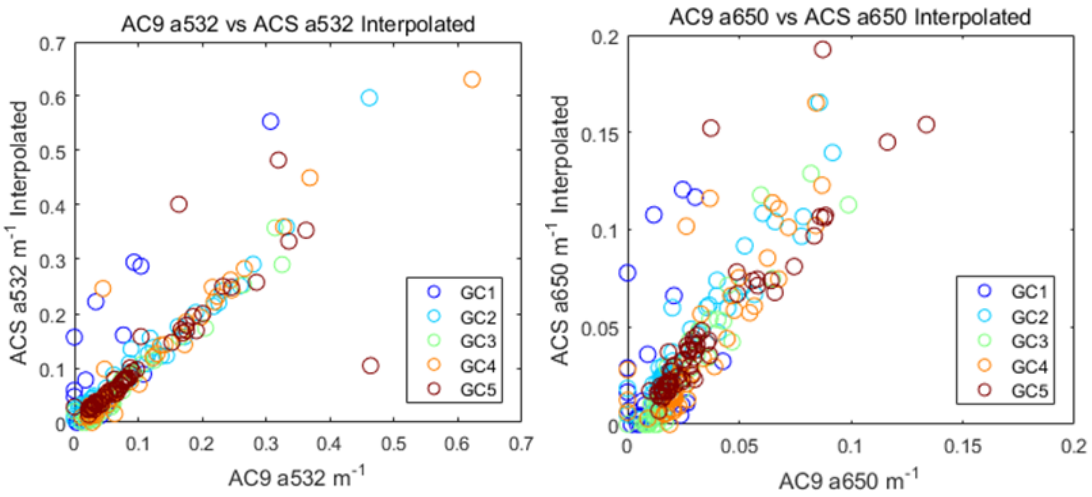

Figure 27. AC9 vs. ACS Absorption Selected Scatter Plots

These plots display selected wavelengths and ranges of data.

The results of the AC9 and ACS absorption coefficient analysis are two-fold. The correlation values are very different for GC1 than for the remaining four cruises. First, let's discuss what happened with the GC2 through GC5 absorption data. For cruises GC2 through GC5, the Spearman correlation values between the absorption sensors are relatively high for eight of the nine wavelengths. These values range from 0.86 ($p = 0.00$) to 0.99 ($p = 0.00$) (Table 21). The ninth wavelength, 715 nm, has much lower correlation coefficients between the absorption sensors than the other eight wavelengths. In fact, these values are so low that there does not appear to be any statistical relationship between the sensors at 715 nm at all. In most cases, the AC9 absorption value at 715 nm

is zero. This low correlation is likely due to 715 nm being used as the reference wavelength for AC9 temperature and salinity adjustments (Pegau et al., 1997). The ACS, on the other hand, usually reports a non-zero value at 715 nm. (Though the absorption value usually reaches zero at nearby wavelengths indicative of a longer wavelength being employed as a reference wavelength (Pegau et al., 1997) for the ACS). For GC4, the lack of any reported correlation value at 715 nm results from all the AC9 data having the value zero.

Unlike cruises GC2 – GC5, for GC1, the Spearman correlation values between the absorption coefficients reported by the two sensors were universally low (0.06, $p = 0.79$ to 0.52, $p = 0.01$). This poor correlation indicated a worrisome lack of agreement between the sensors. This phenomenon was also seen in the GC1 data of the scatter plots in Figure 27. Further analysis was performed.

Table 21

Relationship Between AC9 and ACS Absorption, Filterdepths

Wavelength nm	GC1 AC9 to Interpolated ACS Absorption Spearman Rank Correlation Values			GC2 AC9 to Interpolated ACS Absorption Spearman Rank Correlation Values			GC3 AC9 to Interpolated ACS Absorption Spearman Rank Correlation Values		
	ρ	p	n	ρ	p	n	ρ	p	n
412	0.50	0.01	23	0.88	0.00	63	0.98	0.00	36
440	0.43	0.04	23	0.96	0.00	63	0.97	0.00	36
488	0.47	0.02	23	0.93	0.00	63	0.98	0.00	36
510	0.41	0.05	23	0.91	0.00	63	0.96	0.00	36
532	0.41	0.05	23	0.90	0.00	63	0.94	0.00	36
555	0.40	0.06	23	0.91	0.00	63	0.93	0.00	36
650	0.20	0.35	23	0.91	0.00	63	0.93	0.00	36
676	-0.07	0.75	23	0.87	0.00	63	0.86	0.00	36
715	0.20	0.35	23	0.22	0.09	63	0.06	0.74	36

Table 21 (continued).

Wavelength nm	GC4 AC9 to Interpolated ACS Absorption Spearman Rank Correlation Values			GC5 AC9 to Interpolated ACS Absorption Spearman Rank Correlation Values			GC2 - GC5 AC9 to Interpolated ACS Absorption Spearman Rank Correlation Values		
	ρ	p	n	ρ	p	n	ρ	p	n
412	0.86	0.00	49	0.99	0.00	70	0.86	0.00	218
440	0.98	0.00	49	0.99	0.00	70	0.98	0.00	218
488	0.94	0.00	49	0.98	0.00	70	0.94	0.00	218
510	0.92	0.00	49	0.99	0.00	70	0.92	0.00	218
532	0.90	0.00	49	0.98	0.00	70	0.90	0.00	218
555	0.92	0.00	49	0.96	0.00	70	0.92	0.00	218
650	0.90	0.00	49	0.94	0.00	70	0.90	0.00	218
676	0.82	0.00	49	0.94	0.00	70	0.82	0.00	218
715	NaN	NaN	49	0.01	0.90	70	NaN	NaN	218

Notes: Salinity and profiler induced turbidity-based exclusions were applied. The ACS data filter was applied. Visual inspection exclusions were applied.

To further investigate the quality of the absorption data and gain additional insight into the low correlation values between the AC9 and the ACS for GC1, the data were also evaluated by calculating the spectral Spearman's ρ between the absorption coefficient and SPM concentration for both sensors and each cruise (Figure 28). Data exclusions based upon salinity comparisons, bottom disturbance, and ACS quality control procedures were applied prior to producing this figure. Since the AC9 and the ACS were deployed side-by-side, it was expected that these absorption-to-SPM correlation coefficients would coincide where similar wavelengths were recorded.

While the expectation of well-matched absorption-to-SPM correlation coefficients between the AC9 and ACS generally occurred, there were a couple of glaring discrepancies reported by the different sensors. A notable trend of low correlation between SPM concentration and absorption coefficients at all nine wavelengths of the AC9 occurred during GC1. This result was similar to the low correlation values calculated between all nine wavelengths of the two absorption datasets from GC1. Significantly, all of the correlation values for absorption by the ACS sensor in relation to SPM were close to either 1 or -1 for all five cruises, even during GC1. (The exception to this is seen between 700 nm and 730 nm and applied to both sensors.) The circumstance of high ACS absorption-to-SPM correlation coupled with the low GC1 correlation values between absorption coefficient values measured by the AC9 and the ACS (Table 21) indicated that there was something wrong either with the AC9 sensor or with the processing of that cruise's absorption data. (An environmental cause for low absorption-to-SPM correlation values should have been evident in the relationship between SPM and the ACS absorption data in addition to the relationship between SPM and the AC9

absorption values.) Since similar trends were not evident in the remaining four cruises, and since the same problem of low SPM-to-IOP correlation also occurred with the attenuation sensor of the AC9, it was concluded that the GC1 calibrations related to the AC9 for the second half of the cruise were inaccurate. (This was the only part of cruise GC1 where data from the filter samples were trusted.) Therefore, the absorption values reported by the AC9 during GC1 were excluded from further analysis and algorithm development. (Note. It is possible that this problem was not experienced during the first half of GC1, prior to the mid-cruise calibration event. Since SPM samples from this period were not evaluated, concurrent AC9 data from the first half of GC1 were also not evaluated for calibration error using the methods described here.)

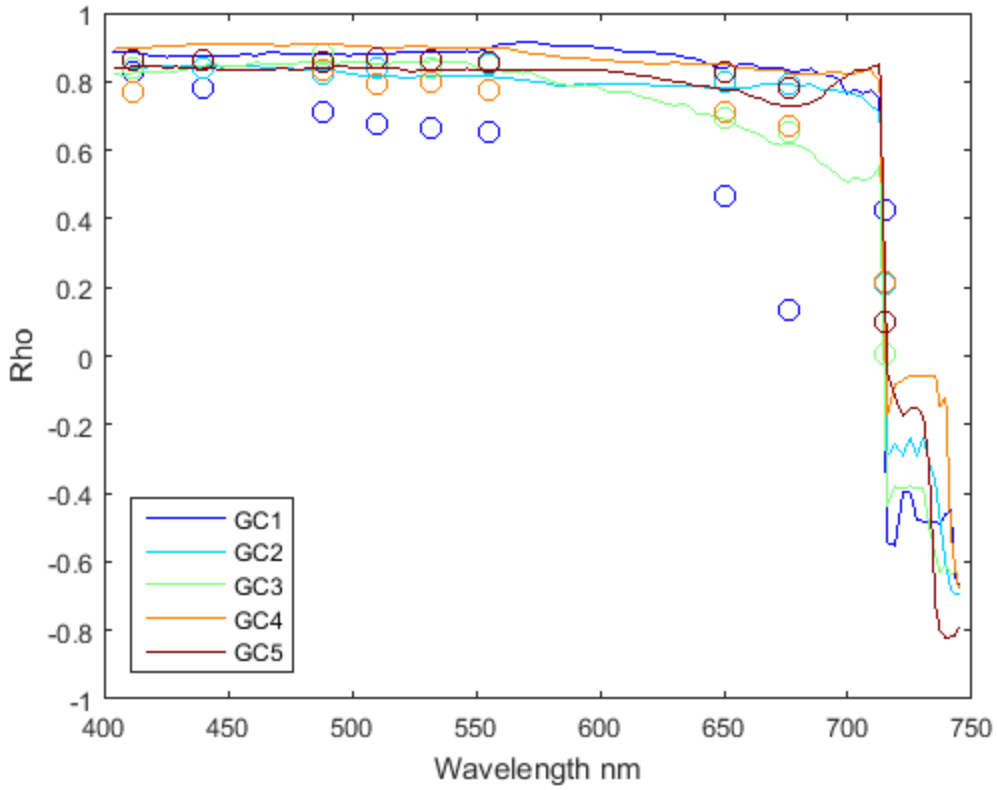

Figure 28. Spectral Spearman's Rho Relating SPM to Absorption

The plot of Spearman's rho relating SPM to absorption calculated from AC9 and ACS observations. Continuous lines represent this relationship using ACS data. Dots represent this relationship using AC9 data.

The second case of lower SPM-to-absorption correlation coefficients occurred during GC3 (Figure 28). For all cruises, absorption-to-SPM correlation coefficients decreased nonlinearly with increasing wavelength between about 530 nm and 715 nm. During GC3, this trend was more evident. Since this phenomenon did not occur to such a noticeable extent in the ACS data for the other four cruises, it was thought that there might have been a calibration problem similar to the one experienced by the AC9 during GC1. To further examine that idea, the absorption data from both AC sensors were divided into two groups depending upon whether they were collected before or after the mid-cruise calibration for cruises GC2 and GC3. (Mid-cruise calibration events did not occur during GC4, or GC5 and data from the AC9 were not used during GC1, therefore

only cruises GC2, and GC3 had this analysis applied to them.) Both absorption-to-absorption correlation values and absorption-to-SPM correlation values were evaluated for the first and second halves of each cruise.

The examination of the quality of the absorption data relative to mid-cruise sensor calibration events yields slightly lower correlation values between the longer wavelengths of the absorption sensors for the first parts of GC2 and GC3. Furthermore, there is a much weaker relationship between SPM and the longer wavelengths during the first half of GC3 (calibration 1) than during the second half (calibration 2) for the AC9. Similar correlation calculations between SPM and absorption wavelengths of the ACS revealed lower values for the longer wavelengths relative to shorter ones. These ACS values remained consistent across the mid-cruise calibration event. Since the sensor-based absorption-to-absorption values were fairly well correlated, it appears that the poorer correlation between SPM and the longer wavelengths of absorption was produced by the state of the water parcels sampled rather than by mechanical or processing errors.

Another potential source of uncertainty in the absorption data is the inherent error associated with pure water absorption (a_w). Figure 29 is based on the work of Smith and Baker (R. C. Smith & Baker, 1981) who performed a careful analysis of this property. Observation wavelengths used by the AC9 and BB9 are noted in this figure. With increasing wavelength, increasing absorption values and uncertainties can be observed. (Though the a_w coefficients in the blue wavelengths are small compared to other parts of the absorption spectrum, later research has suggested that these values may have suffered some scattering contamination which effectively increased the a_w values reported below 500 nm by two or three-fold (Fry, 2013). Even though the Smith and Baker values of a_w

are not applied to the AC9 and ACS observations, the possibility of a_w, represented pure water calibration events, being enhanced by forward scattering for the shorter wavelengths may influence the shape of spectral absorption curves.) Likewise, it is possible that the slightly lower correlation coefficients between absorption and SPM at higher wavelengths are influenced by the greater amount of variability associated with the a_w at the longer wavelengths. Additionally, absorption values produced by the AC sensors generally decrease with increasing wavelength (Figure 21) making any uncertainties related to pure water absorption more pronounced in the longer wavelengths.

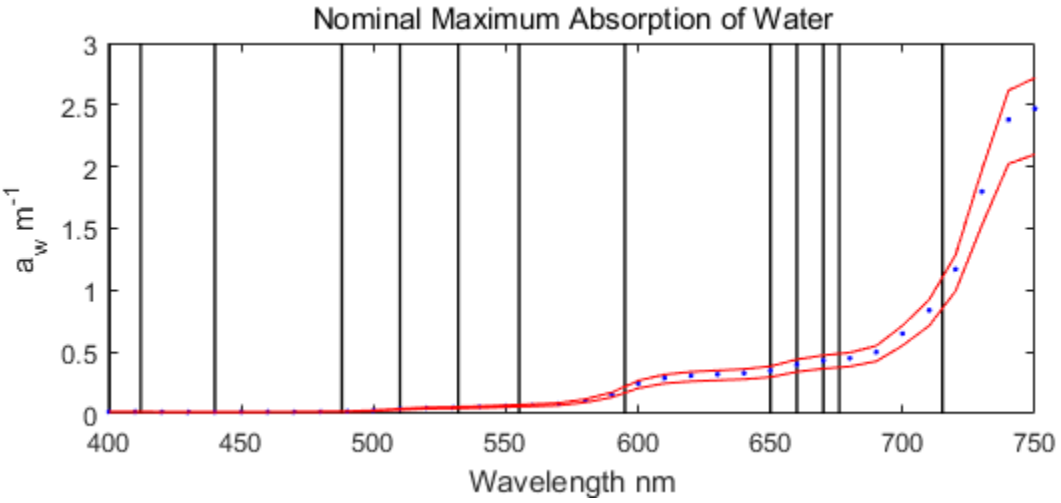

Figure 29. Absorption Spectrum of Pure Water

Nominal maximum absorption of pure water (blue dots) with uncertainty (red lines) based on Smith and Baker (R. C. Smith & Baker, 1981). AC9, BB9, and LISST wavelengths are noted with vertical lines.

As a final process for quality control of absorption data, a visual inspection was performed of each filterdepth spectrum. (Examples may be viewed in Figure 30.) Some of those plots displayed highly suspicious features in relation to spectra recorded at nearby depths raising questions about the validity of the affected sensor reports. These

features included spiky spectra or absorption values ≤ 0 over a large range of wavelengths. These anomalies were most often noted in the near-surface subset of the filterdepth data and were removed from algorithm development after visual inspection.

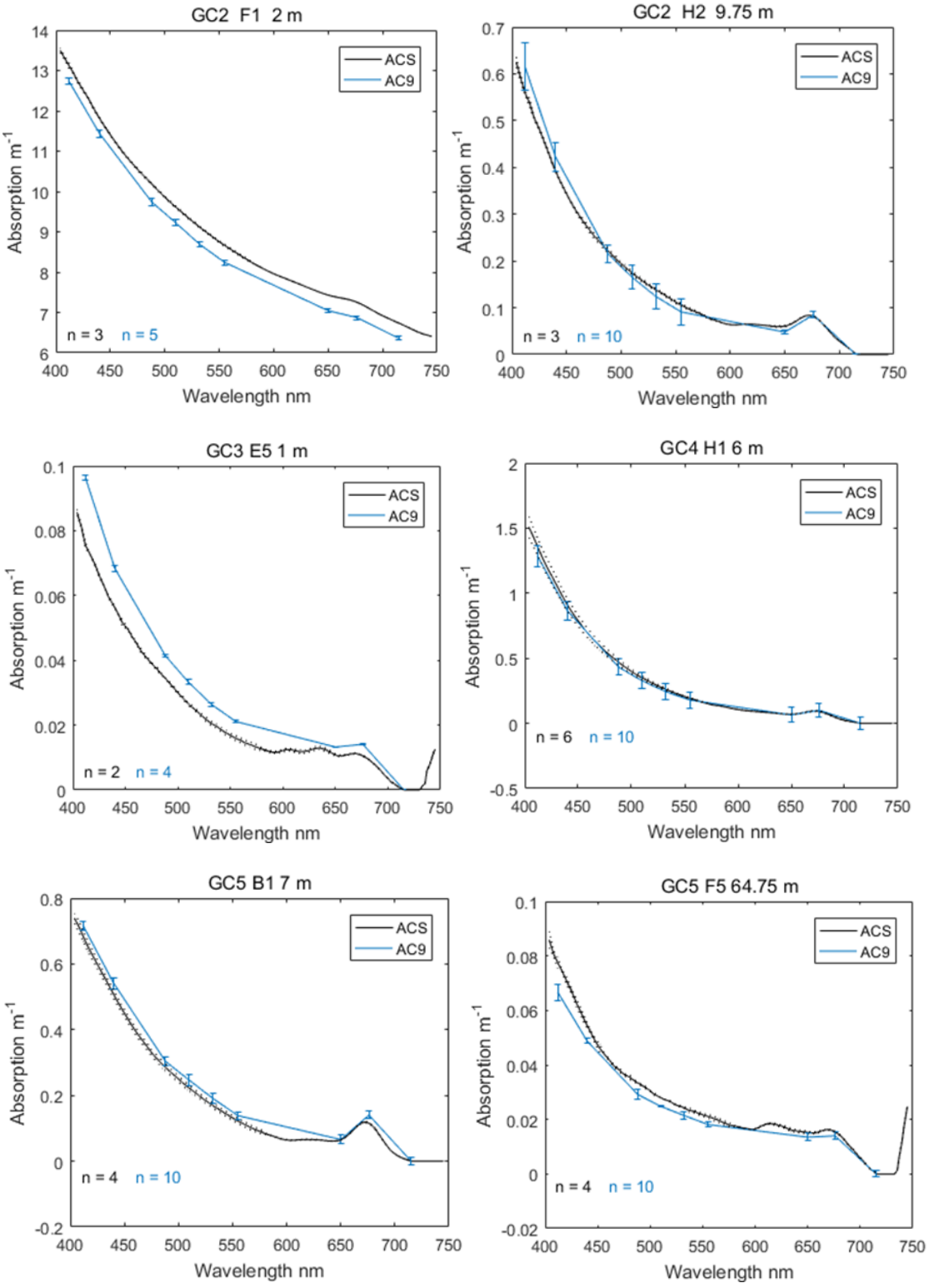

Figure 30. Absorption Spectra Examples

Cruise, station, and filterdetpths are identified at the top of each plot. Dotted lines and intervals represent MAD values.

AC9 & ACS Data Quality: Attenuation

The initial quality assessment procedure for the attenuation data produced by the AC9 and the ACS was identical to the treatment of the absorption data. Thus, ACS mid-spectral artifacts were removed from further analysis using the methods described. Plots for spectral attenuation reported by the AC9 and the ACS are drawn for each filterdepth following all data quality checks. Examples may be viewed in Figure 31. These plots also include the quality-accepted attenuation data from the transmissometer and LISST sensors. (The differences between the reported values between these sensors and the AC instruments are addressed later in this chapter.) Similar to the absorption spectra at filterdepths, these plots make it clear that although the attenuation from the AC9 and the ACS are related, they frequently do not report the same values, even though the sensors are deployed side-by-side. Table 22 shows the results of the Spearman correlation analysis between the attenuation coefficients as reported by the two sensors. Example scatter plots relating attenuation between the two AC sensors are drawn in Figure 31.

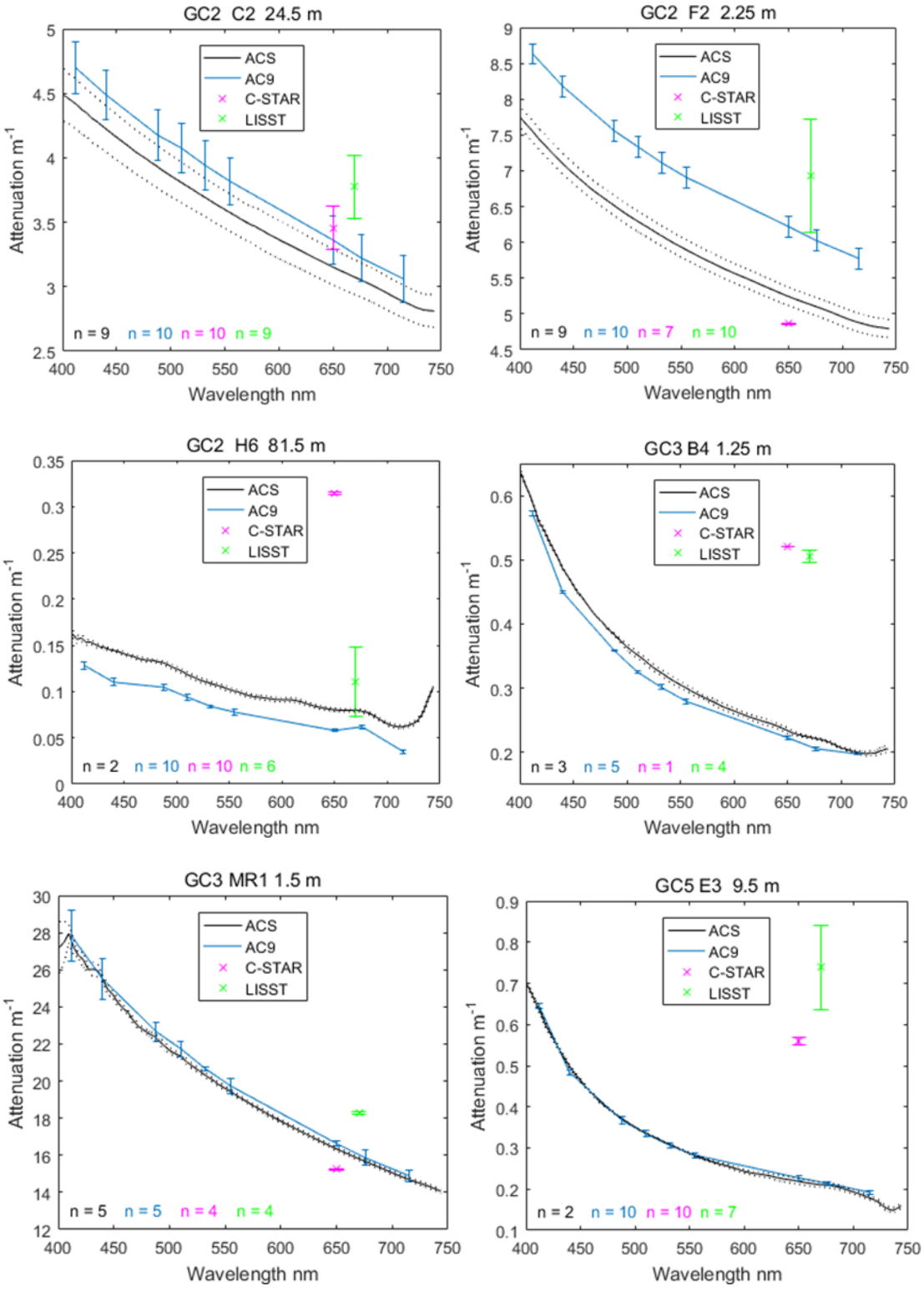

Figure 31. Example Attenuation Spectra

Cruise, station, and filterdetpths are identified at the top of each plot. Dotted lines and intervals represent MAD values.

Table 22

Relationship Between AC9 & ACS Attenuation, Filterdepths

Wavelength nm	GC1 AC9 to Interpolated ACS Attenuation Spearman Rank Correlation Values			GC2 AC9 to Interpolated ACS Attenuation Spearman Rank Correlation Values			GC3 AC9 to Interpolated ACS Attenuation Spearman Rank Correlation Values		
	ρ	p	n	ρ	p	n	ρ	p	n
412	0.50	0.01	25	0.97	0.00	61	1.00	0.00	54
440	0.47	0.02	25	0.97	0.00	61	1.00	0.00	54
488	0.33	0.10	25	0.97	0.00	61	1.00	0.00	54
510	0.19	0.35	25	0.97	0.00	61	1.00	0.00	54
532	0.17	0.42	25	0.97	0.00	61	1.00	0.00	54
555	0.20	0.33	25	0.97	0.00	61	1.00	0.00	54
650	0.11	0.59	25	0.97	0.00	61	0.99	0.00	54
676	0.11	0.60	25	0.97	0.00	61	0.99	0.00	54
715	-0.06	0.78	25	0.97	0.00	61	0.99	0.00	54

Table 22 (continued).

Wavelength nm	GC4 AC9 to Interpolated ACS Attenuation Spearman Rank Correlation Values			GC5 AC9 to Interpolated ACS Attenuation Spearman Rank Correlation Values			GC2 - GC5 AC9 to Interpolated ACS Absorption Spearman Rank Correlation Values		
	ρ	p	n	ρ	p	n	ρ	p	n
412	0.96	0.00	56	0.98	0.00	79	0.96	0.00	250
440	0.96	0.00	56	0.98	0.00	79	0.96	0.00	250
488	0.95	0.00	56	0.98	0.00	79	0.95	0.00	250
510	0.95	0.00	56	0.98	0.00	79	0.95	0.00	250
532	0.95	0.00	56	0.98	0.00	79	0.95	0.00	250
555	0.95	0.00	56	0.98	0.00	79	0.95	0.00	250
650	0.95	0.00	56	0.98	0.00	79	0.95	0.00	250
676	0.95	0.00	56	0.98	0.00	79	0.95	0.00	250
715	0.95	0.00	56	0.98	0.00	79	0.95	0.00	250

Notes: Salinity and profiler induced turbidity-based exclusions were applied. The ACS data filter was applied. Visual inspection exclusions were applied.

Regarding cruises GC2 through GC5, the correlation values of the attenuation coefficients between the sensors are relatively high for eight of the nine wavelengths (all wavelengths except for 715 nm) ranging from 0.94 (p = 0.00) to 1.00 (p = 0.00). Overall, there is a better agreement between the two attenuation sensors than the absorption sensors. Similar to the results of the quality analysis of the absorption data, the Spearman Rank correlation values between the attenuation coefficients as reported by the two sensors for GC1 were universally low, again indicating a lack of agreement between the sensors for at least the second half of that cruise. The scatter plots in Figure 32 clearly demonstrate this lack of correlation for GC1.

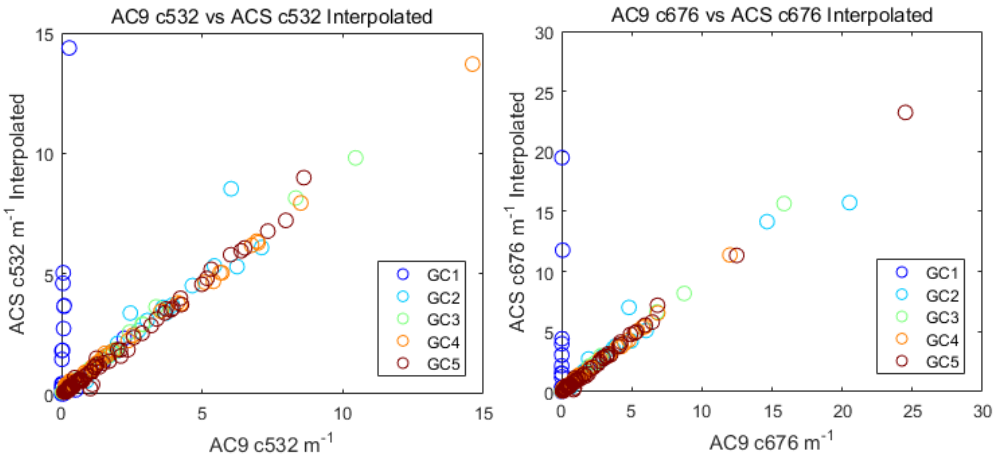

Figure 32. AC9 c vs. ACS c Selected Scatter Plots

These plots display selected wavelengths and ranges of data.

As with the absorption data, the quality of the attenuation data for GC1 was considered questionable and further evaluated by calculating the spectral Spearman's rho between attenuation and SPM concentration for each cruise (Figure 33). It was expected that the SPM-attenuation correlation coefficients would match up well between the AC9 and ACS datasets where similar wavelengths were recorded. Generally, that is what

occurred for cruises GC2 thru GC5. As with the absorption sensor on the AC9, it was concluded that the GC1 calibration values for attenuation were inaccurate for at least the second half of the cruise. Consequently, the GC1 attenuation data produced by the AC9 were excluded from further evaluation and algorithm development. Unlike the absorption data, the accepted attenuation data correlation coefficients are stable across the observed wavelengths. The attenuation data did not demonstrate a lessening of correlation to SPM with increasing wavelength during GC3.

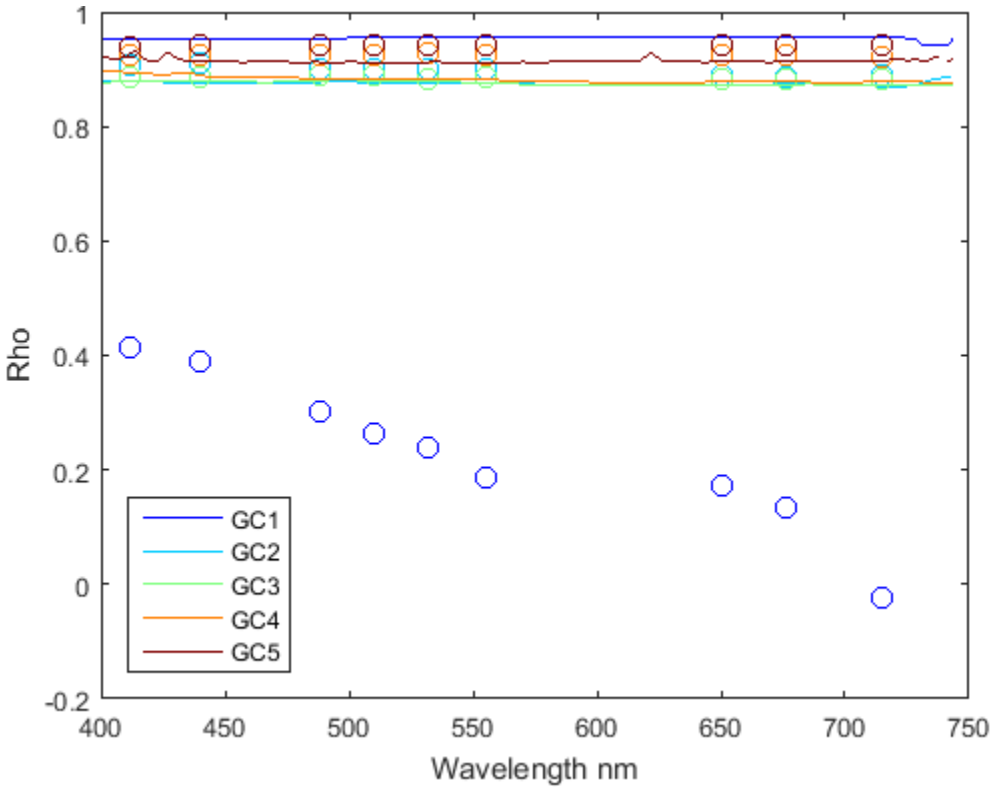

Figure 33. Spectral Spearman's Rho Relating SPM to Attenuation

The plot of Spearman's rho relating SPM to attenuation calculated from AC9 and ACS observations. Continuous lines represent this relationship using ACS data. Dots represent this relationship using AC9 data.

Finally, a visual inspection was performed of the median ± MAD plots of the filterdepth spectra for attenuation values related to both the AC9 and the ACS sensors.

Spectra that were obviously distorted were removed from the working data set. Most of these affected spectra were collected near the sea surface where it is believed bubbles may have interfered with the signal.

Transmissometer Data Quality: Attenuation 650 nm

The C-Star transmissometer deployed on the CTD profiler of the R/V Cape Hatteras provided attenuation data at 650 nm. It was unique among the optical sensors used in this research in that it was deployed on the CTD profiler rather than on the optical profiler. The location of this sensor on the CTD profiler means that SPM estimates provided from transmissometer data may reach depths that far exceeded the maximum depths reached by the optical profiler. (That platform was generally not deployed to depths greater than 200 m.) Data quality issues evaluated relative to the transmissometer include sensor saturation, and how well its attenuation values correlated with attenuation reported by the AC9 and the ACS.

Examination of the individual profiles in this project revealed that the transmissometer reached saturation at c (650 nm) = 55.262 m^{-1}. In most cases, saturation appeared to be associated with CTD-T (Chapter III) as determined by visual inspection of profile data. However, during this project, there were two occurrences where it appeared that natural environmental conditions caused saturation (Figure 34). Both instances occurred during GC2. Since a closer examination of these two points produced a procedural modification related to one of these instances, these two transmissometer saturation events are characterized here.

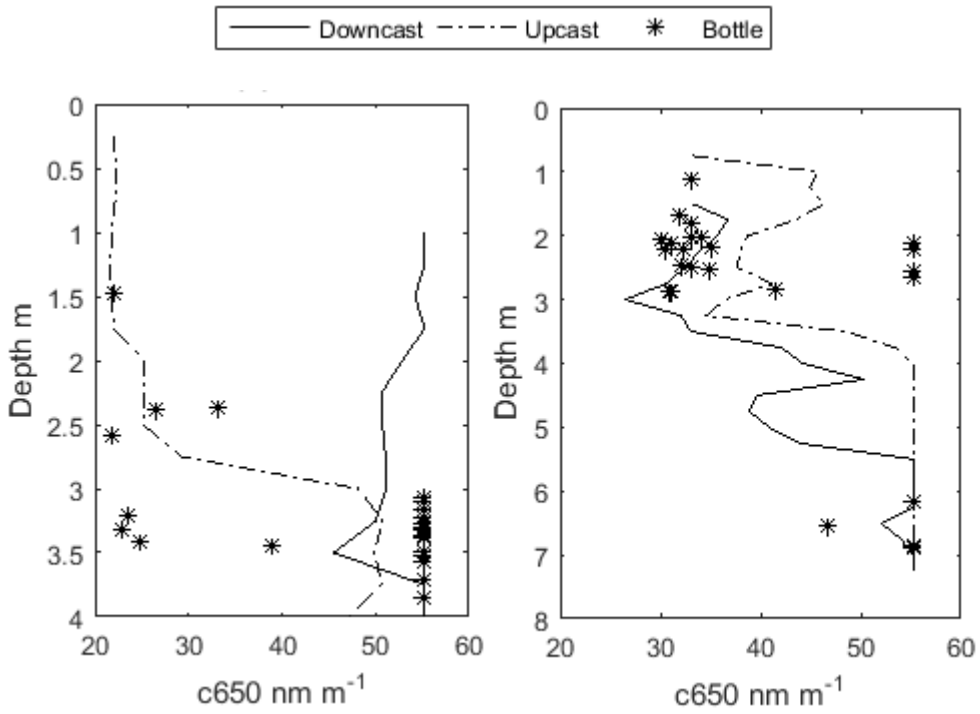

Figure 34. Transmissometer Saturation

These occurrences of transmissometer saturation take place during GC2 at stations E1 (left) and H1 (right). The * symbols show c650 nm values observed at the time and depth of a water capture event. “Bottle” indicates the attenuation reported by the transmissometer at the moment the water sampler was ordered to close its top and bottom hatches. These events always took place during the upcast of the profiler.

A detailed evaluation was performed on both instances of environmentally induced transmissometer saturation. First, at station H1 (right portion of the figure), it appears that attenuation should have been higher than reported around 6 m depth for both the downcast and upcast profiles. As no filter samples were obtained below this depth, data removal wasn’t necessary for this location.

Station E1 (left portion of the figure), showed a very unusual circumstance where the downcast data reached saturation at both the top and bottom of the profile. This circumstance indicated that while CTD-T may have occurred at the bottom of the profile, something else must have happened at the top of the water column for saturation to have

been reached at the start of the profiling event. Furthermore, at the first water capture event (Niskin bottle #1) the transmissometer recorded the value 38.927 m^{-1}. The next 16 bottle capture events were accompanied by the transmissometer saturation value (depth range 3.1 – 3.8 m). After that, the bottle capture events recorded steadily decreasing attenuation (at 650 nm) values. At the time of the bottle #23 capture event (the bottle from which filtered SPM was extracted), the transmissometer recorded a value of 24.7443 m^{-1}. Once the vertical offset was applied, the median value of c650 from the C-Star transmissometer at 2.5 m depth (the filterdepth) was 49.42. The downcast data for that filterdepth had a median value of 51.9041 m^{-1}. However, if one only used the upcast data, the median value of the transmissometer data at filterdepth 2.5 m was 25.35 m^{-1}. Additionally, the median value of c652.1 from the ACS at the same depth was 27.85. These similar values suggest that conditions were comparable during the CTD upcast and the entire optical profiler observation event at the filterdepth in question. For the combined reasons of saturation on the downcast of the CTD profiler and the similar conditions observed by the CTD profiler upcast and the optical profiler cast, the downcast transmissometer data for GC2, E1 was removed from further analysis while the upcast data was retained. This station represents the only point where the downcast data was eliminated from consideration below the depth of 2 m in this project.

Attenuation values recorded by the transmissometer were evaluated relative to the c650 reported by the AC9 and the interpolated c650 values from the ACS data. The strong relationship between the attenuation measured by the transmissometer, attenuation recorded by the AC9 and the interpolated attenuation at 650 nm from the ACS is shown

in Table 23. Where available, the correlation values with the AC9 are slightly stronger than the values relating the transmissometer to the ACS.

Table 23

Transmissometer c650 Related to AC9 and Interpolated ACS Values

Cruise	Transmissometer vs. AC9			Transmissometer vs. ACS		
	Spearman's ρ	Spearman's p	n	Spearman's ρ	Spearman's p	n
GC1	NA	NA	NA	1.00	0.00	25
GC2	0.98	0.00	65	0.95	0.00	58
GC3	0.97	0.00	60	0.97	0.00	59
GC5	0.97	0.00	86	0.94	0.00	81
GCALL	0.97	0.00	211	0.93	0.00	223

Notes. GCALL combines the data from all available cruises. Salinity, CTD-T, AC9 and ACS exclusions are applied. Transmissometer saturation exclusions are also applied.

Figure 35 shows the scatter plots of these sensor-to-sensor analyses. Here, the transmissometer and ACS appear to experience some sensor drift relative to one another, especially regarding the GC1 data. Cruises GC2, GC3, and GC5 also demonstrate an increasing transmissometer bias relative to the AC sensors. Larger offsets are observed with increasing cruise number. This project notes these offsets as sources of uncertainty when considering SPM concentration estimates based upon these different sensors, but it does not propose steps to mitigate this effect. Similar system bias in transmissometer data may be seen in Figure 35 where there is a discernable separation between the SPM relationship to transmissometer attenuation for GC1 and the SPM-to-transmissometer attenuation for GC5.

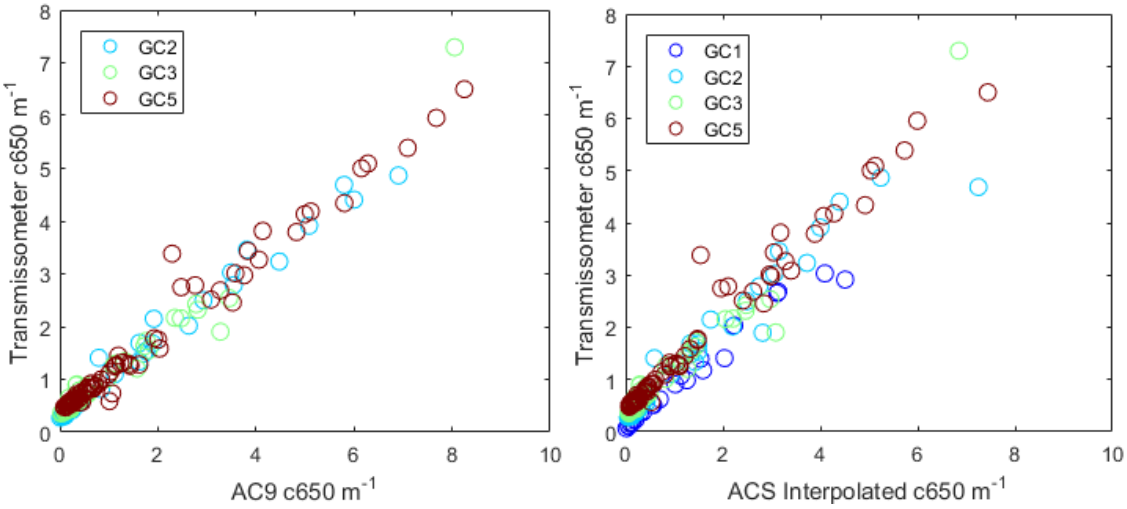

Figure 35. Transmissometer c vs. AC9 c and ACS c Scatter Plots

These plots display selected ranges of data.

LISST Data Quality: Attenuation 670 nm

Four different quality issues arose with the LISST datasets. All of them were improved with the steps discussed here. First, LISST observations from GC4 contained a variable depth bias. The problem was identified when it was noted that LISST observations made while the sensor was still on the deck reported depths often exceeding 2 m (Figure 36). This phenomenon did not occur during the other cruises. The problem may have been caused by a hose clamp attaching the LISST to the optical profiler being placed too near the pressure sensor. Each GC4 LISST profile dataset was given an additional station-specific vertical offset to account for these pressure sensor differences. Each offset consisted of the station specific median value of the sensor depth measurements recorded prior to sensor immersion.

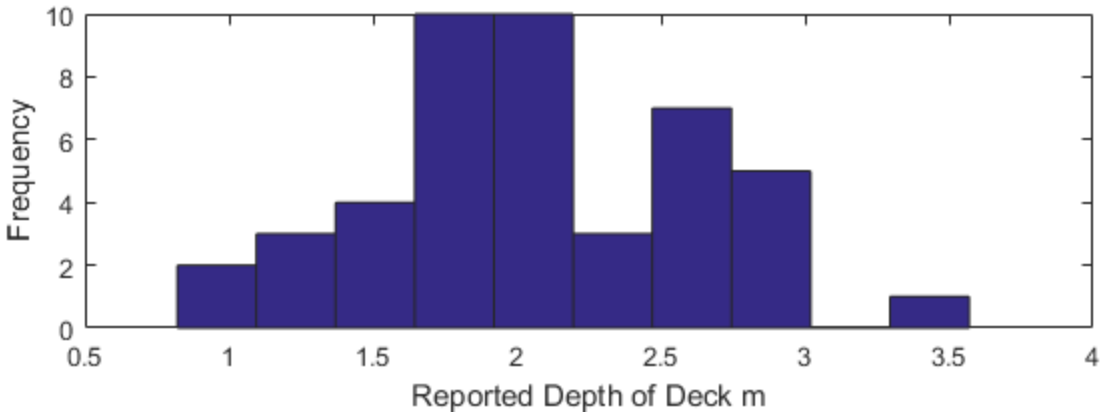

Figure 36. GC4 LISST Depth Offsets Histogram

Histogram of the recorded depths of the LISST while the sensor was on the deck during cruise GC4. n = 45

While the primary purpose of the LISST sensor was to estimate the particle size distribution, another data product of the sensor was the attenuation coefficient at 670 nm. These attenuation values related well to ACS attenuation (Table 24). However, a systematic bias in the actual attenuation values became apparent in the related scatter plots (Figure 37) for cruises GC2 and GC3. This bias constituted the second quality issue identified in the LISST data set. During these cruises, the LISST-reported c670 appeared to be approximately 1 m^{-1} greater than the ACS interpolated c670 relative to the paired data of the other three research cruises (Figure 37). Similar biases for cruises GC2 and GC3 also appear in the scatter plot comparing LISST c670 to SPM. By contrast, the offsets between the cruises of the transmissometer data (Figure 35), were an order of magnitude smaller between each successive cruise than the bias shown in the LISST data between GC2 and GC3 relative to the remaining three cruises.

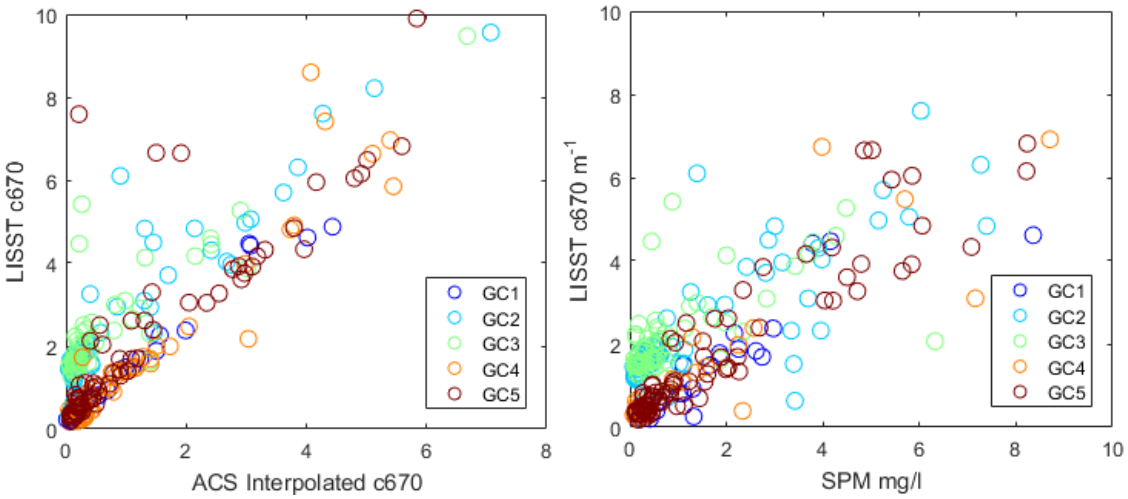

Figure 37. LISST c670 Relationships with Bias

Notes. Left: LISST attenuation in relation to ACS attenuation at 670 nm. Right: LISST attenuation in relation to SPM. The plots display a selected range of data. Salinity, CTD-T and ACS exclusions have been applied.

The correlation coefficients between LISST c670 and ACS c670 ($\rho = 0.93$ $p = 0.00$ $n = 55$ for GC2 and $\rho = 0.84$ $p = 0.00$ $n = 72$ for GC3) were like those calculated between the two sensors for cruises GC1, GC4 and GC5 (Table 24). However, the effect that the biases in cruises GC2 and GC3 had upon the combined data sets (GCALL) resulted in a lower correlation ($\rho = 0.76$ $p = 0.00$ $n = 286$) than was seen for any of the individual cruises. Closer analysis indicated that these features were related to the choice of calibration data applied to the in-situ observations.

In the initial processing of the LISST data, the lab-based clear-water test performed closest in time to the cruise event was applied as the calibration file. To determine if the GC2 and GC3 biases were related to sensor calibration, several benchtop clear water testing events, performed either in the lab, or on the ship, were plotted for inspection (Figure 38). In most cases, the lab and factory based bench tests were similar in spectral shape and amplitude. However, the 13 September 2009 in-lab bench test

displayed a different system response between rings six and twenty-three than were observed during other clear-water tests. A similar system response was recorded during a bench-test while at sea during GC3 (23 July 2009) using ship-supplied Milli-Q.

Even larger amplitudes were recorded on 28 July 2009 (during the same cruise). The two tests performed that day demonstrated a lot of variation in the system response to clear water within a short period. Therefore, neither of the 28 July 2009 test events were considered good candidates for use as calibration data sets.

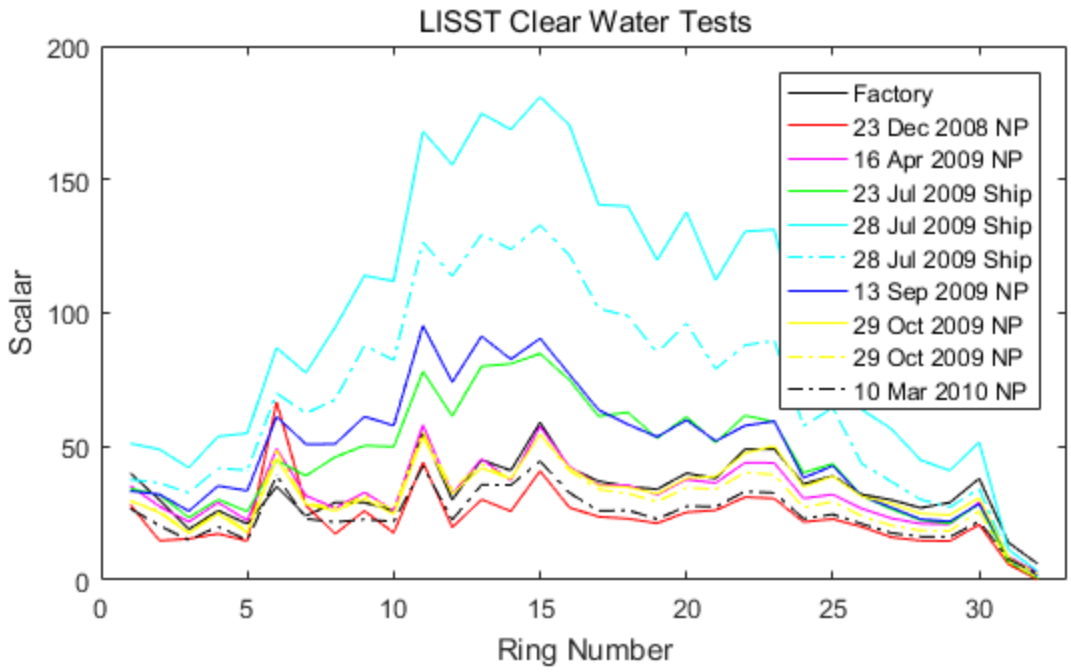

Figure 38. LISST Clear Water Tests

NP represents Nano-pure. "Ship" represents polished water provided by the R/V Cape Hatteras. The ring number represents each of the 32 concentric rings of the LISST that receive the laser signal.

After evaluating the clear water bench tests, the GC2 and GC3 LISST datasets were reprocessed using the 23 July 2009 and 13 September 2009 clear-water tests respectively. The resulting scatter plots relating the LISST attenuation to the ACS attenuation and SPM concentration (Figures 39 and 48) no longer displayed systemic

bias. This exercise effectively demonstrated the importance of frequent clear water tests for the LISST sensor.

Third, it was observed that during GC2, along transects B, C, and D, the LISST reported negative attenuation values in connection with low total data output. (This occurred at stations B4, B5, C4, C5, D4, and D5.) Affected profiles of LISST data were not used in this research. The reported negative values may have been the result of the LISST being set to record data after a predetermined number of observations had been averaged. The speed of the optical profiler (and its rapidly changing depth) may have caused the sensor to purge its data captures before enough counts were received to meet operating specifications and record the averaged data thus causing problems with the output data. Mid-cruise (GC2), the LISST settings had been adjusted to record data more rapidly and data averaging were left to the post-processing depth-binning functions that were applied to all profiler data during this research. GC3 stations and depths that reported a value of zero for total attenuation were also removed from further attenuation analysis. These modifications resulted in slightly larger correlation values between the LISST and ACS attenuation values for GC2 and GC3 (Table 24 “No Suspected Schlieren Removal“ values).

Table 24

LISST c670 Related to Interpolated ACS c670

Cruise	No Suspected Schlieren Removal LISST c670 vs. ACS Interpolated c670			Suspected Schlieren Removed LISST c670 vs. ACS Interpolated c670		
	Spearman's ρ	Spearman's p	n	Spearman's ρ	Spearman's p	n
GC1	0.92	0.00	30	0.99	0.00	13
GC2	0.93	0.00	54	0.93	0.00	43
GC3	0.87	0.00	74	0.91	0.00	54
GC4	0.90	0.00	63	0.92	0.00	34
GC5	0.83	0.00	100	0.97	0.00	39
GCALL	0.86	0.00	321	0.93	0.00	183

Notes. GC ALL combines the data from all available cruises. Salinity and CTD-T exclusions are not applied as both sensors were deployed on the same profiler. Spectral ACS attenuation removals by visual inspection are applied. The system biases originally noted in GC2 and GC3 were corrected prior to these correlation calculations.

The final quality challenge faced with the LISST datasets occurred when the sensor encountered density differences within the observed sample space. This effect, called schlieren, as it relates to LISST observations has been previously studied (Emmanuel Boss et al., 2009; Mikkelsen et al., 2008; Styles, 2006). During that research, schlieren was observed in the presence of pycnoclines. The small density differences resulted in multiple fluid-based refractive indexes within the sensor field of view. Consequently, the sensor assumed all changes in the refractive index to have been caused by particulates, not the water. The result was a decrease in diffraction angle for the forward-scattering light which in turn caused an increase in the amount of photonic energy recorded at the receiver. In the presence of schlieren, the diffraction-based, very small acceptance angle LISST recorded higher attenuation values than other optical sensors at some depths. Figure 39, where LISST c670 was plotted against ACS c670 (interpolated), indicated that schlieren was present in the LISST filterdepth dataset as most of the scatter were biased. Specifically, most of the scatter occurred because the LISST reported much higher attenuation values than the ACS.

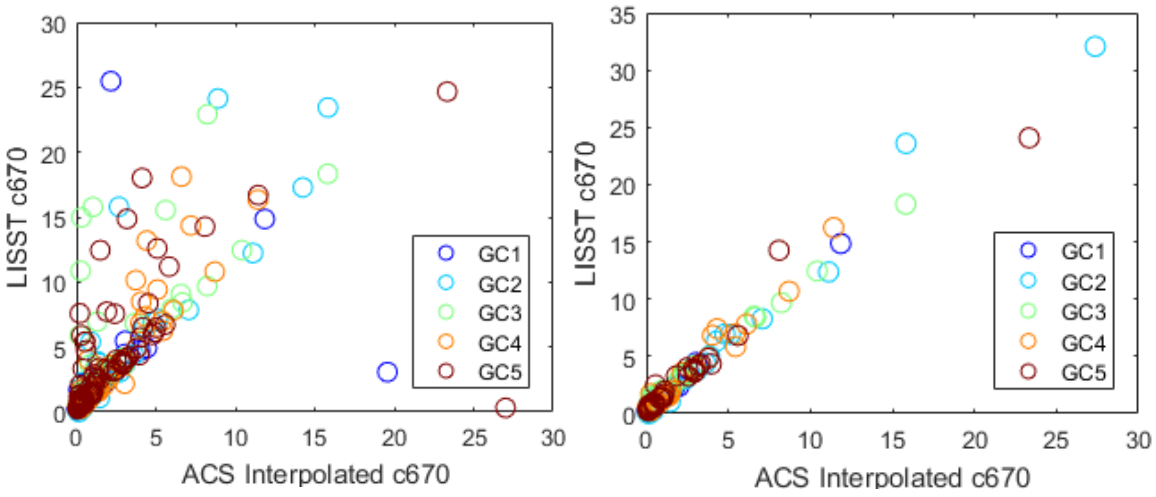

Figure 39. LISST c670 vs. ACS c670 Before & After Suspect Schlieren Removal

This plot displays selected ranges of data.

In the past, schlieren has been identified by artifacts seen in photographic images that were gathered nearly simultaneously as the LISST data (Mikkelsen et al., 2008). In the 2008 study, these occurrences happened in the presence of buoyancy frequency (N s^{-1}) that was relatively high compared to the remainder of the depths in the profile data. Another study attempted to identify the presence of schlieren in LISST sensor data by proposing that this phenomenon occurred over an N threshold of 0.01 s^{-1} (A. Karageorgis, Georgopoulos, Gardner, Mikkelsen, & Velaoras, 2015). However, using a threshold of N $\geq$ 0.01 s^{-1} as the only metric to eliminate LISST data from further analysis due to the influence of suspected schlieren is inappropriate for this research project. This conclusion was determined because it appears that imposing this threshold would remove many data points where schlieren did not seem to occur (Figure 40).

In evaluating the LISST data of this research to identify any filterdepths likely to have been affected by schlieren, profiles of LISST attenuation (c670), ACS attenuation (c669.3) (similar to the work of (Xi, Larouche, Tang, & Michel, 2014)), along with

temperature, salinity and buoyancy frequency were plotted side-by-side (Figure 40). Additionally, LISST total suspended matter (TSM) values (µl/l), or LISST-derived median particle size (D50) were also plotted with the buoyancy frequencies. Depths of filter samples were also noted on these plots.

The buoyancy frequency (N) was evaluated using the equation:

$$N = \sqrt{\left(\frac{g}{\rho_o} * \frac{\delta\rho}{\delta z}\right)} \tag{4.7}$$

where g was gravity (9.8067 m/s^2), ρ_o was the median density of the profile in question and $\frac{\delta\rho}{\delta z}$ was the change in seawater density over a 0.25 m depth range. The density values used in these calculations were reported with the CTD sensor data on the optical profiler.

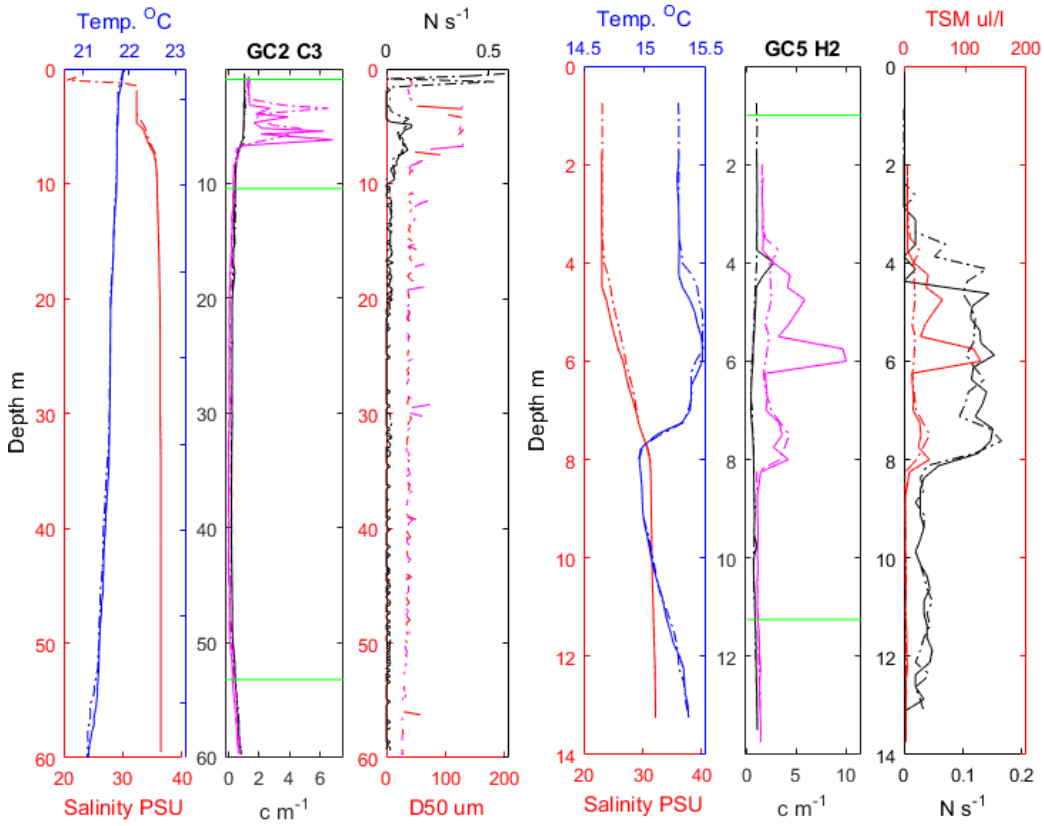

Figure 40. Examples of LISST Attenuation Affected by Schlieren

Left: Temperature and salinity. Middle: LISST c670 nm (magenta) and ACS c669.3 nm (black). Right: Buoyancy frequency based on CTD data and D50 or TSM from the LISST. Green lines represent depths of filter samples.

The left example in Figure 40 (GC2, C3) shows a pycnocline between 4 and 10 m depth. Between the ranges of 2 and 7 m, the LISST c670 dramatically increases in value and becomes spiky relative to the c669.3 recorded by the ACS. These LISST data features are presumed to be the result of schlieren. Between 20 m depth and the bottom of the profile, the highest N values are 0.027 s^{-1}, well above the recommended N threshold recommended by Karageorgis (A. Karageorgis et al., 2015). Yet, in that depth range, there are no signs of interference (high values relative to the ACS attenuation or spikes) due to schlieren, indicating that removing the LISST data from that part of the profile would be inappropriate in this case.

The data profiles drawn on the right in Figure 40 depict another example of suspected schlieren. Here, the nearly simultaneous changes in the temperature, salinity, LISST-attenuation, LISST-TSM, and N values, without similar changes noted in the ACS attenuation data, all indicate that schlieren occurred between approximately 2.5 m through 8.5 m depth. Had a filter sample been collected within this depth range, a LISST-to-SPM evaluation would not have occurred at that point as all LISST data would have been removed from further analysis.

To evaluate the quality of the LISST data for this project profiles like the ones found in Figure 40 were plotted for each station of each cruise and visually evaluated to identify LISST-observed filterdepth data likely to have been influenced by schlieren. Instances of large N values (relative to the remainder of the vertical profile in question) and occurrences of relatively large temperature and salinity changes also helped to identify potential problem areas. As with the Mikkelsen study (Mikkelsen et al., 2008), instances of high TSM or markedly different D50 values were often associated with these pycnoclines. Ultimately, a LISST filterdepth position was removed from further consideration if LISST attenuation was significantly larger and spikier than the ACS data at the same depth.

BB9 Data Quality (b_{bt} & b_{bp})

Quality of the BB9 data products were evaluated using the b_{bp} dataset. Scatter plots of the b_{bp} values and the SPM filtered data revealed features that suggested there were some limitations related to the BB9 (Figure 41). At a different value for each wavelength, all b_{bp} and b_{bt} data would report approximately the same values, regardless of the SPM concentration value connected to the same location. (See Figure 41 for

examples.) The apparent saturation values of the BB9 are 0.73 m^{-1} for 400 nm, 0.48 m^{-1} for 440 nm, 0.30 m^{-1} for 488 nm, 0.24 m^{-1} for 510 nm, 0.21 m^{-1} for 532 nm, 0.13 m^{-1} for 595 nm, 0.10 m^{-1} for 660 nm, 0.09 m^{-1} for 676 nm, and 0.06 m^{-1} for 715 nm.

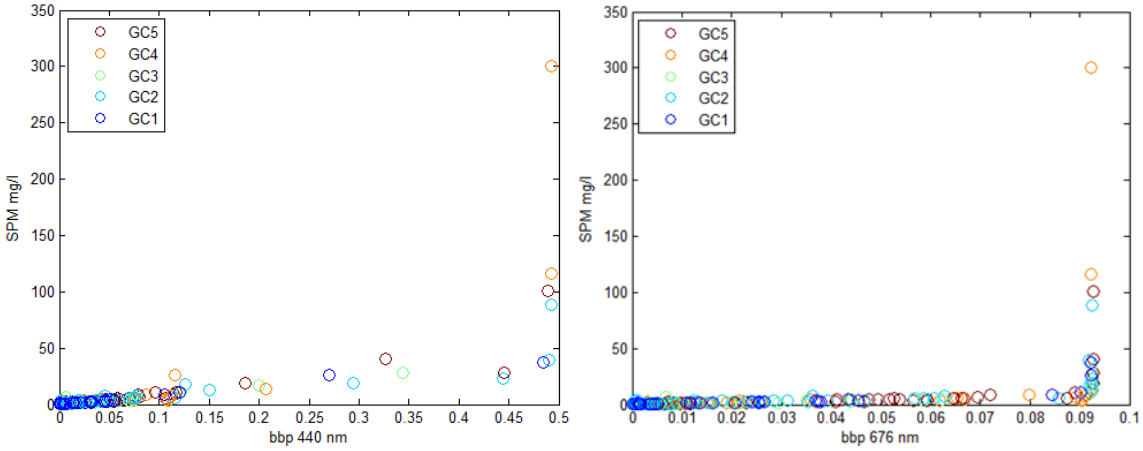

Figure 41. BB9 Saturation thresholds

Examples of bbp versus SPM with saturation thresholds. SPM related to bbp440 nm is shown on the left; SPM related to bbp676 nm is shown on the right.

Examination of raw BB9 data at a few different stations from GC2 provided clarification of this phenomenon. According to the user's guide (WET_Labs, 2008b), the signal range of the sensor's receivers is 0 to 4120 counts of return signal per measurement. Raw data files from the GulfCarbon project indicate that this was indeed correct for the specific BB9 used in this project at wavelengths less than 532 nm. However, for wavelengths 532 nm through 715 nm, the maximum number of counts of the return signal was 4122. At these two maximum count thresholds, the sensor apparently reached saturation. Examples of saturation from GC2 are shown in Figure 42. At station E0 (second cast), wavelengths 488 nm through 715 nm were saturated for the full duration of the profiling event. At station E2, (first cast), maximum detectable counts were reached for wavelengths 595 nm through 715 nm for part of the profiling event.

Therefore, it can be concluded that the data limits noted in the SPM versus b_{bp} scatter plots represent sensor saturation. These saturation values appear to be similar to the sensor limits detected by researchers in the Bristol Channel (David McKee et al., 2009). Wavelength-dependent BB9 saturation has also been noted by other researchers (David McKee et al., 2009).

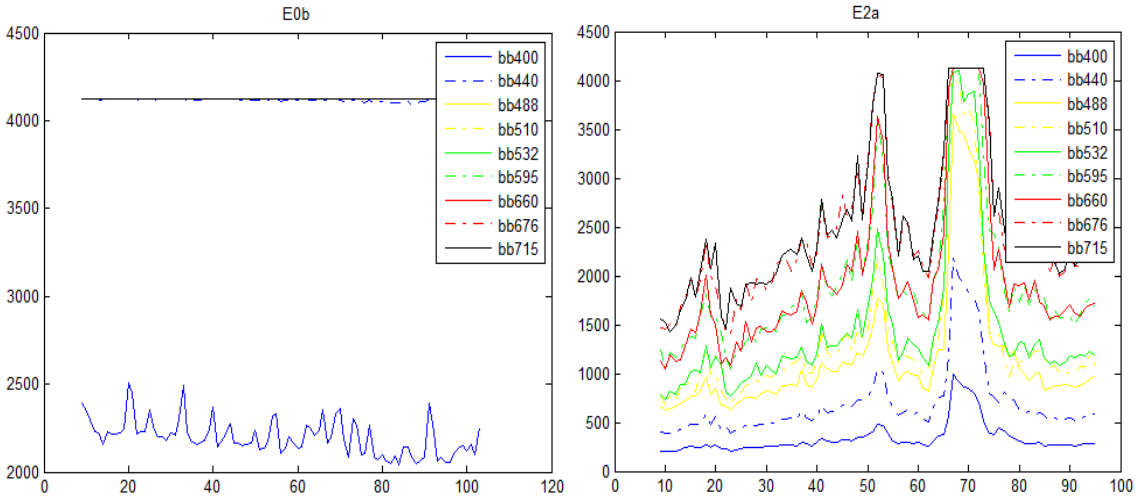

Figure 42. Raw Data, BB9

Examples of raw BB9 data from GC2. The x-axes represent time(s). The y-axes represent counts of the return signal.

Prior to further analysis and algorithm development, all b_{bt} and b_{bp} data that met or exceeded the estimated saturation limits were removed. The parameters for data exclusions derived from the b_{bp} dataset were also applied to the b_{bt} data. Figure 57 shows a summary of the b_{bp} spectra at filterdepths for all five cruises after quality control procedures were applied.

Sensor Acceptance Angles

The acceptance angles of attenuation sensors influence the values recorded by the individual instrument (Emmanuel Boss et al., 2009). Equation 2.7 describes how attenuation is calculated from the transmission signal. Attenuation itself is defined as $c \equiv$

a + b (Mobley, 1994). The effect of absorption in the calculation of attenuation from a transmission signal is straightforward. “Extra” absorption is neither added nor subtracted from the transmission signal during the sampling process. However, the scattering of light, particularly in the forward direction provides practical challenges to sensor-measured transmission signals. This difficulty occurs because the total scattering coefficient (b) represents the full amount of incident light scattered into all directions, or

$$b(\lambda) = 2\pi \int_0^{\pi} \beta(\psi;\lambda)\, sin\psi\, d\psi \qquad (4.8)$$

(Davies, McKee, Bowers, Graham, & Nimmo-Smith, 2014; Mobley, 1994; Petzold, 1972) where β is the volume scattering function, (see equations 2.1, 2.2 and 2.3) (D. Doxaran et al., 2012) and ψ represents the specific angle under consideration for the integration process. Some scattered light is inevitably received by the various transmissometers and processed as part of the transmission signal (Emmanuel Boss et al., 2009; Voss & Austin, 1993; Zaneveld, 1994). This means that a sensor-produced attenuation value actually represents the relationship

$$c_{reported} = a + 2\pi \int_{\theta_{acceptance}}^{\pi} \beta(\theta)\, sin\theta\, d\theta \quad . \qquad (4.9)$$

Wavelength notations are implied rather than expressed here. (It is important to note that the Zaneveld definition of acceptance angle appears to be twice that of Boss’ definition.) Effectively, a “cone” of forward scattered light is always missing from each scattering event in the sample space for the calculation of attenuation. The size of that cone relative to the volume scattering function (β) is directly related to the acceptance angle as in equation 4.9. Conversely, the measured transmission component is increased by the

forward scattered light within that cone. The exaggerated portion of $c_{reported}$ due to forward scattering is represented by

$$b_{0\rightarrow\theta_{acceptance}} = 2\pi \int_0^{\theta_{acceptance}} \beta\,(\theta)\, sin\theta\, d\theta \qquad (4.10)$$

(Pegau, Zaneveld, & Voss, 1995; Zaneveld, 1994). The associated error to the calculation of c in equation 2.7 is over-estimated by a factor of $e^{b_{0\rightarrow\theta_{acceptance}}}$ (Zaneveld, 1994).

Three different acceptance angles are used by the sensors engaged in this research. The LISST has the smallest acceptance angle at 0.0269^{O} (Sequoia_Scientific). The AC9 and ACS sensors both have acceptance angles of 0.93^{O} (WET_Labs, 2008a, 2009) and the C-Star transmissometer has an acceptance angle of ~1^{O} (WET_Labs, 2011). However, a value of 1.2^{O} has been used to represent the C-Star transmissometer acceptance angle in the past (Emmanuel Boss et al., 2009). Because of the relationship between attenuation and transmission in equation 2.7, one expects that the sensors with smaller acceptance angles produce higher attenuation values than the sensors with larger acceptance angles (Emmanuel Boss et al., 2009). Examples of actual differences in attenuation values from this research can be seen in the attenuation spectra plots in Figure 35.

Understanding the source of attenuation over-estimation and quantifying the forward scattering component of $c_{measured}$ are two different matters. If the intensity of the angular scattering were isotropic about a scattering particle, then approximating the missing forward scattering component (equation 4.10) and adjusting the $c_{measured}$ value would be reasonably straightforward calculation when absorption measurements were also taken as was done in this project. Mie theory (also known as Lorenz-Mie theory (Horvath, 2009; Jerlov, 1976; Lock & Gouesbet, 2009)) suggests that angular scatter of

particulates in the single-scattering paradigm is enhanced in the forward direction relative to the backward direction (Chu & Churchill, 1955; Horvath, 2009; Kirk, 1994; Mobley, 1994). Mie theory presumes that the observed particles consist only of homogeneous spheres. Even though natural particle populations are not characterized by these properties, it is apparent that Mie-like scattering (enhanced forward scatter relative to backscatter) occurs based on the backscatter efficiency evaluations performed in Chapter V of this research. Other researchers have also reported greater scatter in the forward direction produced by marine particles (Berthon, Lee, Shybanov, & Zibordi, 2007; Emmanuel Boss et al., 2009; Spinrad, Zaneveld, & Pak, 1978).

Correlation values, while useful in establishing relationships between datasets, do not indicate whether the values of the analyzed data differ significantly. The calculation of median ratios of paired datasets does offer this perspective. Therefore, this evaluation tool was applied to the attenuation datasets used in this dissertation.

Strong correlation coefficients between the attenuation values of the different sensors used in this project have already been established. (See Tables 22, 23 and 24). As expected, the ratios between the attenuation coefficients from AC9 and ACS (both of which have the acceptance angle of 0.93^{O}) are approximately 1 (Table 25). The only exception to this was seen in GC5 where the AC9 consistently had higher attenuation values than the ACS for all common wavelengths. Even when considering the MAD values, those ratios were all higher than 1.0.

Table 25

AC9 to ACS Attenuation Ratios: GC2 – GC5

Wavelength nm	Median	MAD	n
412	1.03	0.09	305
440	1.02	0.10	305
488	1.02	0.10	305
510	1.03	0.10	305
532	1.02	0.10	305
555	1.03	0.10	305
650	1.03	0.10	305
676	1.02	0.10	305
715	1.03	0.11	305

Notes. MAD is the median absolute deviation.

The results of calculating the ratios of the C-Star transmissometer attenuation to the AC9 and ACS attenuation coefficients were less consistent than those relating the AC9 to the ACS. These ratios for GC1 were far less than those produced for the remaining three cruises of transmissometer data and the sensor-to-sensor ratios of the combined dataset (Table 26). The very large difference in attenuation ratios noted here may have been caused by a couple of different circumstances. It is possible that the transmissometer may have been operating under a very different calibration for GC1 than it did for the remaining three cruises on the R/V Cape Hatteras. It is also possible that the transmissometer was replaced between GC1 and GC2. If this second possibility occurred, then it seems likely that the first transmissometer had a larger acceptance angle than the second one. The different transmissometer acceptance angles reported by the manufacturer (WET_Labs, 2010b) and by Boss (Emmanuel Boss et al., 2009), suggests that individual transmissometers may have different acceptance angles from each other

particularly since the manufacturer only reports an approximate acceptance angle on the sensor specifications.

It is also worth noting that the MAD values of the attenuation-to-attenuation ratios between the transmissometer and both AC sensors are very high (0.41 to 1.05) for cruises GC2, GC3 and GC5 whereas the MAD is very low for the available data from GC1. These MAD values have the effect of making the attenuation ratios between the transmissometer and AC sensors statistically equal to 1 for cruises GC2, GC3, and GC5, whereas the attenuation-attenuation ratio for GC1 remains much smaller than 1, even when the MAD value is considered (Table 26). This small ratio value from GC1 suggests that when using transmissometer data to predict SPM concentration, it would be inappropriate to combine the paired data from all four available cruises to generate linear algorithm coefficients. Instead, it would be prudent to keep the GC1 data separate from the rest and use the combined data sets from cruises GC2, GC3 and GC4 for general SPM prediction (see Chapter V).

Table 26

Transmissometer to AC9 & ACS c650 Ratios

Cruise	Transmissometer vs. AC9			Transmissometer vs. ACS		
	Median	MAD	n	Median	MAD	n
GC1	N/A	N/A	N/A	0.91	0.17	25
GC2	2.31	1.32	66	1.85	0.75	58
GC3	2.34	1.18	61	2.20	0.87	60
GC5	1.55	0.63	86	1.77	0.78	79
GC2, GC3 & GC5	1.88	0.90	213	1.92	0.83	197
GCALL	1.88	0.90	213	1.71	0.72	222

Notes: There was not any transmissometer data available for GC4. MAD is the median absolute deviation.

The results of the ACS to LISST attenuation ratios are reported in Table 27. As the ACS acceptance angle was much larger than the acceptance angle for the LISST, these relatively small attenuation-to-attenuation ratios were expected. Cruises GC1, GC2, GC4 and GC5 all have statistically equivalent ratios when both the median and MAD components are considered. GC3 is statistically comparable to GC1, GC2 and GC5 and significantly smaller than GC4. The large difference in the available number of filterdepths between cruises GC3 and GC4 may account for some of that difference.

Table 27

ACS to LISST c670 Ratios

Cruise	Median	MAD	n
GC1	0.71	0.09	20
GC2	0.68	0.16	47
GC3	0.42	0.17	57
GC4	0.79	0.17	16
GC5	0.57	0.16	57
GCALL	0.60	0.19	197

Notes. The analysis was performed after data points suspected to be affected by schlieren were removed. MAD is the median absolute deviation.

For the sake of completeness, the AC9 to ACS absorption-to-absorption ratios were also calculated (Table 28). The acceptance angles for the measurement of absorption do not have similar significance to that of attenuation. In the measurement of absorption by the AC sensors, light scattered in the forward direction is supposed to be removed from the observation cylinders through the combined effects of multiple scattering and eventual absorption into the walls of the sensors' flow tubes. (Additionally, the acceptance angle is the same for both absorption sensors at 0.93^{O}.) However, the AC9 to ACS absorption ratios were calculated to see how well they compared to the

attenuation ratios related to the same instruments. Results of the absorption-absorption calculations are in Table 28. The combined dataset (Table 28) shows very good agreement between the sensors (the ratios are statistically equal to 1) for eight of the nine common wavelengths. The lack of correlation at 715 nm between the AC sensors has been previously discussed and appears to be related to the pre-processing of the AC9 data.

Table 28

AC9 to ACS Absorption Ratios: GC2 – GC5

Wavelength nm	Median	MAD	n
412	0.98	0.07	268
440	1.02	0.07	268
488	0.99	0.08	268
510	1.02	0.09	268
532	1.00	0.11	268
555	0.99	0.11	268
650	0.97	0.15	268
676	1.09	0.15	268
715	*	*	*

Notes. MAD is the median absolute deviation. Most absorption values for the AC9 and many of the absorption values for the ACS at 715 nm were zero making accurate ratios at this wavelength difficult to determine.

Conclusions

This chapter is associated with Hypothesis 1 that "data from sequential casts of the same profiler or of different profilers can be used to represent the same sample space." This is true because the transmissometer attenuation (from the sensor located on the CTD profiler) was evaluated relative to the attenuation coefficients produced by the AC9, ACS, and LISST (which were mounted on the optical profiler). Additionally, interests of Hypothesis 2 were also served as quality-assessed data better benefits the

purpose of predicting SPM concentration from IOPs. Most importantly, this chapter describes the processes and procedures imposed on the quality-checked and approved profiling optical datasets employed later in this dissertation research. Some of the steps taken as a result of these analyses are pertinent to the data used in this dissertation research alone. Other procedures developed here should prove useful to fellow researchers using similar sensors.

Several subsets of data were removed from use for SPM prediction following the methods and techniques described here. All AC9 data (both absorption and attenuation) from GC1 were removed from further algorithm development. A method was devised to automatically identify mid-spectral artifacts in both absorption and attenuation data reported by the ACS. Subsequently, large quantities of ACS data were also removed from algorithm development. Instances of BB9 saturation were also pinpointed and removed from the working dataset. Filterdepth locations where it appeared that schlieren affected the LISST sensor were determined and eliminated from further investigation.

The effects of the acceptance angle on the reported attenuation values of the various sensors were considered. As expected, it influenced these values. It also appeared that the transmissometer mounted on the CTD profiler of the R/V Cape Hatteras underwent a significant calibration or sensor replacement event between cruises GC1 and GC2 making it prudent to separate the GC1 data from GCALL considerations.

This chapter provides the ground-work for some of the decisions and opinions described in Chapter V. It also explored how well various profiling optical sensors perform relative to one another during simultaneous or closely-related-in-time-and-space observations. These analyses effectively demonstrate that SPM algorithms based upon

data from one sensor may not always be applied to data from sensors that nominally report the same optical property. This principle is especially true for attenuation, where the acceptance angles of individual sensors have proven to be critical in the derivation of attenuation from transmission signals.

CHAPTER V – RELATIONSHIPS BETWEEN IOPS AND SPM

Introduction

Inherent optical properties (IOPs) are frequently used for SPM quantification and characterization (Astoreca, Doxaran, Ruddick, Rousseau, & Lancelot, 2012; Emmanuel Boss et al., 2009; Bourrin et al., 2015; D. Doxaran et al., 2012; Jago & Bull, 2000; Jouon et al., 2008; Miles et al., 2016; Qiao et al., 2011; Wegner et al., 2003). This chapter determines estimated SPM concentration derived from linear least squares regression of SPM filter samples and quality-accepted data from the various optical sensors. Nine hundred thirty- nine linear models for SPM prediction are reported. The 169 sets algorithm coefficients derived from the combined datasets of all five research cruises were then evaluated using various methods.

The term "GCALL" is used numerous times in Chapter 5. It refers to the utilization of the quality-passed datasets from all five research cruises associated with this project combined. This research mostly focuses on evaluations involving GCALL data. However, many evaluations and discussions involve datasets on a cruise by cruise basis.

This chapter first considers the relationship between SPM and single IOPs (absorption (a), attenuation (c), total scatter (b) and backscatter (b_b)). Then it examines SPMs relationship with specific IOP combinations. These combinations are backscatter ratio (b_b/b), partial attenuation ($a + b_b$) and finally the ratio $b_b / (a + b_b)$ which is a defining characteristic of remote sensing reflectance (R_{rs}). Each IOP or IOP-combination is evaluated with respect to SPM by first calculating the Spearman correlation coefficient followed by the determination of linear SPM models. After these processes, the SPM models are submitted to a battery of tests to identify the best IOPs and IOP combinations

(see above) for SPM prediction. Special attention is given to three groups of algorithms with special significance to airborne bathymetric lidar surveys. These groups of algorithms include those utilizing the wavelength 532 nm (bathymetric lidar wavelength). The second group of algorithms given extra scrutiny are based upon the IOP combination $a + b_{bp}$. The final group is based upon the IOP combination $b_b / (a + b_b)$.

Single IOPs

IOP Absorption (a)

The conventional way of expressing the components of total absorption is

$$a(\lambda) = a_w + a_\phi + a_{NAP} + a_{CDOM} \quad (5.1)$$

(Babin, Stramski, et al., 2003; Naik, D'Sa, Gomes, Goés, & Mouw, 2013), where $a(\lambda)$ represents total absorption at a given wavelength (λ), a_w represents the absorption of pure water, a_ϕ represents the phytoplankton contribution to absorption, a_{NAP} corresponds to absorption of non-algal particles, and a_{CDOM} stands for absorption by color dissolved organic matter.

The absorption spectra provided by the AC9 and ACS sensors represent the sum of $a_{particulates}$ and a_{CDOM} where $a_{particulates}$ includes absorption by both living and detrital organic matter as well as lithogenic particles. Through sensor calibration procedures, the portion of total absorption contributed by pure water (a_w) is not represented in these spectra, though the maximum contribution it could provide to total absorption is estimated in Figure 29. There we can see that both the value of a_w and its uncertainty expands nonlinearly and substantially with increasing wavelength. Using the cleaned AC9 and ACS datasets for GC2 – GC5 and GC1 – GC5 respectively, Spearman correlation coefficients are calculated between paired data sets of absorption and SPM

(Table 29). In the areas that are influenced by plumes, SPM is generally accompanied by a greater abundance of CDOM which absorbs light well but is a poor scatterer.

Tables 29 and 58 along with Figure 43 demonstrate the relationships between SPM and total non-water absorption (denoted as "a") in this project. (Some researchers use the same notation for this value (Astoreca et al., 2012; D. Doxaran et al., 2012; Hommersom, Peters, Wernand, & Boer, 2009; Oubelkheir, Claustre, Sciandra, & Babin, 2005), while others utilize a_n (David McKee et al., 2009) or a_{t-w} (Chang et al., 2002; Doron, Babin, Mangin, & Hembise, 2007; Tzortziou et al., 2006), or various additional notations (Aurin & Dierssen, 2012; D. McKee, Cunningham, Slater, Jones, & Griffiths, 2003).) The correlation values between SPM and absorption are somewhat stronger for the blue and green wavelengths (412-595 nm) than for the longer wavelengths (650 – 715 nm). These relationships hold true for both sensors.

From a cruise by cruise point of view, (Table 58) the absorption to SPM correlation coefficients were universally stronger for all wavelengths from cruise GC4 than for any of the other cruises. This observation held true for both the AC9 and the ACS, indicating that particulate absorption was a prominent IOP in the project area during GC4. For the other four cruises, the correlations were not as high, though they still showed a strong association between SPM and absorption for some wavelengths. The cruise to cruise variability demonstrates the temporal inconstancy of the region.

Table 29

Relationship Between SPM and Absorption (AC9 & ACS)

Wavelength nm	GC2 – GC5 AC9 a vs. Measured SPM Spearman Correlation Coefficients			GC1- GC5 ACS a vs. Measured SPM Spearman Correlation Coefficients		
	ρ	p	n	ρ	p	n
412	0.86	0.00	268	0.86	0.00	248
440	0.87	0.00	268	0.86	0.00	248
488	0.85	0.00	268	0.86	0.00	248
510	0.86	0.00	268	0.85	0.00	248
532	0.85	0.00	268	0.85	0.00	248
555	0.84	0.00	268	0.83	0.00	248
595	N/A	N/A	N/A	0.78	0.00	248
650	0.78	0.00	268	0.72	0.00	248
660	N/A	N/A	N/A	0.72	0.00	248
670	N/A	N/A	N/A	0.72	0.00	248
676	0.76	0.00	268	0.72	0.00	248
715	0.13	0.03	268	0.64	0.00	248

Note: Salinity, profiler induced turbidity, and visual inspection exclusions were applied. See Table 58 for cruise by cruise coefficients.

The plots relating absorption to SPM display scatter suggesting bifurcation above SPM of about 1.5 mg/l (Figures 43 and 44). This phenomenon occurred during all five cruises and was reported in the data related to all considered wavelengths (except for 715 nm from the AC9) from both the AC9 and the ACS. If this bifurcation is real then at concentrations above 1.5 mg/l, SPM can expect to have two solutions predicted from the same absorption coefficient. Also, two different observed values of absorption can predict the same concentration of SPM. This is due, in large part, to the fact that the project area contains multiple water types with different absorption budgets

(Chakraborty, 2013). (The contributions of a_{φ}, $a_{NAP,}$ and a_{CDOM} vary both spatially and temporally (D'Sa & Miller, 2003; Pope, Weidemann, & Fry, 2000).)

The a_{CDOM} components for the cruises considered in this research were previously evaluated (Chakraborty, 2013; Shen, Fichot, Liang, & Benner, 2016). Furthermore, an absorption budget for the cruise events related to this research was also reported (Chakraborty, 2013). Chakraborty's research also included designating station types for the GulfCarbon cruises. These groups were derived by principal component analysis (PCA) using the following parameters: temperature, salinity, mixed layer depth, dissolved inorganic nitrogen, phosphate, ammonia, silicate, surface currents, wind stress vectors, total chlorophyll-a, diatoms, cryptophytes haptophytes, and prochlorophytes (Chakraborty, 2013). These station types (estuaries, inner shelf, mid-shelf, and slope/offshore) are considered later in this analysis, so they are summarized in Table 30. It is essential to be cognizant that the water types observed at stationary locations may be subject to change over time (Groom et al., 2009). This appears to be the case over the course of this study, as the behavior of absorption measured by the AC9 and the ACS appears to change on a cruise by cruise basis. Absorption behavior observed by station types changes from one cruise to another.

Table 30

Chakraborty GulfCarbon Station Types

Estuaries							
A1	B1	C0	E0	E1	H1	MR1	MR2
Inner Shelf							
A2	B2	B	C1	C2	D1	D2	E2
E3	F1	F2	F3	G1	G2	H2	
Mid-Shelf							
A3	A4	C3	D3	E4	E5	F4	F5
G3	G4	G5	H3	H4	H5	H6	
Slope/Offshore							
A5	A6	B4	B5	C4	C5	D4	D5
E6	F6						

GulfCarbon station types as determined by Sumit Chakraborty (Chakraborty, 2013). See Figure 5 for a map of the project area including station names.

CDOM plays an important, wavelength-dependent role in spectral absorption (D. A. Siegel, Maritorena, Nelson, Hansell, & Lorenzi-Kayser, 2002). It varies considerably in the northern Gulf of Mexico (Chakraborty, 2013; Singh, D'Sa, & Swenson, 2010). The abundance and composition of $a_{CDOM,}$ and therefore its contribution to the absorption budget, is dependent on multiple factors (M. L. Wells, 2004) including terrestrial input (R. F. Chen et al., 2004; Couturier, Nozais, & Chaillou, 2016), fluvial input (R. F. Chen et al., 2004; Zhu, Tian, Yu, & Becker, 2013), export by wind and currents and reduction by photobleaching (Shank & Evans, 2011).

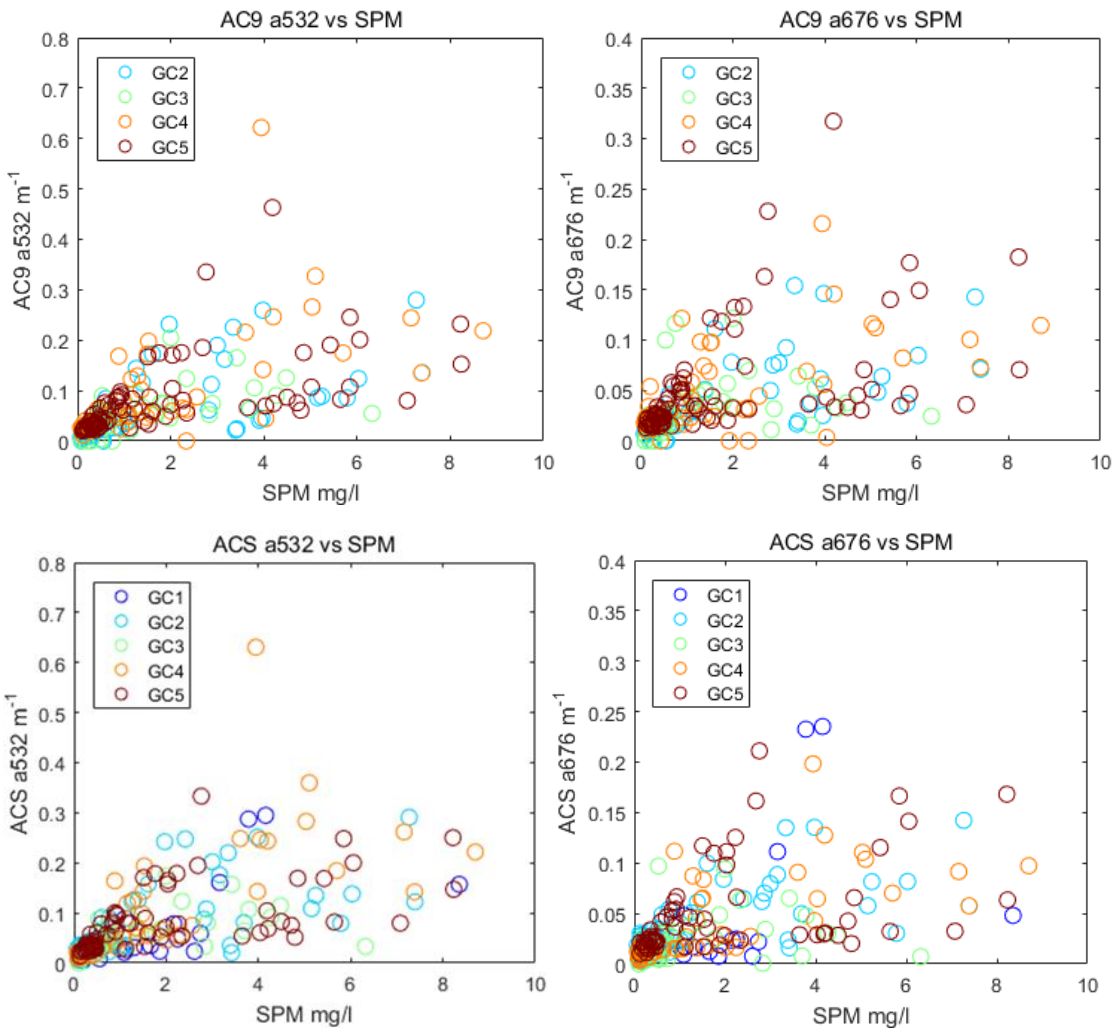

Figure 43. SPM vs. AC9 a & ACS a Selected Scatter Plots

These plots display selected wavelengths and ranges of data.

To further understand the branching trends in the absorption versus SPM scatter plots, the data pairs were sorted into the Chakraborty station types for the GulfCarbon cruises and replotted. Figure 44 and displays SPM and absorption data pairs for selected wavelengths and cruises, emphasizing station type. The plots that combine all cruise data provide very little insight into reasons for apparent bifurcation. Individual plots presenting only one cruise and one wavelength (and one sensor) of absorption related to SPM at a time provide a little more insight. At mid-shelf stations, most of the paired

absorption to SPM data is plotted on the "lower branch" of the bifurcated data. The data pairs from the inner shelf stations are usually plotted along both the upper and lower branches. Most of the SPM sampled on the outer shelf/slope stations have concentrations less than 1.5 mg/l and generally did not bifurcate.

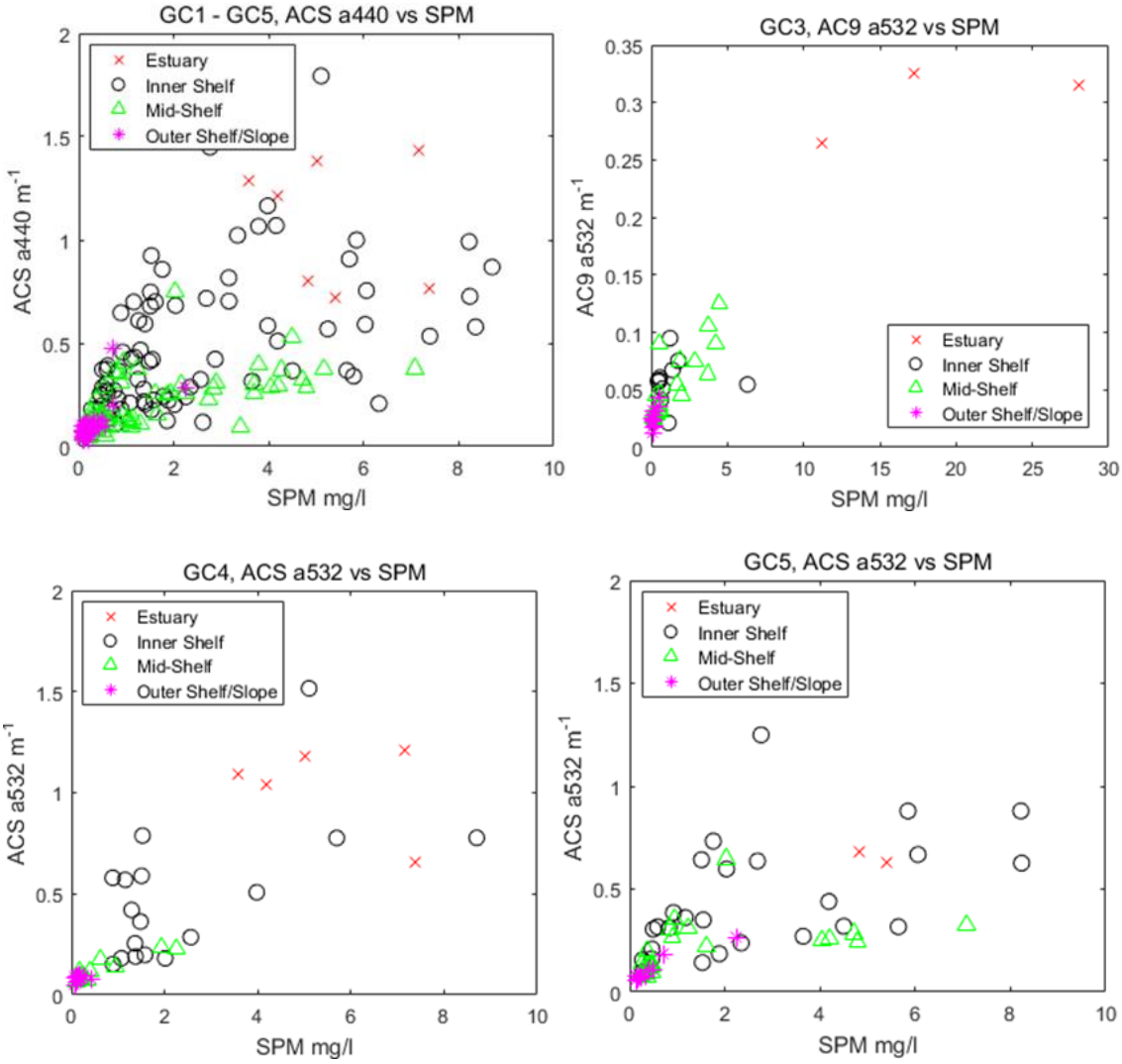

Figure 44. SPM vs. AC9 a & ACS a By Station Type, Selected Scatter Plots

These plots display selected cruises, wavelengths and ranges of data.

The absorption budget for the northern Gulf of Mexico during the sampling periods of this research reported by Sumit Chakraborty (Chakraborty, 2013) provides

some insight into the bifurcation of the absorption versus SPM data and is summarized here. Absorption from non-algal particles (analyzed at 440 nm) was highest in the Chakraborty estuary and inner-shelf stations and lower in the mid-shelf and outer-shelf/slope stations. The reported Pearson linear correlation coefficient between a_{NAP} and SPM was $r^2 = 0.91$, $p < 0.001$, $n = 229$ (Chakraborty, 2013), higher than this work's report of $\rho = 0.87$ or 0.86 for the AC9 and ACS respectively between *a* and SPM. Absorption by algal particles a_{φ} (440 nm) was higher in the estuary and inner-shelf waters and very high at end-member stations C0 (Terrebonne Bay), E1 (Atchafalaya River) and MR2 (Mississippi River). Absorption caused by CDOM and phytoplankton (measured using different methods at 440 nm) were also high in the estuary and inner-shelf waters and lower elsewhere. The a_{CDOM} displayed seasonal variability in the inner shelf waters and was strongly influenced by river discharge. The percentages that each of these absorption contributors added to the total absorption budget have already been reported (Chakraborty, 2013).

Previous work has suggested that CDOM is generally the largest contributor to total absorption at the shorter visible light wavelengths makes a much less substantial (even negligible) impact on the longer visible wavelengths including 650, 660 and 670 nm, (D. Doxaran et al., 2012) which are utilized by various sensors in this project.

SPM Prediction Based Upon Absorption

In calculating the linear algorithm coefficients to predict SPM from absorption reported by the AC9 and the ACS, the data were evaluated as a whole set, and not further divided into the branched groups as seen on the scatter plots. These coefficients are found in Tables 31 (based on GCALL data pairs) and 68 (based on individual cruise data pairs).

The SPM predictive models from the GCALL datasets are plotted in Figure 45. Upon looking at these tables and plots, it is clear that these algorithm coefficients are not interchangeable by wavelength or sensor.

The modeled SPM slopes generally increase with wavelength. Most of the y-axis intercepts are well above zero. Translated into terms of SPM, this means that even if the AC sensors report a value of zero absorption at a given wavelength, the observed sample space is assumed to contain an appreciable amount of SPM. In other words, these algorithm coefficients assume that there is always up to at least the intercept amount (in mg/l) SPM in the water. (Even in the clearest waters, the algorithm using AC9 absorption values at 715 nm will predict an SPM concentration of at least 3.5 mg/l.) This problem becomes more acute as wavelengths increase. Though absorption is not a good SPM predictor, it is a key component for calculating other optical properties (such as scatter) and is a contributor to some of the IOP combinations under consideration.

Table 31

SPM Algorithm Coefficients from AC9 & ACS Absorption Coefficients

Wavelength nm	AC9 GC2 - GC5		ACS GC1 - GC5	
	m (Uncertainty)	b (Uncertainty)	m (Uncertainty)	b (Uncertainty)
412	11.942 (0.040)	-1.859 (0.065)	9.666 (0.030)	-1.338 (0.067)
440	12.308 (0.039)	-1.042 (0.064)	10.394 (0.032)	-0.393 (0.066)
488	14.134 (0.044)	0.161 (0.063)	12.149 (0.037)	0.701 (0.065)
510	15.526 (0.048)	0.59 (0.062)	13.093 (0.040)	1.073 (0.065)
532	17.261 (0.053)	1.003 (0.062)	14.006 (0.043)	1.382 (0.065)
555	17.694 (0.055)	1.353 (0.062)	15.097 (0.046)	1.667 (0.064)
595	N/A	N/A	16.944 (0.052)	2.208 (0.064)
650	21.837 (0.070)	2.071 (0.062)	22.006 (0.073)	2.299 (0.064)
660	N/A	N/A	21.339 (0.068)	2.170 (0.064)
670	N/A	N/A	20.987 (0.066)	2.014 (0.064)
676	22.077 (0.073)	1.938 (0.062)	19.498 (0.061)	2.117 (0.064)
715	23.228 (0.077)	2.978 (0.061)	24.204 (0.081)	3.113 (0.064)

Notes. The slopes and intercepts are for linear SPM predictive algorithms y = mx + b. The uncertainty for the regression slopes and intercepts were calculated using singular value decomposition. Salinity exclusions and coarse visual inspection exclusions were applied. SPM algorithm coefficients calculated from data produced during individual cruises are found in Table 68.

In addition to the initial offset (y-intercept) indicating a presumed presence of SPM, the plots and tables of the SPM prediction algorithms from absorption provide some additional insight into sensor performance. The SPM models (both slope and intercept) from the ACS sensors progress upward in a regular fashion with respect to wavelength. The same general trend is seen with the AC9 models but is not as regular as it is with the ACS. The models utilizing wavelengths 412 nm and 532 nm stand out due to a large intercept (2.116 ±0.063) and small slope (11.026 ±0.042) respectively relative to the other AC9 wavelengths. However, both slopes are statistically close to one another, and the intercepts are statistically the same for these two wavelengths for both the AC9 and the ACS. The lack of regular progression noted in the ACS models demonstrated by the AC9 models is probably related to the fact that each wavelength was measured from an individual light source rather than a single light source whose outgoing wavelength is modified by a rotating filter (Chapters II and IV).

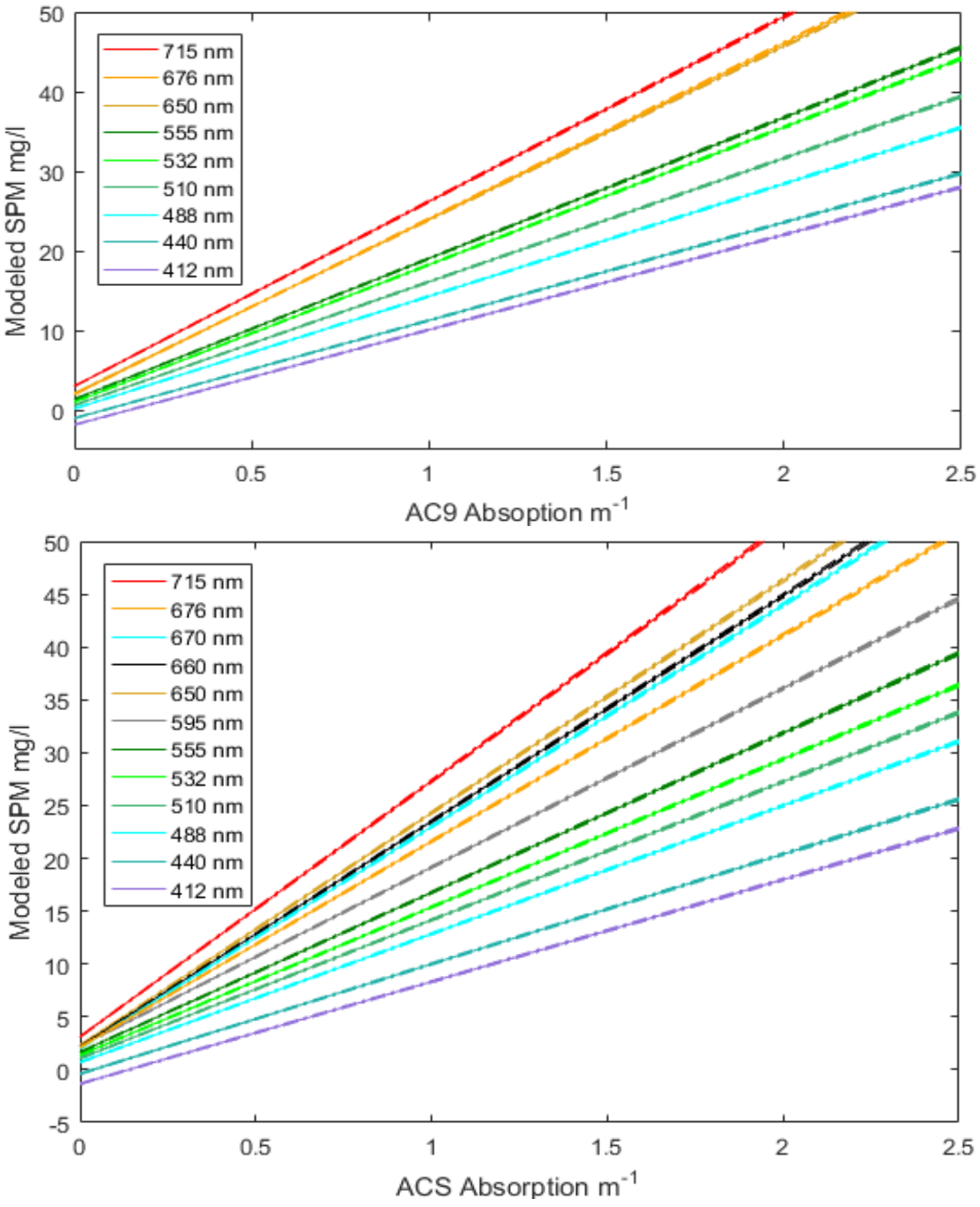

Figure 45. AC9 & ACS Absorption Based SPM Models

Notes: Modeled SPM concentration based on absorption at nine wavelengths. Upper and lower boundaries determined by uncertainty of the algorithm coefficients are plotted above and below the modeled SPM at each wavelength. (They are barely discernable at this resolution.) The AC9 coefficients are based on data from GC2 – GC5. The ACS coefficients are based on data from GC1 - GC5. For the ACS plot (bottom), the wavelengths observed by the AC9, BB9, C-Star transmissometer and LISST are plotted.

IOP Attenuation (c)

Beam attenuation is frequently used to characterize SPM concentration both independently and as part of an IOP combination (Ackleson, 2006; Emmanuel Boss et al., 2009; David Doxaran et al., 2009; Halper & McGrail, 1988; Hill, Boss, Newgard, Law, & Milligan, 2011; Hommersom et al., 2009; Jones, Noble, & Dickey, 2002; Joyce, Bishop, & Brown, 1992; Krivtsov et al., 2008; Lane et al., 2000; Lindsay, Balls, & West, 1996; McCave et al., 2001; Pak, Zaneveld, & Spinrad, 1984; Albert Palanques & Biscaye, 1992; Puig & Palanques, 1998; Ribó, Puig, Salat, & Palanques, 2013; A. Weeks & Simpson, 1991; A. R. Weeks, Simpson, & Bowers, 1993; Wild-Allen, Lane, & Tett, 2002; R. E. Wilson, 1979; Ziervogel et al., 2016). The IOP attenuation (c) is composed of three parts, attenuation due to particles, attenuation due to water and attenuation due to CDOM. In other words, $c = c_p + c_w + c_{CDOM}$ (A. P. Karageorgis et al., 2014). Some researchers further delineate the relationship between SPM and particulate attenuation (c_p) by subtracting an observed attenuation value representing "clear water" from the datasets collected during each project (Bishop, 1986; Chung et al., 1996; Fennel & Boss, 2003; Ferreira, Garcia, Dogliotti, & Garcia, 2013; Garcia et al., 2011; A. P. Karageorgis et al., 2012; Loisel & Morel, 1998; Mishonov, Gardner, & Jo Richardson, 2003; Puig et al., 2013; A. M. Wilson, Raine, Mohn, & White, 2015). Occasionally it has been noted that these clear water values differ from a pure water assumption (Biscaye & Eittreim, 1977; Jacobs, Thorndike, & Ewing, 1973). Additional methods have also been used to determine c_p (Loisel, Me´riaux, Berthon, & Poteau, 2007; Oubelkheir et al., 2006; Ribó et al., 2013; Westberry, Dall?Olmo, Boss, Behrenfeld, & Moutin, 2010; Xing et al., 2014). Still other researchers have specified that c reported by transmissometers using equation

2.7 is an adequate representation of c_p for their research (Hurley, Hill, Milligan, & Law, 2016; Kheireddine & Antoine, 2014; Lorenzoni et al., 2012; Lorenzoni et al., 2009; Lund-Hansen, Andersen, Nielsen, & Pejrup, 2010; G. Neukermans, Loisel, Meriaux, Astoreca, & Mckee, 2012).

In this project, SPM was related directly to c as reported by various sensors. Additional procedures to estimate c_p were not taken in this research. Others have also utilized this approach (Ackleson & O'Donnell, 2011; Baker, 1984; Bergmann, Fahnenstiel, Lohrenz, Millie, & Schofield, 2004; Churchill, Biscaye, & Aikman Iii, 1988; D. Doxaran et al., 2012; Durrieu de Madron et al., 2005; Hawley & Lesht, 1992; McCandliss, Jones, Hearn, Latter, & Jago, 2002; A. Palanques, Guille´n, & Puig, 2001; Puig & Palanques, 1998; L. E. Wells et al., 2006).

The effect of CDOM absorption in the spectral region of c650, c660, and c670 is considered to be negligible (Ackleson & O'Donnell, 2011). Recalling that c = a + b, reports of attenuation in red wavelengths should be most affected by scattering components of living and nonliving material. (Absorption by pure water is already removed from these sensor reports during calibration events.) Furthermore, in general, absorption values are relatively small at these longer wavelengths thus explaining the selection of red light utilized by most single-wavelength transmissometers.

This research shows that the relationship between SPM and attenuation is significantly stronger than between SPM and absorption. The correlation coefficients are both higher and more similar to each other regardless of the wavelength (Tables 31, 32, and 59). This may also be seen in two other visualizations relating SPM to absorption and SPM to attenuation. First are the plots of spectral Spearman’s rho between SPM in

relation to absorption (Figure 28) and SPM in relation to attenuation (Figure 33). Second, the differences between the relationship between SPM and absorption and SPM and attenuation may be viewed by comparing the scatter plots in Figure 43 and Figure 46. There is generally more scatter in the plots between SPM and absorption than there is between SPM and attenuation. Additionally, the bifurcation observed in the SPM versus absorption scatter plots is not observed in the plots relating SPM to attenuation.

When considering the cruise-by-cruise data (Table 59), it is noted that the GC5 correlation values between attenuation and SPM are universally higher regardless of the sensor used or the wavelength studied. For the ACS, the $\rho = 0.96$ for all wavelengths studied for GC5. Additionally, the relationship between ACS c and SPM also reported high correlation coefficients of either 0.95 and 0.96 ($p = 0.00$) for all wavelengths under consideration.

Table 32

Relationship Between SPM and Attenuation (AC9 & ACS)

Wavelength nm	AC9 c vs. Measured SPM Spearman Correlation Coefficients			ACS c vs. Measured SPM Spearman Correlation Coefficients		
	ρ	p	n	ρ	p	n
412	0.91	0.00	273	0.90	0.00	280
440	0.91	0.00	273	0.90	0.00	280
488	0.91	0.00	273	0.90	0.00	280
510	0.91	0.00	273	0.90	0.00	280
532	0.91	0.00	273	0.89	0.00	280
555	0.91	0.00	273	0.89	0.00	280
595	N/A	N/A	N/A	0.89	0.00	280
650	0.91	0.00	273	0.89	0.00	280
660	N/A	N/A	N/A	0.89	0.00	280
670	N/A	N/A	N/A	0.89	0.00	280
676	0.91	0.00	273	0.89	0.00	280
715	0.91	0.00	273	0.89	0.00	280

Note: Salinity, profiler induced turbidity, and visual inspection exclusions were applied. See Table 59 for cruise by cruise coefficients.

The results of this dissertation research correlate well with another project that utilized an AC9 to study the relationship between attenuation and SPM. At the Mackenzie River plume in the western Canadian Arctic, it was reported that at c(555) there was a strong correlation coefficient (Pearson) $R^2 = 0.97$, n = 35 to SPM concentration (D. Doxaran et al., 2012). As with this research, an AC9 was used to obtain the c(555) values.

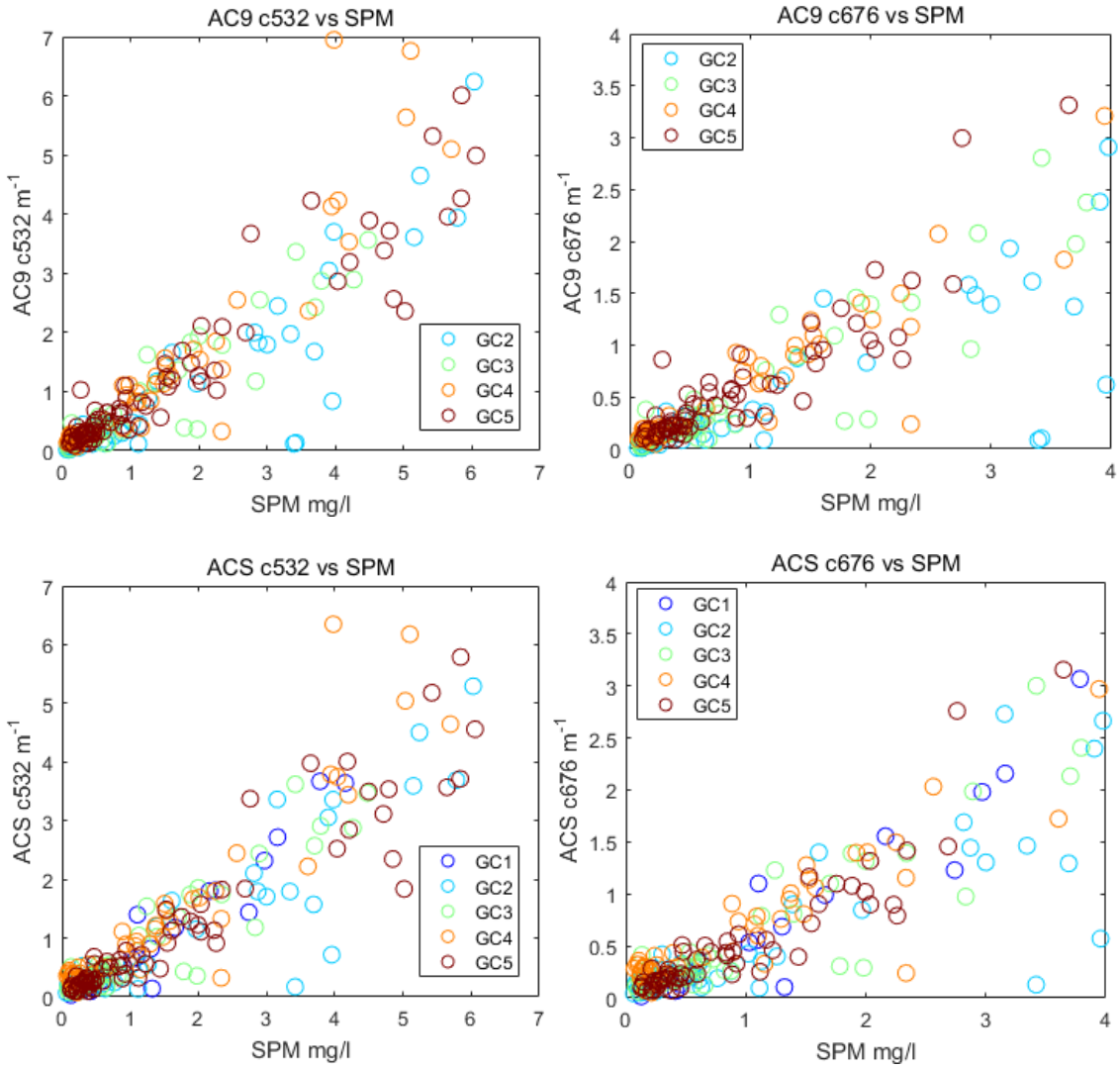

Figure 46. SPM vs. AC9 c & ACS c Selected Scatter Plots

These plots display selected wavelengths and ranges of data.

In addition to analyzing the relationship between SPM and c reported by the AC9 and the ACS sensors, the attenuation coefficients detected by the transmissometer (650 nm) and the LISST (670 nm) were also considered (Tables 33 and 34, also Figures 47 and 48). The correlations between SPM and these attenuation values were also strong. While these correlations were typically high, the LISST reported somewhat lower correlation coefficients to SPM concentration even after data suspected of being

influenced by schlieren were removed from the working dataset. This effect is likely caused by the differences in measurement utilized by these two sensors. Similar to circumstances recorded by both the AC9 and ACS sensors, GC5 was noted for exceptionally high (relative to GCALL) correlation values between SPM and attenuation reported by both the transmissometer and the LISST. Also, as with the ACS, the LISST reported a high correlation value between the two properties for GC1 as well.

Table 33

Relationship Between SPM and Attenuation (Transmissometer)

Cruise	Spearman's ρ	Spearman's p	n
GC1	0.92	0.00	36
GC2	0.92	0.00	92
GC3	0.93	0.00	93
GC5	0.97	0.00	97
GC2, GC3 & GC5	0.92	0.00	282
GCALL	0.91	0.00	318

Notes. The row GC2, GC3 & GC5 combines the data from the specified cruises. GCALL combines the data from all available cruises. Transmissometer saturation exclusions are applied.

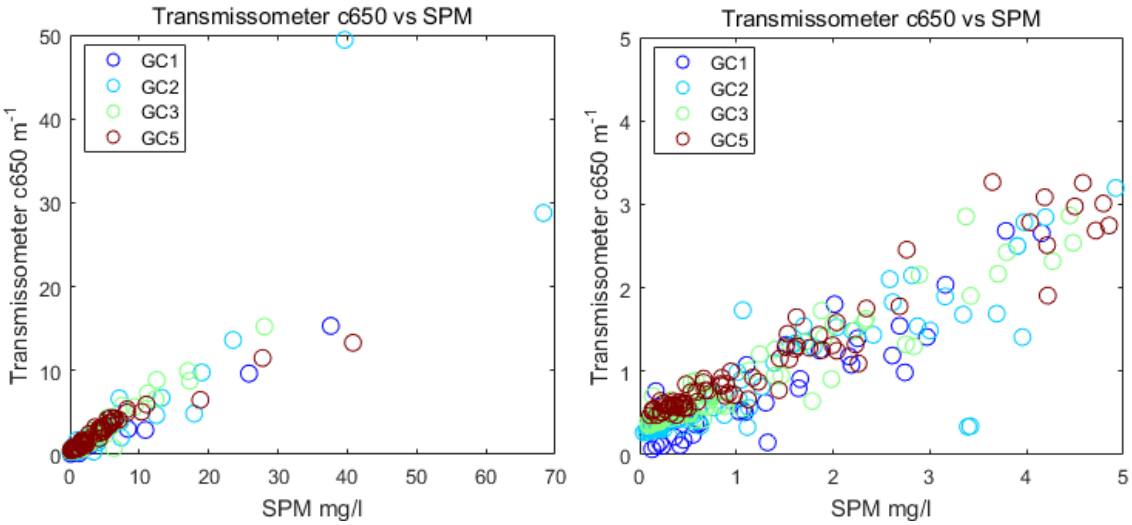

Figure 47. SPM vs. Transmissometer c Scatter Plots

The plot on the left displays all available data. The plot on the right displays selected ranges of data.

Table 34

Relationship Between SPM and Attenuation (LISST)

Cruise	No Suspected Schlieren Removal			Suspected Schlieren Removed		
	Spearman's ρ	Spearman's p	n	Spearman's ρ	Spearman's p	n
GC1	0.94	0.00	29	0.95	0.00	20
GC2	0.84	0.00	75	0.79	0.00	47
GC3	0.77	0.00	67	0.79	0.00	56
GC4	0.83	0.00	59	0.73	0.00	29
GC5	0.93	0.00	86	0.94	0.00	51
GC1, GC2, GC3, GC5	0.85	0.00	257	0.83	0.00	174
GCALL	0.84	0.00	316	0.83	0.00	202

Notes. GCALL combines the data from all available cruises. Salinity data exclusions were applied.

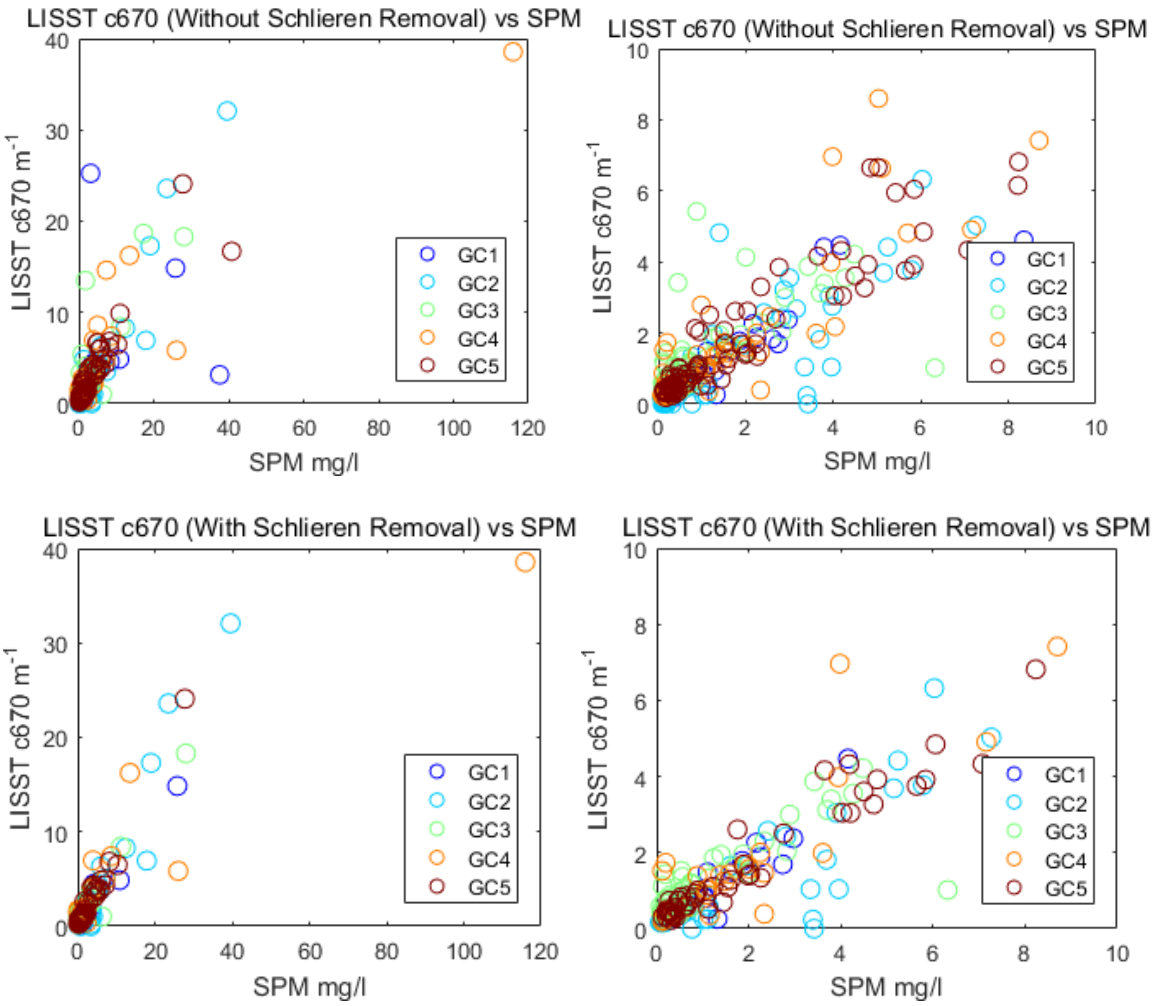

Figure 48. SPM vs. LISST c Scatter Plots

The plots on the left display all available data. The plot on the right displays selected ranges of data. Upper plots show the complete dataset. The lower plots show the same dataset after instances of suspected schlieren were removed. Salinity and CTD-T based exclusions were also removed.

SPM Prediction Based Upon Attenuation

Linear algorithm coefficients for the prediction of SPM using attenuation coefficients are reported for the AC9 and ACS datasets at wavelengths 412 nm, 440 nm, 488 nm, 510 nm, 532 nm, 555 nm, 650 nm, 676 nm, and 715 nm (Tables 35 and 69). Additional algorithm coefficients for attenuation observed from the transmissometer and LISST are found in Tables 36 and 37 respectively. Uncertainties for the algorithm

coefficients were calculated using singular value decomposition. The models were then plotted (Figures 49, 50 and 51) along with the uncertainties related to algorithm coefficients. The attenuation-based SPM models using the AC9 are relatively disordered in relation to wavelength progression. Conversely, the absorption-based SPM models using the ACS have patterns of increasing slopes (m) and origin offsets (b) with increasing wavelength.

Table 35

SPM Algorithm Coefficients from AC9 & ACS Attenuation Coefficients

Wavelength nm	AC9 GC2 - GC5 m (Uncertainty)	AC9 GC2 - GC5 b (Uncertainty)	ACS GC1 - GC5 m (Uncertainty)	ACS GC1 - GC5 b (Uncertainty)
412	0.925 (0.013)	0.304 (0.068)	1.226 (0.015)	-0.130 (0.069)
440	1.099 (0.015)	0.146 (0.069)	1.244 (0.015)	0.003 (0.068)
488	1.195 (0.017)	0.181 (0.068)	1.350 (0.016)	0.051 (0.068)
510	1.226 (0.017)	0.207 (0.068)	1.396 (0.017)	0.066 (0.068)
532	1.266 (0.018)	0.227 (0.068)	1.441 (0.017)	0.081 (0.068)
555	1.307 (0.018)	0.237 (0.068)	1.484 (0.018)	0.099 (0.068)
595	N/A	N/A	1.560 (0.019)	0.128 (0.068)
650	1.461 (0.021)	0.296 (0.068)	1.663 (0.020)	0.155 (0.068)
660	N/A	N/A	1.681 (0.020)	0.161 (0.068)
670	N/A	N/A	1.699 (0.021)	0.163 (0.068)
676	1.506 (0.021)	0.312 (0.068)	1.708 (0.021)	0.164 (0.068)
715	1.574 (0.022)	0.336 (0.068)	1.782 (0.022)	0.212 (0.067)

Notes. The slopes and intercepts are for linear SPM predictive algorithms y = mx + b. The uncertainty for the regression slopes and intercepts were calculated using singular value decomposition. Salinity exclusions and visual inspection exclusions were applied. SPM algorithm coefficients calculated from data produced during individual cruises are found in Table 69.

At the Mackenzie River Plume (Canadian Arctic) it was reported in predicting SPM from c(555) that the slope was nearly 1.00 and that there was “a negligible intercept” which is understood to be statistically zero (D. Doxaran et al., 2012). There was clearly a difference between that project area and the northern Gulf of Mexico where the SPM prediction slopes and intercepts from c555 are significantly greater than 1.00 and 0.00 respectively. Another set of linear regression estimates of SPM from an AC9 630 nm dataset produced $y = 1.8828\ x - 0.5047$ ($R^2 = 0.9019$) where x and y are c(630) and SPM respectively (Bergmann et al., 2004). These regressed values do not fit well between the comparable coefficients reported for the bounding wavelengths (555 and 650 nm for the AC9 and 595 and 650 for the ACS) reported in this project. As both projects mentioned here used an AC9 for attenuation measurements, the acceptance angles of the two AC9 sensors are assumed to have been the same at 0.93^{O}. Therefore the differences between the linear regressions may be attributed to regional or temporal differences in the population components for SPM and CDOM.

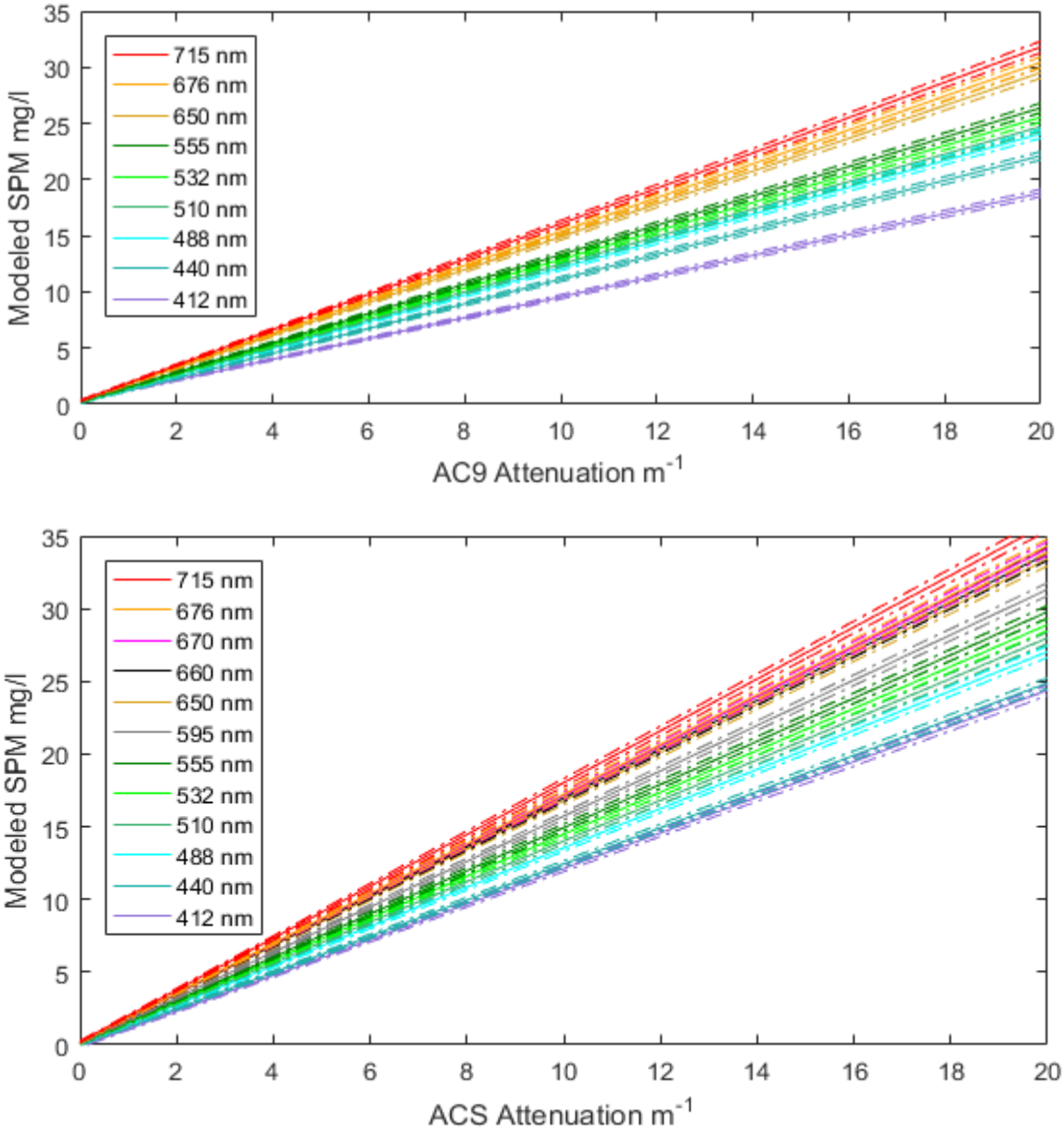

Figure 49. AC9 & ACS Attenuation-Based SPM Models

Modeled SPM concentration based on attenuation. Upper and lower boundaries determined by uncertainty of the algorithm coefficients are plotted above and below the modeled SPM at each wavelength. (They are barely discernable at this resolution.) The AC9 coefficients are based on data from GC2 – GC5. The ACS coefficients are based on data from GC1 - GC5. The plotted ACS wavelengths represent the wavelengths observed by the AC9, BB9, C-Star transmissometer and the LISST.

Table 36

SPM Algorithm Coefficients from Attenuation (Transmissometer)

Cruise	m (uncertainty)	b (uncertainty)	n
GC1	2.533 (0.058)	-0.532 (0.192)	36
GC2	1.250 (0.017)	0.738 (0.111)	92
GC3	1.761 (0.042)	-0.442 (0.125)	93
GC5	2.503 (0.048)	-1.657 (0.135)	97
GC2, GC3 & GC5	1.440 (0.015)	0.236 (0.066)	282
GCALL	1.505 (0.014)	0.227 (0.062)	318

Notes. The slopes and intercepts are for linear SPM predictive algorithms y = mx + b. The uncertainty for the regression slopes and intercepts were calculated using singular value decomposition. The row GC2, GC3 & GC5 combines the data from the specified cruises. GCALL combines the data from all available cruises. Transmissometer exclusions are applied.

Transmissometer based SPM models are reported in Table 36 and Figure 50. For comparison, a C-Star transmissometer based SPM linear algorithm was published in 2006 (L. E. Wells et al., 2006): SPM = 2.778*c660 – 0.130. While the slopes of GC1 and GC5 are similar to the linear regression performed in the Canadian Arctic (L. E. Wells et al., 2006), the absolute values of y-intercepts are all much smaller. These researchers used a WET Labs C-Star transmissometer using wavelength 660 nm, rather than at 650 nm (the wavelength utilized in the northern Gulf of Mexico). Current specifications state that C-Star transmissometers utilize the 650 nm wavelength. However, since the specifications also claim that the sensor has ~20 nm bandwidth, perhaps this 10 nm difference doesn't signify given the receiver angle uncertainty discussed in Chapter IV.

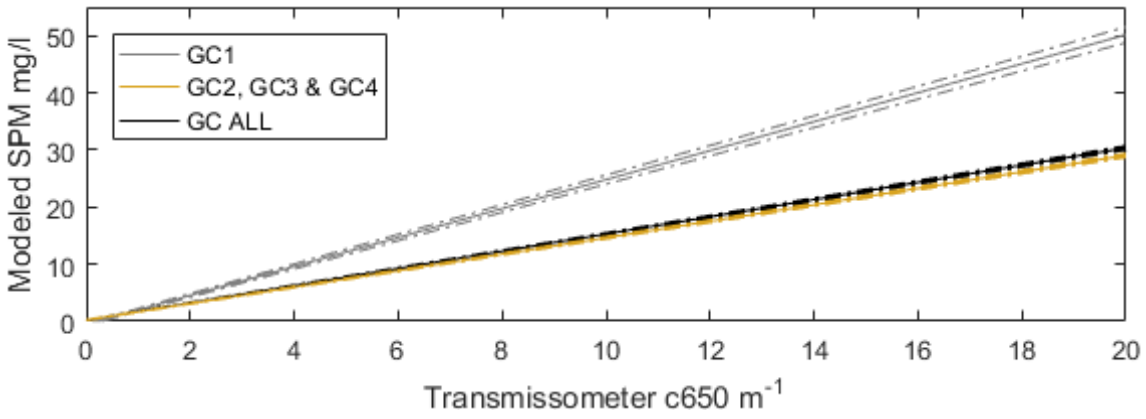

Figure 50. Transmissometer Attenuation-Based SPM Models

Modeled SPM concentration based on attenuation. Upper and lower boundaries determined by uncertainty of the algorithm coefficients are plotted above and below the modeled SPM at each wavelength. (They are barely discernable at this resolution.) The upper model represents GC1. The x-axis is plotted at the same resolution as the AC9 and ACS models based upon attenuation.

The SPM models based upon attenuation calculated from LISST observations are reported in Table 37 and Figure 51. The cruise by cruise regressions were developed using relatively low sample numbers. This means that the variability of these coefficients may reflect spatial differences as well as temporal ones. The algorithm slope and intercept are both lower than those reported for the ACS using the GCALL dataset.

Table 37

SPM Algorithm Coefficients from Attenuation (LISST)

Cruise	m (Uncertainty)	b (Uncertainty)	n
GC1	1.747 (0.070)	-0.548 (0.266)	20
GC2	1.161 (0.024)	0.526 (0.162)	47
GC3	1.491 (0.051)	-0.670 (0.157)	56
GC4	2.979 (0.027)	-2.801 (0.204)	29
GC5	1.197 (0.040)	0.014 (0.164)	51
GC1, GC2, GC3 & GC5	1.258 (0.018)	-0.009 (0.086)	174
GCALL	1.186 (0.015)	-0.922 (0.078)	203

Notes. The slopes and intercepts are for linear SPM predictive algorithms y = mx + b. The uncertainty for the regression slopes and intercepts were calculated using singular value decomposition. GC ALL combines the data from all available cruises. Coefficients were calculated after locations of suspected schlieren were removed.

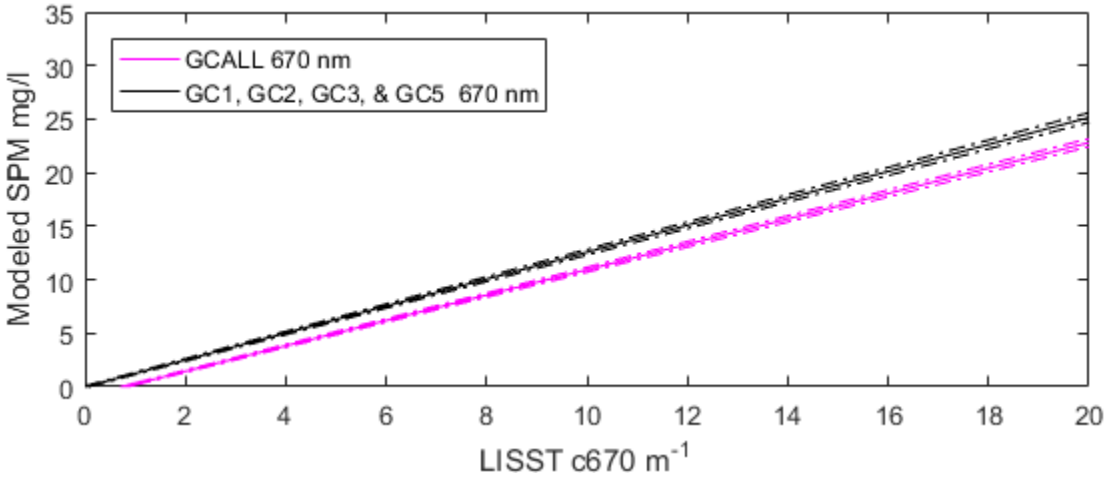

Figure 51. LISST Attenuation-Based SPM Model

Modeled SPM concentration based on attenuation. Upper and lower boundaries determined by uncertainty of the algorithm coefficients are plotted above and below the modeled SPM at each wavelength. (They are barely discernable at this resolution.) This figure is plotted at the same resolution as the AC9 and ACS models based upon attenuation.

Some drawbacks in using attenuation as a proxy for bulk SPM have been documented. In one study, changes in attenuation were noted even though the concentration of SPM remained relatively unchanged (Curran et al., 2007). Also, smaller particles scatter light more effectively (and at larger angles) than larger particles thus

creating a non-uniform response to populations of the same concentrations but consisting of different particle sizes (Ellis, Bowers, & Jones, 2004). Others have also noted that the attenuation coefficient has been known to change relative to the index of refraction and particle size distribution of SPM (Behrenfeld & Boss, 2003; Campbell & Spinrad, 1987; W. D. Gardner, Mishonov, & Richardson, 2006; Jago & Bull, 2000; Kitchen & Zaneveld, 1992; Oubelkheir et al., 2005).

IOP Total Scatter (b) from the AC9 & ACS

Total scatter values have previously been used to estimate SPM (Babin, Morel, Fournier-Sicre, Fell, & Stramski, 2003; Bowers, Braithwaite, Nimmo-Smith, & Grahamb, 2009). Uncertainty associated with the relation of b to SPM has been attributed to variability in the organic components of SPM (Martinez-Vicente, Land, Tilstone, Widdicombe, & Fishwick, 2010). In addition to being useful as an SPM predictor on its own, total scattering values are necessary components for backscatter ratio calculations (performed later in this research). In some open ocean studies, $c_p(660)$ has been used as a proxy for $b_p(660)$ (Loisel et al., 2007). Total scatter (and sometimes total particulate scatter) has previously been estimated by subtracting AC9 and ACS absorption measurements from the corresponding attenuation coefficients without imposing any further offsets (Emmanuel Boss et al., 2013; Doron et al., 2007; D. Doxaran et al., 2012; David Doxaran et al., 2009; Loisel et al., 2007; Martinez-Vicente et al., 2010; David McKee et al., 2009; David McKee & Cunningham, 2006; Oubelkheir et al., 2006; Sipelgas & Raudsepp, 2015; Terrie, Ladner, & Gould, 1997). This method was employed in this research. Where applicable, total scatter (minus the contribution from pure water measured during sensor calibrations) was calculated at filterdepths for the AC9 and the

ACS using the relationship b = c - a. Sometimes the coefficient for total scatter is also written as b_t.

The relationships between b and SPM for this project are reported in Table 38 and 60. These values are relatively high (0.89 p = 0.00 to 0.93 p = 0.00) for all nine evaluated wavelengths from both sensors. Cruise by cruise evaluations indicate variation of these values by space and time. These variations have similar causes to the differences noted in the correlation calculations between SPM and attenuation (particle size and index of refraction). The temporal variations are fairly easy to identify. For example, the SPM to b_t correlation values for GC2 are lower than those calculated for any of the other cruises regardless of which attenuation sensor was used. Conversely, the correlation values between SPM and b from GC5 are universally high regardless of the sensor used to as the source for absorption and attenuation data. The similarity of correlation values of the sensors for the cruises (GC2, GC4, and GC5) indicates minor temporal variation in how well natural water scatters light in the project area (marginally well during GC2 and better during GC4 and GC5). Spatial variation in how well SPM correlates to b may be inferred from the fact that larger differences in correlation values are seen by a sensor to sensor comparison for each cruise than in the combined cruise data sets. The ACS cruise-by-cruise data pairs of SPM and IOP values are significantly smaller than similar datasets related to the AC9. (This is similar to the low n-values associated with the quality-approved LISST data.)

Considering that there were often large differences in the number of b_t data available from the different sensors, it is clear that AC9 b_t data was available at positions that were not procurable in the ACS b_t data set. It is also likely that the ACS b_t dataset

contained some positions not available in the AC9 b_t dataset. The larger n values associated with the total available data sets (265 and 186 for the AC9 and ACS respectively) likely provide a better regional representation than evaluating these datasets cruise-by-cruise by region. As with the attenuation coefficients, there were stronger correlation values associated with GC5 than the other cruises.

Table 38

Relationship Between SPM and b, (AC9 & ACS)

Wavelength nm	GC2 - GC5 AC9			GC1 - GC5 ACS		
	ρ	p	n	ρ	p	n
412	0.89	0.00	257	0.92	0.00	182
440	0.90	0.00	257	0.93	0.00	182
488	0.90	0.00	257	0.93	0.00	182
510	0.90	0.00	257	0.93	0.00	182
532	0.90	0.00	257	0.93	0.00	182
555	0.90	0.00	257	0.93	0.00	182
595	N/A	N/A	N/A	0.93	0.00	182
650	0.90	0.00	256	0.93	0.00	182
660	N/A	N/A	N/A	0.93	0.00	182
670	N/A	N/A	N/A	0.93	0.00	182
676	0.90	0.00	257	0.93	0.00	182
715	0.90	0.00	256	0.93	0.00	181

Notes: Salinity and profiler induced turbidity-based exclusions were applied. The ACS data filter was applied. Visual inspection exclusions of a and c were applied. See Table 60 for cruise by cruise coefficients.

At the Mackenzie River plume in the western Canadian Arctic, it was reported that for b(555) there was a strong determination coefficient $R^2 = 0.98$, n = 35 to SPM concentration (D. Doxaran et al., 2012). As with this research, an AC9 was used to calculate the b(555) values. The results of these two projects correlate well. An earlier (1987 – 1988) study on the Louisiana shelf waters had a strong correlation between b – b_w (at 655 nm) and SPM ($R^2 = 0.846$, n = 29) (Højerslev & Aarup, 2002) where b_w was

the scattering of pure water at 655 nm, and b represented scatter including the water component.

Representative scatter plots relating SPM to b_t in the northern Gulf of Mexico are shown in Figure 52. Not surprisingly, they are similar to the ones depicting SPM and attenuation from the AC9 and the ACS in Figure 46.

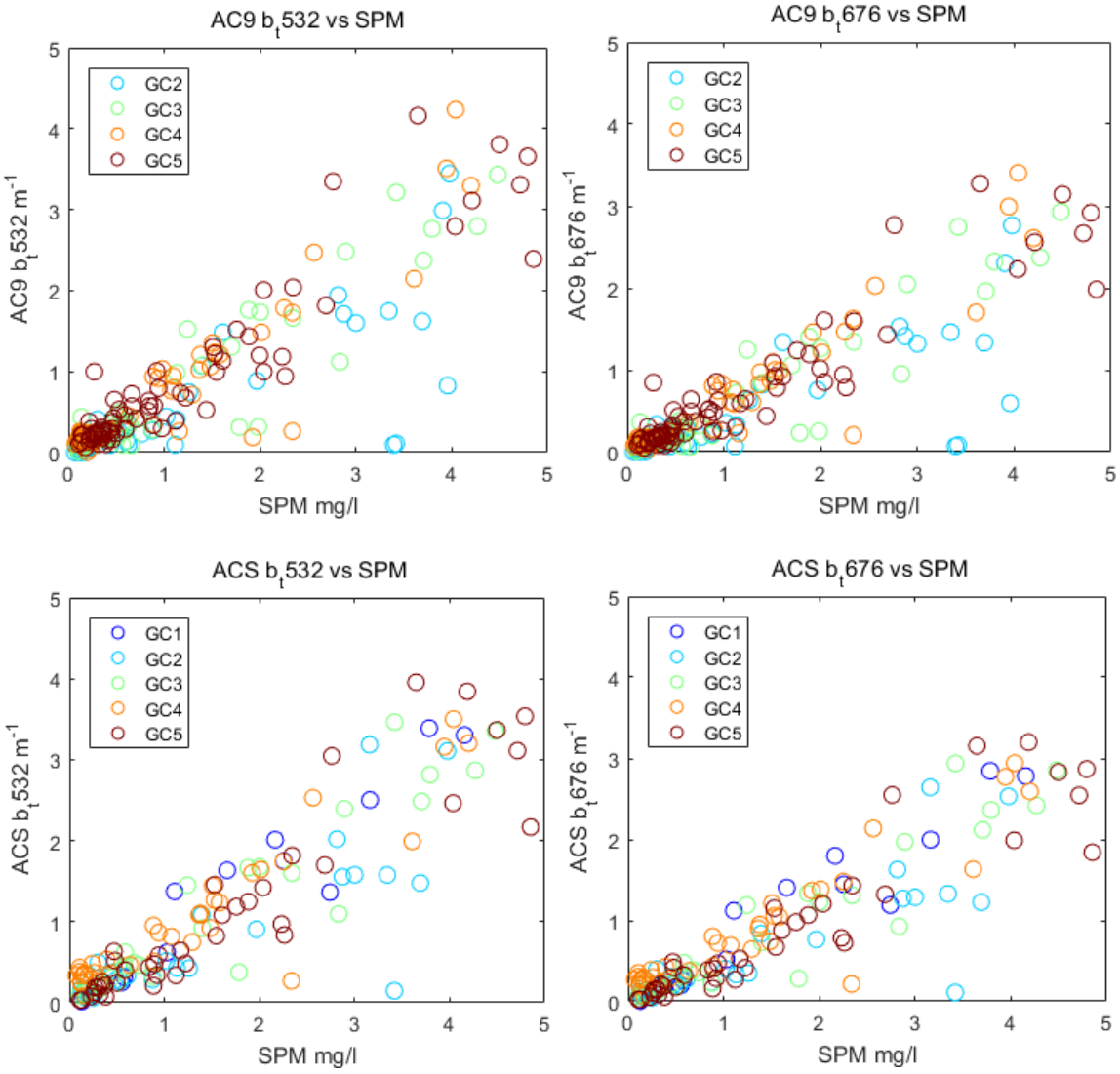

Figure 52. SPM vs. b (AC9 & ACS) Selected Scatter Plots

These plots display selected wavelengths and ranges of data.

The potential impact of clear water on total scatter is very different than the potential effect it has upon absorption. Unlike the absorption of pure water (Figure 29) scattering of pure water decreases with increasing wavelength. Figure 53 was created using data reported by (R. C. Smith & Baker, 1981) of the total molecular scatter of spectral light by pure water and pure sea water. The wavelengths used by the AC9 and the BB9 are denoted. Molecular backscatter by pure fresh water and pure sea water was assumed to be half of the total molecular scatter value based on algorithms reported by Andre Morel (A. Morel, 1974) (WET_Labs, 2008b).

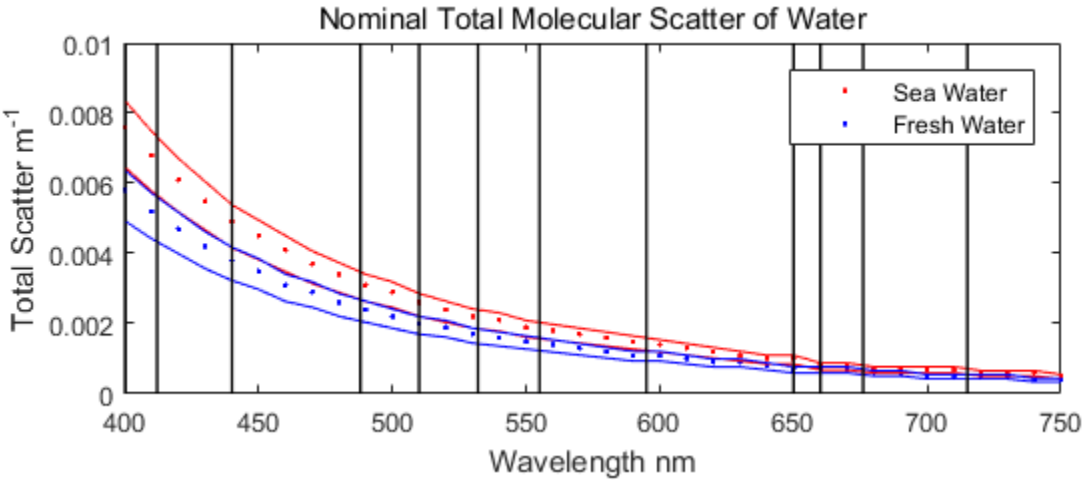

Figure 53. Spectral Total Scatter of Pure Water

This figure is based on (A. Morel, 1974). Vertical lines are plotted at wavelengths observed by the AC9, BB9 and LISST sensors.

SPM Prediction Based Upon Scatter

Table 39 presents the GCALL linear algorithm coefficients for predicting SPM with b_t. Cruise by cruise algorithm coefficients may be found in Table 70. Note that the intercept uncertainties (and most of the slope uncertainties) exceed the expected total scatter of pure water. Plots of the SPM prediction models from b_t derived from the AC9 and the ACS are in Figure 54.

Table 39

SPM Algorithm Coefficients from b, (AC9 & ACS)

Wavelength nm	AC9 GC2 - GC5		ACS GC1 - GC5	
	m (Uncertainty)	b (Uncertainty)	m (Uncertainty)	b (Uncertainty)
412	0.639 (0.009)	1.177 (0.066)	1.383 (0.018)	-0.018 (0.088)
440	0.648 (0.009)	1.250 (0.066)	1.356 (0.017)	0.100 (0.088)
488	0.697 (0.010)	1.215 (0.066)	1.420 (0.018)	0.106 (0.088)
510	1.040 (0.013)	0.643 (0.068)	1.451 (0.018)	0.109 (0.088)
532	1.207 (0.015)	0.420 (0.069)	1.483 (0.019)	0.118 (0.088)
555	1.281 (0.016)	0.358 (0.069)	1.515 (0.019)	0.135 (0.088)
595	NaN	NaN	1.576 (0.020)	0.160 (0.087)
650	1.431 (0.018)	0.388 (0.069)	1.669 (0.021)	0.205 (0.087)
660	NaN	NaN	1.688 (0.022)	0.223 (0.087)
670	NaN	NaN	1.707 (0.022)	0.239 (0.087)
676	1.480 (0.019)	0.415 (0.069)	1.716 (0.022)	0.240 (0.087)
715	1.539 (0.019)	0.388 (0.069)	1.767 (0.023)	0.248 (0.087)

Notes. The slopes and intercepts are for linear SPM predictive algorithms y = mx + b. The uncertainty for the regression slopes and intercepts were calculated using singular value decomposition. SPM algorithm coefficients calculated from data produced during individual cruises are found in Table 70.

A study performed in 1987 and 1988 in Louisiana shelf waters using a scattering sensor at 655 nm reported that SPM = 11.66 * ($b(655) – b_w(655)$) ($R^2 = 0.846$, n = 29) (Højerslev & Aarup, 2002). Since the pure water contributions of both absorption and scattering have already been removed from the scattering coefficients in this work, the last component of the aforementioned equation becomes redundant, and the slope parameter is the only one subject to consideration with respect to this research. That slope parameter (11.66) far exceeds all of the slope coefficients relating b to SPM during this research.

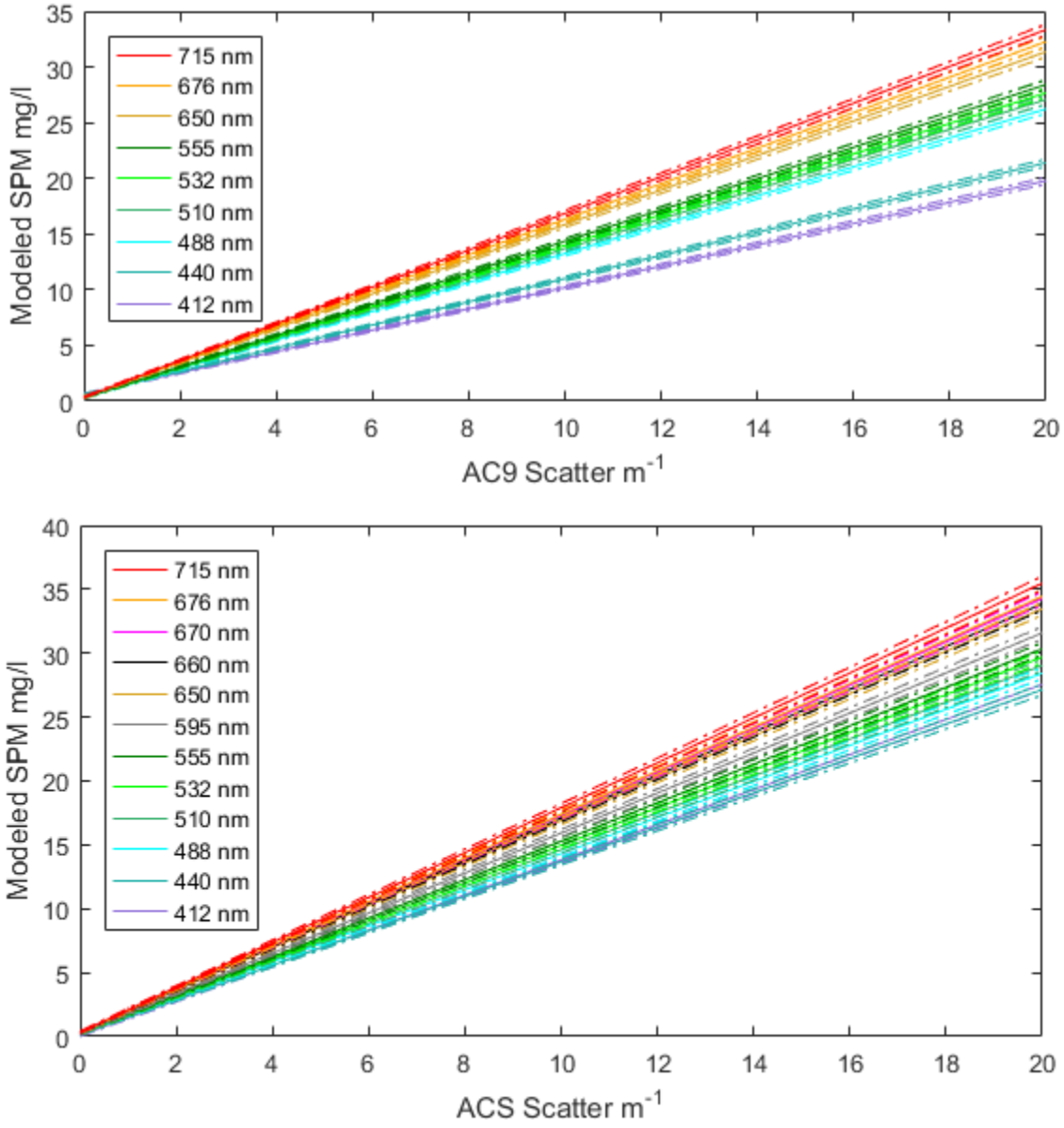

Figure 54. Total Scatter Based SPM Models

Modeled SPM concentration based on total scatter at nine wavelengths for the AC9 and eleven wavelengths for the ACS. Upper and lower boundaries determined by uncertainty of the algorithm coefficients are plotted above and below the modeled SPM at each wavelength. (They are barely discernable at this resolution.) The AC9 coefficients are based on data from GC2 – GC5. The ACS coefficients are based on data from GC1 - GC5.

IOP Backscatter (b_b)

The BB9 was deployed to measure light (400 nm, 440 nm, 488 nm, 510 nm, 532 nm, 660 nm, 676 nm, and 715 nm) backscattered at an angle of 117^O from the incident beams. Other researchers have also used backscatter data products to predict SPM (Emmanuel Boss et al., 2009; G. Neukermans et al., 2012; Reynolds, Stramski, & Neukermans, 2016; Wu, Cui, Duan, Fei, & Liu, 2011) From the BB9 observations, total backscattering coefficients (b_{bt}) and particulate backscattering coefficients (b_{bp}) were calculated. The first coefficient (b_{bt}) represented complete backscatter including estimated contribution from pure sea water based upon a salinity threshold at 35 PSU (WET_Labs, 2008b). The coefficient b_{bp} represented backscatter minus the estimated contribution of pure sea water. The details regarding the estimation of the backscattering of pure sea water are described in Chapter II of this dissertation. The b_b and b_{bp} spectra themselves have often been modeled using a power function (D'Sa et al., 2007; Garcia et al., 2011; Griet Neukermans, Reynolds, & Stramski, 2014; Reynolds et al., 2016; Ruddick, De Cauwer, Park, & Moore, 2006):

$$b_{b[p]}(\lambda) = b_{b[p]}(\lambda_O)\left(\frac{\lambda}{\lambda_O}\right)^{\zeta} \tag{5.2}$$

Here $b_{b[p]}$ represents either b_b or b_{bp}, λ_O, is the designated reference wavelength and ζ is the slope produced by regression. This model is not always a good fit with the observed data as seen in Figure 57. It has also been noted that the departures of actual b_b and b_{bp} from the power law models make using these derived values problematic for SPM concentration estimation (Davies et al., 2014). One project determined the relationship between $b_b(700)$ to SPM to be an exponential one through $SPM = exp\left(\frac{b_b(700)+0.702}{0.302}\right)$

(expression inverted from the approximation of $b_b(700)$ from SPM) in a lacustrine environment (Wu et al., 2011). For this research, linear models are developed for SPM to b_b. This step becomes particularly meaningful in Chapter VI of this dissertation as b_b is sometimes estimated from remote sensing reflectance (Z. Lee, Carder, & Arnone, 2002).

b_{bt}

The relationship between total backscatter at nine wavelengths and SPM is reported in Table 40 and Table 61. For GC1, the correlation coefficients are universally higher than the ones reported by the evaluations performed using the GCALL datasets. The coefficients for cruises GC2 and GC3 are slightly lower than the other three cruises. Figure 55 shows selected scatter plots demonstrating the relationship between SPM and b_{bt} at selected wavelengths.

Table 40

Relationship Between SPM and b_{bt} (BB9)

Wavelength nm	b_{bt} vs. Measured SPM Spearman Correlation Coefficients		
	ρ	p	n
400	0.85	0.00	290
440	0.91	0.00	289
488	0.88	0.00	284
510	0.91	0.00	284
532	0.90	0.00	284
595	0.90	0.00	248
660	0.89	0.00	242
676	0.90	0.00	277
715	0.89	0.00	274

Notes. Data from all cruises were used in the calculation of these correlations. Salinity and CTD-T exclusions were applied. BB9 saturation exclusions were also applied. See Table 61 for individual cruise results.

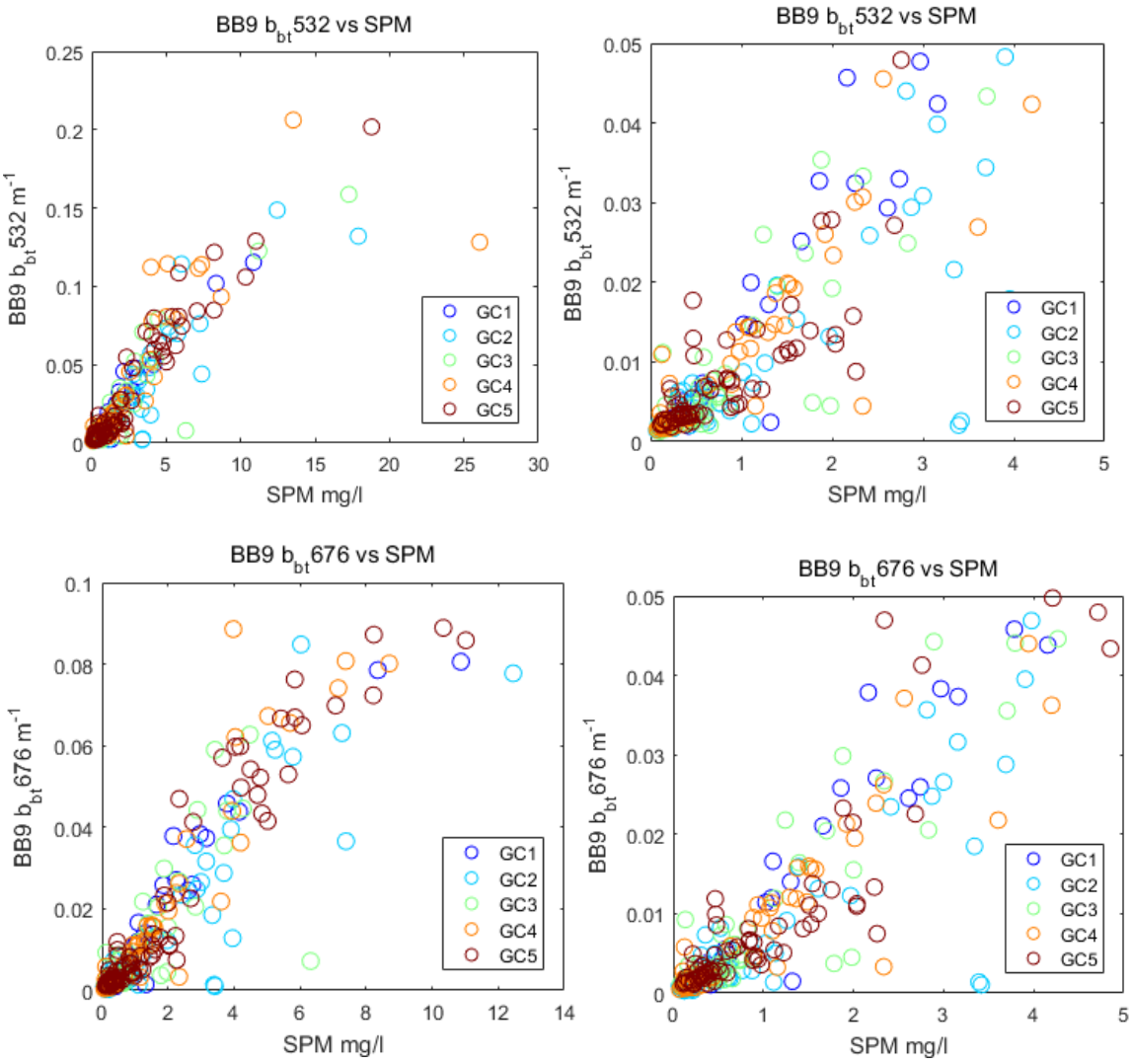

Figure 55. SPM vs. b_{bt} Selected Scatter Plots

These plots display selected wavelengths and ranges of data. Plots on the left display full datasets.

b_{bp}

The authors of peer-reviewed literature generally prefer to work with particulate backscatter (b_{bp}) (Reynolds et al., 2016) rather than total backscatter (b_{bt}). Since the traditional way of differentiating b_{bp} from b_{bt} appears to be somewhat arbitrary in the choice of pure fresh water versus pure seawater subtraction, both parameters are considered in this research. Others have also subtracted half of the Smith and Baker (R.

C. Smith & Baker, 1981) (Figure 53) total scattering values from backscattering coefficients to produce b_{bp} values (Neil et al., 2011; Tzortziou et al., 2007).

An argument could be made that interpolated values between saline pure water (35-39 PSU) and fresh pure water (0 – 34 PSU) might be appropriate for calculating b_{bt} in project areas similar to this one where the in-situ salinity measurements approach both extremes of this range (see Figure 53). However, the published uncertainties of these two types total pure water scattering draws into question the significance of using an interpolated pure water value for the calculation of b_{bt}.

Many different kinds of particles and size ranges contribute to b_{bp} (Stramski et al., 2004). One team even studied the effect of viruses on bacterial particulate backscatter as a result of infection (Balch et al., 2002). Other studies have reported spectral shapes of b_{bp} (David McKee et al., 2009) that are similar to the ones produced in this research (Figure 56). It has been put forward that particulate attenuation and particulate backscatter cannot be used interchangeably for SPM prediction (Kheireddine & Antoine, 2014). This claim indicates that still other researchers have previously attempted to do so. As an alternative to using linear regression, some investigators have used a power function to fit $b_{bp}(550)$ to SPM such that $b_{bp}(550) = k1*SPM^{k2}$ where k1 and k2 values were calculated by the researchers (Reynolds et al., 2016). One project determined the relationship between $b_b(700)$ to SPM to be an exponential one through $SPM = exp\left(\frac{b_b(700)+0.702}{0.302}\right)$ (expression inverted from the approximation of $b_b(700)$ from SPM) in a lacustrine environment (Wu et al., 2011).

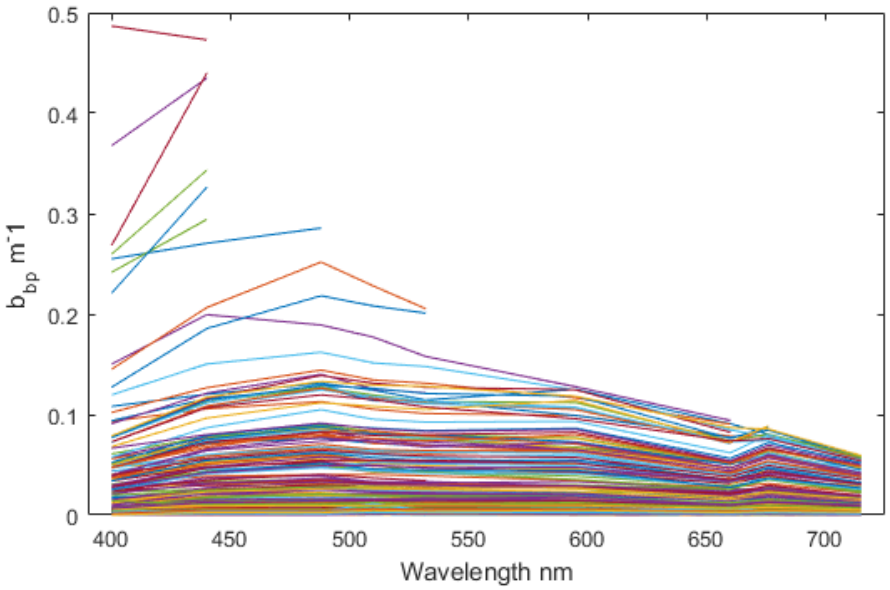

Figure 56. b_{bp} Spectra

The spectra of b_{bp} coefficients at filterdepths for GC1 – GC5.

Spearman correlation values were calculated between b_{bp} and SPM. Table 41 and Table 61 show the results of these evaluations. For GC2, the correlation values were all lower than the values calculated using the GCALL datasets. For GC1, the correlation values were all higher than the GCALL datasets. And for GC5 the values were all slightly higher than the GCALL data sets demonstrating temporal variability in this relationship. The relationship between SPM and b_{bp} is also displayed in Figure 57.

Table 41

Relationship Between SPM and b_{bp} (BB9)

Wavelength nm	GC1 - GC5		
	ρ	p	n
400	0.87	0.00	290
440	0.91	0.00	289
488	0.89	0.00	284
510	0.91	0.00	284
532	0.91	0.00	284
595	0.90	0.00	248
660	0.89	0.00	282
676	0.90	0.00	277
715	0.89	0.00	274

Notes. Data from all cruises were used in the calculation of these correlations. Salinity and CTD-T exclusions were applied. BB9 saturation exclusions were also applied. See Table 61 for cruise by cruise coefficients.

An earlier study in the northern Gulf of Mexico produced the value $r^2 = 0.87$ between SPM and $b_{bp}(555)$ (D'Sa et al., 2007). At the Mackenzie River plume, the correlation coefficient (believed to be Pearson's correlation coefficient) between $b_{bp}(715)$ and SPM concentration was $R^2 = 0.98$, n = 35 (D. Doxaran et al., 2012). Like the Spearman correlation coefficients listed in Table 41, these two reports are consistent with a strong to very strong relationship between b_{bp} and SPM. Finally, another project utilizing particulate backscatter in the Beaufort and Chukchi seas, found the determination coefficient, R^2, between log-transformed SPM concentration and $b_{bp}(550)$ to be 0.88, n = 274 (Reynolds et al., 2016).

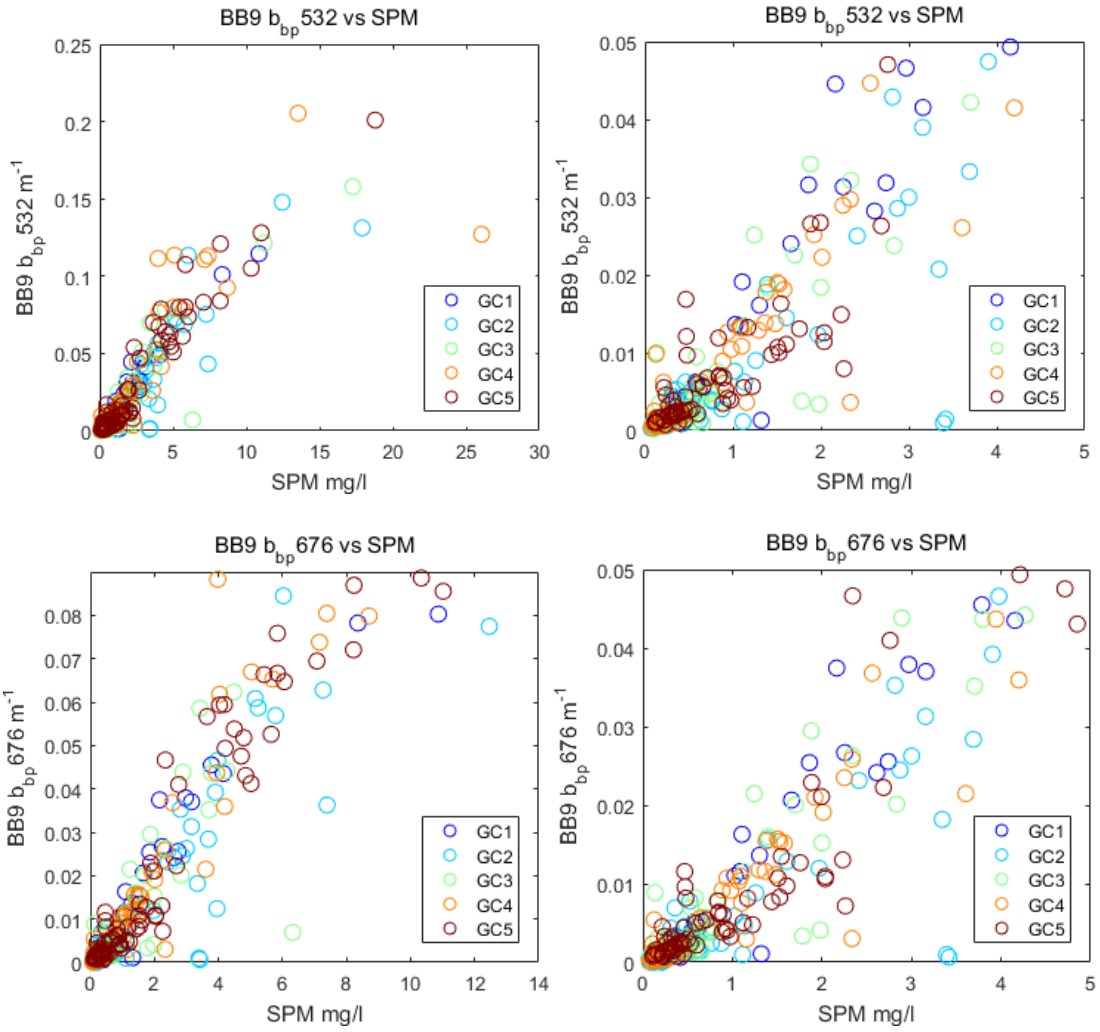

Figure 57. SPM vs. b_{bp} Selected Scatter Plots

These plots display selected wavelengths and ranges of data. Plots on the left display full datasets.

SPM Prediction Based Upon Backscatter

The coefficients for the linear SPM prediction models based upon backscatter are tabulated in Tables 42 (for b_{bt}) and 43 (for b_{bp}). Cruise by cruise algorithm coefficients may be found in Table 71. Likewise, the GCALL models, with uncertainty ranges are plotted in Figures 58 and 59. As part of these figures, a plot is included indicating the observational limits of the BB9 sensor used in this study.

Table 42

SPM Algorithm Coefficients from b_{bt}

Wavelength nm	m (Uncertainty)	b (Uncertainty)
400	94.613 (1.165)	0.428 (0.064)
440	75.461 (1.023)	0.209 (0.066)
488	71.300 (1.496)	0.175 (0.070)
510	77.096 (1.612)	0.122 (0.070)
532	80.725 (1.686)	0.138 (0.070)
595	86.488 (2.076)	0.167 (0.076)
660	124.739 (2.871)	0.186 (0.070)
676	88.150 (2.746)	0.270 (0.073)
715	128.68 (4.237)	0.265 (0.073)

Notes. The slopes and intercepts are for linear SPM predictive algorithms y = mx + b. The uncertainty for the regression slopes and intercepts were calculated using singular value decomposition. Data from all five cruises were used to calculate these values. SPM algorithm coefficients calculated from data produced during individual cruises are found in Table 71.

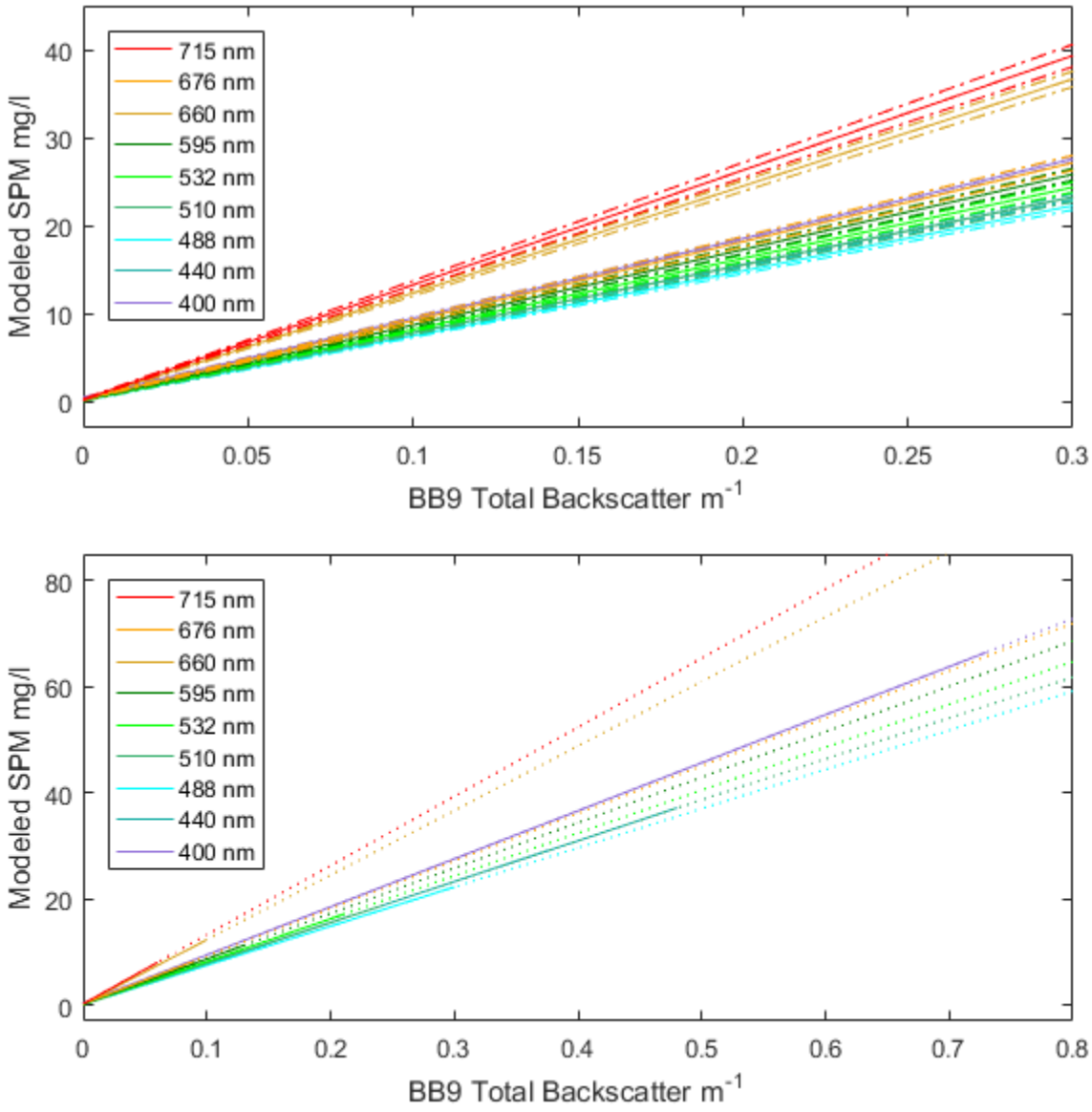

Figure 58. Modeled SPM Based on b_{bt}

Modeled SPM concentration based on particulate backscatter at nine wavelengths based on data from GC1 - GC5. Top plot: Upper and lower boundaries determined by uncertainty of the algorithm coefficients are plotted above and below the modeled SPM at each wavelength. Bottom plot: Solid lines indicate ranges of SPM concentrations estimates possible within the range of the BB9.

Table 43

SPM Algorithm Coefficients from b_{bt}

Wavelength nm	GC1 - GC5	
	m (Uncertainty)	b (Uncertainty)
400	94.977 (1.170)	0.664 (0.063)
440	75.368 (1.022)	0.382 (0.065)
488	71.261 (1.495)	0.278 (0.069)
510	77.015 (1.611)	0.218 (0.069)
532	80.653 (1.685)	0.222 (0.069)
595	86.425 (2.074)	0.223 (0.075)
660	124.751 (2.870)	0.234 (0.070)
676	88.120 (2.744)	0.303 (0.072)
715	128.635 (4.235)	0.303 (0.072)

Notes. The slopes and intercepts are for linear SPM predictive algorithm y = mx + b. The uncertainty for the regression slopes and intercepts were calculated using singular value decomposition. Salinity, CTD turbulence, and BB9 saturation exclusions were applied. SPM algorithm coefficients calculated from data produced during individual cruises are found in Table 71.

Previously in the northern Gulf of Mexico, the following regressed relationship was reported: SPM = 106.93*b_{bp}(555) + 0.61 (D'Sa et al., 2007). The linear relationship describing SPM from b_{bp}(715) at the Mackenzie River delta is quite different at SPM = 54.7*b_{bp}(715) (D. Doxaran et al., 2012). Neither of these regressions fit well with the algorithms produced in this project.

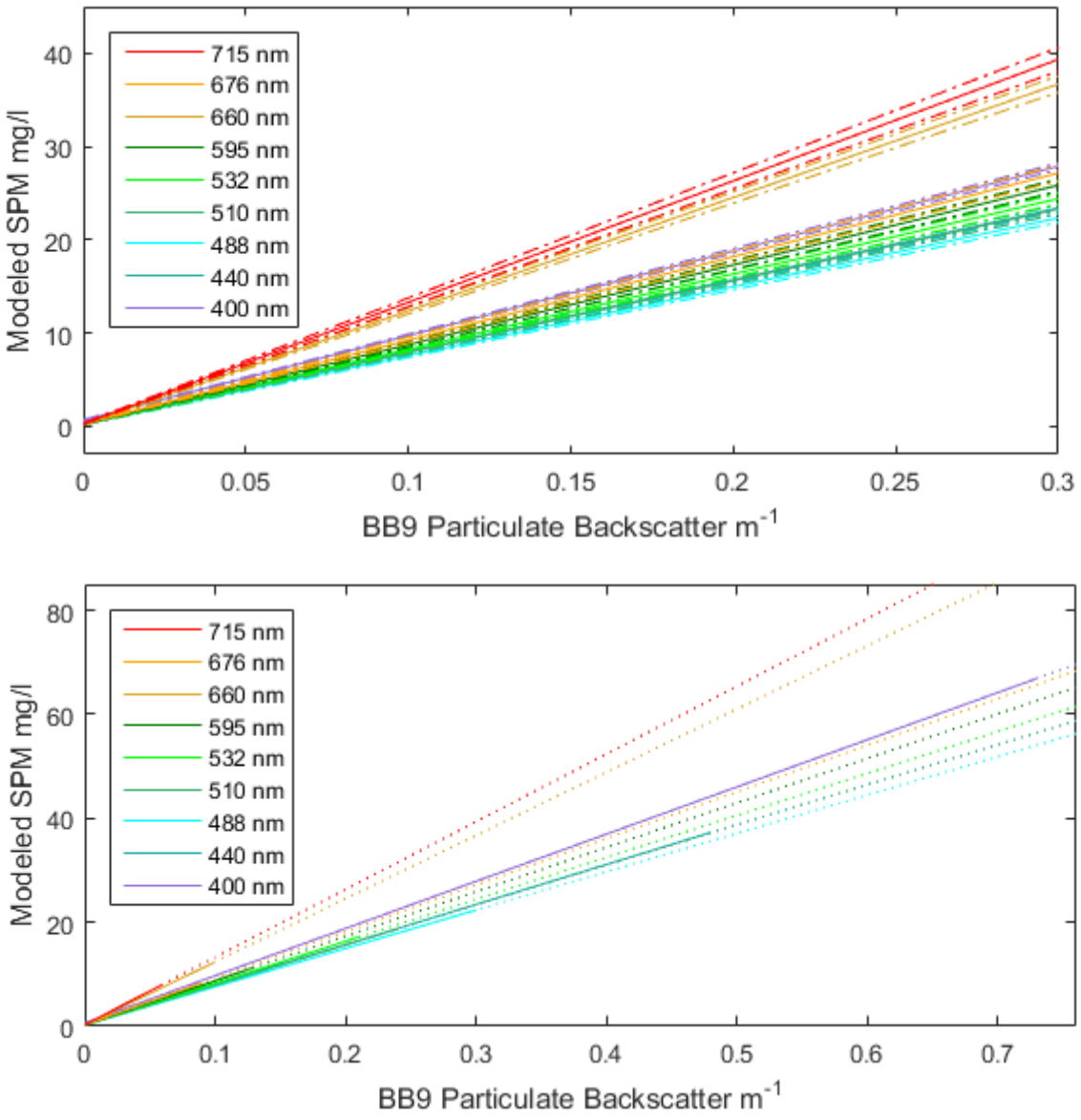

Figure 59. Modeled SPM Based on b_{bp}

Modeled SPM concentration based on particulate backscatter at nine wavelengths based on data from GC1 - GC5. Top plot: Upper and lower boundaries determined by uncertainty of the algorithm coefficients are plotted above and below the modeled SPM at each wavelength. Bottom plot: Solid lines indicate ranges of SPM concentrations estimates possible within the range of the BB9.

IOPs in Combination

By considering combinations of IOPs, the optical environment of natural waters may be more fully characterized. Some of the IOP combinations considered here are (such as $a + b_b$ and $b_b / (a + b_b)$) relevant to observations made with an airborne bathymetric lidar or a hyperspectral sensor. Others (such as the backscatter ratio) are easily determined with available observations and evaluated here.

Backscatter Ratio $\frac{b_b}{b}$

The particulate backscatter ratio $\frac{b_{bp}}{b_t}$ and total backscatter ratio $\frac{b_{bt}}{b_t}$ may be estimated using the coefficients derived from the BB9 and the AC9 or ACS where b_t represents total scatter, $b_t = c - a$. Backscatter ratio estimates describe the behavior of scattered light in natural waters and includes the effects of particulates, dissolved substances and the water itself. Studies have been made in the past relating specific phytoplanktoners to spectral backscattering ratios (Ahn, Bricaud, & Morel, 1992).

A published proxy for the particulate backscattering ratio is the ratio $b_{bp}(550)/c_p(660)$ (Kheireddine & Antoine, 2014). Several researchers have noted that backscatter ratio values typically increase with increasing mineral content and decrease as organic content becomes dominant (Ackleson & O'Donnell, 2011; Bowers, Hill, & Braithwaite, 2014; D. Doxaran et al., 2012; Loisel et al., 2007). Additionally, the use of multiple sensors to calculate an IOP combination value introduces uncertainty not necessarily associated with single IOP component values (David McKee et al., 2009).

For this project, some of the effects of water are removed during the determination of a, c and b_{bp} as described in the methods. The six wavelengths observed

by both the AC9 and BB9 data are 440 nm, 488 nm, 510 nm, 532 nm, 676 nm, and 715 nm. When the ACS data is interpolated to each nm wavelength, eight common wavelengths may be utilized in the determination of backscattering ratios (440 nm, 488 nm, 510 nm, 532 nm, 595 nm, 660 nm, 676 nm, and 715 nm). This research evaluates two versions of the backscattering ratio, b_{bt}/b, and b_{bp}/b. Due to the large percentages of data removed from the ACS derived absorption and attenuation coefficient datasets resulting from the persistent mid-spectral anomaly, and the elimination of many near surface data due to other anomalies (identified by visual evaluation of each absorption and attenuation spectrum for all filterdepths), the number of scattering values available for further analysis of near-surface waters is limited. The effect of the ACS data losses of both absorption and attenuation data can be seen in the low n values reported through the use of these sensors relative to the AC9 in Tables 44 and 45.

b_{bt}/b

The Spearman Rank correlation coefficients between b_{bt}/b and SPM are quite low and even indicate instances of no correlation thru high p values (> 0.05) (Tables 44, and 62). There is also great inconsistency when comparing correlation values between SPM and b_{bt}/b calculated using the AC9 reports versus the ACS data (Table 44). Based on this information, there is very little value (if any) in using the GCALL datasets to predict SPM from IOP combination b_{bt}/b. However, based upon the cruise-by-cruise Spearman correlation coefficients (Table 62) the values in the total backscattering ratio may demonstrate stronger relationships to SPM under favorable circumstances. Such circumstances existed during GC4 when the ACS-derived IOP combination had significant correlation values with SPM. Those values range from 0.67 to 0.86 ($p = 0.00$).

During the same cruise, however, the AC9-derived backscatter ratios had much lower correlation values and some higher p values to SPM than those reported by the ACS. The most meaningful (or useful) wavelengths of b_{bt}/b for SPM prediction appear to be 676 nm and 715 nm for the AC9 related to GC4.

Table 44

Relationship Between SPM and b_{bt}/b (AC9 & ACS)

Wavelength nm	b_{bt}/b (AC9) vs. Measured SPM Spearman Correlation Coefficients			b_{bt}/b (ACS) vs. Measured SPM Spearman Correlation Coefficients		
	ρ	p	n	ρ	p	n
440	-0.41	0.00	256	0.01	0.87	164
488	-0.01	0.84	251	0.32	0.00	159
510	-0.27	0.00	251	0.17	0.04	157
532	-0.11	0.08	251	0.30	0.00	157
595	N/A	N/A	N/A	0.36	0.00	143
660	N/A	N/A	N/A	0.51	0.00	153
676	0.16	0.02	244	0.39	0.00	149
715	0.18	0.00	240	0.40	0.00	155

Notes. Data from all cruises were used in the calculation of these correlations. Salinity and CTD-T exclusions were applied. BB9 saturation and AC9 and ACS exclusions were also applied. See Table 62 for cruise by cruise values.

The scatter plots in Figure 60 give an additional perspective on the relationship between b_{bt}/b and SPM. The plots using the AC9 data suggest that the regional temporal variation of the b_{bt}/b to SPM relationship occurs, especially at low concentrations of SPM (<1.0 mg/l). (The ratio b_{bt}/b is generally higher for these low SPM concentrations during cruises GC2 and GC3 than they are for cruises GC4 and GC5.) This phenomenon is less apparent in the b_{bt}/b data using ACS observations where there is less information available to analyze these relationships.

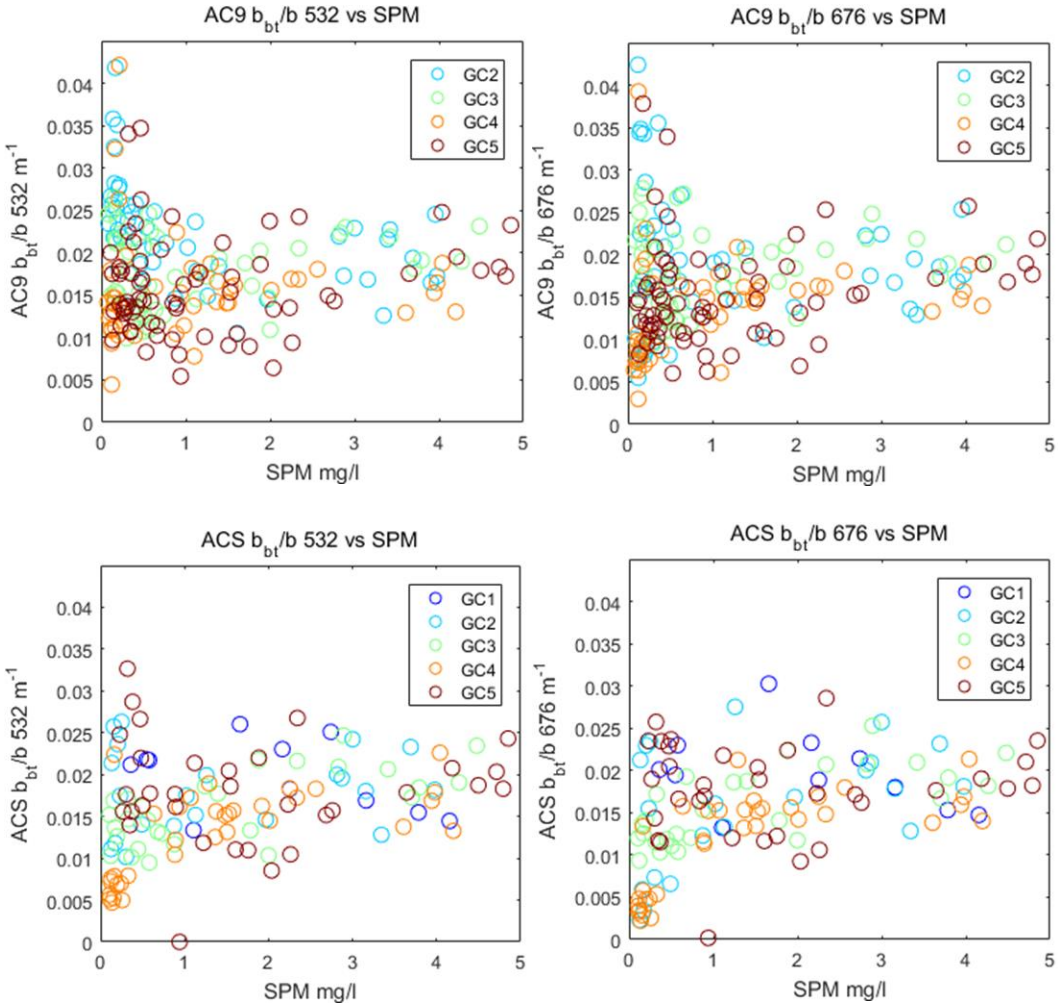

Figure 60. SPM vs. b_{bt}/b (AC9 & ACS)

These plots display selected wavelengths and ranges of data.

b_{bp}/b

For the b_{bp}/b value, the effects of pure water are mitigated (if not entirely removed) prior to the calculation of this ratio. The relationship between b_{bp}/b and SPM, represented by the Spearman correlation coefficient between the datasets (Table 45) is considerably stronger than the values representing the relationship between SPM and b_{bt}/b. However, as with the b_{bt}/b relationship to SPM, there is considerable disagreement between the correlation values derived using the AC9 versus the ACS data. It is also

worth noting that all correlation values for the GCALL datasets actually represent a relationship between b_{bp}/b and SPM given that all p-values are 0.00 in Table 45. (In contrast, the SPM to b_{bt}/b ratios did not always appear to be statistically related to each other as indicated by high p-values.) The scatter plots for the GCALL data pairs are in Figure 61. Regarding the cruise-by-cruise datasets, the distinction noted between cruises GC2 and GC3 relative to GC4, and GC5 are not as apparent with the b_{bp}/b to SPM data pairs as they are in the b_{bt}/b data pairs (Figure 60). The highest correlation values evaluated between b_{bp}/b and SPM occurred during GC4. This was experienced by both sensors and all wavelengths (Table 63). Some cruises (such as GC1 and GC5 for the ACS and GC3 for the AC9) produced unacceptably high p-values between the paired datasets.

Table 45

SPM in Relation to b_{bp}/b (AC9 & ACS)

Wavelength nm	b_{bp}/b (AC9) vs. Measured SPM Spearman Correlation Coefficients			b_{bp}/b (ACS) vs. Measured SPM Spearman Correlation Coefficients		
	ρ	p	n	ρ	p	n
440	0.46	0.00	258	0.70	0.00	164
488	0.56	0.00	253	0.69	0.00	161
510	0.37	0.00	253	0.53	0.00	159
532	0.51	0.00	253	0.58	0.00	159
595	N/A	N/A	N/A	0.59	0.00	143
660	N/A	N/A	N/A	0.62	0.00	155
676	0.39	0.00	246	0.50	0.00	151
715	0.46	0.00	243	0.54	0.00	148

Notes. Data from all cruises were used in the calculation of these correlations. Salinity and CTD-T exclusions were applied. BB9 saturation and AC9 and ACS exclusions were also applied. See Table 63 for cruise by cruise evaluations.

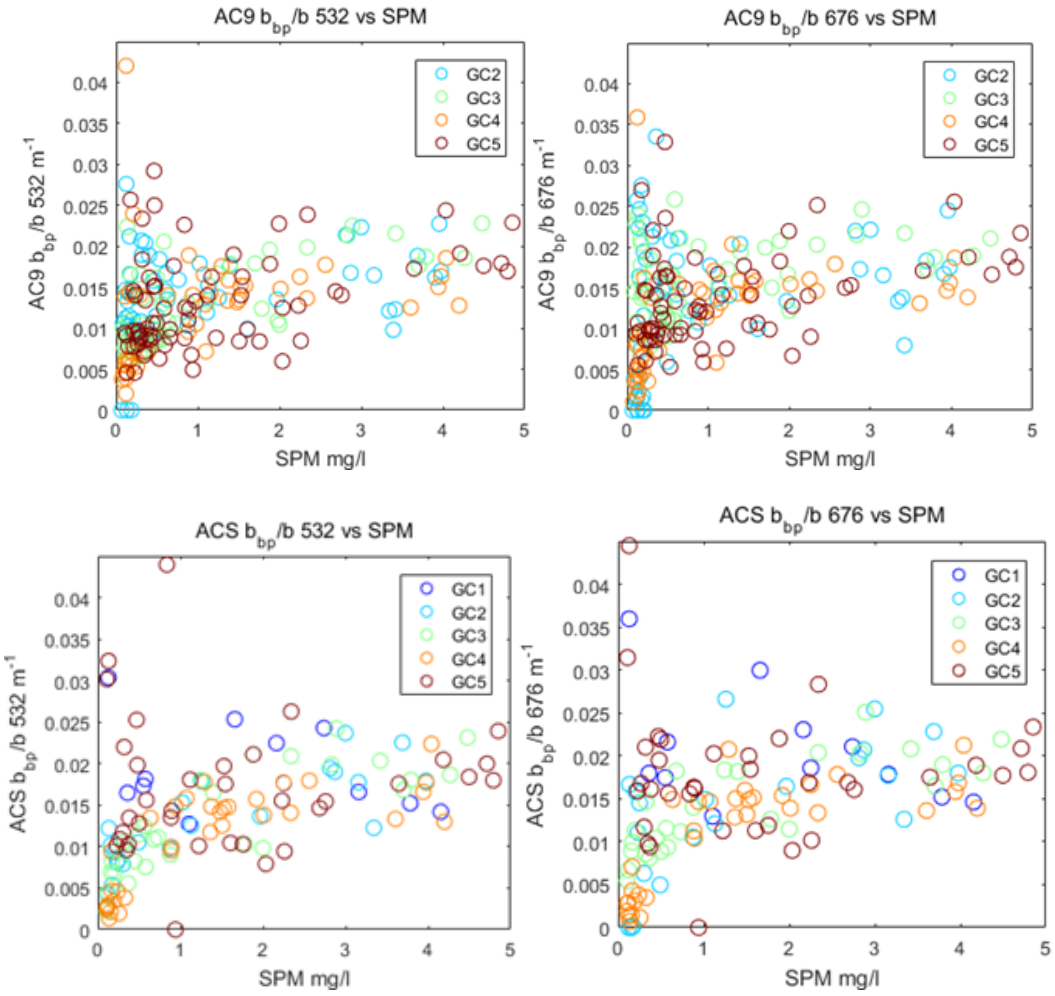

Figure 61. SPM vs. b_{pb}/b (AC9 & ACS) Selected Scatter Plots

These plots display selected wavelengths and ranges of data.

SPM Prediction Based Upon b_b/b

The linear algorithm coefficients for predicting SPM from b_{bt}/b and b_{bp}/b are in Tables 46 and 47 respectively. Modeled SPM based upon the linear algorithm coefficients calculated using b_{bt}/b and b_{bp}/b are found in Figures 62 and 60 respectively. These models are not grouped well by wavelength as perceived in other IOP based SPM models (Figures 45, 49, 54, 58 and 59). The wavelength-dependent slopes for the b_b/b - based SPM models may be either positive or negative. Also, many of the y-intercepts for

the algorithms are far too large (Tables 46 and 47) to make the b_{bt}/b and b_{bp}/b - based models meaningful for practical use.

Table 46

SPM Algorithm Coefficients from b_{bt}/b (AC9 & ACS)

Wavelength nm	b_{bt}/b (AC9) GC2 - GC5		b_{bt}/b (ACS) GC1 - GC5	
	m (Uncertainty)	b (Uncertainty)	m (Uncertainty)	b (Uncertainty)
440	-15.321 (1.609)	2.995 (0.075)	-26.518 (6.613)*	4.354 (0.143)*
488	-3.217 (1.272)*	2.167 (0.069)*	28.576 (7.295)	2.599 (0.155)
510	-16.623 (2.930)	2.462 (0.091)	-3.588 (7.051)	2.978 (0.155)
532	-18.684 (4.045)*	2.465 (0.102)*	29.238 (8.608)	2.400 (0.170)
595	N/A	N/A	89.079 (12.544)	1.512 (0.214)
660	N/A	N/A	99.334 (12.267)	1.536 (0.173)
676	-1.859 (1.110)	1.743 (0.068)	39.143 (9.078)	1.642 (0.170)
715	10.638 (9.552)	1.511 (0.131)	130.740 (18.568)	0.685 (0.230)

Notes. The slopes and intercepts are for linear SPM predictive algorithm y = mx + b. The uncertainty for the regression slopes and intercepts were calculated using singular value decomposition. Salinity, CTD turbulence, and BB9 saturation exclusions were applied. * The GCALL data pairs of b_{bt}/b and SPM are statistically unrelated. SPM algorithm coefficients calculated from data produced during individual cruises are found in Table 72.

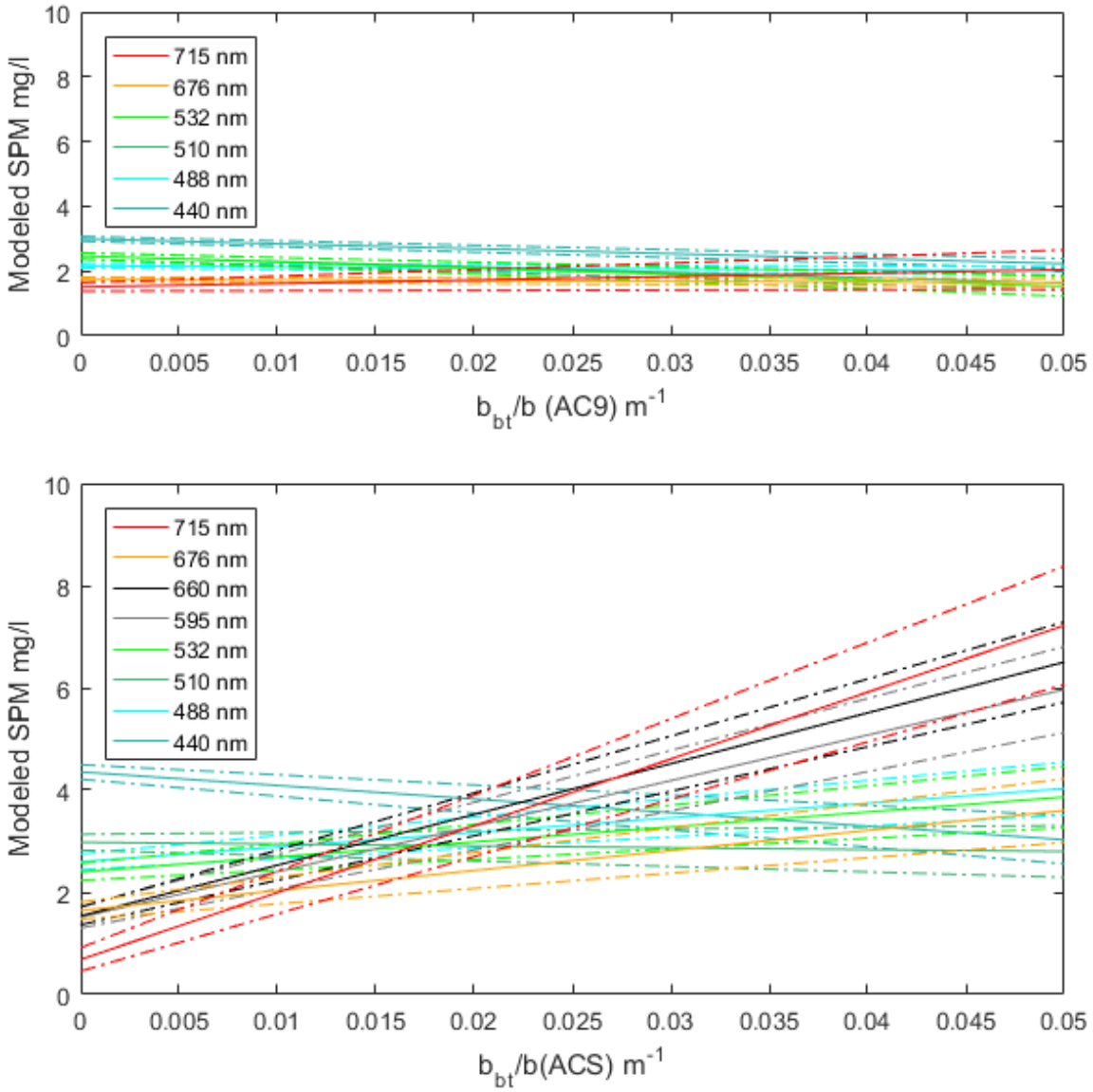

Figure 62. b_{bt}/b (AC9 & ACS) Based SPM Models

Modeled SPM concentration based on backscatter ratio (using total backscatter) at six wavelengths for the AC9 and eight wavelengths for the ACS. Upper and lower boundaries determined by uncertainty of the algorithm coefficients are plotted above and below the modeled SPM at each wavelength. The AC9 coefficients are based on data from GC2 – GC5. The ACS coefficients are based on data from GC1 - GC5.

Table 47

SPM Algorithm Coefficients from b_{bp}/b (AC9 & ACS)

Wavelength nm	b_{bp}/b (AC9) GC2 - GC5		b_{bp}/b (ACS) GC1 - GC5	
	m (Uncertainty)	b (Uncertainty)	m (Uncertainty)	b (Uncertainty)
440	20.142 (3.732)	2.315 (0.079)	452.512 (13.914)	-1.809 (0.191)
488	189.915 (9.044)	-0.343 (0.131)	247.801 (10.983)	-0.502 (0.177)
510	144.040 (10.971)	-0.061 (0.175)	114.900 (10.674)	1.058 (0.186)
532	154.502 (10.197)	-0.038 (0.153)	193.112 (11.982)	0.022 (0.194)
595	N/A	N/A	213.450 (13.212)	-0.231 (0.206)
660	N/A	N/A	247.822 (14.715)	0.011 (0.181)
676	1.222 (2.148)	1.671 (0.073)	108.961 (11.689)	0.604 (0.195)
715	128.892 (12.832)	0.369 (0.140)	118.283 (14.849)	0.877 (0.180)

Notes. The slopes and intercepts are for linear SPM predictive algorithm y = mx + b. The uncertainty for the regression slopes and intercepts were calculated using singular value decomposition. Salinity, CTD turbulence, and BB9 saturation exclusions were applied. SPM algorithm coefficients calculated from data produced during individual cruises are found in Table 73.

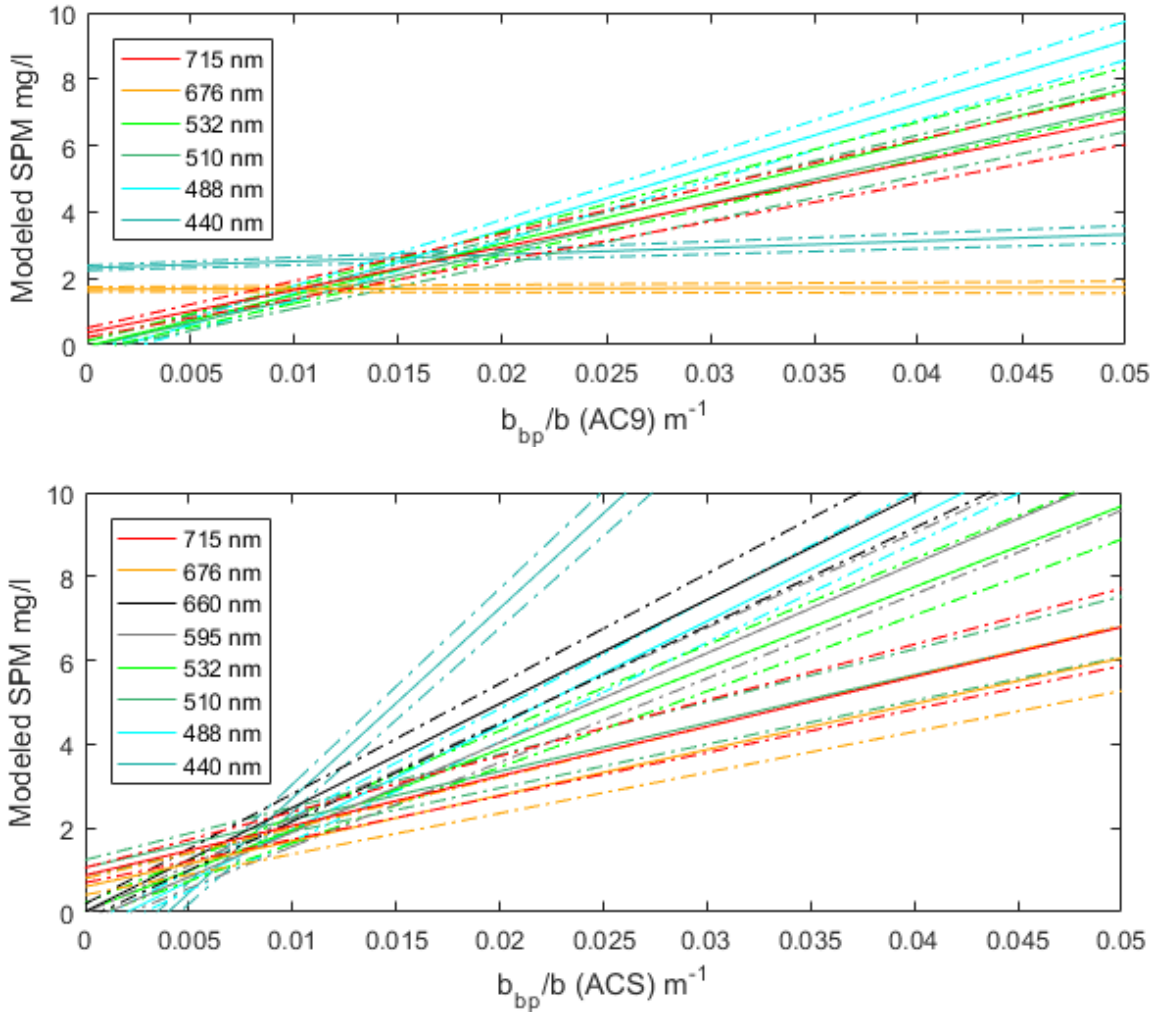

Figure 63. b_{bp}/b (AC9 & ACS) Based SPM Models

Modeled SPM concentration based on backscatter efficiency (using particulate backscatter) at six wavelengths for the AC9 and eight wavelengths for the ACS. Upper and lower boundaries determined by uncertainty of the algorithm coefficients are plotted above and below the modeled SPM at each wavelength. The AC9 coefficients are based on data from GC2 – GC5. The ACS coefficients are based on data from GC1 - GC5.

IOP Partial Attenuation $a + b_b$

The partial attenuation coefficient represents a summation of backscatter and absorption ($a + b_b$). At 532 nm, $a + b_b$ is offered as a data product of the CZMIL lidar. From REA and Hydrofusion software systems, $a + b_b$ at 532 nm can be reported as depth specific estimates which allows for high resolution coverage of this IOP

combination from airborne hydrographic survey systems (Viktor I. Feygels et al., 2013; Moonkoo Kim et al., 2016; Macon et al., 2008). This "effective attenuation" is affected by the lidar field of view (Minsu Kim et al., 2014) and is thus sensor specific. Based on published data (A. Morel, 1974; R. C. Smith & Baker, 1981) (see Figures 29 and 53), one can expect $a + b_b$ at 532 nm to have a range of 0.0432 m^{-1} thru 0.0578 m^{-1} for pure water and 0.0430 m^{-1} thru 0.0581 m^{-1} for pure sea water. Since $a + b_b$ can be calculated for six wavelengths using BB9 data and eight wavelengths using ACS data these IOP combinations were also calculated and evaluated with respect to SPM. Finally, this partial attenuation coefficient also consists of most of the components contributing to the IOP combination $b_b / (a + b_b)$ which is discussed later in this chapter.

The Spearman correlation coefficients relating $a + b_{bt}$ to SPM are in Tables 48 and 64. As absorption values tend to be much larger than backscatter values, it was thought that the correlation coefficients between SPM and $a + b_{bt}$ would resemble the coefficients between SPM and absorption (found in Table 29). That expectation proved true for the AC9 contributions to $a + b_{bt}$ for wavelengths 440 nm, 488, nm 510 nm and 532 nm and incorrect for the remainder of the GCALL evaluations. At wavelengths 676 nm and 715 nm, the $a + b_{bt}$ correlation coefficients are significantly stronger than for absorption alone. This phenomenon makes sense as absorption values are much lower at these wavelengths than for the shorter ones. Therefore, the backscatter contributions to this IOP combinations are much more important at the longer wavelengths. Where the ACS contributed absorption values to the IOP combination, the SPM correlation values were stronger (significantly so for the longer wavelengths) than ACS a to SPM values. The n-values for $a + b_{bt}$ are much smaller (n = 136 to 165) contingent upon wavelength

than the n-values (n = 248) for the SPM to ACS absorption evaluations. Scatter plots relating SPM to $a + b_{bt}$ are in Figure 64.

Table 48

SPM in Relation to $a + b_{bt}$ (AC9 & ACS)

Wavelength nm	$a + b_{bt}$ (AC9) vs. Measured SPM Spearman Correlation Coefficients			$a + b_{bt}$ (ACS) vs. Measured SPM Spearman Correlation Coefficients		
	ρ	p	n	ρ	p	n
440	0.85	0.00	265	0.88	0.00	165
488	0.85	0.00	260	0.89	0.00	160
510	0.85	0.00	260	0.89	0.00	157
532	0.84	0.00	260	0.90	0.00	157
595	N/A	N/A	N/A	0.90	0.00	155
660	N/A	N/A	N/A	0.86	0.00	154
676	0.82	0.00	253	0.85	0.00	149
715	0.85	0.00	244	0.92	0.00	139

Notes. Data from all cruises were used in the calculation of these correlations. Salinity and CTD-T exclusions were applied. BB9 saturation and AC9 and ACS exclusions were also applied. See also Table 64.

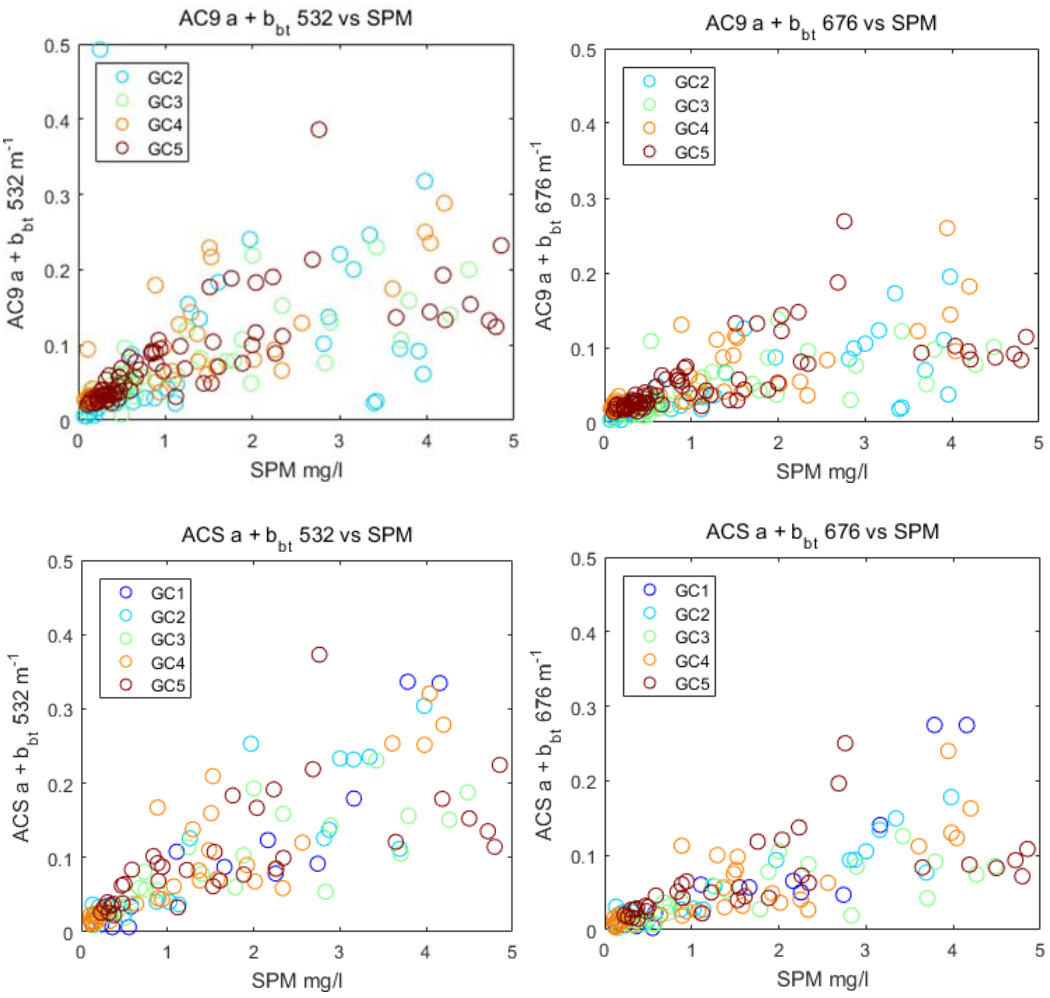

Figure 64. SPM vs. a + b_{bt} (AC9 & ACS) Selected Scatter Plots

These plots display selected wavelengths and ranges of data.

The IOP combination a + b_{bp} was also considered during this research. The results of this evaluation were expected to be similar to those of a + b_{bt} as these values are also mostly controlled by the absorption values. In other words, the elimination of the estimated pure water contribution of backscatter was expected to have a negligible effect on the IOP combination a + b_{bp}. This appears to be the case as there is very little difference between the values reported in Table 48 relative to Table 49 (and Tables 64 and 65) where the Spearman correlation values between a + b_{bt} or a + b_{bp} and SPM are

presented respectively. The minor differences that are reflected between these two tables indicate a slightly stronger relationship between $a + b_{bp}$ and SPM than $a + b_{bt}$ and SPM as might be expected. Likewise, the scatter plots in Figure 65 are very similar to those in Figure 64.

Table 49

SPM in Relation to $a + b_{bp}$ (AC9 & ACS)

Wavelength nm	$a + b_{bp}$ (AC9) vs. Measured SPM Spearman Correlation Coefficients			$a + b_{bp}$ (ACS) vs. Measured SPM Spearman Correlation Coefficients		
	ρ	p	n	ρ	p	n
440	0.85	0.00	265	0.88	0.00	167
488	0.85	0.00	260	0.89	0.00	162
510	0.85	0.00	260	0.89	0.00	159
532	0.85	0.00	260	0.90	0.00	159
595	N/A	N/A	N/A	0.90	0.00	157
660	N/A	N/A	N/A	0.86	0.00	156
676	0.82	0.00	253	0.85	0.00	151
715	0.86	0.00	250	0.93	0.00	145

Notes. Data from all cruises were used in the calculation of these correlations. Salinity and CTD-T exclusions were applied. BB9 saturation and AC9 and ACS exclusions were also applied.

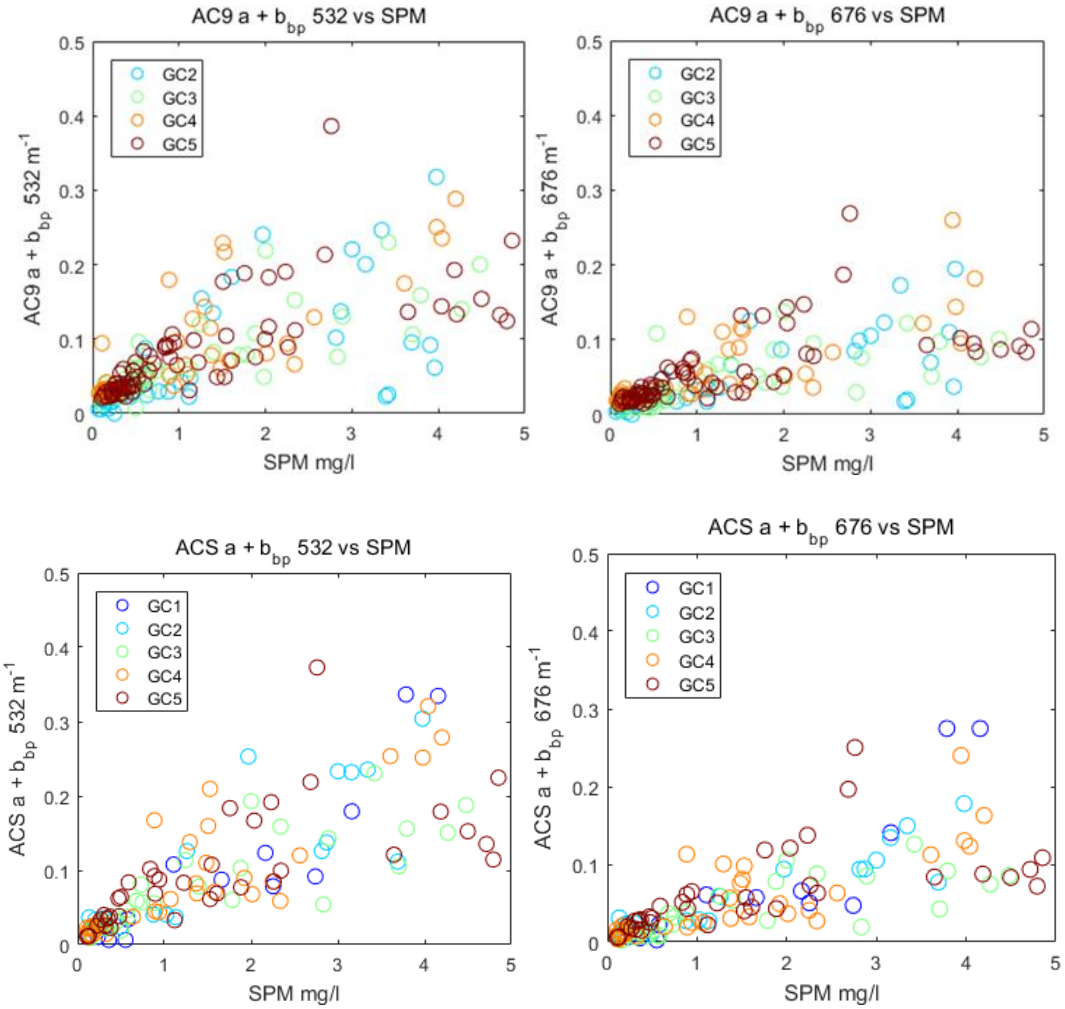

Figure 65. SPM vs. a + b_{bp} (AC9 & ACS) Selected Scatter Plots

These plots display selected wavelengths and ranges of data.

SPM Prediction Based Upon a + b_b

The linear algorithm coefficients for predicting SPM based upon a + b_{bt} and a + b_{bp} are in Tables 50 and 51 for the GCALL datasets and Tables 74 and 75 for the individual cruises. The models derived using the GCALL data pairs are plotted in Figures 66 and 67. These figures demonstrate substantial differences between the models derived from the AC9 and ACS sensors. These differences are best discerned when noting that the x and y-axes of all four plots in these two figures are identical.

Table 50

SPM Algorithm Coefficients from $a + b_{bt}$ (AC9 & ACS)

Wavelength nm	$a + b_{bt}$ (AC9) GC2 - GC5		$a + b_{bt}$ (ACS) GC1 - GC5	
	m (Uncertainty)	b (Uncertainty)	m (Uncertainty)	b (Uncertainty)
440	8.190 (0.070)	-0.162 (0.067)	8.652 (0.145)	0.220 (0.099)
488	11.916 (0.123)	-0.009 (0.067)	14.236 (0.352)	-0.050 (0.111)
510	19.042 (0.199)	-0.482 (0.069)	17.268 (0.508)	0.025 (0.117)
532	8.969 (0.103)	1.063 (0.064)	22.241 (0.639)	-0.089 (0.118)
595	N/A	N/A	40.517 (1.180)	-0.153 (0.118)
660	N/A	N/A	41.774 (1.390)	0.058 (0.121)
676	9.846 (0.094)	0.962 (0.064)	26.489 (1.214)	0.384 (0.120)
715	8.745 (0.099)	1.466 (0.064)	122.598 (5.350)	0.437 (0.117)

Notes. The slopes and intercepts are for linear SPM predictive algorithm y = mx + b. The uncertainty for the regression slopes and intercepts were calculated using singular value decomposition. Salinity, CTD turbulence, and BB9 saturation exclusions were applied. SPM algorithm coefficients calculated from data produced during individual cruises are found in Table 74.

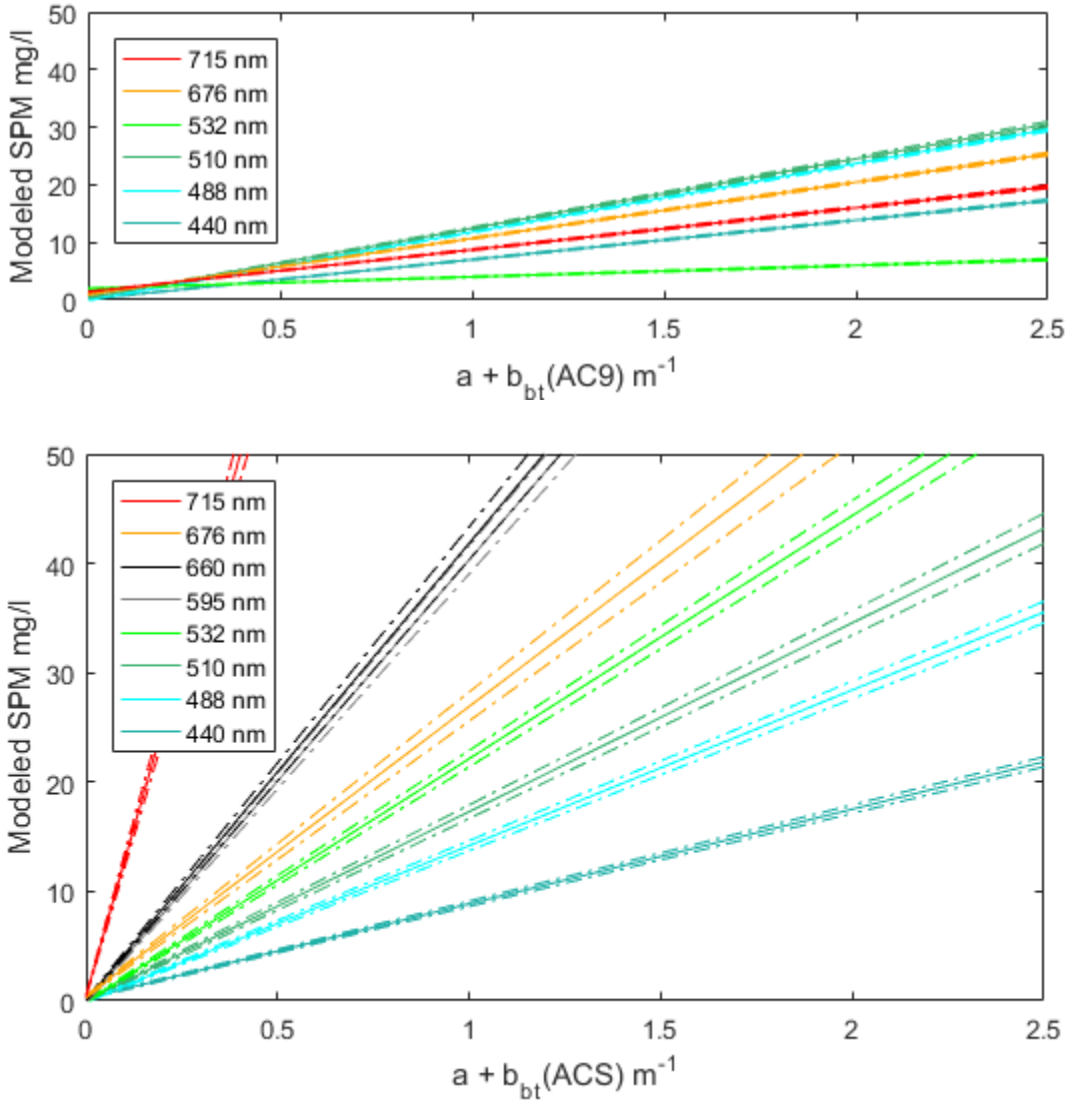

Figure 66. a + b_{bt} Based SPM Models (AC9 & ACS)

Modeled SPM concentration based on partial attenuation (using total backscatter) at six wavelengths for the AC9 and eight wavelengths for the ACS. Upper and lower boundaries determined by uncertainty of the algorithm coefficients are plotted above and below the modeled SPM at each wavelength. The AC9 coefficients are based on data from GC2 – GC5. The ACS coefficients are based on data from GC1 - GC5.

Table 51

SPM Algorithm Coefficients from $a + b_{bp}$ (AC9 & ACS)

Wavelength nm	$a + b_{bp}$ (AC9) GC2 - GC5		$a + b_{bp}$ (ACS) GC1 - GC5	
	m (Uncertainty)	b (Uncertainty)	m (Uncertainty)	b (Uncertainty)
440	8.19 (0.07)	-0.162 (0.067)	8.657 (0.144)	0.213 (0.098)
488	11.914 (0.123)	-0.005 (0.067)	14.238 (0.35)	-0.051 (0.11)
510	19.035 (0.199)	-0.476 (0.069)	17.277 (0.505)	0.022 (0.115)
532	8.989 (0.103)	1.077 (0.064)	22.245 (0.635)	-0.09 (0.116)
595	N/A	N/A	40.522 (1.173)	-0.154 (0.117)
660	N/A	N/A	41.818 (1.381)	0.052 (0.119)
676	9.846 (0.094)	0.963 (0.064)	26.57 (1.207)	0.373 (0.118)
715	8.751 (0.099)	1.434 (0.064)	123.2 (5.251)	0.418 (0.112)

Notes. The slopes and intercepts are for linear SPM predictive algorithm y = mx + b. The uncertainty for the regression slopes and intercepts were calculated using singular value decomposition. Salinity, CTD turbulence, and BB9 saturation exclusions were applied. SPM algorithm coefficients calculated from data produced during individual cruises are found in Table 75.

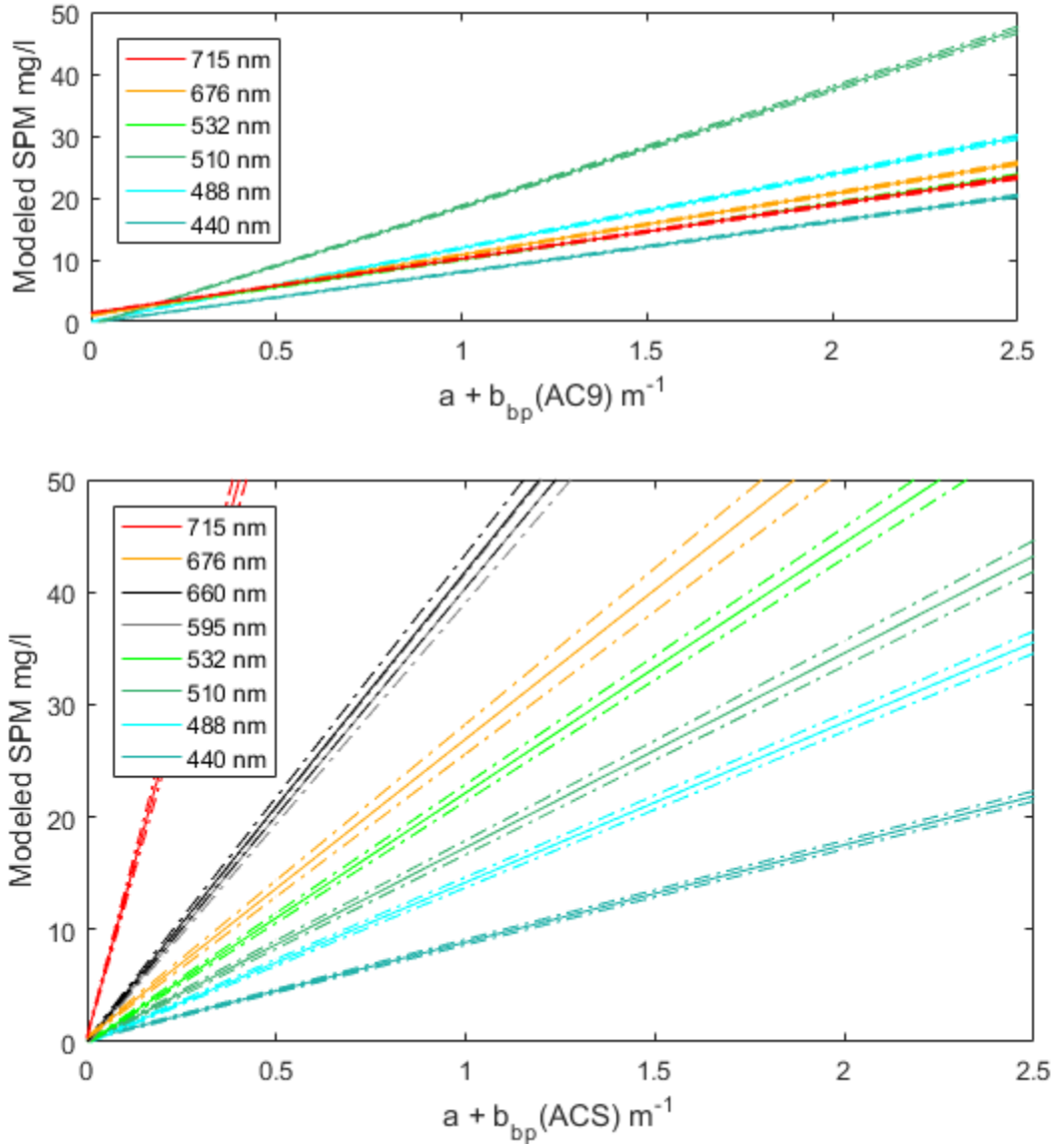

Figure 67. a + b_{bp} Based SPM Models (AC9 & ACS)

Modeled SPM concentration based on partial attenuation (using particulate backscatter) at six wavelengths for the AC9 and eight wavelengths for the ACS. Upper and lower boundaries determined by uncertainty of the algorithm coefficients are plotted above and below the modeled SPM at each wavelength. The AC9 coefficients are based on data from GC2 – GC5. The ACS coefficients are based on data from GC1 - GC5.

IOP Combination $b_b / (a + b_b)$

The data-fused value $b_b / (a + b_b)$ represents the IOP contribution to the apparent optical property (AOP) remote sensing reflectance (R_{rs}) (Aurin & Dierssen, 2012; Gallegos, Werdell, & McClain, 2011; Kobayashi et al., 2011; Kowalczuk, Durako, Cooper, Wells, & Souza, 2006; Z. Lee et al., 2002; Z. Lee et al., 2016; Many et al., 2016; Montes-Hugo, Churnside, Gould, Arnone, & Foy, 2010; Naik et al., 2013; Ogashawara et al., 2016; Sydor, 2007; Tzortziou et al., 2007; Wynne, Stumpf, & Richardson, 2006). Therefore, its relationship to SPM is evaluated in this project. As before, variations including b_{bt} and b_{bp} are considered.

Table 52 and Figure 68 describe the relationship between SPM and $b_{bt} / (a + b_{bt})$ for the GCALL paired data. Some of the cruise-by-cruise evaluations (see Table 66) differ wildly from the values reported in Table 52. For example, during GC2, the correlation values between $b_{bt} / (a + b_{bt})$ (where the AC9 contributed to the IOP combination) and SPM were negative for five of the six available wavelengths. At 715 nm where the p-value was so high that it was clear that there was no correlation between SPM and the IOP combination. For that matter, regarding AC9 contributions to the $b_{bt} / (a + b_{bt})$ values at 715 nm, none of the datasets for individual cruises or the GCALL dataset reported p-values low enough to indicate a statistical relationship between the tested parameters. The ACS did not exhibit the same difficulty. As with the sensor-to-sensor analysis performed in Chapter IV, the low correlation at 715 nm was likely due to 715 nm being used as the reference wavelength for AC9 temperature and salinity adjustments (Pegau et al., 1997).

Table 52

SPM in Relation to $b_{bt} / (a + b_{bt})$, (AC9 & ACS)

Wavelength nm	$b_{bt} / (a + b_{bt})$ (AC9) vs. Measured SPM Spearman Correlation Coefficients			$b_{bt} / (a + b_{bt})$ (ACS) vs. Measured SPM Spearman Correlation Coefficients		
	ρ	p	n	ρ	p	n
440	0.35	0.00	265	0.55	0.00	165
488	0.53	0.00	260	0.59	0.00	160
510	0.46	0.00	260	0.57	0.00	157
532	0.57	0.00	260	0.62	0.00	157
595	N/A	N/A	N/A	0.60	0.00	140
660	N/A	N/A	N/A	0.68	0.00	153
676	0.67	0.00	253	0.65	0.00	149
715	-0.03	0.65	246	-0.31	0.00	145

Notes. Data from all cruises were used in the calculation of these correlations. Salinity and CTD-T exclusions were applied. BB9 saturation and AC9 and ACS exclusions were also applied. See Table 66 for cruise by cruise evaluations.

Regarding the relationship between SPM and $b_{bt} / (a + b_{bt})$ where the ACS contributed to the IOP combination's value, two of the cruises stand out (Table 66). First, for GC1 (ACS and BB9 sensors), none of the correlation values have significant meaning as the p-values are far above the 0.05 threshold indicating that the IOP combination and SPM two parameters are not related for all eight tested wavelengths. This cruise also had the least numbers of data pairs with which to perform this analysis ($n < 14$ for all wavelengths). Conversely, GC2 reported the highest correlation values between SPM and $b_{bt} / (a + b_{bt})$ for all wavelengths related to the ACS. (In all cases the correlations values between SPM and $b_{bt} / (a + b_{bt})$ are significantly greater for GC2 than for the GCALL datasets.) In other cases, certain wavelengths also had stronger correlation values

between these two parameters than the GCALL evaluations. This phenomenon indicates that $b_{bt} / (a + b_{bt})$ may not be the best resource available for SPM prediction.

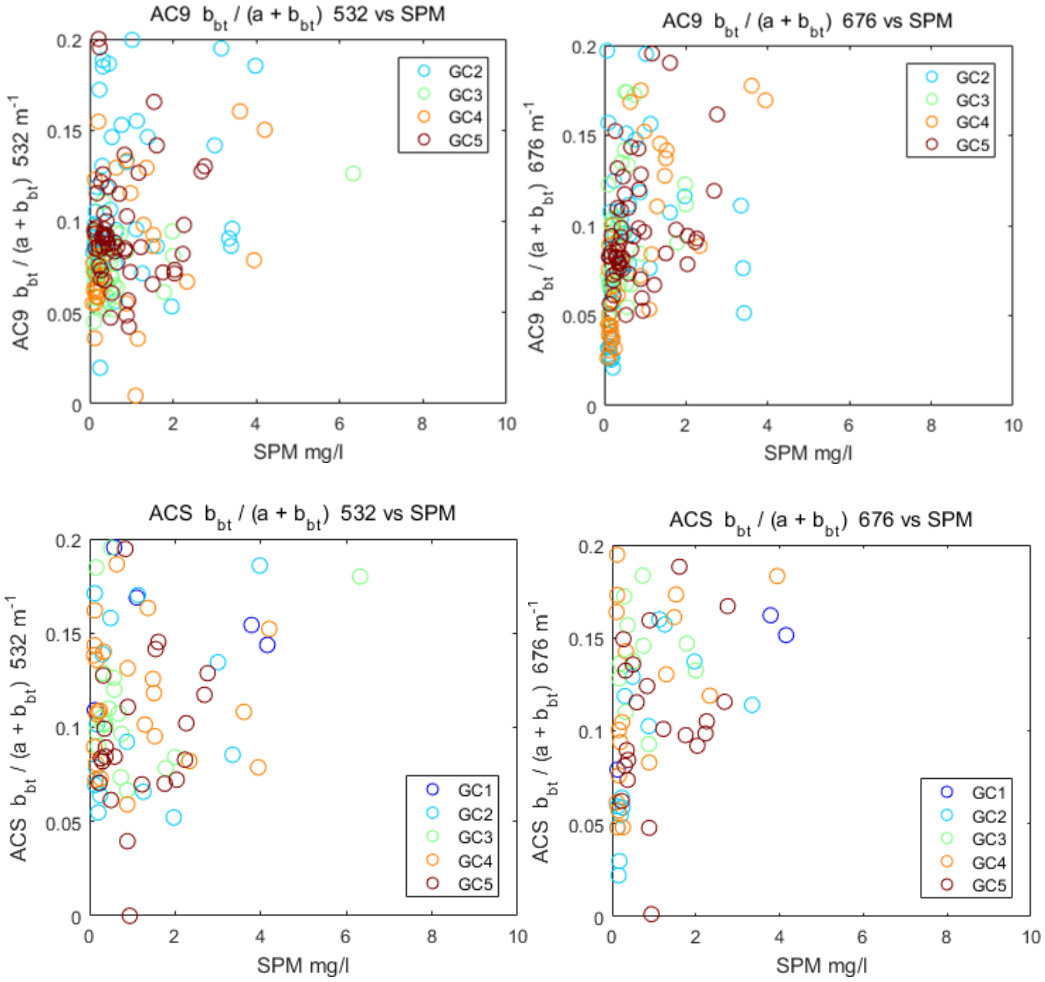

Figure 68. SPM vs. $b_{bt} / (a + b_{bt})$, (AC9 & ACS) Selected Scatter Plots

These plots display selected wavelengths and ranges of data.

Regarding the relationship between SPM and $b_{bp} / (a + b_{bp})$, the correlation values in Table 53 are very similar to those reported in Table 52. Likewise, the scatter plots in Figure 60 and resemble those in Figure 58. As with the $a + b_b$ IOP combination, the absorption value dominates the value of $b_b / (a + b_b)$ for both the $b_{bt} / (a + b_{bt})$, and $b_{bp} / (a + b_{bp})$ variations. Concerning wavelength 715 nm, all sets of $b_b / (a + b_b)$ models utilizing

these data from both AC sensors should be regarded as suspect given universally low correlation values (and very high p values related to the AC9 observations).

Table 53

SPM in Relation to $b_{bp} / (a + b_{bp})$, (AC9 & ACS)

Wavelength nm	$b_{bp} / (a + b_{bp})$ (AC9) vs. Measured SPM Spearman Correlation Coefficients			$b_{bp} / (a + b_{bp})$ (ACS) vs. Measured SPM Spearman Correlation Coefficients		
	ρ	p	n	ρ	p	n
440	0.36	0.00	265	0.54	0.00	167
488	0.53	0.00	260	0.59	0.00	162
510	0.46	0.00	260	0.56	0.00	159
532	0.57	0.00	260	0.61	0.00	159
595	N/A	N/A	N/A	0.60	0.00	142
660	N/A	N/A	N/A	0.68	0.00	156
676	0.67	0.00	253	0.64	0.00	151
715	0.07	0.24	250	-0.26	0.00	147

Notes. Data from all cruises were used in the calculation of these correlations. Salinity and CTD-T exclusions were applied. BB9 saturation and AC9 and ACS exclusions were also applied. Cruise by cruise correlation coefficients are reported in Table 67.

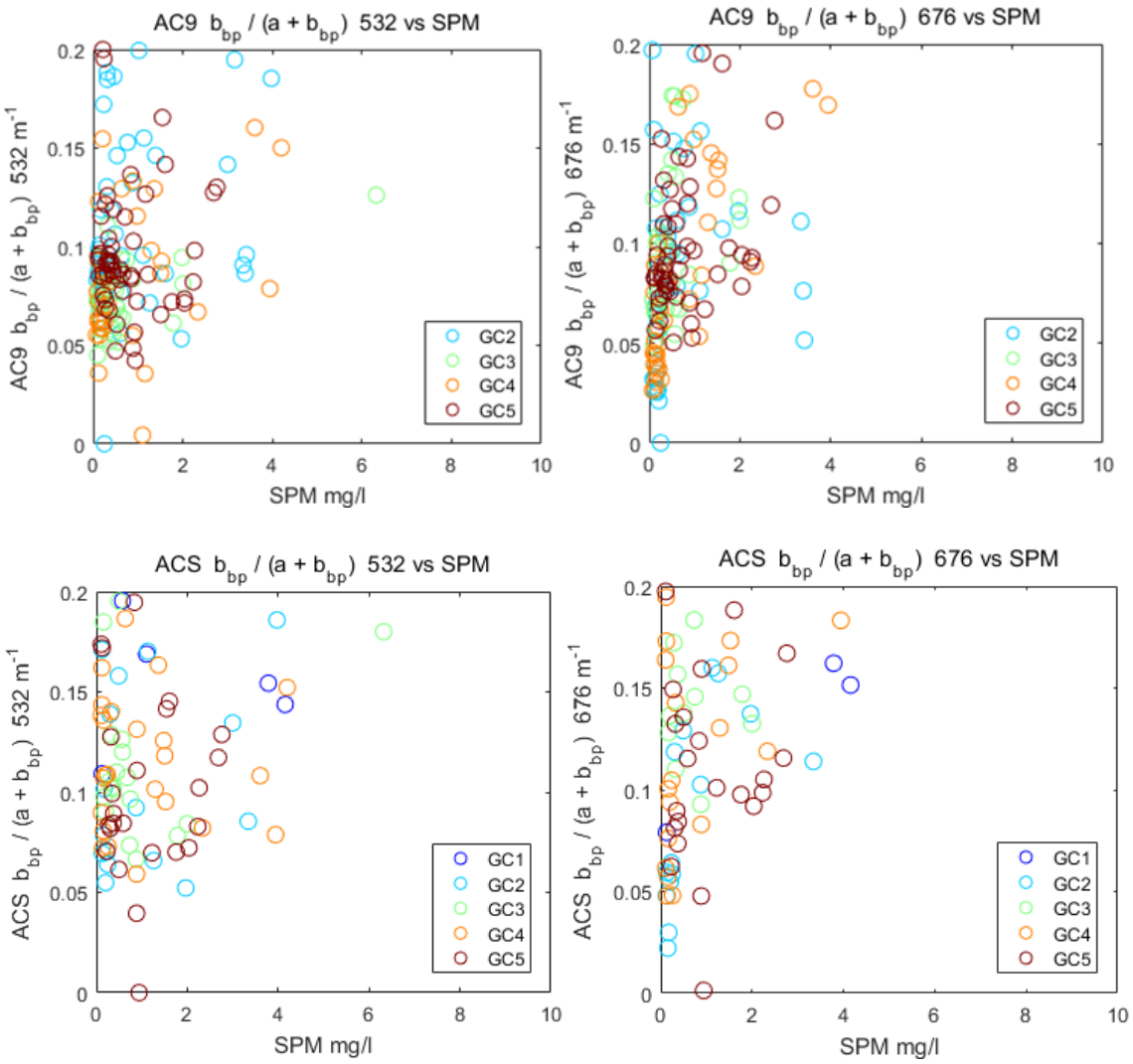

Figure 69. SPM vs. b_{bp} / (a + b_{bp}), (AC9 & ACS) Selected Scatter Plots

These plots display selected wavelengths and ranges of data.

SPM Prediction Based Upon b_b / (a + b_b)

The linear algorithm coefficients to predict SPM from b_{bt} / (a + b_{bt}), and b_{bp} / (a + b_{bp}) respectively are in Tables 54 and 55. The cruise by cruise algorithm coefficients are in Tables 76 and 77. The plotted GCALL models are displayed in Figures 70 and 71. The slope of predicted SPM decreases monotonically with increasing wavelength for both b_{bt} / (a + b_{bt}) and b_{bp} / (a + b_{bp}) (excluding the wavelength 715 nm).

Table 54

SPM Algorithm Coefficients from $b_{bt} / (a + b_{bt})$, (AC9 & ACS)

Wavelength nm	$b_{bt} / (a + b_{bt})$ (AC9) GC2 - GC5		$b_{bt} / (a + b_{bt})$ (ACS) GC1 - GC5	
	m (Uncertainty)	b (Uncertainty)	m (Uncertainty)	b (Uncertainty)
440	17.874 (0.823)	1.442 (0.093)	40.359 (1.188)	-0.143 (0.141)
488	12.329 (0.586)	0.917 (0.097)	16.374 (0.709)	0.465 (0.139)
510	10.584 (0.569)	0.871 (0.107)	14.702 (0.678)	0.096 (0.153)
532	9.841 (0.479)	0.792 (0.103)	12.649 (0.570)	0.151 (0.148)
595	N/A	N/A	8.403 (0.435)	0.140 (0.169)
660	N/A	N/A	4.854 (0.312)	1.338 (0.123)
676	5.008 (0.357)	1.098 (0.096)	4.777 (0.369)	0.863 (0.137)
715	-1.850 (0.125)*	3.964 (0.142)*	-0.185 (0.039)	2.467 (0.101)

Notes. The slopes and intercepts are for linear SPM predictive algorithm y = mx + b. The uncertainty for the regression slopes and intercepts were calculated using singular value decomposition. * The GCALL data pairs of b_{bt}/b and SPM are statistically unrelated. Salinity, CTD turbulence, and BB9 saturation exclusions were applied. SPM algorithm coefficients calculated from data produced during individual cruises are found in Table 76.

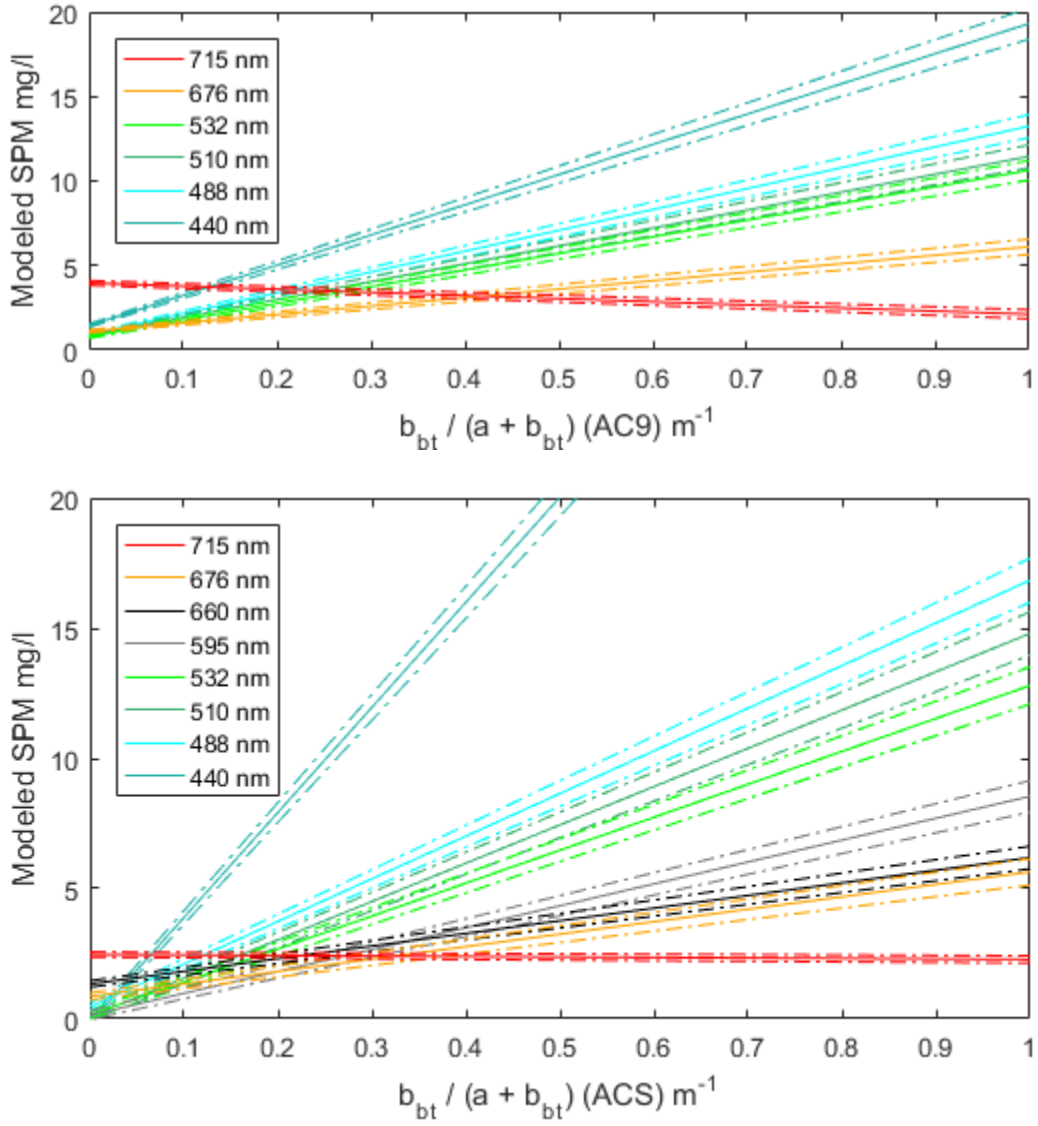

Figure 70. b_{bt} / (a + b_{bt}) SPM Models (AC9 & ACS)

Modeled SPM concentration at six wavelengths for the AC9 and eight wavelengths for the ACS. Upper and lower boundaries determined by uncertainty of the algorithm coefficients are plotted above and below the modeled SPM at each wavelength. The AC9 coefficients are based on data from GC2 – GC5. The ACS coefficients are based on data from GC1 - GC5.

Table 55

SPM Algorithm Coefficients from $b_{bp} / (a + b_{bp})$, (AC9 & ACS)

Wavelength nm	$b_{bp} / (a + b_{bp})$ (AC9) GC2 - GC5		$b_{bp} / (a + b_{bp})$ (ACS) GC1 - GC5	
	m (Uncertainty)	b (Uncertainty)	m (Uncertainty)	b (Uncertainty)
440	30.202 (1.027)	0.482 (0.104)	40.493 (1.188)	-0.193 (0.141)
488	12.386 (0.585)	0.917 (0.097)	16.506 (0.707)	0.422 (0.138)
510	10.578 (0.569)	0.873 (0.107)	14.725 (0.678)	0.058 (0.152)
532	9.838 (0.478)	0.794 (0.103)	12.714 (0.570)	0.109 (0.147)
595	N/A	N/A	8.487 (0.433)	0.087 (0.167)
660	N/A	N/A	4.939 (0.310)	1.281 (0.121)
676	5.012 (0.357)	1.099 (0.096)	4.821 (0.369)	0.827 (0.137)
715	-1.615 (0.121)	3.666 (0.136)	-0.221 (0.047)	2.473 (0.105)

Notes. The slopes and intercepts are for linear SPM predictive algorithm y = mx + b. The uncertainty for the regression slopes and intercepts were calculated using singular value decomposition. Salinity, CTD turbulence, and BB9 saturation exclusions were applied. SPM algorithm coefficients calculated from data produced during individual cruises are found in Table 77.

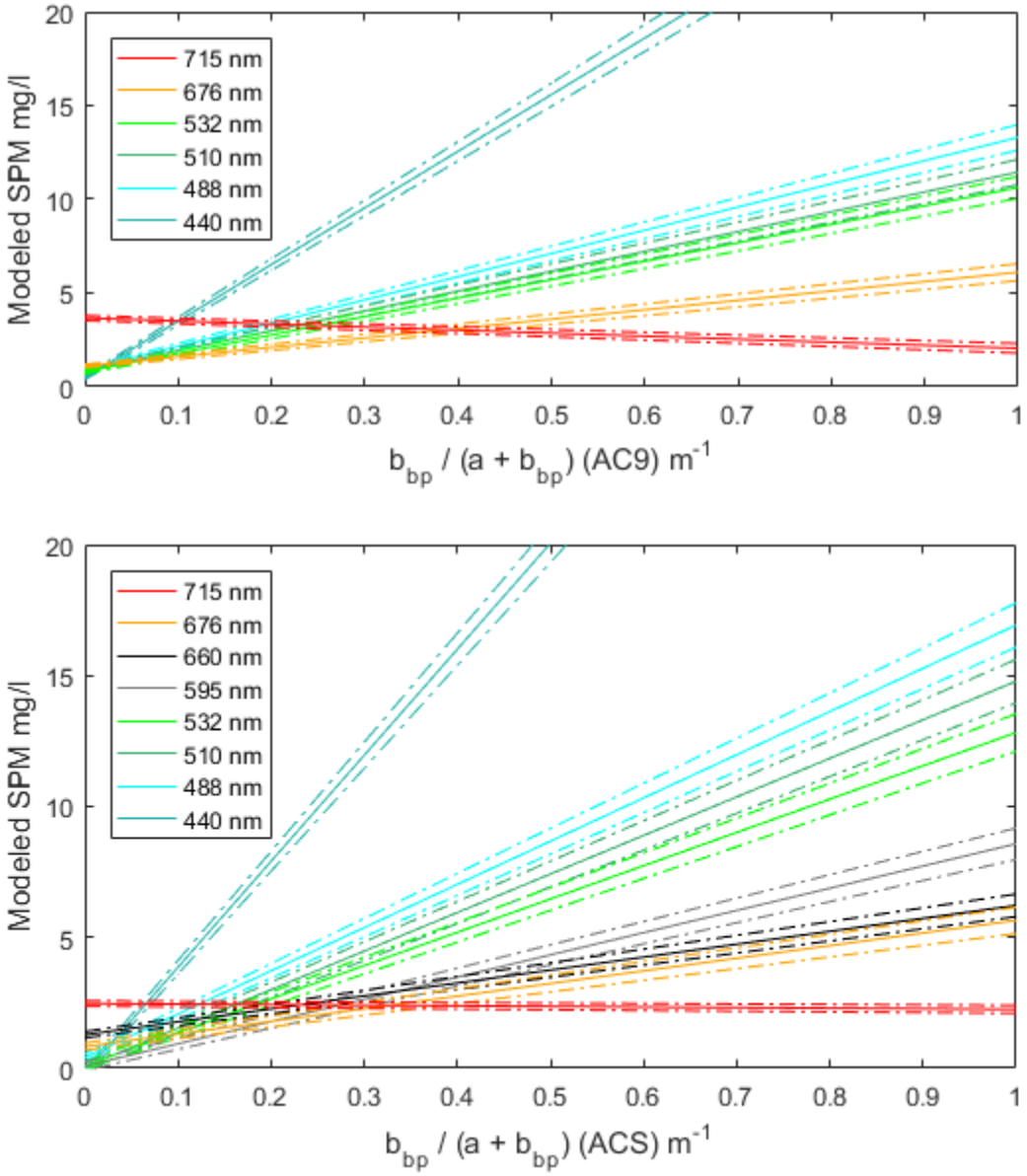

Figure 71. b_{bp} / (a + b_{bp}) SPM Models (AC9 & ACS)

Modeled SPM concentration at six wavelengths for the AC9 and eight wavelengths for the ACS. Upper and lower boundaries determined by uncertainty of the algorithm coefficients are plotted above and below the modeled SPM at each wavelength. The AC9 coefficients are based on data from GC2 – GC5. The ACS coefficients are based on data from GC1 - GC5.

Best SPM Approximation Models

Some SPM predictors have more value than others. For example, researchers have suggested that particulate attenuation (c_p), particulate backscatter (b_{bp}) and (sometimes) side scattering (not addressed in this research) provide the best estimations for SPM concentration (D'Sa et al., 2007; D. Doxaran et al., 2012; G. Neukermans et al., 2012). This project verifies that relationship between SPM and absorption is poor compared to the relationships between SPM and b_t, b_{bp}, and c. Conversely, the correlation between absorption and SPM is better than the relationship between SPM and $b_b / (a + b_b)$, and much stronger than b_b/b and SPM. The IOPs b_b, b, and c almost always have strong correlations to SPM. This chapter section analyzes the regressions produced in this research and suggests the best estimators for SPM concentration.

SPM Prediction Accuracy Analysis

Each of the 169 IOP - based SPM algorithms created using GCALL datasets was submitted to an evaluation of the model's accuracy. The specific steps used in these analyses are detailed presently. These tests involved the same datasets from which they were developed, so the results of the evaluations are presumed to be somewhat stronger than if independent datasets were used for validation.

The complete filtered SPM sample set (minus the underway samples described in Chapter II) has non-gaussian distribution (Figure 72). It has a median value of 1.12 ±8.03 (MAD) mg/l and a range of over 300 mg/l (n = 458). (Underway samples were not considered during this evaluation because no water column profile measurements were obtained at these locations.) Understanding this distribution is important to decisions made in subsampling this dataset for additional quantitative evaluations.

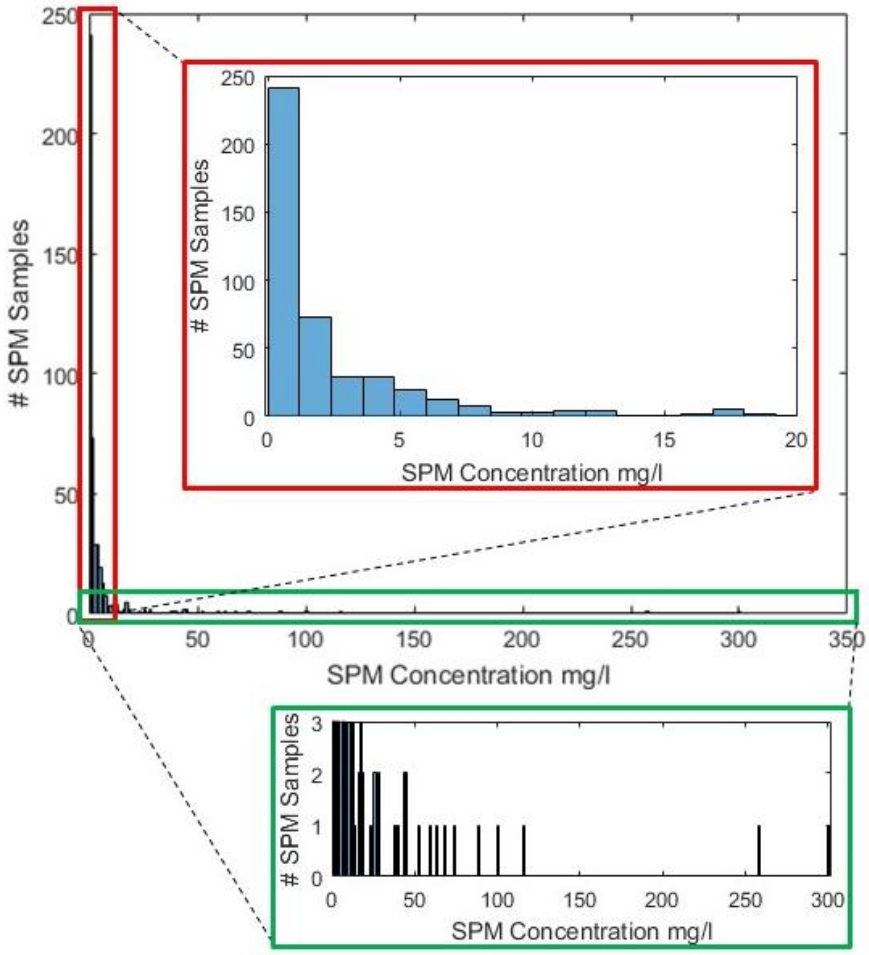

Figure 72. Filtered SPM Concentration Histogram, GCALL

The smaller plots in this figure represent magnified portions of the complete frequency distribution.

One quantitative method used for evaluating SPM predictive models from IOPs was to calculate the model's uncertainty for both slope and intercept components (previously determined using singular value decomposition). These results were reported alongside the various linear algorithm coefficients in the tables of this chapter. This project utilizes SPM filter samples with measured uncertainty through the evaluation of multiple samples from the same location. Where multiples were not collected, the estimated uncertainty of ±8.56% of the concentration was imposed. (See Chapter VII for the determination of this value.) Similarly, the measured or calculated IOPs or IOP

combinations with measurement uncertainties associated with each value at each all filterdepths sampled are applied to this analysis.

A MATLAB script was written to utilize the measured and computed IOPs and IOP combinations so that each of these parameters at filterdepths were evaluated three times. First, the estimated SPM concentration was calculated for the model in question. Second, upper and lower limits of predicted SPM concentration were computed using the combined uncertainties from both the IOP (or IOP combination) and the model, thus producing uncertainty values associated with each calculated SPM concentration. Once this step was complete, it became possible to compare the measured versus modeled SPM concentration with uncertainties attached to both parameters.

If there was overlap in the uncertainty ranges of measured and modeled SPM at a given filterdepth, the SPM prediction of the model under evaluation was considered an "accurate prediction" by the script. If the uncertainty ranges did not overlap, it was determined whether the model underestimated or overestimated actual SPM concentration. The percentages of accurate predictions, underestimated predictions, and overpredicted estimations were computed for each IOP - based SPM model. Stacked bar-plots were made of the results for the GCALL models (Figures 73 and 74). In these figures, the straight horizontal lines represent 33.33%. While it would be preferable for the SPM algorithms to have 100% accuracy, this is not a reasonable assumption. That 33.33% line is noted because the least acceptable results of this accuracy analysis would be to have one-third of any given model's predictions to be accurate, one third to be underestimated and the final third to be overestimated. In other words, a predictive algorithm with a 33.33% (or better) accuracy performance might be considered useful.

The line of asterisks on these plots mark the position of the 50th percentile of inaccurate predictions added to the number of accurate predictions for each model. If the asterisk marks the division between underpredicted SPM percentages and overpredicted SPM percentages, then the performance of that algorithm is in balance relative to the SPM datasets evaluated. Figures 73 and 74 both indicate such balance was rarely achieved. These accuracy analyses were performed for the full GCALL dataset (Figure 73).

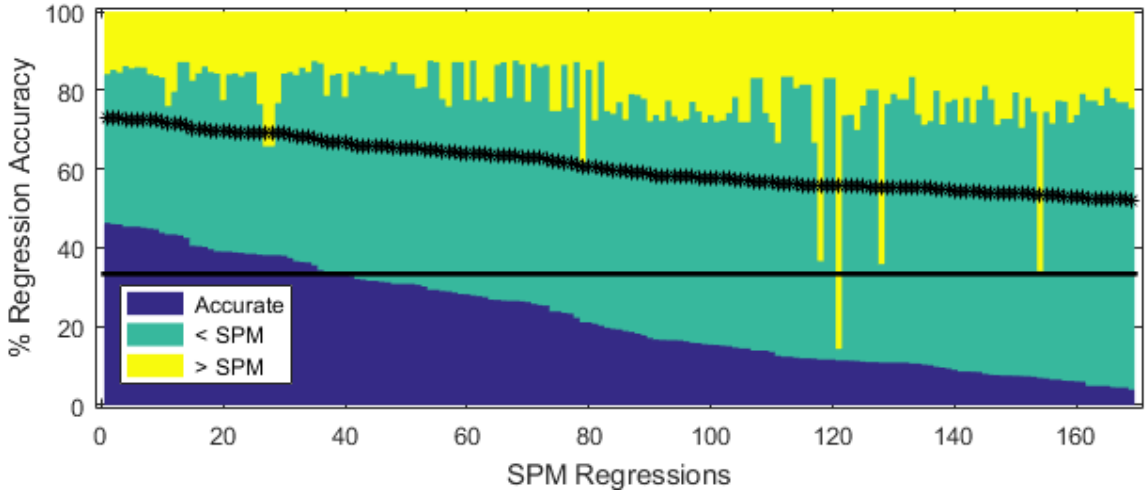

Figure 73. Accuracy Assessments of GCALL SPM Models, Full GCALL Datasets

Each stacked bar (with three parts for each bar) represents the accuracy evaluation results of a single SPM model. There are 168 models based upon the GCALL datasets. Blue bars represent the percentage of accurate SPM predictions determined by this test. Green and yellow bars percentages of underestimated and overestimated concentrations respectively. Algorithms produced using individual cruise data are not represented here.

Figure 73 is a bar-plot showing the results of the GCALL SPM models tested by the GCALL datasets. It is a bit surprising to see that only 39 of the 169 GCALL SPM models perform at 33.33% accuracy or better. Even then, 46.28% accurate predictions represent the best performance for this analysis (from the model using IOP b_{bp} at 660 nm, n = 309, RMSE = 1.36). Of these 39 models considered to be functional by this test, the following IOPs (or IOP combinations) are represented in that group for various

wavelengths the stated number of times: b_{bp} (8), b_{bt} (8), b (7), c (9), a + b_{bp} (4), a + b_{bt} (3). RMSE values from this group of functional models range from 0.82 (b_{bp} and b_{bt} at 715 nm, % accuracy = 40.20% and 45.85% respectively) to 5.01 (AC9 a + b_{bt} at 510 nm and ACS a + b_{bt} at 510 nm, % accuracy = 34.23% in both cases).

Next, it was thought to be beneficial to know how well these algorithms worked for specific concentration ranges within the complete available dataset. In addition to calculating the accuracy percentages for these specified concentration ranges, the RMSE values were also determined during these tests. Since the GCALL filtered sample dataset was non-gaussian (Figure 72) for this evaluation, the full set of measured versus modeled data pairs was divided into four groups based upon quarter percentiles of that distribution. The first subgroup of test values was for the 25th percentile of the measured SPM concentration range. The second subgroup represented the 50th percentile minus the 25th percentile concentration range; the third subgroup represented the 75th percentile minus the 50th percentile concentration range, and the fourth group represented the 75th thru 100th percentile concentration range. This translates into 0 – 0.31 mg/l, 0.32 – 1.06 mg/l, 1.07 – 3.41 mg/l, and 3.42 – 301.0 mg/l concentration ranges respectively. The results are shown in Figure 74.

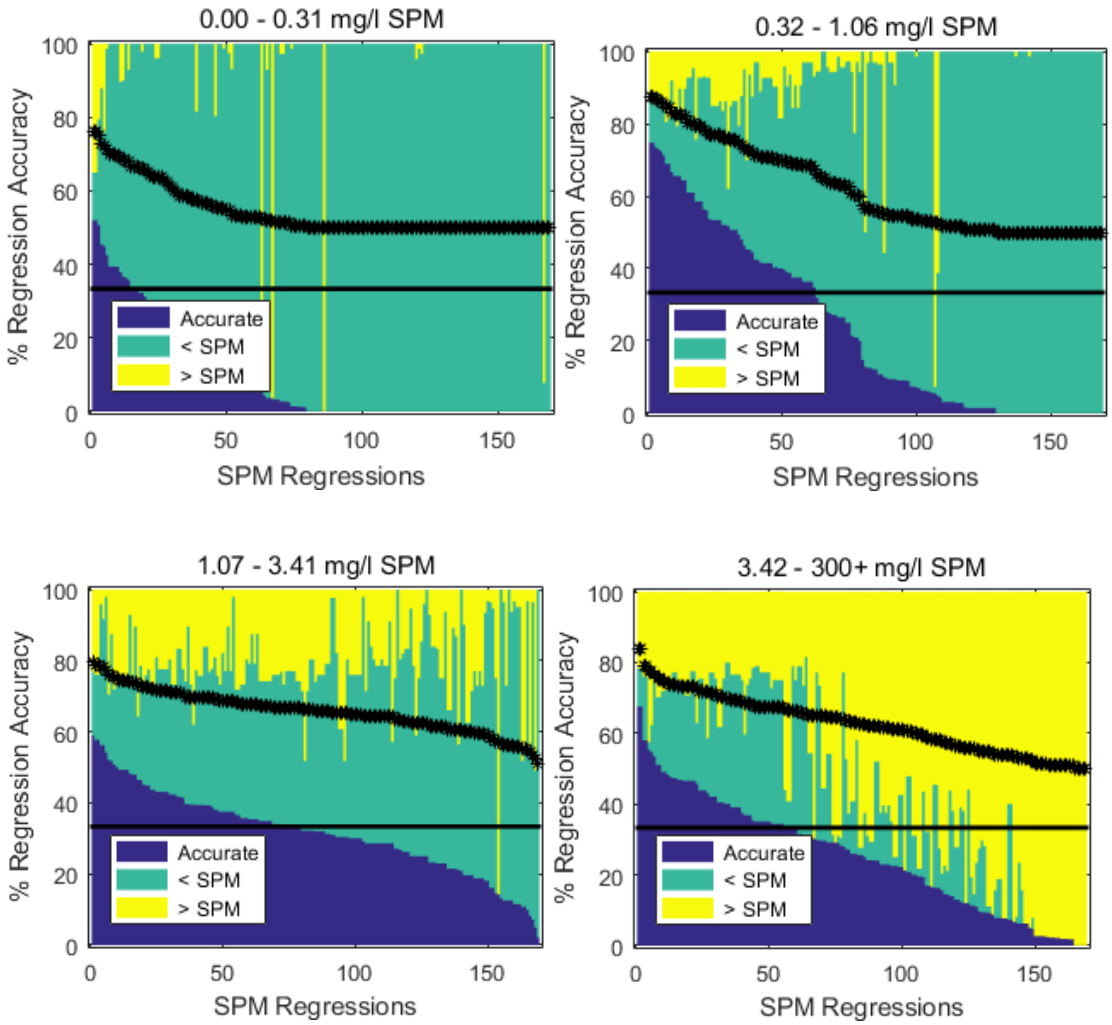

Figure 74. Accuracy Assessments of GCALL SPM Models, Modified Quarter-Percentile Concentration Ranges

Each stacked bar (with three parts for each bar) represents the accuracy evaluation results of a single SPM model. There are 168 models based upon the GCALL datasets. Algorithms produced using individual cruise data are not represented here. The top left plot shows the 25th percentile of the full measured SPM concentration range. The top right and bottom left plots show the 50th percentile minus the 25th percentile, and 75th percentile minus 50th percentile ranges respectively. Finally, the bottom plot shows the 100th percentile minus the 75th percentile concentration range. This translates into 0 – 0.31 mg/l, 0.32 – 1.06 mg/l, 1.07 – 3.41 mg/l, and 3.42 – 301.0 mg/l concentration ranges respectively.

The results of the accuracy evaluations for the modified quarter percentile SPM concentration ranges reveal a few additional interesting things about how well these models work relative to the filtered SPM datasets upon which they were created. First,

more models provide meaningful results (accuracy >33.33%) in the modified 25^{th} – 50^{th} (62 models), and 50^{th} – 75^{th} (79 models) and 75^{th} – 100^{th} (59 models) percentile ranges, than for the 25^{th} percentile (16 models). Figure 74 also shows a strong trend of SPM concentration underestimation of the models in thein all but the 75^{th} - 100^{th} percentile plots. This trend decreases as the SPM concentration gets larger until, finally, the 100^{th} minus 75^{th} percentile concentration range displays a strong tendency for the algorithms to overestimate SPM when not producing accurate results.

RMSE Parameter and Scoring Scheme

While accuracy analysis was useful in detecting these general trends, it did not provide enough information by itself to definitively determine which algorithms were best for SPM concentration prediction. For example, for each of these modified percentile-based SPM concentration test ranges, the top 23 performers (representing 20% of the subset sizes) were identified and grouped into a single dataset. The number of times any given algorithm occurred within this new dataset provided a relative indication of overall performance. None of the IOPs in the new dataset was present four times. Seven algorithms occurred three times within this dataset (all based upon b_b); twenty algorithms had two incidences, and the rest only appeared once. Furthermore, there was a sizable amount of variation between separate occurrences of the same algorithm within this combined dataset of top 20% performers. For example, for $b_{bp}(660)$, even though it occurred three times in the top 20% of performers for all four concentration ranges tested, its accuracy ranged from 32.26% to 68.97%, and the associated RMSE values ranged from 0.19 to 0.93.

To better assess the GCALL SPM algorithms, a quantitative analysis was developed to identify the most reliable SPM models and their associated IOPs. A scoring system was developed to rank the GCALL algorithms based upon performance accuracy and RMSE. The results of the four modified-percentile based subset analyses were used for this evaluation. The RMSE values determined for each SPM concentration range tested were used to create an RMSE parameter, $h_{RMSE,}$ associated with each test. This parameter was formed by scaling the RMSE values within each subset of SPM measured versus modeled data pairs tested. It is defined as

$$h_{RMSE} = 100 - 100 * g' \tag{5.3}$$

where

$$g' = \frac{g - g_{min}}{g_{max} - g_{min}} \tag{5.4}$$

and g represents RMSE values produced by each modified-percentile based SPM concentration range.

The resulting RMSE scoring parameter has parity with the percent accuracy in that both parameters were required, by definition, to have values between 0.00 and 100.00. Also, for both the percent accuracy and h_{RMSE}, high values indicate better quality algorithms. When summed together, the result could have a maximum score of 200. This case would represent an SPM model having both 100% accuracy and an RMSE value of 0.00 for the specific measured versus modeled dataset evaluated within the SPM concentration range tested.

Since each algorithm was tested four times, a maximum combined score would have been 800.The relative values of each GCALL IOP based SPM algorithm were ranked based upon these combined scores. The five instances where the p-values

associated with the Spearman correlation coefficients indicated that SPM and the IOP under consideration were not statistically related for the GCALL dataset were flagged, and the corresponding algorithms were ranked last. The results are reported in Table 56. In this table, the recorded RMSE values were determined using the complete measured versus modeled SPM concentrations dataset for GCALL.

Table 56

Best IOPs by Rank for SPM Analysis (GCALL Algorithms)

Total Score	Rank	IOP(s)	Wavelength nm	Sensor(s)	RMSE	n
582.77	1	b_{bt}	715	BB9	0.82	301
579.80	2	b_{bt}	676	BB9	0.86	304
577.66	3	b_{bp}	676	BB9	0.86	304
574.92	4	b_{bp}	510	BB9	1.36	311
574.57	5	b_{bt}	510	BB9	1.37	311
574.28	6	b_{bt}	532	BB9	1.36	311
572.07	7	b_{bp}	660	BB9	1.36	309
571.74	8	b_{bp}	532	BB9	1.36	311
570.81	9	b_{bt}	660	BB9	1.36	309
565.98	10	b_{bp}	715	BB9	0.82	301
565.35	11	b_{bp}	595	BB9	1.43	275
553.40	12	$a + b_{bp}$	715	ACS & BB9	0.95	141
552.81	13	c	412	ACS	2.04	279
552.73	14	b_{bt}	595	BB9	1.56	309
552.68	15	b_{bt}	488	BB9	1.41	312
547.52	16	b_{bp}	488	BB9	1.41	312
543.63	17	$a + b_{bt}$	715	ACS & BB9	0.96	137
542.44	18	b	412	ACS	2.55	182
542.30	19	c	440	ACS	2.11	279
540.24	20	b	488	ACS	2.60	182
539.56	21	b	440	ACS	2.56	182
538.68	22	c	510	ACS	2.13	279
536.95	23	c	488	ACS	2.13	279
536.66	24	b	510	ACS	2.61	182
535.95	25	b	532	ACS	2.62	182
534.34	26	c	532	ACS	2.14	279
530.62	27	b_{bt}	440	BB9	1.79	318
529.37	28	b	555	ACS	2.64	182
528.29	29	c	555	ACS	2.15	279

Table 56 (continued).

Total Score	Rank	IOP(s)	Wavelength nm	Sensor(s)	RMSE	n
526.52	30	b_{bp}	440	BB9	1.79	318
522.00	31	b	595	ACS	2.66	182
515.47	32	c	595	ACS	2.17	279
515.21	33	$a + b_{bp}$	595	ACS & BB9	2.27	157
515.12	34	c	650	ACS	2.19	279
514.32	35	c	440	AC9	2.05	273
513.92	36	$a + b_{bt}$	595	ACS & BB9	2.29	155
512.44	37	c	660	ACS	2.20	279
511.83	38***	c	670	LISST***	1.35	154
511.37	39	c	488	AC9	2.08	273
508.02	40	c	670	ACS	2.20	279
507.93	41	c	676	ACS	2.21	279
506.10	42	c	715	ACS	2.22	279
505.76	43	c	532	AC9	2.12	273
505.67	44	c	510	AC9	2.10	273
502.21	45	c	555	AC9	2.13	273
499.84	46	c	676	AC9	2.20	273
497.86	47	c	715	AC9	2.22	273
495.19	48	b	650	ACS	2.70	182
494.64	49	b	715	ACS	2.75	181
492.99	50	c	650	AC9	2.18	273
492.65	51	$a + b_{bp}$	532	ACS & BB9	2.55	159
490.61	52	b	660	ACS	2.70	182
490.09	53	b	670	ACS	2.71	182
490.00	54	b	676	ACS	2.71	182
487.59	55	$a + b_{bt}$	532	ACS & BB9	2.57	157
484.52	56	b	715	AC9	2.29	256
484.40	57	b_{bt}	400	BB9	2.04	319
484.39	58	b	532	AC9	2.24	257
483.61	59	b_{bp}	400	BB9	2.70	319
483.21	60	b	555	AC9	2.20	257
480.19	61	b	650	AC9	2.26	256
479.41	62	b	676	AC9	2.28	257

Table 56 (continued).

Total Score	Rank	IOP(s)	Wavelength nm	Sensor(s)	RMSE	n
475.36	63	c	412	AC9	2.26	273
464.72	64	$a + b_{bt}$	660	ACS & BB9	2.54	154
464.38	65	$a + b_{bp}$	660	ACS & BB9	2.52	156
462.85	66	$a + b_{bp}$	488	ACS & BB9	2.78	162
458.48	67	$a + b_{bp}$	510	ACS & BB9	2.62	159
458.4	68	$a + b_{bp}$	676	ACS & BB9	1.43	151
457.17	69	$a + b_{bt}$	488	ACS & BB9	2.79	160
455.20	70	$a + b_{bt}$	676	ACS & BB9	1.44	149
452.11	71	$a + b_{bt}$	510	ACS & BB9	2.64	157
450.47	72	b	510	AC9	2.48	257
445.4	73	c	650	Transmissometer	3.37	257
442.49	74**	c	650	Transmissometer**	3.33	228
389.12	75	b_{bp}/b	715	AC9 & BB9	1.98	243
386.51	76	a	440	ACS	6.13	247
380.71	77	b	412	AC9	3.03	257
380.26	78	$a + b_{bp}$	440	ACS & BB9	3.90	167
377.48	79	$a + b_{bt}$	440	ACS & BB9	3.92	165
371.70	80	b	488	AC9	3.21	257
370.14	81	b	440	AC9	3.24	257
366.88	82	b_{bt}/b	715	AC9 & BB9	2.09	240
365.69	83	b_{bp}/b	595	ACS & BB9	3.41	142
362.64	84	$b_{bp} / (a + b_{bp})$	676	ACS & BB9	2.03	151
360.11	85	b_{bt}/b	715	ACS & BB9	2.08	145
358.26	86	$b_{bt} / (a + b_{bt})$	676	ACS & BB9	2.03	149
357.09	87	b_{bp}/b	676	ACS& BB9	2.18	150
356.46	88	b_{bp}/b	488	AC9 & BB9	3.08	249
348.01	89	b_{bp}/b	715	ACS & BB9	2.07	147
344.43	90	b_{bp}/b	510	AC9 & BB9	3.22	253
343.84	91	b_{bp}/b	676	AC9 & BB9	2.19	246
343.64	92	a	488	AC9	6.09	268

Table 56 (continued).

Total Score	Rank	IOP(s)	Wavelength nm	Sensor(s)	RMSE	n
343.45	93	$a + b_{bt}$	510	AC9 & BB9	5.01	260
343.42	94	$a + b_{bp}$	510	AC9 & BB9	5.01	260
343.10	95	b_{bt}/b	676	ACS & BB9	2.27	149
341.03	96	b_{bt}/b	676	AC9 & BB9	2.19	244
340.41	97	b_{bp}/b	532	AC9 & BB9	3.17	253
335.08	98	$b_{bp} / (a + b_{bp})$	715	ACS & BB9	2.12	144
334.75	99	a	510	AC9	5.73	268
331.18	100	b_{bp}/b	532	ACS & BB9	3.57	158
329.34	101	$b_{bt} / (a + b_{bt})$	715	ACS & BB9	2.13	144
320.84	102	a	488	ACS	5.69	247
320.58	103	c	670	LISST	5.47	203
320.19	104	$b_{bt} / (a + b_{bt})$	532	ACS & BB9	3.35	156
318.83	105	$b_{bp} / (a + b_{bp})$	532	ACS & BB9	3.34	158
316.80	106	$b_{bt} / (a + b_{bt})$	510	ACS & BB9	3.36	157
316.38	107	$b_{bp} / (a + b_{bp})$	510	ACS & BB9	3.36	159
314.16	108	a	440	AC9	7.47	268
312.62	109	$b_{bp} / (a + b_{bp})$	595	ACS & BB9	3.32	142
311.39	110	$b_{bt} / (a + b_{bt})$	595	ACS & BB9	3.34	140
309.12	111	a	532	AC9	6.18	268
308.47	112	b_{bt}/b	510	AC9 & BB9	3.30	251
308.20	113	$a + b_{bt}$	440	AC9 & BB9	4.55	265
308.20	114	$a + b_{bp}$	440	AC9 & BB9	4.55	265
306.34	115	b_{bp}/b	660	ACS & BB9	3.24	155
301.01	116	b_{bp}/b	510	ACS & BB9	3.68	159
300.80	117	a	510	ACS	5.93	247
297.66	118	$b_{bp} / (a + b_{bp})$	676	AC9 & BB9	7.44	253
297.64	119	$b_{bt} / (a + b_{bt})$	676	AC9 & BB9	7.44	253
292.35	120	$b_{bt} / (a + b_{bt})$	660	ACS & BB9	3.28	153
291.60	121	$b_{bp} / (a + b_{bp})$	660	ACS & BB9	3.26	156
285.97	122	a	555	AC9	6.46	268

Table 56 (continued).

Total Score	Rank	IOP(s)	Wavelength nm	Sensor(s)	RMSE	n
285.85	123	b_{bt}/b	660	ACS	3.46	153
283.44	124	$b_{bt} / (a + b_{bt})$	510	AC9 & BB9	7.68	260
283.41	125	$b_{bp} / (a + b_{bp})$	510	AC9 & BB9	7.68	260
283.35	126	$b_{bp} / (a + b_{bp})$	488	ACS & BB9	3.83	161
283.23	127	$b_{bt} / (a + b_{bt})$	488	ACS & BB9	3.85	159
282.71	128	$a + b_{bt}$	676	AC9 & BB9	3.52	253
282.69	129	$a + b_{bp}$	676	AC9 & BB9	3.52	253
282.44	130	a	532	ACS	6.20	247
280.58	131	a	412	ACS	7.48	247
279.16	132	$b_{bt} / (a + b_{bt})$	532	AC9 & BB9	7.65	260
279.13	133	$b_{bp} / (a + b_{bp})$	532	AC9 & BB9	7.65	260
273.65	134	a	555	ACS	6.24	247
273.27	135	$a + b_{bt}$	488	AC9 & BB9	4.96	260
273.25	136	$b_{bp} / (a + b_{bp})$	488	AC9 & BB9	7.66	260
273.09	137	$b_{bt} / (a + b_{bt})$	488	AC9 & BB9	7.66	260
270.47	138	$a + b_{bp}$	488	AC9 & BB9	4.95	260
267.86	139	b_{bt}/b	595	ACS & BB9	3.65	143
266.03	140	b_{bp}/b	488	ACS & BB9	3.92	156
258.19	141	b_{bt}/b	532	ACS & BB9	3.79	156
257.57	142	b_{bt}/b	510	ACS& BB9	3.79	157
254.73	143	b_{bp}/b	440	AC9 & BB9	4.93	258
248.37	144	a	595	ACS	6.58	247
245.78	145	b_{bp}/b	440	ACS & BB9	5.57	163
239.97	146	$b_{bp} / (a + b_{bp})$	440	ACS & BB9	5.48	166
239.68	147	a	412	AC9	10.09	268
238.59	148	$b_{bt} / (a + b_{bt})$	440	ACS & BB9	5.50	164
238.57	149	b_{bt}/b	488	ACS & BB9	4.26	158
232.99	150	$a + b_{bp}$	715	AC9 & BB9	5.02	250
228.42	151	$a + b_{bt}$	715	AC9 & BB9	5.08	244
227.23	152	$a + b_{bp}$	532	AC9 & BB9	5.56	260

Table 56 (continued).

Total Score	Rank	IOP(s)	Wavelength nm	Sensor(s)	RMSE	n
225.94	153	$a + b_{bt}$	532	AC9 & BB9	5.57	260
223.14	154	a	676	ACS	7.17	247
222.16	155	a	650	AC9	8.11	268
221.50	156	$b_{bp} / (a + b_{bp})$	440	AC9 & BB9	8.30	265
217.78	157	$b_{bt} / (a + b_{bt})$	440	AC9 & BB9	8.39	265
207.63	158	a	670	ACS	8.93	247
202.44	159	a	660	ACS	8.89	247
194.42	160	a	676	AC9	9.56	268
185.71	161	a	650	ACS	10.00	247
172.41	162	b_{bt}/b	440	ACS & BB9	6.11	163
165.21	163	a	715	AC9	9.78	268
155.04	164	a	715	ACS	10.38	247
310.96	165*	b_{bt}/b	488	AC9 & BB9	3.32	251
305.30	165*	b_{bt}/b	532	AC9 & BB9	3.31	251
243.33	165*	b_{bt}/b	440	AC9 & BB9	4.92	256
240.30	165*	$b_{bp} / (a + b_{bp})$	715	AC9 & BB9	7.46	250
237.43	165*	$b_{bt} / (a + b_{bt})$	715	AC9 & BB9	7.50	246

*Spearman rank correlation coefficients indicate that SPM is not statistically related to these IOP combinations and wavelengths for the GCALL datasets. **This algorithm is from GC2, GC3, and GC5. RMSE values were computed using the GCALL dataset. Maximum potential total score was 800.

The scores from Table 56 were reduced to percentages of 800 and plotted in a histogram (Figure 75). This bimodal distribution clearly distinguishes two groups of SPM algorithms based upon score - percentages. The right group, containing the highest score - percentages, consists of all of the representatives of IOPs c, b_{bt} and b_{bp}. Additionally, all but three of the SPM models based on b were present along with seven wavelengths for the IOP combinations $a + b_{bp}$ and $a + b_{bt}$ each. These latter two groups of IOP combinations represent all of the ACS contributions to $+ b_b$ except for at 440 nm

wavelength. The left group in the histogram in Figure 75 consists of IOP – based SPM algorithms representing the lower score - based percentages contained all of the models formed by a, b_{bt} / (a + b_{bt}), b_{bp} / (a + b_{bp}), b_{bt}/b, and b_{bp}/b. All of the IOP combination models that were based upon a + b_{bt} and a + b_{bp} utilizing the AC9, and three b models using the AC9 were also represented in this group.

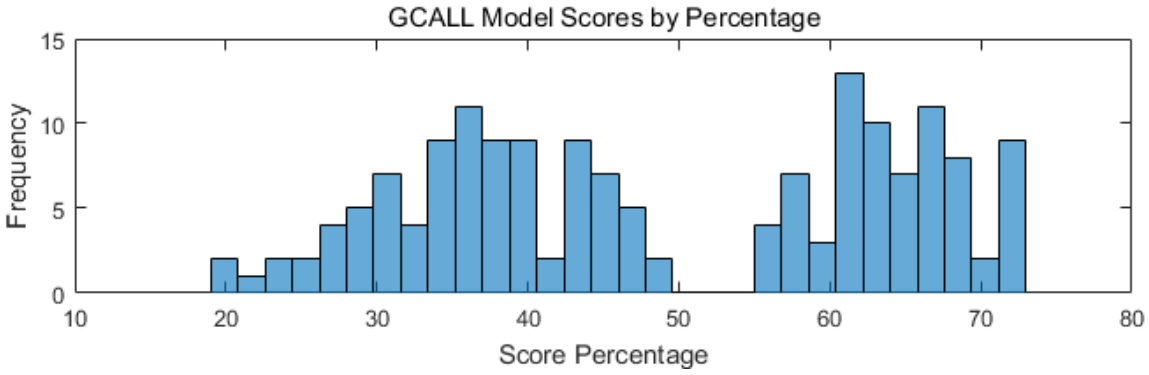

Figure 75. Reduced Scores of GCALL SPM Models

As this project is particularly interested in products that might be related to airborne bathymetric lidar systems including a co-located hyperspectral sensor, extra consideration was given to a few specific groups of algorithms. Regarding the algorithms utilizing IOPs at 532 nm, Figure 76 includes a histogram similar to the one in Figure 75, showing the score – based percentages for the 532 nm based SPM models. The SPM models based on b_{bt} and b_{bp} rank 6th and 8th overall and represent the highest two scoring 532 nm based SPM models. The other stronger scoring 532 nm IOP based models utilized IOPs b and c. The IOP combinations a + b_{bt} and a + b_{bp} where the ACS was the contributing absorption sensor were also among that group. Since the same IOP combinations based upon AC9 observations occur in the lower scoring group of algorithms, it appears that this particular IOP parameter at 532 nm may be strongly dependent on individual sensors.

Figure 76 also shows a histogram highlighting the score - percentages of the SPM models based upon the IOP combination $a + b_b$ for all wavelengths, sensors, and varieties (including particulate backscatter and total backscatter) evaluated in this project. The highest scoring group for this class of SPM algorithms all derive from measurements taken by the ACS. All of the AC9 contributions to this class (along with both contributions of the ACS at 440 nm wavelength) occur in the lower scoring group in this class. It may be important to note that the n-values of samples that could be tested for the ACS-derived models are just over half of the number of samples that could be (and were) used to evaluate the various SPM models based on $a + b_b$ using AC9 observations. The top scoring wavelengths in this analysis are 715 nm, 595 nm, and 532 respectively.

The histogram showing the score - percentages of SPM algorithms utilizing the IOP combination $b_b / (a + b_b)$ is shown in the lower plot of Figure 76. Unlike the other specialized subgroups of models considered here, all of these algorithms have score percentage values less than 50% indicating that other methods of SPM prediction would be preferred if available. The best performing models of this group involved the ACS and the wavelength of 676 nm. As with the $a + b_b$ models, the AC9 - based models had more measured versus modeled SPM data pairs to work with than the ACS-based algorithms. The AC9 – founded algorithms also did not perform as well as the ACS - based algorithms.

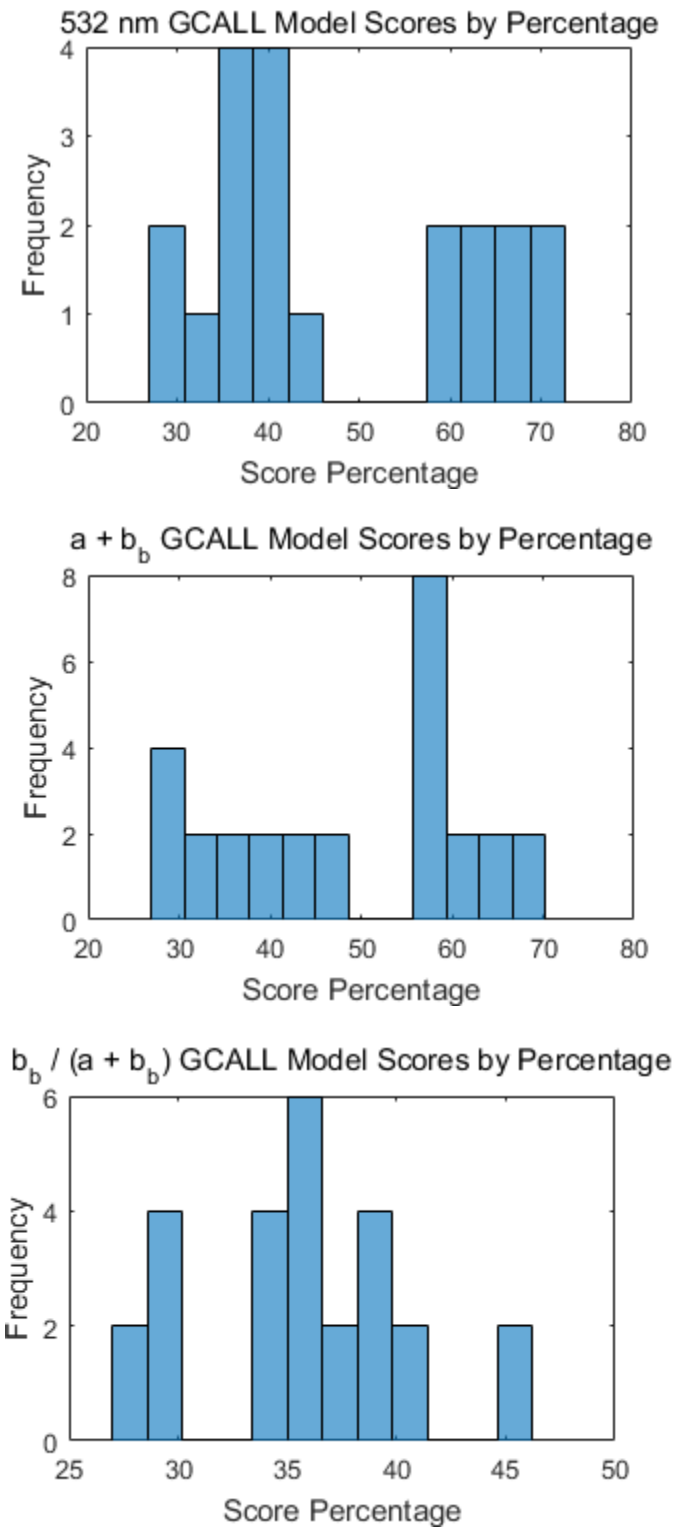

Figure 76. Reduced Scores of Selected GCALL SPM Models

X_{IOP} Analysis

Another quantitative method used for evaluating SPM predictive models from IOPs included reversing the variables of each linear model. Specifically, SPM concentrations were held at fixed levels for each linear model such that

$$X_{IOP} = \frac{(b-SPM)}{m} \tag{5.5}$$

where m and b represent the slope and intercept coefficients. The resulting X_{IOP} is the value required by the IOP or IOP combination to produce SPM at the desired concentration level. Table 57 shows examples of X_{IOP} values needed to produce estimated SPM concentrations at the 25th, 50th, and 75th percentiles of the filtered SPM dataset used in algorithm generation and testing procedures. Additionally, concentration values of 0.10 and 10.00 mg/l are also presented in this table. During this evaluation, the saturation thresholds of the BB9 (Chapter IV) were also considered so that if a X_{IOP} value would have required a BB9 input exceeding those tolerances, a numerical result was not provided in the table. For instances where X_{IOP} calculations were negative, the cell that would have contained that value in Table 57 was also left blank. This evaluation is useful in that it demonstrates that sometimes the IOP input required to produce a specific SPM concentration is a negative value. In the sampling environment, negative IOP values usually indicate a difficulty with a sensor (usually a calibration issue). Therefore, instances requiring a negative X_{IOP} value to achieve a specified SPM concentration represent unobtainable (or at least undesirable) sampling situations. To better understand the value of this table, consider the IOP b at 532 nm calculated from ACS observations. The SPM algorithm produced using these data requires a negative X_{IOP} value (represented by a blank table cell) to predict an SPM concentration of 0.10 mg/l. SPM at

a concentration of 0.37 mg/l, however, can be predicted by this model if the measured or calculated total scatter has a value of 0.1362 m^{-1}. Therefore, it may be inferred that at some point between 0.10 mg/l and 0.37 mg/l that algorithm begins to become capable of predicting SPM concentration. According to this table, some SPM models are capable of predicting low concentrations of SPM, such as those depending upon absorption at short wavelengths. Other models such as the ones based upon b_{bf}/b utilizing the AC9 drop out at larger SPM concentration predictions. This occurs because the required BB9 inputs for these calculations exceed the pertinent saturation threshold. While the X_{IOP} evaluation does not give any indication of a model's accuracy, and only provides limited information about the tolerances of specific sensors, it does supply information about its utility (such as the fact that the LISST based algorithm can be used to predict SPM concentrations $\leq$0.10 mg/l).

Table 57

X_{IOP} Examples

IOP(s)	Wavelength nm	Sensor(s)	X_{IOP} Needed to Calculate ___ mg/l SPM				
			0.1	0.32	1.07	3.42	10
a	412	AC9	0.164	0.1825	0.2453	0.4421	0.993
a	440	AC9	0.0928	0.1107	0.1716	0.3625	0.8971
a	488	AC9		0.0112	0.0643	0.2306	0.6961
a	510	AC9			0.0309	0.1823	0.6061
a	532	AC9			0.0039	0.14	0.5212
a	555	AC9				0.1168	0.4887
a	650	AC9				0.0618	0.3631
a	676	AC9				0.0671	0.3652
a	715	AC9				0.019	0.3023
$a + b_{bp}$	440	AC9 & BB9	0.032	0.0589	0.1504	0.4374	1.2408
$a + b_{bp}$	488	AC9 & BB9	0.0088	0.0273	0.0902	0.2875	0.8398
$a + b_{bp}$	510	AC9 & BB9	0.0303	0.0418	0.0812	0.2047	0.5504
$a + b_{bp}$	532	AC9 & BB9				0.2607	0.9927
$a + b_{bp}$	676	AC9 & BB9			0.0109	0.2495	0.9178
$a + b_{bp}$	715	AC9 & BB9				0.2269	0.9789
$a + b_{bt}$	440	AC9 & BB9	0.032	0.0589	0.1504	0.4374	1.2408
$a + b_{bt}$	488	AC9 & BB9	0.0091	0.0276	0.0906	0.2878	0.84

Table 57 (continued).

IOP(s)	Wavelength nm	Sensor(s)	X_{IOP} Needed to Calculate ___ mg/l SPM				
			0.1	0.32	1.07	3.42	10
$a + b_{bt}$	510	AC9 & BB9	0.0306	0.0421	0.0815	0.2049	0.5505
$a + b_{bt}$	532	AC9 & BB9			0.0008	0.2628	0.9964
$a + b_{bt}$	676	AC9 & BB9			0.011	0.2496	0.9179
$a + b_{bt}$	715	AC9 & BB9				0.2234	0.9759
b	412	AC9				3.5102	13.8075
b	440	AC9				3.3488	13.5031
b	488	AC9				3.1636	12.604
b	510	AC9			0.4106	2.6702	8.9971
b	532	AC9			0.5385	2.4855	7.937
b	555	AC9			0.5558	2.3903	7.5269
b	650	AC9			0.4766	2.1188	6.717
b	676	AC9			0.4426	2.0304	6.4764
b	715	AC9			0.4431	1.9701	6.2456
$b_{bp} / (a + b_{bp})$	440	AC9 & BB9			0.0195	0.0973	0.3151
$b_{bp} / (a + b_{bp})$	488	AC9 & BB9			0.0124	0.2021	0.7333
$b_{bp} / (a + b_{bp})$	510	AC9 & BB9			0.0186	0.2408	0.8628
$b_{bp} / (a + b_{bp})$	532	AC9 & BB9			0.0281	0.2669	0.9358
$b_{bp} / (a + b_{bp})$	676	AC9 & BB9				0.4631	1.7759
$b_{bp} / (a + b_{bp})$	715	AC9 & BB9	2.208	2.0718	1.6074	0.1523	

Table 57 (continued).

IOP(s)	Wavelength nm	Sensor(s)	X_{IOP} Needed to Calculate ___ mg/l SPM				
			0.1	0.32	1.07	3.42	10
$b_{bt} / (a + b_{bt})$	440	AC9 & BB9				0.1107	0.4788
$b_{bt} / (a + b_{bt})$	488	AC9 & BB9			0.0124	0.203	0.7367
$b_{bt} / (a + b_{bt})$	510	AC9 & BB9			0.0188	0.2408	0.8625
$b_{bt} / (a + b_{bt})$	532	AC9 & BB9			0.0282	0.267	0.9357
$b_{bt} / (a + b_{bt})$	676	AC9 & BB9				0.4637	1.7776
$b_{bt} / (a + b_{bt})$	715	AC9 & BB9	2.0886	1.9697	1.5643	0.2941	
c	412	AC9		0.0173	0.8281	3.3686	10.4822
c	440	AC9		0.1583	0.8408	2.9791	8.9663
c	488	AC9		0.1163	0.7439	2.7105	8.2167
c	510	AC9		0.0922	0.7039	2.6207	7.9878
c	532	AC9		0.0735	0.6659	2.5221	7.7196
c	555	AC9		0.0635	0.6373	2.4353	7.4698
c	650	AC9		0.0164	0.5298	2.1383	6.642
c	676	AC9		0.0053	0.5033	2.0637	6.4329
c	715	AC9			0.4663	1.9593	6.1398
b_{bp}/b	440	AC9 & BB9				0.0549	0.3815
b_{bp}/b	488	AC9 & BB9	0.0023	0.0035	0.0074	0.0198	0.0545
b_{bp}/b	510	AC9 & BB9	0.0011	0.0026	0.0079	0.0242	0.0698
b_{bp}/b	532	AC9 & BB9	0.0009	0.0023	0.0072	0.0224	0.065

Table 57 (continued).

IOP(s)	Wavelength nm	Sensor(s)	X_{IOP} Needed to Calculate ___ mg/l SPM				
			0.1	0.32	1.07	3.42	10
b_{bp}/b	676	AC9 & BB9				1.4313	6.8159
b_{bp}/b	715	AC9 & BB9			0.0054	0.0237	0.0747
b_{bt}/b	440	AC9 & BB9	0.189	0.1746	0.1256		
b_{bt}/b	488	AC9 & BB9	0.6425	0.5741	0.341		
b_{bt}/b	510	AC9 & BB9	0.1421	0.1289	0.0837		
b_{bt}/b	532	AC9 & BB9	0.1266	0.1148	0.0747		
b_{bt}/b	676	AC9 & BB9	0.8838	0.7655	0.362		
b_{bt}/b	715	AC9 & BB9				0.1795	0.798
a	412	ACS	0.1488	0.1715	0.2491	0.4922	1.173
a	440	ACS	0.0474	0.0686	0.1408	0.3668	0.9999
a	488	ACS			0.0304	0.2238	0.7654
a	510	ACS				0.1793	0.6818
a	532	ACS				0.1455	0.6153
a	555	ACS				0.1161	0.552
a	595	ACS				0.0715	0.4599
a	650	ACS				0.0509	0.35
a	660	ACS				0.0586	0.3669
a	670	ACS				0.067	0.3805
a	676	ACS				0.0668	0.4043

Table 57 (continued).

IOP(s)	Wavelength nm	Sensor(s)	X_{IOP} Needed to Calculate ___ mg/l SPM				
			0.1	0.32	1.07	3.42	10
a	715	ACS				0.0127	0.2845
$a + b_{bp}$	440	ACS & BB9		0.0124	0.099	0.3705	1.1305
$a + b_{bp}$	488	ACS & BB9	0.0106	0.0261	0.0787	0.2438	0.7059
$a + b_{bp}$	510	ACS & BB9	0.0045	0.0172	0.0607	0.1967	0.5775
$a + b_{bp}$	532	ACS & BB9	0.0085	0.0184	0.0521	0.1578	0.4536
$a + b_{bp}$	595	ACS & BB9	0.0063	0.0117	0.0302	0.0882	0.2506
$a + b_{bp}$	660	ACS & BB9	0.0011	0.0064	0.0243	0.0805	0.2379
$a + b_{bp}$	676	ACS & BB9			0.0262	0.1147	0.3623
$a + b_{bp}$	715	ACS & BB9			0.0053	0.0244	0.0778
$a + b_{bt}$	440	ACS & BB9		0.0116	0.0982	0.3699	1.1304
$a + b_{bt}$	488	ACS & BB9	0.0105	0.026	0.0787	0.2437	0.706
$a + b_{bt}$	510	ACS & BB9	0.0043	0.0171	0.0605	0.1966	0.5777
$a + b_{bt}$	532	ACS & BB9	0.0085	0.0184	0.0521	0.1578	0.4536
$a + b_{bt}$	595	ACS & BB9	0.0062	0.0117	0.0302	0.0882	0.2506
$a + b_{bt}$	660	ACS & BB9	0.001	0.0063	0.0242	0.0805	0.238
$a + b_{bt}$	676	ACS & BB9			0.0259	0.1146	0.363
$a + b_{bt}$	715	ACS & BB9			0.0052	0.0243	0.078
b	412	ACS	0.0853	0.2444	0.7867	2.4859	7.2437

Table 57 (continued).

IOP(s)	Wavelength nm	Sensor(s)	X_{IOP} Needed to Calculate ___ mg/l SPM				
			0.1	0.32	1.07	3.42	10
b	440	ACS	0	0.1622	0.7153	2.4484	7.3009
b	488	ACS		0.1507	0.6789	2.3338	6.9676
b	510	ACS		0.1454	0.6623	2.2819	6.8167
b	532	ACS		0.1362	0.6419	2.2266	6.6635
b	555	ACS		0.1221	0.6172	2.1683	6.5116
b	595	ACS		0.1015	0.5774	2.0685	6.2437
b	650	ACS		0.0689	0.5183	1.9263	5.8688
b	660	ACS		0.0575	0.5018	1.894	5.7921
b	670	ACS		0.0475	0.4868	1.8635	5.7182
b	676	ACS		0.0466	0.4837	1.8531	5.6876
b	715	ACS		0.0407	0.4652	1.7951	5.519
$b_{bp} / (a + b_{bp})$	440	ACS & BB9	0.0072	0.0127	0.0312	0.0892	0.2517
$b_{bp} / (a + b_{bp})$	488	ACS & BB9			0.0393	0.1816	0.5803
$b_{bp} / (a + b_{bp})$	510	ACS & BB9	0.0029	0.0178	0.0687	0.2283	0.6752
$b_{bp} / (a + b_{bp})$	532	ACS & BB9		0.0166	0.0756	0.2604	0.778
$b_{bp} / (a + b_{bp})$	595	ACS & BB9	0.0015	0.0275	0.1158	0.3927	1.168
$b_{bp} / (a + b_{bp})$	660	ACS & BB9				0.4331	1.7653
$b_{bp} / (a + b_{bp})$	676	ACS & BB9			0.0504	0.5379	1.9027
$b_{bp} / (a + b_{bp})$	715	ACS & BB9	10.7376	9.7421	6.3484		

Table 57 (continued).

IOP(s)	Wavelength nm	Sensor(s)	X_{IOP} Needed to Calculate ___ mg/l SPM				
			0.1	0.32	1.07	3.42	10
$b_{bt} / (a + b_{bt})$	440	ACS & BB9	0.006	0.0115	0.0301	0.0883	0.2513
$b_{bt} / (a + b_{bt})$	488	ACS & BB9			0.0369	0.1805	0.5823
$b_{bt} / (a + b_{bt})$	510	ACS & BB9	0.0003	0.0152	0.0662	0.2261	0.6736
$b_{bt} / (a + b_{bt})$	532	ACS & BB9		0.0134	0.0727	0.2584	0.7786
$b_{bt} / (a + b_{bt})$	595	ACS & BB9		0.0214	0.1107	0.3903	1.1734
$b_{bt} / (a + b_{bt})$	660	ACS & BB9				0.4289	1.7845
$b_{bt} / (a + b_{bt})$	676	ACS & BB9			0.0433	0.5353	1.9127
$b_{bt} / (a + b_{bt})$	715	ACS & BB9	12.7946	11.6054	7.5514		
c	412	ACS	0.1876	0.367	0.9788	2.8956	8.2626
c	440	ACS	0.078	0.2548	0.8577	2.7468	8.0362
c	488	ACS	0.0363	0.1993	0.7548	2.4956	7.3696
c	510	ACS	0.0244	0.1819	0.7192	2.4026	7.116
c	532	ACS	0.0132	0.1659	0.6863	2.3171	6.8834
c	555	ACS	0.0007	0.1489	0.6543	2.2379	6.6718
c	595	ACS		0.1231	0.6038	2.1103	6.3282
c	650	ACS		0.0992	0.5502	1.9633	5.92
c	660	ACS		0.0946	0.5407	1.9387	5.8531
c	670	ACS		0.0924	0.5338	1.917	5.7899
c	676	ACS		0.0913	0.5304	1.9063	5.7588

Table 57 (continued).

IOP(s)	Wavelength nm	Sensor(s)	X_{IOP} Needed to Calculate ___ mg/l SPM				
			0.1	0.32	1.07	3.42	10
c	715	ACS		0.0606	0.4815	1.8002	5.4927
b_{bp}/b	440	ACS & BB9	0.0042	0.0047	0.0064	0.0116	0.0261
b_{bp}/b	488	ACS & BB9	0.0024	0.0033	0.0063	0.0158	0.0424
b_{bp}/b	510	ACS & BB9			0.0001	0.0206	0.0778
b_{bp}/b	532	ACS & BB9	0.0004	0.0015	0.0054	0.0176	0.0517
b_{bp}/b	595	ACS & BB9	0.0016	0.0026	0.0061	0.0171	0.0479
b_{bp}/b	660	ACS & BB9	0.0004	0.0012	0.0043	0.0138	0.0403
b_{bp}/b	676	ACS & BB9			0.0043	0.0258	0.0862
b_{bp}/b	715	ACS & BB9			0.0016	0.0215	0.0771
b_{bt}/b	440	ACS & BB9	0.1604	0.1521	0.1238	0.0352	
b_{bt}/b	488	ACS & BB9				0.0287	0.259
b_{bt}/b	510	ACS & BB9	0.8021	0.7408	0.5318		
b_{bt}/b	532	ACS & BB9				0.0349	0.2599
b_{bt}/b	595	ACS & BB9				0.0214	0.0953
b_{bt}/b	660	ACS & BB9				0.019	0.0852
b_{bt}/b	676	ACS & BB9				0.0454	0.2135
b_{bt}/b	715	ACS & BB9			0.0029	0.0209	0.0712

Table 57 (continued).

IOP(s)	Wavelength nm	Sensor(s)	X_{IOP} Needed to Calculate ___ mg/l SPM				
			0.1	0.32	1.07	3.42	10
b_{bp}	400	BB9			0.006	0.0253	0.0794
b_{bp}	440	BB9			0.0091	0.0403	0.1276
b_{bp}	488	BB9		0.0006	0.0111	0.0441	0.1364
b_{bp}	510	BB9		0.0013	0.0111	0.0416	0.127
b_{bp}	532	BB9		0.0012	0.0105	0.0397	0.1212
b_{bp}	595	BB9		0.0011	0.0098	0.037	0.1131
b_{bp}	660	BB9		0.0007	0.0067	0.0255	0.0783
b_{bp}	676	BB9		0.0002	0.0087	0.0354	0.11
b_{bp}	715	BB9		0.0001	0.006	0.0242	0.0754
b_{bt}	400	BB9			0.0068	0.0316	0.1012
b_{bt}	440	BB9		0.0015	0.0114	0.0426	0.1297
b_{bt}	488	BB9		0.002	0.0126	0.0455	0.1378
b_{bt}	510	BB9		0.0026	0.0123	0.0428	0.1281
b_{bt}	532	BB9		0.0023	0.0115	0.0407	0.1222
b_{bt}	595	BB9		0.0018	0.0104	0.0376	0.1137
b_{bt}	660	BB9		0.0011	0.0071	0.0259	0.0787
b_{bt}	676	BB9		0.0006	0.0091	0.0357	0.1104

Table 57 (continued).

IOP(s)	Wavelength nm	Sensor(s)	X_{IOP} Needed to Calculate ___ mg/l SPM				
			0.1	0.32	1.07	3.42	10
b_{bt}	715	BB9		0.0004	0.0063	0.0245	0.0757
c	670	LISST	0.04	0.252	0.8485	2.9443	7.8108
c	650	Transmissometer		0.095	0.6	2.3741	6.4937
c	650	Transmissometer*		0.0931	0.6208	2.475	6.7806

Notes. SPM concentrations 0.32, 1.07 and 3.42 mg/l represent the SPM concentration values at the 25th, 50th and 75th percentiles of the GCALL filtered samples dataset. Concentration values of 0.10 and 10.00 mg/l are provided to add end-members to this example. *This algorithm was created using data from cruises GC2, GC3, and GC5.

Conclusions

Chapter V of this dissertation addressed Hypothesis 2 which states the hull hypothesis that" all IOPs are equivalent SPM predictors." Through correlation analysis, linear algorithm development, and the testing of those algorithms, it was determined that the IOPs b_{bt}, b_{bp}, and c are the top performing SPM forecasters. The IOP b made a good showing, and somewhat surprisingly, several wavelengths of $a + b_{bp}$ and $a + b_{bt}$ did well if the ACS sensor was utilized to contribute the absorption component of this IOP combination. Cruise specific relationships between SPM and the IOPs and IOP combinations were also evaluated and corresponding algorithms produced. However, they were not subjected to the full battery of algorithm evaluations as preliminary results indicated, as expected, that these algorithms have better results than the GCALL algorithms when applied to specific cruises. However, any algorithm used for predicting future SPM concentrations in the northern Gulf of Mexico are best predicated upon complete sets of quality-passed data.

Tables: Cruise by Cruise Coefficients

The tables in the final section of Chapter V are too long to fit well into the text of this chapter. However, they are essential to some of the discussions herein. Tables 58 thru 67 report the Spearman correlation coefficients calculated on a cruise-by-cruise basis. The linear algorithm coefficients for individual cruises are in shared in Tables 68 thru 77.

Table 58

Relationship Between SPM and Absorption, Cruise by Cruise

Cruise	Wavelength nm	AC9 a vs. Measured SPM Spearman Correlation Coefficients			ACS a vs. Measured SPM Spearman Correlation Coefficients		
		ρ	p	n	ρ	p	n
GC1	412	N/A	N/A	N/A	0.87	0.00	23
GC1	440	N/A	N/A	N/A	0.86	0.00	23
GC1	488	N/A	N/A	N/A	0.86	0.00	23
GC1	510	N/A	N/A	N/A	0.87	0.00	23
GC1	532	N/A	N/A	N/A	0.88	0.00	23
GC1	555	N/A	N/A	N/A	0.89	0.00	23
GC1	595	N/A	N/A	N/A	0.90	0.00	23
GC1	650	N/A	N/A	N/A	0.83	0.00	23
GC1	660	N/A	N/A	N/A	0.84	0.00	23
GC1	670	N/A	N/A	N/A	0.83	0.00	23
GC1	676	N/A	N/A	N/A	0.81	0.00	23
GC1	715	N/A	N/A	N/A	0.55	0.01	23
GC2	412	0.85	0.00	69	0.84	0.00	65
GC2	440	0.84	0.00	69	0.84	0.00	65
GC2	488	0.82	0.00	69	0.83	0.00	65
GC2	510	0.83	0.00	69	0.82	0.00	65
GC2	532	0.83	0.00	69	0.82	0.00	65
GC2	555	0.83	0.00	69	0.81	0.00	65
GC2	595	N/A	N/A	N/A	0.79	0.00	65
GC2	650	0.79	0.00	69	0.78	0.00	65
GC2	660	N/A	N/A	N/A	0.78	0.00	65
GC2	670	N/A	N/A	N/A	0.79	0.00	65
GC2	676	0.80	0.00	69	0.79	0.00	65
GC2	715	0.21	0.09	69	0.70	0.00	65
GC3	412	0.84	0.00	54	0.80	0.00	40
GC3	440	0.86	0.00	54	0.83	0.00	40
GC3	488	0.88	0.00	54	0.83	0.00	40
GC3	510	0.87	0.00	54	0.83	0.00	40
GC3	532	0.84	0.00	54	0.84	0.00	40
GC3	555	0.86	0.00	54	0.81	0.00	40
GC3	595	N/A	N/A	N/A	0.76	0.00	40

Table 58 (continued).

Cruise	Wavelength nm	AC9 a vs. Measured SPM Spearman Correlation Coefficients			ACS a vs. Measured SPM Spearman Correlation Coefficients		
		ρ	p	n	ρ	p	n
GC3	650	0.69	0.00	54	0.65	0.00	40
GC3	660	N/A	N/A	N/A	0.61	0.00	40
GC3	670	N/A	N/A	N/A	0.57	0.00	40
GC3	676	0.65	0.00	54	0.56	0.00	40
GC3	715	0.00	0.97	54	-0.37	0.02	40
GC4	412	0.90	0.00	58	0.90	0.00	50
GC4	440	0.92	0.00	58	0.91	0.00	50
GC4	488	0.90	0.00	58	0.91	0.00	50
GC4	510	0.90	0.00	58	0.91	0.00	50
GC4	532	0.90	0.00	58	0.91	0.00	50
GC4	555	0.88	0.00	58	0.90	0.00	50
GC4	595	N/A	N/A	N/A	0.87	0.00	50
GC4	650	0.84	0.00	58	0.86	0.00	50
GC4	660	N/A	N/A	N/A	0.85	0.00	50
GC4	670	N/A	N/A	N/A	0.85	0.00	50
GC4	676	0.77	0.00	58	0.84	0.00	50
GC4	715	0.23	0.09	58	0.81	0.00	50
GC5	412	0.86	0.00	87	0.84	0.00	70
GC5	440	0.86	0.00	87	0.83	0.00	70
GC5	488	0.85	0.00	87	0.83	0.00	70
GC5	510	0.86	0.00	87	0.83	0.00	70
GC5	532	0.86	0.00	87	0.83	0.00	70
GC5	555	0.85	0.00	87	0.83	0.00	70
GC5	595	N/A	N/A	N/A	0.83	0.00	70
GC5	650	0.82	0.00	87	0.77	0.00	70
GC5	660	N/A	N/A	N/A	0.75	0.00	70
GC5	670	N/A	N/A	N/A	0.72	0.00	70
GC5	676	0.78	0.00	87	0.72	0.00	70
GC5	715	0.10	0.34	87	0.84	0.00	70

Notes. These selected wavelengths were interpolated from the ACS output and include the wavelengths observed by the AC9 and the BB9 (except 400 nm which is beyond the range of the ACS). Salinity exclusions and visual inspection exclusions were applied.

Table 59

Relationship Between SPM and Attenuation, Cruise by Cruise

Cruise	Wavelength nm	AC9 c vs. Measured SPM Spearman Correlation Coefficients			ACS c vs. Measured SPM Spearman Correlation Coefficients		
		ρ	p	n	ρ	p	n
GC1	412	N/A	N/A	N/A	0.95	0.00	25
GC1	440	N/A	N/A	N/A	0.95	0.00	25
GC1	488	N/A	N/A	N/A	0.95	0.00	25
GC1	510	N/A	N/A	N/A	0.96	0.00	25
GC1	532	N/A	N/A	N/A	0.96	0.00	25
GC1	555	N/A	N/A	N/A	0.96	0.00	25
GC1	595	N/A	N/A	N/A	0.96	0.00	25
GC1	650	N/A	N/A	N/A	0.96	0.00	25
GC1	660	N/A	N/A	N/A	0.96	0.00	25
GC1	670	N/A	N/A	N/A	0.96	0.00	25
GC1	676	N/A	N/A	N/A	0.96	0.00	25
GC1	715	N/A	N/A	N/A	0.96	0.00	25
GC2	412	0.90	0.00	69	0.87	0.00	61
GC2	440	0.91	0.00	69	0.87	0.00	61
GC2	488	0.90	0.00	69	0.87	0.00	61
GC2	510	0.90	0.00	69	0.87	0.00	61
GC2	532	0.90	0.00	69	0.87	0.00	61
GC2	555	0.90	0.00	69	0.87	0.00	61
GC2	595	N/A	N/A	N/A	0.86	0.00	61
GC2	650	0.89	0.00	69	0.87	0.00	61
GC2	660	N/A	N/A	N/A	0.86	0.00	61
GC2	670	N/A	N/A	N/A	0.87	0.00	61
GC2	676	0.88	0.00	69	0.87	0.00	61
GC2	715	0.89	0.00	69	0.86	0.00	61
GC3	412	0.89	0.00	60	0.88	0.00	59
GC3	440	0.89	0.00	60	0.88	0.00	59
GC3	488	0.89	0.00	60	0.88	0.00	59
GC3	510	0.89	0.00	60	0.88	0.00	59
GC3	532	0.88	0.00	60	0.88	0.00	59
GC3	555	0.89	0.00	60	0.88	0.00	59
GC3	595	N/A	N/A	N/A	0.87	0.00	59

Table 59 (continued).

Cruise	Wavelength nm	AC9 c vs. Measured SPM Spearman Correlation Coefficients			ACS c vs. Measured SPM Spearman Correlation Coefficients		
		ρ	p	n	ρ	p	n
GC3	650	0.88	0.00	60	0.87	0.00	59
GC3	660	N/A	N/A	N/A	0.87	0.00	59
GC3	670	N/A	N/A	N/A	0.87	0.00	59
GC3	676	0.88	0.00	60	0.87	0.00	59
GC3	715	0.88	0.00	60	0.87	0.00	59
GC4	412	0.92	0.00	59	0.89	0.00	56
GC4	440	0.93	0.00	59	0.89	0.00	56
GC4	488	0.93	0.00	59	0.88	0.00	56
GC4	510	0.92	0.00	59	0.88	0.00	56
GC4	532	0.93	0.00	59	0.88	0.00	56
GC4	555	0.93	0.00	59	0.88	0.00	56
GC4	595	N/A	N/A	N/A	0.88	0.00	56
GC4	650	0.92	0.00	59	0.88	0.00	56
GC4	660	N/A	N/A	N/A	0.88	0.00	56
GC4	670	N/A	N/A	N/A	0.88	0.00	56
GC4	676	0.92	0.00	59	0.88	0.00	56
GC4	715	0.92	0.00	59	0.88	0.00	56
GC5	412	0.94	0.00	85	0.96	0.00	79
GC5	440	0.94	0.00	85	0.96	0.00	79
GC5	488	0.94	0.00	85	0.96	0.00	79
GC5	510	0.94	0.00	85	0.96	0.00	79
GC5	532	0.95	0.00	85	0.96	0.00	79
GC5	555	0.94	0.00	85	0.96	0.00	79
GC5	595	N/A	N/A	N/A	0.96	0.00	79
GC5	650	0.94	0.00	85	0.96	0.00	79
GC5	660	N/A	N/A	N/A	0.96	0.00	79
GC5	670	N/A	N/A	N/A	0.96	0.00	79
GC5	676	0.94	0.00	85	0.96	0.00	79
GC5	715	0.94	0.00	85	0.96	0.00	79

Notes. These selected wavelengths were interpolated from the ACS output and include the wavelengths observed by the AC9 and the BB9 (except 400 nm which is beyond the range of the ACS). Salinity exclusions and visual inspection exclusions were applied.

Table 60

Relationship Between SPM and b_t, Cruise by Cruise

Cruise	Wavelength nm	AC9 b_t vs. Measured SPM Spearman Correlation Coefficients			ACS b_t vs. Measured SPM Spearman Correlation Coefficients		
		ρ	p	n	ρ	p	n
GC1	412	N/A	N/A	N/A	0.96	0.00	15
GC1	440	N/A	N/A	N/A	0.96	0.00	15
GC1	488	N/A	N/A	N/A	0.96	0.00	15
GC1	510	N/A	N/A	N/A	0.96	0.00	15
GC1	532	N/A	N/A	N/A	0.96	0.00	15
GC1	555	N/A	N/A	N/A	0.97	0.00	15
GC1	595	N/A	N/A	N/A	0.97	0.00	15
GC1	650	N/A	N/A	N/A	0.97	0.00	15
GC1	660	N/A	N/A	N/A	0.97	0.00	15
GC1	670	N/A	N/A	N/A	0.97	0.00	15
GC1	676	N/A	N/A	N/A	0.97	0.00	15
GC1	715	N/A	N/A	N/A	0.96	0.00	14
GC2	412	0.88	0.00	63	0.91	0.00	36
GC2	440	0.89	0.00	63	0.91	0.00	36
GC2	488	0.90	0.00	63	0.91	0.00	36
GC2	510	0.90	0.00	63	0.91	0.00	36
GC2	532	0.90	0.00	63	0.91	0.00	36
GC2	555	0.91	0.00	63	0.91	0.00	36
GC2	595	N/A	N/A	N/A	0.92	0.00	36
GC2	650	0.90	0.00	62	0.91	0.00	36
GC2	660	N/A	N/A	N/A	0.91	0.00	36
GC2	670	N/A	N/A	N/A	0.91	0.00	36
GC2	676	0.89	0.00	63	0.91	0.00	36
GC2	715	0.89	0.00	62	0.91	0.00	36
GC3	412	0.86	0.00	54	0.93	0.00	33
GC3	440	0.87	0.00	54	0.93	0.00	33
GC3	488	0.87	0.00	54	0.93	0.00	33
GC3	510	0.87	0.00	54	0.94	0.00	33
GC3	532	0.87	0.00	54	0.94	0.00	33
GC3	555	0.87	0.00	54	0.94	0.00	33
GC3	595	N/A	N/A	N/A	0.94	0.00	33

Table 60 (continued).

Cruise	Wavelength nm	AC9 b_t vs. Measured SPM Spearman Correlation Coefficients			ACS b_t vs. Measured SPM Spearman Correlation Coefficients		
		ρ	p	n	ρ	p	n
GC3	650	0.87	0.00	54	0.94	0.00	33
GC3	660	N/A	N/A	N/A	0.94	0.00	33
GC3	670	N/A	N/A	N/A	0.94	0.00	33
GC3	676	0.86	0.00	54	0.94	0.00	33
GC3	715	0.87	0.00	54	0.94	0.00	33
GC4	412	0.90	0.00	55	0.91	0.00	45
GC4	440	0.90	0.00	55	0.90	0.00	45
GC4	488	0.91	0.00	55	0.91	0.00	45
GC4	510	0.92	0.00	55	0.90	0.00	45
GC4	532	0.92	0.00	55	0.91	0.00	45
GC4	555	0.92	0.00	55	0.91	0.00	45
GC4	595	N/A	N/A	N/A	0.91	0.00	45
GC4	650	0.92	0.00	55	0.91	0.00	45
GC4	660	N/A	N/A	N/A	0.91	0.00	45
GC4	670	N/A	N/A	N/A	0.91	0.00	45
GC4	676	0.92	0.00	55	0.91	0.00	45
GC4	715	0.92	0.00	55	0.91	0.00	45
GC5	412	0.93	0.00	85	0.97	0.00	53
GC5	440	0.93	0.00	85	0.97	0.00	53
GC5	488	0.94	0.00	85	0.97	0.00	53
GC5	510	0.94	0.00	85	0.97	0.00	53
GC5	532	0.94	0.00	85	0.97	0.00	53
GC5	555	0.94	0.00	85	0.97	0.00	53
GC5	595	N/A	N/A	N/A	0.97	0.00	53
GC5	650	0.94	0.00	85	0.97	0.00	53
GC5	660	N/A	N/A	N/A	0.97	0.00	53
GC5	670	N/A	N/A	N/A	0.97	0.00	53
GC5	676	0.94	0.00	85	0.97	0.00	53
GC5	715	0.94	0.00	85	0.98	0.00	53

Notes. These selected wavelengths were interpolated from the ACS output and include the wavelengths observed by the AC9 and the BB9 (except 400 nm which is beyond the range of the ACS). Salinity exclusions and visual inspection exclusions were applied.

Table 61

Relationship Between SPM and b_b, Cruise by Cruise

Cruise	Wavelength nm	b_{bt} vs. Measured SPM Spearman Correlation Coefficients			b_{bp} vs. Measured SPM Spearman Correlation Coefficients		
		ρ	p	n	ρ	p	n
GC1	400	0.94	0.00	29	0.94	0.00	29
GC1	440	0.95	0.00	29	0.95	0.00	29
GC1	488	0.94	0.00	28	0.94	0.00	28
GC1	510	0.94	0.00	27	0.94	0.00	27
GC1	532	0.94	0.00	27	0.94	0.00	27
GC1	595	0.94	0.00	27	0.94	0.00	27
GC1	660	0.94	0.00	27	0.94	0.00	27
GC1	676	0.94	0.00	27	0.94	0.00	27
GC1	715	0.95	0.00	27	0.95	0.00	27
GC2	400	0.75	0.00	74	0.79	0.00	75
GC2	440	0.88	0.00	74	0.88	0.00	74
GC2	488	0.85	0.00	72	0.85	0.00	72
GC2	510	0.86	0.00	72	0.86	0.00	72
GC2	532	0.87	0.00	72	0.87	0.00	72
GC2	595	0.87	0.00	72	0.87	0.00	72
GC2	660	0.81	0.00	72	0.80	0.00	72
GC2	676	0.85	0.00	71	0.86	0.00	71
GC2	715	0.86	0.00	71	0.86	0.00	71
GC3	400	0.86	0.00	68	0.85	0.00	68
GC3	440	0.87	0.00	68	0.87	0.00	68
GC3	488	0.88	0.00	67	0.88	0.00	67
GC3	510	0.89	0.00	67	0.89	0.00	67
GC3	532	0.88	0.00	67	0.88	0.00	67
GC3	595	0.83	0.00	33	0.83	0.00	33
GC3	660	0.89	0.00	67	0.89	0.00	67
GC3	676	0.87	0.00	65	0.87	0.00	65
GC3	715	0.87	0.00	65	0.87	0.00	65
GC4	400	0.90	0.00	60	0.91	0.00	60
GC4	440	0.92	0.00	60	0.92	0.00	60
GC4	488	0.92	0.00	60	0.93	0.00	60
GC4	510	0.93	0.00	60	0.93	0.00	60

Table 61 (continued).

Cruise	Wavelength nm	b_{bt} vs. Measured SPM Spearman Correlation Coefficients			b_{bp} vs. Measured SPM Spearman Correlation Coefficients		
		ρ	p	n	ρ	p	n
GC4	532	0.92	0.00	60	0.92	0.00	60
GC4	595	0.91	0.00	59	0.91	0.00	59
GC4	660	0.92	0.00	59	0.92	0.00	59
GC4	676	0.91	0.00	57	0.91	0.00	57
GC4	715	0.91	0.00	56	0.91	0.00	56
GC5	400	0.89	0.00	87	0.92	0.00	88
GC5	440	0.93	0.00	87	0.93	0.00	87
GC5	488	0.93	0.00	85	0.93	0.00	85
GC5	510	0.93	0.00	85	0.93	0.00	85
GC5	532	0.92	0.00	85	0.93	0.00	85
GC5	595	0.93	0.00	84	0.93	0.00	84
GC5	660	0.93	0.00	84	0.93	0.00	84
GC5	676	0.93	0.00	84	0.93	0.00	84
GC5	715	0.93	0.00	82	0.93	0.00	82

Notes: Salinity and profiler induced turbidity based exclusions were applied. Sensor saturation exclusions were applied.

Table 62

Relationship Between SPM and b_{bt}/b, Cruise by Cruise

Cruise	Wavelength nm	b_{bt}/b (AC9) vs. Measured SPM Spearman Correlation Coefficients			b_{bt}/b (ACS) vs. Measured SPM Spearman Correlation Coefficients		
		ρ	p	n	ρ	p	n
GC1	440	N/A	N/A	N/A	0.56	0.05	13
GC1	488	N/A	N/A	N/A	0.56	0.05	13
GC1	510	N/A	N/A	N/A	0.62	0.03	12
GC1	532	N/A	N/A	N/A	0.49	0.11	12
GC1	595	N/A	N/A	N/A	0.40	0.20	12
GC1	660	N/A	N/A	N/A	0.59	0.05	12
GC1	676	N/A	N/A	N/A	0.54	0.07	12
GC1	715	N/A	N/A	N/A	0.57	0.07	11
GC2	440	0.77	0.00	62	0.25	0.17	31
GC2	488	0.17	0.19	60	0.24	0.20	29
GC2	510	0.70	0.00	60	0.02	0.90	29
GC2	532	0.67	0.00	60	0.11	0.57	29
GC2	595	N/A	N/A	N/A	0.41	0.03	29
GC2	660	N/A	N/A	N/A	0.78	0.00	27
GC2	676	0.04	0.77	59	0.32	0.10	27
GC2	715	0.03	0.80	58	0.55	0.00	27
GC3	440	0.54	0.00	54	0.25	0.61	32
GC3	488	0.41	0.00	53	0.22	0.22	31
GC3	510	0.41	0.00	53	0.29	0.11	31
GC3	532	0.17	0.23	53	0.48	0.01	31
GC3	595	N/A	N/A	N/A	-0.16	0.54	18
GC3	660	N/A	N/A	N/A	0.53	0.00	31
GC3	676	0.08	0.57	51	0.63	0.00	29
GC3	715	0.09	0.52	51	0.47	0.01	29
GC4	440	0.30	0.03	55	0.67	0.00	42
GC4	488	-0.14	0.30	55	0.72	0.00	42
GC4	510	-0.03	0.81	55	0.74	0.00	41
GC4	532	0.30	0.03	55	0.73	0.00	41
GC4	595	N/A	N/A	N/A	0.73	0.00	41
GC4	660	N/A	N/A	N/A	0.86	0.00	41
GC4	676	0.52	0.00	52	0.82	0.00	38

Table 62 (continued),

Cruise	Wavelength nm	b_{bt}/b (AC9) vs. Measured SPM Spearman Correlation Coefficients			b_{bt}/b (ACS) vs. Measured SPM Spearman Correlation Coefficients		
		ρ	p	n	ρ	p	n
GC4	715	0.51	0.00	51	0.70	0.00	37
GC5	440	0.22	0.04	85	0.32	0.03	46
GC5	488	0.44	0.00	83	0.28	0.06	44
GC5	510	-0.05	0.65	83	0.33	0.03	44
GC5	532	0.10	0.37	83	0.09	0.57	44
GC5	595	N/A	N/A	N/A	-0.04	0.79	43
GC5	660	N/A	N/A	N/A	0.01	0.97	42
GC5	676	0.28	0.01	82	-0.10	0.53	43
GC5	715	0.34	0.00	80	0.15	0.33	41

Table 63

Relationship Between SPM and b_{bp}/b, Cruise by Cruise

Cruise	Wavelength nm	b_{bp}/b (AC9) vs. Measured SPM Spearman Correlation Coefficients			b_{bp}/b (ACS) vs. Measured SPM Spearman Correlation Coefficients		
		ρ	p	n	ρ	p	n
GC1	440	N/A	N/A	N/A	0.26	0.42	12
GC1	488	N/A	N/A	N/A	0.34	0.25	13
GC1	510	N/A	N/A	N/A	0.52	0.08	12
GC1	532	N/A	N/A	N/A	0.35	0.27	12
GC1	595	N/A	N/A	N/A	0.35	0.27	12
GC1	660	N/A	N/A	N/A	-0.03	0.94	12
GC1	676	N/A	N/A	N/A	0.41	0.18	12
GC1	715	N/A	N/A	N/A	0.17	0.60	12
GC2	440	0.26	0.04	64	0.72	0.00	31
GC2	488	0.71	0.00	62	0.76	0.00	29
GC2	510	0.28	0.03	62	0.63	0.00	29
GC2	532	0.40	0.00	62	0.76	0.00	29
GC2	595	N/A	N/A	N/A	0.74	0.00	29
GC2	660	N/A	N/A	N/A	0.81	0.00	28
GC2	676	-0.26	0.04	61	0.65	0.00	27
GC2	715	0.44	0.00	61	0.73	0.00	27
GC3	440	-0.42	0.00	54	0.72	0.00	31
GC3	488	0.30	0.03	53	0.74	0.00	31
GC3	510	0.26	0.06	53	0.75	0.00	31
GC3	532	0.64	0.00	53	0.78	0.00	31
GC3	595	N/A	N/A	N/A	0.76	0.00	16
GC3	660	N/A	N/A	N/A	0.72	0.00	31
GC3	676	0.23	0.10	51	0.77	0.00	29
GC3	715	0.23	0.10	51	0.73	0.00	29
GC4	440	0.73	0.00	55	0.88	0.00	42
GC4	488	0.64	0.00	55	0.85	0.00	42
GC4	510	0.59	0.00	55	0.84	0.00	41
GC4	532	0.63	0.00	55	0.84	0.00	41
GC4	595	N/A	N/A	N/A	0.81	0.00	41
GC4	660	N/A	N/A	N/A	0.89	0.00	40
GC4	676	0.72	0.00	52	0.84	0.00	38

Table 63 (continued).

Cruise	Wavelength nm	b_{bp}/b (AC9) vs. Measured SPM Spearman Correlation Coefficients			b_{bp}/b (ACS) vs. Measured SPM Spearman Correlation Coefficients		
		ρ	p	n	ρ	p	n
GC4	715	0.66	0.00	51	0.81	0.00	37
GC5	440	0.64	0.00	85	0.58	0.00	48
GC5	488	0.76	0.00	83	0.63	0.00	46
GC5	510	0.42	0.00	83	0.06	0.70	46
GC5	532	0.45	0.00	83	0.15	0.31	46
GC5	595	N/A	N/A	N/A	0.15	0.34	45
GC5	660	N/A	N/A	N/A	0.16	0.31	44
GC5	676	0.45	0.00	82	-0.05	0.76	45
GC5	715	0.50	0.00	80	-0.01	0.97	43

Table 64

Relationship Between SPM and a + b_{bt}, Cruise by Cruise

Cruise	Wavelength nm	a + b_{bt} (AC9) vs. Measured SPM Spearman Correlation Coefficients			a + b_{bt} (ACS) vs. Measured SPM Spearman Correlation Coefficients		
		ρ	p	n	ρ	p	n
GC1	440	N/A	N/A	N/A	0.91	0.00	13
GC1	488	N/A	N/A	N/A	0.89	0.00	13
GC1	510	N/A	N/A	N/A	0.87	0.00	12
GC1	532	N/A	N/A	N/A	0.87	0.00	12
GC1	595	N/A	N/A	N/A	0.92	0.00	11
GC1	660	N/A	N/A	N/A	0.86	0.00	12
GC1	676	N/A	N/A	N/A	0.85	0.00	12
GC1	715	N/A	N/A	N/A	0.82	0.01	10
GC2	440	0.84	0.00	67	0.85	0.00	31
GC2	488	0.83	0.00	65	0.84	0.00	29
GC2	510	0.84	0.00	65	0.86	0.00	29
GC2	532	0.82	0.00	65	0.87	0.00	29
GC2	595	N/A	N/A	N/A	0.89	0.00	29
GC2	660	N/A	N/A	N/A	0.88	0.00	28
GC2	676	0.82	0.00	64	0.84	0.00	27
GC2	715	0.87	0.00	58	0.93	0.00	23
GC3	440	0.87	0.00	54	0.85	0.00	33
GC3	488	0.89	0.00	53	0.85	0.00	32
GC3	510	0.88	0.00	53	0.84	0.00	31
GC3	532	0.88	0.00	53	0.86	0.00	31
GC3	595	N/A	N/A	N/A	0.84	0.00	31
GC3	660	N/A	N/A	N/A	0.76	0.00	31
GC3	676	0.77	0.00	51	0.73	0.00	29
GC3	715	0.86	0.00	51	0.91	0.00	30
GC4	440	0.81	0.00	57	0.90	0.00	42
GC4	488	0.81	0.00	57	0.91	0.00	42
GC4	510	0.81	0.00	57	0.90	0.00	41
GC4	532	0.81	0.00	57	0.91	0.00	41
GC4	595	N/A	N/A	N/A	0.91	0.00	41
GC4	660	N/A	N/A	N/A	0.91	0.00	41

Table 64 (continued).

Cruise	Wavelength nm	$a + b_{bt}$ (AC9) vs. Measured SPM Spearman Correlation Coefficients			$a + b_{bt}$ (ACS) vs. Measured SPM Spearman Correlation Coefficients		
		ρ	p	n	ρ	p	n
GC4	676	0.79	0.00	54	0.89	0.00	38
GC4	715	0.80	0.00	53	0.94	0.00	35
GC5	440	0.90	0.00	87	0.87	0.00	46
GC5	488	0.91	0.00	85	0.89	0.00	44
GC5	510	0.92	0.00	85	0.89	0.00	44
GC5	532	0.91	0.00	85	0.89	0.00	44
GC5	595	N/A	N/A	N/A	0.94	0.00	43
GC5	660	N/A	N/A	N/A	0.89	0.00	42
GC5	676	0.90	0.00	84	0.89	0.00	43
GC5	715	0.90	0.00	82	0.92	0.00	41

Table 65

Relationship Between SPM and a + b_{bp}, Cruise by Cruise

Cruise	Wavelength nm	a + b_{bp} (AC9) vs. Measured SPM Spearman Correlation Coefficients			a + b_{bp} (ACS) vs. Measured SPM Spearman Correlation Coefficients		
		ρ	p	n	ρ	p	n
GC1	440	N/A	N/A	N/A	0.91	0.00	13
GC1	488	N/A	N/A	N/A	0.89	0.00	13
GC1	510	N/A	N/A	N/A	0.87	0.00	12
GC1	532	N/A	N/A	N/A	0.87	0.00	12
GC1	595	N/A	N/A	N/A	0.92	0.00	11
GC1	660	N/A	N/A	N/A	0.86	0.00	12
GC1	676	N/A	N/A	N/A	0.85	0.00	12
GC1	715	N/A	N/A	N/A	0.82	0.01	10
GC2	440	0.84	0.00	67	0.85	0.00	31
GC2	488	0.83	0.00	65	0.84	0.00	29
GC2	510	0.84	0.00	65	0.86	0.00	29
GC2	532	0.85	0.00	65	0.87	0.00	29
GC2	595	N/A	N/A	N/A	0.89	0.00	29
GC2	660	N/A	N/A	N/A	0.88	0.00	28
GC2	676	0.82	0.00	64	0.84	0.00	27
GC2	715	0.87	0.00	64	0.94	0.00	27
GC3	440	0.87	0.00	54	0.85	0.00	33
GC3	488	0.89	0.00	53	0.85	0.00	32
GC3	510	0.88	0.00	53	0.84	0.00	31
GC3	532	0.88	0.00	53	0.86	0.00	31
GC3	595	N/A	N/A	N/A	0.84	0.00	31
GC3	660	N/A	N/A	N/A	0.76	0.00	31
GC3	676	0.77	0.00	51	0.73	0.00	29
GC3	715	0.86	0.00	51	0.91	0.00	30
GC4	440	0.81	0.00	57	0.90	0.00	42
GC4	488	0.81	0.00	57	0.91	0.00	42
GC4	510	0.81	0.00	57	0.90	0.00	41
GC4	532	0.81	0.00	57	0.91	0.00	41
GC4	595	N/A	N/A	N/A	0.91	0.00	41
GC4	660	N/A	N/A	N/A	0.91	0.00	41

Table 65 (continued).

Cruise	Wavelength nm	$a + b_{bp}$ (AC9) vs. Measured SPM Spearman Correlation Coefficients			$a + b_{bp}$ (ACS) vs. Measured SPM Spearman Correlation Coefficients		
		ρ	p	n	ρ	p	n
GC4	676	0.79	0.00	54	0.89	0.00	38
GC4	715	0.80	0.00	53	0.94	0.00	35
GC5	440	0.90	0.00	87	0.88	0.00	48
GC5	488	0.91	0.00	85	0.90	0.00	46
GC5	510	0.92	0.00	85	0.90	0.00	46
GC5	532	0.91	0.00	85	0.91	0.00	46
GC5	595	N/A	N/A	N/A	0.95	0.00	45
GC5	660	N/A	N/A	N/A	0.91	0.00	44
GC5	676	0.90	0.00	84	0.90	0.00	45
GC5	715	0.90	0.00	82	0.92	0.00	43

Table 66

Relationship Between SPM and $b_{bt} / (a + b_{bt})$, Cruise by Cruise

Cruise	Wavelength nm	$b_{bt} / (a + b_{bt})$ (AC9) vs. Measured SPM Spearman Correlation Coefficients			$b_{bt} / (a + b_{bt})$ (ACS) vs. Measured SPM Spearman Correlation Coefficients		
		ρ	p	n	ρ	p	n
GC1	440	N/A	N/A	N/A	0.09	0.76	13
GC1	488	N/A	N/A	N/A	-0.16	0.59	13
GC1	510	N/A	N/A	N/A	0.10	0.75	12
GC1	532	N/A	N/A	N/A	0.11	0.73	12
GC1	595	N/A	N/A	N/A	0.05	0.88	11
GC1	660	N/A	N/A	N/A	0.05	0.89	12
GC1	676	N/A	N/A	N/A	0.12	0.72	12
GC1	715	N/A	N/A	N/A	-0.38	0.25	11
GC2	440	0.23	0.06	67	0.63	0.00	31
GC2	488	0.47	0.00	65	0.81	0.00	29
GC2	510	0.36	0.00	65	0.67	0.00	29
GC2	532	0.49	0.00	65	0.74	0.00	29
GC2	595	N/A	N/A	N/A	0.87	0.00	29
GC2	660	N/A	N/A	N/A	0.88	0.00	27
GC2	676	0.64	0.00	64	0.90	0.00	27
GC2	715	-0.07	0.59	60	0.42	0.04	26
GC3	440	0.47	0.00	54	0.63	0.00	33
GC3	488	0.51	0.00	53	0.44	0.01	32
GC3	510	0.52	0.00	53	0.59	0.00	31
GC3	532	0.59	0.00	53	0.62	0.00	31
GC3	595	N/A	N/A	N/A	0.23	0.39	16
GC3	660	N/A	N/A	N/A	0.56	0.00	31
GC3	676	0.59	0.00	51	0.63	0.00	29
GC3	715	-0.02	0.89	51	0.29	0.12	30
GC4	440	-0.26	0.05	57	0.49	0.00	42
GC4	488	-0.49	0.00	57	0.59	0.00	42
GC4	510	-0.49	0.00	57	0.51	0.00	41
GC4	532	-0.57	0.00	57	0.57	0.00	41
GC4	595	N/A	N/A	N/A	0.67	0.00	41
GC4	660	N/A	N/A	N/A	0.80	0.00	41

Table 66 (continued).

Cruise	Wavelength nm	$b_{bt} / (a + b_{bt})$ (AC9) vs. Measured SPM Spearman Correlation Coefficients			$b_{bt} / (a + b_{bt})$ (ACS) vs. Measured SPM Spearman Correlation Coefficients		
		ρ	p	n	ρ	p	n
GC4	676	-0.71	0.00	54	0.69	0.00	38
GC4	715	0.05	0.70	53	0.43	0.01	37
GC5	440	0.44	0.00	87	0.56	0.00	46
GC5	488	0.65	0.00	85	0.66	0.00	44
GC5	510	0.49	0.00	85	0.58	0.00	44
GC5	532	0.55	0.00	85	0.62	0.00	44
GC5	595	N/A	N/A	N/A	0.75	0.00	43
GC5	660	N/A	N/A	N/A	0.70	0.00	42
GC5	676	0.66	0.00	84	0.64	0.00	43
GC5	715	-0.04	0.72	82	0.69	0.00	41

Table 67

Relationship Between SPM and $b_{bp} / (a + b_{bp})$, Cruise by Cruise

Cruise	Wavelength nm	$b_{bp} / (a + b_{bp})$ (AC9) vs. Measured SPM Spearman Correlation Coefficients			$b_{bp} / (a + b_{bp})$ (ACS) vs. Measured SPM Spearman Correlation Coefficients		
		ρ	p	n	ρ	p	n
GC1	440	N/A	N/A	N/A	0.09	0.76	13
GC1	488	N/A	N/A	N/A	-0.16	0.59	13
GC1	510	N/A	N/A	N/A	0.10	0.75	12
GC1	532	N/A	N/A	N/A	0.11	0.73	12
GC1	595	N/A	N/A	N/A	0.05	0.88	11
GC1	660	N/A	N/A	N/A	0.05	0.89	12
GC1	676	N/A	N/A	N/A	0.12	0.72	12
GC1	715	N/A	N/A	N/A	-0.38	0.25	11
GC2	440	0.26	0.04	67	0.63	0.00	31
GC2	488	0.48	0.00	65	0.81	0.00	29
GC2	510	0.36	0.00	65	0.67	0.00	29
GC2	532	0.49	0.00	65	0.74	0.00	29
GC2	595	N/A	N/A	N/A	0.87	0.00	29
GC2	660	N/A	N/A	N/A	0.88	0.00	28
GC2	676	0.64	0.00	64	0.90	0.00	27
GC2	715	0.22	0.08	64	0.42	0.03	26
GC3	440	0.47	0.00	54	0.63	0.00	33
GC3	488	0.51	0.00	53	0.44	0.01	32
GC3	510	0.52	0.00	53	0.59	0.00	31
GC3	532	0.59	0.00	53	0.62	0.00	31
GC3	595	N/A	N/A	N/A	0.23	0.39	16
GC3	660	N/A	N/A	N/A	0.56	0.00	31
GC3	676	0.59	0.00	51	0.63	0.00	29
GC3	715	-0.02	0.89	51	0.29	0.12	30
GC4	440	-0.26	0.05	57	0.49	0.00	42
GC4	488	-0.49	0.00	57	0.59	0.00	42
GC4	510	-0.49	0.00	57	0.51	0.00	41
GC4	532	-0.57	0.00	57	0.57	0.00	41
GC4	595	N/A	N/A	N/A	0.67	0.00	41
GC4	660	N/A	N/A	N/A	0.80	0.00	41

Table 67 (continued).

Cruise	Wavelength nm	$b_{bp} / (a + b_{bp})$ (AC9) vs. Measured SPM Spearman Correlation Coefficients			$b_{bp} / (a + b_{bp})$ (ACS) vs. Measured SPM Spearman Correlation Coefficients		
		ρ	p	n	ρ	p	n
GC4	676	-0.71	0.00	54	0.69	0.00	38
GC4	715	0.05	0.70	53	0.43	0.01	37
GC5	440	0.44	0.00	87	0.54	0.00	48
GC5	488	0.65	0.00	85	0.64	0.00	46
GC5	510	0.49	0.00	85	0.55	0.00	46
GC5	532	0.55	0.00	85	0.59	0.00	46
GC5	595	N/A	N/A	N/A	0.72	0.00	45
GC5	660	N/A	N/A	N/A	0.67	0.00	44
GC5	676	0.66	0.00	84	0.61	0.00	45
GC5	715	-0.04	0.72	82	0.47	0.00	43

Table 68

SPM Algorithm Coefficients from Absorption, Cruise by Cruise

Cruise	Wavelength nm	AC9		ACS	
		m (Uncertainty)	b (Uncertainty)	m (Uncertainty)	b (Uncertainty)
GC1	412	N/A	N/A	11.733 (0.295)	-0.933 (0.256)
GC1	440	N/A	N/A	16.283 (0.415)	-1.004 (0.258)
GC1	488	N/A	N/A	27.530 (0.696)	-0.914 (0.256)
GC1	510	N/A	N/A	35.272 (0.891)	-0.842 (0.255)
GC1	532	N/A	N/A	45.691 (1.153)	-0.870 (0.255)
GC1	555	N/A	N/A	62.523 (1.567)	-0.954 (0.256)
GC1	595	N/A	N/A	104.541 (2.599)	-0.818 (0.253)
GC1	650	N/A	N/A	138.325 (3.866)	-0.909 (0.265)
GC1	660	N/A	N/A	100.337 (3.210)	-0.084 (0.264)
GC1	670	N/A	N/A	70.554 (2.594)	0.681 (0.261)
GC1	676	N/A	N/A	69.848 (2.654)	0.835 (0.261)
GC1	715	N/A	N/A	10938.016 (291.943)	-1.141 (0.264)
GC2	412	6.294 (0.067)	0.453 (0.127)	6.494 (0.068)	0.219 (0.132)
GC2	440	7.070 (0.075)	0.811 (0.126)	6.797 (0.072)	0.769 (0.130)
GC2	488	8.636 (0.091)	1.350 (0.124)	8.068 (0.086)	1.304 (0.129)
GC2	510	9.997 (0.108)	1.734 (0.123)	8.537 (0.091)	1.516 (0.128)
GC2	532	10.355 (0.116)	2.155 (0.123)	8.980 (0.096)	1.686 (0.128)
GC2	555	10.702 (0.123)	2.395 (0.122)	9.837 (0.105)	1.831 (0.127)

Table 68 (continued).

Cruise	Wavelength nm	AC9		ACS	
		m (Uncertainty)	b (Uncertainty)	m (Uncertainty)	b (Uncertainty)
GC2	595	N/A	N/A	11.151 (0.126)	2.469 (0.126)
GC2	650	12.282 (0.144)	2.679 (0.122)	11.676 (0.136)	2.693 (0.126)
GC2	660	N/A	N/A	11.813 (0.137)	2.636 (0.126)
GC2	670	N/A	N/A	11.953 (0.139)	2.553 (0.126)
GC2	676	12.711 (0.147)	2.501 (0.122)	12.035 (0.140)	2.565 (0.126)
GC2	715	13.380 (0.158)*	3.052 (0.121)*	12.623 (0.150)	3.144 (0.125)
GC3	412	12.681 (0.412)	-1.334 (0.177)	11.488 (0.375)	-1.110 (0.202)
GC3	440	16.270 (0.521)	-1.320 (0.176)	17.835 (0.593)	-1.478 (0.211)
GC3	488	30.701 (0.988)	-1.496 (0.180)	32.272 (1.080)	-1.537 (0.213)
GC3	510	41.012 (1.338)	-1.552 (0.182)	44.466 (1.507)	-1.596 (0.216)
GC3	532	57.323 (1.995)	-1.664 (0.190)	60.441 (2.083)	-1.722 (0.221)
GC3	555	76.587 (2.725)	-1.731 (0.194)	80.560 (2.909)	-1.696 (0.225)
GC3	595	N/A	N/A	131.506 (5.009)	-1.354 (0.222)
GC3	650	166.970 (7.340)	-1.772 (0.22)	133.934 (7.006)	-0.230 (0.222)
GC3	660	N/A	N/A	99.942 (6.071)	0.137 (0.224)
GC3	670	N/A	N/A	69.968 (4.983)	0.558 (0.222)
GC3	676	68.671 (4.534)	-0.067 (0.200)	68.496 (5.025)	0.673 (0.219)
GC3	715	-133.142 (82.963)*	2.183 (0.137)*	-47.602 (46.981)	2.788 (0.165)
GC4	412	16.522 (0.055)	-4.866 (0.140)	10.797 (0.036)	-3.157 (0.149)
GC4	440	14.510 (0.047)	-2.668 (0.137)	11.331 (0.037)	-1.745 (0.147)

Table 68 (continued).

Cruise	Wavelength nm	AC9		ACS	
		m (Uncertainty)	b (Uncertainty)	m (Uncertainty)	b (Uncertainty)
GC4	488	15.764 (0.051)	-0.787 (0.135)	13.021 (0.042)	-0.198 (0.146)
GC4	510	16.835 (0.054)	-0.277 (0.135)	14.105 (0.045)	0.275 (0.145)
GC4	532	19.055 (0.061)	0.211 (0.135)	15.176 (0.049)	0.656 (0.145)
GC4	555	19.410 (0.062)	0.554 (0.134)	16.292 (0.052)	0.970 (0.145)
GC4	595	N/A	N/A	18.093 (0.058)	1.431 (0.145)
GC4	650	24.693 (0.081)	2.492 (0.133)	26.067 (0.087)	1.407 (0.145)
GC4	660	N/A	N/A	24.448 (0.080)	1.280 (0.145)
GC4	670	N/A	N/A	23.66 (0.077)	1.142 (0.145)
GC4	676	25.003 (0.085)	3.013 (0.133)	21.202 (0.068)	1.355 (0.145)
GC4	715	26.243 (0.089)*	4.325 (0.132)*	29.078 (0.097)	2.324 (0.144)
GC5	412	5.946 (0.153)	0.452 (0.125)	5.535 (0.137)	0.549 (0.139)
GC5	440	9.357 (0.221)	-0.028 (0.128)	8.495 (0.209)	0.349 (0.141)
GC5	488	15.464 (0.373)	0.197 (0.126)	15.296 (0.376)	0.314 (0.141)
GC5	510	19.643 (0.494)	0.204 (0.127)	19.039 (0.476)	0.432 (0.140)
GC5	532	24.360 (0.680)	0.437 (0.128)	24.733 (0.627)	0.451 (0.141)
GC5	555	26.636 (0.846)	0.886 (0.125)	32.416 (0.836)	0.516 (0.141)
GC5	595	N/A	N/A	51.390 (1.370)	0.562 (0.141)
GC5	650	51.606 (1.900)	0.793 (0.133)	84.894 (2.34)	-0.305 (0.157)
GC5	660	N/A	N/A	74.306 (2.148)	-0.405 (0.162)

Table 68 (continued).

Cruise	Wavelength nm	AC9		ACS	
		m (Uncertainty)	b (Uncertainty)	m (Uncertainty)	b (Uncertainty)
GC5	670	N/A	N/A	59.415 (1.853)	-0.260 (0.165)
GC5	676	43.394 (1.63)	0.357 (0.145)	59.754 (1.901)	-0.201 (0.165)
GC5	715	4.71 (3.755)*	2.923 (0.108)*	8808.098 (206.925)	-1.425 (0.164)

Notes. The slopes and intercepts are for linear SPM predictive algorithms y = mx + b. The uncertainty for the regression slopes and intercepts were calculated using singular value decomposition. These selected wavelengths were interpolated from the ACS output and included the wavelengths observed by the AC9 and the BB9 (except 400 nm which is beyond the range of the ACS). Salinity exclusions and visual inspection exclusions were applied. *Spearman correlation coefficients indicate that SPM is statistically unrelated to the IOP in question for the cruise-data tested.

Table 69

SPM Algorithm Coefficients from Attenuation, Cruise by Cruise

Cruise	Wavelength nm	AC9		ACS	
		m (Uncertainty)	b (Uncertainty)	m (Uncertainty)	b (Uncertainty)
GC1	412	N/A	N/A	1.431 (0.034)	-0.335 (0.231)
GC1	440	N/A	N/A	1.485 (0.035)	-0.264 (0.230)
GC1	488	N/A	N/A	1.609 (0.038)	-0.252 (0.230)
GC1	510	N/A	N/A	1.655 (0.039)	-0.233 (0.230)
GC1	532	N/A	N/A	1.701 (0.040)	-0.218 (0.230)
GC1	555	N/A	N/A	1.747 (0.041)	-0.203 (0.230)
GC1	595	N/A	N/A	1.831 (0.043)	-0.175 (0.229)
GC1	650	N/A	N/A	1.948 (0.046)	-0.171 (0.229)
GC1	660	N/A	N/A	1.969 (0.046)	-0.165 (0.229)
GC1	670	N/A	N/A	1.989 (0.047)	-0.168 (0.229)
GC1	676	N/A	N/A	2.000 (0.047)	-0.170 (0.229)
GC1	715	N/A	N/A	2.083 (0.049)	-0.078 (0.228)
GC2	412	0.920 (0.027)	0.517 (0.133)	1.061 (0.031)	0.281 (0.146)
GC2	440	0.976 (0.028)	0.551 (0.132)	1.129 (0.033)	0.316 (0.145)
GC2	488	1.049 (0.031)	0.597 (0.132)	1.211 (0.035)	0.380 (0.145)
GC2	510	1.073 (0.031)	0.612 (0.132)	1.248 (0.036)	0.402 (0.144)
GC2	532	1.106 (0.032)	0.631 (0.131)	1.286 (0.038)	0.421 (0.144)
GC2	555	1.140 (0.033)	0.644 (0.131)	1.325 (0.039)	0.438 (0.144)

Table 69 (continued).

Cruise	Wavelength nm	AC9		ACS	
		m (Uncertainty)	b (Uncertainty)	m (Uncertainty)	b (Uncertainty)
GC2	595	N/A	N/A	1.391 (0.041)	0.464 (0.143)
GC2	650	1.268 (0.037)	0.691 (0.131)	1.484 (0.043)	0.489 (0.143)
GC2	660	N/A	N/A	1.500 (0.044)	0.494 (0.143)
GC2	670	N/A	N/A	1.516 (0.044)	0.495 (0.143)
GC2	676	1.306 (0.038)	0.702 (0.131)	1.526 (0.045)	0.496 (0.143)
GC2	715	1.367 (0.040)	0.727 (0.130)	1.594 (0.047)	0.528 (0.143)
GC3	412	1.058 (0.032)	0.117 (0.141)	1.077 (0.033)	0.095 (0.143)
GC3	440	1.142 (0.035)	0.132 (0.141)	1.157 (0.035)	0.101 (0.143)
GC3	488	1.272 (0.038)	0.120 (0.141)	1.301 (0.039)	0.088 (0.143)
GC3	510	1.321 (0.040)	0.124 (0.141)	1.356 (0.041)	0.092 (0.143)
GC3	532	1.383 (0.042)	0.126 (0.141)	1.416 (0.043)	0.091 (0.143)
GC3	555	1.442 (0.043)	0.121 (0.141)	1.476 (0.045)	0.091 (0.143)
GC3	595	N/A	N/A	1.582 (0.048)	0.093 (0.143)
GC3	650	1.683 (0.051)	0.121 (0.141)	1.729 (0.052)	0.090 (0.143)
GC3	660	N/A	N/A	1.755 (0.053)	0.089 (0.143)
GC3	670	N/A	N/A	1.782 (0.054)	0.084 (0.143)
GC3	676	1.758 (0.053)	0.112 (0.141)	1.797 (0.054)	0.081 (0.143)
GC3	715	1.861 (0.056)	0.121 (0.141)	1.904 (0.058)	0.098 (0.142)
GC4	412	0.891 (0.038)	0.110 (0.160)	0.978 (0.043)	0.026 (0.169)
GC4	440	0.958 (0.041)	0.134 (0.159)	1.053 (0.046)	0.039 (0.168)

Table 69 (continued).

Cruise	Wavelength nm	AC9		ACS	
		m (Uncertainty)	b (Uncertainty)	m (Uncertainty)	b (Uncertainty)
GC4	488	1.061 (0.045)	0.144 (0.158)	1.162 (0.050)	0.056 (0.167)
GC4	510	1.104 (0.046)	0.148 (0.158)	1.206 (0.052)	0.061 (0.167)
GC4	532	1.151 (0.048)	0.150 (0.158)	1.252 (0.053)	0.064 (0.167)
GC4	555	1.195 (0.050)	0.148 (0.158)	1.298 (0.055)	0.065 (0.166)
GC4	595	N/A	N/A	1.377 (0.058)	0.070 (0.166)
GC4	650	1.373 (0.057)	0.151 (0.157)	1.481 (0.063)	0.069 (0.166)
GC4	660	N/A	N/A	1.500 (0.063)	0.071 (0.166)
GC4	670	N/A	N/A	1.516 (0.064)	0.072 (0.166)
GC4	676	1.422 (0.059)	0.163 (0.157)	1.523 (0.064)	0.073 (0.166)
GC4	715	1.491 (0.062)	0.173 (0.157)	1.599 (0.067)	0.098 (0.165)
GC5	412	0.891 (0.019)	0.400 (0.122)	1.426 (0.028)	-0.489 (0.134)
GC5	440	1.227 (0.025)	-0.121 (0.125)	1.284 (0.027)	-0.004 (0.13)
GC5	488	1.326 (0.027)	-0.065 (0.125)	1.369 (0.029)	0.095 (0.13)
GC5	510	1.347 (0.028)	-0.006 (0.125)	1.416 (0.030)	0.114 (0.13)
GC5	532	1.382 (0.029)	0.032 (0.124)	1.456 (0.031)	0.141 (0.129)
GC5	555	1.420 (0.030)	0.054 (0.124)	1.490 (0.032)	0.179 (0.129)
GC5	595	N/A	N/A	1.550 (0.033)	0.236 (0.129)
GC5	650	1.552 (0.033)	0.175 (0.123)	1.631 (0.035)	0.299 (0.128)
GC5	660	N/A	N/A	1.646 (0.035)	0.311 (0.128)

Table 69 (continued).

Cruise	Wavelength nm	AC9		ACS	
		m (Uncertainty)	b (Uncertainty)	m (Uncertainty)	b (Uncertainty)
GC5	670	N/A	N/A	1.658 (0.036)	0.320 (0.128)
GC5	676	1.591 (0.034)	0.211 (0.123)	1.666 (0.036)	0.323 (0.128)
GC5	715	1.650 (0.035)	0.249 (0.123)	1.723 (0.037)	0.398 (0.128)

Notes. The slopes and intercepts are for linear SPM predictive algorithms y = mx + b. The uncertainty for the regression slopes and intercepts were calculated using singular value decomposition. These selected wavelengths were interpolated from the ACS output and included the wavelengths observed by the AC9 and the BB9 (except 400 nm which is beyond the range of the ACS). Salinity exclusions and visual inspection exclusions were applied.

Table 70

SPM Algorithm Coefficients from b_t, Cruise by Cruise

Cruise	Wavelength nm	AC9		ACS	
		m (Uncertainty)	b (Uncertainty)	m (Uncertainty)	b (Uncertainty)
GC1	412	N/A	N/A	1.638 (0.041)	-0.731 (0.305)
GC1	440	N/A	N/A	1.633 (0.040)	-0.628 (0.303)
GC1	488	N/A	N/A	1.716 (0.043)	-0.662 (0.304)
GC1	510	N/A	N/A	1.746 (0.043)	-0.659 (0.304)
GC1	532	N/A	N/A	1.776 (0.044)	-0.647 (0.304)
GC1	555	N/A	N/A	1.811 (0.045)	-0.638 (0.304)
GC1	595	N/A	N/A	1.882 (0.047)	-0.624 (0.303)
GC1	650	N/A	N/A	1.990 (0.049)	-0.589 (0.303)
GC1	660	N/A	N/A	2.012 (0.050)	-0.556 (0.303)
GC1	670	N/A	N/A	2.035 (0.050)	-0.532 (0.302)
GC1	676	N/A	N/A	2.045 (0.051)	-0.535 (0.302)
GC1	715	N/A	N/A	2.112 (0.053)	-0.587 (0.317)
GC2	412	0.486 (0.011)	1.626 (0.131)	1.111 (0.035)	0.770 (0.198)
GC2	440	0.480 (0.010)	1.675 (0.131)	1.161 (0.037)	0.748 (0.198)
GC2	488	0.518 (0.011)	1.652 (0.131)	1.213 (0.039)	0.772 (0.198)
GC2	510	0.838 (0.017)	1.123 (0.133)	1.241 (0.04)	0.778 (0.197)
GC2	532	1.043 (0.021)	0.857 (0.135)	1.271 (0.041)	0.788 (0.197)
GC2	555	1.137 (0.023)	0.773 (0.136)	1.301 (0.042)	0.800 (0.197)

Table 70 (continued).

Cruise	Wavelength nm	AC9		ACS	
		m (Uncertainty)	b (Uncertainty)	m (Uncertainty)	b (Uncertainty)
GC2	595	N/A	N/A	1.357 (0.043)	0.820 (0.197)
GC2	650	1.287 (0.026)	0.790 (0.137)	1.442 (0.046)	0.858 (0.196)
GC2	660	N/A	N/A	1.458 (0.047)	0.872 (0.196)
GC2	670	N/A	N/A	1.475 (0.047)	0.885 (0.196)
GC2	676	1.333 (0.027)	0.791 (0.136)	1.484 (0.047)	0.885 (0.196)
GC2	715	1.397 (0.028)	0.781 (0.137)	1.538 (0.049)	0.864 (0.196)
GC3	412	1.123 (0.034)	0.272 (0.148)	1.165 (0.037)	0.366 (0.197)
GC3	440	1.215 (0.037)	0.270 (0.148)	1.222 (0.039)	0.331 (0.197)
GC3	488	1.318 (0.040)	0.207 (0.148)	1.347 (0.043)	0.242 (0.198)
GC3	510	1.354 (0.041)	0.194 (0.149)	1.390 (0.044)	0.225 (0.198)
GC3	532	1.404 (0.043)	0.183 (0.149)	1.443 (0.046)	0.207 (0.199)
GC3	555	1.456 (0.044)	0.169 (0.149)	1.496 (0.048)	0.193 (0.199)
GC3	595	N/A	N/A	1.596 (0.051)	0.168 (0.199)
GC3	650	1.684 (0.051)	0.141 (0.149)	1.739 (0.055)	0.149 (0.199)
GC3	660	N/A	N/A	1.766 (0.056)	0.153 (0.199)
GC3	670	N/A	N/A	1.794 (0.057)	0.153 (0.199)
GC3	676	1.759 (0.054)	0.144 (0.149)	1.810 (0.058)	0.147 (0.199)
GC3	715	1.856 (0.056)	0.119 (0.149)	1.906 (0.061)	0.126 (0.200)
GC4	412	0.993 (0.043)	0.273 (0.162)	1.140 (0.052)	0.195 (0.191)
GC4	440	1.054 (0.045)	0.248 (0.162)	1.173 (0.053)	0.187 (0.191)

Table 70 (continued).

Cruise	Wavelength nm	AC9		ACS	
		m (Uncertainty)	b (Uncertainty)	m (Uncertainty)	b (Uncertainty)
GC4	488	1.120 (0.047)	0.214 (0.163)	1.233 (0.056)	0.162 (0.191)
GC4	510	1.149 (0.049)	0.210 (0.163)	1.260 (0.057)	0.155 (0.191)
GC4	532	1.179 (0.050)	0.207 (0.163)	1.293 (0.058)	0.147 (0.191)
GC4	555	1.218 (0.051)	0.192 (0.163)	1.330 (0.059)	0.137 (0.191)
GC4	595	N/A	N/A	1.398 (0.062)	0.122 (0.191)
GC4	650	1.384 (0.058)	0.184 (0.163)	1.498 (0.066)	0.115 (0.191)
GC4	660	N/A	N/A	1.521 (0.067)	0.118 (0.191)
GC4	670	N/A	N/A	1.543 (0.068)	0.121 (0.191)
GC4	676	1.443 (0.060)	0.202 (0.162)	1.551 (0.068)	0.122 (0.191)
GC4	715	1.489 (0.062)	0.171 (0.163)	1.596 (0.070)	0.125 (0.191)
GC5	412	1.020 (0.022)	0.463 (0.121)	1.777 (0.037)	-0.812 (0.172)
GC5	440	1.382 (0.028)	-0.069 (0.125)	1.464 (0.032)	-0.048 (0.165)
GC5	488	1.432 (0.029)	-0.052 (0.125)	1.482 (0.033)	0.079 (0.164)
GC5	510	1.435 (0.030)	0.002 (0.124)	1.509 (0.033)	0.100 (0.164)
GC5	532	1.451 (0.030)	0.032 (0.124)	1.530 (0.034)	0.139 (0.164)
GC5	555	1.475 (0.031)	0.051 (0.124)	1.543 (0.034)	0.198 (0.164)
GC5	595	N/A	N/A	1.579 (0.035)	0.284 (0.163)
GC5	650	1.574 (0.033)	0.198 (0.123)	1.642 (0.037)	0.399 (0.162)
GC5	660	N/A	N/A	1.656 (0.038)	0.430 (0.162)

Table 70 (continued).

Cruise	Wavelength nm	AC9		ACS	
		m (Uncertainty)	b (Uncertainty)	m (Uncertainty)	b (Uncertainty)
GC5	670	N/A	N/A	1.669 (0.038)	0.461 (0.161)
GC5	676	676	1.616 (0.034)	1.675 (0.038)	0.468 (0.161)
GC5	715	715	1.651 (0.035)	1.704 (0.039)	0.505 (0.161)

Notes. The slopes and intercepts are for linear SPM predictive algorithms y = mx + b. The uncertainty for the regression slopes and intercepts were calculated using singular value decomposition. These selected wavelengths were interpolated from the ACS output and included the wavelengths observed by the AC9 and the BB9 (except 400 nm which is beyond the range of the ACS). Salinity exclusions and visual inspection exclusions were applied.

Table 71

SPM Algorithm Coefficients from b_b, Cruise by Cruise

Cruise	Wavelength nm	b_{bt}		b_{bp}	
		m (Uncertainty)	b (Uncertainty)	m (Uncertainty)	b (Uncertainty)
GC1	400	82.231 (1.923)	-0.077 (0.210)	82.061 (1.919)	0.219 (0.207)
GC1	440	83.142 (1.937)	-0.249 (0.212)	83.014 (1.934)	-0.048 (0.21)
GC1	488	86.719 (3.304)	-0.509 (0.230)	86.556 (3.298)	-0.37 (0.227)
GC1	510	78.571 (6.345)	-0.133 (0.263)	78.342 (6.326)	-0.026 (0.257)
GC1	532	82.793 (6.713)	-0.118 (0.262)	82.582 (6.695)	-0.024 (0.257)
GC1	595	79.459 (6.406)	-0.009 (0.256)	79.341 (6.397)	0.047 (0.253)
GC1	660	103.858 (8.435)	-0.071 (0.260)	103.72 (8.423)	-0.024 (0.257)
GC1	676	105.980 (8.787)	-0.154 (0.267)	105.859 (8.776)	-0.111 (0.265)
GC1	715	146.405 (12.112)	-0.132 (0.266)	146.206 (12.096)	-0.085 (0.263)
GC2	400	77.700 (1.536)	0.610 (0.124)	77.948 (1.542)	0.777 (0.122)
GC2	440	62.046 (1.788)	0.516 (0.127)	61.952 (1.784)	0.664 (0.126)
GC2	488	78.781 (3.446)	0.237 (0.136)	78.715 (3.444)	0.349 (0.134)
GC2	510	85.932 (3.751)	0.171 (0.138)	85.733 (3.742)	0.283 (0.135)
GC2	532	88.197 (3.852)	0.216 (0.137)	88.024 (3.844)	0.312 (0.135)
GC2	595	100.110 (4.363)	0.215 (0.137)	99.964 (4.356)	0.283 (0.135)
GC2	660	130.047 (5.685)	0.294 (0.135)	130.197 (5.691)	0.336 (0.134)
GC2	676	101.339 (5.941)	0.316 (0.140)	101.241 (5.935)	0.356 (0.139)
GC2	715	148.782 (8.683)	0.316 (0.140)	148.627 (8.673)	0.361 (0.138)

Table 71 (continued).

Cruise	Wavelength nm	b_{bt}		b_{bp}	
		m (Uncertainty)	b (Uncertainty)	m (Uncertainty)	b (Uncertainty)
GC3	400	106.189 (3.183)	0.026 (0.132)	106.419 (3.189)	0.354 (0.129)
GC3	440	80.384 (2.413)	0.046 (0.132)	80.369 (2.412)	0.229 (0.13)
GC3	488	74.605 (3.740)	0.037 (0.140)	74.681 (3.741)	0.145 (0.137)
GC3	510	82.406 (4.104)	0.049 (0.139)	82.481 (4.106)	0.148 (0.137)
GC3	532	86.663 (4.366)	0.084 (0.139)	86.74 (4.367)	0.171 (0.137)
GC3	595	118.685 (7.144)	0.215 (0.188)	118.718 (7.143)	0.289 (0.187)
GC3	660	143.806 (7.258)	0.110 (0.138)	143.889 (7.26)	0.168 (0.137)
GC3	676	70.030 (8.711)	0.352 (0.148)	70.121 (8.719)	0.377 (0.146)
GC3	715	107.112 (13.382)	0.359 (0.148)	107.273 (13.397)	0.39 (0.146)
GC4	400	108.165 (4.406)	0.386 (0.150)	110.281 (4.515)	0.546 (0.147)
GC4	440	77.991 (3.160)	0.073 (0.157)	77.676 (3.15)	0.256 (0.153)
GC4	488	66.177 (2.669)	0.142 (0.155)	66.034 (2.665)	0.242 (0.153)
GC4	510	72.587 (2.91)	0.106 (0.155)	72.444 (2.906)	0.197 (0.153)
GC4	532	77.812 (3.098)	0.072 (0.156)	77.673 (3.094)	0.154 (0.154)
GC4	595	87.542 (3.840)	-0.027 (0.159)	87.418 (3.836)	0.03 (0.158)
GC4	660	130.365 (5.735)	0.036 (0.158)	130.191 (5.729)	0.091 (0.157)
GC4	676	78.819 (5.577)	0.264 (0.162)	78.748 (5.571)	0.294 (0.161)
GC4	715	128.945 (9.056)	0.154 (0.166)	128.789 (9.044)	0.192 (0.164)
GC5	400	129.405 (2.534)	-0.097 (0.123)	194.71 (1.89)	-0.724 (0.116)
GC5	440	83.692 (1.657)	0.089 (0.121)	83.651 (1.656)	0.274 (0.119)

Table 71 (continued).

Cruise	Wavelength nm	b_{bt}		b_{bp}	
		m (Uncertainty)	b (Uncertainty)	m (Uncertainty)	b (Uncertainty)
GC5	488	71.099 (2.654)	0.203 (0.132)	71.13 (2.654)	0.301 (0.13)
GC5	510	75.171 (2.804)	0.088 (0.134)	75.155 (2.802)	0.178 (0.132)
GC5	532	77.885 (2.896)	0.111 (0.133)	77.879 (2.895)	0.188 (0.132)
GC5	595	73.714 (3.423)	0.222 (0.137)	73.717 (3.422)	0.268 (0.136)
GC5	660	109.204 (5.085)	0.257 (0.136)	109.198 (5.084)	0.301 (0.135)
GC5	676	91.623 (4.288)	0.200 (0.138)	91.624 (4.288)	0.233 (0.137)
GC5	715	123.899 (6.623)	0.236 (0.139)	123.906 (6.623)	0.271 (0.138)

Notes. The slopes and intercepts are for linear SPM predictive algorithms y = mx + b. The uncertainty for the regression slopes and intercepts were calculated using singular value decomposition. Salinity and CTD-T exclusions were applied. Sensor saturation exclusions were also applied.

Table 72

SPM Algorithm Coefficients from b_{bt}/b, Cruise by Cruise

Cruise	Wavelength nm	AC9		ACS	
		m (Uncertainty)	b (Uncertainty)	m (Uncertainty)	b (Uncertainty)
GC1	440	N/A	N/A	-37.695 (8.443)*	4.846 (0.374)*
GC1	488	N/A	N/A	-40.865 (9.066)*	4.985 (0.393)*
GC1	510	N/A	N/A	-21.742 (10.279)	2.519 (0.416)
GC1	532	N/A	N/A	-24.180 (11.639)*	2.543 (0.428)*
GC1	595	N/A	N/A	-47.403 (25.260)*	2.965 (0.643)*
GC1	660	N/A	N/A	-43.901 (19.766)*	2.890 (0.536)*
GC1	676	N/A	N/A	-26.540 (12.769)*	2.590 (0.445)*
GC1	715	N/A	N/A	-146.722 (59.109)*	4.421 (1.003)*
GC2	440	-23.488 (2.749)	3.594 (0.165)	-150.870 (20.776)*	7.734 (0.474)*
GC2	488	-3.124 (1.319)*	2.188 (0.137)*	166.796 (29.482)*	0.396 (0.561)*
GC2	510	-15.443 (3.401)	2.564 (0.168)	-32.045 (13.319)*	4.071 (0.337)*
GC2	532	-23.090 (4.792)	2.722 (0.186)	139.126 (43.323)*	0.855 (0.812)*
GC2	595	N/A	N/A	329.441 (43.239)	-1.826 (0.710)
GC2	660	N/A	N/A	415.251 (36.373)	-1.920 (0.486)
GC2	676	-2.299 (1.132)*	1.893 (0.137)*	124.460 (29.420)*	0.468 (0.522)*
GC2	715	-13.151 (22.561)*	2.015 (0.332)*	303.792 (49.117)	-0.806 (0.571)
GC3	440	-9.208 (2.151)	2.479 (0.156)	-155.145 (37.717)*	5.908 (0.662)*
GC3	488	-25.480 (7.289)	2.328 (0.234)	100.471 (43.215)*	0.596 (0.832)*

Table 72 (continued).

Cruise	Wavelength nm	AC9		ACS	
		m (Uncertainty)	b (Uncertainty)	m (Uncertainty)	b (Uncertainty)
GC3	510	-26.674 (8.151)	2.291 (0.236)	125.397 (48.069)*	0.322 (0.848)*
GC3	532	-29.863 (12.969)*	2.251 (0.289)*	212.390 (44.204)	-0.892 (0.725)
GC3	595	N/A	N/A	-73.189 (44.937)*	3.892 (0.567)*
GC3	660	N/A	N/A	264.348 (57.859)	-0.496 (0.677)
GC3	676	-11.933 (12.700)*	1.411 (0.291)*	197.313 (43.152)	-1.427 (0.703)
GC3	715	-14.761 (12.735)*	1.375 (0.225)*	235.578 (63.874)	-0.902 (0.722)
GC4	440	-52.117 (12.010)	3.295 (0.253)	238.973 (28.553)	-0.383 (0.433)
GC4	488	-11.064 (17.586)*	2.567 (0.343)*	353.070 (26.663)	-2.605 (0.451)
GC4	510	-26.261 (17.487)*	2.833 (0.338)*	380.781 (29.215)	-2.965 (0.465)
GC4	532	12.317 (18.927)	2.168 (0.337)	404.891 (28.529)	-2.932 (0.430)
GC4	595	N/A	N/A	372.943 (26.702)	-2.249 (0.390)
GC4	660	N/A	N/A	522.330 (34.188)	-2.179 (0.358)
GC4	676	96.285 (24.505)	0.320 (0.365)	237.640 (26.645)	-1.037 (0.372)
GC4	715	73.538 (31.845)	0.840 (0.358)	310.527 (38.395)	-1.004 (0.394)
GC5	440	-23.473 (13.934)	3.340 (0.254)	-46.139 (23.340)	5.460 (0.427)
GC5	488	208.150 (19.286)	-0.753 (0.295)	181.890 (29.552)*	0.288 (0.515)*
GC5	510	10.085 (17.116)*	2.022 (0.319)*	-113.434 (27.745)	5.509 (0.556)
GC5	532	29.279 (17.649)*	1.717 (0.310)*	-29.525 (21.869)*	3.868 (0.432)*
GC5	595	N/A	N/A	49.406 (30.500)*	2.094 (0.557)*
GC5	660	N/A	N/A	51.918 (48.837)*	2.312 (0.674)*

Table 72 (continued).

Cruise	Wavelength nm	AC9		ACS	
		m (Uncertainty)	b (Uncertainty)	m (Uncertainty)	b (Uncertainty)
GC5	676	77.795 (20.10)	0.800 (0.328)	5.947 (30.836)*	2.857 (0.562)*
GC5	715	164.074 (28.392)	0.078 (0.320)	-30.900 (36.698)*	3.057 (0.505)*

Notes. The slopes and intercepts are for linear SPM predictive algorithms y = mx + b. The uncertainty for the regression slopes and intercepts were calculated using singular value decomposition. Salinity and CTD-T exclusions were applied. Sensor saturation exclusions were also applied. *Spearman correlation coefficients indicate that SPM is statistically unrelated to the IOP in question for the cruise-data tested.

Table 73

Algorithm Coefficients from b_{bp} / b, Cruise by Cruise

Cruise	Wavelength nm	AC9		ACS	
		m (Uncertainty)	b (Uncertainty)	m (Uncertainty)	b (Uncertainty)
GC1	440	N/A	N/A	86.101 (69.802)*	2.54 (1.241)*
GC1	488	N/A	N/A	-158.946 (42.956)*	7.148 (0.965)*
GC1	510	N/A	N/A	-88.375 (47.937)*	3.689 (1.019)*
GC1	532	N/A	N/A	-84.166 (57.466)*	3.506 (1.142)*
GC1	595	N/A	N/A	79.643 (63.641)*	0.464 (1.173)*
GC1	660	N/A	N/A	27.788 (52.559)*	1.422 (0.926)*
GC1	676	N/A	N/A	-89.607 (45.543)*	3.727 (0.979)*
GC1	715	N/A	N/A	-13.871 (46.826)*	2.084 (0.727)*
GC2	440	48.990 (16.887)	1.857 (0.290)	587.988 (34.222)	-3.831 (0.520)
GC2	488	209.678 (16.797)	-0.455 (0.235)	299.467 (23.959)	-0.762 (0.381)
GC2	510	171.898 (23.605)	-0.693 (0.393)	41.554 (16.367)	2.684 (0.336)
GC2	532	95.613 (17.41)	0.559 (0.294)	447.198 (34.915)	-3.184 (0.546)
GC2	595	N/A	N/A	390.387 (32.630)	-1.895 (0.479)
GC2	660	N/A	N/A	331.095 (27.301)	-0.388 (0.342)
GC2	676	-1.919 (2.199)	1.794 (0.137)	173.910 (27.013)	-0.046 (0.443)
GC2	715	153.694 (22.610)	0.280 (0.252)	309.801 (39.489)	-0.456 (0.425)
GC3	440	-3.267 (4.019)	2.21 (0.153)	315.177 (32.599)	-0.373 (0.428)
GC3	488	98.395 (25.076)	0.009 (0.444)	259.307 (31.366)	-1.412 (0.504)

Table 73 (continued).

Cruise	Wavelength nm	AC9		ACS	
		m (Uncertainty)	b (Uncertainty)	m (Uncertainty)	b (Uncertainty)
GC3	510	41.437 (20.298)*	0.995 (0.356)*	288.662 (35.195)	-1.568 (0.526)
GC3	532	218.444 (28.037)	-1.188 (0.391)	253.263 (30.906)	-0.834 (0.443)
GC3	595	N/A	N/A	406.057 (52.595)	-1.751 (0.607)
GC3	660	N/A	N/A	317.182 (44.486)	-0.638 (0.473)
GC3	676	28.210 (21.123)*	0.695 (0.383)*	186.166 (35.318)	-0.988 (0.538)
GC3	715	23.950 (25.106)*	0.911 (0.307)*	272.356 (52.677)	-0.955 (0.541)
GC4	440	343.125 (26.279)	-1.024 (0.293)	442.655 (26.469)	-1.687 (0.320)
GC4	488	281.714 (24.170)	-1.338 (0.345)	384.302 (23.110)	-2.196 (0.349)
GC4	510	233.721 (25.188)	-0.788 (0.366)	402.695 (25.645)	-2.477 (0.368)
GC4	532	186.124 (20.999)	-0.001 (0.299)	377.877 (24.278)	-1.893 (0.337)
GC4	595	N/A	N/A	350.997 (23.858)	-1.558 (0.332)
GC4	660	N/A	N/A	474.053 (30.948)	-1.355 (0.315)
GC4	676	145.256 (22.491)	-0.080 (0.301)	224.295 (24.381)	-0.678 (0.329)
GC4	715	152.001 (30.359)	0.251 (0.304)	317.494 (35.823)	-0.826 (0.348)
GC5	440	464.011 (20.351)	-1.872 (0.238)	636.815 (28.791)	-3.427 (0.385)
GC5	488	257.033 (15.719)	-0.526 (0.200)	252.407 (20.607)	-0.181 (0.312)
GC5	510	214.166 (21.135)	-0.850 (0.320)	14.770 (26.574)	2.923 (0.489)
GC5	532	186.754 (19.749)	-0.344 (0.290)	37.788 (20.897)*	2.540 (0.385)*
GC5	595	N/A	N/A	63.630 (25.271)*	1.764 (0.451)*
GC5	660	N/A	N/A	142.792 (40.735)*	1.070 (0.538)*

Table 73 (continued).

Cruise	Wavelength nm	AC9		ACS	
		m (Uncertainty)	b (Uncertainty)	m (Uncertainty)	b (Uncertainty)
GC5	676	149.711 (20.643)	-0.108 (0.310)	-6.652 (22.838)*	2.951 (0.426)*
GC5	715	230.724 (27.341)	-0.389 (0.284)	-33.272 (24.596)*	2.974 (0.358)*

Notes. The slopes and intercepts are for linear SPM predictive algorithms y = mx + b. The uncertainty for the regression slopes and intercepts were calculated using singular value decomposition. Salinity and CTD-T exclusions were applied. Sensor saturation exclusions were also applied. *Spearman correlation coefficients indicate that SPM is statistically unrelated to the IOP in question for the cruise-data tested.

Table 74

SPM Algorithm Coefficients from $a + b_{bt}$, Cruise by Cruise

Cruise	Wavelength nm	AC9		ACS	
		m (Uncertainty)	b (Uncertainty)	m (Uncertainty)	b (Uncertainty)
GC1	440	N/A	N/A	11.711 (0.539)	-1.262 (0.36)
GC1	488	N/A	N/A	18.797 (0.861)	-1.246 (0.359)
GC1	510	N/A	N/A	8.640 (2.088)	0.619 (0.419)
GC1	532	N/A	N/A	11.020 (2.637)	0.588 (0.422)
GC1	595	N/A	N/A	22.509 (5.526)	0.415 (0.492)
GC1	660	N/A	N/A	16.069 (3.906)	0.736 (0.400)
GC1	676	N/A	N/A	12.642 (3.126)	0.812 (0.391)
GC1	715	N/A	N/A	100.487 (31.412)	0.242 (0.693)
GC2	440	10.201 (0.341)	-0.071 (0.150)	11.244 (0.435)	-0.222 (0.257)
GC2	488	14.725 (0.836)	0.080 (0.162)	15.159 (1.043)	0.142 (0.291)
GC2	510	19.485 (1.052)	-0.060 (0.164)	20.817 (1.353)	-0.155 (0.296)
GC2	532	19.106 (1.200)	0.267 (0.162)	27.680 (1.700)	-0.469 (0.301)
GC2	595	N/A	N/A	52.824 (2.896)	-0.978 (0.303)
GC2	660	N/A	N/A	55.326 (3.591)	-0.831 (0.316)
GC2	676	36.006 (2.465)	-0.038 (0.172)	33.744 (3.337)	-0.026 (0.317)
GC2	715	146.961 (8.962)	0.426 (0.157)	124.64 (12.843)	0.790 (0.303)
GC3	440	14.236 (0.449)	-1.197 (0.172)	15.092 (0.500)	-1.201 (0.227)
GC3	488	19.700 (1.044)	-0.820 (0.190)	20.204 (1.173)	-0.674 (0.253)

Table 74 (continued).

Cruise	Wavelength nm	AC9		ACS	
		m (Uncertainty)	b (Uncertainty)	m (Uncertainty)	b (Uncertainty)
GC3	510	24.366 (1.278)	-0.766 (0.187)	25.176 (1.444)	-0.622 (0.254)
GC3	532	30.383 (1.596)	-0.737 (0.187)	31.280 (1.816)	-0.630 (0.256)
GC3	595	N/A	N/A	66.390 (3.738)	-0.153 (0.234)
GC3	660	N/A	N/A	60.925 (3.914)	-0.139 (0.247)
GC3	676	25.828 (4.328)	0.159 (0.220)	24.853 (5.323)	0.676 (0.287)
GC3	715	102.855 (13.778)	0.442 (0.171)	94.551 (15.085)	0.686 (0.238)
GC4	440	8.027 (0.080)	-1.523 (0.145)	5.421 (0.330)	0.699 (0.209)
GC4	488	11.861 (0.133)	-0.994 (0.145)	10.124 (0.562)	0.425 (0.211)
GC4	510	19.248 (0.219)	-1.411 (0.148)	12.642 (0.829)	0.435 (0.218)
GC4	532	8.737 (0.106)	0.859 (0.139)	16.556 (1.042)	0.323 (0.218)
GC4	595	N/A	N/A	34.913 (1.903)	-0.120 (0.221)
GC4	660	N/A	N/A	47.827 (2.838)	-0.184 (0.234)
GC4	676	9.818 (0.095)	0.323 (0.140)	28.138 (2.643)	0.127 (0.236)
GC4	715	8.751 (0.101)	1.107 (0.141)	127.259 (10.867)	0.299 (0.222)
GC5	440	8.816 (0.197)	-0.111 (0.127)	7.908 (0.200)	0.689 (0.178)
GC5	488	16.190 (0.662)	-0.483 (0.154)	16.082 (0.767)	-0.408 (0.233)
GC5	510	20.090 (0.818)	-0.556 (0.156)	20.466 (0.964)	-0.504 (0.235)
GC5	532	22.200 (1.151)	-0.118 (0.162)	26.073 (1.216)	-0.610 (0.237)
GC5	595	N/A	N/A	41.103 (2.403)	-0.496 (0.253)
GC5	660	N/A	N/A	37.566 (2.486)	0.0750 (0.248)

Table 74 (continued).

Cruise	Wavelength nm	AC9		ACS	
		m (Uncertainty)	b (Uncertainty)	m (Uncertainty)	b (Uncertainty)
GC5	676	29.552 (1.596)	-0.113 (0.158)	29.410 (1.975)	0.211 (0.240)
GC5	715	123.201 (6.596)	0.283 (0.138)	129.326 (8.592)	0.343 (0.219)

Notes. The slopes and intercepts are for linear SPM predictive algorithms y = mx + b. The uncertainty for the regression slopes and intercepts were calculated using singular value decomposition. Salinity and CTD-T exclusions were applied. Sensor saturation exclusions were also applied.

Table 75

SPM Algorithm Coefficients from $a + b_{bp}$, Cruise by Cruise

Cruise	Wavelength nm	AC9		ACS	
		m (Uncertainty)	b (Uncertainty)	m (Uncertainty)	b (Uncertainty)
GC1	440	N/A	N/A	11.711 (0.539)	-1.262 (0.360)
GC1	488	N/A	N/A	18.797 (0.861)	-1.246 (0.359)
GC1	510	N/A	N/A	8.640 (2.088)	0.619 (0.419)
GC1	532	N/A	N/A	11.020 (2.637)	0.588 (0.422)
GC1	595	N/A	N/A	22.509 (5.526)	0.415 (0.492)
GC1	660	N/A	N/A	16.069 (3.906)	0.736 (0.400)
GC1	676	N/A	N/A	12.642 (3.126)	0.812 (0.391)
GC1	715	N/A	N/A	100.487 (31.412)	0.242 (0.693)
GC2	440	10.200 (0.341)	-0.071 (0.150)	11.244 (0.435)	-0.222 (0.257)
GC2	488	14.680 (0.832)	0.100 (0.162)	15.159 (1.043)	0.142 (0.291)
GC2	510	19.418 (1.047)	-0.031 (0.163)	20.817 (1.353)	-0.155 (0.296)
GC2	532	26.381 (1.367)	-0.163 (0.165)	27.680 (1.700)	-0.469 (0.301)
GC2	595	N/A	N/A	52.824 (2.896)	-0.978 (0.303)
GC2	660	N/A	N/A	55.326 (3.591)	-0.831 (0.316)
GC2	676	35.900 (2.459)	-0.027 (0.171)	33.744 (3.337)	-0.026 (0.317)
GC2	715	147.920 (8.783)	0.401 (0.146)	129.388 (11.877)	0.637 (0.259)
GC3	440	14.236 (0.449)	-1.197 (0.172)	15.092 (0.500)	-1.201 (0.227)
GC3	488	19.700 (1.044)	-0.820 (0.190)	20.204 (1.173)	-0.674 (0.253)

Table 75 (continued).

Cruise	Wavelength nm	AC9		ACS	
		m (Uncertainty)	b (Uncertainty)	m (Uncertainty)	b (Uncertainty)
GC3	510	24.366 (1.278)	-0.766 (0.187)	25.176 (1.444)	-0.622 (0.254)
GC3	532	30.383 (1.596)	-0.737 (0.187)	31.280 (1.816)	-0.630 (0.256)
GC3	595	N/A	N/A	66.390 (3.738)	-0.153 (0.234)
GC3	660	N/A	N/A	60.925 (3.914)	-0.139 (0.247)
GC3	676	25.828 (4.328)	0.159 (0.220)	24.853 (5.323)	0.676 (0.287)
GC3	715	102.855 (13.778)	0.442 (0.171)	94.551 (15.085)	0.686 (0.238)
GC4	440	8.027 (0.080)	-1.523 (0.145)	5.421 (0.330)	0.699 (0.209)
GC4	488	11.861 (0.133)	-0.994 (0.145)	10.124 (0.562)	0.425 (0.211)
GC4	510	19.248 (0.219)	-1.411 (0.148)	12.642 (0.829)	0.435 (0.218)
GC4	532	8.737 (0.106)	0.859 (0.139)	16.556 (1.042)	0.323 (0.218)
GC4	595	N/A	N/A	34.913 (1.903)	-0.120 (0.221)
GC4	660	N/A	N/A	47.827 (2.838)	-0.184 (0.234)
GC4	676	9.818 (0.095)	0.323 (0.140)	28.138 (2.643)	0.127 (0.236)
GC4	715	8.751 (0.101)	1.107 (0.141)	127.259 (10.867)	0.299 (0.222)
GC5	440	8.816 (0.197)	-0.111 (0.127)	7.937 (0.198)	0.641 (0.173)
GC5	488	16.190 (0.662)	-0.483 (0.154)	16.014 (0.747)	-0.380 (0.222)
GC5	510	20.090 (0.818)	-0.556 (0.156)	20.360 (0.939)	-0.469 (0.224)
GC5	532	22.200 (1.151)	-0.118 (0.162)	25.910 (1.184)	-0.567 (0.226)
GC5	595	N/A	N/A	40.855 (2.328)	-0.462 (0.240)
GC5	660	N/A	N/A	37.719 (2.414)	0.054 (0.235)

Table 75 (continued).

Cruise	Wavelength nm	AC9		ACS	
		m (Uncertainty)	b (Uncertainty)	m (Uncertainty)	b (Uncertainty)
GC5	676	29.552 (1.596)	-0.113 (0.158)	29.578 (1.921)	0.184 (0.228)
GC5	715	123.201 (6.596)	0.283 (0.138)	129.863 (8.405)	0.324 (0.209)

Notes. The slopes and intercepts are for linear SPM predictive algorithms y = mx + b. The uncertainty for the regression slopes and intercepts were calculated using singular value decomposition. Salinity and CTD-T exclusions were applied. Sensor saturation exclusions were also applied.

Table 76

SPM Algorithm Coefficients from $b_{bt} / (a + b_{bt})$, Cruise by Cruise

Cruise	Wavelength nm	AC9		ACS	
		m (Uncertainty)	b (Uncertainty)	m (Uncertainty)	b (Uncertainty)
GC1	440	N/A	N/A	11.711 (0.539)*	-1.262 (0.360)*
GC1	488	N/A	N/A	18.797 (0.861)*	-1.246 (0.359)*
GC1	510	N/A	N/A	8.640 (2.088)*	0.619 (0.419)*
GC1	532	N/A	N/A	11.020 (2.637)*	0.588 (0.422)*
GC1	595	N/A	N/A	22.509 (5.526)*	0.415 (0.492)*
GC1	660	N/A	N/A	16.069 (3.906)*	0.736 (0.400)*
GC1	676	N/A	N/A	12.642 (3.126)*	0.812 (0.391)*
GC1	715	N/A	N/A	100.487 (31.412)*	0.242 (0.693)*
GC2	440	10.200 (0.341)*	-0.071 (0.150)*	11.244 (0.435)	-0.222 (0.257)
GC2	488	14.680 (0.832)	0.100 (0.162)	15.159 (1.043)	0.142 (0.291)
GC2	510	19.418 (1.047)	-0.031 (0.163)	20.817 (1.353)	-0.155 (0.296)
GC2	532	26.381 (1.367)	-0.163 (0.165)	27.680 (1.700)	-0.469 (0.301)
GC2	595	N/A	N/A	52.824 (2.896)	-0.978 (0.303)
GC2	660	N/A	N/A	55.326 (3.591)	-0.831 (0.316)
GC2	676	35.900 (2.459)	-0.027 (0.171)	33.744 (3.337)	-0.026 (0.317)
GC2	715	147.920 (8.783)*	0.401 (0.146)*	129.388 (11.877)	0.637 (0.259)
GC3	440	14.236 (0.449)	-1.197 (0.172)	15.092 (0.500)	-1.201 (0.227)
GC3	488	19.700 (1.044)	-0.820 (0.190)	20.204 (1.173)	-0.674 (0.253)

Table 76 (continued).

Cruise	Wavelength nm	AC9		ACS	
		m (Uncertainty)	b (Uncertainty)	m (Uncertainty)	b (Uncertainty)
GC3	510	24.366 (1.278)	-0.766 (0.187)	25.176 (1.444)	-0.622 (0.254)
GC3	532	30.383 (1.596)	-0.737 (0.187)	31.280 (1.816)	-0.630 (0.256)
GC3	595	N/A	N/A	66.390 (3.738)*	-0.153 (0.234)*
GC3	660	N/A	N/A	60.925 (3.914)	-0.139 (0.247)
GC3	676	25.828 (4.328)	0.159 (0.220)	24.853 (5.323)	0.676 (0.287)
GC3	715	102.855 (13.778)*	0.442 (0.171)*	94.551 (15.085)*	0.686 (0.238)*
GC4	440	8.027 (0.080)*	-1.523 (0.145)*	5.421 (0.330)	0.699 (0.209)
GC4	488	11.861 (0.133)	-0.994 (0.145)	10.124 (0.562)	0.425 (0.211)
GC4	510	19.248 (0.219)	-1.411 (0.148)	12.642 (0.829)	0.435 (0.218)
GC4	532	8.737 (0.106)	0.859 (0.139)	16.556 (1.042)	0.323 (0.218)
GC4	595	N/A	N/A	34.913 (1.903)	-0.120 (0.221)
GC4	660	N/A	N/A	47.827 (2.838)	-0.184 (0.234)
GC4	676	9.818 (0.095)	0.323 (0.140)	28.138 (2.643)	0.127 (0.236)
GC4	715	8.751 (0.101)*	1.107 (0.141)*	127.259 (10.867)	0.299 (0.222)
GC5	440	8.816 (0.197)	-0.111 (0.127)	7.937 (0.198)	0.641 (0.173)
GC5	488	16.19 (0.662)	-0.483 (0.154)	16.014 (0.747)	-0.380 (0.222)
GC5	510	20.090 (0.818)	-0.556 (0.156)	20.360 (0.939)	-0.469 (0.224)
GC5	532	22.200 (1.151)	-0.118 (0.162)	25.910 (1.184)	-0.567 (0.226)
GC5	595	N/A	N/A	40.855 (2.328)	-0.462 (0.240)
GC5	660	N/A	N/A	37.719 (2.414)	0.054 (0.235)

Table 76 (continued).

Cruise	Wavelength nm	AC9		ACS	
		m (Uncertainty)	b (Uncertainty)	m (Uncertainty)	b (Uncertainty)
GC5	676	29.552 (1.596)	-0.113 (0.158)	29.578 (1.921)	0.184 (0.228)
GC5	715	123.201 (6.596)*	0.283 (0.138)*	129.863 (8.405)	0.324 (0.209)

Notes. The slopes and intercepts are for linear SPM predictive algorithms y = mx + b. The uncertainty for the regression slopes and intercepts were calculated using singular value decomposition. Salinity and CTD-T exclusions were applied. Sensor saturation exclusions were also applied. *Spearman correlation coefficients indicate that SPM is statistically unrelated to the IOP in question for the cruise-data tested.

Table 77

SPM Algorithm Coefficients from $b_{bp} / (a + b_{bp})$, Cruise by Cruise

Cruise	Wavelength nm	AC9		ACS	
		m (Uncertainty)	b (Uncertainty)	m (Uncertainty)	b (Uncertainty)
GC1	440	N/A	N/A	8.261 (4.799)*	2.694 (0.657)*
GC1	488	N/A	N/A	2.096 (3.097)*	3.268 (0.721)*
GC1	510	N/A	N/A	-2.443 (2.296)*	2.511 (0.662)*
GC1	532	N/A	N/A	-1.674 (1.705)*	2.385 (0.593)*
GC1	595	N/A	N/A	1.482 (1.793)*	1.347 (0.842)*
GC1	660	N/A	N/A	-0.540 (0.487)*	2.161 (0.386)*
GC1	676	N/A	N/A	-0.886 (0.888)*	2.257 (0.478)*
GC1	715	N/A	N/A	-0.217 (0.113)*	2.428 (0.367)*
GC2	440	42.508 (1.954)	-1.709 (0.229)	55.276 (2.363)	-1.823 (0.326)
GC2	488	13.517 (1.045)	0.130 (0.186)	24.464 (1.591)	-0.276 (0.302)
GC2	510	14.329 (1.096)	-0.415 (0.218)	23.490 (1.594)	-1.029 (0.353)
GC2	532	15.787 (0.986)	-0.845 (0.213)	21.035 (1.367)	-1.001 (0.341)
GC2	595	N/A	N/A	16.349 (1.010)	-1.334 (0.346)
GC2	660	N/A	N/A	15.136 (1.054)	-0.361 (0.305)
GC2	676	9.233 (0.746)	-0.090 (0.190)	11.601 (1.134)	-0.131 (0.323)
GC2	715	1.598 (0.504)*	0.194 (0.485)*	-0.264 (0.057)	3.236 (0.238)
GC3	440	46.283 (2.468)	-1.314 (0.230)	49.280 (2.981)	-1.555 (0.337)
GC3	488	17.455 (1.526)	-0.519 (0.235)	11.856 (1.590)	0.416 (0.323)

Table 77 (continued).

Cruise	Wavelength nm	AC9		ACS	
		m (Uncertainty)	b (Uncertainty)	m (Uncertainty)	b (Uncertainty)
GC3	510	16.345 (1.420)	-0.647 (0.243)	18.117 (1.733)	-0.826 (0.366)
GC3	532	10.847 (1.063)	-0.112 (0.222)	16.250 (1.484)	-0.835 (0.354)
GC3	595	N/A	N/A	-2.813 (1.186)*	4.523 (0.528)*
GC3	660	N/A	N/A	7.756 (0.865)	-0.099 (0.342)
GC3	676	5.246 (0.797)	0.008 (0.225)	4.800 (0.818)	0.020 (0.341)
GC3	715	0.672 (1.095)*	0.511 (1.085)*	1.244 (0.749)*	0.483 (0.724)*
GC4	440	-11.634 (2.724)*	5.158 (0.236)*	46.116 (3.230)	-0.737 (0.304)
GC4	488	-1.004 (1.534)	4.446 (0.228)	28.585 (1.850)	-1.130 (0.309)
GC4	510	-5.220 (1.358)	5.055 (0.232)	22.673 (1.698)	-1.124 (0.329)
GC4	532	-2.958 (1.092)	4.804 (0.221)	19.574 (1.434)	-1.093 (0.322)
GC4	595	N/A	N/A	13.198 (0.972)	-1.405 (0.343)
GC4	660	N/A	N/A	13.775 (0.861)	-0.863 (0.274)
GC4	676	-5.112 (0.805)	4.668 (0.200)	6.264 (0.881)	0.228 (0.292)
GC4	715	-2.096 (0.127)*	6.036 (0.196)*	-1.058 (0.281)	3.234 (0.391)
GC5	440	34.837 (1.671)	0.123 (0.172)	30.260 (2.007)	1.497 (0.245)
GC5	488	15.287 (0.933)	0.252 (0.161)	13.057 (1.149)	1.108 (0.235)
GC5	510	14.191 (0.915)	-0.074 (0.182)	11.883 (1.097)	0.812 (0.264)
GC5	532	12.932 (0.791)	-0.151 (0.180)	10.817 (0.937)	0.709 (0.260)
GC5	595	N/A	N/A	8.841 (0.705)	-0.130 (0.279)
GC5	660	N/A	N/A	8.487 (0.760)	0.590 (0.254)

Table 77 (continued).

Cruise	Wavelength nm	AC9		ACS	
		m (Uncertainty)	b (Uncertainty)	m (Uncertainty)	b (Uncertainty)
GC5	676	8.682 (0.589)	0.109 (0.168)	6.812 (0.692)	0.865 (0.249)
GC5	715	0.608 (1.006)*	1.224 (1.000)*	-0.425 (0.370)	2.989 (0.424)

Notes. The slopes and intercepts are for linear SPM predictive algorithms y = mx + b. The uncertainty for the regression slopes and intercepts were calculated using singular value decomposition. Salinity and CTD-T exclusions were applied. Sensor saturation exclusions were also applied. Sensor saturation exclusions were also applied. *Spearman correlation coefficients indicate that SPM is statistically unrelated to the IOP in question for the cruise-data tested.

CHAPTER VI - AOP R_{rs}: DATA QUALITY AND RELATIONSHIP TO SPM

Introduction

In some cases, specific properties of SPM are studied to better understand optical signals (Neil et al., 2011; Woźniak, Meler, Lednicka, Zdun, & Stoń-Egiert, 2011). Employing a reversal of perspective, apparent optical properties are frequently used for SPM estimation and characterization (Avinash et al., 2012; Cai, Tang, & Li, 2015; Fettweis, Monbaliu, Baeye, Nechad, & Van den Eynde, 2012; He et al., 2013; Mao, Chen, Pan, Tao, & Zhu, 2012; Qiu, 2013; Volpe, Silvestri, & Marani, 2011; Woźniak, Darecki, Zabłocka, Burska, & Dera, 2016 in press). This chapter discusses the remote sensing reflectance (R_{rs}) spectra developed during this research and determines their relationship to SPM concentration. A novel way of predicting SPM from R_{rs} is established.

AOP Hyperspectral R_{rs}

The R_{rs} spectra in this project (Figure 77) were calculated using the methods described in Chapter II for the ASD and HyperSaS sensors. The locations where necessary data for R_{rs} estimations were collected were limited to station visits when there was sufficient daylight to make observations. Table 77 summarizes locations where R_{rs} data are available. Examples of resultant spectra with 95% confidence intervals (CI) are plotted in Figure 87. The CIs were calculated using Student-T coefficients. Similar 95% CI values of R_{rs} spectra have also been reported by other researchers (Kobayashi et al., 2011).

Table 78

Cruises and Stations with R_{rs} Data Availability

Station	Cruise and ^{O}Field of View			
	GC2	GC3	GC4	GC5
A1	3, 25 (2 dates)	25	10	1
A2	3, 25		10	1
A3	25	25		
B1				1, 10
B2				1, 10, 25
B4	3, 25	25		
C0		25	10, 25	1
C1				1, 10, 25
C2		25	10	1
C3		25		
D2		25	10	
D3			10	1, 10, 25
D4		25		1, 10, 25
E0	25			1, 10
E1	3, 25		10, 25	1, 10, 25
E2	3		10	1
E3		25		
F4	25	25		
F5	25	25		1, 10, 25
G2	3, 25			1, 10, 25
G3	3			1, 10, 25
G4	3, 25	25		1, 10, 25
H1		25		
H2	3, 25	25		1, 10
H3	3, 25			1, 10, 25
H4				1
MR1		25		1
MR2		25		1, 10, 25
MR3		25		
NGI8		25		

R_{rs} data is available at selected stations from cruises GC2, GC3, GC4, and GC5. Field of view options include 1^{O}, 3^{O}, 10^{O}, and 25^{O}. Several stations have R_{rs} "replicate" data from multiple FOV options (Figure 87).

This study included water types ranging from fluvial to coastal to offshore. These diverse water types have different characteristic R_{rs} spectral shapes are noted and often associated with different water types. Figure 77 shows examples of R_{rs} spectra representing river, nearshore and offshore waters of this project. Other R_{rs} studies that have sampled multiple water types (or optically complex waters) also show different spectral shape types. These study areas include the Gulf of Lyons (Sylvain Ouillon & Petrenko, 2005), the Santa Barbara Channel (Toole & Siegel, 2001), Patagonian shelf break waters (Ferreira et al., 2013), French Guiana (Froidefond, Gardel, Guiral, Parra, & Ternon, 2002), coastal waters of Hokkaido, Japan (Isada et al., 2015), the Gulf of Thailand (Kobayashi et al., 2011), the English Channel and southern North Sea (Lubac & Loisel, 2007), western India (Menon, Lotliker, & Nayak, 2005) and various Chinese shelf waters (J. Chen, Cui, Qiu, & Lin, 2014).

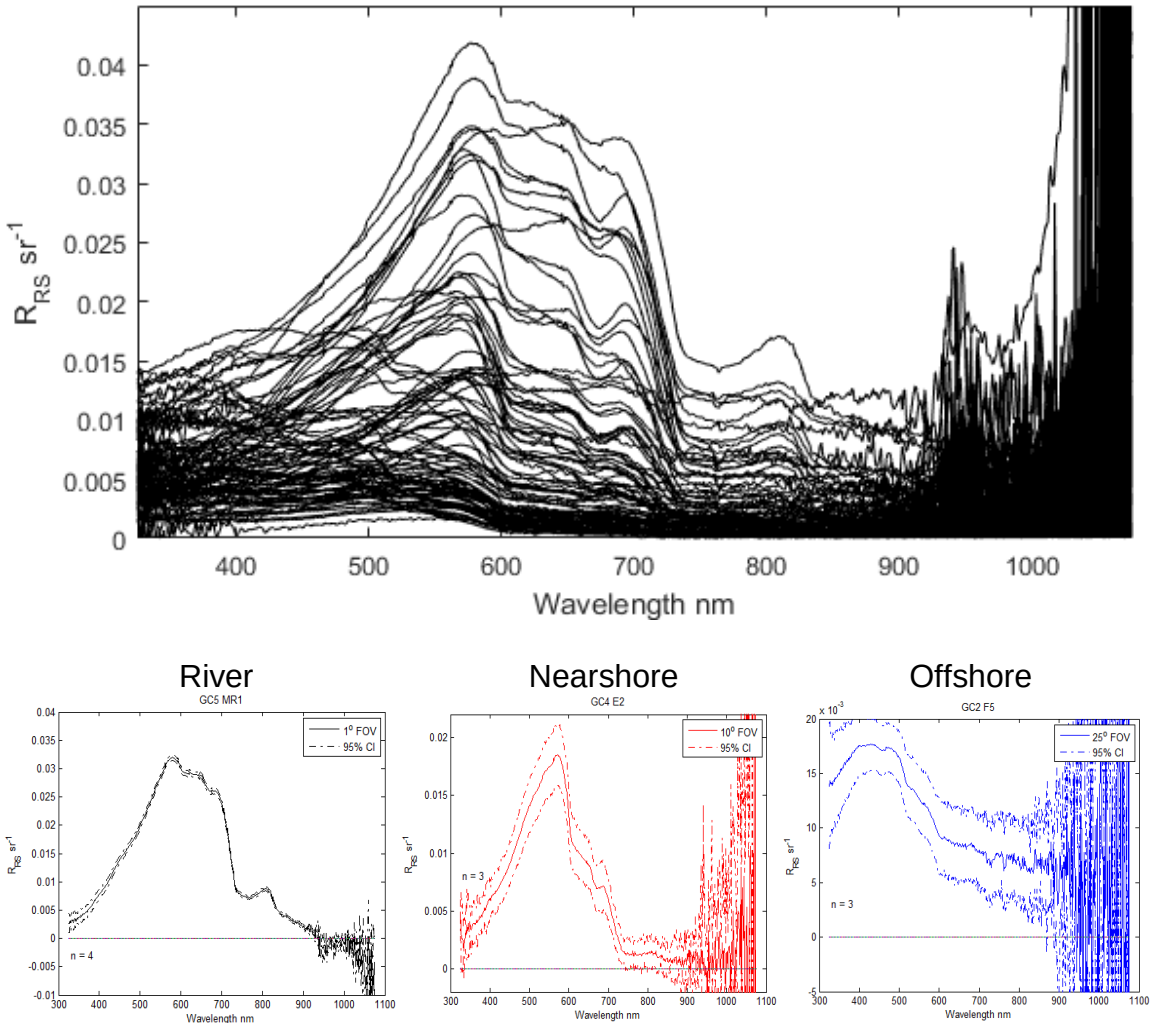

Figure 77. R_{rs} Spectra

R_{rs} spectra for each observed site and each available FOV option. (Where multiple spectra are available for a give FOV option, the mean R_{rs} spectrum is plotted.) Results from the ASD and HyperSaS are shown. n = 97 in the upper plot. The lower three R_{rs} plots show examples of spectral shapes for fluvial waters (left: station MR1, cruise GC5), nearshore waters (middle: station E2, cruise GC4) and offshore (right: station F5, GC2). All four plots in this figure display a lot of noise in the near-infrared wavelengths. These wavelengths are not utilized for SPM prediction.

R_{rs} Data Quality

HyperSaS derived R_{rs} data were available from cruise GC2 for this research. The general data quality assessment began with a qualitative graphical analysis of the R_{rs} spectra derived from that sensor. Several examples are plotted in Figure 87 (located at the

end of the chapter). Overall these R_{rs} spectra had smaller 95% CIs and greater n values than the R_{rs} spectra calculated using the ASD data (Figure 87). The HyperSaS sensor was intended for use while the research vessel was in transit. Therefore, it was turned off during station occupation events. Consequently, for this project, the closest available R_{rs} spectra to the stations visited during GC2 were applied to this research. The mean distance between the locations where the HyperSaS R_{rs} spectra were measured and their associated stations ranged from 42 m at H2 to 7048 m at station G4. Example mean distance values between the station and HyperSaS observations are noted on the individual R_{rs} spectra plots in Figure 87. This offset between observations from the HyperSaS sensor and the station appears to influence the spectral shape of the data related to station A1, located at the mouth of Mobile Bay but is not discernable when compared to ASD data from the other stations (Figure 87).

R_{rs} amplitude differences are apparent between the HyperSaS data, which were obtained using a 3^{O} FOV seaward looking sensor, and the ASD sensor which was employed with the 25^{O} FOV option during cruise GC2. Since amplitude differences were also observed between the different FOV options employed by the ASD sensor at the same stations in cruises GC4 and GC5, this matter is addressed later where differences between all FOV options were considered.

ASD data general quality assessment also began with a qualitative graphical analysis of the R_{rs} spectra derived from that sensor. The available ultraviolet wavelengths (325 nm – 399 nm) were rather noisy (Figure 77). It is believed that glint caused negative sloping R_{rs} features recorded in the ultraviolet region in some of the 25^{O} FOV observations and even in a few instances in the 10^{O} and 1^{O} FOV data from the ASD.

Figure 78 shows two examples of these features. This phenomenon may also be noted in some of the R_{rs} spectra plotted in Figure 87 including cruise GC2, stations A2 and G4, cruise GC4, station C0, and cruise GC5, stations G3 and G4. The CIs are larger in association with these features than they are in relation to the remaining wavelengths of the affected spectra.

At the other end of the observational spectrum, the data became extremely noisy in the infrared wavelengths greater than 900 nm. Therefore, R_{rs} data for 900 nm thru 1075 nm were not considered in this study. In spectra that did not have a universally large 95% CI, such as the ones seen at cruise GC2, station E0 (Figure 79), the greatest amount of uncertainty often took place between 325 nm and 450 nm as seen in cruise GC2, station A3 (Figure 78) and in various plots in Figure 87.

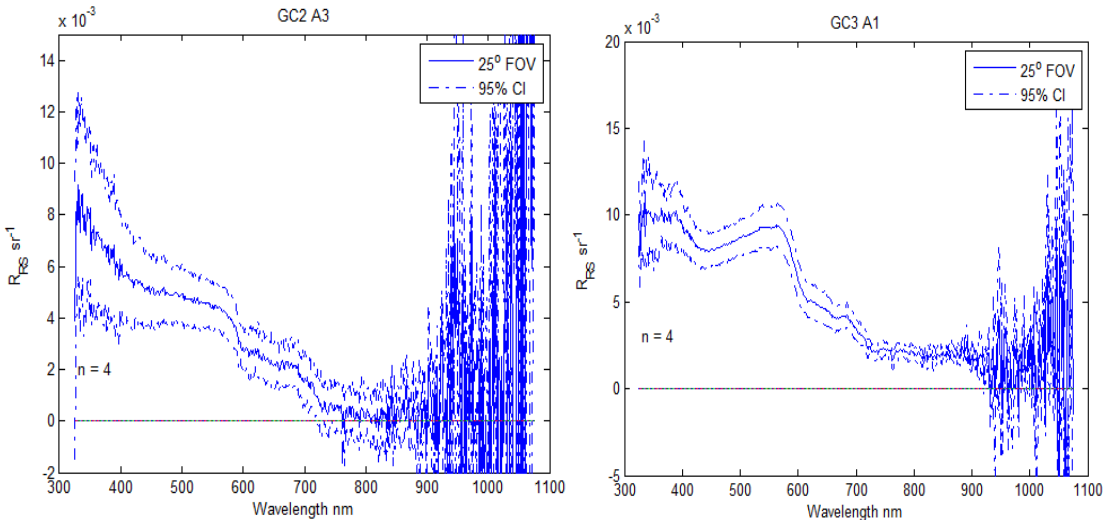

Figure 78. Examples of ASD R_{rs} Spectra

Examples of suspected glint affecting 300 nm thru 400 nm. Examples of infrared noise are also displayed.

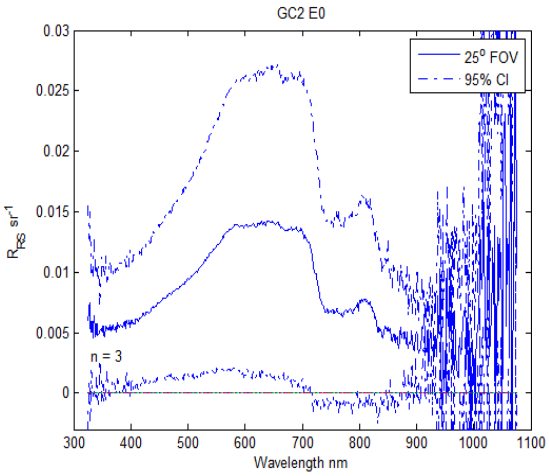

Figure 79. ASD R_{rs} at Station E0, Cruise GC2

This figure shows an example of a very large 95% CI. It also demonstrates noise typical in this project in the NIR. The mean R_{rs} spectrum is representative of river outlet waters associated with the Atchafayala River.

Several ASD R_{rs} spectra unexpectedly displayed regions of negative values at wavelengths less than 900 nm (Figure 77). (See also Figure 87 for additional examples including cruise GC2, stations A1a, A2, and H3, and cruise GC5, station B2.) In all cases but one (GC5, B2), this phenomenon was observed in spectra collected by the ASD using a 25° field of view instrument configuration. When negative R_{rs} values occurred, sea radiance observations had greater values than sky radiance observations. One possible reason for these abnormal circumstances could be due to the under-sampling of the calibrated surfaces. These surfaces were usually observed once (where n usually equaled 5) for each FOV attachment at each station rather than after each sky-sea observational pair. This procedure imposed varying time lapses between the sky-sea observational pairs and the calibrated surface. Longer time lapses allowed greater potential for variations in the natural light, especially when overhead conditions included cloud cover. Since the sea observations were much lower in value than the sky observations, these radiometric corrections involving the calibrated surfaces would have a much greater impact on the

sea values than the sky values. Another possible reason for observations of higher upwelling radiance values from the sea surface than the estimated downwelling radiance (E_d) from the sky could have been due to sea surface focusing, or glint. This phenomenon of negative R_{rs} values casts doubt on the validity of the absolute amplitude accuracy of the R_{rs} values particularly when measurements were collected with a 25^O FOV. However, value may still be attributed to relative amplitude or spectral shape of the R_{rs} values. Steps taken towards that achievement are detailed hereafter.

Data quality procedures applied to both sensors helped to quantify uncertainty. One data quality assessment technique used in evaluating R_{rs} spectra was the calculation of the spectral noise to signal ratio (NSR) of the data. Spectral NSR was calculated for each FOV at each station. (See Figure 80 for examples.) This procedure was done to determine if the data had quantitative value. Ratio values greater than or equal to 1 indicate that the R_{rs} data associated with that particular station, FOV and affected wavelengths were too noisy to produce a meaningful R_{rs} value. NSR values were calculated using the relationship

$$NSR(\lambda) = \frac{STD_{R_{rs}S}(\lambda)}{mean_{R_{rs}S}(\lambda)} \ . \qquad (6.1)$$

Here, $S(\lambda)$ represented R_{rs} signal strength for a specific wavelength. STD_{Rrs} and $mean_{Rrs}$ were the standard deviation and mean of wavelength specific R_{rs} value respectively.

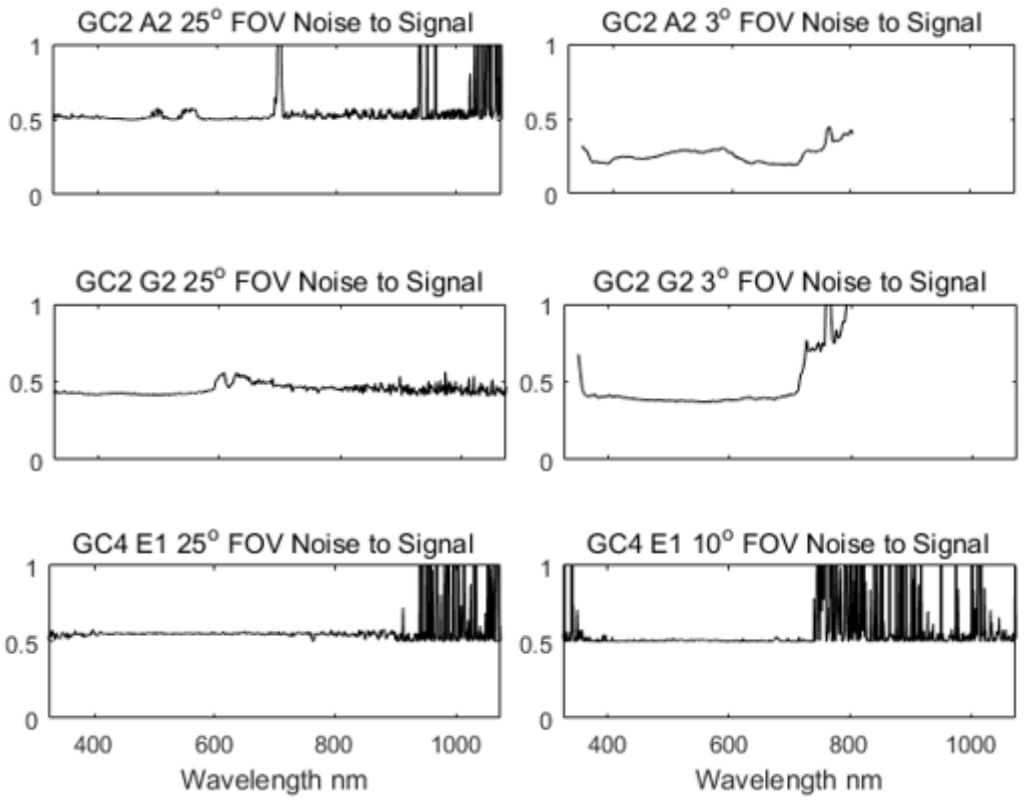

Figure 80. Noise to Signal Ratios for Selected Cruises and Stations

This figure displays examples of spectral NSR from the ASD sensor using 25^{O} and 10^{O} fore-optic attachments. Examples of HyperSaS data represented by 3^{O} FOV are also provided.

Overall the NSRs related to the R_{rs} values calculated using ASD data were rather high near 0.5. Conversely, R_{rs} values derived using HyperSaS data were less noisy with NSR values at about 0.3 in the visible light range and approaching 0.5 – 0.6 in the near-infrared region. These generally lower NSR values associated with the HyperSaS could be due to the large volume of R_{rs} spectra relative to the small number of R_{rs} values produced using the ASD. Though the summary plot in Figure 81 shows fairly consistent NSR values across the spectral range of the ASD sensor, there was a lot of individual variation at the different stations and FOV options. (Spectral NSRs based upon the field

of view are seen in Figure 82). The median and MAD values of spectral R_{rs} NSR utilized in this project are also displayed in Figure 81.

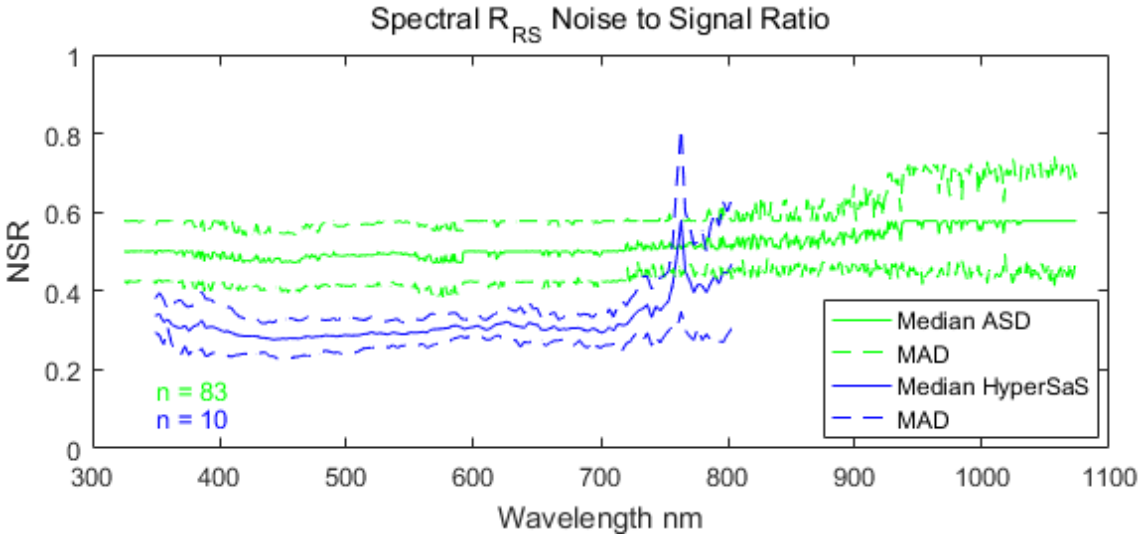

Figure 81. R_{rs} Noise to Signal Ratios by Sensor

Median and MAD R_{rs} NSR spectra for the ASD and HyperSaS sensors.

In Figure 81, no distinction was made between the FOVs for the R_{rs} derived from the ASD data. (In other words, all ASD based R_{rs} spectra, regardless of the FOV option used for data collection were used to calculate the median and MAD valued of the NSR for that sensor in Figure 81.) In contrast, Figure 82 shows spectral median and MAD NSR values using all available data for each field of view. This figure suggests that FOV option might affect the NSR particularly between 500 nm and 600 nm for the 25º FOV and above 900 nm for the 10º FOV. Figure 82 further suggests that the NSR increases with increasing FOV angular option of the ASD.

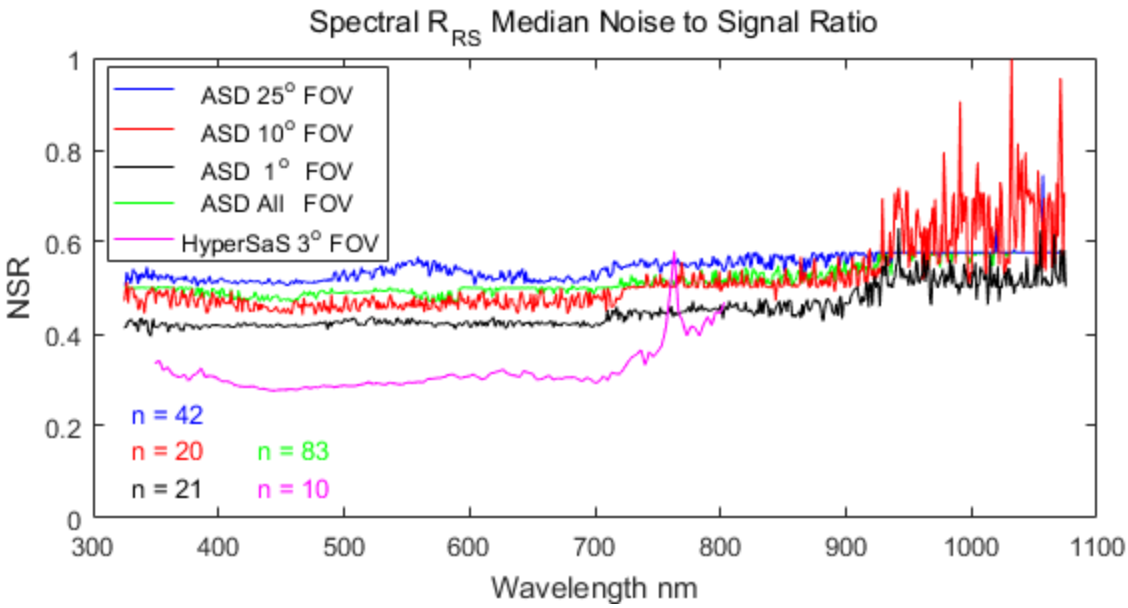

Figure 82. R_{rs} Noise to Signal Ratios by FOV

Medians of the R_{rs} spectral NSR are plotted. Median ± MAD values are not plotted since the result was too busy to provide a meaningful visual reference.

In most cases, however, not all FOV options were employed for the ASD at all stations. In every case where HyperSaS data was available in conjunction with ASD data, only the FOV option of 25° was used. However, during GC5, there were nine instances where all three FOV options for the ASD were successfully employed at the same station. These observations occurred at stations B2, C1, D4, E1, F5, G3, G4, H3, and MR2. To evaluate whether the FOV option had a significant impact on the NSR, median and MAD NSR values were calculated for the three different FOV options using the data from these nine stations (Figure 82). There was 100% overlap between the median ± MAD ranges for the 25° FOV to 10 ° FOV evaluation and for the 10° FOV to 1° FOV comparison. This means that the spectral NSR ratios were statistically the same. For most wavelengths, there was also overlap in the median ± MAD ranges for the 25° FOV to 1° FOV evaluation with four exceptions in the visible light range. These occurred at 588 nm, 599

nm, 603 nm and 606 nm and had values less than 0.01. Additional wavelengths of non-overlap within the 25^{O} FOV to 1^{o} FOV comparison occurred in the near infrared (700 nm – 900 nm) wavelength range at 704 nm, 710 nm, and 815 nm. The largest of these values occurred at 704 nm with a value of 0.0244. These results suggest that the FOV option used with the ASD sensor had little to no effect on the on the NSRs of the resultant R_{rs} values. It is worth noting that though the NSR values are high between 900 nm and 1075 nm in Figures 82 and 83 for all three FOV options, this noisiness is not a universal feature as demonstrated in Figure 80.

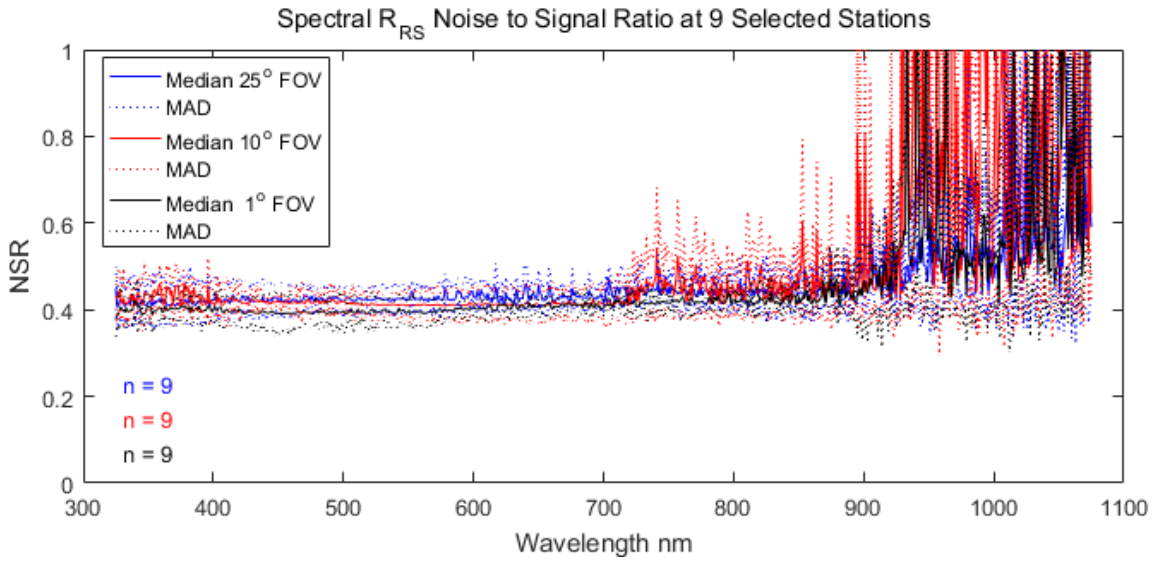

Figure 83. R_{rs} NSR for Stations Observed with Three ASD FOV Options

Medians of the R_{rs} with± MAD values are plotted for stations where all three ASD FOV options were employed. This occurred during GC5 at stations B2, C1, D4, E1, G3, G4, H3, and MR2.

Environmental sources of uncertainty in R_{rs} spectra include the effects of entrained bubbles (Stramski & Tegowski, 2001) and glint (Monzon, Forester, Burkhart, & Bellemare, 2006; André Morel & Gentili, 2008; Mustard, Staid, & Fripp, 2001). There has been a great deal of discussion about the effect of sun glint off faceted sea surfaces (Dev & Shanmugam, 2014; Kutser, Vahtmäe, Paavel, & Kauer, 2013; Kutser, Vahtmäe,

& Praks, 2009; Mobley, 1999). There is disagreement about how best to address this problem. Glint correction methods have been put forth by applying uniform and non-uniform, linear and non-linear solutions upon affected spectra (Dev & Shanmugam, 2014; Kutser et al., 2013; Kutser et al., 2009). None of these methods appear to be appropriate for the entire R_{rs} data set in the northern Gulf of Mexico as several different water types are represented in the project area.

Normalization of R_{rs} Data

One approach to working with meaningful versions of R_{rs} spectra in order to produce results relevant to future work includes subjecting the data to a researcher-defined (i.e., arbitrarily defined) normalization process (de Moraes Rudorff et al., 2014; David Doxaran, Froidefond, Lavender, & Castaing, 2002; Giannini, Garcia, Tavano, & Ciotti, 2013; Hooker, Morrow, & Matsuoka, 2013; Ma et al., 2011; Simis & Olsson, 2013; Torrecilla, Stramski, Reynolds, Millán-Núñez, & Piera, 2011). To minimize the potential effects of glint and sub-zero R_{rs} values occasionally encountered in the ret to near-infrared wavelengths, this concept was applied to the R_{rs} data in this study. Each R_{rs} spectrum was normalized so that between the range of 350 nm to 802 nm, the lowest value was set to zero and the highest value set to one. The range considered during the normalization process was selected because it was the largest interval produced when the HyperSaS R_{rs} data was interpolated (linearly) to each integer wavelength. As a result, some of the normalized data from the ASD exceeded the zero-to-one boundaries for wavelengths in the ranges 235 nm - 349 nm and 803 – 900 nm. (Data from these two wavelength ranges were not used for SPM prediction.) ASD R_{rs} data beyond 900 nm were not normalized. Once each spectrum for each FOV option at each station was

normalized, median and MAD spectral values were calculated of the new datasets (Figure 84).

Since many R_{rs} and normalized R_{rs} spectra evidence a minor peak near 800 nm, a second range for normalization of ASD R_{rs} spectra was performed to see if data quality could be improved in the near-infrared wavelengths by extending the wavelength range for normalization evaluation from 400 nm to 900 nm (Figure 84). The frequent noisiness of the wavelengths greater than 803 nm caused the lowest values (which were adjusted to zero) to shift to the right. The result of this shift created a reduction of the vertical exaggeration of the spectral shapes. It appears that the new minimum values were related to noise rather than to minimal values associated with small peaks near 800 nm as those features were not better resolved by applying this normalization procedure. This range of normalization also appeared to increase the overall noisiness of the resultant spectra between 725 nm and 900 nm. Consequently, no further analysis was performed on normalized R_{rs} spectra that used an evaluation range of 400 nm – 900 nm.

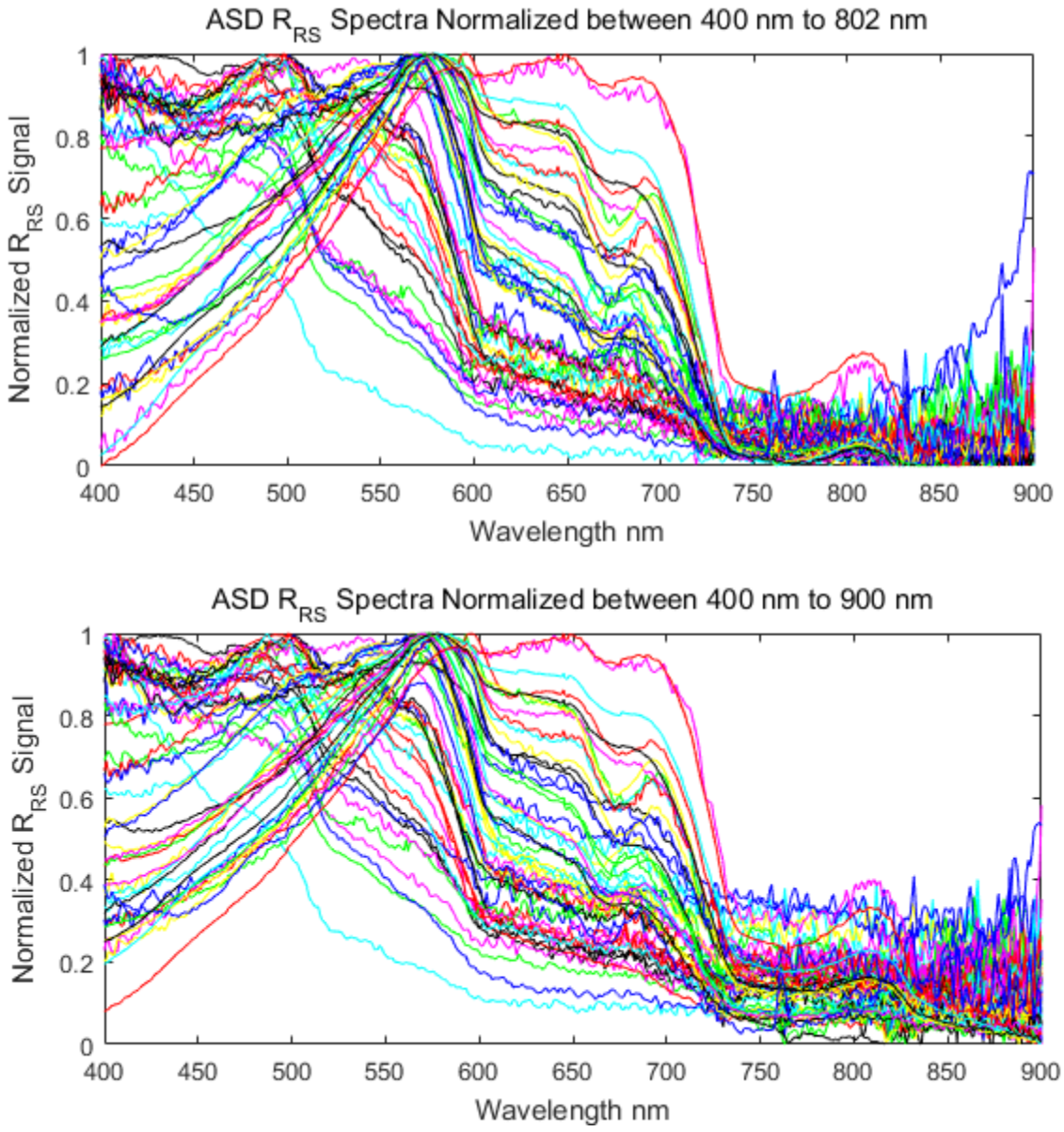

Figure 84. Spectral Normalization Using Two Wavelength Ranges

Top: ASD normalized R_{rs} spectra were calculated using maximum and minimum data within the 400 nm to 802 nm wavelength range. Bottom: ASD normalized R_{rs} spectra were calculated using maximum and minimum data within the 400 nm to 90 nm wavelength range.

SPM Prediction from R_{rs}

The normalized spectra (plotted in Figures 84 and 87) make it easier to see two things. First, regardless of the field of view used for observation, the wavelengths of

maximum R_{rs} (or normalized R_{rs}) appear to be approximately the same. Second, the suspected glint features noted in some spectra between 300 nm and 400 nm diminish with the decreased angular field of view. Furthermore, as the maximum peak of the R_{rs} spectra moves to longer wavelengths, SPM concentration generally increases. This trend has also been noticed by other researchers (Jian Li, Chen, Tian, Huang, & Feng, 2015), but not yet used for estimating SPM concentration. Figure 85 shows this relationship between SPM and the normalized wavelength of maximum R_{rs} value. This relationship has a strong correlation value of $\rho = 0.88$ ($p = 0.00$, $n = 63$).

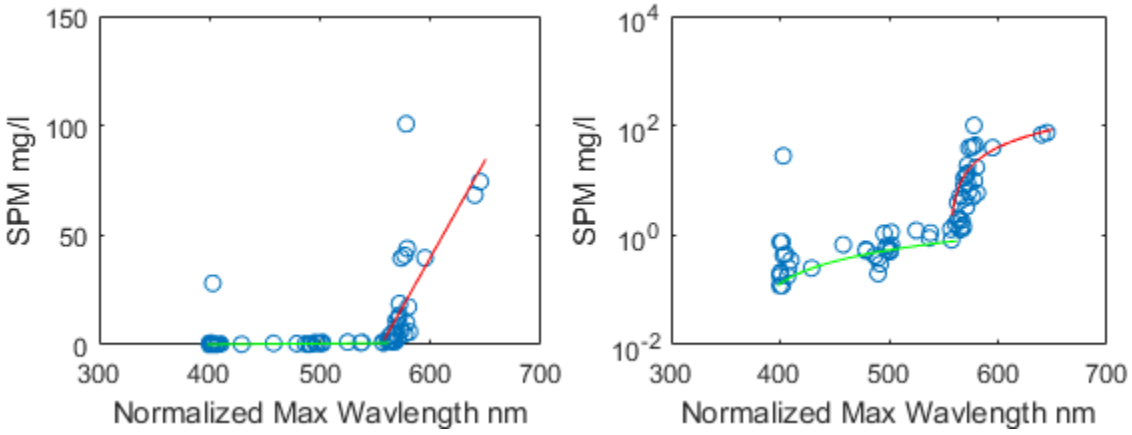

Figure 85. SPM vs. Normalized Maximum R_{rs} Wavelength

Note: the y-axis on the left plot is linear while it is in log scale on the right. n = 63

Two linear regressions were applied to these datasets. The first regression was for wavelengths 400 nm thru 560 nm. The second was for 560 nm thru 650 nm. The results are described in equations 6.2 and 6.3.

For $\lambda \leq 560$: $SPM = 0.00440\ (\pm 0.00327) * \lambda - 1.49005\ (\pm 1.52007)$ (6.2)

For $\lambda > 560$: $SPM = 0.89618\ (\pm 0.00968) * \lambda - 497.79175\ (\pm 5.58446)$ (6.3)

Algorithm coefficient uncertainties determined through singular value decomposition are in parentheses. λ represents the wavelength of normalized maximum R_{rs} value. The

RMSE values are 4.77 and 18.11 for equations 6.2 and 6.3 respectively. Neither of these linear regressions utilized the outlier point at λ = 403 nm and SPM = 28.05 mg/l, though this point was used in the RMSE evaluation for equation 6.2. However, if this outlier is removed from RMSE calculations, that value drops dramatically to RMSE = 0.24. This outlier occurred at Station MR1 during GC3 using the 25^{O} field of view (Figure 86). The peak occurring at 403 nm for this observation does not occur in the R_{rs} spectra of other high SPM concentration locations observed during this research suggesting that it might be a glint artifact.

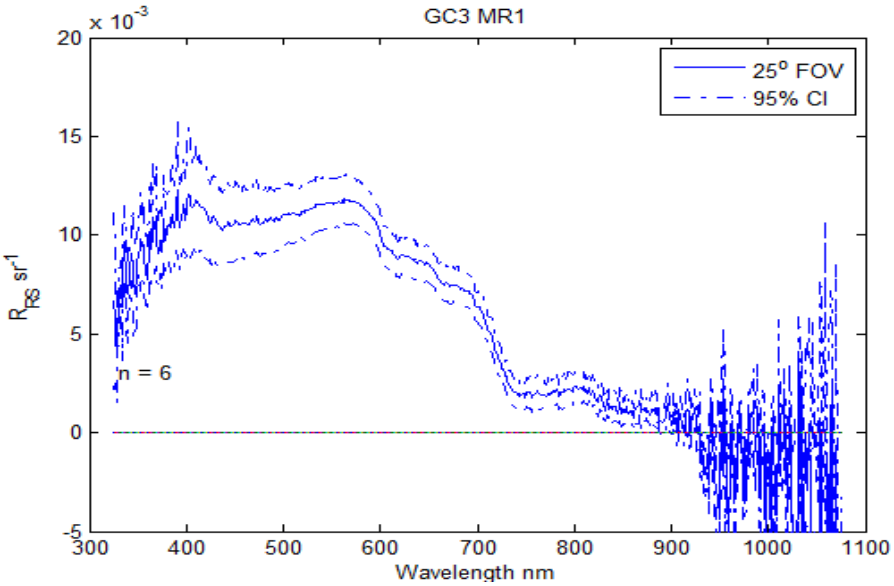

Figure 86. R_{rs} at Station MR1, Cruise GC3

This figure shows the mean and 95% CI of R_{rs} at this station.

The SPM prediction based upon the wavelength of maximum R_{rs} value represents a new way to estimate SPM from an AOP. The large uncertainties associated with these algorithms make these regression-based models produced here less useful than many of the IOP-based SPM models discussed in Chapter V. Unfortunately, an RMSE based scoring parameter cannot be established for these two equations, so scores cannot be

developed for comparison with the IOP based SPM models. However, the R_{rs} based algorithm may be useful in first-order SPM estimation in locations where in-situ data is not available.

It is also possible that an improved sampling scheme for the ASD sensor would produce data yielding better-tuned results. Those modifications would include the exclusive use of the 1^{O} FOV fore-optic attachment. Also, reference surfaces would be observed between each set of sky and sea observations so that each calculated R_{rs} spectrum would be completely independent.

Hopefully, these two modifications to the methods used in this research would eliminate some of the noisiness that was particularly noticeable in some of the 25^{O} FOV spectra in this project. This noisiness can be detected in several plots of Figure 87. In this research, that noisiness had an effect on the calculation of wavelength used in the data pairs plotted in Figure 84. This effect was noticed in three of the nine cases where all three FOV options were utilized at the same place. Table 79 demonstrates the effect of using 25^{O} FOV R_{rs} data on the determination of the wavelength of the maximum R_{rs} signal. Referencing information available in Table 79, one may use extrapolation to hypothesize that approximately one-third of the 25^{O} FOV R_{rs} spectra in this project exhibit significantly different wavelengths of maximum R_{rs} signal than R_{rs} spectra produced using smaller FOV options would have. This suggests that better-tuned SPM algorithms based upon the wavelength of maximum R_{rs} signals are possible. Additionally, if the negatively sloping features noted in some of the R_{rs} spectra can be proven to be glint artifacts, their removal may also improve the calculated relationship between SPM and R_{rs} spectra.

Table 79

Examples of 25^{O} FOV Influence on Wavelength of Maximum R_{rs} Signal

Station	FOV^{O}	Wavelength Max nm	Mean Wavelength nm	STD	Wavelength Max Without 25^{O} FOV nm	Wavelength STD Without 25^{O} FOV nm
B2	1	563	556.7	13.7	564.5	2.1
	10	566				
	25	541				
C1	1	568	568.7	0.6		
	10	569				
	25	569				
D4	1	486	458.0	46.8	485.0	1.4
	10	484				
	25	404				
E1	1	577	578.3	1.2		
	10	579				
	25	579				
F5	1	400	401.3	2.3		
	10	400				
	25	404				
G3	1	539	525.0	21.7	537.5	2.1
	10	536				
	25	500				
G4	1	501	497.3	4.0		
	10	498				
	25	493				
H3	1	546	557.3	10.0		
	10	565				
	25	561				
MR2	1	578	576.7	1.2		
	10	576				
	25	576				

Conclusions

This chapter addressed Hypothesis 3 which stated that "SPM can be predicted with varying degrees of uncertainty from inherent optical properties and apparent optical properties." Per Objective 1 of that hypothesis which was to evaluate SPM relative to the "apparent optical property remote sensing reflectance data from above deck sensors. Correlation parameters between R_{rs} and SPM were calculated." The AOP R_{rs} data were analyzed and utilized for SPM prediction. Unlike the IOP SPM models, R_{rs} cannot predict SPM with a single linear regression. Instead, multiple linear regressions were produced to estimate SPM from two different wavelength ranges in a novel approach to estimate SPM concentration. Suggestions were made to improve future R_{rs} research using the ASD.

Plots

The plots in Figure 87 show R_{rs} spectra developed using different FOV options. Plots on the right display the normalized versions of those spectra. Ninety-five percent CIs were plotted in all cases. "Mean Diff." plots show the differences between the various mean values. Plots labeled "Outliers" display differences between maximum and minimum CIs when those boundaries did not overlap between the means.

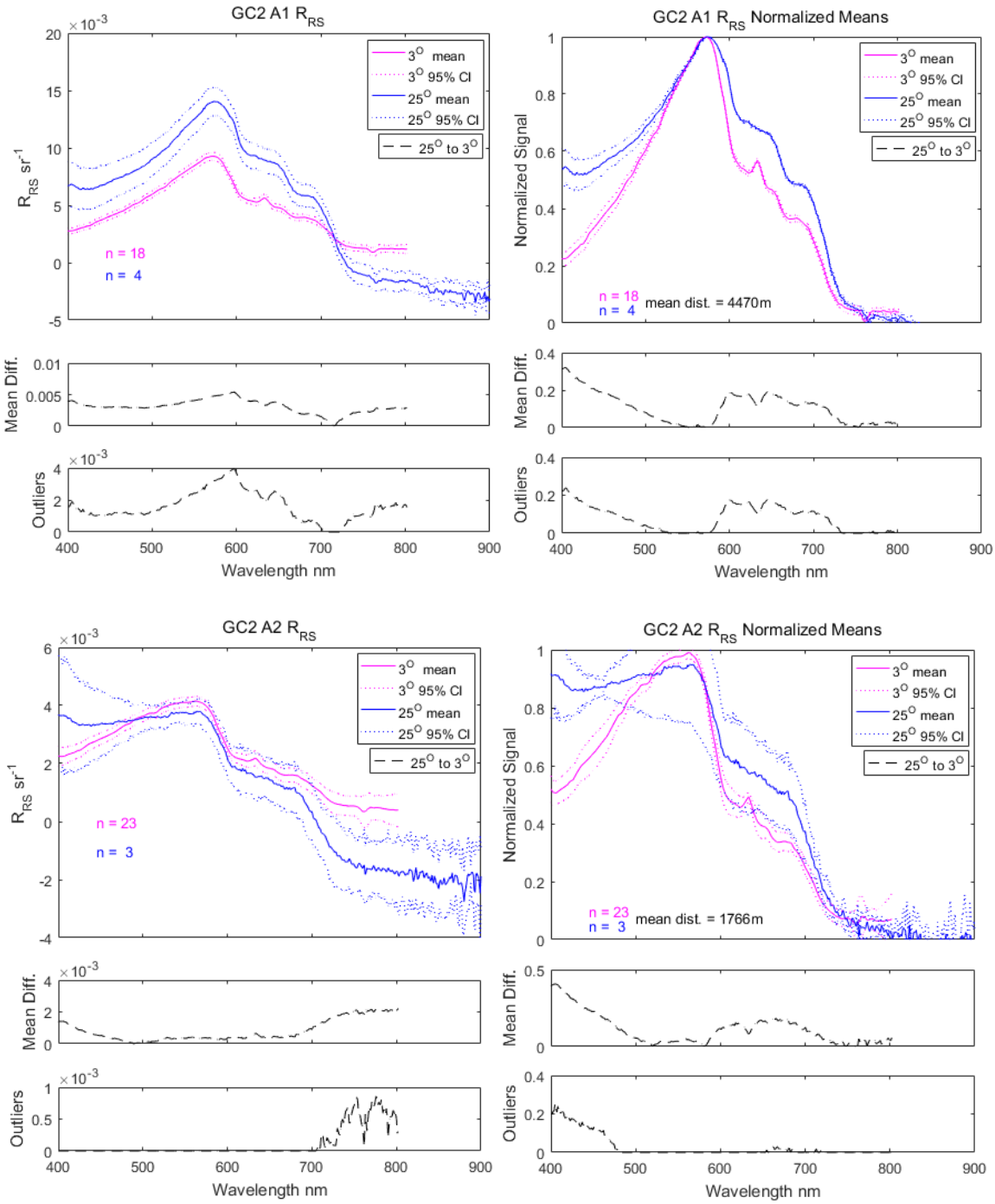

Figure 87. R_{rs} & Normalized R_{rs} Spectral Shape Comparisons

Plots on the left display mean R_{rs} spectra with 95% CIs. Plots on the right display normalized mean R_{rs} spectra with 95% CIs for the same datasets. Mean Diff. plots show the differences between the various mean values. Plots labeled “Outliers” display differences between maximum and minimum CIs when those boundaries did not overlap between the means.

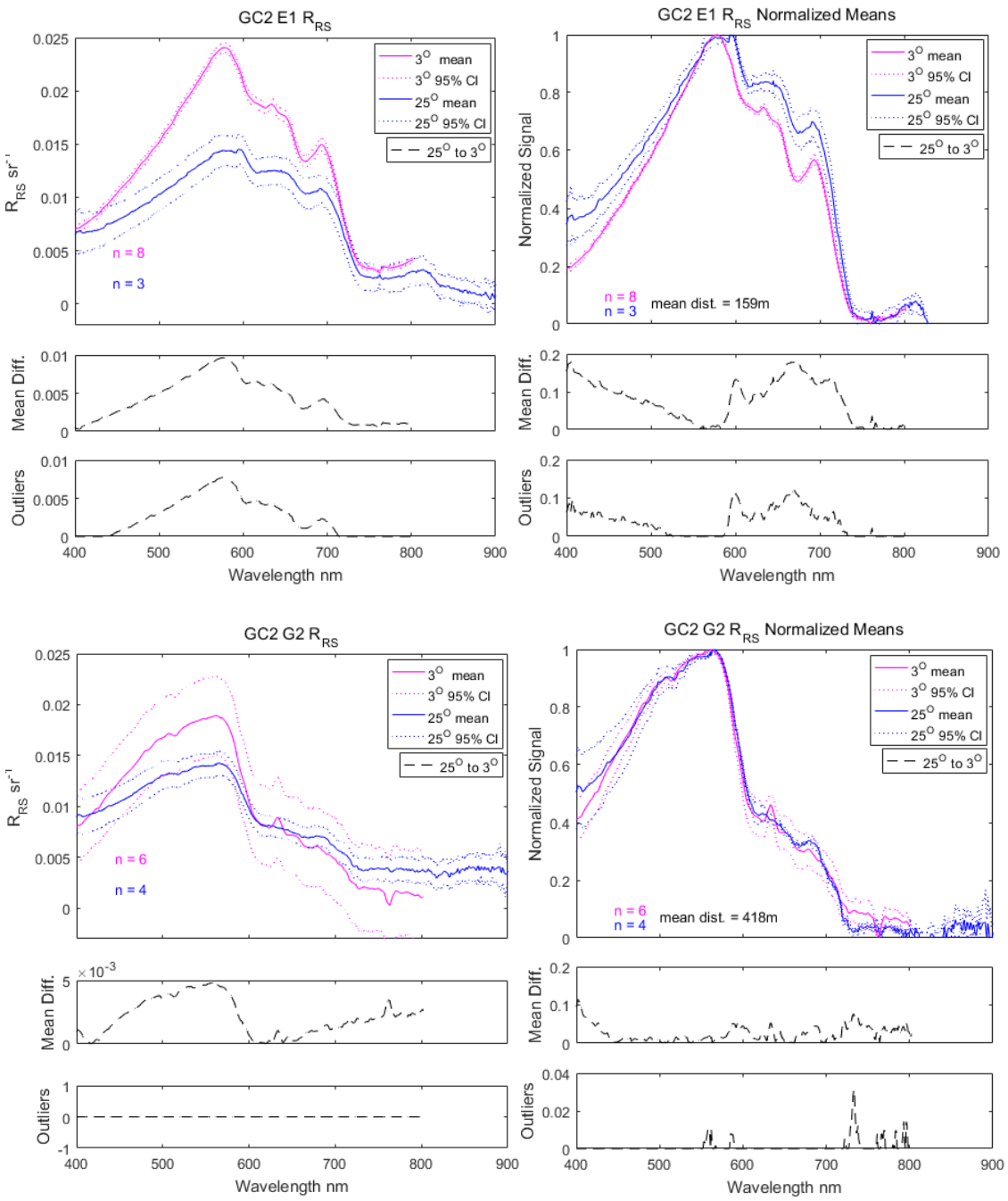

Figure 87 (continued). R_{rs} & Normalized R_{rs} Spectral Shape Comparisons

Plots on the left display mean R_{rs} spectra with 95% CIs. Plots on the right display normalized mean R_{rs} spectra with 95% CIs for the same datasets. Mean Diff. plots show the differences between the various mean values. Plots labeled “Outliers” display differences between maximum and minimum CIs when those boundaries did not overlap between the means.

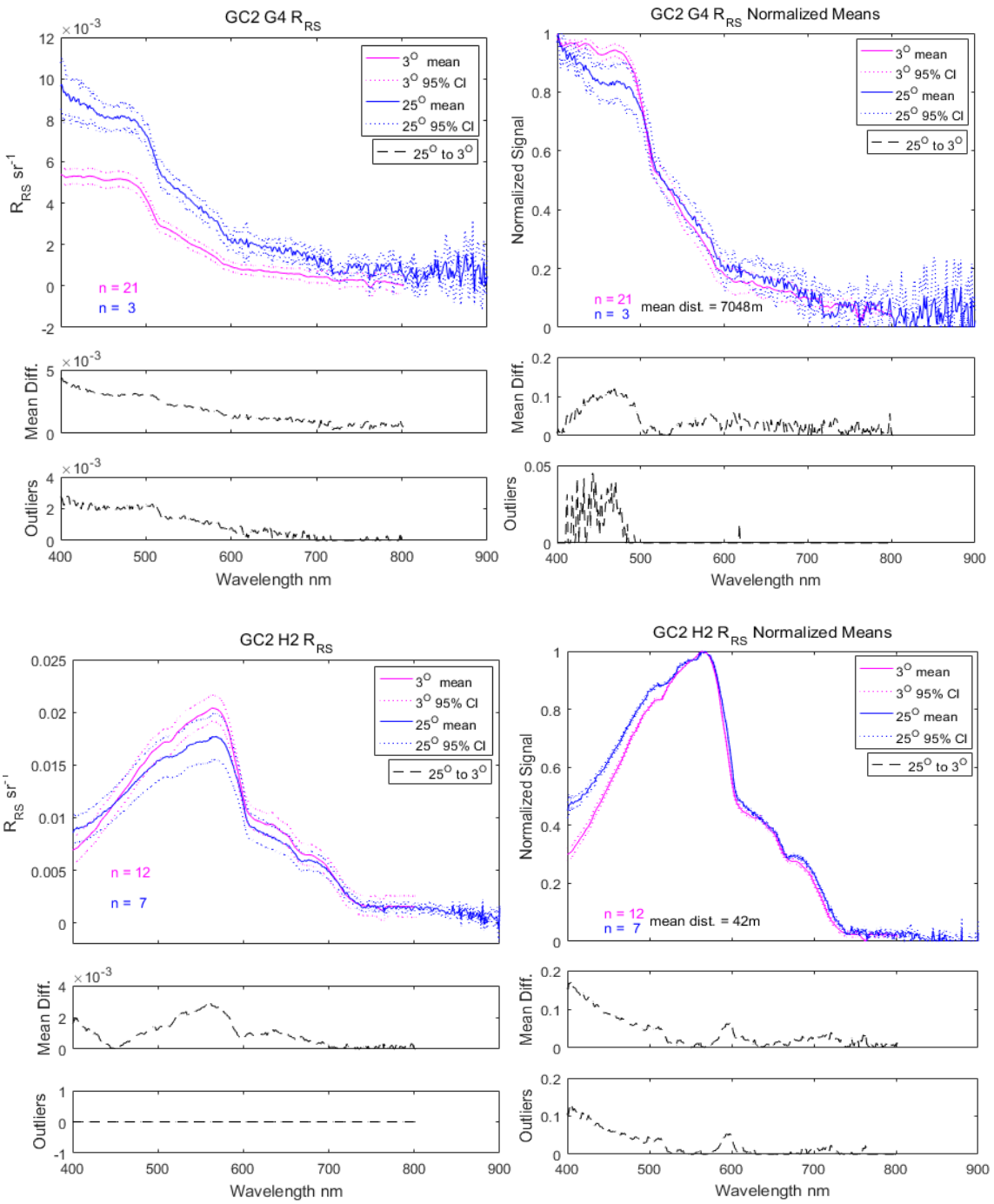

Figure 87 (continued). R_{rs} & Normalized R_{rs} Spectral Shape Comparisons

Plots on the left display mean R_{rs} spectra with 95% CIs. Plots on the right display normalized mean R_{rs} spectra with 95% CIs for the same datasets. Mean Diff. plots show the differences between the various mean values. Plots labeled “Outliers” display differences between maximum and minimum CIs when those boundaries did not overlap between the means.

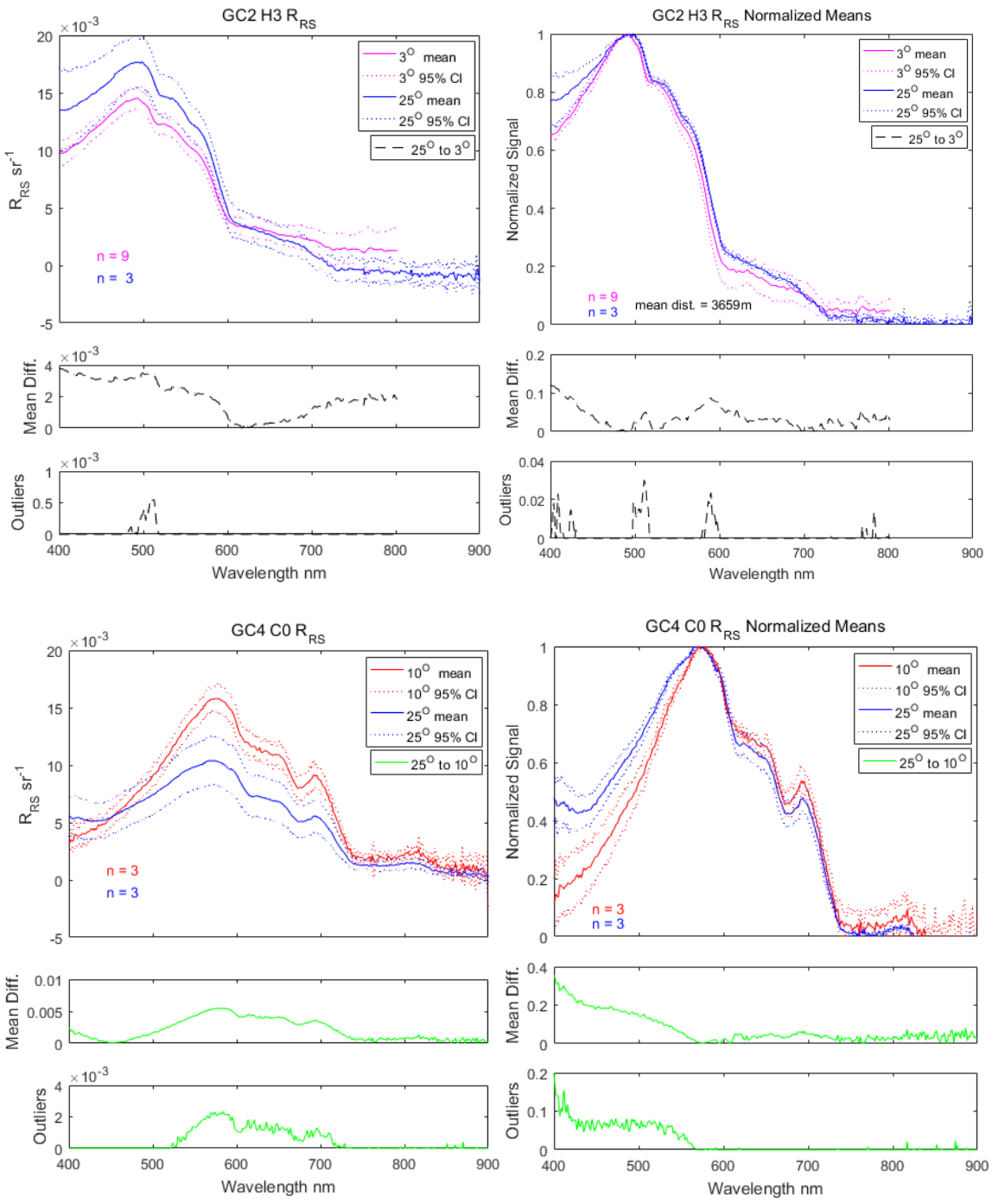

Figure 87 (continued). R_{rs} & Normalized R_{rs} Spectral Shape Comparisons

Plots on the left display mean R_{rs} spectra with 95% CIs. Plots on the right display normalized mean R_{rs} spectra with 95% CIs for the same datasets. Mean Diff. plots show the differences between the various mean values. Plots labeled “Outliers” display differences between maximum and minimum CIs when those boundaries did not overlap between the means.

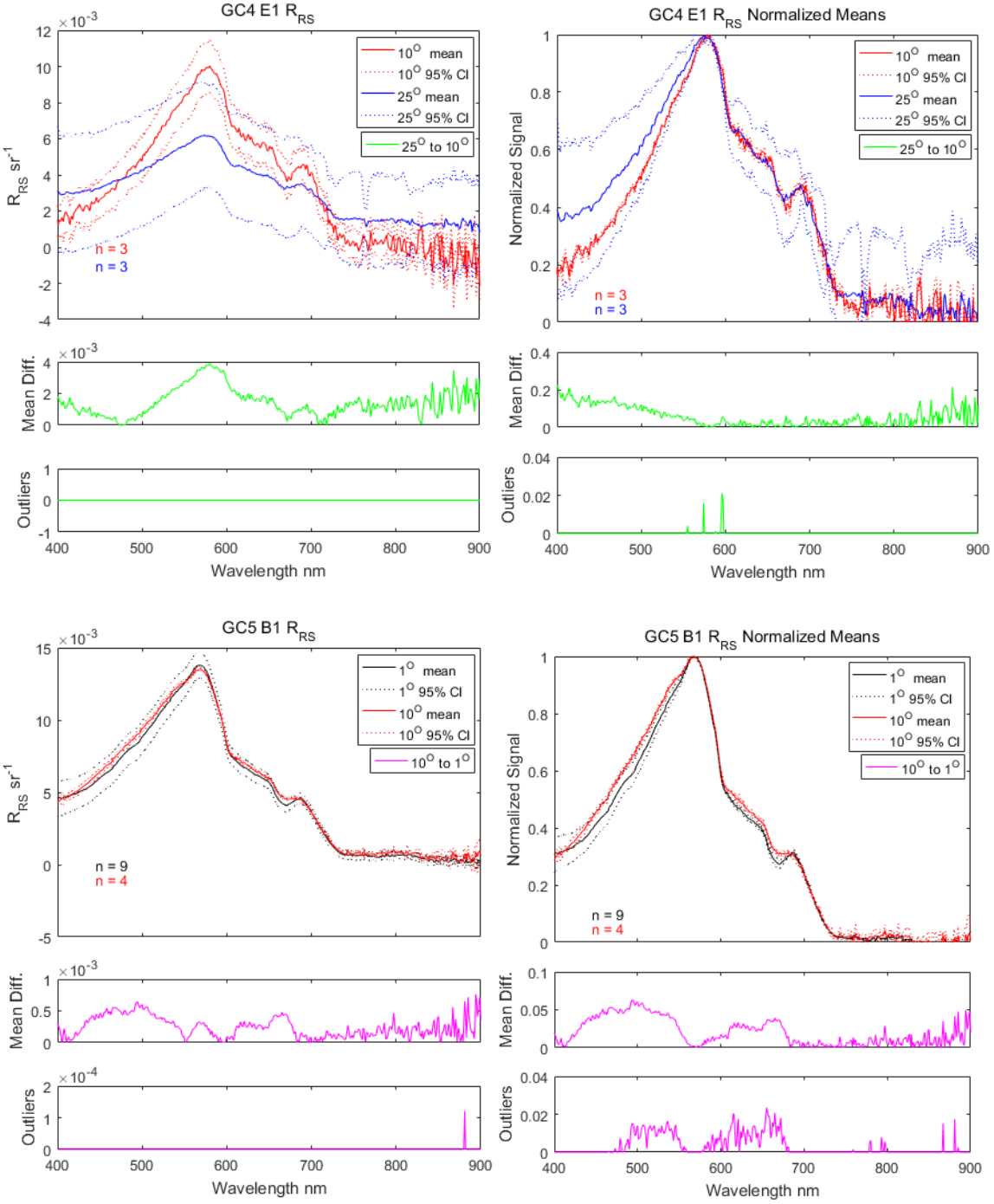

Figure 87 (continued). R_{rs} & Normalized R_{rs} Spectral Shape Comparisons

Plots on the left display mean R_{rs} spectra with 95% CIs. Plots on the right display normalized mean R_{rs} spectra with 95% CIs for the same datasets. Mean Diff. plots show the differences between the various mean values. Plots labeled “Outliers” display differences between maximum and minimum CIs when those boundaries did not overlap between the means.

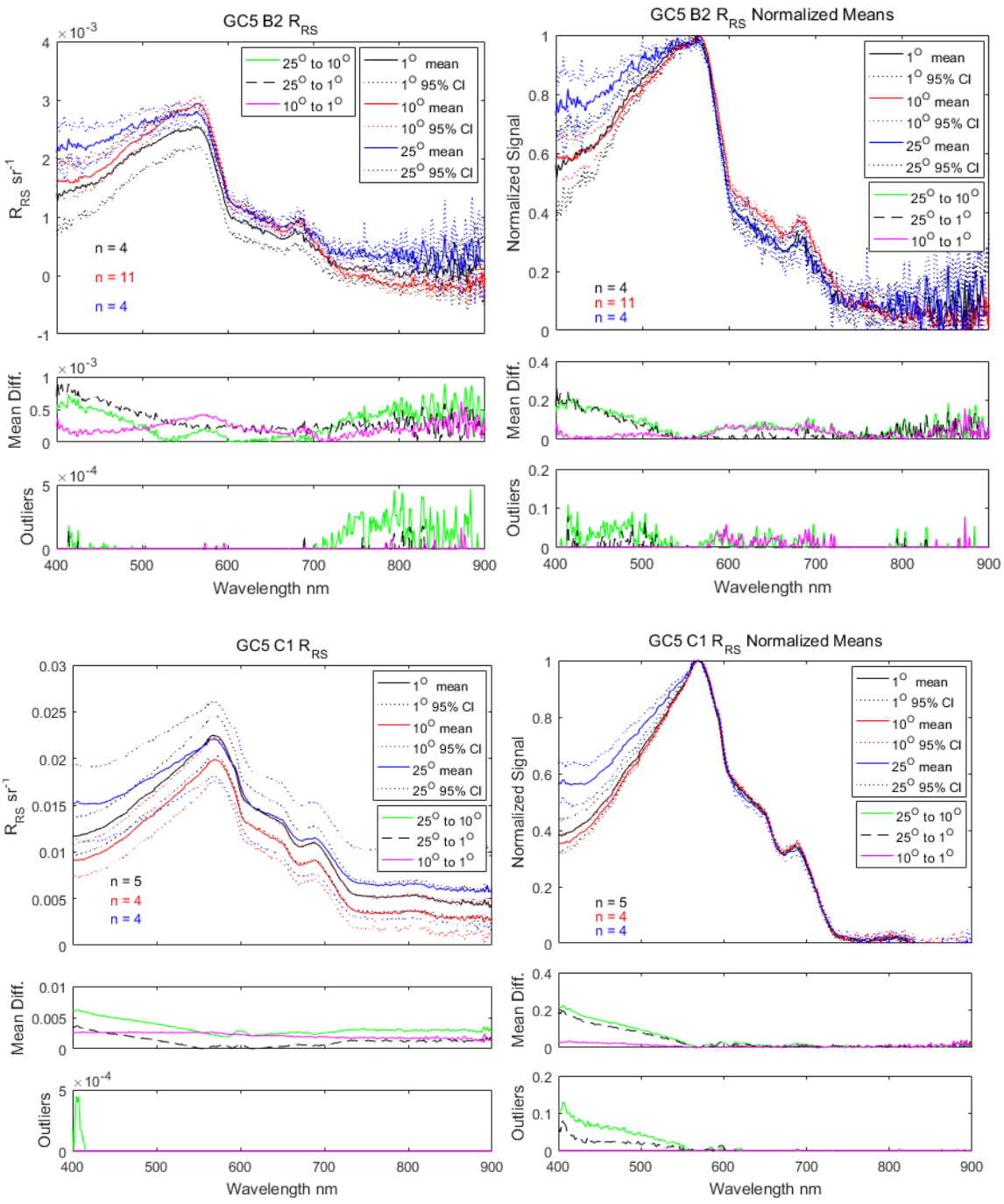

Figure 87 (continued). R_{rs} & Normalized R_{rs} Spectral Shape Comparisons

Plots on the left display mean R_{rs} spectra with 95% CIs. Plots on the right display normalized mean R_{rs} spectra with 95% CIs for the same datasets. Mean Diff. plots show the differences between the various mean values. Plots labeled "Outliers" display differences between maximum and minimum CIs when those boundaries did not overlap between the means.

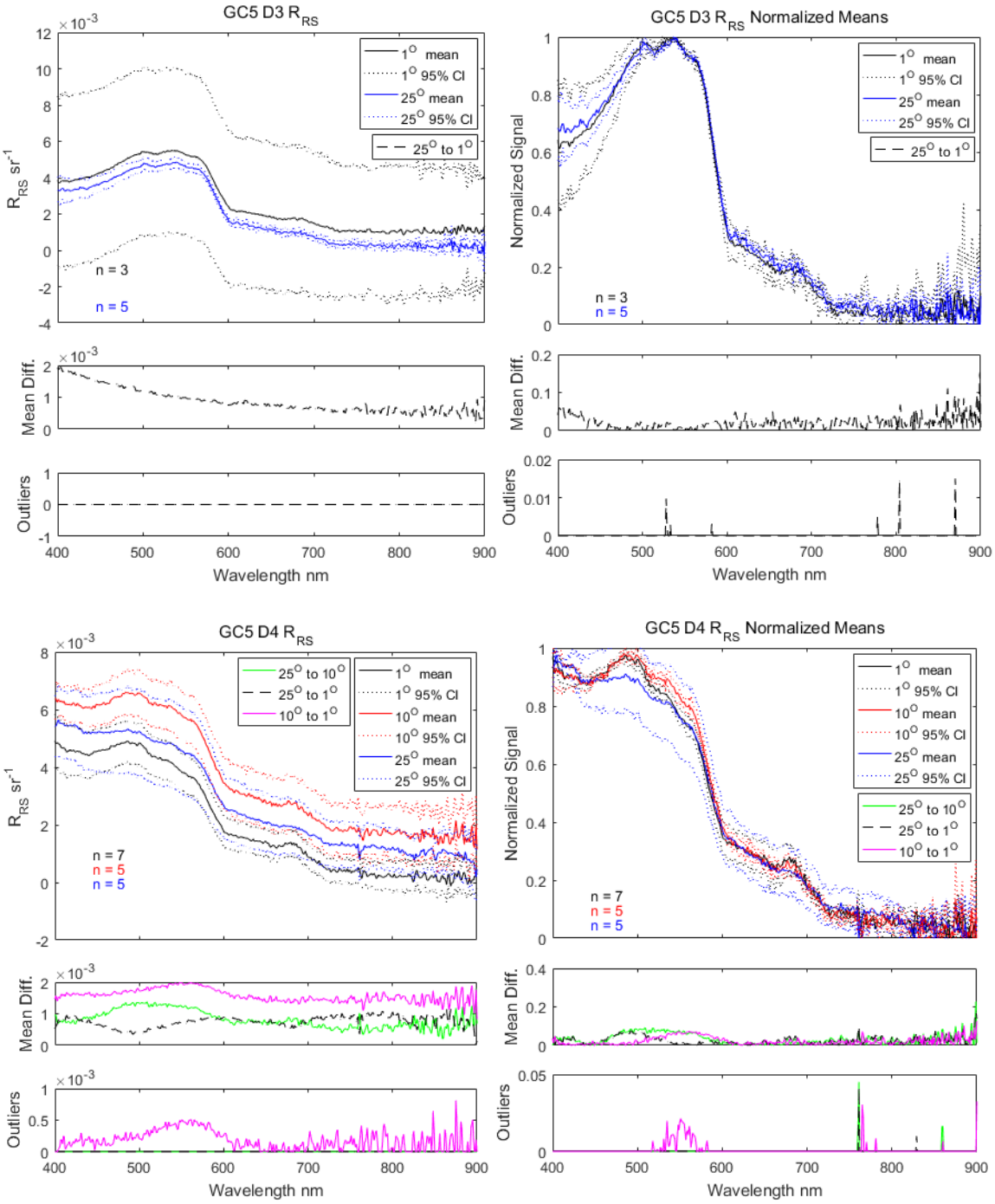

Figure 87 (continued). R_{rs} & Normalized R_{rs} Spectral Shape Comparisons

Plots on the left display mean R_{rs} spectra with 95% CIs. Plots on the right display normalized mean R_{rs} spectra with 95% CIs for the same datasets. Mean Diff. plots show the differences between the various mean values. Plots labeled “Outliers” display differences between maximum and minimum CIs when those boundaries did not overlap between the means.

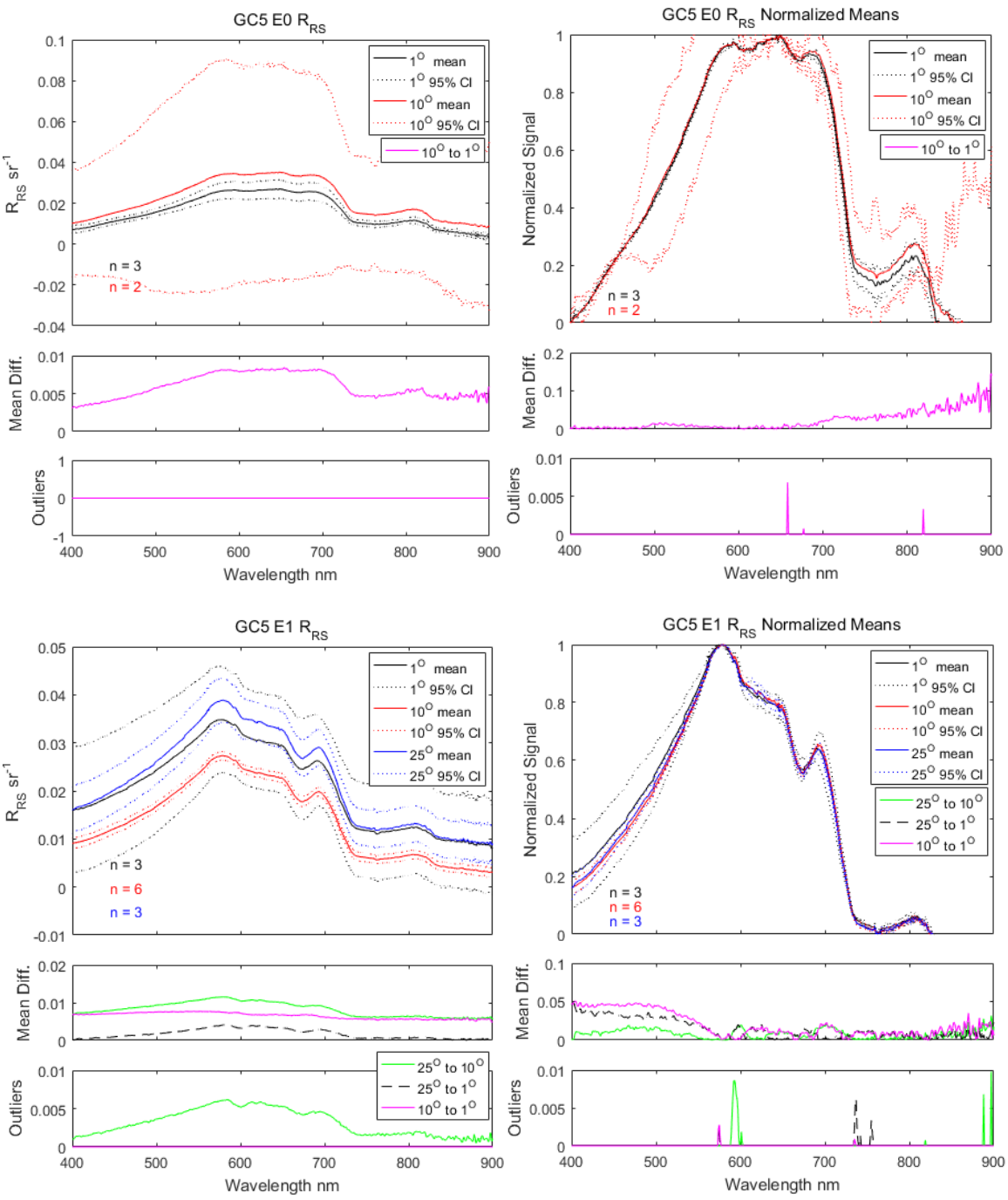

Figure 87 (continued). R_{rs} & Normalized R_{rs} Spectral Shape Comparisons

Plots on the left display mean R_{rs} spectra with 95% CIs. Plots on the right display normalized mean R_{rs} spectra with 95% CIs for the same datasets. Mean Diff. plots show the differences between the various mean values. Plots labeled “Outliers” display differences between maximum and minimum CIs when those boundaries did not overlap between the means.

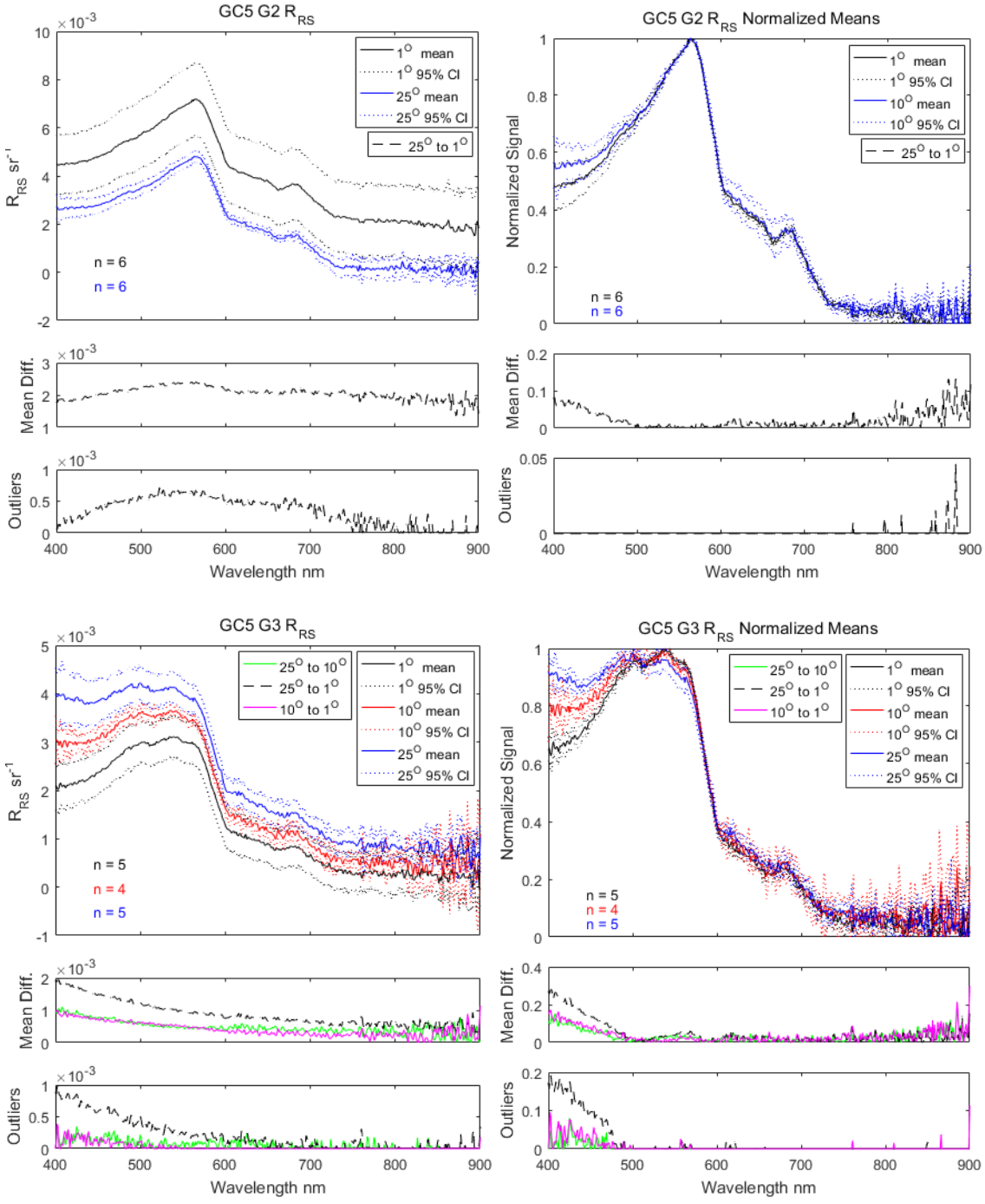

Figure 87 (continued). R_{rs} & Normalized R_{rs} Spectral Shape Comparisons

Plots on the left display mean R_{rs} spectra with 95% CIs. Plots on the right display normalized mean R_{rs} spectra with 95% CIs for the same datasets. Mean Diff. plots show the differences between the various mean values. Plots labeled “Outliers” display differences between maximum and minimum CIs when those boundaries did not overlap between the means.

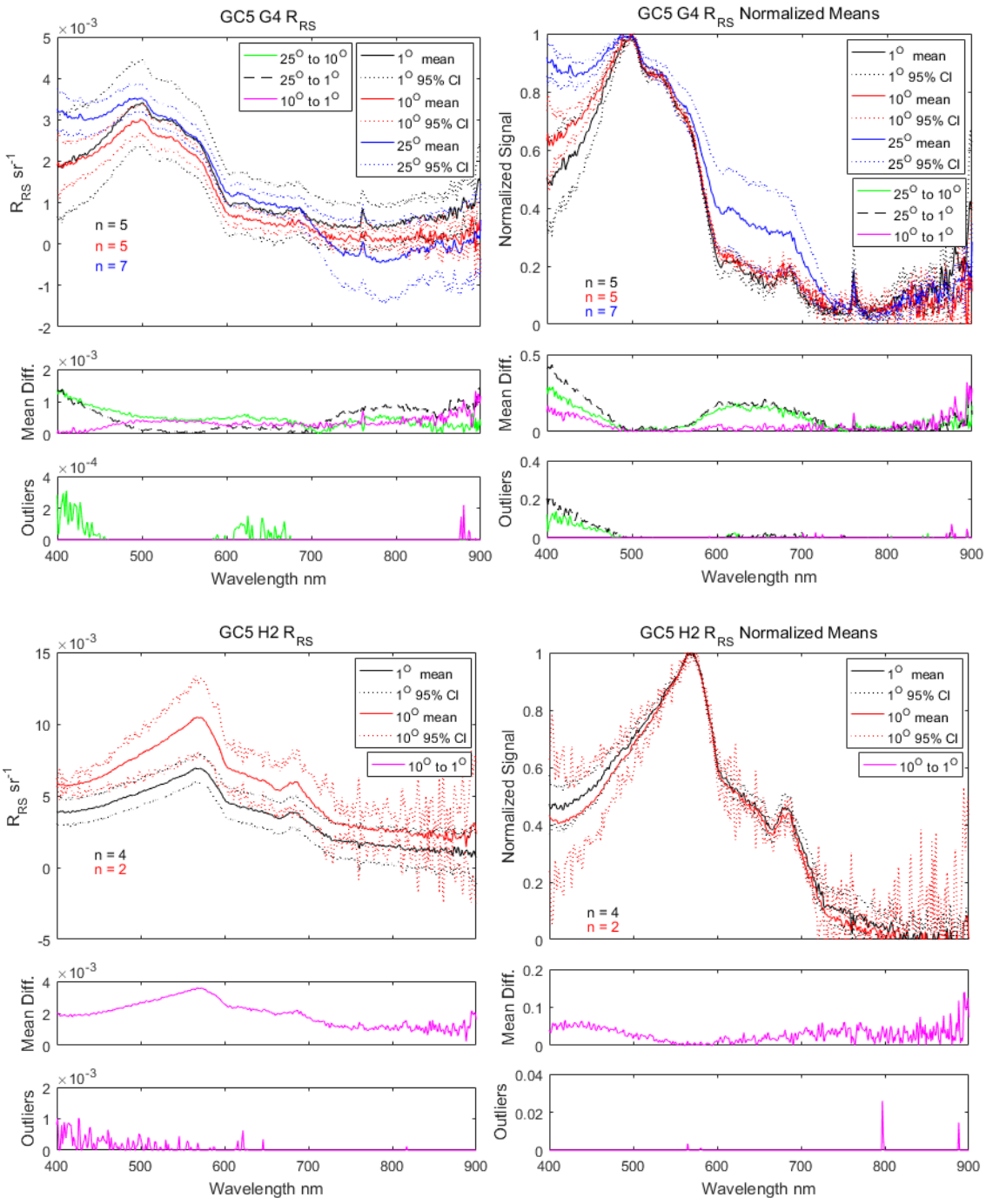

Figure 87 (continued). R_{rs} & Normalized R_{rs} Spectral Shape Comparisons

Plots on the left display mean R_{rs} spectra with 95% CIs. Plots on the right display normalized mean R_{rs} spectra with 95% CIs for the same datasets. Mean Diff. plots show the differences between the various mean values. Plots labeled “Outliers” display differences between maximum and minimum CIs when those boundaries did not overlap between the means.

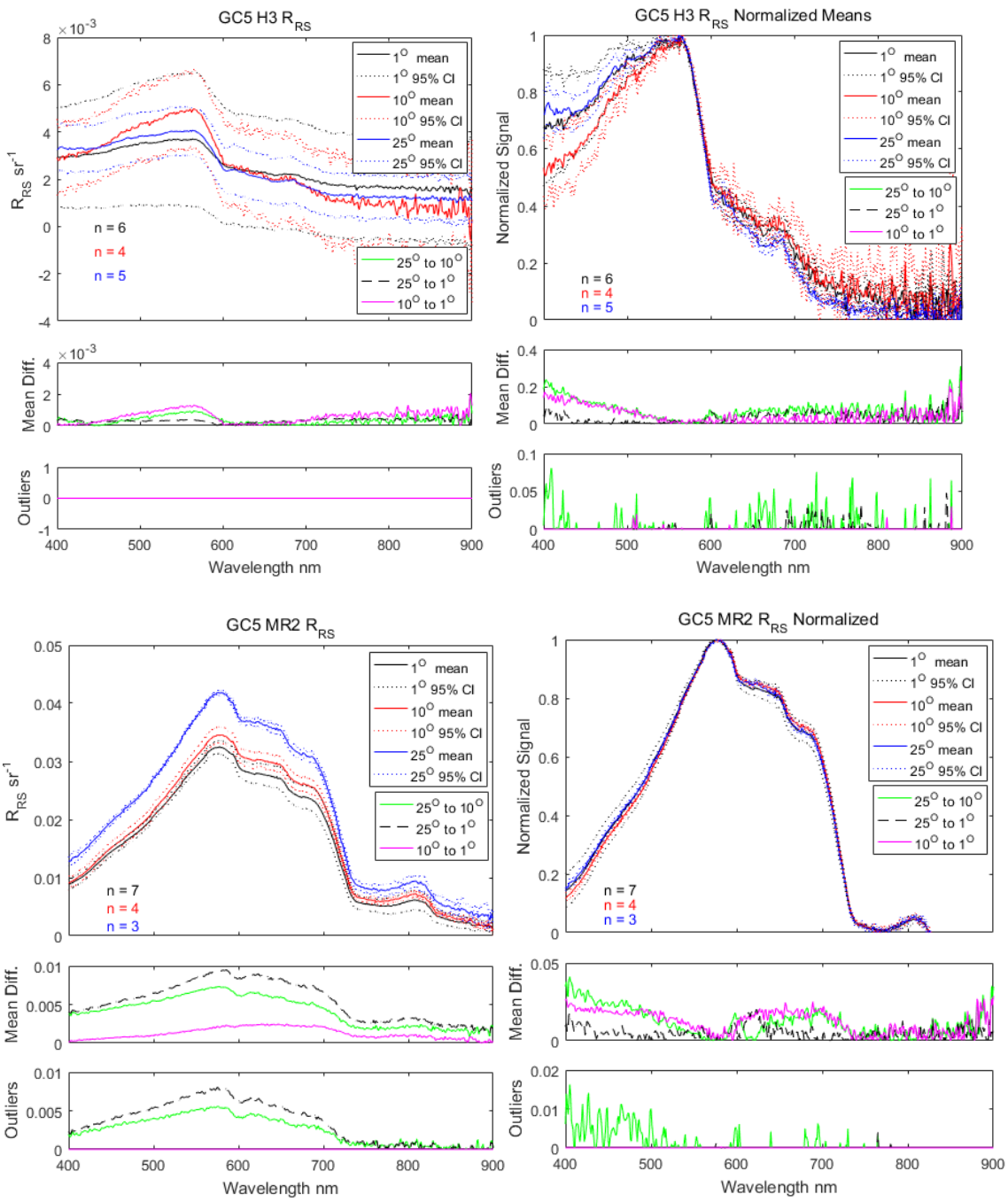

Figure 87 (continued). R_{rs} & Normalized R_{rs} Spectral Shape Comparisons

Plots on the left display mean R_{rs} spectra with 95% CIs. Plots on the right display normalized mean R_{rs} spectra with 95% CIs for the same datasets. Mean Diff. plots show the differences between the various mean values. Plots labeled "Outliers" display differences between maximum and minimum CIs when those boundaries did not overlap between the means.

CHAPTER VII - SPM PROPERTIES & DISTRIBUTION

Introduction

This chapter illustrates the temporal and spatial distributions of SPM and other selected properties in the project area. It demonstrates that even in the same place the mean particle diameter and particulate carbon content varies over time. This, in turn, indicates that particle populations in SPM vary in material and origin. The presence and bulk characteristics of suspended particulate matter influence marine organisms by regulating light availability. Additionally, it serves as transport for nutrients, pollutants, and biological materials. It affects anthropogenic activities by contributing to in-filling harbors (de-Nijs et al., 2009) and shipping channels. It may also contribute to the fouling of marine instruments. Sources of SPM include fluvial inputs, re-suspension of bottom particulates (Bartholomä et al., 2009) and in - situ generation by marine organisms.

Filtration methods for the measurement of SPM concentration vary from study to study. Methods utilized have ranged from paper filters used in the 1950s in applications with turbid waters to more modern membrane filters and glass fiber filters (Harris, 1971). There is some inconsistency in the literature about the minimum size of SPM (Harris, 1971; Stramski et al., 2004) which defines the distinction between particulate matter and colloidal materials. For this study, suspended particulate matter is defined as material located in the water column which may be captured on a 0.4 µm filtration membrane, as these types of filters were used throughout this study. Other researchers have the same pore-sized membranes for their filter samples (Jafar-Sidik, Gohin, Bowers, Howarth, & Hull, 2017; J. T. Liu et al., 2009; McCave et al., 2001; McPhee-Shaw et al., 2004; A.

Palanques et al., 2001; Tsompanoglou et al., 2017), effectively using the same definition of SPM as this dissertation.

SPM may be composed of many different types of particles. The organic fraction of SPM may consist of living or deceased matter. Mineral particles are also present in the marine environment and become suspended in the water column through aeolian (dust), fluvial or re-suspension processes. Flocs are aggregates consisting of mineral particles attached to organic membranes. Each one can contain as many as 10^6 component particles (Baugh & Manning, 2007). The formation and disassembly of these aggregates depend upon the availability of constituent materials and the local turbulent flow regime (Bartholomä et al., 2009; Bowers, 2003). It has been demonstrated that floc density and size have an inverse relationship (Bowers et al., 2011). The observation of intact flocs becomes problematic due to their fragility, although in - situ methods for observing them are improving. The identification of flocs, as opposed to individual SPM particles, are not addressed in this project, but these aggregates are expected to have been present in the survey area during this study.

SPM samples provided the baseline material for this dissertation. The samples were collected at many different depths during this project. Particular attention was given to sampling near-surface waters defined by depths of the shallowest water-capture events by the CTD profilers. Near-surface filter samples had a median depth of 1.25 m with 0.25 m and 2.75 m minimum and maximum depths. Near-bottom samples were collected with increasing regularity as the cruises progressed. Incidents of CTD-induced turbidity were identified and removed from the near-bottom SPM data set. Additional SPM samples

were collected at various depths of opportunity for comparison with datasets from the sensors.

In this chapter, measurement uncertainty of SPM filter samples is quantified. The distribution of SPM in the northern Gulf of Mexico during this research period is examined. Various parameters available from quality-passed LISST data are considered. The horizontal distribution of SPM near the seafloor is evaluated. Bottom nepheloid layers (BNLs) and intermediate nepheloid layers (INLs) are considered. The total carbon content of selected near-surface SPM filter samples is also analyzed.

Filtration Uncertainty

Uncertainty in estimates of SPM concentrations could be attributed to various sources, including natural variability in the distribution of SPM within the water being sampled as well as uncertainties associated with the methodology. Analyses of multiple filtered samples were made using water from the same source. The effects of salt retention on the filters and variations of SPM concentration reported by filters with different pore sizes were also examined.

Multiple samples were filtered from the same bulk water bottle at 113 locations throughout the series of cruises involved in this project. Multiple filter samples from a given water bottle were assumed to represent random observations of a normally distributed population. This data set of multiple samples from the same water source was therefore treated as normally distributed. Overall, this treatment of the data revealed an 8.56% uncertainty (standard deviation) in the SPM concentration dataset using 0.4 μm pore sized filters. This uncertainty value compares well with similar data quality

evaluation of SPM samples filtered onto 0.4 µm pore sized polycarbonate filters for a project located in the St. Lawrence estuary (Larouche & Boyer-Villemaire, 2010).

Another way of expressing the uncertainty of filtration replicates is to determine the percentage of SPM represented by the coefficient of variation (D. Doxaran et al., 2012). In the work of D. Doxaran et al. (2012), the mean uncertainty calculated by this method for samples collected at the Mackenzie River plume represented ± 16%, 10% and 2% for SPM concentrations of 0.04 – 1.00 mg/l, 1 – 10 mg/l and 10 – 100 mg/l respectively. In this study, the coefficient of variation is ± 46.5% (n = 38), 6.3% (n = 51) and 0.4% (n = 23) for concentration ranges 0.12 – 1 mg/l, 1 – 10 mg/l, and 10 – 300 mg/l respectively.

In Chapter II, it was explained that the extraction techniques used for subsampling water captured by the sampling bottles on the CTD profile changed mid-cruise during GC1. Filter sample data from the first half of that cruise were therefore not applied to this research. During GC1, an effort was made to quantify how the different water extraction techniques from the Niskin bottles affected SPM concentration. The results reported in Table 80 are mixed. The “old method” refers to the technique of subsampling the Niskin bottle using the spigot near the base of the bottle. The “new method” refers to the draining of the entire Niskin bottle into a clean carboy and subsampling it after agitating the bulk sample in to homogenize it.

Table 80

Analysis of Niskin Bottle Drainage Techniques

Station	SPM Concentration mg/l			% Difference of New Method
	Old Method	New Method	Difference (New - Old)	
E1	21.51	27.97	6.46	23.09
E0	236.87	257.75	20.88	8.1
E1*	24.56	19.38	-5.18	-26.75
H5	1.17	1.07	-0.1	-9.77

Notes. All comparisons were conducted during GC1. Old method refers to spigot drainage of Niskin bottles. New method refers to complete Niskin drainage by bottom removal. *This station was visited twice during GC1. n = 2 for all comparisons.

Consideration was given to the question of what happens to SPM concentration measurement if the sample was not properly rinsed prior to freezing or desiccation. Table 81 shows examples where this idea was tested. While this is not enough information to fully quantify what happens to improperly rinsed samples, it is clear that salt retention would be extremely detrimental to the quantification of SPM concentration if procedures were not correctly followed. During this project, great care was taken to ensure that all SPM samples were well rinsed.

Table 81

Salt Blanks Without Rinse

Cruise	Concentration (STD) mg/l
GC2[a]	31.00 (17.91)
GC4	1.83 (0.21)

Note: All filters have a pore size of 0.4 µm. [a]Water pre-filtered with a 0.2 µm filter. STD is the standard deviation.

cruise GC1. At some point during the excursion, the onboard water ultra-purification system failed. This means that rinse-water for the samples consisted of deionized water rather than Milli-Q water. Samples of polished water (MilliQ, Nano-pure, or deionized water) were obtained and processed as SPM samples for three of the cruises to gain some idea of what kind of background signal they might contribute to the SPM dataset. The results are in Table 82. There may have been an appreciable effect on SPM concentration related to the failure of the Milli-Q system during GC1. During the other cruises, however, the background signal appears to have been negligible.

Table 82

Polished Water Blanks Provided by Research Vessels

Cruise	Concentration (STD) mg/l	Water Type
GC1	0.13	MilliQ
GC1	0.1	Deionized
GC2	0.03	MilliQ
GC5	0.01 (0.01)	Nano-pure

Note: During GC1 the MilliQ filter system failed.

Analyses were also performed to determine the effect of different types of filters used to process the samples upon the resulting SPM concentrations. The operational definition of SPM varies from project to project (Bowers & Binding, 2006). This project routinely used 0.4 µm pore size filter membranes for sampling; however, at several locations, samples were also collected on 0.2 µm filters and GF/F filters for a comparison of methods. The GF/F filters had a nominal pore size greater than 0.4 µm (Stramski et al.,

2004). Systematic differences among filter types were observed and were not necessarily intuitive. It was expected that the smaller pore size filters would capture more SPM per unit volume (i.e., SPM per unit volume was expected to be highest for the 0.2 µm pore size filters, intermediate for the 0.4 µm pore size filters, and lowest for the GF/F filters).

Overall, the 0.2 µm pore sized filters captured approximately the same amount of SPM as the 0.4 µm pore sized filters. The mean differences between the SPM concentrations represented 0.99% ± 43.95% of SPM concentration, n = 69. In an unexpected development, the GF/F filters, with a nominal pore size greater than 0.4 µm, exhibited the highest SPM concentration per unit volume, higher than both the 0.4 µm pore sized filters (34.14% ± 38.36%, n = 38), and the 0.2 µm pore size filters (32.41% ± 36.21%, n = 32). Other researchers have also noted high retention of SPM onto GF/F filters relative to the 0.4 µm pore sized polycarbonate filters (Larouche & Boyer-Villemaire, 2010).

One possible reason for the large differences seen between the Nuclepore membrane filters and the GF/F filters may have been attributable to salt and colloidal matter retention by the GF/F filters. SPM filtrate was drawn through 0.2 µm, 0.4 µm and GF/F filters, which were subsequently rinsed three times with MilliQ, dried, and weighed, as was normally done for all other SPM samples (Table 83) to evaluate this possibility. It was found that there was 35.68% higher residual material retained on the 0.2 µm filter compared to that on the 0.4 µm filters, and 93.42% and 91.08% higher residual material on the GF/F compared to the 0.4 and 0.2 µm filters respectively (nearly twice the mass in both cases). These results indicated that both the GF/F filters and the 0.2 µm filters retained additional mass not evident on the 0.4 µm filters.

Table 83

Salt Blanks with Rinse

Cruise	Concentration (STD) mg/l	Pore Size	Notes
GC3	0.24 (0.08)	0.4 µm	dried prior to rinse
GC3	0.15	0.4 µm	
GC4	0.43 (0.33)	0.4 µm	dried prior to rinse
GC5	0.03 (0.00)	0.4 µm	not allowed to dry before rinse
GC5	0.04	0.2 µm	not allowed to dry before rinse
GC5	0.47	GF/F	not allowed to dry before rinse

While the higher retention of mass per unit volume was expected for the 0.2 µm relative to the 0.4 µm filters, the GF/F behavior was more difficult to explain. Perhaps salt was retained on the filter and contributed to a higher background signal. Alternatively, the structure of the GF/F filters may have promoted the retention of particles far smaller than 0.4 µm, especially as interstitial spaces began to fill. Regardless of what caused the differences observed in SPM concentration due to filter selection, it was clear that consistency of filter type was essential for comparative analyses both within and between cruises.

Suspended Particulate Matter in the northern Gulf of Mexico

Histograms of the full dataset of 0.4 µm pore based filter samples for SPM have already been presented in Chapter V (Best SPM Approximation Models section). Some attention is given to a few additional characteristics of SPM that were derived from the LISST and transmissometer sensors. Additionally, salinity and total carbon content in relation to near-surface SPM are also considered.

LISST-Derived SPM Characteristics

Several parameters were calculated from the LISST data and applied to this project. During these evaluations, all points where schlieren was suspected to influence LISST observations (see Chapter IV) were removed from the working datasets. The mean particle diameter (D50) in µm was calculated using the MATLAB script compute_mean.m provided by Sequoia Scientific. Second, an abundance index was determined defined by the following equation:

$$Abundance\ Index = \sum_i \frac{v_i}{d_i} \quad \frac{\mu l}{l}\ \mu m^{-1} \tag{7.1}$$

where *v* and *d* were the volume and median diameter of each particle size bin of the LISST. Finally, total suspended matter (µl/l) was determined by summing the volumes of SPM from all 32 bins of the sensor. The correlation coefficients between each of these parameters and SPM are presented in Table 84.

In evaluating the relationship between LISST – derived properties and SPM, an additional subset of the GCALL dataset was formed consisting of all quality-passed information (see LISST Quality section in Chapter IV) from cruises GC1, GC2, GC3 and GC5 combined. This was done because significant differences were seen in the relationship between LISST attenuation and SPM (Tables 34 and 37) compared to the remaining four research cruises in the project.

Table 84

Relationship Between SPM Concentration & LISST-Derived SPM Properties

Cruise	LISST Property	Spearman Correlation Coefficients		n
		ρ	p	
GC1	D50 µm	0.14	0.55	20
GC2	D50 µm	0.29	0.05	47
GC3	D50 µm	-0.76	0.00	56
GC4	D50 µm	-0.5	0.01	30
GC5	D50 µm	-0.58	0.00	68
GCALL	D50 µm	-0.39	0.00	221
GC1, GC2, GC3 & GC5	D50 µm	-0.38	0.00	191
GC1	Abundance Index	0.94	0.00	20
GC2	Abundance Index	0.68	0.00	47
GC3	Abundance Index	0.87	0.00	56
GC4	Abundance Index	0.79	0.00	30
GC5	Abundance Index	0.95	0.00	68
GCALL	Abundance Index	0.81	0.00	221
GC1, GC2, GC3 & GC5	Abundance Index	0.80	0.00	191
GC1	TSM µl/l	0.94	0.00	20
GC2	TSM µl/l	0.74	0.00	47
GC3	TSM µl/l	0.84	0.00	56
GC4	TSM µl/l	0.63	0.00	30
GC5	TSM µl/l	0.91	0.00	68
GCALL	TSM µl/l	0.82	0.00	221
GC1, GC2, GC3 & GC5	TSM µl/l	0.84	0.00	191

According to the p-values generated in the correlation analysis between D50 and SPM, there is no relationship between SPM concentrations and the mean particle size for cruises GC1 and GC2. For the remaining three cruises, there is a correlation (to varying degrees) between these two properties. Further insight into the relationship between these two parameters is plotted in Figure 88. From this figure, it can be seen that the largest diameters associated with any concentration of SPM occurred during GC3.

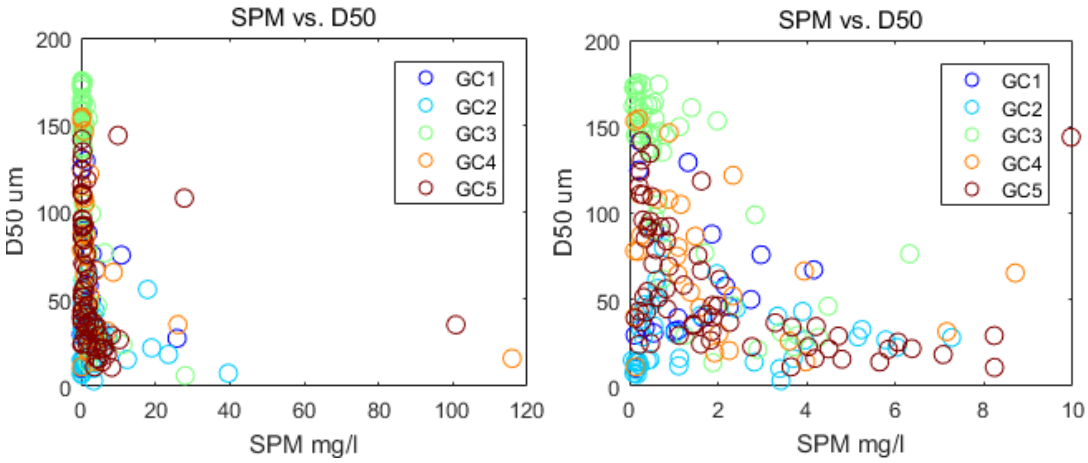

Figure 88. SPM in Relation to D50

Note. The plot on the right is a magnification of the plot on the left.

The SPM abundance index described in equation 7.1 correlates well with SPM concentration for all five cruises. However, this relationship is demonstrably less strong during GC2 (Table 84). Figure 89 shows the scatter plots for SPM and the abundance index.

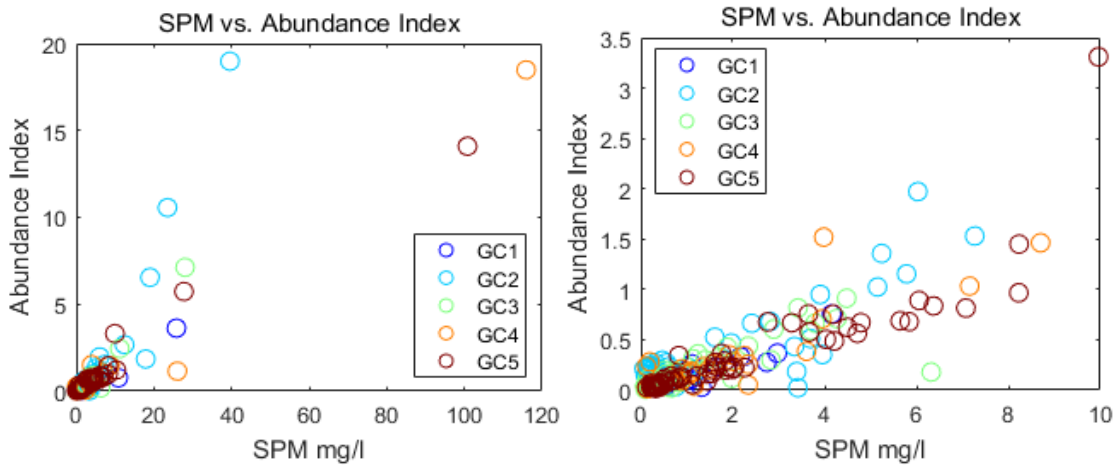

Figure 89. SPM in Relation to Abundance Index

Note. The plot on the right is a magnification of the plot on the left.

Similar to the abundance index, total suspended matter (TSM) concentration in µl/l has a strong correlation with SPM concentration (mg/l) (Table 84). TSM consists of

the sum of the SPM volume estimates reported by the LISST for all 32 of its particle size ranges. Figure 90 shows scatter plots of these relationships.

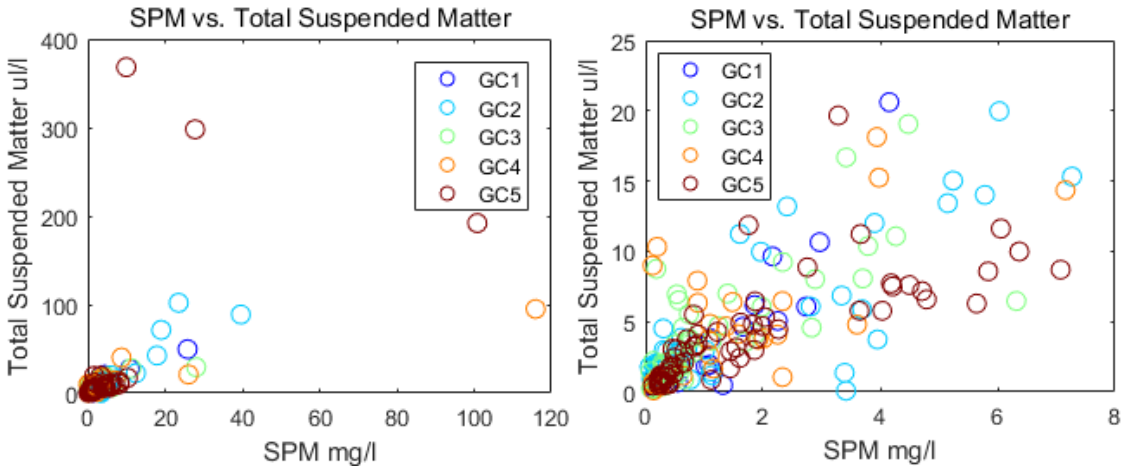

Figure 90. SPM in Relation to TSM

Note. The plot on the right is a magnification of the plot on the left.

SPM in Bottom and Intermediate Waters

Observational methods needed to perform a rigorous study of water near the seafloor, its interaction with the seabed and processes related to the resuspension of benthic matter were not available during this project. However, some information about the distribution of SPM in the near-bottom waters were gained from the data procured during this research.

Near-bottom filter samples were collected at selected stations (Figure 91). During sample collection, the CTD profiling package was lowered to a depth believed to be the minimum safe height above the seafloor before collecting the near-bottom water samples. Acoustic altimeters on the on the CTD profilers helped ships' personnel make the decision to stop profiler descent during each deployment. Minimum altimeter values were not retained. Therefore, an unknown offset between the seafloor and the CTD profilers existed at each site of near-bottom sampling.

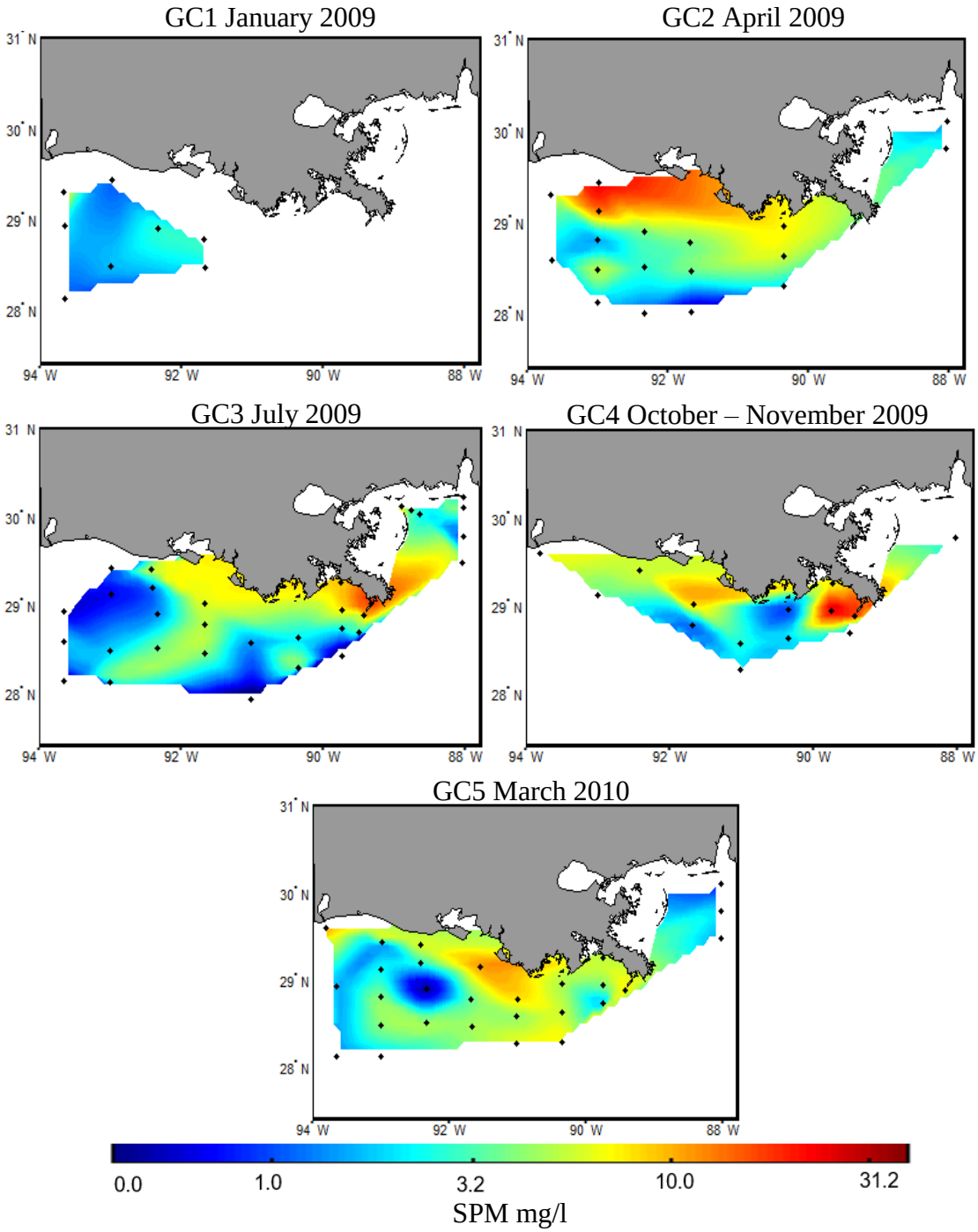

Figure 91. Near – Bottom SPM Distribution, Filter Samples

Samples associated with CTD induced turbidity are not plotted.

Two separate depth observations associated with water sample collection were recorded. First, depth-to-seafloor from the vessel was manually recorded at many (though not all) stations using soundings reported from the vessel's navigational display based upon hull-mounted sonars. The second depth measurement associated with the data acquisition from bottom waters was the depth-from-surface observation recorded by the CTD depth from the pressure sensors on the ships' profilers. In this case, the "bottom" depth was the CTD sensor's depth (located near the base of the rosette) when the first water sample bottle was fired. Naturally, these depth measurements did not match. Reasons for this mismatch can be divided into vertical and horizontal components.

There were several reasons for misalignment of the two "bottom" measurements obtained in this study. First reflecting on the vertical components, the profiler was not routinely allowed to settle on the seafloor. Therefore a minimum of a few decimeters between the CTD depth and the actual seafloor was implied. (For the sake of thoroughness, it should be noted that on a few occasions, the CTD profiler did make contact with the seafloor evidenced by benthic sediments found near the joints and seams at the base of the water sampling profiler. However, these events were very rare.) The second major contributor to the differences between the depth datasets was the fact that the vessels' navigational sonars were mounted on or near the ships' keels. This configuration added a surface-to-sonar misalignment relative to water column depth measurements from the profiler. The published draft depths for the research vessels used in this project were 2.7 m for the R/V Cape Hatteras (Oceanographic Consortium, 2011) and 2.9 m for the R/V Hugh R Sharp (Deleware, 2009), though the actual draft of the vessels may have varied from published values and even from station to station within a

cruise due to dynamic payload weight and distribution (including fuel and sewage). Other potential sources for the misalignment of the depth datasets include legitimate differences in sea-surface-to-seafloor depth that may have been experienced as the vessels drifted between the time of seafloor depth observation by the vessel and the firing of the sampler bottles. Even in cases where the vessel was relatively stationary, there was still an unknown horizontal offset between the two depth sensors. These offsets were most likely on the order of meters to a few tens of meters depending on the location of the navigational sonar and the strength of subsurface currents pulling the profilers away from the vessel. These occurrences were not quantifiable from the metadata gathered at each CTD cast.

A final potential source of depth data misalignment may be attributed to different sensitivities of the depth sensors. The ships' CTD sensors had an expected uncertainty of up to 1.36 m (Table 1). Sonar data requires several supporting datasets to translate raw soundings to highly accurate depth measurements. These data sets include accurate sound speed profiles and offsets related to roll and pitch motions of the research vessel. Since some of the essential equipment and a dry-dock vessel configuration survey was not available during this project, the hand-recorded sonar data was uncorrected for these variables.

Employing the Jarque-Bera goodness-of-fit test for the calculated differences between these two critical depths (from the vessel and the CTD profiler) revealed that this data set had a normal distribution. The mean difference between the depth measured by the CTD at the base of the water sampler rosette and the depth-to-seafloor recorded in the CTD log by manual observation from the ship's navigational sonar was 0.40 m

(±1.57m, n=110) The fact that the mean difference is a positive value suggests that the distance between the CTD profiler and the seafloor was usually less than the distance between the sonar and the sea surface. Therefore, the vertical component of the near-seafloor paradigm for SPM sampling (where it can be claimed that sampling usually occurred within the bottom two or three meters of the water column) is similar to the near-surface sampling events (where sampling usually occurred within the top two meters of the water column).

In addition to the near – bottom distribution of SPM as described by the filter samples in Figure 91, estimates of near bottom SPM were determined using transmissometer data. This was accomplished by utilizing the cruise-specific SPM algorithms developed in Chapter V and applying them to the bottom two meters of the transmissometer profiles. Median predicted near-bottom SPM values were established and plotted in Figure 92.

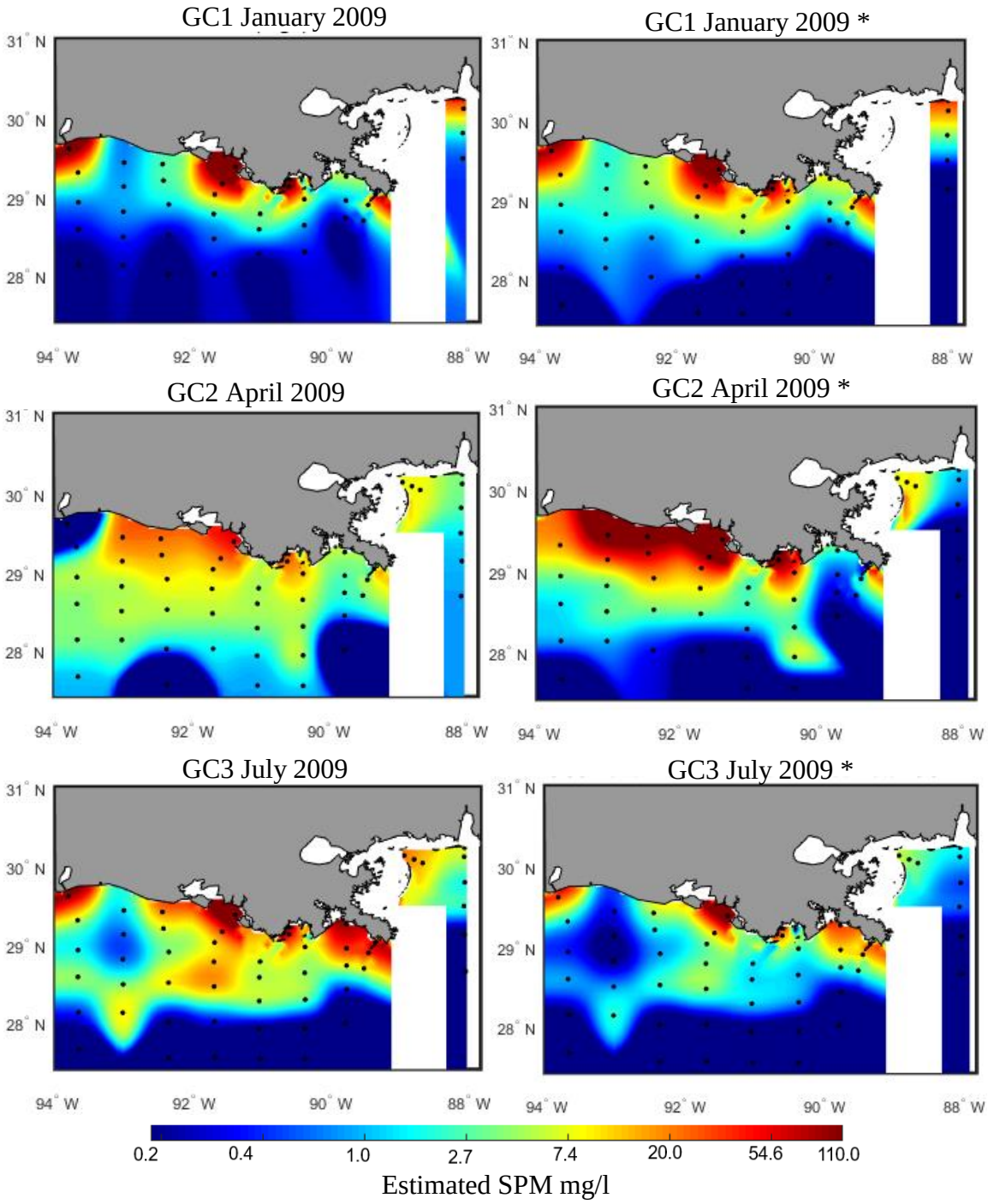

Figure 92. Estimated Near – Bottom SPM, Transmissometer

Notes. SPM is estimated from transmissometer-based algorithms for the individual cruises (left). Plots of the right show SPM estimates using the algorithm based upon the GCALL dataset. (See Chapter V). There is no transmissometer data for GC4.

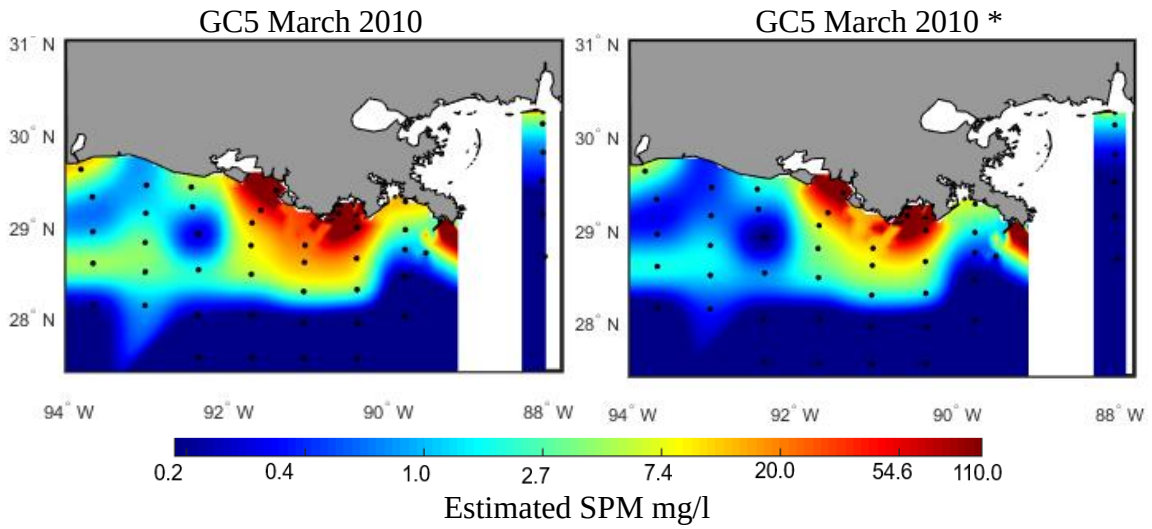

Figure 92 (continued). Estimated Near – Bottom SPM, Transmissometer

Notes. SPM is estimated from transmissometer-based algorithms for the individual cruises (left). Plots of the right show SPM estimates using the algorithm based upon the GCALL dataset. (See Chapter V). There is no transmissometer data for GC4.

Figure 92 (transmissometer based) gives better near – bottom SPM distribution coverage than Figure 91 (filter-sample based). Where there is overlap in coverage between these two figures, general features are in agreement. For example, a hook-shaped feature in both representations of GC3 near – bottom SPM associated with transects E and F can be identified in both figures. (See Figure 5 for station names.) Also, during GC5, similar areas of low SPM concentration are noticeable at Station F3 using both methods of SPM concentration estimation.

Nepheloids

Relatively high concentrations of SPM in proximity to the seafloor are well-known occurrences called nepheloids. Some of these features are identified in the SPM bottom-water data in this project. A nepheloid is defined as “a layer of water in the deep ocean basin that contains significant amounts of suspended sediment” (Bates & Jackson, 1987). Furthermore, Bates and Jackson state that these layers have a range of 200 m thru 1000 m

in thickness. More recently, nepheloid layers are ”defined by enhanced particle content relative to surrounding waters” (Inthorn et al., 2006). This latter interpretation appears to be the more popular definition of these features in recent literature. The term “nepheloid” has also been widely utilized in association with relatively high SPM concentration layers encountered at much shallower depths than the deep ocean. Furthermore, these structures may be subdivided into the categories surface nepheloid layers (SNL), bottom nepheloid layers (BNL) and intermediate nepheloid layers (INL) (Azetsu-Scott, Johnson, & Petrie, 1995; Capello, Budillon, Cutroneo, & Tucci, 2009; Du & Liu, 2017; Inthorn et al., 2006; Lorenzoni et al., 2009; McCave, 1986; McCave et al., 2001; McPhee-Shaw et al., 2004; Oliveira et al., 2002; van Weering, de Stigter, Boer, & de Haas, 2002; Walsh & Nittrouer, 1999). Nepheloid layers are understood to be transport mechanisms for particles (Halper & McGrail, 1988; Masson, Huvenne, de Stigter, Arzola, & LeBas, 2011). Separate nepheloid layers within the same water column (identified by turbidity meter or transmissometer) have previously been examined in relation to SPM (Capello et al., 2009; Puig & Palanques, 1998; Ransom, Shea, Burkett, Bennett, & Baerwald, 1998). Advection contributes to nepheloid layers and particle transport (Rutgers van der Loeff, Meyer, Rudels, & Rachor, 2002). Nepheloids may also be influenced by tides (J. T. Liu, Wang, Lee, & Hsu, 2010), wind forces (S. Ouillon et al., 2010), upwelling and downwelling processes (Oliveira et al., 2002).

BNLs may be formed by the resuspension of benthic sediments by bottom currents followed by advection (Kennett, 1982; J. T. Liu et al., 2009). BNLs may also extend upwards to several hundred meters above the seafloor (Boggs, 1995; Kennett, 1982). The benthic biosphere sometimes contributes particles to BNLs (Rutgers van der

Loeff et al., 2002). Furthermore, it has been put forward that bottom nepheloid layers are a primary source of colloidal organic carbon in the world ocean (Guo & Santschi, 2000). Several researchers add the modifier "permanent" to the bottom nepheloids they study (Bourrin et al., 2015; Wilford D. Gardner, Tucholke, Richardson, & Biscaye, 2017; Many et al., 2016) when there is evidence of persistence. Not all BNLs are considered permanent.

In addition to their presence in deep waters, bottom nepheloid layers have been identified (X. H. Wang, Pinardi, & Malacic, 2007) and studied on continental shelves (Tsompanoglou et al., 2017; Yurkovskis, 2005). Continental shelf nepheloid layers have been studied specifically in a regional context (Oliveira et al., 2002). Additionally, BNLs have sometimes been associated with salinity gradients (Puig et al., 2013; Ribó et al., 2013; Yurkovskis, 2005).

INLs often form at a shelf break where detachment from a BNL occurs along with lateral spreading along isopycnals (de Stigter et al., 2007; Du & Liu, 2017; Lorenzoni et al., 2009). Other INLs may form further down the continental slope (McPhee-Shaw et al., 2004; Albert Palanques et al., 2006). The formation of these INLs may be related to internal waves (Bourgault, Morsilli, Richards, Neumeier, & Kelley, 2014; Masunaga et al., 2017). Surface nepheloid layers are mentioned in literature where INLs or BNLs are studied (Puig & Palanques, 1998). They may get special consideration under that name (SNL) in some studies (Lorenzoni et al., 2009; Many et al., 2016; Oliveira et al., 2002), however it is also common to find projects (like this dissertation) that prefers to address SNLs as plumes, near-surface SPM, blooms or surface layers (Wegner et al., 2003).

An approximately 200 m thick, deep water BNL has been studied recently in the Mississippi Canyon, northern Gulf of Mexico relative to its biological communities (Moss et al., 2015; Ziervogel et al., 2016). Additionally, there has been evidence of INL transport over the Mississippi Canyon where a continental shelf BNL detached (Ross, Gardner, Richardson, & Asper, 2009). The same study noted that an INL was observed in the axis of the Mississippi Canyon (Ross et al., 2009) between 50 and 200 m depth.

BNLs on in the southwest portion of this project area have also been researched (Halper & McGrail, 1988). There, advection appears to have been a stronger influence on the BNL presence than weather driven resuspension events (Halper & McGrail, 1988). However, Halper and McGrail conclude that such storms indirectly affect the shelf BNL by inducing oscillations that adjust the SPM concentration for the bottom 4 m of the BNL by moving particle-rich (nearshore) or particle-poor (offshore) waters over their research site.

For this research, nepheloid layers were detected in transmissometer data. (See Figure 93 for examples of benthic, intermediate and surface nepheloids in the transmissometer data.) No transmissometer data is available for GC4, so only cruises GC1, GC2, GC3 and GC5 are considered in examining BNLs and INLs in the northern Gulf of Mexico.

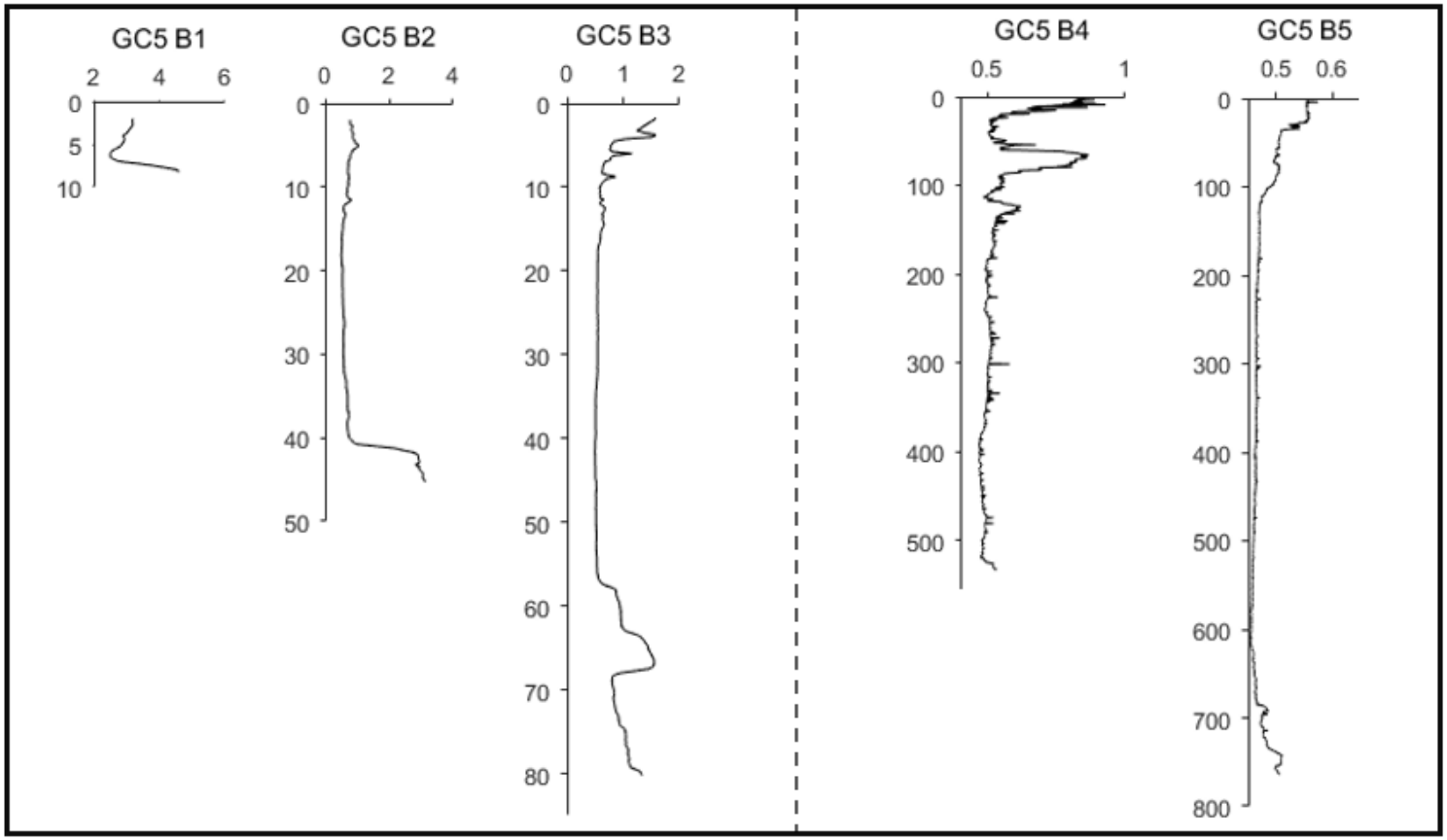

Figure 93. Examples of Transmissometer Profiles

This figure shows the downcast data of the Transmissometer for cruise GC5, Transect B. The x-axes show attenuation and the y-axes show depth in meters. Note that the attenuation axes in these profiles get smaller the further the stations progress along the transect.

Each station in the project area was designated as either a continental shelf station or a continental slope station based upon its approximate depth (Tables 85 and 86). These tables were produced to better understand depth ranges of BNLs and INLs. (See Figure 5 for station locations.)

Table 85

Continental Shelf Stations, Transmissometer Data

Transect	Stations						Depth Range m
A		A1	A2	A3	A4		12 - 41
B		B1	B2	B3			7 - 81
C	C0	C1	C2	C3			4 - 63
D		D1	D2	D3			13 - 67
E	E0	E1	E2	E3	E4	E5	5 - 115
F		F1	F2	F3	F4	F5	11 - 122
G		G1	G2	G3	G4	G5	12 - 80
H		H1	H2	H3	H4	H5	9 - 68
MR		MR1	MR2	MR3			13 - 108
NGI		NGI6	NGI7	NGI8			10 - 17

Note. Approximate depths are referenced to the sea surface at the time of station occupation and are not reduced to a standard vertical datum.

Table 86

Continental Slope Stations, Transmissometer Data

Transect	Stations			Depth Range m
A		A5	A6	712 - 1723
B	B4	B5		564 - 765
C	C4	C5		701 - 1114
D	D4	D5		228 - 896
F			F6	939
H			H6	294

Note. Approximate depths are referenced to the sea surface at the time of station occupation and are not reduced to a standard vertical datum.

All continental shelf stations in this research have depths less than 130 m (median value 23 ± 22 m, n = 41). Uncertainty was estimated by calculating the median absolute deviation. Temporally persistent BNL signatures are recorded in the transmissometer profile data for the 27 shelf stations listed in Table 87. The first region with a persistent BNL appears under stations A2 and A3, along the transect running north-south from Mobile Bay. A BNL was also noted at station A1 for cruises GC1, GC3, and GC5. (As there was only transmissometer data available at two depths for that station during GC2, it is difficult to determine whether or not a BNL existed there at that time.) The persistent BNL at the continental shelf stations along Transect A appears to be geographically isolated from most of the rest of the project area due to the presence of the Mississippi Delta and Mississippi Canyon. (All though all three NGI stations recorded BNL features during the two cruises they were visited, GC2 and GC3.)

Table 87

Continental Shelf Stations with Persistent BNL Signatures

Continental Shelf Stations with Persistent BNL				
A2	D1	F3	H2	MR3
A3	D2	F5	H3	NGI6
B2	E2	G2	H4	NGI7
B3	E3	G3	H5	NGI8
C1	E4	G4		
C2	E5	G5		
C3				

It is important that BNL signatures are recorded in the transmissometer profile data as the presence of a BNL is not always obvious in the plan-view plots of the median SPM values (based on transmissometer data) for the bottom 2 m of each profile (Figure 92). Additionally, not all near-shore continental shelf stations that report high SPM concentration values near the seafloor also have a BNL signature in the transmissometer data. Several of the coastal stations, such as B2, E0, F1, and H1, usually reported high concentrations of SPM near the seafloor that were laterally consistent with stations further along the transects, though a BNL signal was not always distinguishable.

The continental slope is not as well represented by the stations in this project area as the continental shelf. Continental slope stations range in depth from about 225 m thru 1725 m (median value 765 ± 275.2 m, n = 11). Uncertainty was estimated by calculating the median absolute deviation. Of these slope stations, only B4, C4, C5, and D5 had an identifiable BNL for all four cruises. Additionally, station B5 had a BNL for cruises GC1, GC3, and GC5, though no data was available for GC2. Similarly, H6 had a BNL for cruises GC1, GC2, and GC3, but no data for GC5. Therefore, it is possible that these two additional slope stations had a persistent BNL.

INLs in the northern Gulf of Mexico

GC2 reported an interesting array of nepheloid layers. During this cruise, BNLs were apparent at all slope stations except for A5 (depth approximately 712 m). (No data was available for station B5.) Additionally, all outer shelf stations reported a BNL except for Station A4. Also, INLs on all slope stations for GC2 appear to be BNLs that became detached at the shelf break, possibly advecting along isopycnals.

INLs are also recorded on the continental shelf. Nice examples can be seen during cruise GC2, station NGI8, cruise GC3, stations C2 and F5. But INLs are not persistent at any given continental shelf station for all four cruises. Furthermore, it was sometimes difficult to decide from transmissometer records alone if a given INL signature was a distinct feature unto itself, or if it was best-considered part of a BNL or SNL. Examples of this dilemma are located at the feature 45 m – 55 m depth at GC3, station C3, at GC5, station H3, depth range 4 m – 15 m and station D2, 11 m depth.

SNLs

Only a few stations showed persistent SNL signatures in the transmissometer data for all four cruises (Table 88). However, most transects displayed lateral continuity of SPM concentration from nearshore to offshore regardless of the presence or absence of an SNL signal in the transmissometer profile data.

Table 88

Stations with Persistent SNL Signatures

Stations with Persistent SNLs		
A6	C4	MR2
B1	C5	MR3
B3	D4	NGI6
B4	D5	NGI8

SPM in Surface Waters

Consideration was given to SPM in the surface waters. As expected, the greatest concentrations of SPM were found in near-shore waters (particularly in proximity to outflow regions of the major rivers). Also, the near-surface distribution of SPM concentration (determined by filter samples) for each cruise is plotted in Figure 94. Generally, concentrations decreased with increasing distance from shore (see also Tables 89 and 90).

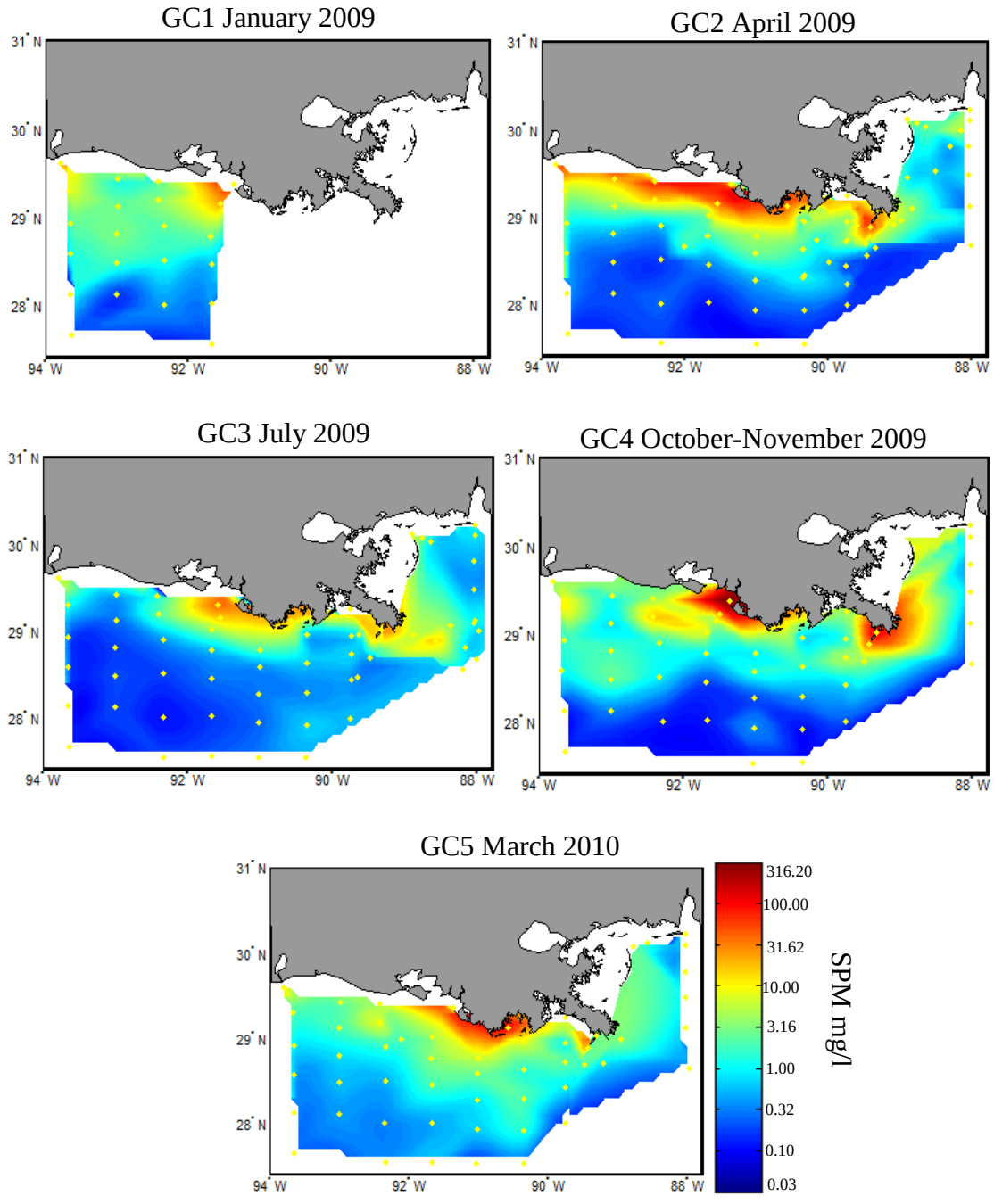

Figure 94. Surface SPM Distribution

Distributions of surface SPM (mg/l) for the five cruise periods using 0.4 µm pore size filters. Sample locations were indicated. Note that the SPM was plotted using a log scale.

In order to characterize regional and temporal patterns of SPM across the study area, a general statistical analysis was performed to determine the high, low and medial concentrations of SPM for each cruise. Since SPM data were available for less than half of the study site for cruise GC1, regional evaluations were performed using two different perspectives. For the first evaluation, only the 19 stations common to all five research cruises were considered. The second perspective for regional SPM evaluation utilized the 44 stations common to cruises GC2 thru GC5.

The surface SPM samples in the northern Gulf of Mexico were determined to be non-gaussian by the asymmetrical shapes of the histograms of surface SPM concentration (Figure 95) and by the interquartile ranges displayed in box and whisker plots of the same datasets (Figure 96); therefore, non-parametric methods were used to calculate the descriptive statistics of each cruise and in the analysis of temporal change from a regional perspective. The regional descriptive statistics of surface water SPM were summarized in Tables 89 and 90.

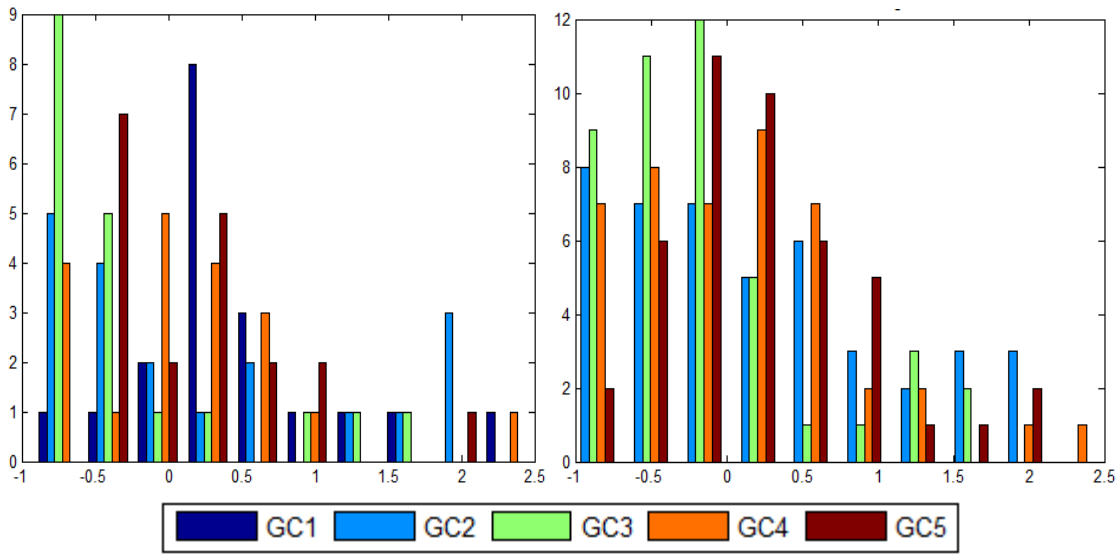

Figure 95. Surface SPM Histograms

Histograms of surface SPM at the stations common to cruises GC1 – GC5 (left) and cruises GC2 – GC5 (right). SPM is expressed as the natural log of SPM concentration.

Table 89

Surface SPM at Stations Common to GC1 – GC5

Cruise	Surface SPM mg/l				Min. Stations	Max Stations
	Median	MAD	Min.	Max		
GC1	2.25	0.93	0.21	257.75	H6	E0
GC2	0.61	0.46	0.12	88.11	E5	F1
GC3	0.29	0.13	0.13	44.25	H5, H6	E0
GC4	1.16	0.96	0.12	300.38	E5, H5, H6	E0
GC5	1.51	1.04	0.28	74.44	H6	E0

Note. MAD is the median absolute deviation. n = 19

Table 90

Surface SPM to Stations Common to GC2 – GC5

Cruise	Surface SPM mg/l				Min. Stations	Max Stations
	Median	MAD	Min.	Max		
GC2	1.03	0.86	0.09	88.11	D5	F1
GC3	0.5	0.3	0.13	44.25	H5, H6	E0
GC4	1.04	0.84	0.09	300.38	C5	E0
GC5	1.56	1.06	0.13	100.8	B5	C0

Note. MAD is the median absolute deviation. n = 44

The box and whisker plots (Figure 96) give an additional perspective on the regional distribution of surface SPM. The largest outliers of the SPM concentration occurred during cruises GC1 and GC4. It was probably not a coincidence that the points of highest concentration for each of these cruises occurred at Station E0, located at the mouth of the Atchafalaya River (Tables 89 and 90). Both cruises were also preceded by an extended period of low flow followed by rapidly increasing discharge of both the Atchafalaya River and the Mississippi River (Figure 98). It is also clear that the regional surface SPM during GC1 was unique as evidenced by the negative skew of this distribution. (All other distributions were positively skewed.) GC1 also had the highest median SPM concentration of the five cruises.

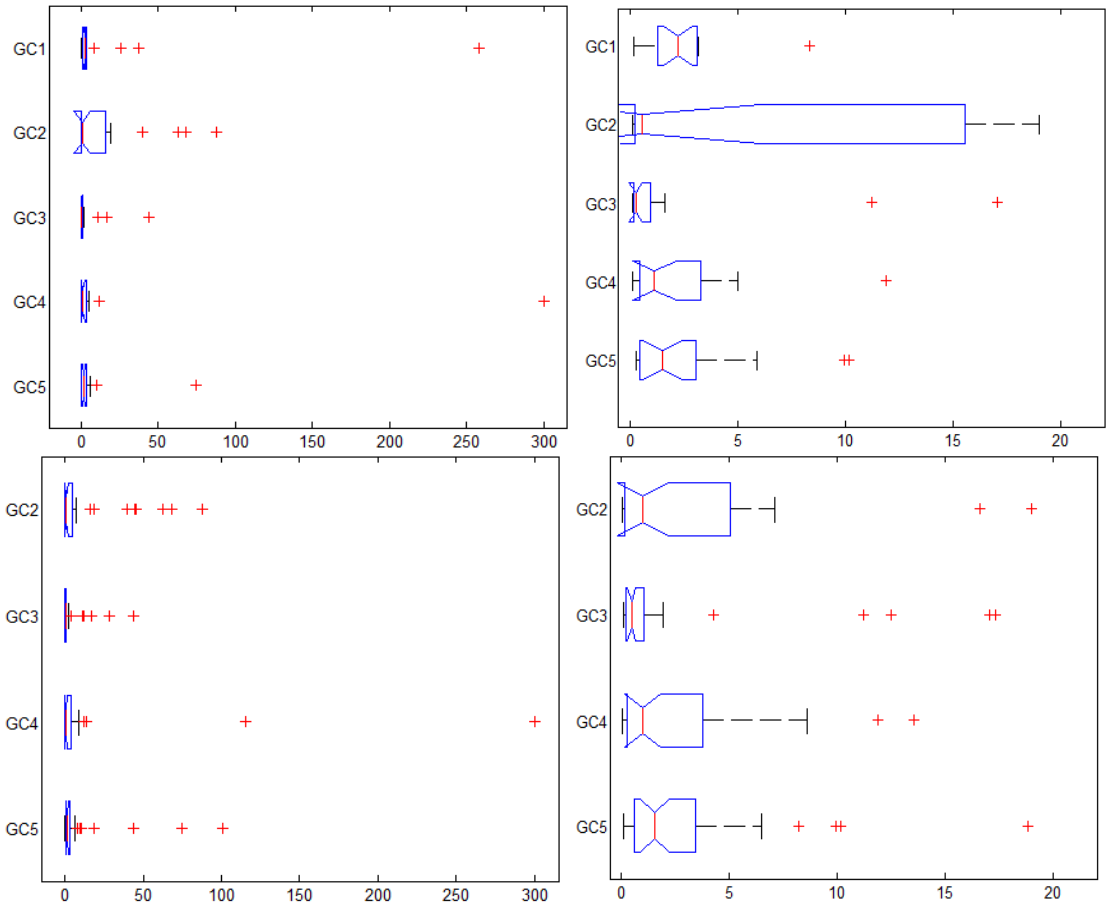

Figure 96. Surface SPM Box & Whisker Plots

Box and whisker plots of surface SPM (mg/l) measured by the filtration method, 0.4 µm pore sized filters. For the top two plots, n = 19. For the bottom two plots, n = 44. Red lines show median SPM concentration. Boxes show the interquartile range (left side 25th percentile, right side 75th percentile). Whiskers extend up to 1.5 beyond the interquartile range. Outliers are marked by red "+" symbols. Where notched areas do not overlap, there is a statistical significance of at least 5% between the cruises. Left plots show all outliers. Right plots are an enlargement of the left plots.

The descriptive statistics of the 19 - point and 44 - point perspectives in Tables 89 and 90 show that the minimum concentration of surface SPM was consistently below 0.20 mg/l. GC1 even fell into that category if station E6, with an SPM concentration value of 0.17 mg/l was included in that consideration. (This value was not reflected in Table 89 because station E6 was not sampled during all five cruises.) All minimum concentration values were located at the southern edge of the project area. Conversely,

the maximum surface SPM concentration values sampled during each cruise (from the stations evaluated for Tables 89 and 90) varied widely in both value and location. It is interesting to note that none of these locations occurred at the Mississippi River stations.

Temporal variation of surface SPM at each station was assumed to be nonparametric in nature. This variation was quantified by calculating the percent-MAD (i.e., the percentage of the median of a given station represented by its median absolute deviation) of SPM measured at each station (Figure 97). Where the 19 common stations for all five cruises were considered, the median percent MAD was 76.41% with minimum and maximum values of 36.66% (Station H6) and 685.36% (Station F1) respectively. Concerning the 44 common stations for cruises GC2 thru GC5, the median percent standard deviation was 63.39% with minimum and maximum values of 17.99% (Station B5) and 641.87% (Station F1) respectively. These values clearly show that certain areas of the project site exhibited more variability over time than others. The regions of greatest fluctuation were seen at the near-shore stations F1 and G1. Stations C1, H1, E4 and G4 were also characterized by relatively large temporal variation in SPM concentrations. Contrary to these areas, Stations MR3 and E1, located at the mouths of the Mississippi and Atchafalaya Rivers respectively, displayed relatively low variation in SPM concentrations over time.

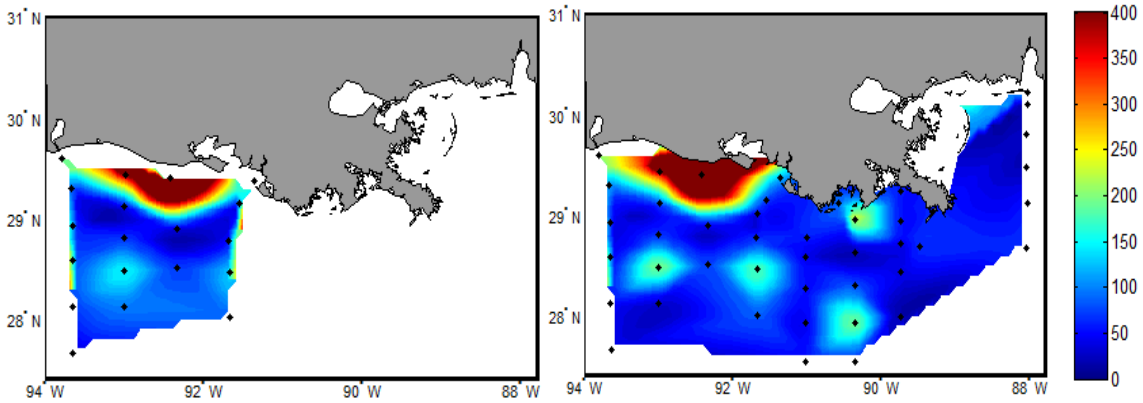

Figure 97. %MAD of Surface SPM

The percent median absolute deviation of surface SPM. Left GC1 thru GC5. Right. GC2 thru GC5.

Surface SPM and Salinity

Fresh was water discharged into the northern Gulf of Mexico during pulse events. Fluvial sources of SPM included multiple rivers discharging into in Mobile Bay, Alabama, the Sabine River at the Texas-Louisiana border and from the Mississippi and Atchafalaya Rivers. The discharge of these latter two rivers are shown in Figure 98. GC3 and GC5 took place during periods of relatively low flow while cruises GC1, GC2, and GC4 were conducted during times of higher river discharge. Figures 99 and 100 show the near-surface distributions for salinity measured by the optical profiler and the MAD values for salinity respectively.

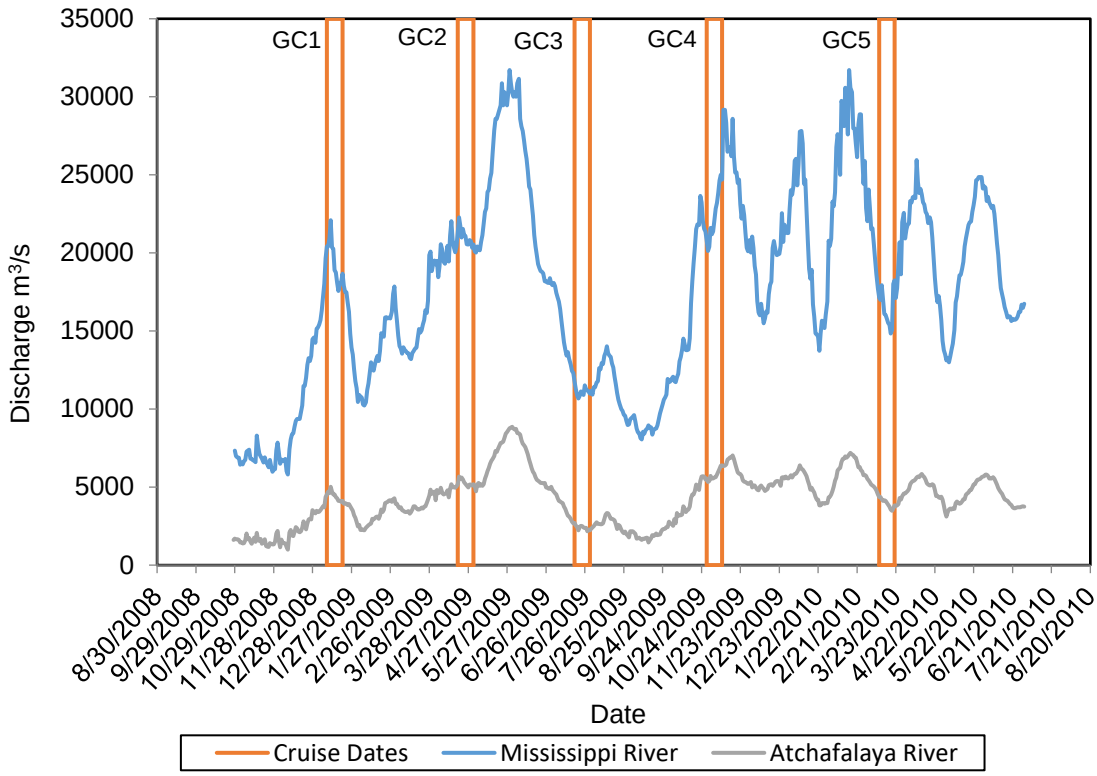

Figure 98. River Discharge, Mississippi & Atchafalaya

Daily discharge from the Mississippi River at USGS Station Belle Chasse, Louisiana an33d from the Atchafalaya River at USGS Station Morgan City, Louisiana. Cruise dates are noted.

From Figure 99 it is evident that the project area experienced regions of freshwater associated with rivers. Oceanic waters were best represented in the southwest of the project area. Many stations experienced conditions somewhere between these two end members. The two plots in Figure 100 are based upon observations from the 19 stations common to all five cruises and upon the 44 stations common to cruises GC2 thru GC5. Figure 100 is particularly useful in demonstrating the variability of surface salinity in the project area. It is interesting that the addition of GC5 salinity data to the western half of the project area had a dampening effect on the MAD values for several stations.

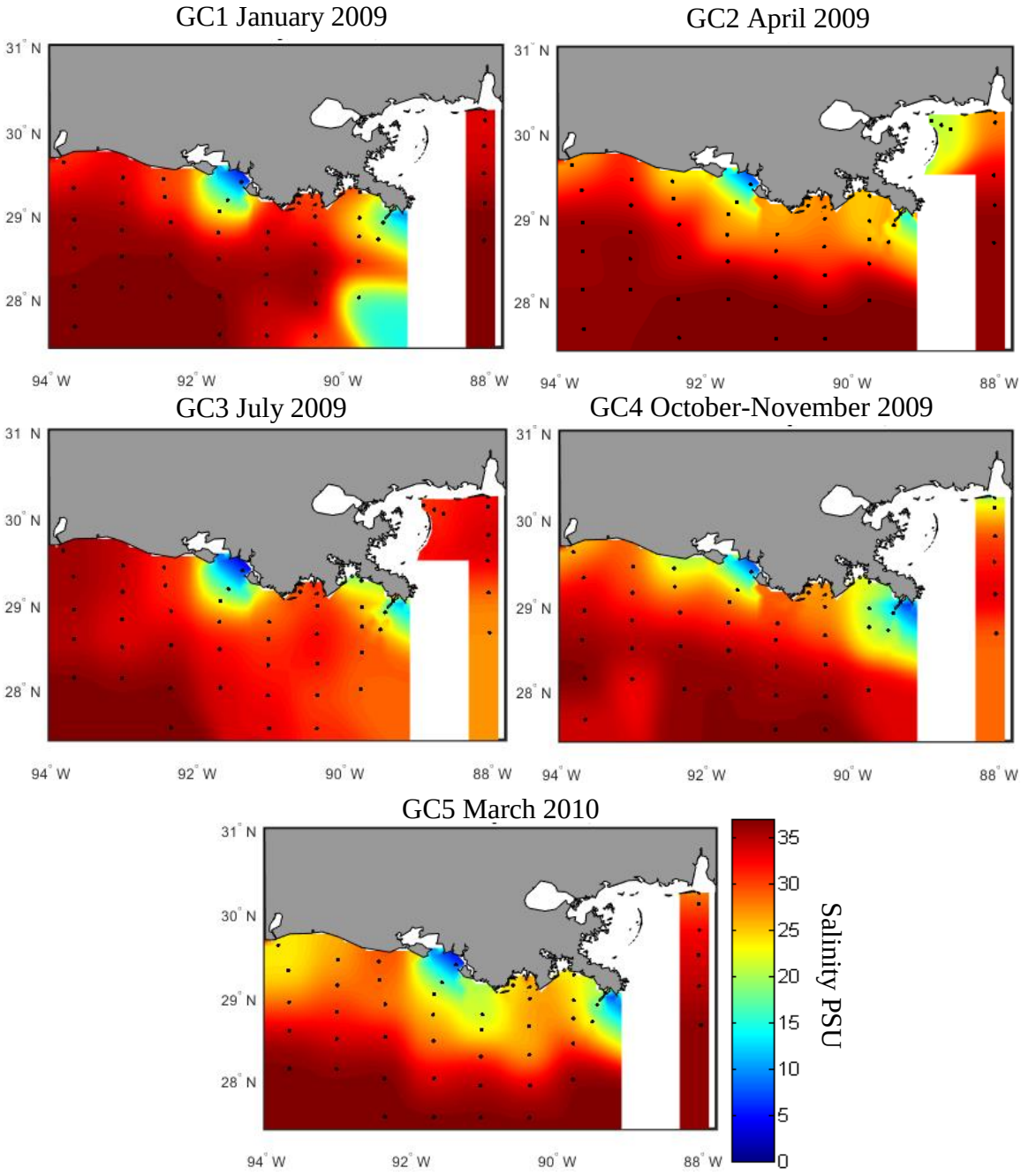

Figure 99. Near – Surface Salinity

Salinity values plotted are the median values of the 0.75 – 2.0 m depth range observed by the SBE49 on the optical profiler.

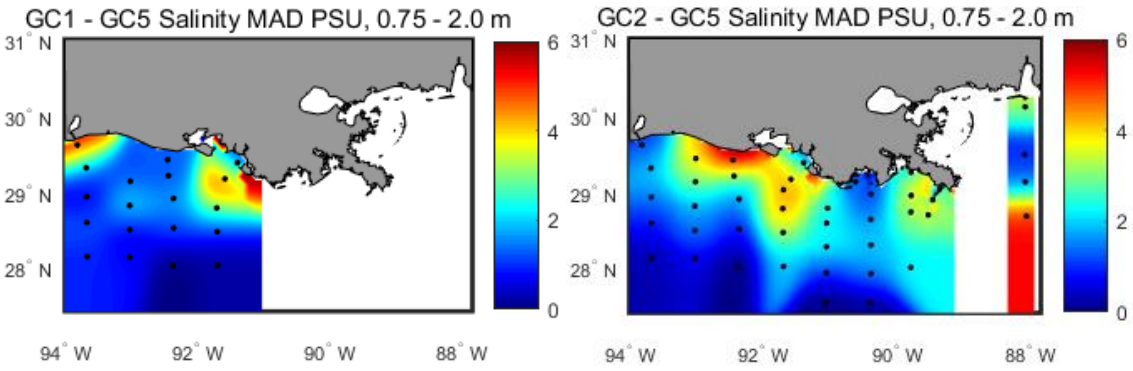

Figure 100. MAD Sea Surface Salinity

Notes. The left plot shows the MAD for the 19 stations common to all five cruises. The right plot shows the MAD for the 44 stations common to cruises GC2 thru GC5.

Table 91 and Figure 101 demonstrate a significant association between SPM and salinity in surface waters. For these evaluations, two different sets of salinity data were utilized. First, SPM was associated with salinity values (from the optical profiler) reported at the filterdepths. Second, the relationship between near-surface salinity and SPM was evaluated using salinity values from the 0.75 – 2.0 m depth range from the optical profiler. As might be expected, Figure 101 shows that large concentrations of SPM are found in areas of low salinity. However, large concentrations of near-surface SPM may also be found at mid-range and even relatively high (~30 PSU) salinity.

Table 91

Relationship Between SPM and Surface Salinity

Cruise	Filterdepth Salinity Spearman Correlation Coefficients			0.75 - 2.0 m Salinity Spearman Correlation Coefficients		
	ρ	p	n	ρ	p	n
GC1	-0.72	0.00	22	-0.79	0.00	21
GC2	-0.84	0.00	49	-0.82	0.00	50
GC3	-0.69	0.00	50	-0.73	0.00	50
GC4	-0.85	0.00	46	-0.74	0.00	46
GC5	-0.90	0.00	49	-0.91	0.00	49
GCALL	-0.79	0.00	215	-0.78	0.00	216

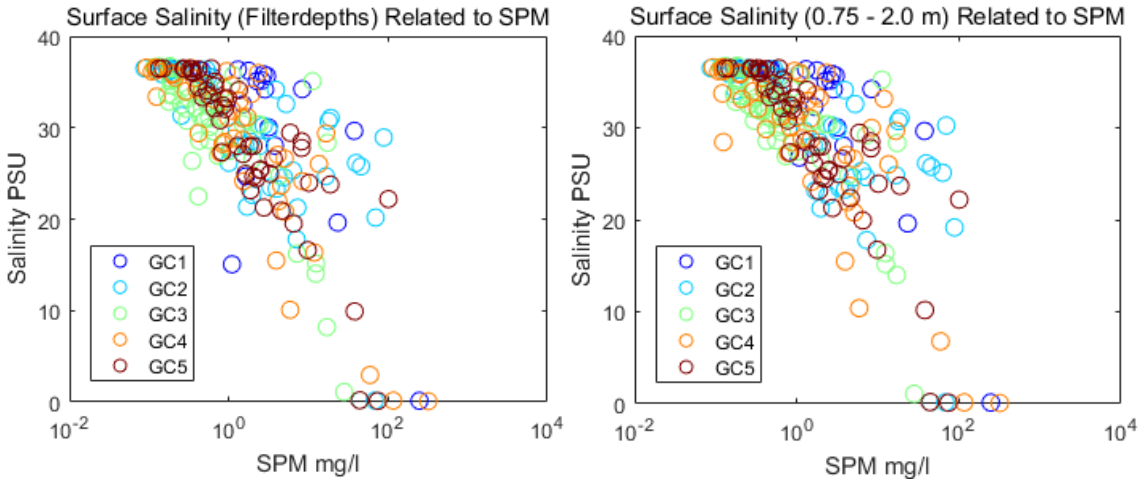

Figure 101. Surface SPM vs. Salinity

Surface SPM and D50

The distribution of the mean diameter of SPM (in µm) was plotted for near – surface waters (1.0 – 2.0 m depth range) for all cruises in Figure 102. Two versions of the plots are offered. The plots on the left include all available D50 data calculated from LISST observations. The tops of all of the LISST based attenuation profiles were examined, and stations where near-surface observations were suspected to have been

influenced by schlieren were identified using the methods described in Chapter IV. These points were removed from the working datasets. The modified datasets were then plotted and are located on the right side of the figure. Regarding cruise GC4, so many near-surface points were removed from the working dataset due to suspected schlieren that a meaningful surface could not be generated with the remaining values. Regarding the other four cruises, the removal of points suspected to have been influenced by schlieren made significant differences on a local scale (especially where the point was removed from the nearshore environment). In most cases though, regional differences due to point removal are not apparent at first glance.

In most cases, the populations of the largest particles (by diameter) occurred in the southern part of the project area. Other areas of mid-range to large particles appear to be associated with the distal portions of the river plumes. The three stations associated with the Atchafalaya river outfall region (E0, E1, and E2) are notable in that for cruises GC1 and GC2, these stations are associated with significantly smaller particles than neighboring stations. Even during GC3, these stations have populations of SPM with smaller particles than the stations just to the south.

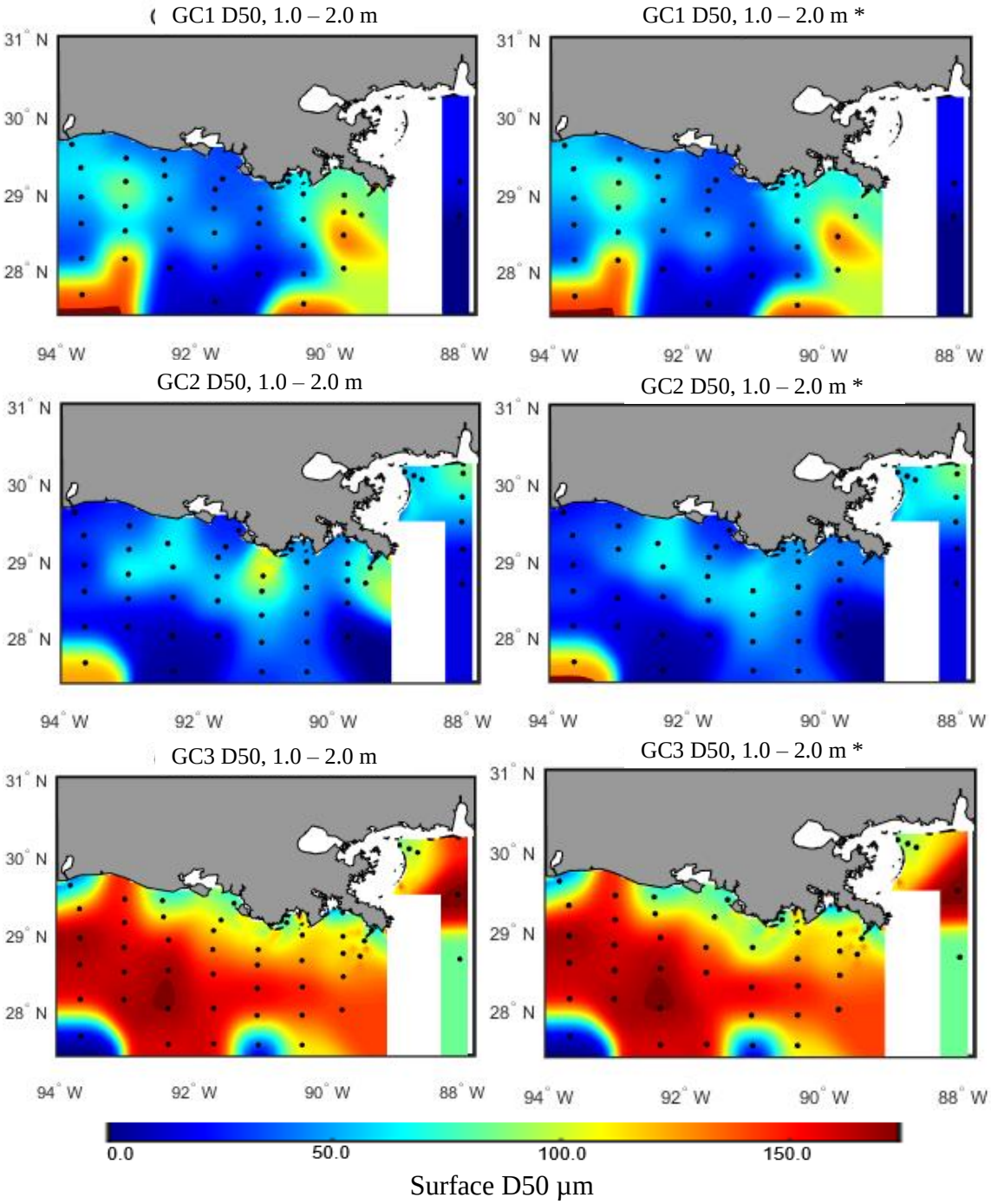

Figure 102. Surface D50

Plots on the left show all available surface station data. Plots on the right show surfaces created using the same datasets after stations with suspected schlieren influence were removed. For GC4, after stations with suspected schlieren artifacts were removed from the dataset, there were not enough remaining points to create a meaningful surface.

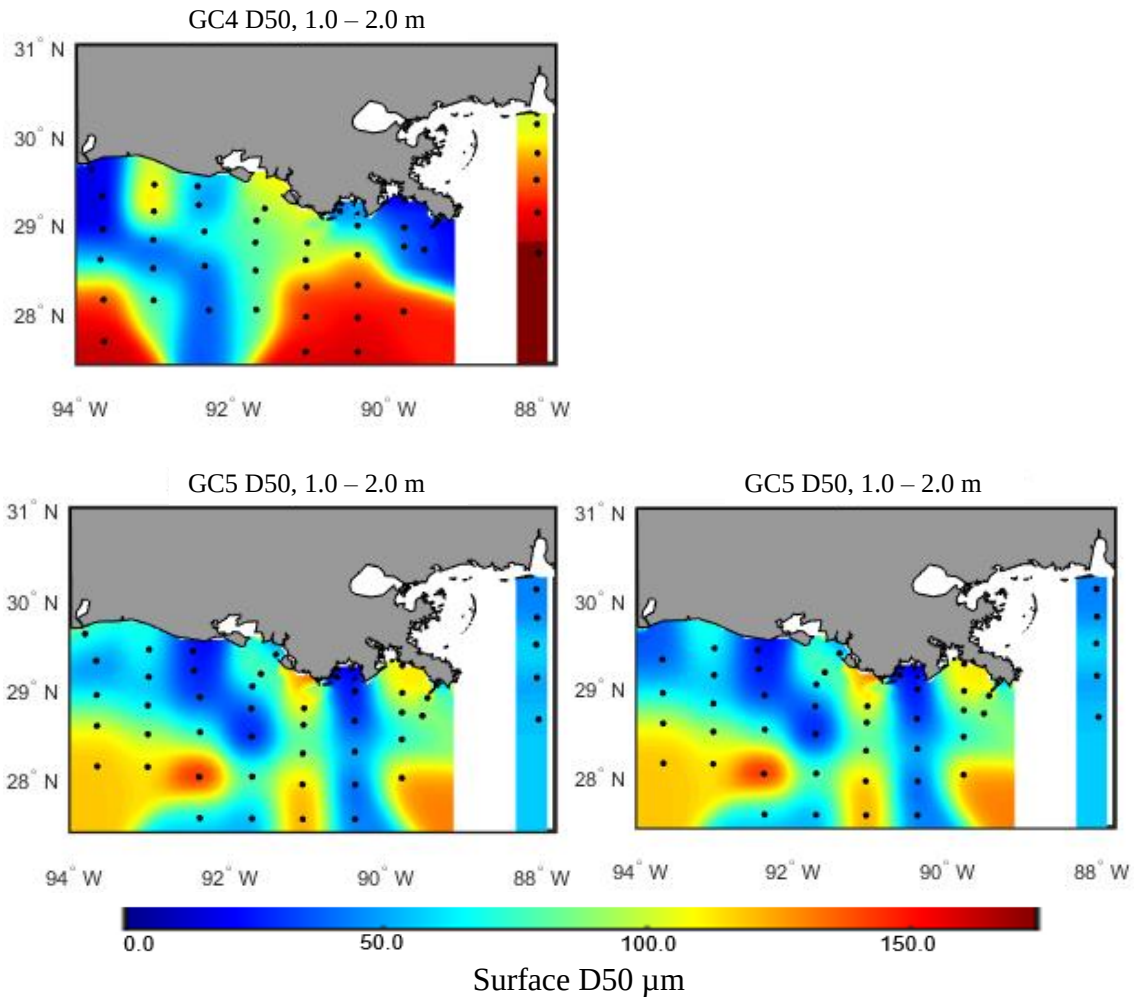

Figure 102 (continued). Surface D50

Plots on the left show all available surface station data. Plots on the right show surfaces created using the same datasets after stations with suspected schlieren influence were removed. For GC4, after stations with suspected schlieren artifacts were removed from the dataset, there were not enough remaining points to create a meaningful surface.

The areas displaying SPM populations with large – diameter particles are likely associated with planktonic organisms as individuals in such populations tend to be larger and less dense than lithogenic particles. The large percentage of particulate carbon associated with near-surface SPM (Figure 103) also suggests a strong biogenic signal in these populations. These data indicate that the study area during GC3, in particular, experienced a lot of organic activity in the surface waters.

Particulate Carbon (PC)

Estimations of organic versus inorganic matter (or living and detrital matter versus lithogenic material) are useful to this research, since having an approximation of the organic component of bulk SPM is applicable in distinguishing between different populations and give some hints about the particulate sources. A previous study estimated the relationship between SPM and particulate organic carbon (POC) to be Organic-Matter/POC = 2.6 g/g (Babin, Morel, et al., 2003). In other words, assuming all PC is, in fact, POC then for SPM to consist of 100% organic matter, SPM would need to be approximately 38.5% PC. In this research, there are several cases where percent PC in SPM is greater than 38.5%.

A different study (Feely, 1975) showed that the population of SPM at two sites in the Gulf of Mexico between the depths of 550 m and 3075 m had the total carbon content (PC) contained between 85.7% to 95.6% POC. Furthermore, the SPM collected at these sites consisted of 16% to 86% PC. For that research, nucleopore filters were used at one site and Millipore filters at the other site indicating that these values should be viewed as estimates only when compared one with another.

For the purposes of this project qualitative estimations of living plus detrital matter are made by measuring the amount of total carbon in SPM. The filtration method used to generate these data are described in Chapter II. The approximate percent of SPM which consisted of PC was also calculated for analysis (hereafter referred to as %PC). The %PC values were determined using concentrations of two separate sets of filter samples. As a result, at locations where the SPM concentrations were low, it was more likely to get less accurate %PC values as the presence or absence of a few planktonic

organisms on either the SPM filters or the PC filters had a significant effect on the calculated concentration of the affected filter sample. The most extreme occurrence of this effect occurred at 1.5 m, station E5, during GC2 where %PC was 102%.

Particulate carbon (PC) samples were collected during each cruise. However, cruises GC1 and GC5 did not have enough of these types of samples collected to consider the regional representation of this attribute. The regional distributions of particulate carbon (PC) and %PC for cruises GC2 thru GC4 are shown in Figure 103.

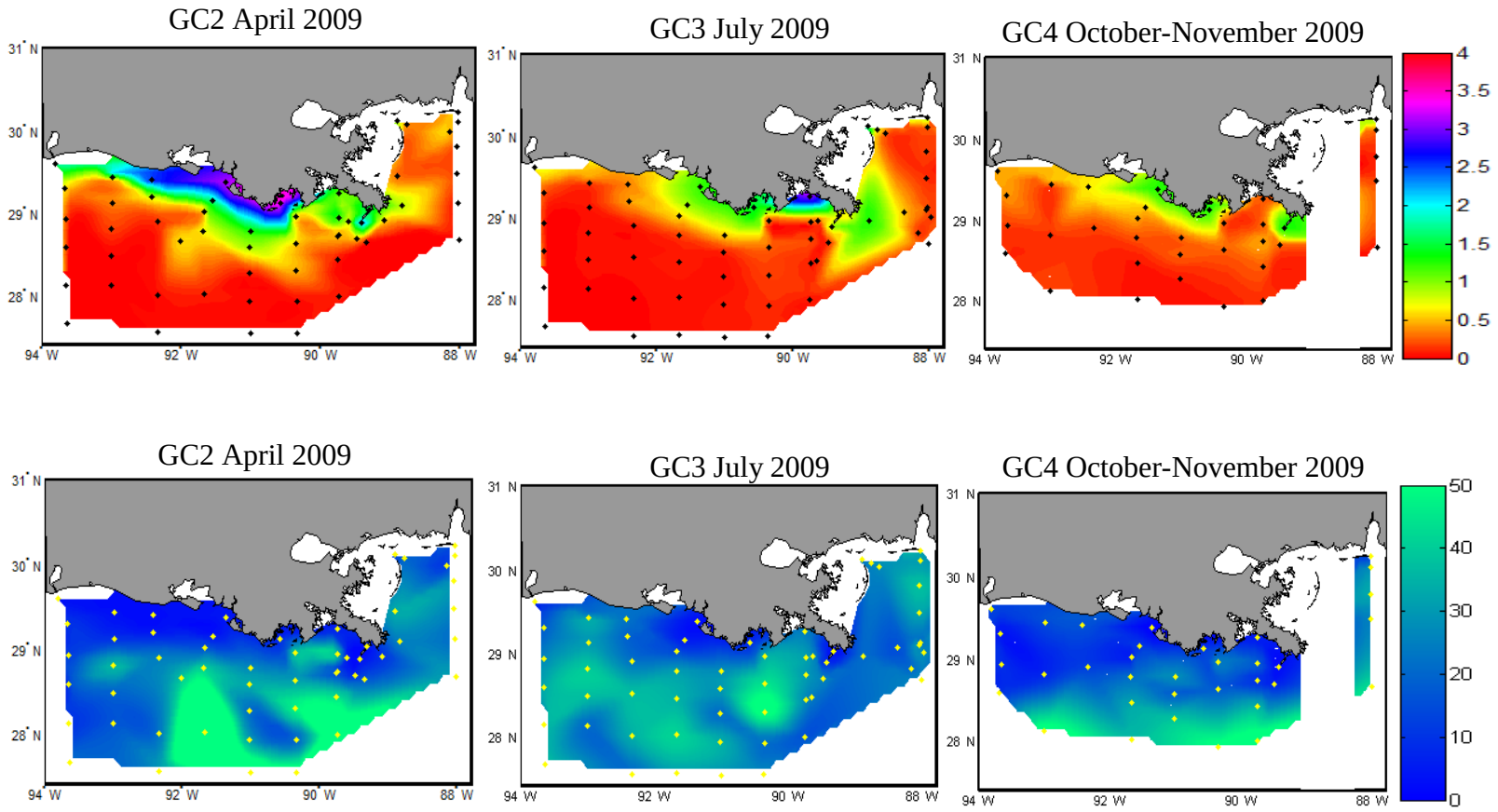

Figure 103. Surface PC Distribution

Top: PC, mg/l, Bottom %PC. Note, for the %PC plots, some surface samples were greater than 50% (four in GC2, one in GC3 and two in GC4). Sample locations are noted.

The highest concentrations of PC were consistently seen in the near-shore portion of the project area with the greatest occurrences of PC concentrations at Stations C0, B1 and MR1 (Tables 93 and 94 and Figure 103). The smallest concentrations of PC were observed in the southwest portion of the study site at stations E5 and G5. Figure 104 shows the distribution of concentration for all surface PC samples for cruises GC2 thru GC4. Kruskal-Wallis comparisons between the complete surface dataset for these three cruises indicate that each were statistically different from each other (GC2 – GC3 p = 0.07, GC2 – GC4 p = 0.38, GC3 – GC4 p = 0.17).

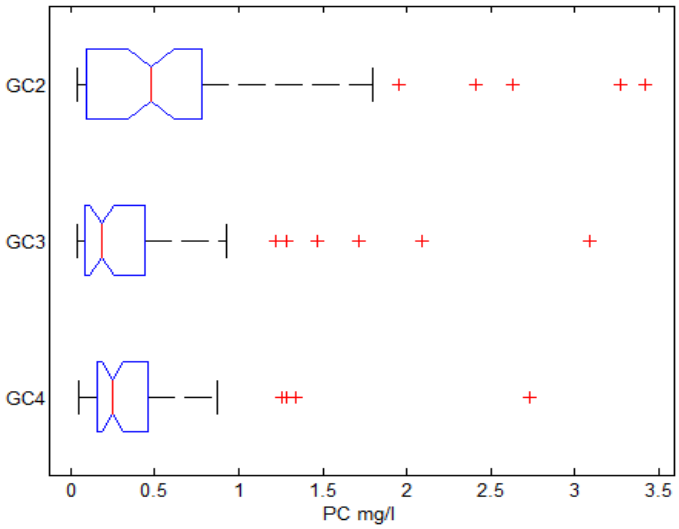

Figure 104. Surface PC Box & Whisker Plots

Box and whisker plot of all surface PC samples for GC2 thru GC4. nGC2 = 57; nGC3 = 62; nGC4= 44. Red lines show median SPM concentration. Boxes show the interquartile range (left side 25th percentile, right side 75th percentile). Whiskers extend to the most extreme values not considered outliers by MATLAB. Outliers are marked by red "+" symbols. Where notched areas do not overlap, there is a statistical significance of at least 5% between the cruises.

Table 92

PC for Stations Common to GC2 – GC4

Cruise	Surface PC mg/l		
	Median	Min. (Station)	Max (Station)
GC2	0.57	0.04 (G5)	3.41 (C0)
GC3	0.19	0.04 (G5)	3.08 (B1)
GC4	0.25	0.05 (E5)	2.73 (MR1)

The study of particulate carbon is relevant to the study of SPM in that it is assumed that a large percentage of PC is organic in nature. Therefore, understanding the particulate carbon content (%PC) of SPM becomes important. Regional distribution of %PC is shown in the lower half of Figure 103. The particulate carbon content (%PC) of SPM generally increases with distance from fluvial influences. Similar distributions have been noted at other locations (Goni et al., 2006). If the Babin ratio (Babin, Morel, et al., 2003) (requiring 38.5% PC to represent a 100% biogenic SPM population holds) true for the northern Gulf of Mexico, then the %PC plots in Figure 103 suggest that large regions of the study area had SPM populations consisting completely of organic matter.

Table 93

%PC for Stations Common to GC2 – GC4

Cruise	Surface %PC of SPM mg/l		
	Median	Min. (Station)	Max (Station)
GC2	19.6	2.99 (F1)	102.55 (E5)
GC3	26.96	2.46 (MR1)	44.77 (C2)
GC4	25.2	0.42 (E0)	342.08 (A6)

Note. Only the stations common to GC2 - GC4 are considered. n = 36

Finally, during GC5, additional filter samples were obtained in the near surface waters to estimate particulate organic carbon (POC) using a mass spectrometer. GF/F

filters were used in establishing this dataset. The distribution of POC and percent POC of the SPM populations are displayed in Figure 105. Similar to the total particulate carbon regional distribution seen in cruises GC2, GC3, and GC4, the highest concentration of POC was located nearshore. Figure 105 shows POC extending further south during GC5 than the PC did during cruises GC2 thru GC4. Since different types of filters were used to collect samples for PC and POC, one cannot be sure about the accuracy of any regional comparison using these two different data types.

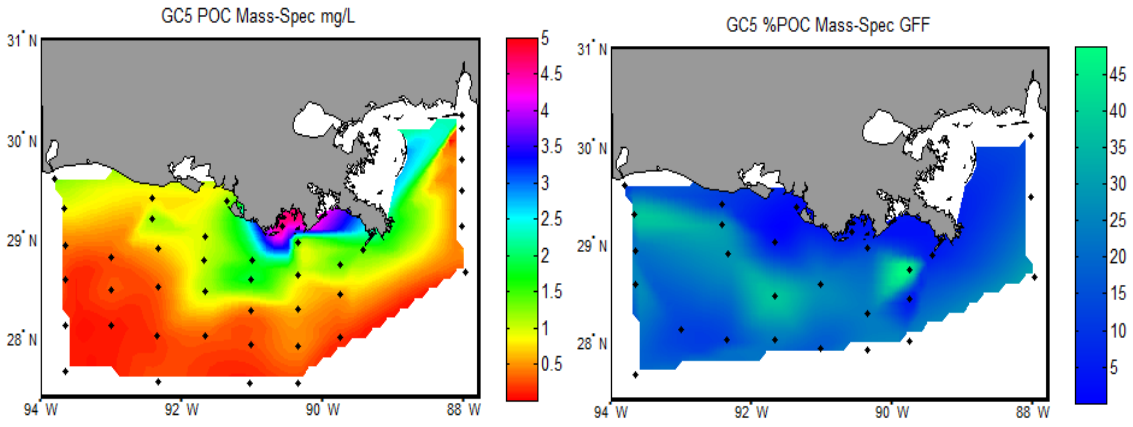

Figure 105. Surface POC & %POC, GC5

Conclusions

Chapter VII addressed and supported Hypothesis 2 of this dissertation that "regional SPM concentration and composition varies over time." All objectives related to this hypothesis were completed and discussed. SPM attributes evaluated in this chapter describe some of the ways SPM populations change both temporally and spatially. Distribution of SPM in the near - surface and near-bottom waters were evaluated.

CHAPTER VIII – CLOSING REMARKS

This dissertation was developed, in part, to serve as a tool for hydrographers wanting to maximize the utility of data products produced during airborne bathymetric lidar surveys, by analyzing the potential for using those data types for estimating SPM concentration. This aim is in keeping with the survey-once, use-many-times concept that is often a goal of current survey programs. These closing remarks are intended to provide counsel to hydrographers, managers and other parties planning airborne bathymetric lidar surveys or intending to use data from previous projects for the purpose of estimating SPM concentration. Here the word "estimating" is used deliberately as even the best models cannot always account for the vagrancies and nuances that occur in natural waters. And, as this dissertation demonstrates, some optical properties are better for SPM prediction than others. The independent signals of both the lidar and hyperspectral sensors are considered. By applying spatially appropriate algorithms, large portions of airborne hydrographic survey project areas may yield first-order SPM concentration approximations.

Though not the ideal data-type for the purpose, the lidar signal itself (and its close association with the IOP combination $a + b_b$ at 532 nm) may be used to predict SPM. (For all that there is promise for using lidar signals for SPM prediction, the results from Chapter V of this work indicate that that the best IOPs for the purpose are b_b, c, and b, but these parameters are not presently attainable from lidar systems.) Since absorption is often the dominating IOP in the combination $a + b_b$, (especially in nearshore waters), *regional* and *temporal* tuning of these SPM models is strongly encouraged. The benefit of

using the modified k_{sys} of the laser signal for estimating SPM is the wonderful spatial resolution available from that source. Therefore, even lower performing SPM models may be of great benefit, so long it is understood that there will likely be large uncertainties associated with them. This work used the IOP combinations $a + b_{bt}$ and $a + b_{bp}$ (sometimes referred to collectively as $a + b_b$) at 532 nm to approximate the lidar's k_{sys} capability. The results of the effectiveness of these IOP combinations to estimate SPM were mixed.

Six wavelengths of the IOP combination $a + b_b$ were evaluated using AC9 and BB9 sensors. None of the algorithms utilizing AC9 data performed well. The $a + b_b$ models utilizing absorption from the AC9 at 532 nm ranked at the very bottom (# 27 and # 28) of the 28 $a + b_b$ algorithms produced in this research. On it's own, this information provides a dim view on the potential for using part of a bathymetric lidar signal to predict SPM, especially when considering that the number of data points available for the formation of these two algorithms at 532 nm from the AC9 ($n = 260$ for both $a + b_{bp}$ and $a + b_{bt}$) far exceeded the number of available data pairs available for $a + b_b$ algorithm production using the ACS ($n = 159$ for $a + b_{bp}$ and $n = 157$ for $a + b_{bt}$). However, the results of the $a + b_b$ algorithms from the ACS are much more encouraging. Eight wavelengths of the IOP combination $a + b_b$ were evaluated using the ACS and BB9 sensors. The 532 nm models ranked # 5 and # 6 of the 28 $a + b_b$ algorithms produced. (The 532 nm $a + b_b$ algorithms were outperformed by wavelengths 715 nm and 595 nm, all from the ACS.) These same $a + b_b$ models using the ACS data at 532 nm rank # 51 and # 55 out of over 160 models evaluated (Table 56).

If I were to be put in charge of the data acquired from a CZMIL hydrographic survey, I would feel confident using an R_{rs}–based pair of algorithms (utilizing the wavelengths of maximum signal similar to the ones developed in this research) to calculate first-order approximation values of SPM concentrations. At the present stage of this type of research, I would choose to only employ such algorithms in optically deep waters (where the seafloor does not contribute to R_{rs} signals). As a recommended rule of thumb, and until the question can be given greater attention and research, I would consider the water optically deep if the powered 532 nm lidar signal attenuates before it penetrates deep enough to provide a seafloor return signal. This means that the most likely places for the R_{rs} signals to be useful for SPM prediction will be at the deepest edges of planned survey areas, over plume features, and possibly while the airborne platform is in transit. The R_{rs} based pair of algorithms can be used for first - order SPM approximation.

Future steps for progressing along maximizing the utility of airborne hydrographic survey systems like CZMIL include obtaining simultaneous observations from the sea and the air. High costs and scheduling complications inherent to such data gathering projects means that limited efforts have yet been performed to this end. However, in order to better predict SPM, one will need to evaluate data pairs of the depth-isolated K_{sys} values minus the expected volume scattering of the waveform and measured SPM concentration. (This research used the proxy $a + b_b$ to represent the first value in these data pairs.) Since absorption coefficients can have wild variations both temporally and spatially, the expectation of creating a universal SPM prediction

algorithm using $a + b_b$ alone would be a bad idea. As discussed earlier contributors to the absorption budget (especially by CDOM, non-algal particles and phytoplankton) change over temporal and spatial scales. However, if it is known that a particular area will be regularly surveyed by airborne hydrographic systems such as CZMIL, it might be worth the effort to perform time-series filter sampling of SPM (especially in the surface waters) of a few stations in depths that can be resolved by lidar waveforms and have a significant portion of potential waveforms be composed of water volume scattering so that the median slope may be calculated. This will allow interested parties to better understand the temporal variation of SPM in the area of interest. Finally, it is important to schedule SPM sampling to occur coincidentally with the airborne platform so that the lidar-based SPM algorithm can be tuned. The more coincident sampling that can be done the better! (Also, if the 1054 nm waveforms penetrate the sea surface, these waveforms may be used in a similar manner as the 532 nm waveforms to produce data to be regressed relative to measured SPM concentration in surface waters.)

Additional future research might include determining when an airborne hydrographic survey system flies over optically deep waters relative to the hyperspectral sensor. If a better relationship between optically deep waters (relative to the hyperspectral sensor) and the k_{sys} signal can be identified, that knowledge may significantly increase the portion of each total accumulated R_{rs} dataset that may be easily used for SPM prediction. First, we'd want to verify the hypothesis that when the active laser attenuates before reaching the seafloor, the full observed spectrum for R_{rs} data is observing optically deep waters. (Recall that different wavelengths of visible light interact distinctly from

other wavelengths. Therefore depths that are optically deep for red wavelengths may not be optically deep for blue wavelengths.) This may be approached by using a sensor like Satlantic's HyperPro to generate ship-based profiles of diffuse attenuation (k_d) for multiple visible wavelengths. If these profiles do not show an increase in k_d as the sensor approaches the seafloor (and if the operator cannot see the seafloor with her eyes over the boat rail), then the water is most likely optically deep for visible wavelengths. Since water column constituents (such as SPM) are temporally variable, k_d data collection will need to be done in concert with the airborne platform. One will want to be sure to sample environments where lidar signal extinction is expected (such in waters deeper than 45 m) and where lidar is likely to reach the bottom (such as in areas where the bottom may be seen by ship-borne researchers).

Since it is possible that lidar signals may reach the seafloor in optically deep waters (relative to the hyperspectral sensor), that relationship might also bear some study. Large datasets of paired depth-delimited modified k_{sys} values (as described above) and k_d profiles might allow future research to determine the relationship between optically deep waters (particularly for the shorter wavelengths) and the lidar signal. Again, this relationship is expected to change both spatially and temporally. Consider the difference in near-surface SPM at stations F1 and G1 (Figures 5 and 94).

On can also create a regionally tuned b_b–based SPM models as was done in this dissertation, then use a R_{rs} inversion process such as the quasi-analytical algorithm (QAA) (Z. Lee, Arnone, Hu, Werdell, & Lubac, 2010; Z. Lee et al., 2002) to approximate b_b. This approach to SPM prediction has the disadvantage of utilizing an IOP derived

from inversion (therefore only an estimate of b_b) to run the b_b-based model. However, further experimental efforts may prove that using modeled b_b to (in its turn) model SPM may provide superior results to other methods considered here.

The variability of SPM concentration, particle size distribution, and composition makes it a SPM prediction a difficult subject to study in general terms. Nevertheless, the ability to provide first-order approximations of SPM concentration may be very useful to many parties with interests in the nearshore environment. This type of information becomes even more valuable when additional parameters are known about specific survey areas. For example, if repeat surveys are expected over a site with a known sewage outfall pipe, understanding the distribution of SPM around that feature may help researchers and managers understand residency time, dilution rates and other related properties of the plume.

APPENDIX A – Permission to use Table

SEQUOIA

June 18th, 2018

TO: Sarah Epps
FROM: Sequoia Scientific, Inc.
RE: Approval Letter

Sarah,

We are pleased to give you permission to use the table on page 64 of out publication LISST-100X Particle Size Analyzer, User's Manual Version 4.65 in your dissertation, The Feasibility of using Inherent Optical Properties and the Apparent Optical Property Remote Sensing Reflectance to estimate Suspended Particulate Matter, Particularly for use in Airborne Hydrographic Surveys.

Thank You,

Yogi Agrawal
President/Founder

Sequoia Scientific, Inc.
2700 Richards Road, Suite 107
Bellevue WA 98005 USA
425.641.0944 (T); 425.643.0595 (F)
www.SequoiaSci.com ; info@SequoiaSci.com

REFERENCES

Ackleson, S. G. (2006). Optical determinations of suspended sediment dynamics in western Long Island Sound and the Connecticut River plume. *Journal of Geophysical Research: Oceans, 111*(C7), C07009. doi:10.1029/2005jc003214

Ackleson, S. G., & O'Donnell, J. (2011). Small-scale variability in suspended matter associated with the Connecticut River plume front. *Journal of Geophysical Research: Oceans, 116*(C10), n/a-n/a. doi:10.1029/2011JC007053

Agrawal, Y. C., & Pottsmith, H. C. (2000). Instruments for particle size and settling velocity observations in sediment transport. *Marine Geology, 168*(1-4), 89-114. doi:Doi: 10.1016/s0025-3227(00)00044-x

Agrawal, Y. C., Whitmire, A., Mikkelsen, O. A., & Pottsmith, H. C. (2008). Light scattering by random shaped particles and consequences on measuring suspended sediments by laser diffraction. *Journal of Geophysical Research: Oceans, 113*, C04023, 04021-04011. doi:10.1029/2007JC004403

Ahn, Y.-H., Bricaud, A., & Morel, A. (1992). Light backscattering efficiency and related properties of some phytoplankters. *Deep Sea Research Part A. Oceanographic Research Papers, 39*(11-12), 1835-1855. doi:Doi: 10.1016/0198-0149(92)90002-b

Analytical Spectral Devices, I. (2002). FieldSpec Pro User's Guide (Vol. Rev. C, pp. 136): Boulder, Co.

Analytical Spectral Devices, I. (2003, 12/17/2003). *FieldSpec UV/VNIR HandHeld Spectroradiometer User's Guide, revC*. Analytical Spectral Devices, Boulder.

Astoreca, R., Doxaran, D., Ruddick, K., Rousseau, V., & Lancelot, C. (2012). Influence of suspended particle concentration, composition and size on the variability of inherent optical properties of the Southern North Sea. *Continental Shelf Research, 35*(0), 117-128. doi:http://dx.doi.org/10.1016/j.csr.2012.01.007

Aurin, D. A., & Dierssen, H. M. (2012). Advantages and limitations of ocean color remote sensing in CDOM-dominated, mineral-rich coastal and estuarine waters. *Remote Sensing of Environment, 125*(0), 181-197. doi:http://dx.doi.org/10.1016/j.rse.2012.07.001

Avinash, K., Jena, B., Vinaya, M. S., Jayappa, K. S., Narayana, A. C., & Gangadhara Bhat, H. (2012). Regionally tuned algorithm to study the seasonal variation of suspended sediment concentration using IRS-P4 Ocean Colour Monitor data. *The Egyptian Journal of Remote Sensing and Space Science, 15*(1), 67-81. doi:http://dx.doi.org/10.1016/j.ejrs.2012.05.003

Azetsu-Scott, K., Johnson, B. D., & Petrie, B. (1995). An intermittent, intermediate nepheloid layer in Emerald Basin, Scotian Shelf. *Continental Shelf Research, 15*(2–3), 281-293. doi:http://dx.doi.org/10.1016/0278-4343(93)E0003-Q

Babin, M., Morel, A., Fournier-Sicre, V., Fell, F., & Stramski, D. (2003). Light Scattering Properties of Marine Particles in Coastal and Open Ocean Waters as Related to the Particle Mass Concentration. *Limnology and Oceanography, 48*(2), 843-859.

Babin, M., Stramski, D., Ferrari, G. M., Claustre, H., Bricaud, A., Obolensky, G., & Hoepffner, N. (2003). Variations in the light absorption coefficients of phytoplankton, nonalgal particles, and dissolved organic matter in coastal waters

around Europe. *Journal of Geophysical Research: Oceans, 108*(C7). doi:10.1029/2001JC000882

Baird, M. E., Cherukuru, N., Jones, E., Margvelashvili, N., Mongin, M., Oubelkheir, K., . . . Wild-Allen, K. A. (2016). Remote-sensing reflectance and true colour produced by a coupled hydrodynamic, optical, sediment, biogeochemical model of the Great Barrier Reef, Australia: Comparison with satellite data. *Environmental Modelling & Software, 78*, 79-96. doi:http://dx.doi.org/10.1016/j.envsoft.2015.11.025

Baker, E. T. (1984). Patterns of suspended particle distribution and transport in a large fjordlike estuary. *Journal of Geophysical Research: Oceans, 89*(C4), 6553-6566. doi:10.1029/JC089iC04p06553

Balch, W. M., Vaughn, J. M., Jr., Novotny, J. F., Drapeau, D. T., Goes, J. I., Booth, E., . . . Vaughn, J. M., Jr. (2002). Fundamental changes in light scattering associated with infection of marine bacteria by bacteriophage. *Limnology and Oceanography, 47*(5), 1554-1561. doi:10.4319/lo.2002.47.5.1554

Barth, J. A., & Bogucki, D. J. (2000). Spectral light absorption and attenuation measurements from a towed undulating vehicle. *Deep Sea Research Part I: Oceanographic Research Papers, 47*(2), 323-342. doi:http://dx.doi.org/10.1016/S0967-0637(99)00057-6

Bartholomä, A., Kubicki, A., Badewien, T. H., & Flemming, B. W. (2009). Suspended sediment transport in the German Wadden Sea—seasonal variations and extreme events *Ocean Dynamics, 59*(2), 213-225. doi:10.1007/s10236-009-0193-6

Bates, R. L., & Jackson, J. (1987). *Glossary of Geology* (3rd ed.). Alexandria, VA: American Geological Institute.

Baugh, J. V., & Manning, A. J. (2007). An assessment of a new settling velocity parameterisation for cohesive sediment transport modeling. *Continental Shelf Research, 27*(13), 1835-1855. doi:DOI: 10.1016/j.csr.2007.03.003

Behrenfeld, M. J., & Boss, E. (2003). The beam attenuation to chlorophyll ratio: an optical index of phytoplankton physiology in the surface ocean? *Deep Sea Research Part I: Oceanographic Research Papers, 50*(12), 1537-1549. doi:http://dx.doi.org/10.1016/j.dsr.2003.09.002

Bergmann, T., Fahnenstiel, G., Lohrenz, S., Millie, D., & Schofield, O. (2004). Impacts of a recurrent resuspension event and variable phytoplankton community composition on remote sensing reflectance. *J. Geophys. Res., 109*. doi:10.1029/2002jc001575

Berthon, J.-F., Lee, M., Shybanov, E., & Zibordi, G. (2007). *Measurements of the Volume Scattering Function in a coastal environment.* Paper presented at the Current Research on Remote Sensing, Laser Probing, and Imagery in Natural Waters.

Binding, C. E., Bowers, D. G., & Mitchelson-Jacob, E. G. (2005). Estimating suspended sediment concentrations from ocean colour measurements in moderately turbid waters; the impact of variable particle scattering properties. *Remote Sensing of Environment, 94*, 373-383. doi:10.1016/j.rse.2004.11.002

Biscaye, P. E., & Eittreim, S. L. (1977). Suspended Particulate Loads and Transports in the Nepheloid Layer of the Abyssal Atlantic Ocean*. In C. H. Bruce (Ed.), *Developments in Sedimentology* (Vol. Volume 23, pp. 155-172): Elsevier.

Bishop, J. K. B. (1986). The correction and suspended particulate matter calibration of Sea Tech transmissometer data. *Deep Sea Research Part A. Oceanographic Research Papers, 33*(1), 121-134. doi:http://dx.doi.org/10.1016/0198-0149(86)90111-1

Bishop, J. K. B. (1999). Transmissometer measurement of POC. *Deep Sea Research Part I: Oceanographic Research Papers, 46*(2), 353-369. doi:http://dx.doi.org/10.1016/S0967-0637(98)00069-7

Boggs, S. (1995). *Principles of Sedimentology and Stratigraphy* (Second ed.). New Jersey, United States: Prentice Hall.

Boss, E., & Pegau, W. S. (2001). Relationship of Light Scattering at an Angle in the Backward Direction to the Backscattering Coefficient. *Appl. Opt., 40*(30), 5503-5507.

Boss, E., Picheral, M., Leeuw, T., Chase, A., Karsenti, E., Gorsky, G., . . . Claustre, H. (2013). The characteristics of particulate absorption, scattering and attenuation coefficients in the surface ocean; Contribution of the Tara Oceans expedition. *Methods in Oceanography, 7*, 52-62. doi:http://dx.doi.org/10.1016/j.mio.2013.11.002

Boss, E., Slade, W. H., Behrenfeld, M., & Dall'Olmo, G. (2009). Acceptance angle effects on the beam attenuation in the ocean. *Optics Express, 17*(3), 1535-1550.

Boss, E., Stramski, D., Bergmann, T., Pegau, W. S., & Lewis, M. (2004). Why should we measure the optical backscattering coefficient? *Oceanography, 17*, 44-49.

Boss, E., Taylor, L., Gilbert, S., Gundersen, K., Hawley, N., Janzen, C., . . . Tamburri, M. N. (2009). Comparison of inherent optical properties as a surrogate for particulate matter concentration in coastal waters. *Limnology and Oceanography: Methods, 7*, 803–810.

Bourgault, D., Morsilli, M., Richards, C., Neumeier, U., & Kelley, D. E. (2014). Sediment resuspension and nepheloid layers induced by long internal solitary waves shoaling orthogonally on uniform slopes. *Continental Shelf Research, 72*(0), 21-33. doi:http://dx.doi.org/10.1016/j.csr.2013.10.019

Bourrin, F., Many, G., Durrieu de Madron, X., Martín, J., Puig, P., Houpert, L., . . . Béguery, L. (2015). Glider monitoring of shelf suspended particle dynamics and transport during storm and flooding conditions. *Continental Shelf Research, 109*, 135-149. doi:http://dx.doi.org/10.1016/j.csr.2015.08.031

Bowers, D. G. (2003). A simple turbulent energy-based model of fine suspended sediments in the Irish Sea. *Continental Shelf Research, 23*, 1495–1505. doi:10.1016/j.csr.2003.08.006

Bowers, D. G., & Binding, C. E. (2006). The optical properties of mineral suspended particles: A review and synthesis. *Estuarine, Coastal and Shelf Science, 67*, 219-230. doi:10.1016/j.ecss.2005.11.010

Bowers, D. G., Binding, C. E., & Ellis, K. M. (2007). Satellite remote sensing of the geographical distribution of suspended particle size in an energetic shelf sea.

Estuarine, Coastal and Shelf Science, 73, 457-466. doi:10.1016/j.ecss.2007.02.005

Bowers, D. G., Braithwaite, K. M., Nimmo-Smith, W. A. M., & Graham, G. W. (2011). The optical efficiency of flocs in shelf seas and estuaries. *Estuarine, Coastal and Shelf Science, 91*(3), 341-350. doi:DOI: 10.1016/j.ecss.2010.10.019

Bowers, D. G., Braithwaite, K. M., Nimmo-Smith, W. A. M., & Grahamb, G. W. (2009). Light scattering by particles suspended in the sea:The role of particle size and density. *Continental Shelf Research, 29*, 1748–1755. doi:10.1016/j.csr.2009.06.004

Bowers, D. G., Hill, P. S., & Braithwaite, K. M. (2014). The effect of particulate organic content on the remote sensing of marine suspended sediments. *Remote Sensing of Environment, 144*(0), 172-178. doi:http://dx.doi.org/10.1016/j.rse.2014.01.005

Bunt, J. A. C., Larcombe, P., & Jago, C. F. (1999). Quantifying the response of optical backscatter devices and transmissometers to variations in suspended particulate matter. *Continental Shelf Research, 19*(9), 1199-1220.

Cai, L., Tang, D., & Li, C. (2015). An investigation of spatial variation of suspended sediment concentration induced by a bay bridge based on Landsat TM and OLI data. *Advances in Space Research, 56*(2), 293-303. doi:http://dx.doi.org/10.1016/j.asr.2015.04.015

Campbell, D. E., & Spinrad, R. W. (1987). The relationship between light attenuation and particle characteristics in a turbid estuary. *Estuarine, Coastal and Shelf Science, 25*(1), 53-65. doi:http://dx.doi.org/10.1016/0272-7714(87)90025-4

Capello, M., Budillon, G., Cutroneo, L., & Tucci, S. (2009). The nepheloid bottom layer and water masses at the shelf break of the western Ross Sea. *Deep Sea Research Part II: Topical Studies in Oceanography, 56*(13–14), 843-858. doi:http://dx.doi.org/10.1016/j.dsr2.2008.10.032

Chakraborty, S. (2013). *Phytoplankton community distribution and light absorption properties in the northern Gulf of Mexico.* (3569756 Ph.D.), The University of Southern Mississippi, Ann Arbor. Retrieved from http://lynx.lib.usm.edu/docview/1371926880?accountid=13946 http://linksource.ebsco.com/linking.aspx?sid=Dissertations+%26+Theses+%40+University+of+Southern+Mississippi&fmt=dissertation&genre=dissertations+%26+theses&issn=&volume=&issue=&date=2013-01-01&spage=&title=Phytoplankton+community+distribution+and+light+absorption+properties+in+the+northern+Gulf+of+Mexico&atitle=&au=Chakraborty%2C+Sumit&isbn=9781303072758&jtitle=&btitle= Dissertations & Theses @ University of Southern Mississippi; ProQuest Dissertations & Theses Full Text database.

Chang, G. C., Dickey, T. D., Schofield, O. M., Weidemann, A. D., Boss, E., Pegau, W. S., . . . Glenn, S. M. (2002). Nearshore physical processes and bio-optical properties in the New York Bight. *Journal of Geophysical Research: Oceans, 107*(C9), 3133. doi:10.1029/2001JC001018

Chelsea_Technologies_Group_Ltd. AQUAtracka III, In-situ Fluorimeter, Nephelometer (pp. 2). Surrey, United Kingdom: Chelsea Technologies Group Ltd.

Chen, C.-T. A., Kandasamy, S., Chang, Y.-P., Bai, Y., He, X., Lu, J.-T., & Gao, X. (2017). Geochemical evidence of the indirect pathway of terrestrial particulate material transport to the Okinawa Trough. *Quaternary International, 441*(Part A), 51-61. doi:https://doi.org/10.1016/j.quaint.2016.08.006

Chen, J., Cui, T., Qiu, Z., & Lin, C. (2014). A three-band semi-analytical model for deriving total suspended sediment concentration from HJ-1A/CCD data in turbid coastal waters. *ISPRS Journal of Photogrammetry and Remote Sensing, 93*, 1-13. doi:http://dx.doi.org/10.1016/j.isprsjprs.2014.02.011

Chen, R. F., Bissett, P., Coble, P., Conmy, R., Gardner, G. B., Moran, M. A., . . . Zepp, R. G. (2004). Chromophoric dissolved organic matter (CDOM) source characterization in the Louisiana Bight. *Marine Chemistry, 89*(1–4), 257-272. doi:http://dx.doi.org/10.1016/j.marchem.2004.03.017

Chu, C.-M., & Churchill, S. W. (1955). Representation of the Angular Distribution of Radiation Scattered by a Spherical Particle*. *Journal of the Optical Society of America, 45*(11), 958-962. doi:10.1364/JOSA.45.000958

Chung, S. P., Gardner, W. D., Richardson, M. J., Walsh, I. D., & Landry, M. R. (1996). Beam attenuation and micro-organisms: spatial and temporal variations in small particles along 140°W during the 1992 JGOFS EqPac transects. *Deep Sea Research Part II: Topical Studies in Oceanography, 43*(4–6), 1205-1226. doi:http://dx.doi.org/10.1016/0967-0645(96)00030-6

Churchill, J. H., Biscaye, P. E., & Aikman Iii, F. (1988). The character and motion of suspended particulate matter over the shelf edge and upper slope off Cape Cod.

Continental Shelf Research, 8(5–7), 789-809. doi:http://dx.doi.org/10.1016/0278-4343(88)90077-5

Chust, G., Galparsoro, I., Borja, Á., Franco, J., & Uriarte, A. (2008). Coastal and estuarine habitat mapping, using LIDAR height and intensity and multi-spectral imagery. *Estuarine, Coastal and Shelf Science, 78*(4), 633-643.

Couturier, M., Nozais, C., & Chaillou, G. (2016). Microtidal subterranean estuaries as a source of fresh terrestrial dissolved organic matter to the coastal ocean. *Marine Chemistry, 186*, 46-57. doi:http://dx.doi.org/10.1016/j.marchem.2016.08.001

Curran, K. J., Hill, P. S., Milligan, T. G., Mikkelsen, O. A., Law, B. A., Durrieu de Madron, X., & Bourrin, F. (2007). Settling velocity, effective density, and mass composition of suspended sediment in a coastal bottom boundary layer, Gulf of Lions, France. *Continental Shelf Research, 27*(10-11), 1408-1421. doi:DOI: 10.1016/j.csr.2007.01.014

D'Sa, E. J., & Miller, R. L. (2003). Bio-optical properties in waters influenced by the Mississippi River during low flow conditions. *Remote Sensing of Environment, 84*(4), 538-549. doi:http://dx.doi.org/10.1016/S0034-4257(02)00163-3

D'Sa, E. J., Miller, R. L., & McKee, B. A. (2007). Suspended particulate matter dynamics in coastal waters from ocean color: Application to the northern Gulf of Mexico. *Geophysical Research Letters, 34*, L23611. doi:10.1029/2007GL031192

Davies, E. J., McKee, D., Bowers, D., Graham, G. W., & Nimmo-Smith, W. A. M. (2014). Optically significant particle sizes in seawater. *Applied Optics, 53*(6), 1067-1074. doi:10.1364/AO.53.001067

de-Nijs, M. A. J., Winterwerp, J. C., & Pietrzak, J. D. (2009). On harbor siltation in the fresh-salt water mixing region. *Continental Shelf Research, 29*, 175-193. doi:10.1016/j.csr.2008.01.019

de Moraes Rudorff, N., Frouin, R., Kampel, M., Goyens, C., Meriaux, X., Schieber, B., & Mitchell, B. G. (2014). Ocean-color radiometry across the Southern Atlantic and Southeastern Pacific: Accuracy and remote sensing implications. *Remote Sensing of Environment, 149*(0), 13-32. doi:http://dx.doi.org/10.1016/j.rse.2014.03.029

de Stigter, H. C., Boer, W., de Jesus Mendes, P. A., Jesus, C. C., Thomsen, L., van den Bergh, G. D., & van Weering, T. C. E. (2007). Recent sediment transport and deposition in the Nazaré Canyon, Portuguese continental margin. *Marine Geology, 246*(2–4), 144-164. doi:http://dx.doi.org/10.1016/j.margeo.2007.04.011

Deleware, U. o. (2009). Marine Operations | R/V Hugh R. Sharp. Retrieved from http://www.ceoe.udel.edu/marine/rvSharp.shtml

Deronde, B., Houthys, R., Henriet, J. P., & Van Lancker, V. (2008). Monitoring the sediment dynamics along a sandy shoreline by means of airborne hyperspectral remote sensing and LIDAR: a case study in Belgium. *Earth Surface Processes and Landforms, 33*, 280-294.

Dev, P. J., & Shanmugam, P. (2014). A new theory and its application to remove the effect of surface-reflected light in above-surface radiance data from clear and turbid waters. *Journal of Quantitative Spectroscopy and Radiative Transfer, 142*(0), 75-92. doi:http://dx.doi.org/10.1016/j.jqsrt.2014.03.021

Dolina, I. S., Dolin, L. S., Levin, I. M., Rodionov, A. A., & Savel'ev, V. A. (2007). *Inverse problems of lidar sensing of the ocean*.

Doron, M., Babin, M., Mangin, A., & Hembise, O. (2007). Estimation of light penetration, and horizontal and vertical visibility in oceanic and coastal waters from surface reflectance. *Journal of Geophysical Research: Oceans, 112*(C6), n/a-n/a. doi:10.1029/2006JC004007

Doron, M., Bélanger, S., Doxaran, D., & Babin, M. (2011). Spectral variations in the near-infrared ocean reflectance. *Remote Sensing of Environment, 115*(7), 1617-1631. doi:http://dx.doi.org/10.1016/j.rse.2011.01.015

Doxaran, D., Ehn, J., Bélanger, S., Matsuoka, A., Hooker, S., & Babin, M. (2012). Optical characterisation of suspended particles in the Mackenzie River plume (Canadian Arctic Ocean) and implications for ocean colour remote sensing. *Biogeosciences, 9*(8), 3213-3229. doi:10.5194/bg-9-3213-2012

Doxaran, D., Froidefond, J.-M., Lavender, S., & Castaing, P. (2002). Spectral signature of highly turbid waters: Application with SPOT data to quantify suspended particulate matter concentrations. *Remote Sensing of Environment, 81*(1), 149-161.

Doxaran, D., Ruddick, K., McKee, D., Gentili, B., Tailliez, D., Chami, M., & Babin, M. (2008). *Spectral variations of light scattering by marine particles in coastal waters, from the visible to the near-infrared*. Paper presented at the Ocean Optics XIX, Barger, Italy.

Doxaran, D., Ruddick, K., McKee, D., Gentili, B., Tailliez, D., Chami, M., & Babin, M. (2009). Spectral variations of light scattering by marine particles in coastal waters, from visible to near infrared. *Limnol. Oceanogr., 54*(4), 1257-1271.

Du, X., & Liu, J. T. (2017). Particle dynamics of the surface, intermediate, and benthic nepheloid layers under contrasting conditions of summer monsoon and typhoon winds on the boundary between the Taiwan Strait and East China Sea. *Progress In Oceanography, 156*(Supplement C), 130-144. doi:https://doi.org/10.1016/j.pocean.2017.06.009

Durrieu de Madron, X., Ferré, B., Le Corre, G., Grenz, C., Conan, P., Pujo-Pay, M., . . . Bodiot, O. (2005). Trawling-induced resuspension and dispersal of muddy sediments and dissolved elements in the Gulf of Lion (NW Mediterranean). *Continental Shelf Research, 25*(19–20), 2387-2409. doi:http://dx.doi.org/10.1016/j.csr.2005.08.002

Ellis, K. M., Bowers, D. G., & Jones, S. E. (2004). A study of the temporal variability in particle size in a high-energy regime. *Estuarine, Coastal and Shelf Science, 61*(2), 311-315. doi:http://dx.doi.org/10.1016/j.ecss.2004.06.001

Feely, R. A. (1975). Major-element composition of the particulate matter in the near-bottom nepheloid layer of the gulf of Mexico. *Marine Chemistry, 3*(2), 121-156. doi:http://dx.doi.org/10.1016/0304-4203(75)90019-5

Fennel, K., & Boss, E. (2003). Subsurface maxima of phytoplankton and chlorophyll: Steady-state solutions from a simple model. *Limnol. Oceanogr., 48*(4), 1521-1534.

Ferreira, A., Garcia, C. A. E., Dogliotti, A. I., & Garcia, V. M. T. (2013). Bio-optical characteristics of the Patagonia Shelf break waters: Implications for ocean color algorithms. *Remote Sensing of Environment, 136*, 416-432. doi:10.1016/j.rse.2013.05.022

Fettweis, M., Monbaliu, J., Baeye, M., Nechad, B., & Van den Eynde, D. (2012). Weather and climate induced spatial variability of surface suspended particulate matter concentration in the North Sea and the English Channel. *Methods in Oceanography, 3–4*(0), 25-39. doi:http://dx.doi.org/10.1016/j.mio.2012.11.001

Feygels, V. I., Kopilevich, Y., Tuell, G. H., Surkov, A., LaRocque, P., & Cunningham, A. G. (2007). *Estimation of the water optical properties and bottom reflectance from SHOALS data*.

Feygels, V. I., Park, J. Y., Wozencraft, J., Aitken, J., Macon, C., Mathur, A., . . . Ramnath, V. (2013). *CZMIL (coastal zone mapping and imaging lidar): from first flights to first mission through system validation.* Paper presented at the Ocean Sensing and Monitoring V, Baltimore, Maryland.

Froidefond, J.-M., Gardel, L., Guiral, D., Parra, M., & Ternon, J.-F. (2002). Spectral remote sensing reflectances of coastal waters in French Guiana under the Amazon influence. *Remote Sensing of Environment, 80*(2), 225-232. doi:Doi: 10.1016/s0034-4257(01)00301-7

Fry, E. S. (2013). Studies on some of the inherent optical properties of natural waters [Invited]. *Applied Optics, 52*(5), 930-939. doi:10.1364/ao.52.000930

Gallegos, C. L., Werdell, P. J., & McClain, C. R. (2011). Long-term changes in light scattering in Chesapeake Bay inferred from Secchi depth, light attenuation, and remote sensing measurements. *Journal of Geophysical Research: Oceans, 116*(C7), n/a-n/a. doi:10.1029/2011JC007160

Gao, G. D., Wang, X. H., Bao, X. W., Song, D., Lin, X. P., & Qiao, L. L. (2018). The impacts of land reclamation on suspended-sediment dynamics in Jiaozhou Bay,

Qingdao, China. *Estuarine, Coastal and Shelf Science, 206*, 61-75. doi:https://doi.org/10.1016/j.ecss.2017.01.012

Garcia, C. A. E., Garcia, V. M. T., Dogliotti, A. I., Ferreira, A., Romero, S. I., Mannino, A., . . . Mata, M. M. (2011). Environmental conditions and bio-optical signature of a coccolithophorid bloom in the Patagonian shelf. *Journal of Geophysical Research: Oceans, 116*(C3), n/a-n/a. doi:10.1029/2010JC006595

Gardner, W. D. (1977). Incomplete extraction of rapidly settling particles from water samplers. *Limnology and Oceanography, 22*(4), 764-768. doi:10.4319/lo.1977.22.4.0764

Gardner, W. D., Mishonov, A. V., & Richardson, M. J. (2006). Global POC concentrations from in-situ and satellite data. *Deep Sea Research Part II: Topical Studies in Oceanography, 53*(5-7), 718-740. doi:DOI: 10.1016/j.dsr2.2006.01.029

Gardner, W. D., Tucholke, B. E., Richardson, M. J., & Biscaye, P. E. (2017). Benthic storms, nepheloid layers, and linkage with upper ocean dynamics in the western North Atlantic. *Marine Geology*, *385*(Supplement C), 304-327. doi:https://doi.org/10.1016/j.margeo.2016.12.012

Giannini, M. F. C., Garcia, C. A. E., Tavano, V. M., & Ciotti, Á. M. (2013). Effects of low-salinity and high-turbidity waters on empirical ocean colour algorithms: An example for Southwestern Atlantic waters. *Continental Shelf Research*, *59*(0), 84-96. doi:http://dx.doi.org/10.1016/j.csr.2013.04.013

Goni, M. A., Monacci, N., Gisewhite, R., Ogston, A., Crockett, J., & Nittrouer, C. (2006). Distribution and sources of particulate organic matter in the water column and sediments of the Fly River Delta, Gulf of Papua (Papua New Guinea).

Estuarine, Coastal and Shelf Science, 69(1-2), 225-245. doi:DOI: 10.1016/j.ecss.2006.04.012

Groom, S., Martinez-Vicente, V., Fishwick, J., Tilstone, G., Moore, G., Smyth, T., & Harbour, D. (2009). The Western English Channel observatory: Optical characteristics of station L4. *Journal of Marine Systems, 77*(3), 278-295. doi:DOI: 10.1016/j.jmarsys.2007.12.015

Gundersen, K., Orcutt, K. M., Purdie, D. A., Michaels, A. F., & Knap, A. H. (2001). Particulate organic carbon mass distribution at the Bermuda Atlantic Time-series Study (BATS) site. *Deep Sea Research Part II: Topical Studies in Oceanography, 48*(8-9), 1697-1718.

Guo, L., & Santschi, P. H. (2000). Sedimentary sources of old high molecular weight dissolved organic carbon from the ocean margin benthic nepheloid layer. *Geochimica et Cosmochimica Acta, 64*(4), 651-660. doi:Doi: 10.1016/s0016-7037(99)00335-x

Hakspiel-Segura, C., Martínez-López, A., Pinedo-González, P., Verdugo-Díaz, G., & Acevedo-Acosta, J. D. (2016). Composition of metals in suspended particulate matter of Alfonso basin, southern Gulf of California. *Regional Studies in Marine Science, 3*, 144-153. doi:https://doi.org/10.1016/j.rsma.2015.07.001

Halper, F. B., & McGrail, D. W. (1988). Long-term measurements of near-bottom currents and suspended sediment concentration on the outer Texas-Louisiana continental shelf. *Continental Shelf Research, 8*(1), 23-36. doi:Doi: 10.1016/0278-4343(88)90022-2

Hamers, T., Kamstra, J. H., van Gils, J., Kotte, M. C., & van Hattum, A. G. M. (2015). The influence of extreme river discharge conditions on the quality of suspended particulate matter in Rivers Meuse and Rhine (The Netherlands). *Environmental Research, 143*(Part A), 241-255. doi:https://doi.org/10.1016/j.envres.2015.10.019

Harris, J. E. (1971). *CHARACTERIZATION OF SUSPENDED MATTER IN THE GULF OF MEXICO AND NORTHERN CARIBBEAN SEA.* (7205666 Ph.D.), Texas A&M University, Ann Arbor. Retrieved from http://lynx.lib.usm.edu/docview/302637252?accountid=13946 http://linksource.ebsco.com/linking.aspx?sid=ProQuest+Dissertations+%26+Theses+Full+Text&fmt=dissertation&genre=dissertations+%26+theses&issn=&volume=&issue=&date=1971-01-01&spage=&title=CHARACTERIZATION+OF+SUSPENDED+MATTER+IN+THE+GULF+OF+MEXICO+AND+NORTHERN+CARIBBEAN+SEA&atitle=&au=Harris%2C+John+Elliott&isbn=&jtitle=&btitle= ProQuest Dissertations & Theses Full Text database.

Hawley, N., & Lesht, B. (1992). Sediment resuspension in Lake St. Clair. *Limnol. Oceanogr., 37*(8), 1720-1737.

He, X., Bai, Y., Pan, D., Huang, N., Dong, X., Chen, J., . . . Cui, Q. (2013). Using geostationary satellite ocean color data to map the diurnal dynamics of suspended particulate matter in coastal waters. *Remote Sensing of Environment, 133*(0), 225-239. doi:http://dx.doi.org/10.1016/j.rse.2013.01.023

Helali, M. A., Zaaboub, N., Oueslati, W., Added, A., & Aleya, L. (2016). Suspended particulate matter fluxes along with their associated metals, organic matter and

carbonates in a coastal Mediterranean area affected by mining activities. *Marine Pollution Bulletin, 104*(1), 171-181. doi:https://doi.org/10.1016/j.marpolbul.2016.01.041

Hill, P. S., Boss, E., Newgard, J. P., Law, B. A., & Milligan, T. G. (2011). Observations of the sensitivity of beam attenuation to particle size in a coastal bottom boundary layer. *J. Geophys. Res., 116*(C2), C02023. doi:10.1029/2010jc006539

Højerslev, N. K., & Aarup, T. (2002). Optical Measurements on the Louisiana Shelf off the Mississippi River. *Estuarine, Coastal and Shelf Science, 55*(4), 599-611. doi:http://dx.doi.org/10.1006/ecss.2001.0930

Hommersom, A., Peters, S., Wernand, M. R., & Boer, J. d. (2009). Spatial and temporal variability in bio-optical properties of the Wadden Sea. *Estuarine, Coastal and Shelf Science, 83*, 360-370. doi:10.1016/j.ecss.2009.03.042

Hooker, S. B., Morrow, J. H., & Matsuoka, A. (2013). Apparent optical properties of the Canadian Beaufort Sea -- Part 2: The 1% and 1 cm perspective in deriving and validating AOP data products. *Biogeosciences, 10*(7), 4511-4527. doi:10.5194/bg-10-4511-2013

Horvath, H. (2009). Gustav Mie and the scattering and absorption of light by particles: Historic developments and basics. *Journal of Quantitative Spectroscopy and Radiative Transfer, 110*(11), 787-799. doi:DOI: 10.1016/j.jqsrt.2009.02.022

Hunter, P. D., Tyler, A. N., Présing, M., Kovács, A. W., & Preston, T. (2008). Spectral discrimination of phytoplankton colour groups: The effect of suspended particulate matter and sensor spectral resolution. *Remote Sensing of Environment, 112*(4), 1527-1544.

Hurley, A. J., Hill, P. S., Milligan, T. G., & Law, B. A. (2016). Optical methods for estimating apparent density of sediment in suspension. *Methods in Oceanography, 17*, 153-168. doi:http://dx.doi.org/10.1016/j.mio.2016.09.001

International_Hydrographic_Organization. (2008). IHO Standards for Hydrographic Surveys, 5th edition, Specian Publication N. 44. Monaco: International Hydrographic Bureau.

Inthorn, M., Mohrholz, V., & Zabel, M. (2006). Nepheloid layer distribution in the Benguela upwelling area offshore Namibia. *Deep Sea Research Part I: Oceanographic Research Papers, 53*(8), 1423-1438. doi:http://dx.doi.org/10.1016/j.dsr.2006.06.004

Isada, T., Hirawake, T., Kobayashi, T., Nosaka, Y., Natsuike, M., Imai, I., . . . Saitoh, S.-I. (2015). Hyperspectral optical discrimination of phytoplankton community structure in Funka Bay and its implications for ocean color remote sensing of diatoms. *Remote Sensing of Environment, 159*, 134-151. doi:http://dx.doi.org/10.1016/j.rse.2014.12.006

Jacobs, M. B., Thorndike, E. M., & Ewing, M. (1973). A comparison of suspended particulate matter from nepheloid and clear water. *Marine Geology, 14*(2), 117-128. doi:http://dx.doi.org/10.1016/0025-3227(73)90055-8

Jafar-Sidik, M., Gohin, F., Bowers, D., Howarth, J., & Hull, T. (2017). The relationship between Suspended Particulate Matter and Turbidity at a mooring station in a coastal environment: consequences for satellite-derived products. *Oceanologia, 59*(3), 365-378. doi:https://doi.org/10.1016/j.oceano.2017.04.003

Jago, C. F., & Bull, C. F. J. (2000). Quantification of errors in transmissometer-derived concentration of suspended particulate matter in the coastal zone: implications for flux determinations. *Marine Geology, 169*(3-4), 273-286.

Jarrard, R. D., & Vanden-Berg, M. D. (2006) Sediment Mineralogy Based on Visible and Near-Infrared Reflectance Spectroscopy. *Vol. 267. New Techniques Sed. Core Analysis* (pp. 129 – 140): Geological Society of London.

Jerlov, N. G. (1976). Chapter 2 Scattering. In N. G. Jerlov (Ed.), *Ocean Optics, Elsevier Oceanography Series* (Vol. Volume 14, pp. 13-46): Elsevier.

Jonasz, M., & Fournier, G. (2007). *Light Scattering by Particles in Water Theoretical and Experimental Foundations*. Amsterdam: Elsevier.

Jones, B. H., Noble, M. A., & Dickey, T. D. (2002). Hydrographic and particle distributions over the Palos Verdes Continental Shelf: spatial, seasonal and daily variability. *Continental Shelf Research, 22*(6–7), 945-965. doi:http://dx.doi.org/10.1016/S0278-4343(01)00114-5

Jouon, A., Ouillon, S., Douillet, P., Lefebvre, J. P., Fernandez, J. M., Mari, X., & Froidefond, J.-M. (2008). Spatio-temporal variability in suspended particulate matter concentration and the role of aggregation on size distribution in a coral reef lagoon. *Marine Geology, 256*(1–4), 36-48. doi:http://dx.doi.org/10.1016/j.margeo.2008.09.008

Joyce, T. M., Bishop, J. K. B., & Brown, O. B. (1992). Observations of offshore shelf-water transport induced by a warm-core ring. *Deep Sea Research Part A. Oceanographic Research Papers, 39, Supplement 1*(0), S97-S113. doi:http://dx.doi.org/10.1016/S0198-0149(11)80007-5

Karageorgis, A., Georgopoulos, D., Gardner, W., Mikkelsen, O., & Velaoras, D. (2015). How schlieren affects beam transmissometers and LISST-Deep: an example from the stratified Danube River delta, NW Black Sea. *Mediterranean Marine Science, 16*(2), 366-372. doi:10.12681/mms.1116

Karageorgis, A. P., Gardner, W. D., Mikkelsen, O. A., Georgopoulos, D., Ogston, A. S., Assimakopoulou, G., . . . Papathanassiou, E. (2014). Particle sources over the Danube River delta, Black Sea based on distribution, composition and size using optics, imaging and bulk analyses. *Journal of Marine Systems, 131*(0), 74-90. doi:http://dx.doi.org/10.1016/j.jmarsys.2013.11.013

Karageorgis, A. P., Georgopoulos, D., Kanellopoulos, T. D., Mikkelsen, O. A., Pagou, K., Kontoyiannis, H., . . . Anagnostou, C. (2012). Spatial and seasonal variability of particulate matter optical and size properties in the Eastern Mediterranean Sea. *Journal of Marine Systems, 105–108*(0), 123-134. doi:http://dx.doi.org/10.1016/j.jmarsys.2012.07.003

Kennett, J. (1982). *Marine Geology*. New Jersey, United States: Prentice-Hall Inc.

Kheireddine, M., & Antoine, D. (2014). Diel variability of the beam attenuation and backscattering coefficients in the northwestern Mediterranean Sea (BOUSSOLE site). *Journal of Geophysical Research: Oceans*, n/a-n/a. doi:10.1002/2014JC010007

Kim, M., Feygels, V., Kopilevich, Y., & Park, J. Y. (2014). *Estimation of inherent optical properties from CZMIL lidar.* Paper presented at the Lidar Remote Sensing for Environmental Monitoring XIV, Beijing, China.

Kim, M., Jung, J.-h., Jin, Y., Han, G. M., Lee, T., Hong, S. H., . . . Kannan, N. (2016). Origins of suspended particulate matter based on sterol distribution in low salinity water mass observed in the offshore East China Sea. *Marine Pollution Bulletin, 108*(1–2), 281-288. doi:http://dx.doi.org/10.1016/j.marpolbul.2016.04.049

Kirk, J. T. O. (1994). *Light & Photosynthesis in Aquatic Ecosystems* (2 ed.): Cambridge University Press.

Kitchen, J. C., & Zaneveld, J. R. V. (1992). A three-layered sphere model of the optical properties of phytoplankton. *Limnology and Oceanography*, *37*(8), 1680-1690. doi:10.4319/lo.1992.37.8.1680

Kobayashi, H., Toratani, M., Matsumura, S., Siripong, A., Lirdwitayaprasit, T., & Jintasaeranee, P. (2011). Optical properties of inorganic suspended solids and their influence on ocean colour remote sensing in highly turbid coastal waters. *International Journal of Remote Sensing*, *32*(23), 8393-8420. doi:10.1080/01431161.2010.542193

Kopilevich, Y. I., Feygels, V. I., Tuell, G. H., & Surkov, A. (2005). *Measurement of ocean water optical properties and seafloor reflectance with scanning hydrographic operational airborne lidar survey (SHOALS): I. Theoretical background* Paper presented at the Remote Sensing of the Coastal Oceanic Environment.

Kowalczuk, P., Durako, M. J., Cooper, W. J., Wells, D., & Souza, J. J. (2006). Comparison of radiometric quantities measured in water, above water and derived from seaWiFS imagery in the South Atlantic Bight, North Carolina, USA.

Continental Shelf Research, 26(19), 2433-2453. doi:http://dx.doi.org/10.1016/j.csr.2006.07.024

Krivtsov, V., Howarth, M. J., Jones, S. E., Souza, A. J., & Jago, C. F. (2008). Monitoring and modelling of the Irish Sea and Liverpool Bay: An overview and an SPM case study. *Ecological Modelling, 212*, 37–52. doi:10.1016/j.ecolmodel.2007.10.038

Kumar, A., Equeenuddin, S. M., Mishra, D. R., & Acharya, B. C. (2016). Remote monitoring of sediment dynamics in a coastal lagoon: Long-term spatio-temporal variability of suspended sediment in Chilika. *Estuarine, Coastal and Shelf Science, 170*, 155-172. doi:http://dx.doi.org/10.1016/j.ecss.2016.01.018

Kutser, T., Vahtmäe, E., Paavel, B., & Kauer, T. (2013). Removing glint effects from field radiometry data measured in optically complex coastal and inland waters. *Remote Sensing of Environment, 133*(0), 85-89. doi:http://dx.doi.org/10.1016/j.rse.2013.02.011

Kutser, T., Vahtmäe, E., & Praks, J. (2009). A sun glint correction method for hyperspectral imagery containing areas with non-negligible water leaving NIR signal. *Remote Sensing of Environment, 113*(10), 2267-2262

Download 2274. doi:http://dx.doi.org/10.1016/j.rse.2009.06.016

Lane, A., Riethmüller, R., Herbers, D., Rybaczok, P., Günther, H., & Baumert, H. (2000). Observational data sets for model development. *Coastal Engineering, 41*(1–3), 125-153. doi:http://dx.doi.org/10.1016/S0378-3839(00)00029-6

Larouche, P., & Boyer-Villemaire, U. (2010). Suspended particulate matter in the St. Lawrence estuary and Gulf surface layer and development of a remote sensing

algorithm. *Estuarine, Coastal and Shelf Science, 90*(4), 241-249. doi:DOI: 10.1016/j.ecss.2010.09.005

Le, C., Li, Y., Zha, Y., Sun, D., Huang, C., & Lu, H. (2009). A four-band semi-analytical model for estimating chlorophyll a in highly turbid lakes: The case of Taihu Lake, China. *Remote Sensing of Environment, 113*(6), 1175-1182. doi:http://dx.doi.org/10.1016/j.rse.2009.02.005

Lee, J., Liu, J. T., Hung, C.-C., Lin, S., & Du, X. (2016). River plume induced variability of suspended particle characteristics. *Marine Geology, 380*, 219-230. doi:http://dx.doi.org/10.1016/j.margeo.2016.04.014

Lee, Z., Ahn, Y.-H., Mobley, C., & Arnone, R. (2010). Removal of surface-reflected light for the measurement of remote-sensing reflectance from an above-surface platform. *Optics Express, 18*(25), 26313-26324. doi:10.1364/OE.18.026313

Lee, Z., Carder, K. L., & Arnone, R. A. (2002). Deriving inherent optical properties from water color: a multiband quasi-analytical algorithm for optically deep waters. *Applied Optics, 41*(27), 5755-5772.

Lee, Z., Shang, S., Lin, G., Chen, J., & Doxaran, D. (2016). On the modeling of hyperspectral remote-sensing reflectance of high-sediment-load waters in the visible to shortwave-infrared domain. *Applied Optics, 55*(7), 1738-1750. doi:10.1364/AO.55.001738

Li, J., Chen, X., Tian, L., Huang, J., & Feng, L. (2015). Improved capabilities of the Chinese high-resolution remote sensing satellite GF-1 for monitoring suspended particulate matter (SPM) in inland waters: Radiometric and spatial considerations.

ISPRS Journal of Photogrammetry and Remote Sensing, 106, 145-156. doi:http://dx.doi.org/10.1016/j.isprsjprs.2015.05.009

Li, J., Gao, S., & Wang, Y. (2010). Delineating suspended sediment concentration patterns in surface waters of the Changjaing Estuary by remote sensing analysis. *Acta Oceanologicia Sinica, 29*(4), 38-47.

Lindsay, P., Balls, P. W., & West, J. R. (1996). Influence of Tidal Range and River Discharge on Suspended Particulate Matter Fluxes in the Forth Estuary (Scotland). *Estuarine, Coastal and Shelf Science, 42*(1), 63-82. doi:DOI: 10.1006/ecss.1996.0006

Liu, C., Zhang, L., Fan, C., Xu, F., Chen, K., & Gu, X. (2017). Temporal occurrence and sources of persistent organic pollutants in suspended particulate matter from the most heavily polluted river mouth of Lake Chaohu, China. *Chemosphere, 174*(Supplement C), 39-45. doi:https://doi.org/10.1016/j.chemosphere.2017.01.082

Liu, J. T., Hung, J.-J., Lin, H.-L., Huh, C.-A., Lee, C.-L., Hsu, R. T., . . . Chu, J. C. (2009). From suspended particles to strata: The fate of terrestrial substances in the Gaoping (Kaoping) submarine canyon. *Journal of Marine Systems, 76*(4), 417-432. doi:DOI: 10.1016/j.jmarsys.2008.01.010

Liu, J. T., Wang, Y. H., Lee, I. H., & Hsu, R. T. (2010). Quantifying tidal signatures of the benthic nepheloid layer in Gaoping Submarine Canyon in Southern Taiwan. *Marine Geology, 271*(1-2), 119-130. doi:DOI: 10.1016/j.margeo.2010.01.016

Lock, J. A., & Gouesbet, G. (2009). Generalized Lorenz–Mie theory and applications. *Journal of Quantitative Spectroscopy and Radiative Transfer, 110*(11), 800-807. doi:http://dx.doi.org/10.1016/j.jqsrt.2008.11.013

Lohrenz, S., & Gundersen, K. (2008). Satellite Assessment of CO2 Distribution, Variability and Flux and Understanding of Control Mechanisms in a River Dominated Ocean Margin. Gulf of Mexico: National Science Foundation.

Loisel, H., Me´riaux, X., Berthon, J.-F. o., & Poteau, A. (2007). Investigation of the optical backscattering to scattering ratio of marine particles in relation to their biogeochemical composition in the eastern English Channel and southern North Sea. *Limnol. Oceanogr., 52*(2), 739-752.

Loisel, H., & Morel, A. (1998). Light scattering and chlorophyll concentration in case 1 waters: A reexamination. *Limnol. Oceanogr., 43*(5), 847-858.

Lorenzoni, L., Benitez-Nelson, C. R., Thunell, R. C., Hollander, D., Varela, R., Astor, Y., . . . Muller-Karger, F. E. (2012). Potential role of event-driven sediment transport on sediment accumulation in the Cariaco Basin, Venezuela. *Marine Geology, 307–310*(0), 105-110. doi:http://dx.doi.org/10.1016/j.margeo.2011.12.009

Lorenzoni, L., Thunell, R. C., Benitez-Nelson, C. R., Hollander, D., Martinez, N., Tappa, E., . . . Muller-Karger, F. E. (2009). The importance of subsurface nepheloid layers in transport and delivery of sediments to the eastern Cariaco Basin, Venezuela. *Deep Sea Research Part I: Oceanographic Research Papers, 56*(12), 2249-2262. doi:http://dx.doi.org/10.1016/j.dsr.2009.08.001

Lubac, B., & Loisel, H. (2007). Variability and classification of remote sensing reflectance spectra in the eastern English Channel and southern North Sea.

Remote Sensing of Environment, 110(1), 45-58. doi:DOI: 10.1016/j.rse.2007.02.012

Lund-Hansen, L. C., Andersen, T. J., Nielsen, M. H., & Pejrup, M. (2010). Suspended Matter, Chl-a, CDOM, Grain Sizes, and Optical Properties in the Arctic Fjord-Type Estuary, Kangerlussuaq, West Greenland During Summer. *Estuaries and Coasts, 33*(6), 1442-1451. doi:10.1007/s12237-010-9300-7

Ma, W., Xing, Q., Chen, C., Zhang, Y., Yu, D., & Shi, P. (2011). Using the normalized peak area of remote sensing reflectance in the near-infrared region to estimate total suspended matter. *International Journal of Remote Sensing, 32*(22), 7479-7486. doi:10.1080/01431161.2010.524673

Macon, C., Wozencraft, J., Park, J. Y., & Tuell, G. (2008). *Seafloor and Land Cover Classification through Airborne LIDAR and Hyperspectral Data Fusion* Paper presented at the Geoscience and Remote Sensing Symposium, 2008, Boston, MA.

Many, G., Bourrin, F., Durrieu de Madron, X., Pairaud, I., Gangloff, A., Doxaran, D., . . . Jacquet, M. (2016). Particle assemblage characterization in the Rhone River ROFI. *Journal of Marine Systems, 157*, 39-51. doi:http://dx.doi.org/10.1016/j.jmarsys.2015.12.010

Mao, Z., Chen, J., Pan, D., Tao, B., & Zhu, Q. (2012). A regional remote sensing algorithm for total suspended matter in the East China Sea. *Remote Sensing of Environment, 124*, 819-831. doi:10.1016/j.rse.2012.06.014

Martín, J., Puig, P., Palanques, A., & Ribó, M. (2014). Trawling-induced daily sediment resuspension in the flank of a Mediterranean submarine canyon. *Deep Sea*

Research Part II: Topical Studies in Oceanography, *104*, 174-183. doi:http://dx.doi.org/10.1016/j.dsr2.2013.05.036

Martinez-Vicente, V., Land, P. E., Tilstone, G. H., Widdicombe, C., & Fishwick, J. R. (2010). Particulate scattering and backscattering related to water constituents and seasonal changes in the Western English Channel. *Journal of Plankton Research, 32*(5), 603-619. doi:10.1093/plankt/fbq013

Masson, D. G., Huvenne, V. A. I., de Stigter, H. C., Arzola, R. G., & LeBas, T. P. (2011). Sedimentary processes in the middle Nazaré Canyon. *Deep Sea Research Part II: Topical Studies in Oceanography*, *58*(23–24), 2369-2387. doi:http://dx.doi.org/10.1016/j.dsr2.2011.04.003

Masunaga, E., Arthur, R. S., Fringer, O. B., & Yamazaki, H. (2017). Sediment resuspension and the generation of intermediate nepheloid layers by shoaling internal bores. *Journal of Marine Systems*, *170*(Supplement C), 31-41. doi:https://doi.org/10.1016/j.jmarsys.2017.01.017

McCandliss, R. R., Jones, S. E., Hearn, M., Latter, R., & Jago, C. F. (2002). Dynamics of suspended particles in coastal waters (southern North Sea) during a spring bloom. *Journal of Sea Research*, *47*(3-4), 285-302.

McCarthy, J. C., Pyle, T. E., & Griffin, G. M. (1974). Light transmissivity, suspended sediments and the legal definition of turbidity. *Estuarine and Coastal Marine Science, 2*(3), 291-299. doi:http://dx.doi.org/10.1016/0302-3524(74)90019-X

McCave, I. N. (1986). Local and global aspects of the bottom nepheloid layers in the world ocean. *Netherlands Journal of Sea Research*, *20*(2–3), 167-181. doi:http://dx.doi.org/10.1016/0077-7579(86)90040-2

McCave, I. N., Hall, I. R., Antia, A. N., Chou, L., Dehairs, F., Lampitt, R. S., . . . Wollast, R. (2001). Distribution, composition and flux of particulate material over the European margin at 47°–50°N. *Deep Sea Research Part II: Topical Studies in Oceanography*, *48*(14–15), 3107-3139. doi:http://dx.doi.org/10.1016/S0967-0645(01)00034-0

McKee, D., Chami, M., Brown, I., Calzado, V. S., Doxaran, D., & Cunningham, A. (2009). Role of measurement uncertainties in observed variability in the spectral backscattering ratio: a case study in mineral-rich coastal waters. *Applied Optics, 48*(24), 4663-4675.

McKee, D., & Cunningham, A. (2006). Identification and characterisation of two optical water types in the Irish Sea from in situ inherent optical properties and seawater constituents. *Estuarine, Coastal and Shelf Science, 68*, 305-316. doi:10.1016/j.ecss.2006.02.010

McKee, D., Cunningham, A., Slater, J., Jones, K. J., & Griffiths, C. R. (2003). Inherent and apparent optical properties in coastal waters: a study of the Clyde Sea in early summer. *Estuarine, Coastal and Shelf Science, 56*(2), 369-376. doi:http://dx.doi.org/10.1016/S0272-7714(02)00189-0

McPhee-Shaw, E. E., Sternberg, R. W., Mullenbach, B., & Ogston, A. S. (2004). Observations of intermediate nepheloid layers on the northern California continental margin. *Continental Shelf Research, 24*(6), 693-720. doi:http://dx.doi.org/10.1016/j.csr.2004.01.004

Menon, H. B., Lotliker, A., & Nayak, S. R. (2005). Pre-monsoon bio-optical properties in estuarine, coastal and Lakshadweep waters. *Estuarine, Coastal and Shelf Science, 63*(1–2), 211-223. doi:http://dx.doi.org/10.1016/j.ecss.2004.11.015

Miguel, L. L. A. J., Castro, J. W. A., & Nehama, F. P. J. (2017). Tidal impact on suspended sediments in the Macuse estuary in Mozambique. *Regional Studies in Marine Science, 16*(Supplement C), 1-14. doi:https://doi.org/10.1016/j.rsma.2017.07.002

Mikkelsen, O. A., Milligan, T. G., Hill, P. S., Chant, R. J., Jago, C. F., Jones, S. E., . . . Mitchelson-Jacob, G. (2008). The influence of schlieren on in situ optical measurements used for particle characterization. *Limnology and Oceanography: Methods, 6*, 133–143.

Miles, T., Lee, S. H., Wåhlin, A., Ha, H. K., Kim, T. W., Assmann, K. M., & Schofield, O. (2016). Glider observations of the Dotson Ice Shelf outflow. *Deep Sea Research Part II: Topical Studies in Oceanography, 123*, 16-29. doi:http://dx.doi.org/10.1016/j.dsr2.2015.08.008

Minu, P., Lotliker, A. A., Shaju, S. S., Ashraf, P. M., Kumar, T. S., & Meenakumari, B. (2016). Performance of operational satellite bio-optical algorithms in different water types in the southeastern Arabian Sea. *Oceanologia, 58*(4), 317-326. doi:http://dx.doi.org/10.1016/j.oceano.2016.05.005

Mishonov, A. V., Gardner, W. D., & Jo Richardson, M. (2003). Remote sensing and surface POC concentration in the South Atlantic. *Deep Sea Research Part II: Topical Studies in Oceanography, 50*(22-26), 2997-3015. doi:DOI: 10.1016/j.dsr2.2003.07.007

Mobley, C. D. (1994). *Light and Water: Radiative Transfer in Natural Waters*: Academic Press.

Mobley, C. D. (1999). Estimation of the Remote-Sensing Reflectance from Above-Surface Measurements. *Appl. Opt., 38*(36), 7442-7455.

Montes-Hugo, M. A., Churnside, J. H., Gould, R. W., Arnone, R. A., & Foy, R. (2010). Spatial coherence between remotely sensed ocean color data and vertical distribution of lidar backscattering in coastal stratified waters. *Remote Sensing of Environment, 114*(11), 2584-2593. doi:10.1016/j.rse.2010.05.023

Monzon, C., Forester, D. W., Burkhart, R., & Bellemare, J. (2006). Rough ocean surface and sunglint region characteristics. *Applied Optics, 45*(27), 7089-7096. doi:10.1364/ao.45.007089

Morel, A. (1974). Optical properties of pure water and pure sea water. In N. J. Jerlov & E. S. Nielson (Eds.), *Optical aspects of oceanography* (Vol. 1, pp. 1-24). New York: Academic.

Morel, A., & Gentili, B. (2008). Practical application of the "turbid water" flag in ocean color imagery: Interference with sun-glint contaminated pixels in open ocean. *Remote Sensing of Environment, 112*(3), 934-938.

Moss, J. A., McCurry, C., Tominack, S., Romero, I. C., Hollander, D., Jeffrey, W. H., & Snyder, R. A. (2015). Ciliated protists from the nepheloid layer and water column of sites affected by the Deepwater Horizon oil spill in the Northeastern Gulf of Mexico. *Deep Sea Research Part I: Oceanographic Research Papers, 106*, 85-96. doi:http://dx.doi.org/10.1016/j.dsr.2015.10.001

Mustard, J. F., Staid, M. I., & Fripp, W. J. (2001). A Semianalytical Approach to the Calibration of AVIRIS Data to Reflectance over Water: Application in a Temperate Estuary. *Remote Sensing of Environment, 75*(3), 335-349. doi:http://dx.doi.org/10.1016/S0034-4257(00)00177-2

Naik, P., D'Sa, E. J., Gomes, H. d. R., Goés, J. I., & Mouw, C. B. (2013). Light absorption properties of southeastern Bering Sea waters: Analysis, parameterization and implications for remote sensing. *Remote Sensing of Environment, 134*(0), 120-134. doi:http://dx.doi.org/10.1016/j.rse.2013.03.004

Neil, C., Cunningham, A., & McKee, D. (2011). Relationships between suspended mineral concentrations and red-waveband reflectances in moderately turbid shelf seas. *Remote Sensing of Environment, 115*(12), 3719-3730. doi:http://dx.doi.org/10.1016/j.rse.2011.09.010

Neukermans, G., Loisel, H., Meriaux, X., Astoreca, R., & Mckee, D. (2012). In situ variability of mass-specific beam attenuation and backscattering of marine particles with respect to particle size, density, and composition. *Limnology and Oceanography, 57*(1), 124-144. doi:10.4319/lo.2011.57.1.0124

Neukermans, G., Reynolds, R. A., & Stramski, D. (2014). Contrasting inherent optical properties and particle characteristics between an under-ice phytoplankton bloom and open water in the Chukchi Sea. *Deep Sea Research Part II: Topical Studies in Oceanography, 105*, 59-73. doi:http://dx.doi.org/10.1016/j.dsr2.2014.03.014

Oceanographic Consortium, D. U. o. N. C. (2011). RV Cape Hatteras Ship Specs. Retrieved from http://www.rvcapehatteras.org/ship-specs/

Ogashawara, I., Mishra, D. R., Nascimento, R. F. F., Alcântara, E. H., Kampel, M., & Stech, J. L. (2016). Re-parameterization of a quasi-analytical algorithm for colored dissolved organic matter dominant inland waters. *International Journal of Applied Earth Observation and Geoinformation, 53*, 128-145. doi:http://dx.doi.org/10.1016/j.jag.2016.09.001

Oliveira, A., Vitorino, J., Rodrigues, A., Jouanneau, J. M., Dias, J. A., & Weber, O. (2002). Nepheloid layer dynamics in the northern Portuguese shelf. *Progress In Oceanography, 52*(2–4), 195-213. doi:http://dx.doi.org/10.1016/S0079-6611(02)00006-X

Oubelkheir, K., Claustre, H., Sciandra, A., & Babin, M. (2005). Bio-optical and biogeochemical properties of different trophic regimes in oceanic waters. *Limnology and Oceanography, 50*(6), 1795-1809. doi:10.4319/lo.2005.50.6.1795

Oubelkheir, K., Clementson, L. A., Webster, I. T., Ford, P. W., Dekker, A. G., Radke, L. C., & Daniel, P. (2006). Using inherent optical properties to investigate biogeochemical dynamics in a tropical macrotidal coastal system. *Journal of Geophysical Research: Oceans, 111*(C7), n/a-n/a. doi:10.1029/2005JC003113

Ouillon, S., Douillet, P., Lefebvre, J. P., Le Gendre, R., Jouon, A., Bonneton, P., . . . Fichez, R. (2010). Circulation and suspended sediment transport in a coral reef lagoon: The south-west lagoon of New Caledonia. *Marine Pollution Bulletin, 61*(7-12), 269-296. doi:DOI: 10.1016/j.marpolbul.2010.06.023

Ouillon, S., & Petrenko, A. (2005). Above-water measurements of reflectance and chlorophyll-a algorithms in the Gulf of Lions, NW Mediterranean Sea. *Optics Express, 13*(7), 2531-2548. doi:10.1364/opex.13.002531

Pak, H., Zaneveld, J. R. V., & Spinrad, R. W. (1984). Vertical distribution of suspended particulate matter in the Zaire river, estuary and plume. *Netherlands Journal of Sea Research, 17*(2-4), 412-425.

Palanques, A., & Biscaye, P. E. (1992). Patterns and controls of the suspended matter distribution over the shelf and upper slope south of New England. *Continental Shelf Research, 12*(5-6), 577-600. doi:Doi: 10.1016/0278-4343(92)90021-b

Palanques, A., Durrieu de Madron, X., Puig, P., Fabres, J., Guillén, J., Calafat, A., . . . Bonnin, J. (2006). Suspended sediment fluxes and transport processes in the Gulf of Lions submarine canyons. The role of storms and dense water cascading. *Marine Geology, 234*(1–4), 43-61. doi:http://dx.doi.org/10.1016/j.margeo.2006.09.002

Palanques, A., Guille´n, J., & Puig, P. (2001). Impact of bottom trawling on water turbidity and muddy sediment of an unfished continental shelf. *Limnol. Oceanogr., 46*(5), 1100-1110.

Pegau, W. S., Gray, D., & Zaneveld, J. R. V. (1997). Absorption and attenuation of visible and near-infrared light in water: dependence on temperature and salinity. *Applied Optics, 36*(24), 6035-6046.

Pegau, W. S., Zaneveld, J. R. V., & Voss, K. J. (1995). Toward closure of the inherent optical properties of natural waters. *Journal of Geophysical Research: Oceans, 100*(C7), 13193-13199. doi:10.1029/95JC00457

Petzold, T. J. (1972) Volume Scattering Functions for Selected Ocean Waters. *SIO Reference* (pp. 79): UC San Diego, SIO Reference, Scripps Institution of Oceanography.

Pope, R. M., Weidemann, A. D., & Fry, E. S. (2000). Integrating Cavity Absorption Meter measurements of dissolved substances and suspended particles in ocean water. *Dynamics of Atmospheres and Oceans, 31*(1–4), 307-320. doi:http://dx.doi.org/10.1016/S0377-0265(99)00039-1

Puig, P., Madron, X. D. d., Salat, J., Schroeder, K., Martín, J., Karageorgis, A. P., . . . Houpert, L. (2013). Thick bottom nepheloid layers in the western Mediterranean generated by deep dense shelf water cascading. *Progress In Oceanography, 111*(0), 1-23. doi:http://dx.doi.org/10.1016/j.pocean.2012.10.003

Puig, P., & Palanques, A. (1998). Nepheloid structure and hydrographic control on the Barcelona continental margin, northwestern Mediterranean. *Marine Geology, 149*(1–4), 39-54. doi:http://dx.doi.org/10.1016/S0025-3227(98)00037-1

Qiao, L. L., Wang, Y. Z., Li, G. X., Deng, S. G., Liu, Y., & Mu, L. (2011). Distribution of suspended particulate matter in the northern Bohai Bay in summer and its relation with thermocline. *Estuarine, Coastal and Shelf Science, 93*(3), 212-219. doi:DOI: 10.1016/j.ecss.2010.10.027

Qiu, Z. (2013). A simple optical model to estimate suspended particulate matter in Yellow River Estuary. *Optics Express, 21*(23), 27891-27904. doi:10.1364/oe.21.027891

Ransom, B., Shea, K. F., Burkett, P. J., Bennett, R. H., & Baerwald, R. (1998). Comparison of pelagic and nepheloid layer marine snow: implications for carbon cycling. *Marine Geology, 150*(1–4), 39-50. doi:http://dx.doi.org/10.1016/S0025-3227(98)00052-8

Reynolds, R. A., Stramski, D., & Neukermans, G. (2016). Optical backscattering by particles in Arctic seawater and relationships to particle mass concentration, size distribution, and bulk composition. *Limnology and Oceanography, 61*(5), 1869-1890. doi:10.1002/lno.10341

Ribó, M., Puig, P., Salat, J., & Palanques, A. (2013). Nepheloid layer distribution in the Gulf of Valencia, northwestern Mediterranean. *Journal of Marine Systems, 111–112*(0), 130-138. doi:http://dx.doi.org/10.1016/j.jmarsys.2012.10.008

Ross, C. B., Gardner, W. D., Richardson, M. J., & Asper, V. L. (2009). Currents and sediment transport in the Mississippi Canyon and effects of Hurricane Georges. *Continental Shelf Research, 29*(11–12), 1384-1396. doi:http://dx.doi.org/10.1016/j.csr.2009.03.002

Ruddick, K. G., De Cauwer, V., Park, Y. J., & Moore, G. (2006). Seaborne measurements of near infrared water-leaving reflectance: The similarity spectrum for turbid waters. *Limnology and Oceanography, 51*(2), 1167-1179.

Rutgers van der Loeff, M. M., Meyer, R., Rudels, B., & Rachor, E. (2002). Resuspension and particle transport in the benthic nepheloid layer in and near Fram Strait in relation to faunal abundances and 234Th depletion. *Deep Sea Research Part I: Oceanographic Research Papers, 49*(11), 1941-1958. doi:http://dx.doi.org/10.1016/S0967-0637(02)00113-9

Sea-Bird Electronics, I. (2010). SBE 49 FastCAT Conductivity, Temperature, and Pressure Sensor with RS-232 Interface (Vol. Manual Version #013,, pp. 69). Bellevue, Washington: Sea-Bird Electronics, Inc.

Sea-Bird Electronics, I. (2011a). FastCAT CTD Sensor SBE49 Specs (pp. 2).

Sea-Bird Electronics, I. (2011b). SBE 911plus CTD (pp. 6). Bellevue, Washington: Sea-Bird Electronics, Inc.

Sequoia_Scientific. LISST-100X Particle Size Analyzer, User's Manual Version 4.65 (pp. 78). Bellevue, WA: Sequoia Scientific, Inc.

Shank, G. C., & Evans, A. (2011). Distribution and photoreactivity of chromophoric dissolved organic matter in northern Gulf of Mexico shelf waters. *Continental Shelf Research, 31*(10), 1128-1139. doi:http://dx.doi.org/10.1016/j.csr.2011.04.009

Shen, Y., Fichot, C. G., Liang, S.-K., & Benner, R. (2016). Biological hot spots and the accumulation of marine dissolved organic matter in a highly productive ocean margin. *Limnology and Oceanography, 61*(4), 1287-1300. doi:10.1002/lno.10290

Siegel, D. A., Dickey, T. D., Washburn, L., Hamilton, M. K., & Mitchell, B. G. (1989). Optical determination of particulate abundance and production variations in the oligotrophic ocean. *Deep Sea Research Part A. Oceanographic Research Papers, 36*(2), 211-222. doi:http://dx.doi.org/10.1016/0198-0149(89)90134-9

Siegel, D. A., Maritorena, S., Nelson, N. B., Hansell, D. A., & Lorenzi-Kayser, M. (2002). Global distribution and dynamics of colored dissolved and detrital organic materials. *Journal of Geophysical Research: Oceans, 107*(C12), 3228. doi:10.1029/2001JC000965

Simis, S. G. H., & Olsson, J. (2013). Unattended processing of shipborne hyperspectral reflectance measurements. *Remote Sensing of Environment, 135*(0), 202-212. doi:http://dx.doi.org/10.1016/j.rse.2013.04.001

Singh, S., D'Sa, E., & Swenson, E. (2010). Seasonal variability in CDOM absorption and fluorescence properties in the Barataria Basin, Louisiana, USA. *Journal of Environmental Sciences, 22*(10), 1481-1490. doi:http://dx.doi.org/10.1016/S1001-0742(09)60279-5

Sipelgas, L., & Raudsepp, U. (2015). Comparison of hyperspectral measurements of the attenuation and scattering coefficients spectra with modeling results in the north-eastern Baltic Sea. *Estuarine, Coastal and Shelf Science, 165*, 1-9. doi:http://dx.doi.org/10.1016/j.ecss.2015.08.008

Smith, R., Irish, J., & Smith, M. (2000). *Airborne Lidar and Airborne Hyperspectral Imagery: A Fusion of two Proven Sensors for Improved Hydrographic Surveying*. Paper presented at the Canadian Hydrographic Conference 2000, Montreal, Canada.

Smith, R. C., & Baker, K. S. (1981). Optical properties of the clearest natural waters (200-800 nm). *Applied Optics, 20*(2), 177-184.

Son, Y. B., Gardner, W. D., Mishonov, A. V., & Richardson, M. J. (2009). Multispectral remote-sensing algorithms for particulate organic carbon (POC): The Gulf of Mexico. *Remote Sensing of Environment, 113*(1), 50-61. doi:10.1016/j.rse.2008.08.011

Spinrad, R. W., Zaneveld, J. R. V., & Pak, H. (1978). Volume scattering function of suspended particulate matter at near-forward angles: a comparison of experimental and theoretical values. *Appl. Opt., 17*(7), 1125-1130.

Stramski, D., Boss, E., Bogucki, D., & Voss, K. J. (2004). The role of seawater constituents in light backscattering in the ocean. *Progress In Oceanography, 61*(1), 27-56.

Stramski, D., & Tegowski, J. (2001). Effects of intermittent entrainment of air bubbles by breaking wind waves on ocean reflectance and underwater light field. *Journal of Geophysical Research: Oceans, 106*(C12), 31345-31360. doi:10.1029/2000JC000461

Styles, R. (2006). Labratory evaluation of the LISST in a stratified fluid. *Marine Geology, 227*(1-2), 151– 162. doi:10.1016/j.margeo.2005.11.011

Sydor, M. (2007). Statistical Treatment of Remote Sensing Reflectance from Coastal Ocean Water: Proportionality of Reflectance from Multiple Scattering to Source Function b/a. *Journal of Coastal Research, 23*(5), 1183-1192.

Terrie, G., Ladner, S., & Gould, R. (1997). *Effects of suspended sediment concentration on the absorption and scattering coefficients*.

Tiessen, M. C. H., Eleveld, M. A., Nauw, J. J., Nechad, B., & Gerkema, T. (2017). Depth dependence and intra-tidal variability of Suspended Particulate Matter transport in the East Anglian plume. *Journal of Sea Research, 127*(Supplement C), 2-11. doi:https://doi.org/10.1016/j.seares.2017.03.008

Toole, D. A., & Siegel, D. A. (2001). Modes and mechanisms of ocean color variability in the Santa Barbara Channel. *Journal of Geophysical Research: Oceans, 106*(C11), 26985-27000. doi:10.1029/2000JC000371

Torrecilla, E., Stramski, D., Reynolds, R. A., Millán-Núñez, E., & Piera, J. (2011). Cluster analysis of hyperspectral optical data for discriminating phytoplankton

pigment assemblages in the open ocean. *Remote Sensing of Environment, 115*(10), 2578-2593. doi:http://dx.doi.org/10.1016/j.rse.2011.05.014

Tsompanoglou, K., Anagnostou, C., Krasakopoulou, E., Pagou, K., Karageorgis, A. P., Pavlidou, A., . . . Tsirambides, A. (2017). Distribution and geochemical composition of suspended particulate material in the shallow embayment of northern Thermaikos Gulf, Greece. *Continental Shelf Research, 143*(Supplement C), 295-310. doi:https://doi.org/10.1016/j.csr.2017.05.002

Tuell, G., Barbor, K., & Wozencraft, J. (2010). *Overview of the Coastal Zone Mapping and Imaging Lidar (CZMIL): A New Multi-sensor Airborne Mapping System for the U.S. Army Corps of Engineers*. Paper presented at the Algorithms and Technologies for Multispectral, Hyperspectral, and Ultraspectral Imagery XVI, Orlando, FL.

Twardowski, M. S., Boss, E., Macdonald, J. B., Pegau, W. S., Barnard, A. H., & Zaneveld, J. R. V. (2001). A model for estimating bulk refractive index from the optical backscattering ratio and the implications for understanding particle composition in case I and case II waters. *Journal of Geophysical Research-Oceans, 106*(C7), 14129-14142. doi:Doi 10.1029/2000jc000404

Tzortziou, M., Herman, J. R., Gallegos, C. L., Neale, P. J., Subramaniam, A., Harding Jr, L. W., & Ahmad, Z. (2006). Bio-optics of the Chesapeake Bay from measurements and radiative transfer closure. *Estuarine, Coastal and Shelf Science, 68*(1–2), 348-362. doi:http://dx.doi.org/10.1016/j.ecss.2006.02.016

Tzortziou, M., Subramaniam, A., Herman, J. R., Gallegos, C. L., Neale, P. J., & Harding Jr, L. W. (2007). Remote sensing reflectance and inherent optical properties in the

mid Chesapeake Bay. *Estuarine, Coastal and Shelf Science, 72*(1–2), 16-32. doi:http://dx.doi.org/10.1016/j.ecss.2006.09.018

Umar, M., Rhoads, B. L., & Greenberg, J. A. (2018). Use of multispectral satellite remote sensing to assess mixing of suspended sediment downstream of large river confluences. *Journal of Hydrology, 556*, 325-338. doi:https://doi.org/10.1016/j.jhydrol.2017.11.026

Unverricht, D., Nguyen, T. C., Heinrich, C., Szczuciński, W., Lahajnar, N., & Stattegger, K. (2014). Suspended sediment dynamics during the inter-monsoon season in the subaqueous Mekong Delta and adjacent shelf, southern Vietnam. *Journal of Asian Earth Sciences, 79, Part A*(0), 509-519. doi:http://dx.doi.org/10.1016/j.jseaes.2012.10.008

van Maren, D. S., Liew, S. C., & Hasan, G. M. J. (2014). The role of terrestrial sediment on turbidity near Singapore's coral reefs. *Continental Shelf Research, 76*(0), 75-88. doi:http://dx.doi.org/10.1016/j.csr.2013.12.001

van Weering, T. C. E., de Stigter, H. C., Boer, W., & de Haas, H. (2002). Recent sediment transport and accumulation on the NW Iberian margin. *Progress In Oceanography, 52*(2–4), 349-371. doi:http://dx.doi.org/10.1016/S0079-6611(02)00015-0

Vercruysse, K., Grabowski, R. C., & Rickson, R. J. (2017). Suspended sediment transport dynamics in rivers: Multi-scale drivers of temporal variation. *Earth-Science Reviews, 166*, 38-52. doi:http://dx.doi.org/10.1016/j.earscirev.2016.12.016

Volpe, V., Silvestri, S., & Marani, M. (2011). Remote sensing retrieval of suspended sediment concentration in shallow waters. *Remote Sensing of Environment, 115*(1), 44-54. doi:http://dx.doi.org/10.1016/j.rse.2010.07.013

Voss, K. J., & Austin, R. W. (1993). Beam-Attenuation Measurement Error Due to Small-Angle Scattering Acceptance. *Journal of Atmospheric and Oceanic Technology, 10*(1), 113-121. doi:10.1175/1520-0426(1993)010<0113:bamedt>2.0.co;2

Walsh, J. P., & Nittrouer, C. A. (1999). Observations of sediment flux to the Eel continental slope, northern California. *Marine Geology, 154*(1–4), 55-68. doi:http://dx.doi.org/10.1016/S0025-3227(98)00103-0

Wang, S., Chen, S., Qiu, Z., Sun, D., Zhang, H., Perrie, W., & Zhang, T. (2016). Variability in the backscattering efficiency of particles in the Bohai and Yellow Seas and related effects on optical properties. *Optics Express, 24*(26), 29360-29379. doi:10.1364/OE.24.029360

Wang, X. H., Pinardi, N., & Malacic, V. (2007). Sediment transport and resuspension due to combined motion of wave and current in the northern Adriatic Sea during a Bora event in January 2001: A numerical modelling study. *Continental Shelf Research, 27*(5), 613-633. doi:DOI: 10.1016/j.csr.2006.10.008

Weeks, A., & Simpson, J. H. (1991). The measurement of suspended particulate concentrations from remotely-sensed data. *International Journal of Remote Sensing, 12*(4), 725-737.

Weeks, A. R., Simpson, J. H., & Bowers, D. (1993). The relationship between concentrations of suspended particulate material and tidal processes in the Irish

Sea. *Continental Shelf Research, 13*(12), 1325-1334. doi:Doi: 10.1016/0278-4343(93)90086-d

Wegner, C., Hölemann, J. A., Dmitrenko, I., Kirillov, S., Tuschling, K., Abramova, E., & Kassens, H. (2003). Suspended particulate matter on the Laptev Sea shelf (Siberian Arctic) during ice-free conditions. *Estuarine, Coastal and Shelf Science, 57*(1-2), 55-64. doi:Doi: 10.1016/s0272-7714(02)00328-1

Wells, L. E., Cordray, M., Bowerman, S., Miller, L. A., Vincent, W. F., & Deming, J. W. (2006). Archaea in particle-rich waters of the Beaufort Shelf and Franklin Bay, Canadian Arctic: Clues to an allochthonous origin? *Limnol. Oceanogr., 5*(1), 47-59.

Wells, M. L. (2004). The colloidal size spectrum of CDOM in the coastal region of the Mississippi Plume using flow field-flow fractionation. *Marine Chemistry, 89*(1–4), 89-102. doi:http://dx.doi.org/10.1016/j.marchem.2004.02.009

Westberry, T. K., Dall?Olmo, G., Boss, E., Behrenfeld, M. J., & Moutin, T. (2010). Coherence of particulate beam attenuation and backscattering coefficients in diverse open ocean environments. *Optics Express, 18*(15), 15419-15425. doi:10.1364/oe.18.015419

WET_Labs. (2006). Spectral Scattering Meter, BB9, Specs (pp. 3): WET Labs, Inc.

WET_Labs. (2008a). *Absorption and Attenuation Meter, (ac-9): User's Guide*. Philomath, OR.

WET_Labs. (2008b, 10 July 2008). *Scattering Meter: ECO BB-9, User's Guide*. User's Guide. Philomath, OR.

WET_Labs. (2009). *Spectral Absorption and Attenuation Meter, ac-s: User's Guide*. Philomath, OR.

WET_Labs. (2010a). ECO 3-Measurement Sensor, (Triplet), User's Guide (pp. 29). Philomath, OR: WET_Labs.

WET_Labs. (2010b). Transmissometer, C-Star, Specs (pp. 1): WET Labs, Inc.

WET_Labs. (2010c). WET Labs Data Handler DH4 (pp. 1): Wet Labs Inc.

WET_Labs. (2011). *Transmissometer, C-Star, User's Guide*. Philomath, OR.

WET_Labs_Inc. (2011). Fluorometer, ECO FL (Y ed.).

Wild-Allen, K., Lane, A., & Tett, P. (2002). Phytoplankton, sediment and optical observations in Netherlands coastal water in spring. *Journal of Sea Research, 47*(3–4), 303-315. doi:http://dx.doi.org/10.1016/S1385-1101(02)00121-1

Wilson, A. M., Raine, R., Mohn, C., & White, M. (2015). Nepheloid layer distribution in the Whittard Canyon, NE Atlantic Margin. *Marine Geology, 367*, 130-142. doi:http://dx.doi.org/10.1016/j.margeo.2015.06.002

Wilson, R. E. (1979). A model for the estimation of the concentrations and spatial extent of suspended sediment plumes. *Estuarine and Coastal Marine Science, 9*(1), 65-78. doi:http://dx.doi.org/10.1016/0302-3524(79)90007-0

Wozencraft, J., & Millar, D. (2005). Airborne Lidar and Integrated Technologies for Coastal Mapping and Nautical Charting. *Marine Technology Society Journal, 39*(3), 27-35. doi:10.4031/002533205787442440

Wozencraft, J. M. (2010). *Requirements for the Coastal Zone Mapping and Imaging Lidar (CZMIL)*. Paper presented at the Algorithms and Technologies for Multispectral, Hyperspectral, and Ultraspectral Imagery XVI, Orlando, FL.

Woźniak, S. B., Darecki, M., Zabłocka, M., Burska, D., & Dera, J. (2016 in press). New simple statistical formulas for estimating surface concentrations of suspended particulate matter (SPM) and particulate organic carbon (POC) from remote-sensing reflectance in the southern Baltic Sea. *Oceanologia*. doi:http://dx.doi.org/10.1016/j.oceano.2016.03.002

Woźniak, S. B., Meler, J., Lednicka, B., Zdun, A., & Stoń-Egiert, J. (2011). Inherent optical properties of suspended particulate matter in the southern Baltic Sea*. *Oceanologia, 53*(3), 691-729. doi:http://dx.doi.org/10.5697/oc.53-3.691

Wu, G., Cui, L., Duan, H., Fei, T., & Liu, Y. (2011). Absorption and backscattering coefficients and their relations to water constituents of Poyang Lake, China. *Applied Optics, 50*(34), 6358-6368. doi:10.1364/ao.50.006358

Wynne, T. T., Stumpf, R. P., & Richardson, A. G. (2006). Discerning resuspended chlorophyll concentrations from ocean color satellite imagery. *Continental Shelf Research, 26*(20), 2583-2597. doi:http://dx.doi.org/10.1016/j.csr.2006.08.003

Xi, H., Larouche, P., Tang, S., & Michel, C. (2014). Characterization and variability of particle size distributions in Hudson Bay, Canada. *Journal of Geophysical Research: Oceans, 119*(6), 3392-3406. doi:10.1002/2013JC009542

Xing, X., Claustre, H., Uitz, J., Mignot, A., Poteau, A., & Wang, H. (2014). Seasonal variations of bio-optical properties and their interrelationships observed by Bio-Argo floats in the subpolar North Atlantic. *Journal of Geophysical Research: Oceans, 119*(10), 7372-7388. doi:10.1002/2014JC010189

Yurkovskis, A. (2005). Seasonal benthic nepheloid layer in the Gulf of Riga, Baltic Sea: Sources, structure and geochemical interactions. *Continental Shelf Research, 25*(18), 2182-2195. doi:DOI: 10.1016/j.csr.2005.08.020

Zaneveld, J. R. V. (1994). Optical Closure: From Theory to Measurement. In R. W. Spinard, K. L. Carder, & M. J. Perry (Eds.), *Ocean Optics* (pp. 59-72). New York: Oxford University Press.

Zege, E., Katsev, I., & Prikhach, A. (2007). *Retrieval of Seawater Inherent Optical Properties Profiles From Lidar Waveforms,*. Paper presented at the Current Research On Remote Sensing, Laser Probing, and Imagery in Natural Waters.

Zhao, X., Zaho, J., Zhang, H., & Zhou, F. (2018). Remote Sensing of Suspended Sediment Concentrations Based on the Waveform Decomposition of Airborne LiDAR Bathymetry. *Remote Sensing, 10*(2).

Zhu, W., Tian, Y. Q., Yu, Q., & Becker, B. L. (2013). Using Hyperion imagery to monitor the spatial and temporal distribution of colored dissolved organic matter in estuarine and coastal regions. *Remote Sensing of Environment, 134*, 342-354. doi:http://dx.doi.org/10.1016/j.rse.2013.03.009

Zhu, W., Yu, Q., & Tian, Y. Q. (2013). Uncertainty analysis of remote sensing of colored dissolved organic matter: Evaluations and comparisons for three rivers in North America. *ISPRS Journal of Photogrammetry & Remote Sensing, 84*, 12-22. doi:10.1016/j.isprsjprs.2013.07.005

Ziervogel, K., Dike, C., Asper, V., Montoya, J., Battles, J., D'souza, N., . . . Arnosti, C. (2016). Enhanced particle fluxes and heterotrophic bacterial activities in Gulf of Mexico bottom waters following storm-induced sediment resuspension. *Deep-Sea*

Research Part Ii-Topical Studies in Oceanography, 129, 77-88. doi:10.1016/j.dsr2.2015.06.017

Zoubir, A., & Iskander, D. R. (1998). Bootstrap Matlab Toolbox v.2.0: School of Electrical & Electronic Systems Engineering, Queensland University of Technology.